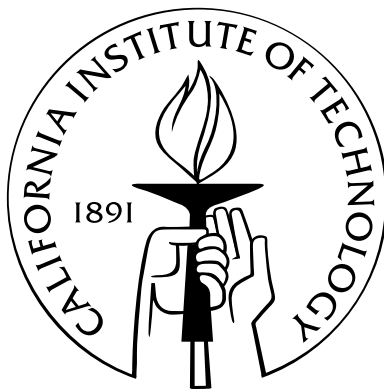


# Simulations of Compressible, Diffusive, Reactive Flows with Detailed Chemistry Using a High-Order Hybrid WENO-CD Scheme

Thesis by  
Jack L. Ziegler

In Partial Fulfillment of the Requirements  
for the Degree of  
Doctor of Philosophy



California Institute of Technology  
Pasadena, California

2012  
(Defended Nov 29, 2011)





# Acknowledgements

I would like to firstly thank my advisors Professors Pullin and Shepherd. Without their guidance, support, and patience, this thesis would not have been possible.

I would also like to thank everyone else that has worked with me and helped me learn about CFD and detonations/reactive flow research throughout my time at Caltech. Firstly, Dr. Shannon Kao helped me learn about gas dynamics, reactive flow, and taught me CANTERA. Dr. David Hill was the first to help me learn about numerical methods and CFD. I also worked with Dr. Ralf Deiterding at ORNL for one summer and owe much to him for learning how to program with AMROC and parallel computers in general. Ralf also continued to help me throughout the PhD process. Later, I collaborated with Dr. Sally Bane and Mr. Jason Damazo and was able to gain experience in learning how to model and compare to actual experiments. I also owe thanks to Professor Guillaume Blanquart, who helped me learn about and develop a reduced hydrocarbon mechanism.

I also thank the Oak Ridge National Lab (ORNL) Jaguar team and the Lawrence Berkeley National Lab (LBNL) NERSC supercomputing team. Lastly, I would like to thank the Department of Energy computational science graduate fellowship (DOE CSGF) for supporting this research.

# Abstract

A hybrid weighted essentially non-oscillatory (WENO)/centered-difference (CD) numerical method, with low numerical dissipation, high-order shock-capturing, and structured adaptive mesh refinement (SAMR), has been developed for the direct numerical simulation (DNS) of the multicomponent, compressive, reactive Navier-Stokes equations. The method enables accurate resolution of diffusive processes within reaction zones. This numerical method is verified with a series of one- and two-dimensional test problems, including a convergence test of a two-dimensional unsteady reactive double Mach reflection problem. Validation of the method is conducted with experimental comparisons of three applications all of which model multi-dimensional, unsteady reactive flow: an irregular propane detonation, shock and detonation bifurcations, and spark ignition deflagrations.

The numerical approach combines time-split reactive source terms with a high-order, shock-capturing scheme specifically designed for diffusive flows. A description of the order-optimized, symmetric, finite difference, flux-based, hybrid WENO / centered-difference scheme is given, along with its implementation in a high-order SAMR framework. The implementation of new techniques for discontinuity flagging, scheme-switching, and high-order prolongation and restriction is described. In particular, the refined methodology does not require upwinded WENO at grid refinement interfaces for stability, allowing high-order prolongation and thereby eliminating a significant source of numerical diffusion within the overall code performance.

A minimally reduced irregular detonation mixture mechanism (22 species and 53 reversible reactions) is developed and combined with the WENO-CD numerical method to accurately model two-dimensional hydrocarbon (propane) detonations with detailed chemistry and transport. First of its kind, resolved double Mach reflection (DMR) detonation simulations with a large hydrocarbon mixture are presented. Detailed discussions and comparisons of the influence of grid resolution, lower-order numerical methods, and inviscid approximations are made in addition to the detailed presentation of fluid dynamics found in an unsteady, highly unstable, reactive DMR

simulation. Also conducted are direct experimental comparisons to soot foils and schlieren images with an unresolved large-scale propane detonation channel simulation.

The numerical method is also applied to the DNS of two other problems, detonation/shock bifurcations and spark ignited deflagrations. Through the resolution of viscous/diffusive scales, new insights into how a bifurcated foot develops after a detonation end wall reflection, and how geometry can influence the development of a flame kernel after spark ignition are found.

# Contents

<b>Contents</b>	<b>vi</b>
<b>List of Figures</b>	<b>xiii</b>
<b>List of Tables</b>	<b>xxiv</b>
<b>1 Introduction</b>	<b>1</b>
1.1 Detonations . . . . .	2
1.1.1 Detonation Theory . . . . .	2
1.1.2 Detonation Shock-Bifurcation . . . . .	3
1.1.3 Detonation Stability . . . . .	5
1.1.4 Simulating Detonations . . . . .	7
1.1.5 Reduced Detonation Mechanisms . . . . .	8
1.1.6 Contemporary Research . . . . .	9
1.2 Spark Ignition . . . . .	10
1.2.1 Theory . . . . .	10
1.2.2 Experiment . . . . .	11
1.2.3 Simulation . . . . .	12
1.3 Overview . . . . .	12
<b>2 equations of Compressible, Diffusive, Reacting Flow</b>	<b>14</b>
2.1 Hyperbolic Systems . . . . .	14
2.2 Euler equations for Compressible Flow . . . . .	15
2.2.1 Inviscid, Adiabatic, One-Dimensional Similarity Flow . . . . .	15
2.2.2 Shock Reflections . . . . .	16
2.2.2.1 Self Similar Approximation . . . . .	18
2.3 Reactive Multi-Component Navier-Stokes equations . . . . .	18
2.3.1 Formulation . . . . .	19
2.3.2 Temperature Evaluation . . . . .	21

2.3.3	Navier-Stokes equations in Axisymmetric Form . . . . .	21
2.4	Shock-Driven Combustion . . . . .	22
2.4.1	Length Scales and Resolution . . . . .	22
2.5	Nondimensionalization . . . . .	23
2.5.1	Non-Reactive Navier-Stokes equations . . . . .	24
2.5.2	Reactive Navier-Stokes equations for Thermally Perfect Mixtures . . . . .	25
2.5.2.1	Navier-Stokes equations for Two Calorically Perfect Gases with One-Step Reaction . . . . .	25
2.6	Eigendecomposition . . . . .	26
<b>3</b>	<b>Numerical Methods</b>	<b>28</b>
3.1	Background on Methods . . . . .	28
3.2	Methods . . . . .	30
3.3	Roe-HLL MUSCL Second-Order Method . . . . .	30
3.4	Advancement to a high-Order Hybrid Scheme . . . . .	31
3.4.1	ENO and WENO Schemes for Conservation Laws . . . . .	32
3.4.1.1	WENO Reconstruction . . . . .	33
3.4.1.2	Characteristic Form . . . . .	34
3.4.2	Enhanced WENO Schemes . . . . .	35
3.4.2.1	WENO-SYM . . . . .	36
3.4.2.2	WENO/CD . . . . .	37
3.4.3	Stability . . . . .	38
3.4.4	Time Discretization . . . . .	40
3.5	SAMR Implementation . . . . .	41
3.5.1	Centered Differences in Flux-Based Form . . . . .	42
3.5.2	Diffusive-Flux Approximation . . . . .	43
3.5.3	Hybrid Method Boundary Flagging . . . . .	44
3.5.4	Higher-Order Accurate Hybrid Prolongation and Restriction . . . . .	46
3.5.5	Adaptive Mesh Refinement . . . . .	48
3.5.6	Multi-Component Chemistry Solver . . . . .	48
3.5.7	Accuracy of the Roe Linearization . . . . .	49
3.6	Stability Criterion . . . . .	50
3.6.1	Non-Reactive Explicit Stability Criterion . . . . .	51
3.6.2	Reactive Multicomponent Explicit Stability Criterion . . . . .	52

<b>4</b>	<b>Verification</b>	<b>53</b>
4.1	Preliminary Verification Study . . . . .	53
4.1.1	One-Dimensional Viscous Shock . . . . .	53
4.1.2	Mass Diffusion/Heat Diffusion Analogy . . . . .	55
4.1.3	Two-Species Laminar Flame Propagation . . . . .	55
4.1.3.1	One Dimension . . . . .	59
4.1.4	One-Dimensional Steady Laminar Flame with Multicomponent Detailed Chemistry . . . . .	61
4.1.4.1	Two Dimensions . . . . .	62
4.1.5	One-Dimensional Unsteady Detonation . . . . .	62
4.1.6	Two-Dimensional Manufactured and Decaying Lamb-Oseen Vor- tex . . . . .	66
4.2	Multi-Dimensional Unsteady Convergence Studies . . . . .	69
4.2.1	The Model Problem . . . . .	69
4.2.2	Initial and Boundary Conditions . . . . .	70
4.2.3	NonReactive Diffusive Double Mach Reflection . . . . .	71
4.2.3.1	Convergence Results . . . . .	74
4.2.4	Double Mach Reflection Detonation . . . . .	77
4.2.4.1	One-Step Chemistry . . . . .	80
4.2.4.2	Convergence Results . . . . .	84
4.2.4.3	Method Comparison . . . . .	86
4.2.5	<b>H<sub>2</sub>-O<sub>2</sub>-Ar</b> Multi-Component Chemistry . . . . .	86
<b>5</b>	<b>Irregular, Diffusive Detonations</b>	<b>92</b>
5.1	Background Research . . . . .	93
5.1.1	Recent Research on Unsteady Effects of Detonations . . . . .	93
5.1.2	Recent Research on Diffusive, Reactive Navier-Stokes . . . . .	95
5.2	Reactive Propane-Air Mechanism . . . . .	96
5.2.1	Reduced Chemistry . . . . .	96
5.2.1.1	Comparison to Detailed Chemistry . . . . .	97
5.2.1.2	Reduced Mechanism Chemistry . . . . .	103
5.3	One-Dimensional Unsteady Results . . . . .	106
5.4	Discussion . . . . .	110
<b>6</b>	<b>Irregular Detonation Double Mach Reflection</b>	<b>111</b>
6.1	Overview of Viscous and Inviscid DMR Simulations . . . . .	112

6.1.1	Pressure Psuedo-Color: 6-Levels, $\mathbf{x}_{\max} = 1$ cm . . . . .	113
6.1.2	Pressure Psuedo-Color: 3-Levels, $\mathbf{x}_{\max} = 8$ cm . . . . .	118
6.1.3	Radical Mass Fraction: 6-Levels, $\mathbf{x}_{\max} = 1$ cm . . . . .	126
6.1.4	Radical Mass Fraction: 5-Levels, $\mathbf{x}_{\max} = 2$ cm . . . . .	131
6.1.5	Radical Mass Fraction: 4-Levels, $\mathbf{x}_{\max} = 4$ cm . . . . .	135
6.1.6	Radical Mass Fraction: 3-Levels, $\mathbf{x}_{\max} = 3$ cm . . . . .	138
6.2	Resolution Comparison . . . . .	145
6.3	MUSCL Comparison . . . . .	145
6.4	Diffusive, Detonation DMR Structural Details . . . . .	150
6.4.1	Velocity Vector Visualizations . . . . .	168
6.5	Detialed Inviscid/Viscous Comparison . . . . .	174
6.5.1	Product Traces . . . . .	179
6.6	Soot Foil Length Scales . . . . .	194
6.6.1	Small-Scale DMR Comparisons . . . . .	195
6.7	Discussion . . . . .	201
<b>7</b>	<b>Irregular Detonation Cell Structure</b>	<b>202</b>
7.1	Thin Channel, Lab Frame Results . . . . .	203
7.1.1	Two Levels, Unresolved . . . . .	203
7.1.2	Four Levels, Marginally Resolved . . . . .	205
7.2	Wide Channel, CJ Frame Results . . . . .	210
7.3	Dominant Cell Size Comparison . . . . .	216
7.3.1	Eight cm Channel Width . . . . .	216
7.3.2	Sixteen cm Channel Width . . . . .	219
7.3.3	Chemiluminescence Comparison . . . . .	230
7.3.4	Statistical Analysis . . . . .	231
7.4	Discussion . . . . .	234
<b>8</b>	<b>Detonation Shock Bifurcation</b>	<b>235</b>
8.1	Motivation . . . . .	235
8.2	Ideal Detonation Reflection Model . . . . .	236
8.3	Experimental Setup . . . . .	237
8.4	Experimental Results . . . . .	238
8.5	Reflected Shock Wave-Boundary Layer Interaction . . . . .	239
8.6	Computational Results: Simple Two-Component . . . . .	240

8.7	Computational Results: Detonation and Shock Bifurcation with Detailed Chemistry and Transport . . . . .	244
8.7.1	Schlieren vs. Multi-Component Simulation Comparisons . . . . .	245
8.7.2	Temperature and Pressure Results: Large-Scale Bifurcations . . . . .	247
8.7.3	Resolved Small-Scale Bifurcations . . . . .	256
8.7.3.1	Air: Isothermal BC . . . . .	256
8.7.3.2	Air: Adiabatic BC . . . . .	263
8.7.3.3	N <sub>2</sub> O: Isothermal BC . . . . .	267
8.7.3.4	N <sub>2</sub> O: Adiabatic BC . . . . .	273
8.7.3.5	H <sub>2</sub> -N <sub>2</sub> O: Adiabatic BC . . . . .	276
8.7.3.6	Specific Heat Ratio . . . . .	283
8.7.4	Foot Geometry . . . . .	284
8.7.4.1	Bifurcation Shock Geometry . . . . .	287
8.7.4.2	Bifurcation H <sub>2</sub> -N <sub>2</sub> O Detonation Geometry . . . . .	294
8.7.5	Pressure Traces . . . . .	296
8.7.5.1	Air . . . . .	297
8.7.5.2	N <sub>2</sub> O . . . . .	300
8.7.5.3	H <sub>2</sub> -N <sub>2</sub> O . . . . .	303
8.7.5.4	Pressure Trace Discussion . . . . .	303
8.8	Discussion . . . . .	304
<b>9</b>	<b>Spark-Ignited Deflagrations</b>	<b>307</b>
9.1	Motivation . . . . .	307
9.2	Simulation Overview . . . . .	309
9.2.1	Approximating a Spark . . . . .	309
9.3	Single-Component Nonreactive Model Problem . . . . .	310
9.3.1	Initial and Boundary Conditions . . . . .	310
9.3.2	Single-Component Nonreactive Results . . . . .	312
9.4	Two-Component Model . . . . .	316
9.5	Four-Species One-Step Model with Constant Transport Properties . . . . .	320
9.5.1	Nonreactive Results . . . . .	321
9.5.2	Reactive Results . . . . .	327
9.6	Multi-Step Reduced Detailed Chemistry Model . . . . .	330
9.6.1	Initial Conditions . . . . .	331
9.6.2	Experimental Comparison: 2 mJ Case . . . . .	331
9.6.2.1	Simulations Details . . . . .	332



9.6.3	Critical Energy Results . . . . .	341
9.6.3.1	One-Dimensional Axisymmetric Case . . . . .	341
9.6.3.2	Two-Dimensional Axisymmetric Cone Case . . . . .	346
9.6.3.3	MIE Experimental Comparison . . . . .	362
9.6.3.4	MIE Analytical Comparison . . . . .	363
9.7	Discussion . . . . .	365
<b>10</b>	<b>Conclusions</b>	<b>366</b>
10.1	Development and Verification of the 6th-Order Hybrid WENO-CD Method for the Multi-Component Reactive Navier-Stokes Equations .	366
10.2	Reduced, Detailed Mechanism Development for the Simulation of a Highly Irregular, Hydrocarbon Detonation . . . . .	368
10.3	Resolved Multi-Component Irregular Detonation Double Mach Reflection	368
10.4	Validation Through Comparisons to Thin Channel Detonation Exper- iments . . . . .	369
10.5	Contribution to Detonation and Shock Bifurcations . . . . .	370
10.6	Contribution to Spark Ignition . . . . .	372
10.7	Future Work and Outlook . . . . .	373
<b>A</b>	<b>Similarity Solution of the One-Dimensional Euler equations</b>	<b>375</b>
<b>B</b>	<b>Shock Reflection Theory</b>	<b>380</b>
B.1	Shock Reflection Background Research . . . . .	380
B.1.1	Relaxation Effects Relevant to Detonations . . . . .	381
B.2	Steady Reflection . . . . .	382
B.3	Unsteady Reflection . . . . .	383
B.3.1	Regular Reflection . . . . .	384
B.3.2	Irregular Reflection . . . . .	384
B.3.3	Single Mach Reflection . . . . .	385
B.3.4	Unsteady Transition Criterion . . . . .	386
B.3.5	Oblique Shock Relations . . . . .	388
B.3.5.1	Shock Polars . . . . .	391
B.3.6	Regular Reflection . . . . .	391
B.3.7	Mach Reflection . . . . .	396
B.3.8	Von Neumann Reflection . . . . .	398
B.3.9	Steady Transition Criterion . . . . .	398

<b>C</b>	<b>Mach Reflection Solution Algorithms</b>	<b>400</b>
C.1	Perfect Gas Algorithm . . . . .	400
C.2	Real Gas Algorithm . . . . .	403
C.3	Law and Glass Algorithm . . . . .	407
C.3.1	Perfect Gas Case . . . . .	408
C.3.2	Real Gas Case . . . . .	411
C.3.3	Comparison of Results with Ben-Dor and Glass . . . . .	417
<b>D</b>	<b>Viscous Flow Physics</b>	<b>419</b>
D.1	Blasius Solution . . . . .	419
D.2	Von Karman Momentum-Integral Technique . . . . .	421
D.3	Inviscid Mixing Layer Linear Stability . . . . .	423
<b>E</b>	<b>Reduced CHEMKIN Mechanisms</b>	<b>426</b>
E.1	Reduced Propane-Air Mechanism . . . . .	426
E.1.1	Chemistry . . . . .	426
E.1.2	Thermodynamics . . . . .	428
E.1.3	Transport . . . . .	429
E.2	Reduced Hydrogen-N <sub>2</sub> O Mechanism . . . . .	430
E.2.1	Chemistry . . . . .	430
E.2.2	Thermodynamics . . . . .	431
E.2.3	Transport . . . . .	432
E.3	Reduced Hydrogen-Air Mechanism . . . . .	432
E.3.1	Chemistry . . . . .	432
E.3.2	Thermodynamics . . . . .	433
E.3.3	Transport . . . . .	434
	<b>Bibliography</b>	<b>436</b>

# List of Figures

1.1	Detonation propagation in tube with a closed end. . . . .	3
1.2	(a) Space-time diagram of an ideal detonation and Taylor wave. (b) Spatial pressure distributions for several times after detonation initiation and prior to reflection. Reprinted from Damazo and Ziegler <i>et al.</i> (35). . . . .	4
1.3	Categorization of the stability of detonations in relation to the longitudinal neutral stability boundary (Shepherd 2008) . . . . .	5
1.4	Diagram of shock waves and triple points in a multi-dimensional detonation (Shepherd 2009). . . . .	6
1.5	Schlieren and PLIF images OH reaction detonation structures $2\text{H}_2\text{-O}_2\text{-12Ar}$ , $P_1 = 20$ kPa (Austin <i>et al.</i> 2005). . . . .	9
1.6	Schlieren and PLIF images OH reaction detonation structures $\text{C}_2\text{H}_4\text{-3O}_2\text{-10.5N}_2$ (Austin <i>et al.</i> 2005). . . . .	9
1.7	Schlieren image of a deflagration wave from spark ignition propagating in a 10 percent hydrogen, 11.37 percent oxygen, 78.63 percent argon mixture in a closed vessel. Reprinted from Bane and Ziegler <i>et al.</i> (10). . . . .	11
2.1	Example shock reflections . . . . .	17
2.2	Velocity vectors in the triple point reference frame, DMR case . . . . .	18
3.1	Set of candidate stencils for two different finite difference WENO methods using flux splitting. . . . .	35
3.2	Shock detection applied to the viscous double Mach reflection problem of §4.2.3. . . .	45
3.3	Fifth-order accurate stencils used by the hybrid-order prolongation and restriction. . .	47
3.4	AMR for the density of a fully resolved viscous jet with AMROC . . . . .	48
4.1	Analytical and numerical solution for the one-dimensional steady shock wave (visually no difference). . . . .	54
4.2	Multicomponent laminar flame with detailed transport. Comparison is with the steady solution of CANTERA. . . . .	55
4.3	Verification of product/reactant mass diffusion with comparison to the heat equation. .	56
4.4	Particle speeds of reactants and products in a steady laminar flame . . . . .	57
4.5	CANTERA and AMROC comparison for the 1D laminar flame . . . . .	58
4.6	Comparing the Transport Properties to CANTERA's results for $T = 300$ to $2500$ K . .	61
4.7	Preliminary unresolved axisymmetric laminar flame results . . . . .	63

4.8	Maximum shock pressure versus time. . . . .	64
4.9	Convergence of the maximum pressure peak of $\sim 99$ for the WENO/CD, WENO, and MUSCL methods. . . . .	65
4.10	One-dimensional inviscid exact solution for the manufactured Lamb-Oseen vortex problem. . . . .	66
4.11	Convergence plot (log-log scale) for the manufactured Lamb-Oseen vortex solution (a) and the viscous decaying vortex (b). . . . .	67
4.12	The model problem of two interacting planar shock waves . . . . .	70
4.13	Boundary conditions for the reactive double Mach reflection problem. . . . .	70
4.14	Vorticity in the mixing layer and the laminar mixing layer thickness as a function of distance from the triple point, Von Karman momentum-integral technique. . . . .	74
4.15	SAMR levels for the DMR convergence test. . . . .	76
4.16	Comparing the initial conditions and transport properties of the one-step two-species with the detailed chemistry case. . . . .	78
4.17	Temperature (K) pseudo-color plot for ZND initial condition with one-step chemistry. . . . .	80
4.18	Pseudo-color plots for a fully-resolved marginally stable detonation with one-step chemistry. . . . .	81
4.19	SAMR levels and WENO usage for the 8-level reactive DMR convergence test. . . . .	81
4.20	DMR density pseudo-color results with detailed chemistry and transport of an $\text{H}_2\text{-O}_2\text{-Ar}$ detonation. . . . .	87
5.1	Detonation induction time comparisons for propane: comparing experimental vs. detailed (22, 21) and reduced mechanisms. The ambient conditions corresponds to $T = 300$ K, $P = 20$ kPa. . . . .	99
5.2	Comparing reduced and detailed mechanism (Blanquart) (22, 21) ZND solutions at different overdrives. . . . .	100
5.3	Comparing specific heats ( $\gamma$ ), Mach number, temperature, and velocities of the reduced (blue) and detailed (red) mechanisms at overdrives of 1.4, 1.0, and 0.8. . . . .	101
5.4	Comparing density, thermicity, molecular weights, and temperature gradients of the reduced (blue) and detailed (red) mechanisms at overdrives of 1.4, 1.0, and 0.8. . . . .	102
5.5	Mole fractions as a function of distance for each species for the reduced mechanism at an overdrive of 1.0 (CJ speed). . . . .	103
5.6	Zoomed in view of the mole fractions as a function of distance for each species for the reduced mechanism at an overdrive of 1.0 (CJ speed). . . . .	104
5.7	Highly zoomed in view of the mole fractions as a function of distance for each species for the reduced mechanism at an overdrive of 1.0 (CJ speed). . . . .	105
5.8	Zoomed in view of the mole fractions of $\text{C}_3\text{H}_7$ and $\text{C}_2\text{H}_5$ as a function of distance for each species for the reduced mechanism at an overdrive of 1.0 (CJ speed). . . . .	105
5.9	Time elapsed nondimensional pressure and temperature for the 1D inviscid case. . . . .	107
5.10	Time elapsed nondimensional pressure for the 1D inviscid case. . . . .	108
5.11	Non-dimensional pressure temperature for the 1D viscous (solid black) and inviscid (dotted red) cases at a time $t = 1.08597 \cdot 10^{-4}$ seconds. . . . .	109
6.1	Pseudo-color pressure plot, 6-levels. . . . .	114

6.2	Pseudo-color pressure plot, 6-levels. . . . .	115
6.3	Pseudo-color pressure plot, 6-levels. . . . .	116
6.4	Pseudo-color pressure plot, 6-levels. . . . .	117
6.5	Incident shock pressure for the inviscid case. . . . .	118
6.6	Pseudo-color plot of the pressure (Pa), 3-levels. . . . .	120
6.7	Pseudo-color plot of the pressure (Pa), 3-levels. . . . .	121
6.8	Pseudo-color plot of the pressure (Pa), 3-levels. . . . .	122
6.9	Pseudo-color plot of the pressure (Pa), 3-levels. . . . .	123
6.10	Pseudo-color plot of the pressure (Pa), 3-levels. . . . .	124
6.11	Pseudo-color plot of the pressure (Pa), 3-levels. . . . .	125
6.12	Pseudo-color plot of the OH radical mass fraction, 6-levels. . . . .	127
6.13	Pseudo-color plot of the OH radical mass fraction, 6-levels. . . . .	128
6.14	Pseudo-color plot of the OH radical mass fraction, 6-levels. . . . .	129
6.15	Pseudo-color plot of the OH radical mass fraction, 6-levels. . . . .	130
6.16	Pseudo-color plot of the O radical mass fraction, 5-levels. . . . .	132
6.17	Pseudo-color plot of the O radical mass fraction, 5-levels. . . . .	133
6.18	Pseudo-color plot of the O radical mass fraction, 5-levels. . . . .	134
6.19	Pseudo-color plot of the O radical mass fraction, 4-levels. . . . .	136
6.20	Pseudo-color plot of the O radical mass fraction, 4-levels. . . . .	137
6.21	Pseudo-color plot of the OH radical mass fraction, 3-levels. . . . .	139
6.22	Pseudo-color plot of the OH radical mass fraction, 3-levels. . . . .	140
6.23	Pseudo-color plot of the OH radical mass fraction, 3-levels. . . . .	141
6.24	Pseudo-color plot of the OH radical mass fraction, 3-levels. . . . .	142
6.25	Pseudo-color plot of the OH radical mass fraction, 3-levels. . . . .	143
6.26	Pseudo-color plot of the OH radical mass fraction, 3-levels. . . . .	144
6.27	Inviscid solutions at a time of $96 \text{ nondim} = 2.90 \cdot 10^{-6} \text{ s}$ . . . . .	146
6.28	Viscous/diffusive solutions at a time of $96 \text{ nondim} = 2.90 \cdot 10^{-6} \text{ s}$ . . . . .	147
6.29	Comparing inviscid CLAWPACK (MUSCL) results to inviscid and viscous/diffusive WENO-CD results. . . . .	148
6.30	Comparing A) inviscid CLAWPACK (MUSCL) O mass fraction results to B) inviscid and C) viscous/diffusive WENO-CD results. . . . .	149
6.31	The interaction of the jet from the shear layer forms a triple point on the Mach Stem shortly after reflection. . . . .	151
6.32	Instabilities of the chemical reactions first appearing in the reflected shock. . . . .	152
6.33	More reflected shocks have appeared within the DMR. . . . .	152
6.34	Showing diffusive results for A) pressure (Pa), B) zoomed in pressure view, C) OH mass fraction, and D) $\text{C}_3\text{H}_8$ mass fraction. . . . .	153
6.35	Showing diffusive results for A) pressure (Pa), B) temperature (K), and C) and D) OH mass fraction. . . . .	154
6.36	Showing diffusive results for A) temperature (K) and B) OH mass fraction. . . . .	155
6.37	Showing diffusive results for A) Pressure (Pa) and B) OH mass fraction. . . . .	156
6.38	Showing diffusive results for A) pressure (Pa), B) temperature (K), C) OH mass fraction, and D) $\text{C}_3\text{H}_8$ mass fraction. . . . .	158

6.39	Showing diffusive results for A) pressure (Pa), B) temperature (K), C) OH mass fraction, and D) nondimensional y-component velocity. . . . .	159
6.40	Showing diffusive results for A) pressure (Pa), B) temperature (K), C) OH mass fraction, and D) nondimensional y-component velocity. . . . .	160
6.41	At a time of $t = 504 \text{ nondim} = 1.52 \cdot 10^{-5}$ seconds, the incident shock/detonation has gone unstable. . . . .	161
6.42	Showing diffusive results for the H mass fraction at subsequent time values of A) $t = 1.52 \cdot 10^{-5}$ sec, B) $1.59 \cdot 10^{-5}$ sec, C) $1.66 \cdot 10^{-5}$ sec, and D) $1.73 \cdot 10^{-5}$ s. . . . .	163
6.43	Showing diffusive results for pressure at subsequent time values, which correspond to the times in figure 6.42. . . . .	164
6.44	Shown is a comparison of the failure of the detonation for the 1D case in a) and an acceleration of the detonation for the 2D case in b). . . . .	165
6.45	Showing diffusive results for the OH mass fraction at a time of $t = 792 \text{ nondim} = 2.39 \cdot 10^{-5}$ s. . . . .	166
6.46	Showing zoomed in views of the development of the keystone like structure created when the incident shock accelerates into the Mach stem. . . . .	167
6.47	Showing velocity vectors superimposed on pressure pseudo-color plots at subsequent time values for the highest resolved 6-level case. . . . .	169
6.48	Showing velocity vectors superimposed on pressure pseudo-color plots ( A, B, and C ) at subsequent time values for the highest resolved 6-level case. . . . .	170
6.49	Showing velocity vectors superimposed on a psuedo-color plot of the $\text{H}_2\text{O}$ mass fraction at the final time of $t = 2.39 \cdot 10^{-5}$ s. . . . .	171
6.50	Showing velocity vectors superimposed on a psuedo-color plot of the H mass fraction at the final time of $t = 2.39 \cdot 10^{-5}$ s. . . . .	172
6.51	Showing velocity vectors superimposed on a psuedo-color plot of the pressure at the final time of $t = 2.39 \cdot 10^{-5}$ s. . . . .	173
6.52	Comparing inviscid (left side) and viscous (right side) solutions of the DMR problem at a time of $t = 36 \text{ nondim} = 1.09 \cdot 10^{-6}$ s. . . . .	176
6.53	Inviscid results of A) pressure (Pa), B) temperature (K), C) O mass fraction, and D) $\text{C}_3\text{H}_8$ mass fraction at the same time step. . . . .	177
6.54	Inviscid results of A) pressure (Pa), B) temperature (K), C) O mass fraction, and D) y-component of the nondimensional velocity at the same time step. . . . .	178
6.55	Key showing traces used without output from the case shown in figure 6.15 is used. . . . .	179
6.56	$\text{H}_2\text{O}$ mass fraction traces starting at $(x,y) = (0,0.05)$ and going to $(0.975,0.05)$ cm. . . . .	180
6.57	$\text{H}_2\text{O}$ mass fraction traces starting at $(x,y) = (0,0.1)$ and going to $(0.975,0.1)$ cm. . . . .	181
6.58	$\text{H}_2\text{O}$ mass fraction traces starting at $(x,y) = (0,0.15)$ and going to $(0.975,0.15)$ cm. . . . .	182
6.59	$\text{H}_2\text{O}$ mass fraction traces starting at $(x,y) = (0.2,0)$ and going to $(0.2,0.32)$ cm. . . . .	183
6.60	$\text{H}_2\text{O}$ mass fraction traces starting at $(x,y) = (0.4,0)$ and going to $(0.4,0.32)$ cm. . . . .	184
6.61	$\text{H}_2\text{O}$ mass fraction traces starting at $(x,y) = (0.6,0)$ and going to $(0.6,0.32)$ cm. . . . .	185
6.62	$\text{H}_2\text{O}$ mass fraction traces starting at $(x,y) = (0.8,0)$ and going to $(0.8,0.32)$ cm. . . . .	185
6.63	$\text{H}_2\text{O}$ mass fraction traces starting at $(x,y) = (0.9,0)$ and going to $(0.9,0.32)$ cm. . . . .	186
6.64	$\text{H}_2\text{O}$ mass fraction traces starting at $(x,y) = (0.58683,0.232936)$ and going to $(0.789084,0.15026)$ cm. . . . .	187

6.65	H <sub>2</sub> O mass fraction traces starting at (x,y) = (0.58683,0.232936) and going to (0.789084,0.15026) cm. . . . .	188
6.66	H <sub>2</sub> O mass fraction traces starting at (x,y) = (0.73852,0.18615) and going to (0.651474,0.288406) cm. . . . .	189
6.67	H <sub>2</sub> O mass fraction traces starting at (x,y) = (0.73852,0.18615) and going to (0.651474,0.288406) cm. . . . .	190
6.68	Key showing traces used with output from the 5-level case shown in figure 6.18 . . . .	191
6.69	H <sub>2</sub> O mass fraction traces starting at (x,y) = (1.3,0) and going to (1.3,0.4) cm. . . . .	192
6.70	H <sub>2</sub> O mass fraction traces starting at (x,y) = (1.3,0) and going to (1.3,0.4) cm. . . . .	192
6.71	H <sub>2</sub> O mass fraction traces starting at (x,y) = (1.3,0) and going to (1.75,0.22) cm. . . .	193
6.72	H <sub>2</sub> O mass fraction traces starting at (x,y) = (1.75,0) and going to (1.75,0.22) cm for MUSCL with 5-levels. . . . .	193
6.73	Soot foil in propane detonation mixture, C <sub>3</sub> H <sub>8</sub> -5O <sub>2</sub> -9N <sub>2</sub> 20 kPa. . . . .	194
6.74	Pseudo-color pressure plot at t=2.39·10 <sup>-5</sup> seconds showing the trace used to estimate a small-scale cell size for the simulated incident wave. . . . .	196
6.75	Pressure trace through the incident wave as shown in figure 6.74. . . . .	196
6.76	Pseudo-color pressure plot at t=2.39·10 <sup>-5</sup> seconds showing the trace used to estimate a small-scale cell size for the simulated “Mach stem” wave. . . . .	197
6.77	Pressure trace through the “Mach stem” wave as shown in figure 6.76. . . . .	197
6.78	Induction time and estimation of substructure cell width . . . . .	198
6.79	Time-resolved shadowgraph images of a detonation propagating in C <sub>3</sub> H <sub>8</sub> -5O <sub>2</sub> -9N <sub>2</sub> in the narrow channel. Time between frames is 1.6 micros. Field of view is about 138 mm. Reprinted from Austin <i>et al.</i> (7). . . . .	199
6.80	Image of a detonation propagating in C <sub>3</sub> H <sub>8</sub> -5O <sub>2</sub> -9N <sub>2</sub> . . . . .	199
6.81	Image of a dominate scale incident shock/Mach stem combination compared to the 3-level simulation result. The schlieren image is from figure 6.80. . . . .	200
7.1	Pressure (kPa) trace key at y=0.5 cm. . . . .	203
7.2	Pressure (kPa) traces at y=0.5 cm. . . . .	204
7.3	Temperature (K) trace key at y=0.5 cm. . . . .	204
7.4	Temperature (K) traces at y=0.5 cm. . . . .	205
7.5	Non-dimensional temperature trace key at y=0.5 cm. . . . .	206
7.6	Non-dimensional temperature traces at y=0.5 cm. . . . .	207
7.7	Non-dimensional pressure traces at y=0.5 cm. . . . .	207
7.8	Non-dimensional pressure trace key at y=0.5 cm. . . . .	208
7.9	Pressure traces at y=0.5 cm. . . . .	209
7.10	Non-dimensional temperature traces at y=0.5 cm. . . . .	209
7.11	Psuedo-color pressure(Pa) and temperature(K) results, showing transition from a steady ZND wave to an unsteady overdriven detonation. 3-levels with $\Delta x_{min} = 1.04167 \cdot 10^{-5}$ m. . . . .	212
7.12	Psuedo-color pressure(Pa) and temperature(K) results, showing transition from a steady ZND wave to an unsteady overdriven detonation. . . . .	213

7.13	Psuedo-color pressure(Pa) and temperature(K) results, showing transition from a steady ZND wave to an unsteady overdriven detonation. . . . .	214
7.14	Psuedo-color pressure(Pa) and temperature(K) results, showing transition from a steady ZND wave to an unsteady overdriven detonation. . . . .	215
7.15	Triple point count during the transition from steady ZND to unsteady detonation cells.	217
7.16	8 cm channel triple point count. . . . .	217
7.17	Soot foil (15 cm wide) in the propane detonation mixture, $C_3H_8-5O_2-9N_2$ . . . . .	218
7.18	8 cm periodic channel triple point tracks from $t = 4896$ (nondim) = $1.47692357 \cdot 10^{-4}$ sec to $t = 7488$ (nondim) = $2.25882428 \cdot 10^{-4}$ sec. . . . .	218
7.19	Soot foil (15 cm wide) in the propane detonation mixture. . . . .	219
7.20	16 cm periodic channel triple point tracks for the last 25 output steps. . . . .	219
7.21	16 cm channel triple point count for the last 35 output steps. . . . .	220
7.22	Psuedo-color nondimensional pressure results starting at $t = 6984$ (nondim). . . . .	221
7.23	Psuedo-color nondimensional pressure results starting at $t = 7848$ (nondim). . . . .	222
7.24	Psuedo-color $H_2O$ mass fraction results starting at $t = 6984$ (nondim). . . . .	223
7.25	Psuedo-color $H_2O$ mass fraction results starting at $t = 7848$ (nondim). . . . .	224
7.26	Psuedo-color OH mass fraction results starting at $t = 6984$ (nondim). . . . .	225
7.27	Psuedo-color OH mass fraction results starting at $t = 7848$ (nondim). . . . .	226
7.28	Psuedo-color nondimensional temperature results starting at $t = 6984$ (nondim). . . . .	227
7.29	Psuedo-color nondimensional temperature results starting at $t = 7848$ (nondim). . . . .	228
7.30	Psuedo-color OH mass fraction, pressure, and temperature. Five detonation cell regions are labeled. . . . .	229
7.31	Psuedo-color OH mass fraction, pressure, and temperature. Four detonation cell regions are labeled. . . . .	229
7.32	OH chemiluminescence images in figure 7.32 found in experiment by Austin (6). . . . .	230
7.33	Comparing OH radical mass fraction results to the OH chemiluminescence images in figure 7.32 found in experiment by Austin (6). . . . .	231
7.34	Nondimensional pressures along the $y = 0$ , $x = [-6000, 3000] \cdot 10^{-3}$ cm cut for the last 18 output steps in the 16 cm wide detonation channel simulation. . . . .	232
7.35	Distribution of all pressures, $y = -8$ cm. . . . .	232
7.36	Distribution of all pressures, $y = 0$ cm. . . . .	233
8.1	Pressure data compared to model results using two different end-wall pressure histories.	238
8.2	Schematic of flow for bifurcated shock wave. Reprinted from Damazo and Ziegler <i>et al.</i> (35). . . . .	240
8.3	Comparison of the approximate pressure model, $P_R(x)$ to the 1D reactive Euler simulation of the TZ wave. . . . .	242
8.4	2D reflected detonation: Density, pressure, and vorticity pseudo-color plots. . . . .	243
8.5	Pressure traces at the heights of 0, 1, 10, and 30 mm from the wall $2.56 \cdot 10^{-5}$ s after reflection. . . . .	244
8.6	Air at 25 kPa. Mach number is 2.2. a) is a schlieren image. b) (isothermal BC) and c) (adiabatic BC) is a pseudo-color plot of the nondimensional density. . . . .	248



8.7	N <sub>2</sub> O at 15 kPa. Mach number is 2.7. a) is a schlieren image. b) (isothermal BC) and c) (adiabatic BC) is a pseudo-color plot of the nondimensional density. . . . .	249
8.8	9:H <sub>2</sub> , 1:N <sub>2</sub> O by mole fraction at 15 kPa. Figure a) is the experimental result. figure b) is a pseudo-color plot of the nondimensional density. . . . .	250
8.9	Adiabatic case: Air at 25 kPa with Mach number 2.2. . . . .	251
8.10	Isothermal case: Air at 25 kPa with Mach number 2.2. . . . .	252
8.11	Adiabatic case: N <sub>2</sub> O at 15 kPa. . . . .	253
8.12	Isothermal case: N <sub>2</sub> O at 15 kPa. . . . .	254
8.13	9:H <sub>2</sub> , 1:N <sub>2</sub> O by mole fraction at 15 kPa. . . . .	255
8.14	Air, isothermal BC case: Incident shock boundary layer. . . . .	257
8.15	Air, isothermal BC case: Incident shock boundary layer traces. . . . .	258
8.16	Isothermal BC case: Velocity vectors superimposed on pseudo-color plots of various quantities for the air shock-bifurcation case with detailed chemistry and transport. . .	259
8.17	Isothermal BC case: Velocity vectors superimposed on pseudo-color plots of various quantities for the air shock-bifurcation case with detailed chemistry and transport. . .	260
8.18	Isothermal BC case: Velocity vectors superimposed on pseudo-color plots of various quantities. . . . .	261
8.19	Isothermal BC case: Velocity vectors superimposed on pseudo-color plots of various quantities. . . . .	262
8.20	Adiabatic BC case: Velocity vectors superimposed on pseudo-color plots of pressure (Pa) and temperature (K) for the air shock-bifurcation case with detailed chemistry and transport. . . . .	263
8.21	Adiabatic BC case: Velocity vectors superimposed on pseudo-color plots of various quantities. . . . .	265
8.22	Adiabatic BC case: Velocity vectors superimposed on pseudo-color plots of various quantities. . . . .	266
8.23	Isothermal BC case: Velocity vectors superimposed on pseudo-color plots of various quantities for the N <sub>2</sub> O shock-bifurcation case with detailed chemistry and transport. .	268
8.24	Isothermal BC case: Velocity vectors superimposed on pseudo-color plots of various quantities. . . . .	269
8.25	Isothermal BC case: Velocity vectors superimposed on pseudo-color plots of various quantities. . . . .	270
8.26	Isothermal BC case: Velocity vectors superimposed on pseudo-color plots of various quantities. . . . .	271
8.27	Isothermal BC case: Velocity vectors superimposed on pseudo-color plots of various quantities. . . . .	272
8.28	Adiabatic BC case: Velocity vectors superimposed on pseudo-color plots of various quantities for the N <sub>2</sub> O shock-bifurcation case with detailed chemistry and transport. .	273
8.29	Adiabatic BC case: Velocity vectors superimposed on pseudo-color plots of various quantities. . . . .	274
8.30	Adiabatic BC case: Velocity vectors superimposed on pseudo-color plots of various quantities. . . . .	275
8.31	Velocity vectors superimposed on a pseudo-color plot of H <sub>2</sub> O mass fraction. . . . .	276

8.32	Velocity vectors superimposed on pseudo-color plots of various quantities for the detonation shock-bifurcation case. . . . .	278
8.33	Velocity vectors superimposed on pseudo-color plots of various quantities for the detonation shock-bifurcation case. . . . .	279
8.34	Velocity vectors superimposed on pseudo-color plots of various quantities for the detonation shock-bifurcation case. . . . .	280
8.35	Velocity vectors superimposed on pseudo-color plots of various quantities for the detonation shock-bifurcation case. . . . .	281
8.36	Velocity vectors superimposed on pseudo-color plots of various quantities for the detonation shock-bifurcation case. . . . .	282
8.37	Specific heat, $\gamma$ A) isothermal wall case, B) adiabatic wall case. . . . .	283
8.38	Schematic of the flow field after shock reflection from the tube end, in the reference frame of the reflected shock's triple point. . . . .	284
8.39	Air: isothermal wall results. . . . .	290
8.40	Air: adiabatic wall results. . . . .	291
8.41	N <sub>2</sub> O: isothermal wall results. . . . .	292
8.42	N <sub>2</sub> O: adiabatic wall results. . . . .	293
8.43	H <sub>2</sub> -N <sub>2</sub> O: adiabatic wall results. . . . .	295
8.44	Air: Pressure (MPa) traces. . . . .	297
8.45	Air: Pressure (MPa) traces. . . . .	298
8.46	Air: $y = 0.5$ cm pressure (MPa) trace. . . . .	299
8.47	N <sub>2</sub> O: Pressure (KPa) traces. . . . .	300
8.48	N <sub>2</sub> O: Pressure (KPa) traces. . . . .	301
8.49	$y = 1.5$ cm pressure (kPa) trace. . . . .	302
8.50	H <sub>2</sub> -N <sub>2</sub> O: Pressure (MPa) traces. . . . .	303
8.51	H <sub>2</sub> -N <sub>2</sub> O: Pressure (MPa) traces. . . . .	304
8.52	$y = 1$ cm pressure (MPa) trace. . . . .	305
9.1	Cartoon of the spark ignition problem demonstrating the two planes in the axisymmetric symmetry . . . . .	309
9.2	Computational domain for the spark ignition simulations. . . . .	311
9.3	Initial Pressure . . . . .	312
9.4	Pressure from axisymmetric shock wave in the early stages of the simulation at $t = 1.5 \cdot 10^{-5}$ sec . . . . .	313
9.5	Zoomed in view of the velocity magnitude near the electrode surface at $t = 6 \cdot 10^{-6}$ s. . . . .	313
9.6	Evolution of density (kg/m <sup>3</sup> ) for nonreactive viscous case. . . . .	314
9.7	Temperature (K) at $t = 2.64 \cdot 10^{-4}$ s for nonreactive viscous case. . . . .	315
9.8	Two-component model: Evolution of density (kg/m <sup>3</sup> ) for nonreactive and reactive case with 2 mm spark gap (2 mJ). . . . .	317
9.9	Two-component model: Evolution of temperature (K) for nonreactive and reactive case with 2 mm spark gap (2 mJ). . . . .	318
9.10	Two-component model: Product mass fraction at $t = 50 \cdot 10^{-6}$ s for reactive case with 2mm spark gap (2 mJ). . . . .	319

9.11	Four-component, nonreactive model: Images from high-speed schlieren visualization (upper set) and simulation density (lower set) of a 2 mJ spark discharge in air with 0.38 mm diameter cylindrical electrodes. . . . .	322
9.12	Four-component, nonreactive model: Images from high-speed schlieren visualization and simulation density of a 2 mJ spark discharge in air with conical electrodes. . . . .	323
9.13	Four-component, nonreactive model: Images from high-speed schlieren visualization and simulation density of a 2 mJ spark discharge in air with 1.6 mm diameter cylindrical electrodes with 19 mm diameter Teflon flanges. . . . .	324
9.14	Four-component, nonreactive model: Simulated pressure field and velocity vectors showing the axisymmetric and spherical portions of the blast wave at time $t = 0.5 \mu s$ . . . . .	325
9.15	Four-component, nonreactive model: Simulation results (vorticity and velocity vectors) showing the vortex pair generated near the tip of the cylindrical electrode at time $t = 10 \mu s$ . . . . .	325
9.16	Four-component, one-step model: Images from high-speed schlieren visualization and simulation of ignition with the thin cylindrical electrodes. . . . .	327
9.17	Four-component, one-step model: Images from high-speed schlieren visualization and simulations of ignition with the conical electrodes. . . . .	328
9.18	Four-component, one-step model: Images from high-speed schlieren visualization and simulation of ignition with the flanged electrodes. . . . .	329
9.19	High-energy case: Images from high-speed schlieren visualization and pseudo-color density results from the simulation of ignition with the thin cylindrical electrodes. . .	333
9.20	High-energy case: Images from high-speed schlieren visualization and pseudo-color density results from the simulation of ignition with the conical electrodes. . . . .	334
9.21	High-energy case: Images from high-speed schlieren visualization and pseudo-color density results from the simulation of ignition with the flanged electrodes. . . . .	335
9.22	Velocity vectors superimposed on pseudo-color plots of $H_2O$ mass fraction for the thin cylindrical electrode case with detailed chemistry and transport. . . . .	337
9.23	Velocity vectors superimposed on pseudo-color plots of $H_2O$ mass fraction for the conical electrode case with detailed chemistry and transport. . . . .	338
9.24	Velocity vectors superimposed on pseudo-color plots for the conical electrode case with detailed chemistry and transport. . . . .	339
9.25	Velocity vectors superimposed on pseudo-color plots of various quantities for the flanged electrode case with detailed chemistry and transport. . . . .	340
9.26	$r = 0.002$ cm: Time-elapsd pseudo-color temperature plots for a spark radius = 0.002 cm with a pressure ratio of 100 with ambient conditions at 10,000 Pa. . . . .	348
9.27	$r = 0.002$ cm: Time-elapsd pseudo-color $H_2O$ mass fraction plots for a spark radius = 0.002 cm with a pressure ratio of 100 with ambient conditions at 10,000 Pa. . . . .	349
9.28	$r = 0.001$ cm: Time-elapsd pseudo-color temperature plots for a spark radius = 0.001 cm with a pressure ratio of 100 with ambient conditions at 10,000 Pa. . . . .	350
9.29	$r = 0.001$ cm: Time-elapsd pseudo-color $H_2O$ mass fraction plots for a spark radius = 0.001 cm with a pressure ratio of 100 with ambient conditions at 10,000 Pa. . . . .	351

9.30	$r = 0.0005$ cm: Time-elapsed pseudo-color temperature plots for a spark radius = 0.0005 cm with a pressure ratio of 100 with ambient conditions at 10,000 Pa. . . . .	352
9.31	$r = 0.0005$ cm: Time-elapsed pseudo-color $H_2O$ mass fraction plots for a spark radius = 0.0005 cm with a pressure ratio of 100 with ambient conditions at 10,000 Pa. . . . .	353
9.32	$r = 0.02$ cm: Time-elapsed pseudo-color temperature plots for a spark radius = 0.02 cm with a pressure ratio of 10 with ambient conditions at 100,000 Pa. Simulation was for $x=(-0.1,0.6)$ and $y=(0,0.5)$ cm with a 280x200 base grid and 4 levels total (3 refinement levels 2x finer each). The number of levels used in the simulation decreased as the gradients became smoother. . . . .	356
9.33	$r = 0.02$ cm: Time-elapsed pseudo-color $H_2O$ mass fraction plots for a spark radius = 0.02 cm with a pressure ratio of 10 with ambient conditions at 100,000 Pa. . . . .	357
9.34	$r = 0.01$ cm: Time-elapsed pseudo-color temperature plots for a spark radius = 0.01 cm with a pressure ratio of 10 with ambient conditions at 100,000 Pa. . . . .	358
9.35	$r = 0.01$ cm: Time-elapsed pseudo-color $H_2O$ mass fraction plots for a spark radius = 0.01 cm with a pressure ratio of 10 with ambient conditions at 100,000 Pa. . . . .	359
9.36	$r = 0.005$ cm: Time-elapsed pseudo-color temperature plots for a spark radius = 0.005 cm with a pressure ratio of 10 with ambient conditions at 100,000 Pa. . . . .	360
9.37	$r = 0.005$ cm: Time-elapsed pseudo-color $H_2O$ mass fraction plots for a spark radius = 0.005 cm with a pressure ratio of 10 with ambient conditions at 100,000 Pa. . . . .	361
9.38	Minimum ignition energy results for hydrogen/inert gas mixtures at $T = 298$ K and $P = 1$ atm. Reprinted from Lewis and von Elbe (102). . . . .	362
A.1	a) Velocity and pressure for the similarity solution at a time, $t = 0.0021$ seconds. b) Velocity and pressure for the similarity solution at a time, $t = 0.11$ seconds. . . . .	378
B.1	Possible steady wedge flows . . . . .	383
B.2	Unsteady reflection . . . . .	384
B.3	Single Mach Reflection, pseudosteady case . . . . .	385
B.4	Pseudosteady transition regions, perfect gas . . . . .	389
B.5	Historical mechanical equilibrium criterion for RR . . . . .	390
B.6	Incident and reflected shock polars . . . . .	392
B.7	Comparing perfect and real gas shock polars . . . . .	392
B.8	Steady flow reflections . . . . .	393
B.9	Steady flow reflection shock polars . . . . .	394
B.10	Shock polar for vNR . . . . .	398
C.1	General algorithm solution, perfect gas . . . . .	402
C.2	Perfect gas results for general algorithm . . . . .	404
C.3	Real gas $\chi(M)$ results for general algorithm . . . . .	407
C.4	Real gas $\frac{P_3}{P_0}(M)$ results for general algorithm . . . . .	408
C.5	Law and Glass algorithm solution, perfect gas . . . . .	409
C.6	Law and Glass algorithm solution with two loops, perfect gas . . . . .	410
C.7	For $N_2$ perfect gas: $\chi(M_s)$ along constant $\chi + \theta_w = \pi/2 - \phi_1$ . . . . .	412
C.8	For $N_2$ perfect gas: $\chi(\theta_w)$ along constant $M_s$ . . . . .	413

C.9	For N <sub>2</sub> perfect gas: $\chi(M_s)$ along constant $\theta_w$ . . . . .	414
C.10	Law and Glass algorithm $\chi(M)$ along constant $\phi_1$ , real gas results . . . . .	415
C.11	Law and Glass algorithm $\chi(M)$ along constant $\theta_w$ , real gas results . . . . .	416
C.12	Comparing Law and Glass algorithm N <sub>2</sub> results with the (18) results . . . . .	417
C.13	Comparing Law and Glass algorithm air results with the (18) Experimental results . .	418
D.1	Vorticity in the Mixing layer . . . . .	419
D.2	Blasius laminar mixing layer solution . . . . .	420
D.3	Laminar mixing layer thickness as a function of distance from the triple point, von Karman momentum-integral technique . . . . .	423
D.4	Inviscid growth rate dependence on the convective Mach number for $\delta'_{ref} = 0.16$ , $s = 1.431$ , and $q = 0.6029$ . . . . .	425

# List of Tables

4.1	$L_1$ -error norms for the three state variables of the viscous shock test problem. . . . .	54
4.2	Input parameters for one-step steady flame model . . . . .	58
4.3	Convergence of the maximum pressure peak for the one-dimensional, unstable two-species detonation problem. . . . .	66
4.4	Convergence on uniform grids using the manufactured solution for the two-dimensional Lamb-Oseen vortex test. . . . .	68
4.5	Convergence results for the decaying (viscous) two-dimensional Lamb-Oseen vortex benchmark . . . . .	69
4.6	Nonreactive diffusive double Mach reflection. . . . .	73
4.7	$L_1$ -error norms for some state variables using the 7-level case as the reference solution. . . . .	75
4.8	$L_1$ -error norms for some state variables using the 7-level case (with $496 \times 86$ base grid) as the reference solution. . . . .	75
4.9	Reactive diffusive double Mach reflection: density, density contour, and mass fraction pseudo-color plots of the DMR structure. . . . .	82
4.10	Reactive diffusive double Mach reflection: density, density contour, and mass fraction pseudo-color plots of the DMR structure. . . . .	83
4.11	$L_1$ -error norms for the state variables using the 8-level case as the reference solution. . . . .	84
4.12	Density errors calculated with a comparison to the highest resolved case (8-levels). . . . .	85
4.13	Comparison of run times for the MUSCL and WENO/CD methods using one-step, two-component chemistry for the DMR problem. . . . .	85
4.14	Reactive diffusive double Mach reflection with detailed chemistry: density, density contour, and mass fraction pseudo-color plots of the DMR structure. . . . .	88
4.15	Detailed chemistry convergence results. . . . .	89
6.1	table of simulation runs for the detonation DMR. . . . .	112
7.1	Comparing the chosen initial condition with the CJ solution for the $T=298$ K, $P = 20$ kPa detonation. . . . .	210
8.1	Pressure gauge locations . . . . .	237
8.2	Gas and chemistry parameters used in computations. . . . .	241
8.3	Summary of bifurcation simulations. . . . .	245

8.4	Table of parameters comparing results from DNS and Mark's Theory using three-shock theory and the <b>Shock and Detonation Toolbox</b> for detailed thermodynamics and chemistry. . . . .	286
9.1	Summary of one- and two-dimensional spark ignition results for different initial spark and ambient conditions. . . . .	342
9.2	Spark ignition results for the 1D axisymmetric problem with a pressure ratio of 100 at ambient (100,000 Pa = 1atm) conditions. . . . .	343
9.3	Spark ignition results for the 1D axisymmetric problem with a pressure ratio of 100 at ambient (10,000 Pa = 0.1atm) conditions with three spark radii: 0.002, 0.001, and 0.0005 cm. . . . .	344
9.4	Spark ignition results for the 1D axisymmetric problem with a pressure ratio of 10 with ambient conditions at 10,000 Pa. Three different spark radii are shown: 0.02, 0.01. and 0.005 cm. . . . .	345
9.5	Comparing experimental ignition energy results for MIE to the 1D and 2D simulation values. . . . .	363
9.6	Analytical ignition energy results and flame parameters used in the calculation. . . . .	364
9.7	Comparing analytical ignition energy results for MIE to the 1D and 2D simulation values.	364

# Chapter 1

## Introduction

Reacting flows have been a topic of on-going research for more than a hundred years. The interaction between hydrodynamic flow and chemical kinetics is complex and even today many phenomena are not very well understood. One of these phenomena is the propagation of detonation waves in gaseous media. Another is the statistical nature of the formation of deflagrations through spark ignition.

Detailed understanding of detonation ignition and propagation in gases is vital for accessing the threat from accidental explosion in piping systems of petrochemical or nuclear fuel processing plants, but also for the innovative propulsion system of the pulse detonation engine. Safety to accidental detonation is especially important in the construction and design of hydrogen delivery systems that are a prerequisite for establishing hydrogen as an alternative energy source (142).

Determining the risk of accidental ignition of flammable mixtures is a topic of tremendous importance in industry and in aviation safety. Experimental work has been done to determine the flammability limits of various fuels in terms of mixture composition (8),(34). These studies were all performed using a very high energy spark ignition source that is assumed strong enough to ignite any mixture with compositions within the flammability limits. It is known that there is a limiting strength of the ignition source. If an ignition source is not strong enough, or is below the minimum ignition energy (MIE) of the particular mixture, the mixture will not ignite. While the numerical modeling of the growth of a flame from a hot gas volume created by an ignition source has been considered for simplified chemistry and transport models or detailed models with unresolved diffusive effects, much is still unknown for real mixtures with detailed chemistry and transport.



## 1.1 Detonations

### 1.1.1 Detonation Theory

Detonation is a process of supersonic combustion in which a shock wave is propagated and supported by the energy release in a reaction zone behind it. It is the more powerful and destructive of the two general classes of combustion, the other more common one being deflagration. In a detonation, the shock compresses the material, thus increasing the temperature to the point of ignition. The ignited material burns behind the shock and releases energy that supports the shock propagation.

The first successful detonation theory was the Chapman and Jouguet (CJ) model to predict the detonation front speed using the conservation laws and thermodynamic properties. Once the detonation velocity is known, the mean flow of the final trailing gas can be completely determined without any consideration of the front. The wave speed is determined by the extent of reaction before the sonic surface is reached, and in this model the reaction is essentially complete at this point making the wave speed independent of the chemistry. This approach is adequate for most simple engineering purposes (98).

As experimental visualization tools improved, more was discovered of detonations, particularly, the finite thickness and multi-dimensional structure. At the head of the detonation wave, the shock wave is followed by a thin reaction zone where the flow is nonuniform behind with a series of periodic striations extending horizontally to the rear of the main flow.

If the effects of the transverse waves are neglected, but the finite reaction zone thickness is accounted for, as shown in figure 1.1, one can apply the ideal reaction zone theory of Zeldovich, Doering, and Von Neumann (ZND) to compute the flow within the reaction zone. The ZND model supposes a steady (time-independent) shock wave followed by chemical reaction in a constant-area, inviscid, compressible flow. The temperature rises and pressure drops as the reactants are converted to intermediates and finally to products. The coupling from the fluid mechanics to the chemistry occurs through the dependence of reaction rates on the species concentrations, pressure, and temperature. The pulse width and the distance to the peak energy release are determined by the chemical reaction mechanism, rates of reaction, and the thermodynamic state behind the shock front.

One finds that, the ideal steady ZND structure is unstable with respect to small disturbances in lead shock shape and speed. The instability is the result of the

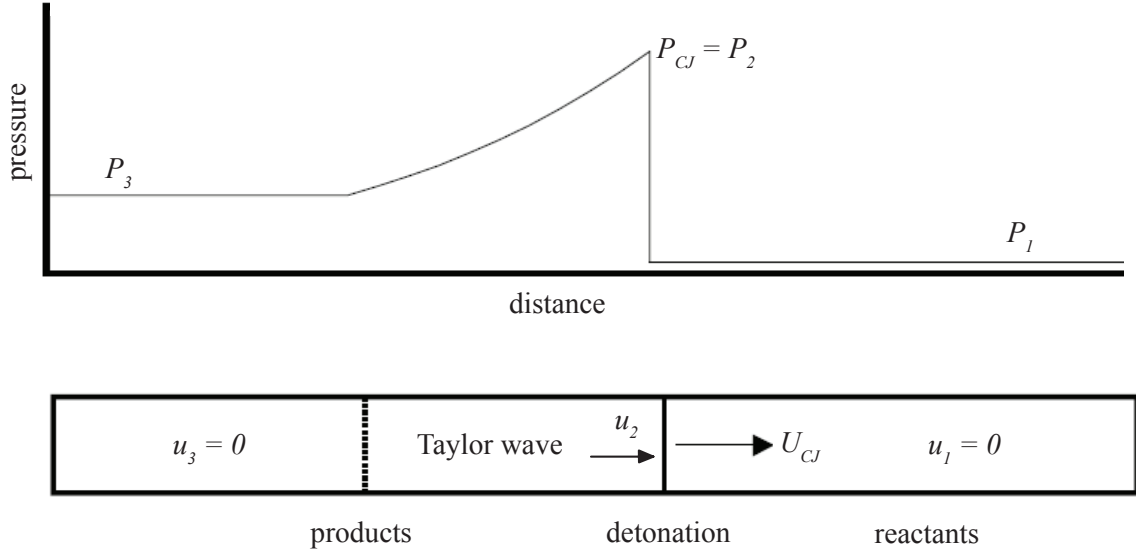


Figure 1.1: Detonation propagation in tube with a closed end.

amplification of acoustic waves trapped in the region between the lead shock and the end of the energy release zone. These instabilities are large enough that they are observed in experiments, showing detonations as multi-front waves. In detonation tube experiments, one observes an average, planar detonation front with an average speed close to the value predicted by CJ theory. But there also exists traverse waves propagating perpendicular the the main front. Using a soot foil, an aluminum sheet that is covered with soot and then placed on the side of the detonation channel, one can observe the detonation instabilities. The soot foils show periodic cells, which coincide with the motion of triple points along the front (142).

### 1.1.2 Detonation Shock-Bifurcation

The generation of a reflected shock wave by an ideal detonation wave is shown in figure 1.2. The detonation travels from the point of ignition to the tube end at the Chapman-Jouget (CJ) speed,  $U_{CJ}$ , as derived in detonation textbooks (98). Trailing the detonation is the Taylor expansion that terminates on the characteristic moving at sound speed  $c_3$ , the sound speed in the constant pressure region behind the expansion. Since  $c_3 > U_{CJ}$ , the expansion broadens as the detonation wave propagates.

Many researchers have investigated the interaction of nonreacting reflected shock waves with boundary layers in the context of shock tube performance and it has been observed (114, 124) that interaction with the boundary layer may cause the reflecting

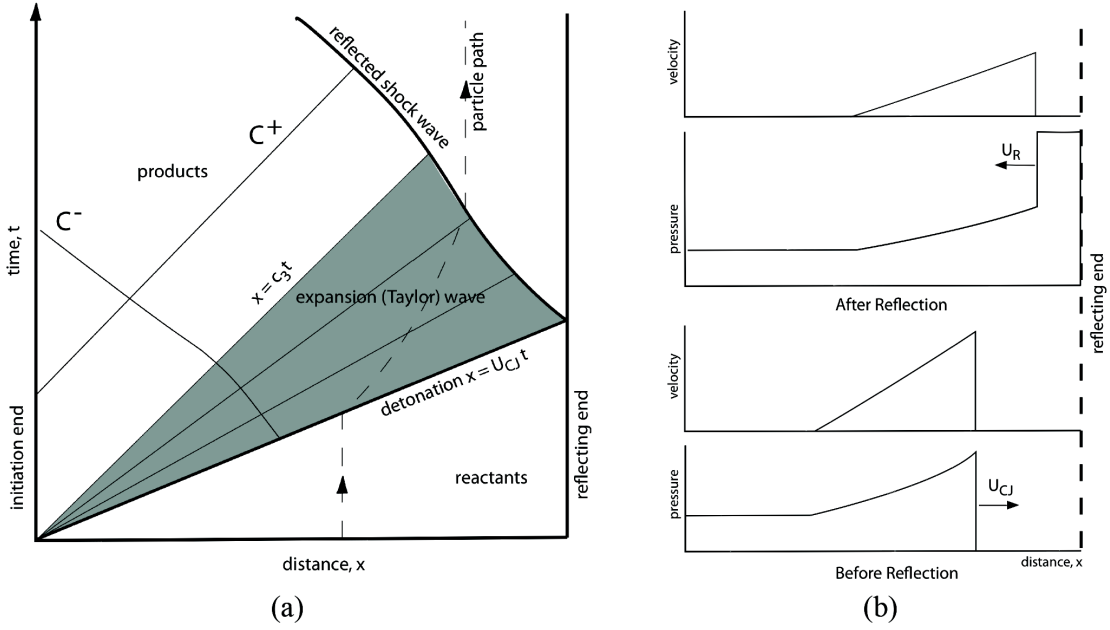


Figure 1.2: (a) Space-time diagram of an ideal detonation and Taylor wave. (b) Spatial pressure distributions for several times after detonation initiation and prior to reflection. Reprinted from Damazo and Ziegler *et al.* (35).

shock wave to bifurcate into an unaffected normal shock wave and a leading angled shock wave or foot that travels along the tube wall. Historical experimental and theoretical comparisons were conducted by Davies *et al.* in 1969 (36), and significant 2D unresolved simulations were conducted by Weber *et al.* in 1995 (159). More recent (2005) work by Gamezo *et al.* (87) has simulated this phenomena in three dimensions using one-step chemistry. The effects of shock wave boundary layer interaction on detonation reflection have had yet to be investigated for real gases that require the use of detailed chemistry and transport. Also, current simulations, while gaining basic insights, have failed to resolve the viscous and diffusive scales in the boundary and shear layers.

Reactive shock bifurcations are likely to form in systems in which shocks, flames, boundary layers, or other velocity gradients are present. These can grow quickly and drastically change the reactive flow structure. They provide a mechanism for a detonationless supersonic flame spread that may accelerate DDT or quickly burn a reactive mixture without creating very strong shocks typical for detonations. This phenomena is important for a broad range of propulsion applications and safety issues (87).

### 1.1.3 Detonation Stability

The dynamic response of detonation fronts is dependent on the regularity of the cellular structure. This regularity is a function of the degree of instability of a particular mixture. The activation energy is the dominant parameter, a function of the Mach number as calculated at the Chapman Jouguet (CJ) point. figure 1.3 shows the degree of instability for some of the commonly analysed mixtures. The distance from the longitudinal neutral stability boundary in reduced activation energy vs. the Mach number coordinates is used to quantify the degree of instability.

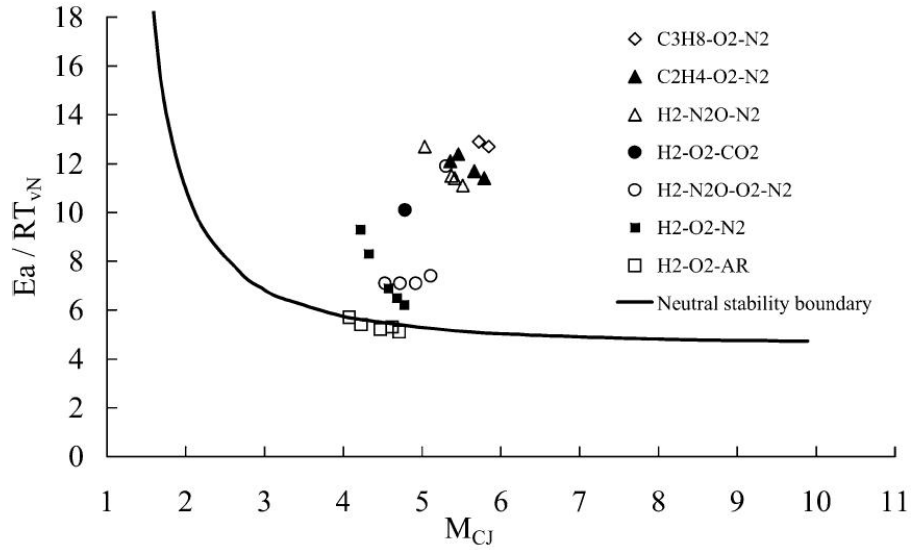


Figure 1.3: Categorization of the stability of detonations in relation to the longitudinal neutral stability boundary (Shepherd 2008)

The effective activation energy,  $E_A$ , can be defined in terms of the variation of the induction length  $\Delta_i$  with post shock temperature.  $E_A$  is found by finding the local slope for  $\ln(\Delta_i)$  vs.  $\frac{1}{T}$  as in the equation

$$\ln(\Delta_i) \frac{E_A}{R} \frac{1}{T} + \text{constant}, \quad (1.1)$$

where  $T$  is the post shock temperature and  $R$  is the particular gas constant for the mixture. A normalized activation energy,  $\theta$ , is defined as  $E_A/R/T$ , and the higher the value, the more unstable the mixture. However, the activation energy alone is not adequate to explain the stability properties of detonations. For example, shortening the energy release zone relative to the induction zone causes more instability.

The instability of detonations has also been examined from a dynamical systems point of view. Linear stability theory predicts that also with increasing activation energy  $\theta$  the ZND structure will become unstable to small perturbations and an increasing number of unstable modes will be accessible with further increases in  $\theta$  (25).

The normalized activation energy of the common mixtures ranges from 5.2 for the regular, marginally unstable argon diluted hydrogen-oxygen mixtures, to 12.7 for the irregular, highly unstable propane-air mixtures. These normalized activation energies of figure 1.3 were calculated by using a  $2 - \gamma$  model approximation of the detailed chemistry, where  $\gamma$  is the specific heat ratio. Note that the mixtures closest to the neutral curve show the greatest cellular regularity, and those farthest from the neutral stability curve show the least regularity (most unstable).

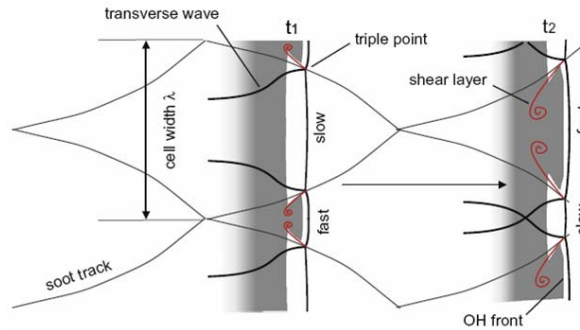


Figure 1.4: Diagram of shock waves and triple points in a multi-dimensional detonation (Shepherd 2009).

A multi-dimensional detonation wave is described as having a periodic structure of transverse waves in addition to the leading shock-reaction front. A key structure in of these shock waves is the three-shock or triple-point configuration. Mach stems and incident shocks are part of the leading shock and the resulting reflected shocks are the transverse waves. The transverse movement of the triple points creates the well known detonation cell pattern, as shown in figure 1.4. Triple points are created when shock waves encounter solid boundaries or in the case of detonations, other incoming shock waves. The regularity or irregularity of these patterns as observed in experiments is what is used to qualitatively describe a detonation as regular or irregular. The most regular cellular patterns are associated with a weakly unstable front with only a single transverse wavelength and smooth wave fronts. The irregular cellular patterns are associated with strongly unstable fronts with a large spectrum of transverse waves parallel and perpendicular to the main front and fine-scale wrinkling on the shock and reaction zones. Macroscopic behavior of detonations, such as initiation, diffraction,

and quenching, is observed to be quantitatively different for these two types (54, 98, 142).

### 1.1.4 Simulating Detonations

Simulating all of the relevant processes in a detonation wave is extremely difficult. Detonations are fundamentally three-dimensional and also multi-scale. In experiments, detonations propagate 1 to 10 m and the reaction zones contain spatial gradients of the order of  $10^{-6}$  to  $10^{-5}$  m. Gradients in the temperatures, velocities, mass fractions occur at even smaller scales due to diffusion. This range of scales makes the direct simulation of detonations computationally expensive. Another issue is the  $10^3$  reactions and  $10^2$  species needed to model the chemistry for larger fuel molecules such as hydrocarbons. This creates further computational expense and storage issues. This simulation of multi-dimensional diffusive, reacting flow which includes shock waves creates many numerical challenges involving efficiency, accuracy, shock capturing, and turbulence modeling (142).

The most complex detonation simulations have typically used either the multi-dimensional Euler (inviscid) formulation with detailed chemistry and no transport, the multi-dimensional Navier-Stokes formulation with two-component, one-step chemistry and transport, or the one-dimensional Navier-Stokes formulation with detailed chemistry and transport. All of these simulations required the use of adaptive mesh refinement (AMR) in order to tackle the large range in scales (131). Powers and Paolucci (132) give the rationale and estimates for determining the minimum chemical length scale that needs to be resolved in detonation simulations. They stress that for the reactive Euler equations, in order for the simulation results to be mathematically correct, the smallest length scale must be resolved. This length is widely different for different chemical kinetic models and is the reciprocal of the magnitude of the real part of each of the eigenvalues of the local Jacobian matrix. Their conclusion is that the finest length scales predicted by a one-dimensional steady analysis of a common stoichiometric CJ hydrogen-air detonation model are roughly three orders of magnitude finer than the induction zone thickness. This suggests that past supposedly accurate calculations using detailed kinetics were formally underresolved.

For more detailed discussion of detonation theory and history from experimental, theoretical, and numerical viewpoints see the review of Shepherd (142) and the textbooks of Lee (98) and Fickett and Davis (54). Also, see Chapter 5 for a discussion of research relevant to diffusive detonations.

### 1.1.5 Reduced Detonation Mechanisms

Currently, when conducting a multi-dimensional detonation simulation, including the full detailed chemistry is prohibitively expensive. Detailed chemistry models are not practical for large-scale multi-dimensional simulations nor suitable for analytical computations that attempt to formulate theories using approximate methods such as activation energy asymptotic analysis. The detonation chemical reaction is a coupled chain-branching, thermal explosion in which exponential growth of radical species, recombination reactions forming products and releasing thermal energy, and competing reaction pathways for intermediates all occur simultaneously. All of these effects are included when a full detailed chemistry model is used for simulation. Substantial efforts have gone into developing reduced detailed chemistry models that only contain the essential species and reactions and also ad hoc models with pseudospecies that mimic some portion of the actual chemical processes. For use in conducting the first direct numerical simulations of detonations, the reduced detailed chemistry mechanisms are the most useful as they preserve more physics than the ad hoc models. Example ad hoc models include Lu *et al.* (111), which uses complex CSP for chemistry reduction, Browne *et al.* (24), who calibrated a five-step, four-species model that simulated hydrogen combustion, and Petrova *et al.* (126) and Fernandez-Galisteo (53), who developed a phenomenological model for hydrocarbons.

These models give insight into the stability properties of detonations, yet, lack many features that are needed to understand the much more complex irregular detonations of larger fuel molecules. Additionally, when using the transport equations, actual rather than ad hoc “dummy” reactants and products must be used. Full detailed chemistry and transport models have been developed for these purposes. Examples include GRI-MECH 3.0 ([www.me.berkeley.edu/gri\\_mech/](http://www.me.berkeley.edu/gri_mech/)), JetSurF2.0 (<http://melchior.usc.edu/JetSurF/JetSurF2.0>), and CaltechMech (22),(21). These mechanisms are complex with a very large number of species and for use in multi-dimensional simulations must be reduced either by hand or by using QSSA (quasi-steady state analysis) (127),(125),(155),(133). All of these reductions are specific for certain mixture types and ranges of initial conditions. Also, of the ones cited, except for the full detailed chemistry, the reductions only create models which are suitable for steady simulations, especially those for hydrocarbons such as in Varatharajan *et al.* (155). One must account for the full range of detonation speeds (overdrives) when modeling the chemistry for a more realistic unsteady simulation. Schultz and Shepherd (141) used constant volume explosion and ZND simulations with the most



detailed reaction mechanisms available at the time for many types of mixtures (hydrogen, ethylene, and propane). They compared the induction times from their numerical model with those from experiments and found on average that for post shock temperatures above 1200 K, the numerical/experimental error is approximately 25 percent. This shows that care must be taken when designing reduced models and multiple unreduced models and experimental comparisons are needed.

### 1.1.6 Contemporary Research

Experimental visualizations of shock and reaction front configurations suggest that the process of supersonic combustion is more complex than previously thought. Although all propagating detonations are unstable, there is a wide range of behavior with one extreme being nearly laminar but unsteady periodic flow and the other a chaotic instability with highly turbulent flow.

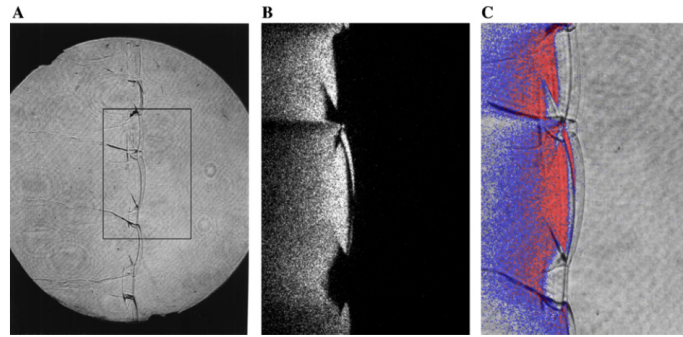


Figure 1.5: Schlieren and PLIF images OH reaction detonation structures  $2\text{H}_2\text{-O}_2\text{-12Ar}$ ,  $P_1 = 20$  kPa (Austin *et al.* 2005).

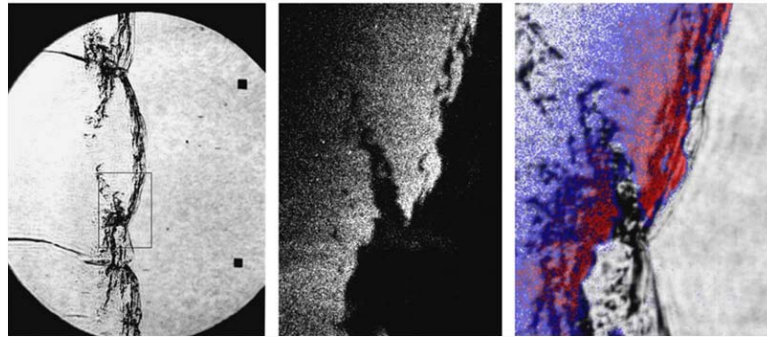


Figure 1.6: Schlieren and PLIF images OH reaction detonation structures  $\text{C}_2\text{H}_4\text{-3O}_2\text{-10.5N}_2$  (Austin *et al.* 2005).



While the typical regular (low activation energy or weakly unstable) detonations of such mixtures as hydrogen and argon have predicable structures as in figure 1.5, the reaction fronts and shear layers for irregular (high activation energy or highly unstable) detonations are highly wrinkled with velocity and density fluctuations on a scale much smaller than the cell width as shown in figure 1.6. Here, ignition delays allow diffusion to compete with convective adiabatic processes as a transport mechanism, causing coupling between fluid dynamics and chemical processes. Also, a significant temporal oscillation in the lead-shock strength can result in disparate induction times across the shear layer, where instabilities can lead to the formation of vortical structures before ignition. Transport of hot products and cold reactants across the mixing/shear layer leads to local detonations, augmenting the fundamental shock induced combustion mechanism in the detonation front.

Using a two-dimensional simulation of the shear layer behind detonation triple points, Massa *et al.* (116) investigated the role of vortical structures associated with Kelvin-Helmholtz instability in the formation of localized ignition using detailed chemical kinetics and transport. Only in the higher effective activation energy mixtures did localized explosions occur in the shear layer. They also found that the ignition is linked to mass and heat diffusion rather than the instability associated with the shear layer. This was the first two-dimensional simulation that addressed the diffusive role of detailed chemical kinetics and transport.

In this thesis, the work of Massa *et al.* (116) was built on, by further investigating the role diffusive mixing has in the triple-point mixing layers of irregular detonations. We now include the shock waves and triples points. The goal of this research is to conduct multi-dimensional simulations of multiple species detonation problems using AMR with detailed chemistry and transport. This models the largely unexplored hydrocarbon detonations.

## 1.2 Spark Ignition

### 1.2.1 Theory

When energy is deposited into a combustible mixture, there are multiple possible outcomes. When an extreme amount of energy is used, a detonation wave results where the chemical reactions follow and support the wave. When a lesser amount of energy is deposited quickly (as with a spark), a shock wave still results, yet, the chemical reactions lag behind, with the propagation speed of the products limited by

a balance of diffusion and convection. Initially, with small enough energy or small enough timescale, a laminar propagating flame, otherwise known as a deflagration, results. Depending on mainly the amount of energy, the laminar deflagration may or may not transition to a turbulent flame. The turbulence depends on instabilities, such as changes in flame front curvature. A turbulent flame is faster and more energetic than the original laminar flame, and more likely to continue to propagate through the combustible mixture.

The physics of turbulent combustion includes many processes and effects. For example, there are tens to thousands of species and reactions depending on the composition of the mixture. The fluid dynamics is inherently three dimensional and includes many forces and effects that cannot be ignored, such as viscosity, mass diffusion, heat conduction, buoyancy, and real gas thermodynamics. Also of importance is the no slip boundary condition at solid complex shaped boundaries and the random, complex, high energy nature of the spark. The spark in reality is a high temperature plasma of ions and free radicals. In combustion theory, it is postulated that both the high temperature and the presence of reaction enhancing radicals are the agents for creating self sustaining deflagrations and detonations.

### 1.2.2 Experiment

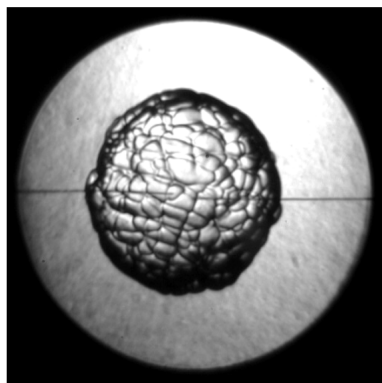


Figure 1.7: Schlieren image of a deflagration wave from spark ignition propagating in a 10 percent hydrogen, 11.37 percent oxygen, 78.63 percent argon mixture in a closed vessel. Reprinted from Bane and Ziegler *et al.* (10).

In terms of deflagrating explosions from spark ignition, the concept of minimum ignition energy (MIE) has traditionally formed the basis for studying ignition hazards of fuels. Standard test methods for determining the MIE use a capacitive spark

discharge as the ignition source, and there have been extensive experimental studies to determine the minimum ignition energies of many different flammable mixtures (11),(12). However, due to the complexity of modeling the ignition process, predicting ignition remains primarily an experimental issue.

### 1.2.3 Simulation

Much of the previous work on simulating ignition has idealized the problem and treated one-dimensional spherical and cylindrical spark kernels. There have been some two-dimensional simulations of spark discharge in a nonreactive gas performed by (91, 3, 136, 51) to investigate the fluid mechanics involved in the spark ignition process and two-dimensional simulations of ignition have been performed in (78, 93, 153, 151, 152, 165). More recent 2D simulations include those of Nakaya et al. (120) and Han et al. (63, 64). The Nakaya et al. work is an improvement on the work done in the Yuasa et al. paper (165). However, none of these studies has made an effort to resolve the diffusive scales (most notably immediately after the blast wave and the boundary layers at solid boundaries) with the appropriate mesh size and AMR or study the diffusive processes and interactions with varying geometries in detail with the combination of detailed chemistry. In all the two-dimensional studies, the classic toroidal shape of the hot gas kernel is observed, which occurs due to fluid flow inward toward the point of symmetry.

In both the simulations and experiments in this study, only very short sparks (on the order of  $10^{-7}$  s) are considered. In some of the previous modeling work (78, 153, 152) sparks with a breakdown phase followed by a long arc phase ( $10^{-5}$  to  $10^{-4}$  s) are used to simulate sparks from circuits with a significant inductance component, e.g., an automotive spark plug, which is very different from sparks encountered by accident from static electricity buildup or that from lightning. Shorter duration ( $< 10^{-6}$  s) sparks are more consistent with electrostatic discharge hazards in aviation and other industries.

## 1.3 Overview

In chapter 2, the key physics found in compressible, reactive, diffusive flow are introduced, starting with hyperbolic systems and moving to the Euler equations and shock reflections and then arriving at the reactive Navier-Stokes equations. In chapter 3, WENO methods are briefly introduced and then extended to describe the symmetric

variant and its hybridization with centered differences. The implementation of the scheme with time-split integration, discontinuity flagging, and flux-based SAMR is developed. One- and two-dimensional nonreactive and reactive verification problems are presented in chapter 4. Convergence results are presented for a fully resolved reactive, diffusive DMR with one-step chemistry, along with results for multi-component flow with detailed transport and chemistry. The present simulations can be viewed as extension and application of the hybrid approach to detonation-driven, diffusive-reactive flows within an SAMR framework, with a focus on the accurate resolution of reactive-diffusive effects.

In the next five chapters, specific applications are developed. In chapter 5, a detailed, reduced mechanism for irregular propane detonations is developed. In chapter 6, this mechanism is used for a diffusive double Mach reflection simulation with a transition to micro-scale cellular structure in the the incident shock. Comparisons between different resolutions and viscous/diffusive and inviscid simulations are conducted. In the next chapter, 7, this mechanism is used to simulate the two dimensional detonation cell pattern for propane. These results are compared to experimental visualizations and soot foils. The next two chapters involve two different applications and also different hydrogen-oxidizer mixtures. In chapter 8, detonation and shock bifurcation is simulated at scales which are observable in experiment. Schlieren images are compared to simulations for different compositions of reactive and nonreactive mixtures. Lastly, in chapter 9, a comparison between spark ignition experiments and simulations is shown and discussed. A systematic study is developed by starting with a simple nonreactive single species model and moving towards the full multi-component detailed chemistry and transport model.

This thesis also includes five appendices which provide supplemental background material and mechanisms. Appendix A shows a similarity solution of the one dimensional Euler equations. appendix B discusses irregular Mach reflections in detail and appendix C provides algorithms which were used in MATLAB programs to explore Mach reflections in detail. Viscous flow physics theory and solutions are developed in appendix D. Lastly, CHEMKIN II mechanisms with detailed chemistry and transport that are used in simulations discussed in this thesis are listed in appendix E.

# Chapter 2

## equations of Compressible, Diffusive, Reacting Flow

The equations of reactive fluid dynamics are described in this section starting with a one-dimensional hyperbolic system and increasing complexity to the Euler and Navier-Stokes equations and then with the full reactive Navier-Stokes with detailed chemistry. Nondimensionalizations and an eigendecomposition are also given.

### 2.1 Hyperbolic Systems

Compressible flow is fundamentally related to the mathematical properties entailed in a simple scalar hyperbolic equation,

$$u_t(x, t) + f_x(u(x, t)) = 0, \quad (2.1)$$

where “ $x$ ” and “ $t$ ” denote  $x$  and  $t$  derivatives. In this equation, a quantity  $u$  is conserved in space and time when a flux,  $f_x$ , of  $u$  is encountered. In this form, the equation is deemed a conservation law. The law is that the change in a quantity is equal to the flux of that quantity. In this chapter, this equation is built on, beginning here with a scalar hyperbolic conservation law. A self-similar nonlinear system of conservation laws with an analytical solution is described. This solution is later used in verification of numerical simulations for the one space dimensional Euler equation. The hyperbolic Euler equations are related to their parabolic Navier-Stokes extension, and also to reacting flow, known for its the stiff source terms.

## 2.2 Euler equations for Compressible Flow

The 3D Euler equations are a nonlinear hyperbolic system and consist of the continuity, momentum, and energy equations. The continuity equation is in differential form

$$\rho_{,t} + (\rho u_i)_{,i} = 0, \quad (2.2)$$

where  $\rho$  is the density and  $u_i$  represents the velocity in the x, y, z directions. The momentum equation is

$$(\rho u_j)_{,t} + (\rho u_i u_j)_{,i} = -p_{,j}, \quad (2.3)$$

where  $p$  is the pressure with  $P_{,j} = P_{,i} \delta_{ij}$ . Unlike the scalar continuity and energy equations, the momentum equation is a vector equation with one equation for each of the three spatial dimensions. The last equation, the energy equation, is expressed as

$$(\rho e_t)_{,t} + (\rho u_i e_t)_{,i} = -(u_i p)_{,i}, \quad (2.4)$$

where  $e_t$  is the total internal energy. Now, for a compact representation, one uses a vector equation, that represents a system of 5 scalar equations. The final result is a nonlinear, time dependent, hyperbolic, vector equation. This 5 degree of freedom equation is written as

$$\mathbf{U}_{,t} + \mathbf{F}_{i,i}^{adv} = 0. \quad (2.5)$$

With

$$\mathbf{U} = \begin{bmatrix} \rho \\ \rho u_1 \\ \rho u_2 \\ \rho u_3 \\ \rho e_t \end{bmatrix}, \quad \mathbf{F}_i^{adv} = u_i \mathbf{U} + p \begin{bmatrix} 0 \\ \delta_{11} \\ \delta_{22} \\ \delta_{33} \\ u_i \end{bmatrix}. \quad (2.6)$$

### 2.2.1 Inviscid, Adiabatic, One-Dimensional Similarity Flow

Inviscid, adiabatic, one dimensional flow as described by the Euler equations has no characteristic length or time scales present. Only a velocity scale dictates the form of the solution. In this case, all derivatives with respect to  $x$  and  $t$  can be expressed

in terms of the similarity parameter  $\xi$ , see (94) §99,

$$\xi = x/t, \quad (2.7)$$

$$\frac{\partial}{\partial x} = \frac{1}{t} \frac{d}{d\xi}, \quad (2.8)$$

$$\frac{\partial}{\partial t} = -\frac{\xi}{t} \frac{d}{d\xi}. \quad (2.9)$$

These expressions can be applied to the continuity and Euler equations

$$\frac{\partial \rho}{\partial t} + \frac{\partial(\rho v)}{\partial x} = 0, \quad (2.10)$$

$$\frac{\partial v}{\partial t} + v \frac{\partial(v)}{\partial x} = -\frac{1}{\rho} \frac{\partial p}{\partial x}, \quad (2.11)$$

with  $v$  as the  $x$  component of the velocity. Now writing all derivatives in terms of  $\xi$ , the  $t$  and  $x$  variables disappear.

$$(v - \xi) \frac{d\rho}{d\xi} + \rho \frac{d(v)}{d\xi} = 0, \quad (2.12)$$

$$(v - \xi) \frac{dv}{d\xi} = -\frac{1}{\rho} \frac{dp}{d\xi}. \quad (2.13)$$

By expressing the equations in terms of the similarity variable, exact solutions can be found, for example for the breaking wave problem, see appendix A. These exact solutions have previously been used for verification of the numerical methods for the inviscid part of the solutions. Understanding similarity flow is also crucial for understanding the physics of shock reflections.

## 2.2.2 Shock Reflections

Shock waves are a fundamental property of the Euler equations and hyperbolic systems in general. To understand supersonic compressible flows, one must study shock wave interactions with solid boundaries and other shocks.

The following section summarizes the basic theory for modeling the interactions of planar shock waves with angled wedges, particularly the properties of the triple point structure. This problem is important for understanding how shock waves interact with boundaries and with other shock waves. When a moving planar shock wave hits a wedge, the shock is reflected and the flow is deflected. This is referred to as the “unsteady problem”. The incident shock wave is moving unchanged, encounters the

wedge, and then moves up the wedge. Unsteady examples are shown in figures 2.1(a), and 2.1(b). For the “steady problem” a stationary shock wave at an oblique angle encounters a boundary and reflects off. An example of where this may occur is in a jet engine inlet or outlet, or in shock tubes with traverse waves. Steady examples are shown in Fig. 2.1(c) and 2.1(d). The unsteady and steady cases are different, however, they have inherently similar fundamental processes involved.

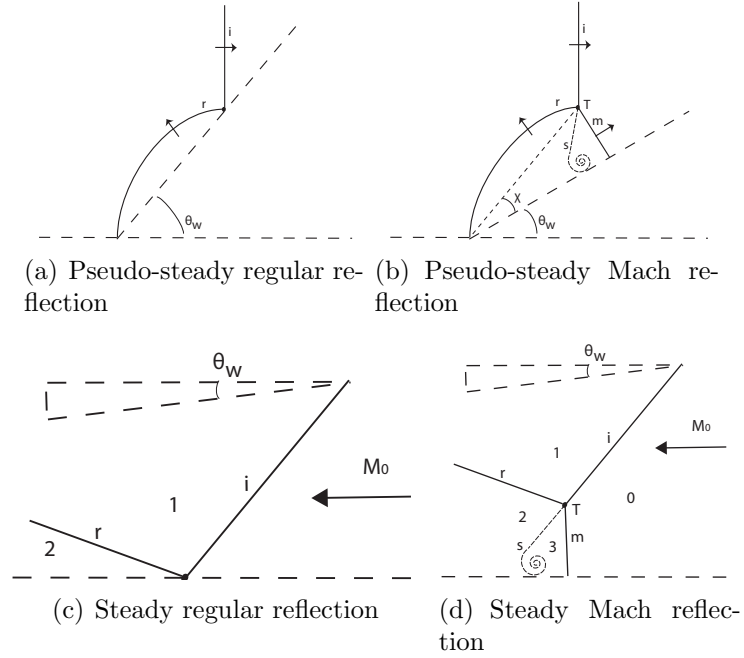


Figure 2.1: Example shock reflections

For both the steady and unsteady cases, the Mach number and the wedge angle are the input parameters for a perfect gas model. For the real gas model, the pressure, temperature, and species data are also required. There also exist different levels of approximation for modeling chemical reactions. In all cases of inviscid theory, *thermodynamic equilibrium* is enforced across all shock waves. The *chemical* post shock state, for example, from dissociation, combustion, or other processes, can be either ignored; (frozen case) as in the case of relatively low temperatures of nonreacting species; assumed to be in local equilibrium (all reaction occur across shock); or assumed to be partially reacted, by simulating the unsteady chemical kinetics.

Approximate solutions known as “two shock theory” and “three shock theory” for the shock reflection phenomenon were developed by (156). The three shock theory models the primary triple point shock structure of the more complex reflection phenomenon known as Mach reflection. For the unsteady problem, the triple point path



angle is found as a function of the incident shock Mach number and the wedge angle. These results agree roughly with experimental results, except at small wedge angles and for strong Mach numbers where the assumptions break down the most (16).

For further developments and examples from these shock theories and a discussion of the various types of shock reflections see Appendices B and C.

### 2.2.2.1 Self Similar Approximation

The unsteady reflection process can be approximated as a self similar, pseudo-steady problem (103), (15), (18). For this simplification, the Mach stem is assumed to be straight and perpendicular to the wedge, and the fluid is modeled as inviscid. By attaching a reference frame to the triple point, the three shock pseudo-steady solution is found. In this frame, the reflected wave of a single Mach reflection (SMR) relative to the triple point path, is straight in the pseudo-steady reference frame. This is demonstrated in figure 2.2, where the velocity vectors are shown in the reference frame of the triple point.

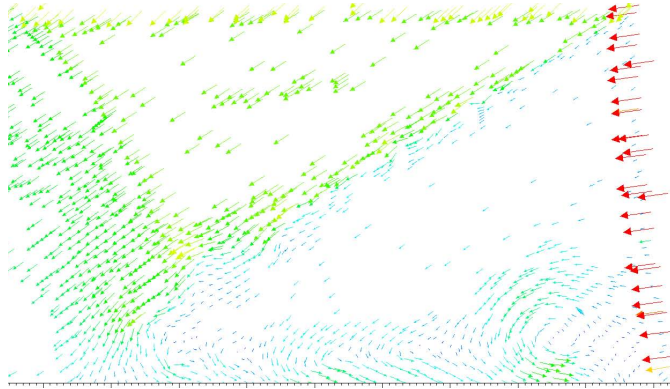


Figure 2.2: Velocity vectors in the triple point reference frame, DMR case

## 2.3 Reactive Multi-Component Navier-Stokes equations

To conduct direct numerical simulations (DNS) of detonations and deflagrations, the compressible Navier-Stokes equations are extended to model multidimensional, multi-component, chemically reacting gas flows. The model assumes an ideal gas mixture with zero bulk viscosity. Soret and Dufour effects of mass diffusion, external body

forces, and radiant heat transfer are neglected. This forms a large system of nonlinear conservation laws containing stiff source terms (52) and both first- and second-order derivative terms from convective and diffusive transport. *Mixture averaged transport* is also assumed. In this approximation, “cross diffusion” terms are neglected and the solution of a matrix equation at each time step is avoided. Note that in this case, there are still separate temperature and pressure dependent diffusivities for each species. For the derivation, see (164).

### 2.3.1 Formulation

The problem is formulated for a mixture of  $N$  species as

$$\partial_t \mathbf{q} + \partial_x \mathbf{f}^{\text{conv}} + \partial_y \mathbf{h}^{\text{conv}} - \partial_x \mathbf{f}^{\text{diff}} - \partial_y \mathbf{h}^{\text{diff}} = \mathbf{s}^{\text{chem}} \quad (2.14)$$

with vector of state  $\mathbf{q} = (\rho u, \rho v, \rho e_t, \rho Y_1, \dots, \rho Y_N)^T$  and the convective fluxes

$$\mathbf{f}^{\text{conv}} = u \mathbf{q} + p (1, 0, u, 0, \dots, 0)^T, \quad \mathbf{h}^{\text{conv}} = v \mathbf{q} + p (0, 1, v, 0, \dots, 0)^T, \quad (2.15)$$

the diffusive fluxes

$$\mathbf{f}^{\text{diff}} = \left( \tau_{xx}, \tau_{xy}, u \tau_{xx} + v \tau_{xy} + k \partial_x T + \rho \sum_{i=1}^N h_i D_i \partial_x Y_i, \rho D_1 \partial_x Y_1, \dots, \rho D_N \partial_x Y_N \right)^T \quad (2.16)$$

and

$$\mathbf{h}^{\text{diff}} = \left( \tau_{xy}, \tau_{yy}, u \tau_{xy} + v \tau_{yy} + k \partial_y T + \rho \sum_{i=1}^N h_i D_i \partial_y Y_i, \rho D_1 \partial_y Y_1, \dots, \rho D_N \partial_y Y_N \right)^T, \quad (2.17)$$

and the reactive source term

$$\mathbf{s}^{\text{chem}} = (0, 0, 0, 0, \dot{\omega}_1(T, p, Y_1, \dots, Y_N), \dots, \dot{\omega}_N(T, p, Y_1, \dots, Y_N))^T, \quad (2.18)$$

where  $\tau$  denotes the stress tensor (defined in appendix 2.5). The mass fraction of the  $i$ -th species is computed from the partial and total density as  $Y_i = \rho_i / \rho$ . The enthalpy of the gas mixture is denoted by  $h$ ,  $\dot{\omega}_i$  is the mass production rate of the  $i$ -th species,  $\mu$  the mixture viscosity,  $k$  the mixture thermal conductivity, and  $D_i$  the mass diffusivity of the  $i$ -th species into the mixture. The mass production rates are specified by Arrhenius rate equations, determined by the particular reaction mechanism. The

contribution of each species to the total energy is obtained by using a mass-fraction-averaged enthalpy, i.e.,

$$h = \sum_{i=1}^N Y_i h_i, \quad \text{where} \quad h = e_t + \frac{p}{\rho} - \frac{u^2 + v^2}{2}. \quad (2.19)$$

To close the system of equations, we have the ideal gas law for the average mixture properties, as derived from the partial pressure equation for each species, that reads

$$p = \sum_{i=1}^N p_i = \sum_{i=1}^N \rho Y_i R_i T = \rho R T, \quad \text{with} \quad R = \sum_{i=1}^N Y_i R_i, \quad R_i = \frac{\mathcal{R}}{W_i}, \quad (2.20)$$

where  $\mathcal{R}$  is the universal gas constant and  $W_i$  the molar mass of each species. The mass production rates are computed by summing the contributions from each chemical reaction. The reactions are all formulated with an Arrhenius rate equation, cf. (164). The sound speed,  $a$ , a parameter that is calculated throughout the simulation, must be derived for a mixture, of thermally perfect, ideal gases. The frozen sound speed is defined as the derivative of the pressure with respect to the density at constant entropy and species concentrations and reads

$$a^2 = \left( \frac{\partial p}{\partial \rho} \right)_{s, Y_1, \dots, Y_N} = \gamma R T = \gamma \frac{p}{\rho} = \gamma \sum_{i=1}^N Y_i T. \quad (2.21)$$

Using a representation of each species' specific heat at constant pressure and constant volume, denoted by  $c_{pi}(T)$  and  $c_{vi}(T)$ , respectively, as a function of  $T$ , the specific heat ratio for each species is

$$\gamma_i(T) = \frac{c_{pi}(T)}{c_{vi}(T)}, \quad c_{vi} = c_{pi}(T) - R_i. \quad (2.22)$$

A mixture value for  $\gamma - 1$  is found using the mole fraction,  $X_i$ , as

$$\gamma(T) = 1 + \left( \sum_{i=1}^N \frac{X_i}{\gamma_i(T) - 1} \right)^{-1}, \quad X_i = \frac{\rho_i}{\rho} = \frac{Y_i W}{W_i}, \quad (2.23)$$

$$\text{with} \quad W = \left( \sum_{i=1}^N \frac{Y_i}{W_i} \right)^{-1} = \sum_{i=1}^N X_i W_i. \quad (2.24)$$

For the canonical eigendecomposition, for instance, of the Jacobian of the flux function  $\mathbf{f}^{\text{conv}}$ , see section 2.6.

### 2.3.2 Temperature Evaluation

Ideal gases require the computation of the temperature from the conserved quantities by solving an implicit equation. Consider the pressure as the sum of partial pressures,

$$p = \sum_{i=1}^N \rho Y_i \frac{\mathcal{R}}{W_i} T, \quad (2.25)$$

and also as related to the enthalpy and internal energy of the mixture,

$$p = H - E = \sum_{i=1}^N \rho_i h_i(T) + \rho e_t, \quad p = \sum_{i=1}^N \rho_i h_i(T) - \rho e_t + \rho \frac{u^2 + v^2}{2}. \quad (2.26)$$

The pressure in (2.25) and (2.26) must be equal, giving the equation

$$0 = \sum_{i=1}^N \rho_i h_i(T) - \rho e_t + \rho \frac{u^2 + v^2}{2} - \sum_{i=1}^N \rho Y_i \frac{\mathcal{R}}{W_i} T. \quad (2.27)$$

### 2.3.3 Navier-Stokes equations in Axisymmetric Form

The Navier-Stokes equations for two-dimensional, compressible, viscous, heat conducting flow in axisymmetric coordinates will be described. These equations consist of the continuity, energy, and momentum equations. With  $u_1 = u$  and  $u_2 = v$  as the axial and radial velocities (x and y velocities viewed in a cross section), the continuity equation is in differential form

$$\rho_{,t} + (\rho u_i)_{,i} = -\frac{1}{r} \rho v, \quad (2.28)$$

where  $\rho$  is the density and  $u_i$  represents the velocity in the x and y directions. The momentum equation is

$$(\rho u_j)_{,t} + (\rho u_i u_j)_{,i} + p_{,j} = (\tau_{ij})_{,i} - \frac{1}{r} \rho v^2, \quad (2.29)$$

where  $\tau_{ij}$  is the viscous stress tensor. The energy equation, is expressed as

$$(\rho e_t)_{,t} + (\rho u_i e_t)_{,i} + (u_i p)_{,i} = (\tau_{ij} u_j)_{,i} - q_{i,i} - \frac{1}{r} (\rho e_t + p) v, \quad (2.30)$$

where  $q_{i,i} = (-kT_{,i})_{,i}$  is the heat flux. This formulation is used in the spark ignition simulations discussed in section §9.

## 2.4 Shock-Driven Combustion

A canonical problem for shock-induced combustion in compressible flow is the detonation wave. A multidimensional detonation wave is described as having a quasi-periodic structure of transverse waves in addition to the leading shock-reaction front. A key repetitive substructure within gaseous detonations is the three-shock or triple point configuration that arises due to a fundamental instability. Here, Mach stems and incident shocks are part of the leading shock and the resulting reflected shocks are the transverse waves. However, Mach reflection structures can also be created when shock waves encounter solid boundaries. In the following, we will concentrate on the length scales required to obtain an accurate DNS simulation of just this fundamental triple point structure.

### 2.4.1 Length Scales and Resolution

In order to achieve accurate numerical simulation results, all physically relevant length and timescales must be resolved, regardless of the order of accuracy of the numerical method. For our method, having at least 10 to  $10^2$  cells across a length scale is required before one can begin testing for convergence. The detonation problem has multiple length scales, which requires care both in setting up an adaptive solution and in interpreting the results. The incident shock thickness is slightly larger than the nondimensional length scale used in the exact one-dimensional viscous shock solution. The shock thickness reads

$$\lambda_{\text{shock}} = \frac{8\mu(T)}{5} \sqrt{\frac{2}{\pi\rho_{\infty}p_{\infty}}}. \quad (2.31)$$

It is of the order of three to five mean free path lengths. Note that in a Mach reflection pattern, the smallest shock thickness is found in the Mach stem. In this thesis, we do not always resolve this length scale and in this sense we are performing pseudo-DNS. With shock-capturing, numerical dissipation will smear the shock in this region, yet, the other areas of the flow field are largely unaffected if their other scales (reactive and viscous) are resolved. The diffusive length scales, which include viscosity, heat, and mass diffusion, are most prevalent in the shear layer. On dimensional grounds, the viscous shear layer thickness,  $\delta_{\text{visc}}$ , grows as

$$\delta_{\text{visc}} \approx \sqrt{\nu t}, \quad (2.32)$$

where  $\nu = \frac{\mu}{\rho}$  is the dynamic viscosity, while the thermal heat conduction layer thickness,  $\delta_{\text{cond}}$ , and the mass diffusion layer thickness,  $\delta_{\text{mass},i}$ , grow as

$$\delta_{\text{cond}} \approx \sqrt{\frac{k_{\text{ref}} t}{\rho c_v}}, \quad \delta_{\text{mass},i} \approx \sqrt{\frac{D_i}{\rho} t}, \quad (2.33)$$

respectively. For hydrogen and hydrocarbon fueled detonations, typically the smallest scale is the viscous shear thickness, followed by the mass, and then the heat diffusion thickness length across the shear layer.

Also, for the chemical reactions, there are two different types of scales. A fundamental time scale comes from each Arrhenius rate equation and for a simple one-step model is

$$\tau_{\text{Arr}} = \frac{1}{AY_1 T^n} \exp\left(\frac{E_a}{RT}\right). \quad (2.34)$$

For a mixture with multiple reactions, associated timescales can differ by orders of magnitude. A further length scale of larger size is the laminar flame thickness, which results from the interaction of the chemical rate equations, diffusion, heat conduction, and convection. For our resolved results, we only run simulations for timescales capturing the flames in the laminar regime. Therefore, for the results presented, we check the resolution of the smallest length scale, the viscous shear layer thickness.

## 2.5 Nondimensionalization

A nondimensionalization or scaling of the fluid dynamic equations is important at the highest resolutions. Without a scaling the equations can be ill-conditioned for a large pressure and small time step (short diffusive and reactive time scale). When simulating diffusive flow with realistic physical parameters and using fine grids in order to show convergence, the time steps become so small that round-off errors and lack of precision pollute the results. Nondimensionalization mitigates this problem. In section §4 for our convergence tests, the nonreactive results were for a shock traveling into standard atmospheric conditions ( $T = 300$  K and  $p = 1.01325 \cdot 10^5$  Pa); however, the preliminary detonation simulations were for a shock propagating into a lower pressure of 6,700 Pa, for which a nondimensionalization was unnecessary.

### 2.5.1 Non-Reactive Navier-Stokes equations

In the nonreactive case, using the length and the time scaling  $x = L_\infty x^*$ ,  $y = L_\infty y^*$  and  $t = \frac{L_\infty}{a_\infty} t^*$ , respectively, the primitive variables are nondimensionalized as

$$u = a_\infty u^*, \quad v = a_\infty v^*, \quad \rho = \rho_\infty \rho^*, \quad p = \rho_\infty a_\infty^2 p^*, \quad T = \frac{a_\infty^2}{c_{p_\infty}} T^*, \quad (2.35)$$

with the  $*$  as nondimensional. The normalized caloric equation and ideal gas law for a single polytropic gas then reads

$$c_p(T) = c_{p_\infty} c_p^*(T^*), \quad R = c_{p_\infty} R^*, \quad p = \rho R T, \quad (2.36)$$

$$(\rho_\infty a_\infty^2 p^*) = (\rho_\infty \rho^*)(c_{p_\infty} R^*) \left( \frac{a_\infty^2}{c_{p_\infty}} T^* \right). \quad (2.37)$$

The validity of this nondimensionalization can be verified easily by substituting these variables into the Navier-Stokes equations and cancelling the factors to derive the results below. The nondimensional nonreactive compressible Navier-Stokes equations in two space dimensions are

$$\frac{\partial \rho^*}{\partial t^*} + \frac{\partial \rho^* u^*}{\partial x^*} + \frac{\partial \rho^* v^*}{\partial y^*} = 0, \quad (2.38)$$

$$\frac{\partial \rho^* u^*}{\partial t^*} + \frac{\partial \rho^* u^{*2}}{\partial x^*} + \frac{\partial \rho^* u^* v^*}{\partial y^*} = \frac{\partial \tau_{xx}^*}{\partial x^*} + \frac{\partial \tau_{xy}^*}{\partial y^*}, \quad (2.39)$$

$$\frac{\partial \rho^* v^*}{\partial t^*} + \frac{\partial \rho^* u^* v^*}{\partial x^*} + \frac{\partial \rho^* v^{*2}}{\partial y^*} + p = \frac{\partial \tau_{xy}^*}{\partial x^*} + \frac{\partial \tau_{yy}^*}{\partial y^*}, \quad (2.40)$$

$$\frac{\partial \rho^* e_t^*}{\partial t^*} + \frac{\partial \rho^* u^* (e_t^* + p^*)}{\partial x^*} + \frac{\partial \rho^* v^* (e_t^* + p^*)}{\partial y^*} = \frac{\partial (u^* \tau_{xx}^* + v^* \tau_{xy}^*)}{\partial x^*} + \frac{\partial (u^* \tau_{xy}^* + v^* \tau_{yy}^*)}{\partial y^*} \quad (2.41)$$

$$+ \frac{\partial q_x^*}{\partial x^*} + \frac{\partial q_y^*}{\partial y^*}, \quad (2.42)$$

where the stresses read

$$\begin{aligned} \tau_{xx}^* &= \mu^*(T^*) \left( 2 \frac{\partial u^*}{\partial x^*} - \frac{2}{3} \left( \frac{\partial u^*}{\partial x^*} + \frac{\partial v^*}{\partial y^*} \right) \right), \\ \tau_{xy}^* &= \mu^*(T^*) \left( \frac{\partial u^*}{\partial y^*} + \frac{\partial v^*}{\partial x^*} \right), \\ \tau_{yy}^* &= \mu^*(T^*) \left( 2 \frac{\partial v^*}{\partial y^*} - \frac{2}{3} \left( \frac{\partial u^*}{\partial x^*} + \frac{\partial v^*}{\partial y^*} \right) \right), \end{aligned} \quad (2.43)$$

and the heat transfer terms are

$$q_x^* = k^*(T^*) \frac{\partial T^*}{\partial x^*}, \quad q_y^* = k^*(T^*) \frac{\partial T^*}{\partial y^*} \quad (2.44)$$

with normalized mixture viscosity and normalized thermal conductivity

$$\mu = a_\infty L_\infty \rho_\infty \mu^*(T^*), \quad k = \rho_\infty a_\infty L_\infty c_{p_\infty} k^*(T^*). \quad (2.45)$$

## 2.5.2 Reactive Navier-Stokes equations for Thermally Perfect Mixtures

For  $N$  thermally perfect species, the normalization of the total and partial densities is  $\rho_\infty = \sum_{i=1}^N \rho_{i_\infty}$ ,  $\rho_i = \rho_\infty \rho_i^*$  and the normalized caloric equations (2.36) take the form

$$c_{p_i}(T) = c_{p_\infty} c_{p_i}^*(T^*), \quad h_i(T) = a_\infty^2 h_i^*, \quad R_i = c_{p_\infty} R_i^*. \quad (2.46)$$

The normalized mass diffusivities read  $D_i(T) = a_\infty L_\infty D_i^*(T^*)$  and, in case of chemical reaction, the normalized Arrhenius parameters are

$$E_i = a_\infty^2 E_i^*, \quad A_i = \frac{a_\infty}{L_\infty} A_i^*. \quad (2.47)$$

### 2.5.2.1 Navier-Stokes equations for Two Calorically Perfect Gases with One-Step Reaction

If only two calorically perfect gases with identical adiabatic coefficient,  $\gamma$ , are considered, (2.46) reduces to

$$c_p = \frac{\gamma R}{\gamma - 1}, \quad c_p = c_p c_p^*, \quad c_p^* = 1, \quad h_1 = q_0 + c_p T, \quad h_2 = c_p T, \quad q_0 = a_\infty^2 q_0^*, \quad R = c_p R^*, \quad (2.48)$$

where the normalized temperature is now given as  $T = \frac{a_\infty^2}{c_p} T^*$ . With the single reaction

$$\frac{d\omega_1}{dt} = \rho_1 A \exp\left(\frac{E_A}{R_u T}\right) = \rho_1 A \exp\left(\frac{E}{RT}\right), \quad (2.49)$$

the normalized Arrhenius parameters of (2.47) read

$$E = \frac{E_A}{W} = E_A \frac{R}{R_u}, \quad E = a_\infty^2 E^*, \quad A = \frac{a_\infty}{L_\infty} A^*. \quad (2.50)$$



## 2.6 Eigendecomposition

An eigendecomposition is needed for the numerical solution of the inviscid part of the reactive Navier-Stokes equations otherwise known as the reactive Euler equations. The eigen values and vectors are required to put the solution in characteristic form and also for approximate Riemann problem solutions, which are used by Roe's method and the shock detection method as described in §3.3 and 3.5.3.

The eigenvalues and eigenvectors of the thermally perfect multi-component Euler equations can be derived in a straightforward algebraic computation, cf. (40). For the state vector of conserved variables  $\mathbf{q} = (\rho u, \rho v, \rho e_t, \rho Y_1, \dots, \rho Y_N)^T$  the inviscid flux in the x-direction, for instance, satisfies  $\mathbf{f}^{\text{conv}} = \mathbf{A}(\mathbf{q})\mathbf{q}$ , with

$$\mathbf{A}(\mathbf{q}) = \begin{bmatrix} (3-\gamma)u & -\bar{\gamma}v & \bar{\gamma} & \phi_1 - u^2 & \dots & \phi_N - u^2 \\ v & u & 0 & -uv & \dots & -uv \\ H - \bar{\gamma}u^2 & -\bar{\gamma}uv & \gamma u & u(\phi_1 - H) & \dots & u(\phi_N - H) \\ Y_1 & 0 & 0 & u(1 - Y_1) & -uY_1 & \dots & -uY_1 \\ & & & -uY_2 & u(1 - Y_2) & & \vdots \\ \vdots & \vdots & \vdots & \vdots & \ddots & & -uY_{N-1} \\ Y_N & 0 & 0 & -uY_N & \dots & -uY_N & u(1 - Y_N) \end{bmatrix} \quad (2.51)$$

denoting the corresponding Jacobian. With eigenvalues  $\lambda_k = \{u - a, u, \dots, u, u + a\}$ , the matrix of right eigenvectors, defined by  $(\mathbf{A} - \lambda_k \mathbf{I})\mathbf{r}_k = 0$ , reads

$$\mathbf{R}(\mathbf{q}) = \begin{bmatrix} u - a & u & \dots & u & 0 & u + a \\ v & v & \dots & v & 1 & v \\ H - ua & u^2 + v^2 - \frac{\phi_1}{\bar{\gamma}} & \dots & u^2 + v^2 - \frac{\phi_N}{\bar{\gamma}} & v & H + ua \\ Y_1 & 1 & 0 & \dots & 0 & Y_1 \\ & 0 & & & & \\ \vdots & \vdots & \ddots & \vdots & \vdots & \vdots \\ Y_N & 0 & \dots & 0 & 1 & 0 & Y_N \end{bmatrix}, \quad (2.52)$$

where  $\phi_i = \frac{\partial p}{\partial \rho_i}$ , the partial derivative of the pressure with respect to the  $i$ -th species' density, is given by

$$\phi_i = \bar{\gamma} \left( \frac{u^2 + v^2}{2} - h_i \right) + \gamma R_i T, \quad (2.53)$$

with  $\bar{\gamma} = \gamma - 1$  and the total specific enthalpy  $H = h + \frac{u^2+v^2}{2}$ .

# Chapter 3

## Numerical Methods

The compressible, reactive Navier-Stokes equations are a mixed-type set of partial differential equations (PDEs) with stiff source terms, presenting a significant challenge for numerical simulation. The result is a multiscale problem containing sharp gradients whose discretized solution is highly sensitive to numerical dissipation. The hyperbolic part of the equations (the inviscid terms as modeled by the Euler equations) is often solved numerically by using a shock-capturing method specifically designed to be stable when discontinuities are present. However, these robust methods introduce numerical dissipation that pollutes the diffusive part of the equations. For a convective-diffusive equation, owing to the physical viscosity, there are no discontinuities in a fully resolved solution, yet, shock-capturing is still necessary to handle sharp gradients without spurious oscillations. Ideally, a method free of numerical dissipation is desired to accurately capture the diffusive terms. However, owing to their lack of shock-capturing dissipation, these schemes tend to lack robustness and stability in a structured adaptive mesh refinement (SAMR) framework. Because of these difficulties, a *hybrid method* has been developed, which combines the introduction of some numerical dissipation at sharp gradients, e.g., across shock waves, with a dissipation-free treatment with centered stencils in regions of smooth flow.

### 3.1 Background on Methods

The present numerical method combines and extends, both to high order and to the resolution of diffusive effects, numerical methods developed originally for large eddy simulation (LES) of turbulence (67, 123) and for efficient inviscid detonation simulation (40). We employ a hybrid WENO/centered-difference scheme (67, 123) with improved scheme switching (106). Dynamic mesh adaptation is used to handle

reactive flow problems of a multiscale nature, for which graded meshes (cf. Lele *et al.* (95)) are usually found insufficient. Our implementation is in flux form throughout, thereby ensuring conservation at scheme-matching boundaries, and uses a skew-symmetric form for the inertial fluxes (123), yielding improved overall kinetic energy conservation and stability. In general, our approach retains the benefits of low numerical dissipation away from shocks, the efficiency of an SAMR algorithm and the effectiveness of time-splitting for source term integration.

Aside from works such as (123, 107, 158, 117), which utilize the AMROC (Adaptive Mesh Refinement in Object-oriented C++) SAMR framework, hybrid WENO methods have mainly been applied on uniform or graded meshes. Recent examples include (2, 129, 115, 33, 96, 29). There has been much work in proving numerically and theoretically the stability of hybrid schemes. Adams *et al.* (2) addressed this problem, and Larsson and Gustafsson (96) give a detailed analysis, particularly proving the stability for a hybrid match between finite difference WENO and centered stencils. Their proof, using Kreiss or GKS theory (61), directly applies to our scheme’s framework in the uniform case, yet, is difficult to extend to the SAMR case with overlapping grids. A brief discussion is provided in §13.4 of (61), where the stability of overlapping grids is theorized to be stable when viewed as an overspecified boundary value problem and deemed provable at least in the one-dimensional case.

Another high-order (in fact fourth-order accurate) method for use with SAMR has been developed for the CHOMBO SAMR software (32) based on a globally conservative finite volume formulation. This approach, while well adapted to inviscid simulations, can suffer from numerical dissipation in smooth flow regions, impeding its suitability for small-scale diffusive and viscous phenomena. The problem is shared by the classical second-order accurate MUSCL (Monotone Upstream-centered Schemes for Conservation Laws) methods and by most pure WENO schemes, thereby motivating the present work.

Diffusive effects in reacting flows have become a topic of recent research interest. Day *et al.* (38), using the BoxLib software, have reported lower-order accurate, SAMR-based, finite volume simulations for subsonic turbulent flames that model detailed chemistry and diffusive mixing. For their flows, the compressibility is small and this allows use of a low-Mach-number formulation. A hybrid essentially nonoscillatory (ENO)/centered-difference method with third-order Runge-Kutta (RK) time integration was used by Fedkiw (52) for the simulation of reacting flow. Uniform grids were employed. Related simulations of diffusive compressible reacting flow with detailed chemistry have been conducted by Massa *et al.* (116). They utilized a third-

order in time, fourth-order in space Rusanov, Kutler, Lomax, and Warming (RKLW) scheme as described by Kennedy and Carpenter (86). This method is not monotone or total variation diminishing (TVD) and a numerical filter, which is not appropriate for shock-capturing and SAMR, was used to damp spurious oscillations. Neglecting shock waves, they conducted a two-dimensional simulation of an equivalent shear layer behind triple points in detonations. Double Mach reflection (DMR) simulations with viscosity and thermal conduction have been reported by Vas Ilev *et al.* (76). No-slip boundary conditions were used, which applies to shock-solid surface interactions rather than shock-shock interactions. Similar work has also been done for two- and three-dimensional, turbulent, compressible, reacting flow by Poludnenko *et al.* (130), using the fixed-grid, massively-parallel framework Athena-RFX. Their numerical method is based on a fully unsplit corner transport upwind (CTU) algorithm and an integration scheme using Colella-Woodward (PPM) spatial reconstruction in conjunction with an approximate nonlinear HLLC Riemann solver to achieve 3rd-order accuracy in space and second-order accuracy in time.

## 3.2 Methods

As a comparison, the Roe-HLL MUSCL second-order method was also used. For the initial verification and development purposes, the MUSCL method was useful. The improvement and extension of problems that were previously simulated with the second-order method, often without diffusive effects, is the focus of this work.

## 3.3 Roe-HLL MUSCL Second-Order Method

All modern high-resolution FV schemes are built upon first-order accurate upwind methods that utilize characteristic information. These methods are based on Roe's method, a method based on the linearization of the Godunov method. The Godunov method solves the full Riemann problem but is expensive to calculate at each cell boundary in the domain, thus the simpler Roe method (40) is most often employed.

Roe's second-order slope-limited finite volume method is second-order in space and time, and has the advantage over finite difference methods in that it includes both normal and tangential fluxes rather than just normal fluxes. Because very fine grids are being used to capture the length scales, this method has advantages over higher-order methods. Because it is faster, one can use finer grids.

Artificial oscillations at strong shock waves are moderated or avoided completely within the Roe scheme by adding numerical viscosity to the flux approximation via the entropy correction. Also, unphysical total energies and densities due to the Roe linearization are circumvented by switching to the robust HLL scheme. These corrections are combined for a Roe-HLL scheme with MUSCL (Monotone Upwind Schemes for Conservation Laws) variable extrapolation.

In MUSCL extrapolation, the cell-wise constant approximation of the Riemann problem is replaced by a linear or quadratic interpolation between the values of its left and right neighbors. This interpolation is second- or first-order accurate, depending on the local gradients in the solution, and the particular slope limiter used. The method is designed such that it is only first-order near shock waves, where the solution appears discontinuous. The best limiter for the Navier-Stokes equations appears to be van Albada limiting, as it has the least numerical dissipation as compared to the Minmod, Superbee, van Leer, and Monotized centered limiters.

The Roe method by itself has the problem of producing negative densities and energies for strong shocks. To avoid the erroneous behavior, the Roe method is replaced where necessary by the flux of the robust HLL method. The Harten-Lax-Van Leer (HLL) scheme is positivity preserving in density and energy, when the numerical signal velocities are within suitable bounds for the physical signal velocities. The HLL scheme is a Godunov-type method that uses a very simple approximative Riemann solver, which approximates the solution of the Riemann problem simply by two discontinuous waves.

### 3.4 Advancement to a high-Order Hybrid Scheme

The shock-capturing component of the present hybrid scheme uses a sixth-order accurate, symmetric enhancement of the classical WENO scheme as developed by Shu (80, 144). In the limit of smooth flow, the method obtains a 6th-order centered stencil. We presently utilize only hybrid WENO/centered-difference schemes for SAMR. Alternatives could also be *pure* WENO schemes with enhanced smoothness measures, such as the Mapped WENO schemes (65, 23), or schemes with improved stability properties, such as the monotonicity preserving schemes (9). Also of interest for nonsteady, reactive, compressible flows is the implementation of WENO with one-dimensional shock-fitting (66).

In the following section, WENO schemes are briefly described and the extension to a symmetric WENO method is elaborated. Also, the time-split approach for reactive

source terms, when using a Runge-Kutta integrator, is detailed.

### 3.4.1 ENO and WENO Schemes for Conservation Laws

ENO and WENO discretizations (144) have revolutionized the solution of nonlinear hyperbolic conservation laws, particularly for the multidimensional Euler equations, which are often used as an inviscid, hyperbolic, nondiffusive approximation of the mixed-type Navier-Stokes equations. This approximation is suited for the simulation of shock waves, contact discontinuities, and other nonsmooth flow features. ENO and WENO schemes have been specifically developed for problems containing both piecewise smooth solutions and discontinuities. They are designed to obtain arbitrarily high order of accuracy in smooth solution regions while minimizing the propagation of first-order errors obtained along discontinuities. WENO schemes are an extension of ENO. Instead of choosing from a group of stencils, the WENO approach uses a convex combination of all stencils. Smoother stencils are given larger weight, yet, at discontinuities, WENO performs exactly as ENO. In the limit of smooth regions, however, the WENO approach obtains a much higher order of accuracy. ENO and WENO schemes can either be finite difference or finite volume, yet, the finite difference variant is commonly chosen for reasons of efficiency (144). For the finite difference schemes, the wider the interpolation stencil, the higher the order of accuracy obtained; however, this is only true provided the solution is smooth. Using centered stencils at discontinuities causes undesirable oscillations in the numerical solution. These oscillations propagate through the domain and can create instabilities in the numerical solution.

When discontinuities are present, the global order of accuracy is always reduced to one (60). ENO, WENO, and, for example, discontinuous Galerkin finite volume methods will not by themselves obtain high order of accuracy near discontinuities. Therefore, these schemes are often referred to as *high-resolution* rather than *high-order* methods. In fluid mechanics, whenever shocks are *captured* (rather than *resolved* as possible with the Navier-Stokes equations), first-order accuracy is obtained. Note that high-resolution schemes are nonetheless useful because complex structures, not resolved by low-order methods, can be studied in greater detail. High order of accuracy can be achieved in some cases, for instance, when a shock-fitting method is used (66). Here, the discontinuity's velocity and shape is tracked, and at each time step the Rankine-Hugoniot equations for the shock are solved exactly. This is easily implemented for one-dimensional problems, yet too expensive in two and three space

dimensions. Difficulties also arise on how to track complex multidimensional structures, cf. (39). Thus, for all but the simplest problems, shock-capturing methods are currently still needed.

#### 3.4.1.1 WENO Reconstruction

For each interpolated flux, the smoothest stencil is chosen among the group of neighboring stencils. In a  $k$ -th-order ENO scheme,  $k$  candidate stencils are considered over a range of  $2k - 1$  cells, but only one stencil is used in the reconstruction. The basis of WENO is to take advantage of this by using a convex combination of all of them. Two properties are desired: ENO-like performance at discontinuities and the usage of all  $k$  stencils in the limit of a smoothly varying solution, yielding  $O(\Delta x^{2k-1})$  convergence. The convex combination is a linear combination of fluxes, where all coefficients (smoothness-biased weights),  $\omega_r$ , are nonnegative and sum up to one, i.e.,  $\omega_r \geq 0$  for  $r = 0, \dots, k - 1$  and  $\sum_{r=0}^{k-1} \omega_r = 1$ . The results from each stencil,  $S_r = \{x_{j-r}, \dots, x_{j-r+k-1}\}$ , are combined with the weights  $\omega_r$  to obtain the approximation of the boundary fluxes  $\hat{f}$ . The combination yields

$$\hat{f}_{j+1/2} = \sum_{r=0}^{k-1} \omega_r c_{r\kappa} f_{j-r+\kappa}. \quad (3.1)$$

Since we are using a structured nongraded mesh, the same set of coefficients,  $c_{r\kappa}$ , is used for each point value. This leads to an approximation of the derivative at the cell center in terms of point fluxes at the cell boundaries. The weights are designed for the limit of smoothly varying flow. In this limit, all smoothness measures are equal and the weights become the predetermined values such that all  $k$  stencils together, act as one large stencil that interpolates the  $2k - 1$  cells, hence obtaining  $(2k - 1)$ -th order of accuracy. The weights  $\omega_r$  approach the coefficients  $d_r$ , which, when multiplied appropriately by each stencil's coefficients  $c_{r\kappa}$  and summed, become exactly those coefficients for a polynomial with  $2k - 1$  interpolation points. Hence, in the limit of smooth solutions, the weights are equal to  $d_r$ , while for a discontinuity, some or all weights become zero, depending on if the discontinuity is located within or at the boundary of a cell. With a smoothness measure  $\beta_r$  for the  $r$ -th stencil defined, the weights are

$$\omega_r = \frac{\alpha_r}{\sum_{s=0}^{k-1} \alpha_s} \quad \text{with} \quad \alpha_r = \frac{d_r}{(\epsilon + \beta_r)^2}, \quad (3.2)$$



where  $\epsilon > 0$  is an arbitrary problem- and mesh-size-dependent parameter which can range from  $10^{-2}$  to  $10^{-30}$ . Shu (144) recommends  $10^{-6}$ . Depending on the type of derivative approximation (for example, with centered differences), numerous formulas for  $\beta_r$  are possible. Thus, measures reported in the literature are varied. Note that in deriving a smoothness measure, it is still required that the  $\beta_r$  become zero when a constant solution is encountered in order to ensure convergence to  $(2k - 1)$ -th order in smooth solution regions.

The optimal  $(2k - 1)$ -th-order stencil can be biased in a particular direction for upwinding or is unbiased for a symmetric centered scheme. For the present DNS, an optimal, symmetric, centered stencil is desired, because the numerical dissipation created otherwise pollutes the sensitive nature of the diffusive part of the solution.

#### 3.4.1.2 Characteristic Form

For the finite difference scheme, aside from solving the exact Riemann problem at the cell boundaries, the highest accuracy is obtained if a characteristic decomposition is adopted. Here, the system of equations are diagonalized using a local approximation of the Jacobian at each cell boundary. The state  $\mathbf{q}_j$  and flux  $\mathbf{f}(\mathbf{q}_j)$  are transformed into the characteristic state  $\mathbf{v}_j$  and flux  $\mathbf{g}(\mathbf{q}_j)$ , as detailed by Shu (144). The exact transformation is determined by the local eigenvectors at the cell boundary. It is unknown and must be approximated. The simplest way of doing this is to use the average state at the right and left cells. For fluid mechanics, an expensive but more accurate method is to use the Roe average, which is suitable for shock waves,

$$\mathbf{f}_{j+1} - \mathbf{f}_j = \mathbf{f}'_{j+\frac{1}{2}}(\mathbf{q}_{j+1} + \mathbf{q}_j)(\mathbf{q}_{j+1} - \mathbf{q}_j), \quad (3.3)$$

from which the eigenvectors of the Jacobian,  $\mathbf{f}'_{j+\frac{1}{2}}$ , can be determined. Note that the canonical eigendecomposition of the inertial fluxes of the Navier-Stokes equations is provided for completeness in appendix C. One important step remains before transforming the fluxes back from the characteristic space. A flux split is conducted, which separates the left- and right-moving contributions, based on the negative and positive characteristics. The most commonly used flux split is the Lax-Friedrichs flux splitting, where for the  $m$ -th component of the flux,

$$g_m^\pm(\mathbf{v}) = \frac{1}{2}(g_m(\mathbf{v}) \pm \alpha_m v_m), \quad (3.4)$$

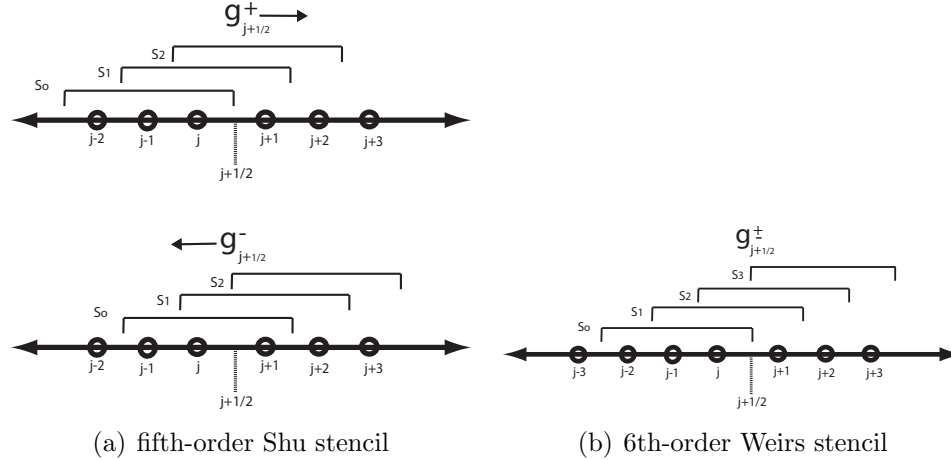


Figure 3.1: Set of candidate stencils for two different finite difference WENO methods using flux splitting. The positive and negative characteristic fluxes,  $g^+$  and  $g^-$ , respectively, are calculated at the cell boundary located at  $x_{j+\frac{1}{2}}$ .

is used. The coefficient  $\alpha_m$  is taken as the maximum of the range of the  $m$ -th eigenvalue in the solution over the whole domain, i.e.,

$$\alpha_m = \max_j |\lambda_{m,j}(\mathbf{q}_j)|. \quad (3.5)$$

With the positive and negative characteristic fluxes found, the finite-difference reconstruction procedure is used twice to derive the positive and negative fluxes at the cell boundaries. As shown in figure 3.1(a), two different sets of stencils and optimal stencils are used. In two space dimensions, the final form of the approximation of the point-wise time derivative for the  $(j, l)$ -th cell is

$$\frac{d\mathbf{q}_{jl}}{dt} = -\frac{1}{\Delta x} \left( \hat{\mathbf{f}}_{j+\frac{1}{2},l} - \hat{\mathbf{f}}_{j-\frac{1}{2},l} \right) - \frac{1}{\Delta y} \left( \hat{\mathbf{h}}_{j,l+\frac{1}{2}} - \hat{\mathbf{h}}_{j,l-\frac{1}{2}} \right). \quad (3.6)$$

### 3.4.2 Enhanced WENO Schemes

WENO schemes perform well for purely hyperbolic PDEs, yet, for mixed equations with physical diffusion, they introduce too much numerical dissipation that tends to artificially remove energy from the highest resolved wave numbers (160). This numerical damping arises from the upwinded, optimal stencils and the smoothness measures. Traditionally, finite difference approximations have been designed to maximize the order of accuracy. However, contemporary research interest in turbulent flow

has expressed the need for minimizing the approximation error of the small turbulent scales. The resulting finite difference schemes are based on *bandwidth*-optimized stencils (see (100)). For our application, DNS, these schemes are the basis for a more general *order*-optimized variant. Our order-optimized scheme includes the symmetric WENO stencils first developed for bandwidth-optimized schemes, e.g., WENO-SYM (160). Our implementation, which we call WENO/CD, is a hybrid approach, extended to an SAMR framework and configured for order optimization.

### 3.4.2.1 WENO-SYM

Weirs (160) used bandwidth optimization techniques to develop symmetric optimal stencils with reduced dissipation and greater resolving efficiency. Using Fourier analysis, the coefficients are chosen to resolve the high frequencies of interest instead of tailoring them for maximal order of accuracy. In this particular case, the optimal fifth-order 5-point stencil, originally constructed with three 3-point stencils, is changed to a symmetric 6th-order, 6-point stencil that is constructed with four 3-point stencils, as shown in figure 3.1(b). Then by bandwidth (rather than order) optimizing the coefficients, a 4th-order accurate optimal stencil is found with the desired spectral properties.

Note the differences between the WENO-SYM stencil and that of the original WENO as depicted in figure 3.1(a). The optimal WENO-SYM stencil is centered at the point at which the flux is being evaluated while the optimal WENO stencil is upwinded in order to mimic the flux in the characteristic directions. The latter is advantageous for correctly modeling the flow of information but introduces numerical dissipation which is undesirable for convergence when resolving small turbulent scales and diffusive mixing. In contrast to Shu's upwinded counterparts (144) only the smoothness measurement introduces dissipation into the WENO-SYM approach, cf. (160). Now with an extra stencil present and all stencils shifted as shown in figure 3.1(b), the WENO-SYM construction is performed with the unchanged stencils  $S_r$  but uses  $\omega_r \geq 0$  for  $r = 0, \dots, k$  with  $\sum_{r=0}^k \omega_r = 1$  and thereby reads

$$\hat{f}_{j+1/2} = \sum_{r=0}^k \omega_r c_{r\kappa} f_{j-r+\kappa}. \quad (3.7)$$

In the limit of smooth flow all  $k + 1$  stencils together act as one large stencil, which interpolates  $2k$  cells obtaining  $(2k)$ -th order of accuracy. For the formally 6th-order accurate WENO-SYM scheme, four 3rd-order-accurate ENO stencils are used. In

this order-optimized implementation for  $k = 3$ , the optimal weights,  $d_r$ , and the ENO stencils, as specified by  $c_{r\kappa}$ , are

$$\begin{aligned} d_r &= \left\{ \frac{1}{20}, \frac{9}{20}, \frac{9}{20}, \frac{1}{20} \right\}, \quad c_{1,\kappa} = \left\{ \frac{2}{6}, \frac{-7}{6}, \frac{11}{6} \right\}, \quad c_{2,\kappa} = \left\{ \frac{-1}{6}, \frac{5}{6}, \frac{2}{6} \right\}, \\ c_{3,\kappa} &= \left\{ \frac{2}{6}, \frac{5}{6}, \frac{-1}{6} \right\}, \quad c_{4,\kappa} = \left\{ \frac{11}{6}, \frac{-7}{6}, \frac{2}{6} \right\}. \end{aligned} \quad (3.8)$$

The evaluation of the smoothness measure for the WENO-SYM scheme is complicated by the fact that a discontinuity could be located exactly at the center of the stencil. This problem is effectively avoided by forcing the right most stencil to have a smoothness parameter,  $\beta_k$ , equal to zero when calculating the positive characteristic flux,  $\mathbf{g}_{j+\frac{1}{2}}^+$ , and similarly forcing the left most stencil to have  $\beta_0$ , equal to zero for the negative characteristic flux,  $\mathbf{g}_{j+\frac{1}{2}}^-$ . For the positive characteristic flux with  $k = 3$  and  $\beta_3 = 0$ , the remaining smoothness measures for  $r = 0, \dots, 2$  are defined as

$$\beta_r = \sum_{n=1}^2 \left( \sum_{l=1}^3 d_{r,n,l} f(q_{j-k+1+r+l}) \right)^2, \quad (3.9)$$

where the smoothness coefficients,  $d_{r,n,l}$ , are given by

$$d_{1,1,l} = \left\{ \frac{1}{2}, \frac{-4}{2}, \frac{3}{2} \right\}, \quad d_{2,1,l} = \left\{ \frac{-1}{2}, 0, \frac{1}{2} \right\}, \quad d_{3,1,l} = \left\{ \frac{3}{2}, \frac{-4}{2}, \frac{1}{2} \right\}, \quad (3.10)$$

$$d_{4,1,l} = \left\{ \frac{-5}{2}, \frac{8}{2}, \frac{-3}{2} \right\}, \quad (3.11)$$

and

$$d_{r,2,l} = \left\{ \sqrt{\frac{13}{12}}, -2\sqrt{\frac{13}{12}}, \sqrt{\frac{13}{12}} \right\}, \quad r = 0, \dots, 3. \quad (3.12)$$

In the limit of smooth flow, all smoothness measures approach zero. Thus, for example, when WENO-SYM is used near but not at shock waves, the equivalent WENO interpolation is still approaching a perfect, zero-dissipation, centered stencil.

### 3.4.2.2 WENO/CD

Hill *et al.* (67) and Pantano *et al.* (123) developed a robust hybrid WENO/tuned centered difference (TCD) method, which combines the TCD stencil with the WENO-SYM scheme. The centered difference stencil was bandwidth-optimized, specifically for weakly compressible decaying turbulence (123). The optimal WENO weights are chosen to match those of the TCD scheme thereby minimizing oscillations at the matching boundaries. The location of the scheme-switching boundary is defined by

a problem dependent switch. By using the relatively inexpensive TCD stencil predominantly in regions where the solution is smooth and WENO-SYM at and around discontinuities, the overall resulting WENO/TCD scheme performs faster and additionally has the spectral resolution desired in turbulence simulations. For DNS, however, where all scales are resolved, a symmetric order-optimized stencil is ideal. Therefore, for our application a WENO/CD rather than WENO/TCD method is used.

For schemes based on centered stencils, no numerical viscosity is present, yet care is needed to avoid nonlinear instabilities that may develop (123). Such instabilities can be alleviated by using a skew-symmetric formulation that conserves the kinetic energy (69) and prevents the convective terms of the momentum and energy equations from artificially producing or dissipating global kinetic energy. Without this, it has been found that in unstable flow simulations, the entropy of the system decreases with time, a clear violation of the second law of thermodynamics.

### 3.4.3 Stability

For WENO and other high-order spatial methods, at least second-order TVD (total variation diminishing) time integration is required for stability. Higher-order integrators, often up to fifth order, have been used, but can be very computationally expensive. Also, in viscous and reactive-flow simulations, the approximation error due to the spatial discretization is usually assumed to be dominant. Additionally, any temporal discretization exhibits its own numerical dissipation, but whose influence is assumed to be smaller than that introduced by the WENO interpolation or the upwinding. Recent research on the time integration of compressible flows has generally focused on efficiency and stability rather than the reduction of temporal numerical dissipation.

The commonly chosen time discretization for hyperbolic problems is the *method of lines*. The most popular methods used with the Euler equations are explicit TVD or strong stability preserving Runge-Kutta (SSPRK) methods, where each of these is designed for a specific  $n$ -th order of time accuracy,  $O(\Delta t^n)$ . Also, note that each TVD scheme has a critical Courant-Friedrichs-Lewy (CFL) number,  $\nu$ , above which the method is not guaranteed to be stable. A typical definition (for the 1D inviscid case only) would be  $\nu := \frac{\Delta t}{\Delta x} |\lambda_{\max}| \leq 1$ , where  $\lambda_{\max}$  is the maximal eigenvalue encountered in the domain at a particular time,  $t$ , (101). For PDEs with diffusion and convection, the latter relation needs to be adjusted (see section §3.6 for the case of two-dimensional

reactive Navier-Stokes equations).

Note that in practice we use the stability limits of linear systems of equations for our nonlinear system. The stability of a numerical method can be discussed in terms of having a bounded norm. For smooth problems, linearizing the equations and using, for instance, the  $L_2$ -norm is sufficient. However, for problems with discontinuities, a bounded  $L_2$ -norm does not ensure that the solution is nonoscillatory. For a nonoscillatory solution, at least the TV (total variation) or similarly the  $L_{\max}$ -norm must exist (58). The TV semi-norm is defined as  $\|u\|_{TV} = \sum_{j=0}^N |u_{j+1} - u_j|$ .

Finite volume methods with order of accuracy  $>2$  have not been proven to be TVD (121). The intrinsic complexity of WENO and hybrid methods with order  $\geq 3$  has made any analytical proof of nonoscillatory solutions difficult. In practice, SSPRK integration is therefore used for WENO methods. The SSP property is a very strong requirement that guarantees strong monotonicity in arbitrary convex functionals, for arbitrary starting values and arbitrary nonlinear, nonautonomous equations (58). The stability in the TVD sense of these methods is ensured for a particular CFL parameter,  $\nu$ , if the spatial discretization is also stable when used with the 1st-order accurate forward Euler method for temporal integration. However, proof of the TVD stability of WENO methods, that use spatial reconstruction with order 3 or higher, cannot be made as any such operator is linearly unstable when combined with the forward Euler method (157) or any explicit Runge-Kutta method with less than third-order accuracy. Nevertheless, SSPRK methods work well in practice with WENO operators and provide *essentially* nonoscillatory solutions.

Therefore, to date, in order to make some estimates of the stability region, analogies with second-order accurate spatial discretizations with forward Euler time-integration are commonly used. Note that the MUSCL method is second-order accurate both in space and time, and hence, its stability limit of  $\nu \leq 1$  cannot be used as an analogy (cf. (101)). WENO/ENO methods with second-order spatial accuracy are equivalent to slope-limited MUSCL schemes. When combining these methods with the forward Euler method in time, the analytical nonlinear TVD stability result (when using example equations such as the advection equation and Burger's equation and Harten's lemma) ranges from  $\nu \leq \frac{1}{2}$  to  $\nu \leq \frac{2}{3}$  (58), depending on the limiter. It is surmised that WENO/ENO hybrid methods should perform similarly; yet, for numerous problems, such as the ones presented in here, they perform so well in practice that convergence in the  $L_1$ - and  $L_2$ -norm can be established for  $\nu \leq 1$  (see below). This by no means proves that using  $\nu \leq 1$  will work for all possible solutions of the Euler and Navier-Stokes equations; a smaller value, such as  $\nu \leq \frac{1}{2}$ , is a generally safe choice. Note, that

for a full study of stability properties, an analysis of the convergence in the  $L_{\max}$ -norm is also needed.

### 3.4.4 Time Discretization

The typical third-order, three-step SSPRK(3,3) scheme, integrating from time step  $n$  to  $n + 1$ , is

$$q^{(1)} = q(n) + \Delta t L(q(n)), \quad q^{(2)} = \frac{3}{4}q(n) + \frac{1}{4}q^{(1)} + \frac{1}{4}\Delta t L(q^{(1)}), \quad (3.13)$$

$$q(n+1) = \frac{1}{3}q(n) + \frac{2}{3}q^{(2)} + \frac{2}{3}\Delta t L(q^{(2)}). \quad (3.14)$$

In this case, the *linear* stability limit is  $\nu \leq 1.434$  (58). For our *nonlinear* problem we used the limit  $\nu \leq 1$ . This method has an SSP coefficient  $c = 1$ , thereby permitting a time step size similar to the forward Euler method. The costs of the overall method are three times a forward-Euler update. In the last equation,  $L(q)$  is the numerical approximation of the spatial differential operator of the hyperbolic equation. For smooth solutions approximated with a three-step Runge-Kutta method (RK3) and sixth-order accurate WENO, we therefore have

$$q_t = L(q) + O(\Delta x^6) + O(\Delta t^3). \quad (3.15)$$

When viscous scales are also being resolved, we must consider how numerical viscosity from the spatial discretization scales with the CFL number. Using the advection-diffusion equation as an example, if one uses first-order Euler time integration, upwinding on the advection term and a centered difference approximation of the diffusive term, one finds that the numerical viscosity from the space discretization (which scales with  $\Delta x^4$  in this case) approaches zero as the CFL number approaches one. Therefore, for mixed-type PDEs with advection and diffusion terms, the highest possible stable time step should be used.

For the reactive simulations, owing to the large difference in time scales between the fluid dynamics and the reactive source terms, a time-splitting method is used in combination with the SSPRK(3,3) method of Ketcheson *et al.* (58). The stiff source terms are integrated separately in each cell utilizing the 4th-order accurate semi-implicit GRK4A method of Kaps and Rentrop (82), which avoids a globally coupled implicit problem. Using the Strang splitting approach, the maximal temporal order of accuracy is limited to two (101). An easily neglected detail for Runge-Kutta

schemes is the proper time update within the substeps, which is vital to ensure the correctness of time-dependent boundary conditions, as used, for instance, at SAMR-level boundaries when hierarchical time step refinement is employed. Therefore, we sketch the application of Strang splitting with SSPRK(3,3) below. With  $s_{step_\iota} = (1, -\frac{1}{2}, \frac{1}{2})$  the algorithm reads

Integrate chemistry from  $t$  to  $t + \frac{\Delta t}{2}$   
 for  $\iota = 1, 2, 3$ :  
   Update ghost cells at  $t + \Delta t \cdot s_{step_\iota}$   
   Integrate fluid to  $t + \Delta t \cdot s_{step_\iota}$   
 Integrate chemistry from  $t + \frac{\Delta t}{2}$  to  $t + \Delta t$ .

Also, for the nonreactive preliminary simulations, a 10-step, 4th-order Runge-Kutta scheme, SSPRK(10,4) (58), is used. While typically higher than 3rd-order SSP/TVD Runge-Kutta schemes have a stability coefficient smaller than one, for this unique scheme the stable region is for  $\nu = 6$ . This scheme is more efficient than SSPRK(3,3), however, is more difficult to integrate with a time-splitting scheme owing to its 10 as compared to 3 substeps. The 4th-order scheme is stable for the collective 10 steps with a CFL number six times larger than that of the 3rd-order scheme with its collective 3 steps, leading to a scheme that is almost twice as efficient. This 4th-order scheme can also be compared to the four-step 4th-order scheme, SSPRK(4,4), which has  $\nu = 0.624$  (59). Note that  $\nu$  corresponds to the total time-step as computed from the contribution of all substeps. The SSPRK(10,4) scheme reads

for  $\iota = 1, \dots, 10$ :  
   if ( $\iota \neq 10$ ):  $q^{(\iota)} = q^{(\iota-1)} + \frac{\Delta t}{6} L(q^{(\iota-1)})$   
   if ( $\iota = 5$ ):  $q^{(5)} = q^{(4)} + \frac{\Delta t}{6} L(q^{(4)})$ ,  $q^{(*)} = \frac{1}{25}q^n + \frac{9}{25}q^{(5)}$ ,  
                $q^{(5)} = 15q^{(*)} - 5q^{(5)}$   
   if ( $\iota = 10$ ):  $q(n+1) = \frac{6}{10}q^{(9)} + \frac{\Delta t}{10} L(q^{(9)}) + q^{(*)}$ .

### 3.5 SAMR Implementation

We utilize the fluid-solver framework AMROC, version 2.0, integrated into the Virtual Test Facility (47, 48, 46), which is based on the block-structured adaptive mesh refinement algorithm pioneered by Berger and Oliger (20) and refined by Berger and Colella (19). This algorithm is designed especially for the solution of hyperbolic partial differential equations with SAMR, where the computational grid is implemented



as a collection of rectangular grid components. Finite-difference methods are limited to either uniform grids or SAMR, while the finite-volume approach can also be used with unstructured meshes. The SAMR method follows a patch-wise refinement strategy. Cells are flagged by error indicators and clustered into rectangular boxes of appropriate size. Refined grids are derived recursively from the coarser level and a hierarchy of successively embedded grid patches is constructed. With its parallel distribution strategy, described in detail in (41) and (40), AMROC synchronizes the overlapping ghost cell regions of neighboring patches user-transparently over processor borders whenever boundary conditions are applied. An efficient partitioning strategy for distributed memory machines is used for high-performance simulations with MPI-library, cf. (41).

Typically, a second-order accurate Cartesian finite volume method (commonly of the MUSCL type) is used with SAMR implementations. AMROC has been employed very successfully with such schemes to efficiently simulate shock-induced combustion, particularly detonation waves, with simplified (24) and detailed chemical kinetics (42, 44). From the standpoint of DNS, however, the low numerical dissipation of the 6th-order hybrid WENO/CD scheme should provide faster grid-wise convergence than a second-order scheme. Also, it is predicted that for three-dimensional simulations, owing to the multiscale nature of the problem, it will be very expensive to obtain the desired resolution needed in the diffusive mixing and reaction zones. In the case where the simulation is memory rather than compute time limited (i.e., the available memory determines the highest possible resolution), the 6th-order accurate method yields superior results.

In order to prescribe nonrectangular domains in §4.2.3 we utilize a level-set-based embedded boundary method, that has been demonstrated and verified in detail for chemically reactive flows in (43).

### 3.5.1 Centered Differences in Flux-Based Form

WENO schemes themselves are naturally flux-based formulations, but a flux-based formulation of the centered-difference method is also required in order to enforce conservation at the WENO-SYM/CD scheme-matching points. For the  $j$ -th point at the cell center, the flux in the  $x$ -direction can be approximated with a 7-point centered stencil as

$$\left. \frac{\partial f}{\partial x} \right|_j \approx \frac{1}{\Delta x} (\alpha(f_{j+3} - f_{j-3}) + \beta(f_{j+2} - f_{j-2}) + \gamma(f_{j+1} - f_{j-1})), \quad (3.16)$$

where  $\alpha = 1/60$ ,  $\beta = -3/20$ , and  $\gamma = 3/4$  are constants selected for the 6th-order accurate stencil. However, in order to enforce conservation, we must consider the fluxes at the cell boundaries  $f_{j+\frac{1}{2}}$  and  $f_{j-\frac{1}{2}}$ . For the inertial fluxes, the local  $f_j$  at the cell centers are explicitly known. However, the local cell-centered diffusive fluxes must be calculated with a stencil similar to that of (3.16) as discussed in §3.5.2. These together are used to obtain the fluxes at the cell walls, obtaining the final desired conservative approximation of the flux at the cell center, i.e.,

$$\left. \frac{\partial f}{\partial x} \right|_j \approx \frac{1}{\Delta x} \left( f_{j+\frac{1}{2}} - f_{j-\frac{1}{2}} \right), \quad (3.17)$$

where  $f_{j+\frac{1}{2}}$  and  $f_{j-\frac{1}{2}}$  are calculated using

$$f_{j+\frac{1}{2}} = (\bar{\alpha}(f_{j+3} + f_{j-2}) + \bar{\beta}(f_{j+2} + f_{j-1}) + \bar{\gamma}(f_j + f_{j+1})) \quad (3.18)$$

with  $\bar{\alpha} = 1/60$ ,  $\bar{\beta} = -2/15$ , and  $\bar{\gamma} = 37/60$ . However, directly using this is not advised. Presently, we utilize the skew-symmetric form on each piece of the decomposed flux (see Pantano *et al.* (123) for details). The derivative of the flux at the cell center is obtained by adding the contributions from the cell boundaries in (3.17). Note that in this formulation, conservation is ensured but at the cost of a second-order error at cell interfaces where the centered difference (CD) stencil is matched with the WENO-SYM scheme. Since WENO is only used at shock waves, this loss of accuracy is negligible compared to the dominating first-order error along the discontinuity. The forced conservation ensures the stability of the method in an SAMR framework.

### 3.5.2 Diffusive-Flux Approximation

The approximation of the diffusive fluxes shares the previously encountered problem that the numerical fluxes must be calculated at the cell walls in a conservative fashion. For orders of accuracy greater than two, it is difficult to obtain derivatives (nonlinear combinations of first and second derivatives) at the cell walls without allowing for stencil widening. To obtain a 6th-order accurate diffusive-flux approximation, the fluxes need to be first evaluated at the cell centers. However, in order to obtain these approximations, first derivatives of the velocities, mass fractions, and temperatures, must be calculated. For this a standard 7-point centered stencil for the derivative is used. As an example for the velocity, the derivative in the  $y$ -direction of the  $v$ -velocity

is calculated as

$$\left. \frac{\partial v}{\partial y} \right|_l = \frac{1}{\Delta y} (\alpha(v_{l+3} - v_{l-3}) + \beta(v_{l+2} - v_{l-2}) + \gamma(v_{l+1} - v_{l-1})), \quad (3.19)$$

where  $l$  denotes the cell index in the  $y$ -direction. The appropriate diffusive-flux terms are then known at the cell centers with 6th-order accuracy. Yet, for the SAMR framework, fluxes at the cell walls are needed. Therefore, these cell-centered values are interpolated to the cell walls using (3.17) such that, when the wall fluxes are combined with (3.18), the resulting flux at the cell center is conservative at the scheme boundaries and of the desired 6th order of accuracy. In this case, the final cell-centered flux is influenced by a total of 12 cells for each direction. Hence, 6 ghost/boundary cells are required in the SAMR implementation. One may devise a way to calculate the wall fluxes directly in a way that only uses 6 cells for 6th-order accuracy, however, difficulties arise when attempting to calculate cross-derivative terms, such as  $\tau_{xy}$  (cf. appendix 2.5), as it is not straightforward to simultaneously use less than 12 cells and ensure a conservative form.

### 3.5.3 Hybrid Method Boundary Flagging

The WENO/CD scheme requires an explicit switch, from regions of smooth flow (using CD) to regions of extremely high gradients, that require WENO, such as shocks. The normalized curvature of pressure and density was used by Hill and Pullin (67). However, this flagging criterion can be sensitive to the resolution of the mesh in the sense that a smooth flow can appear almost discontinuous if a sufficiently coarse mesh is employed. The problems encountered with this switch motivated development of an alternative, shock-detection based technique (106). The new technique is robust, accurate, and efficient. While reminiscent of shock-fitting in terms of location strong shock waves, it preserves efficiency by not requiring a deformable mesh.

The shock-based detection is suitable for the high-speed DMR problems, studied in depth below, because the shocks continually bound the mixing layer as shown in figure 3.2. The technique uses an approximate Riemann solver to detect the existence and orientation of strong shock waves, while ignoring weak ones. The approximate solution to the Riemann problem is computed using Roe-averaged quantities from the given left ( $L$ ) and right ( $R$ ) state. Liu's entropy condition allows for characterizing the type of the wave encountered at the characteristic associated with the eigenvalues  $u \pm a$  (shock or rarefaction wave). A shock is produced if and only if the central state

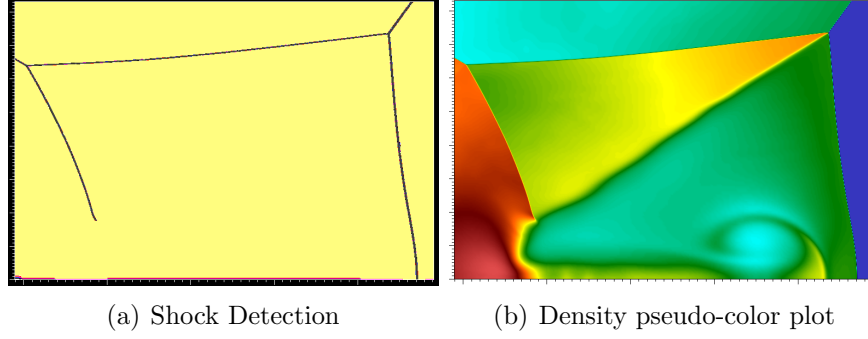


Figure 3.2: Shock detection applied to the viscous double Mach reflection problem of §4.2.3.

satisfies the condition

$$|u_R \pm a_R| < |u_* \pm a_*| < |u_L \pm a_L|. \quad (3.20)$$

Here,  $a_{L,R}$  is computed by evaluating the speed of sound,  $a = \sqrt{\gamma p / \rho}$ , at the left or right cell faces, and the central state  $(u_*, a_*)$  corresponds to the Roe averages,

$$u_* = \frac{\sqrt{\rho_L} u_L + \sqrt{\rho_R} u_R}{\sqrt{\rho_L} + \sqrt{\rho_R}}, \quad a_* = \sqrt{(\gamma_* - 1)(h_* - \frac{1}{2} u_*^2)}, \quad (3.21)$$

where

$$\begin{aligned} h_* &= \frac{\sqrt{\rho_L} h_L + \sqrt{\rho_R} h_R}{\sqrt{\rho_L} + \sqrt{\rho_R}}, & c_{p,*} &= \frac{\sqrt{\rho_L} c_{p,L} + \sqrt{\rho_R} c_{p,R}}{\sqrt{\rho_L} + \sqrt{\rho_R}}, \\ \gamma_* &= \frac{c_{p,*}}{c_{p,*} - R_*}, & R_* &= \frac{\sqrt{\rho_L} R_L + \sqrt{\rho_R} R_R}{\sqrt{\rho_L} + \sqrt{\rho_R}}, \end{aligned} \quad (3.22)$$

and  $h_*$ ,  $\gamma_*$ ,  $c_{p,*}$ , and  $R_*$  are the Roe-averaged specific enthalpy, heat ratio, specific heat for constant pressure, and gas constant, respectively. When testing the validity of the inequalities (3.20), a threshold value  $\alpha_{\text{Liu}}/a$  is considered to eliminate weak acoustic waves that could be easily handled by the CD scheme. For better efficiency and flexibility, this criterion is combined with a geometrical test based on a mapping of the normalized pressure gradient,  $\theta_j$ , that reads (106)

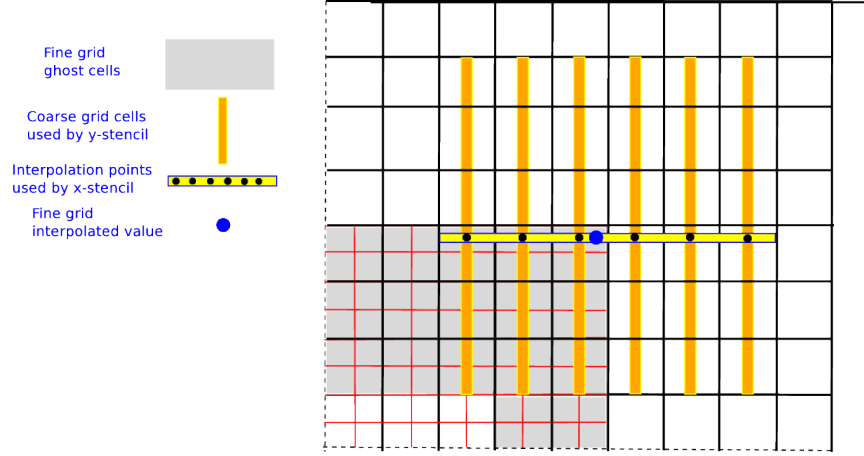
$$\phi(\theta_j) = \frac{2\theta_j}{(1 + \theta_j)^2}, \quad \text{with} \quad \theta_j = \frac{|p_{j+1} - p_j|}{|p_{j+1} + p_j|}. \quad (3.23)$$

If equation (3.20) is satisfied for a cell wall bounded by cells  $j$  and  $j + 1$  with values different by at least  $\alpha_{\text{Liu}}/a$  and also  $\phi(\theta_j) > \alpha_{\text{Map}}$  holds true, then WENO is set to be used at the cell wall. This algorithm is applied independently in each spatial

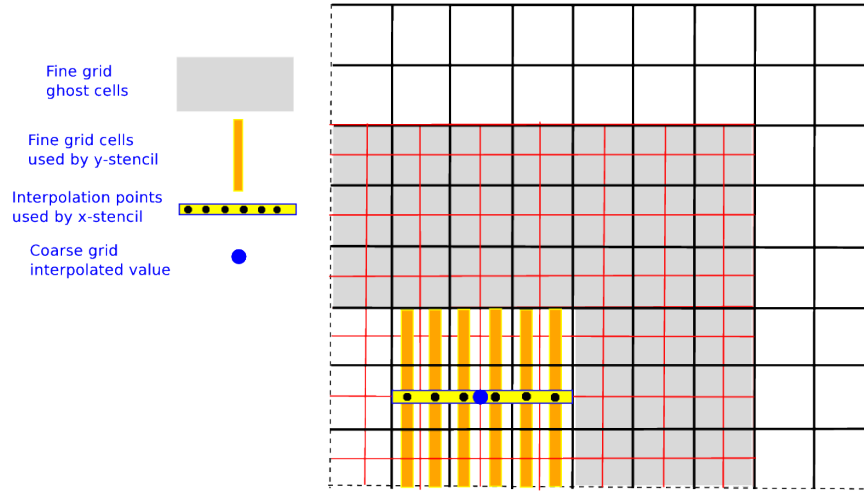
direction and we additionally employ it in multiple rotated frames of reference. The latter allows us to efficiently detect shocks that are not grid aligned. In our two-dimensional simulations, to be discussed below, we use the shock-detection criterion also for rotational angles  $\pm 45$  and  $\pm 135$  degrees to capture shock waves perpendicular to the diagonal directions of the mesh.

### 3.5.4 Higher-Order Accurate Hybrid Prolongation and Restriction

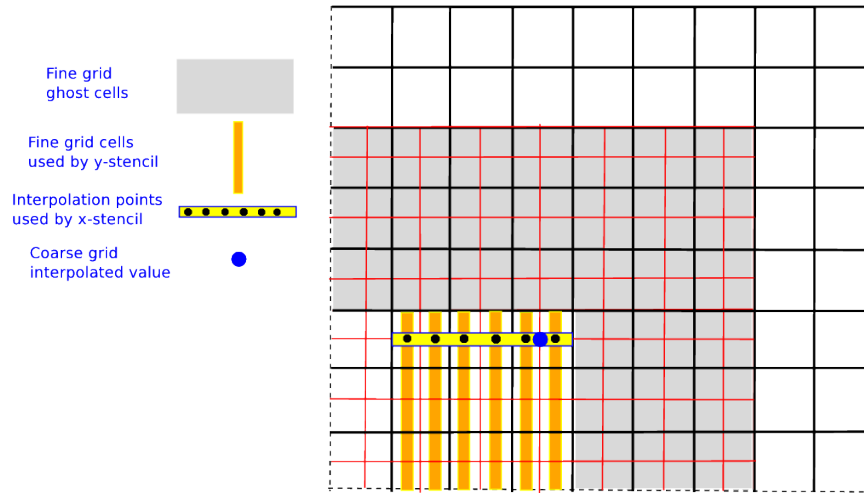
Prolongation involves the interpolation of cell-centered vector of state variables at a coarse level to the next finest level’s ghost or newly refined interior cells. Restriction involves the interpolation (for finite difference methods) or just simple averaging (for finite volume methods) of the fine level states onto the underlying coarse level mesh. We have extended the prolongation and restriction operators commonly used (cf. (19)) from first-order to fifth-order accuracy. In order to construct the interpolation stencils, the Aitken method (122), based on Lagrange interpolation, is used sequentially in each spatial direction. The coefficients are calculated recursively allowing for different refinement factors, for example 2, 4, or 8 times finer grids. Wherever possible, centered stencils are selected as shown in figures 3.3(a) and 3.3(b). Exactly centered or slightly upwinded (by half a cell width) stencils are used in most cases. For coarse cells adjacent to mesh boundaries, as in figure 3.3(c), a stencil upwinded by one cell is required, which is a result of having 6-point fifth-order accurate stencils when 6 ghost cells are available. With our implementation, owing to the treatment of the time step stability criterion as described in the appendix 3.6, WENO is *not* needed at coarse/fine SAMR boundaries for stability. The hybrid prolongation and restriction operators have been applied successfully both with reactive and nonreactive simulations using the WENO/CD method and the shock-based discontinuity detection. With the fifth-order accurate operators, overall 6th-order convergence was found in the two-dimensional verification problems which had smooth flow. At present, these operators are unconstrained and permit local conservation errors within the order of accuracy of the used interpolation. We note that where a discontinuity is flagged, for example with the shock-based detection, the operator defaults to the stable first-order accurate interpolation. One can view this method as a simplified version of mesh interface “WENO” interpolation. In this respect, by making the WENO smoothness measures accessible to the prolongation and restriction functions, fifth-order fully upwinded stencils could be used at the shocks. However, in our case the option of de-



(a) Prolongation: coarse grid to fine ghost cells, upwinded



(b) Restriction: fine to coarse grid underlying cells, centered



(c) Restriction: upwinded case

Figure 3.3: Fifth-order accurate stencils used by the hybrid-order prolongation and restriction. These stencils are used when nondiscontinuous flow is encountered. Note, that all stencils are centered except for the boundary coarse grid cells set in the restriction operation.

faulting to first-order accurate interpolation at discontinuities is chosen for simplicity.

### 3.5.5 Adaptive Mesh Refinement

As an example of how the Navier-Stokes equations can be fully resolved, we show some results for a supersonic mixing jet. Relative to the viscous length scale (which is determined by the gradients of the velocity), there are approximately 100 cells. Shown in figure 3.4(a) are some zoomed in views of the results to demonstrate the detail captured.

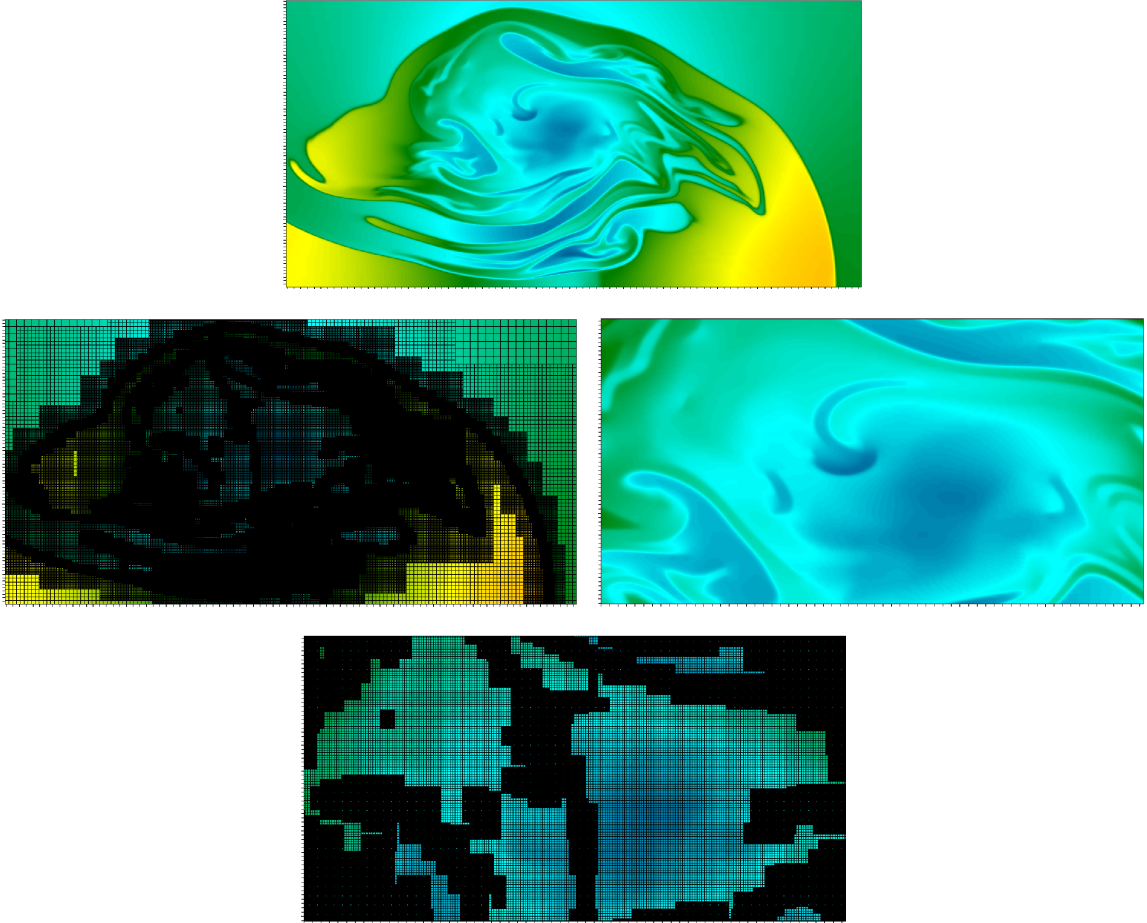


Figure 3.4: AMR for the density of a fully resolved viscous jet with AMROC

### 3.5.6 Multi-Component Chemistry Solver

The detailed multi-component chemistry and transport are implemented through the use of the CHEMKIN-II library (85). This chemical kinetics package is utilized to eval-

uate the reaction rates, enthalpies, specific heats, and transport coefficients according to a particular reaction mechanism and thermodynamic model. The temperature is found by applying a standard Newton method to an implicit temperature equation. If the Newton method does not converge in a reasonable number of iterations, a standard bisection technique is applied. The bisection method is always guaranteed to converge (40). In order to speed up the evaluation of temperature-dependent specific heats and enthalpies, two constant tables are constructed for each species during the start-up of the computational code (45).

### 3.5.7 Accuracy of the Roe Linearization

To determine the accuracy of the numerical method, the size and order of magnitude truncation error must be investigated. To gain some insight, the one dimensional advection-diffusion equation is discussed,

$$\frac{\partial \phi}{\partial t} + u \frac{\partial \phi}{\partial x} = K \frac{\partial^2 \phi}{\partial x^2}, \quad (3.24)$$

Now, consider the Beam-Warming Method (101). For simplicity of argument, the advection equation is considered to determine the influence of the approximate advective derivatives on the numerical diffusion and dispersion. In this case the finite difference method uses a second-order approximation of the derivatives. As in the first order upwinded method, it is assumed that  $u > 0$ ,

$$\phi_i^{n+1} = \phi_i^n - \frac{\Delta t}{2\Delta x}(3\phi_i^n - 4\phi_{i-1}^n + \phi_{i-2}^n) + \frac{\Delta t^2}{2\Delta x^2}(\phi_i^n - 2\phi_{i-1}^n + \phi_{i-2}^n). \quad (3.25)$$

In this case the modified equation is

$$\frac{\partial \phi}{\partial t} + u \frac{\partial \phi}{\partial x} = \frac{-1}{6}u\Delta x^2(2 - 3C + C^2)\frac{\partial^3 \phi}{\partial x^3} + \dots \quad (3.26)$$

The lowest-order error is of order  $\Delta x^2$  and is dispersive in nature. The numerical viscosity is of order  $\Delta x^3$  and scales with the fourth derivative. This method is the 1D linearized analogue to the second-order sloped limited Roe methods for multi-dimensional nonlinear hyperbolic problems. For the Euler equations in particular, the beam-warming method represents the linearized version of a stencil in which one particular characteristic variable found along a positive characteristic, therefore,  $u$  corresponds to the local  $u \pm a$  characteristic speed, where  $a$  is the sound speed. Therefore, when using a "high-resolution" flux/slope limited Finite volume method,



with adequate resolution, the numerical viscosity scales with  $\delta x^3$  and is practically zero. However, one must also note that is only true when the approximate Jacobian (eigenvalue decomposition in Roe's method for example) has a lowest order error of  $\Delta x^2$ ,

$$\frac{\partial \phi}{\partial t} + f(\phi) = 0, \quad (3.27)$$

$$\frac{\partial \phi}{\partial t} + A \frac{\partial \phi}{\partial x} = 0, \quad (3.28)$$

$$A(\phi(x), \phi(x + \Delta x)) = \frac{\partial f(\phi(x + \Delta x/2))}{\partial x} + O(\Delta x^2). \quad (3.29)$$

This means the Roe linearization must be second-order accurate, which for it is for the Euler equations.

### 3.6 Stability Criterion

Special care must be taken when defining a stable, explicit, time-step criterion for mixed type nonlinear PDEs. By considering a straightforward explicit finite difference scheme for the closely related multidimensional but scalar advection-diffusion equation with constant coefficients

$$\frac{\partial \phi}{\partial t} + u \frac{\partial \phi}{\partial x} + v \frac{\partial \phi}{\partial y} = K_x \frac{\partial^2 \phi}{\partial x^2} + K_y \frac{\partial^2 \phi}{\partial y^2}, \quad (3.30)$$

an approximate criterion for explicit methods for the Navier-Stokes equations is constructed. The stability criterion for a finite difference method for (3.30) is found by Von Neumann stability analysis. Then using this results as an analogue, a combined stability criterion for explicit schemes for the Navier-Stokes equations is derived. The parameters resulting from this analysis are

$$\alpha_x = \frac{2K_x \Delta t}{\Delta x^2}, \quad C_x = \frac{u \Delta t}{\Delta x}, \quad \alpha_y = \frac{2K_y \Delta t}{\Delta y^2}, \quad C_y = \frac{v \Delta t}{\Delta y}, \quad (3.31)$$

where  $\alpha_{x,y}$  and  $C_{x,y}$  are the diffusion parameters and the Courant numbers for (3.30), respectively. The stability criterion for a hybrid finite difference method with forward in time, upwinded advection (backward space) and centered diffusion (FT-BS/CS) scheme in two space dimensions is simply (68)

$$\alpha_x + C_x + \alpha_y + C_y \leq 1. \quad (3.32)$$

### 3.6.1 Non-Reactive Explicit Stability Criterion

To determine the stability limit for the used schemes for the nonreactive single-component Navier-Stokes equations one must look at each of the four conservation equations and determine the corresponding Courant numbers and diffusion parameters. For all four equations, the Courant number is the typical CFL number as for the inviscid Euler equations, cf. §3.4.4. The continuity equation for the density has only the Courant number stability criterion. The two momentum equations have the Courant number and a diffusion parameter, where the equivalent  $K_x$ ,  $K_y$  values for an advection-diffusion equation analogue are both  $\frac{4}{3} \frac{\mu}{\rho}$ . In the equation of the total energy density, the dissipative term from the viscosity does not directly affect the stability of  $e_t$  and therefore the diffusion parameter comes from the heat conduction term, where now the analogous condition is  $K_{x,y} \equiv \frac{k}{c_v \rho}$ , with  $k$  denoting the heat diffusivity and  $c_v$  the specific heat at constant volume,  $c_v = c_p - R$ . Then, one splits the convective and diffusive parts, and the maximum time steps are constrained by different convective and diffusive scales. The maximum time step is limited by the combination of the convective CFL number with the diffusion parameters from viscosity and conductivity in the  $x$ - and  $y$ -direction. For example, just from the  $x$ -direction, there is

$$\nu_{\text{conv},x} = \frac{\Delta t}{\Delta x} \max |\lambda|, \quad (3.33)$$

and the diffusive “CFL analogue” parameters are

$$\nu_{\text{diff,visc},x} = \frac{8\mu\Delta t}{3\rho(\Delta x)^2}, \quad \nu_{\text{diff,cond},x} = \frac{2k\Delta t}{c_v\rho(\Delta x)^2}. \quad (3.34)$$

The complete stability condition encompassing convection, viscous diffusion, and heat diffusion is

$$\nu = \max( \nu_{\text{conv}} + \nu_{\text{diff,visc}}, \nu_{\text{conv}} + \nu_{\text{diff,cond}} ) \leq 1, \quad (3.35)$$

where in the two-dimensional case those quantities take the forms

$$\begin{aligned} \nu_{\text{conv}} &= \frac{\Delta t}{\Delta x} \max(|u| + a) + \frac{\Delta t}{\Delta y} \max(|v| + a), \quad \nu_{\text{diff,visc}} = \frac{8\mu\Delta t}{3\rho(\Delta x)^2} + \frac{8\mu\Delta t}{3\rho(\Delta y)^2}, \\ \nu_{\text{diff,cond}} &= \frac{2k\Delta t}{c_v\rho(\Delta x)^2} + \frac{2k\Delta t}{c_v\rho(\Delta y)^2}. \end{aligned} \quad (3.36)$$

Note that in this case the stability limit is computed from the contribution of the CFL numbers for all dimensions rather than taking the maximum of each dimension separately. The viscous and heat conduction scales are separated as they affect the stability of the momentum and energy equations separately. One must also note that

in the case of using the SSPRK(10,4) scheme, the complete stability criterion is for  $\nu \leq 6$ , rather than  $\nu \leq 1$ , cf. §3.4.4. This criterion is for the total  $\Delta t$ , after all substeps have been taken. If one considers each substep separately, then on average the CFL number is for  $\nu_{avg} \leq 0.6$ .

### 3.6.2 Reactive Multicomponent Explicit Stability Criterion

The stability of the two-dimensional multi-component, reactive Navier-Stokes equations is found in the same fashion as for the nonreactive equations. The difference is now that the mass-averaged density, viscosity, and thermal conductivity are used for the convective, viscous, and thermal criterion. However, the mass diffusion of each species must be considered separately. In this case, the explicit stability condition is

$$\nu = \max( \nu_{\text{conv}} + \nu_{\text{diff,visc}}, \quad \nu_{\text{conv}} + \nu_{\text{diff,cond}}, \quad \nu_{\text{conv}} + \nu_{\text{diff,mass}} ) \leq 1, \quad (3.37)$$

with  $\nu_{\text{diff,mass}} = \frac{D_i}{(\Delta x)^2} + \frac{D_i}{(\Delta y)^2}$ , where  $D_i$  is the mass diffusion parameter of the  $i$ -th species, cf. §2.3.

# Chapter 4

## Verification

### 4.1 Preliminary Verification Study

A systematic verification study of the described hybrid WENO/CD method within an SAMR framework has been conducted. The presentation starts with nonreacting and reacting diffusive perfect gas flows in one space dimensions, and considers some two-dimensional benchmarks subsequently. This work has also appeared in Ziegler et al. (166).

#### 4.1.1 One-Dimensional Viscous Shock

An analytical one-dimensional solution of a stationary viscous shock profile was used to verify the implementation separately in the  $x$ - and  $y$ -directions. The analytical solution is formulated in nondimensional form, where the upstream density, pressure, and velocity (indexed with 0) in addition to an equivalent perfect gas mean free path are used as scaling parameters. See Kramer (92) for the implicit solution (with Prandtl number of  $\frac{3}{4}$  and  $\gamma = 1.4$ ), which is expressed as a function of the Mach number and specific heat ratio, and relates the nondimensional velocity and position. The specific mean free path, if only used as a length scale, can be arbitrary. For the adopted solution it is  $\lambda_0 = \frac{8\mu}{5} \sqrt{\frac{2}{\pi \rho_0 p_0}}$ . The density, pressure, and hence the total energy are found with the relations,

$$\rho u = \rho_0 u_0, \quad \bar{u} = \frac{u}{u_0}, \quad \frac{p}{p_0} = \frac{-M^2((\gamma - 1)\bar{u}^2 - (\gamma - 1))) - 2}{2\bar{u}}. \quad (4.1)$$

By using the analytical solution as an initial condition, the Navier-Stokes equations were marched forward in time until the computation reached a stationary state. Typical shock profiles are shown in figure 4.1, where exact and numerical solutions are

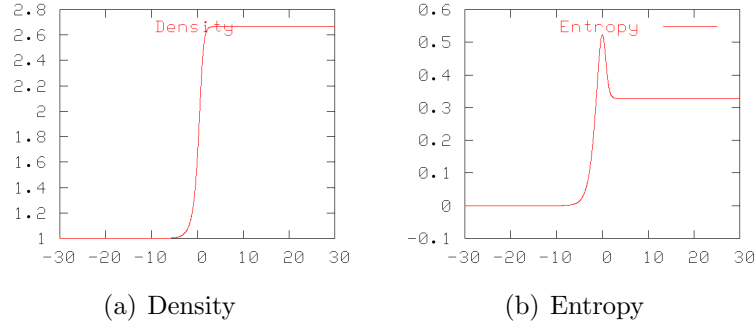


Figure 4.1: Analytical and numerical solution for the one-dimensional steady shock wave (visually no difference).

indistinguishable. The  $L_1$ -error norm of the difference between the exact and the numerical solution was then used to verify 6th-order convergence of WENO and CD solvers, with viscous and heat conduction terms, for a perfect gas. Since this test case has a smooth solution, the WENO and CD methods were tested separately. The low convergence rates at coarse resolution (cf. table 4.1) are the result of an insufficient number of points spanning the shock thickness, and the WENO and CD stencils (6 points wide), but particularly, the viscous flux stencils (12 points wide) show degraded convergence. This is generally true for all possible length scales encountered in a simulation. Note that for this and all following verification studies, because finite difference rather than finite volume methods are used, cell centered rather than cell averaged values are used in convergence tests.

Cells	Density $L_1$ -error	rate	Momentum $L_1$ -error	rate	Total energy $L_1$ -error	rate
Pure CD						
256	2.31E-6	-	1.71E-5	-	1.62E-5	-
512	7.08E-7	1.71	2.73E-7	5.97	3.36E-6	2.27
1024	1.14E-8	5.96	4.38E-9	5.96	5.44E-8	5.95
2048	1.81E-10	5.98	6.94E-11	5.98	8.59E-10	5.99
Pure WENO						
256	2.78E-5	-	4.01E-5	-	1.41E-4	-
512	1.03E-5	1.43	8.49E-6	2.24	4.45E-5	1.66
1024	2.36E-7	5.45	2.09E-7	5.34	1.03E-6	5.43
2048	5.19E-9	5.51	1.75E-8	3.58	2.52E-8	5.35

Table 4.1:  $L_1$ -error norms for the three state variables of the viscous shock test problem. For the pure WENO method the  $\epsilon$  value, cf. equation (3.2), was set to  $10^{-4}$ .

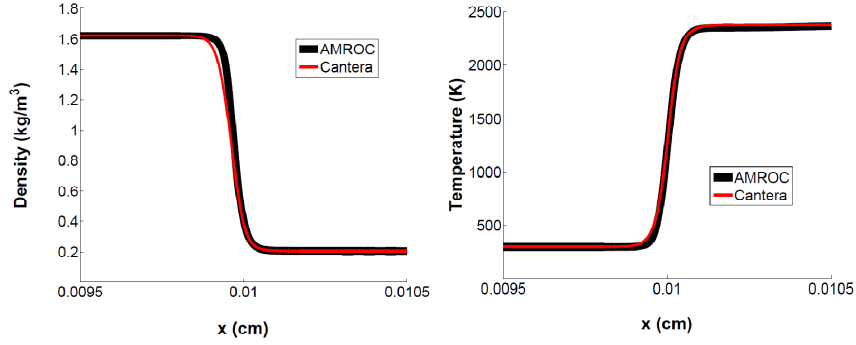


Figure 4.2: Multicomponent laminar flame with detailed transport. Comparison is with the steady solution of CANTERA.

#### 4.1.2 Mass Diffusion/Heat Diffusion Analogy

The two-dimensional analytical heat equation solution was used to verify the mass diffusion of the two-species model. This analytical solution is based on the diffusion of a delta function. Using a 2D Fourier transform the solution is found as a symmetrical Gaussian function.

The exact solution at a time  $t = t_0$  as a function of the  $x$  and  $y$  position is

$$\Delta\rho = \frac{1}{4\pi t} e^{\frac{-x^2}{4t}} e^{\frac{-y^2}{4t}}, \quad (4.2)$$

$$\rho_{product} = \frac{1}{2}(1 + \Delta\rho), \quad (4.3)$$

$$\rho_{reactant} = \frac{1}{2}(1 - \Delta\rho). \quad (4.4)$$

We choose a time of  $t_0 = \frac{1}{4}$  as the initial condition and observe that the  $\Delta\rho$  value follows the exact solution.

#### 4.1.3 Two-Species Laminar Flame Propagation

Using **CANTERA** to construct a reference solution, we designed a perfect gas, two-species, one-step chemistry model that approximates the propagation of a laminar flame in one dimension. For this model we matched the flame velocity and temperature by changing the species' heat release, specific heat, and molecular weight. Also, an approximate one-step reaction rate and activation energy was chosen,

$$\dot{\omega} = -AT^n\rho\lambda e^{-\frac{E_a}{RT}}. \quad (4.5)$$

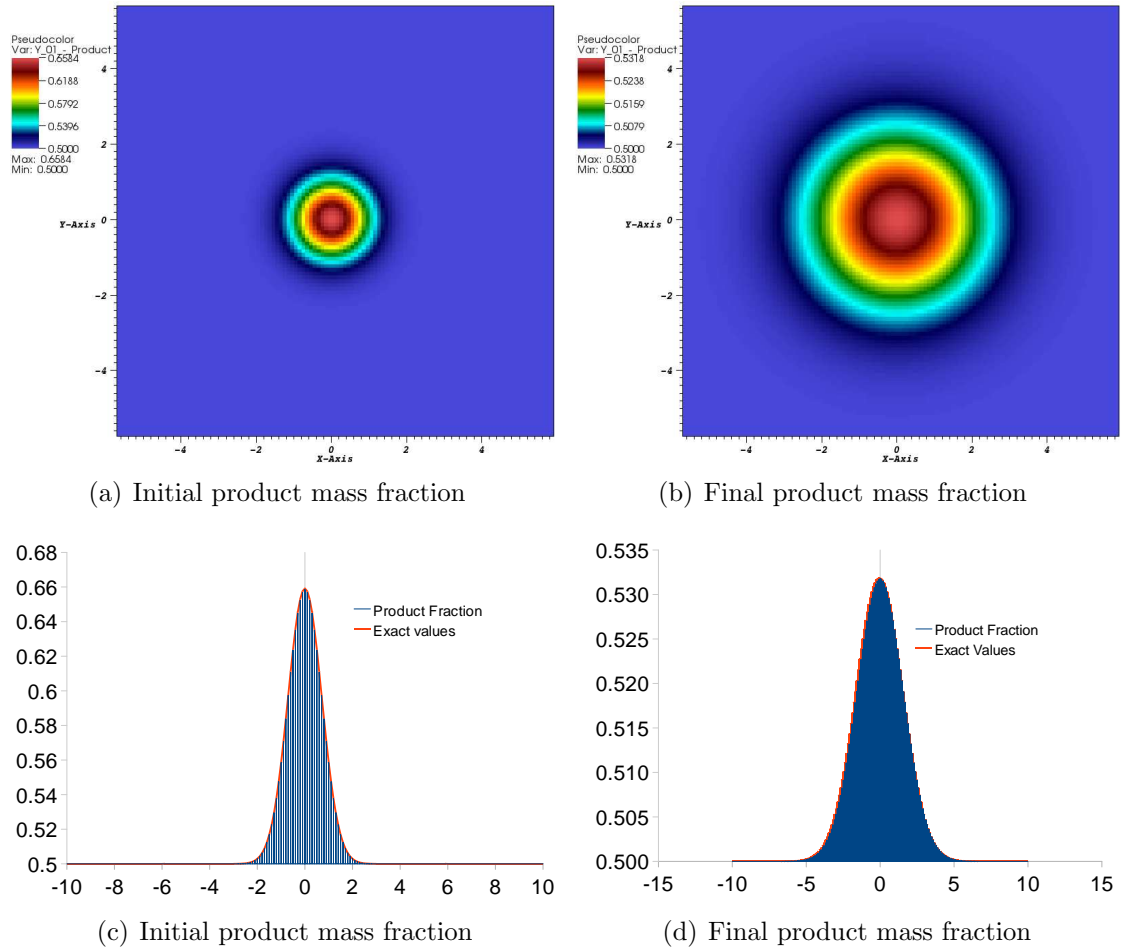


Figure 4.3: Verification of product/reactant mass diffusion with comparison to the heat equation.

When  $\lambda$ , the reaction progress variable is specified as the mass fraction of the reactants, then  $\dot{\omega}$  is the mass production rate for the reactant.  $A$  is the pre-exponential factor,  $n$  the temperature factor (zero in our model),  $E_a$  the activation energy in units of (energy/mass), and  $R$  the gas constant. Note that if the common units of (energy/mol) are used for the activation energy, then the universal gas constant  $\mathcal{R}$  must be used.

The laminar flame speed is defined as the velocity at which reactants propagate through a stationary flame front, see Williams(164) §5.1. In this case, the reactants are approaching the flame front at a constant speed, and then are accelerated to a higher speed as they react and expand. figure 4.4, shows the convention, which one notes is similar to that for a steady shock front.

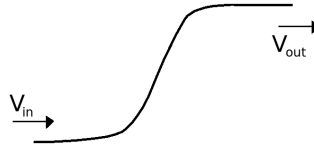


Figure 4.4: Particle speeds of reactants and products in a steady laminar flame

The laminar flame velocity is determined mainly by the energy equation, where there is a balance of heat conduction and mass diffusion of the different enthalpies of the reactants and products. For a one-step model, there is the diffusion of the heat release, which is transported by the products' and reactants' mass diffusion mechanisms. These diffusion rates are controlled by the mass and thermal diffusion coefficients which are functions highly dependent on temperature and inversely dependent on pressure.

We used a simple one-step mechanism with CANTERA's FreeFlame model and mixture transport to obtain an exemplary solution shown in figure 4.5(b) for a mixture starting at standard temperature and pressure. Our parameters, which were obtained by modifying the CANTERA argon mechanism and adding a reaction are shown in figure 4.2.



Property	Value	Units	Comments
Initial Density	1.623	kg/m <sup>3</sup>	density at 300 K, 1 atm
Reactant Specific Heat ( $C_p$ )	20.79	J/mol*K	$C_p/R$ in cti file (1st polynomial coefficient)
Product Specific Heat ( $C_p$ )	20.79	J/mol*K	$C_p/R$ in cti file (1st polynomial coefficient)
Gamma $\gamma$	1.67		calculated from $C_p/C_v$
Heat Release $q$	1074.86	kJ/kg	$R^*(\Delta a_s^\circ)$ where $\Delta() = ()_R - ()_P$
Activation Energy $E_a$	17000	cal/mol	chosen as part of one-step model
	71128	J/mol	common units
Pre-exponential A	9.62E+07	s <sup>-1</sup>	chosen as part of one-step model
Temperature Power n	0		no $T^n$ dependence of reaction rate

Table 4.2: Input parameters for one-step steady flame model

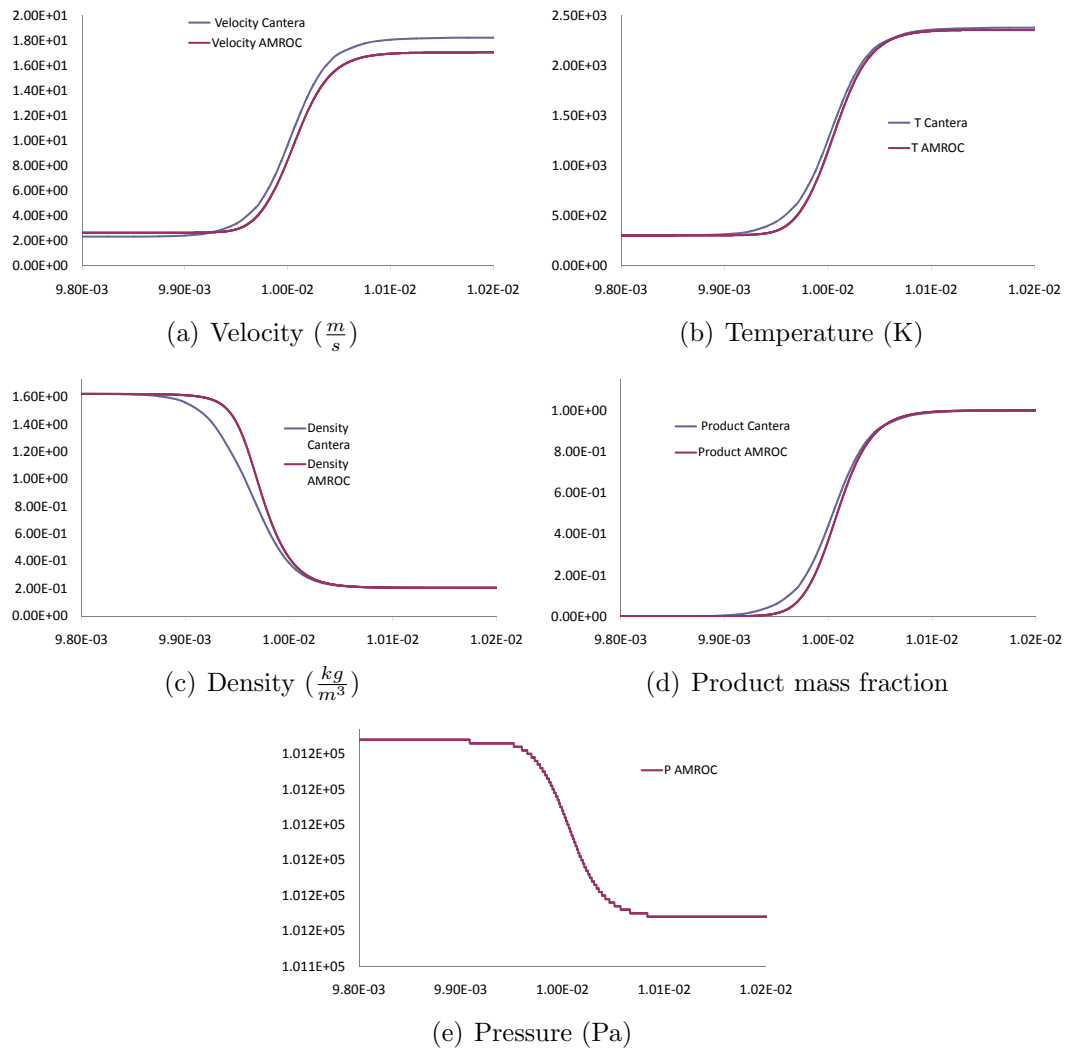


Figure 4.5: CANTERA and AMROC comparison for the 1D laminar flame

#### 4.1.3.1 One Dimension

Using the 1D reactive flow equations in AMROC a laminar steady flame was simulated and compared the reference solution produced with CANTERA. We used a two-species model with the total energy defined by the heat release per unit mass parameter,  $q$ .

$$\gamma = \gamma_1 = \gamma_2, p = \rho RT, R = R_1 = R_2, \quad (4.6)$$

$$\rho = \rho_1 + \rho_2, \rho_1 = \rho Y_1, \rho_2 = \rho Y_2, \quad (4.7)$$

$$\rho e_t = \frac{p}{(\gamma - 1)} + \frac{1}{2}\rho(u^2 + v^2) + \rho_2 q, \quad (4.8)$$

$$e_t = \frac{p}{(\gamma - 1)\rho} + \frac{1}{2}(u^2 + v^2) + qY_2. \quad (4.9)$$

$$(4.10)$$

This is equivalent to having product and reactant enthalpies of the form

$$h_1 = h_0 + c_p T, \quad (4.11)$$

$$h_2 = h_0 + q_0 + c_p T, \quad (4.12)$$

$$h_1 - h_2 = h_{prod} - h_{react} = \Delta h_{reaction} = -q_0. \quad (4.13)$$

Also, note that in general for a two-species model, the sound speed used in the numerical simulation is the frozen sound speed, where

$$c = \sqrt{\frac{\gamma p}{\rho_1 + \rho_2}}, \quad (4.14)$$

$$\gamma = 1 + \frac{X_1}{\gamma_1 - 1} + \frac{X_2}{\gamma_2 - 1}, \quad (4.15)$$

$$X_1 = \rho \frac{Y_1}{W_1}, X_2 = \rho \frac{Y_2}{W_2}, \quad (4.16)$$

where  $X_i$  is the mole fraction and  $W_i$  is the molar mass;

Now, for the special case of a one-dimensional model assuming perfect gases, reactants and products having the same molecular weight, constant conductivity and mass diffusivities, and zero viscosity, the conservation equations for mass, momentum,

and energy are as follows,

$$\frac{\partial(\rho Y_1)}{\partial t} + \frac{\partial(\rho u Y_1)}{\partial x} = \frac{\partial}{\partial x} \left( \rho D \frac{\partial Y_1}{\partial x} \right) + \dot{\omega}_1, \quad (4.17)$$

$$\frac{\partial(\rho Y_2)}{\partial t} + \frac{\partial(\rho u Y_2)}{\partial x} = \frac{\partial}{\partial x} \left( \rho D \frac{\partial Y_2}{\partial x} \right) + \dot{\omega}_2, \quad (4.18)$$

$$\frac{\partial(\rho u)}{\partial t} + \frac{\partial(\rho u^2 + p)}{\partial x} = 0, \quad (4.19)$$

$$\frac{\partial(\rho e_t)}{\partial t} + \frac{\partial(\rho u(e_t + p))}{\partial x} = \frac{\partial}{\partial x} \left( \rho D q_0 \frac{\partial Y_2}{\partial x} \right) + \frac{\partial}{\partial x} \left( k \frac{\partial T}{\partial x} \right), \quad (4.20)$$

where  $Y_1$ ,  $Y_2$ ,  $D$ , and  $k$  are the reactant and product mass fractions, mass diffusivity, and thermal diffusivity. First, using constant conductivity and mass diffusivities, we started the laminar flame using a compressed and pressurized region of products. By the ideal gas law this corresponds to an increase in temperature. After a transient period, a steady propagating laminar flame resulted. Initially, a weak shock wave travels out slightly raising the temperature and pressure in front of the flame. There is an expansion fan behind the shock wave, which cools reactants close to ambient conditions.

In this first simulation using constant diffusivities corresponding the ambient values, the laminar flame speed was found to be about half of that expected from CANTERA, which uses a temperature dependent transport model. Subsequently, another simulation was conducted using temperature dependent conductivity and temperature and pressure dependent mass diffusivity that match CANTERA's. The temperature dependent Sutherland law is used for the viscosity and conductivity, however, to match the CANTERA solution, the viscosity was neglected,

$$\mu = \mu_{ref} \left\{ \frac{T}{T_{ref}} \right\}^{\frac{3}{2}} \frac{T_{ref} + s_\mu}{T + s_\mu}, \quad (4.21)$$

$$k = k_{ref} \left\{ \frac{T}{T_{ref}} \right\}^{\frac{3}{2}} \frac{T_{ref} + s_k}{T + s_k}. \quad (4.22)$$

The following equation was used for the mass diffusivity,

$$D = D_{ref} \left\{ \frac{D}{D_{ref}} \right\}_k^{1.71} \frac{p}{p_{ref}}, \quad (4.23)$$

where  $p_{ref}$  is defined as atmospheric pressure. For our temperature ranges of 300 to 2500 K, these approximate functions are very close to CANTERA's as shown in

figure 4.6.

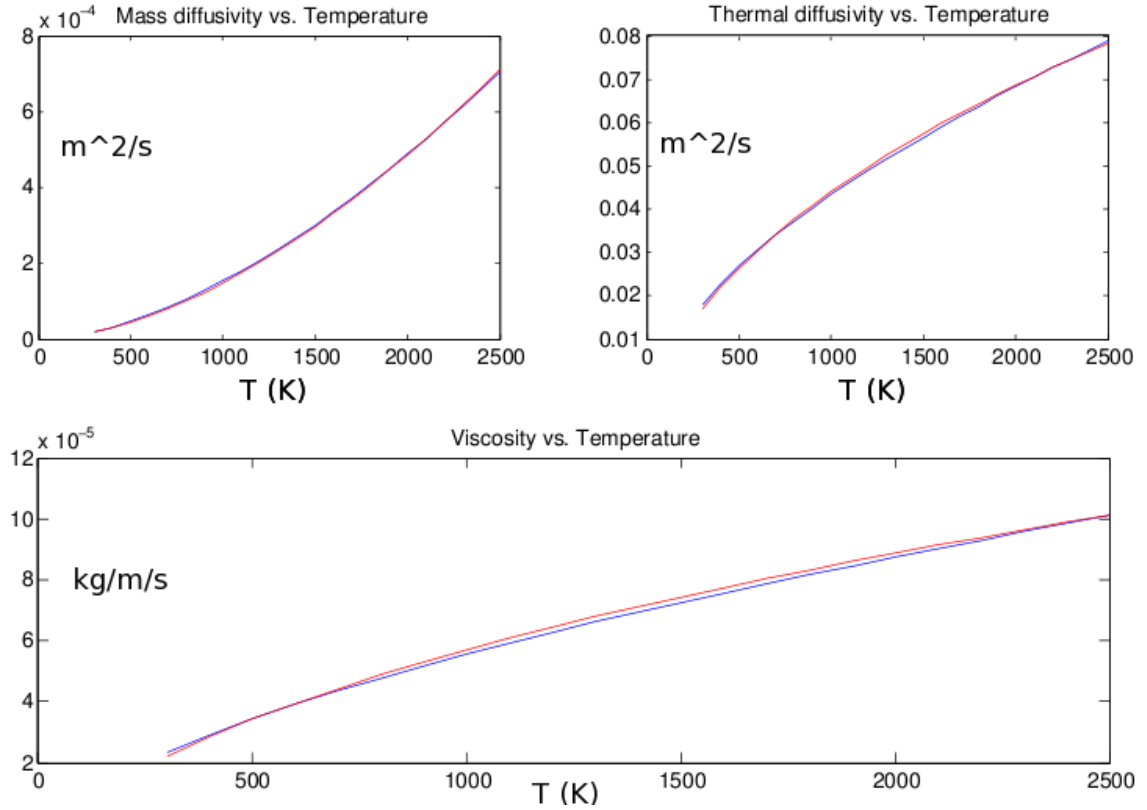


Figure 4.6: Comparing the Transport Properties to CANTERA's results for  $T = 300$  to 2500 K

Using the temperature and pressure dependent transport values, the results were much closer. The discrepancies are surmised to be the result of CANTERA using a constant pressure assumption in its solution (the momentum equation is ignored), and the slight differences in the transport properties. Since the CANTERA solution is not exact for the momentum equation, there are differences in the steady state results between the full diffusive Navier-Stokes (ignoring viscosity) equations of AMROC and the CANTERA energy and continuity based result.

#### 4.1.4 One-Dimensional Steady Laminar Flame with Multi-component Detailed Chemistry

As a multi-component verification of flows with chemistry, we compared our solution for a 4-species one-step model of hydrogen-air combustion using CHEMKIN-II and

the full one-dimensional reactive multi-component Navier-Stokes equation to the approximate FreeFlame model of CANTERA<sup>1</sup> using the same mixture transport and kinetic model. The flame velocity and temperature were matched to that of a typical hydrogen-air flame by changing the heat release and one-step Arrhenius reaction rate and activation energy. Physical transport properties were used for the H<sub>2</sub>O, N<sub>2</sub>, H<sub>2</sub>, O<sub>2</sub> mixture.

The small discrepancies in the compared solutions are expected and interpreted as the result of CANTERA using a constant pressure assumption in its solution. Since the CANTERA solution is not exact for the momentum equation, there are slight differences in the steady state results to the full diffusive Navier-Stokes equations of AMROC. For our AMROC solution, the CANTERA result is used as the initial condition and the solution undergoes a transient process (as the pressure adjusts) to reach a slightly different steady state. To the authors' best knowledge, there exist no analytical or semi-analytical, implicit solutions for multi-component, reacting, diffusive flow. The difficulty is primarily due to modeling both mass diffusion and pressure gradients. Therefore, a comparison to CANTERA's widely accepted approximate flame solution was warranted.

#### 4.1.4.1 Two Dimensions

In axisymmetric coordinates we simulated the evolution of a laminar flame, for an initial condition as box of hot products. First, similar to the unreactive cases, a shock wave (in this case very weak) propagates out and pre-compresses and pressures the surrounding fluid. Then heat conduction and mass diffusion (as in the 1D case viscosity is neglected) show their effects, as shown in figure 4.7(a). First we observe how a low energy flame propagates in axisymmetric coordinates with the symmetry BCs, but with out the influence of solid boundaries as will later be the case for an electrode surface. These 2D results are different from the 1D reference solution mainly with the fact the simulation is not in the reference frame of a flame front.

#### 4.1.5 One-Dimensional Unsteady Detonation

An unsteady reactive one-dimensional problem was used to verify the interaction of the time-split chemistry terms with the reactive fluid solver. A standard unsteady detonation problem with specific heat  $\gamma = 1.2$ , nondimensional heat release  $q = 50$ , activation energy  $E = 50$ , gas constant  $R = 1$ , reaction rate coefficient  $A = 230.75$ ,

---

<sup>1</sup><http://www.cantera.org>

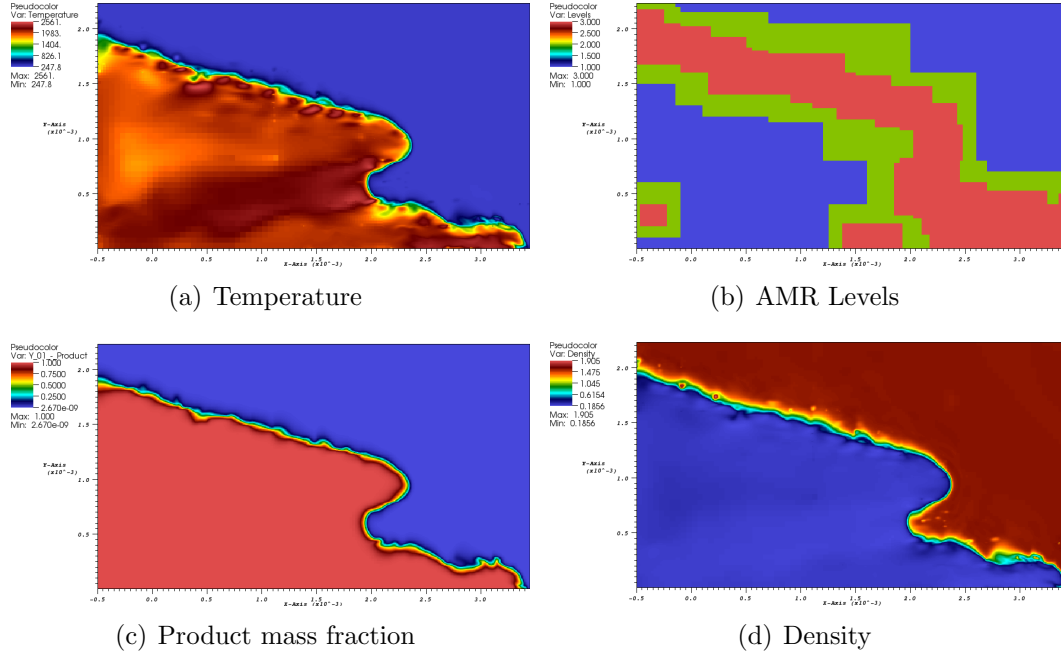
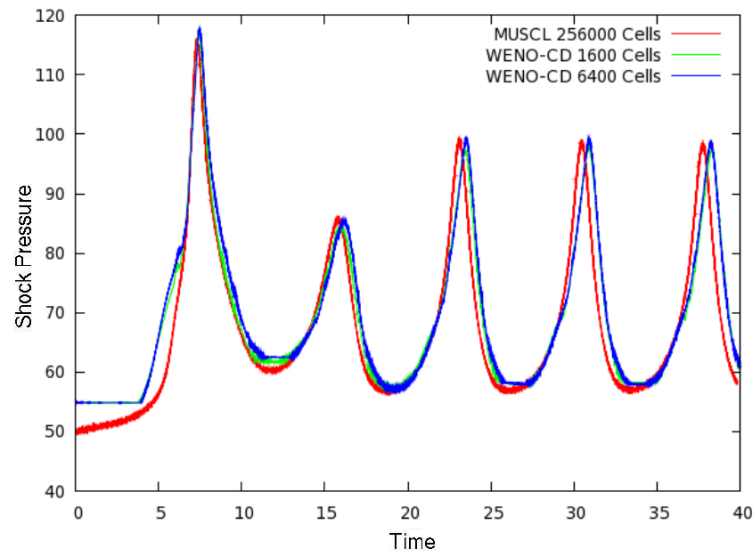


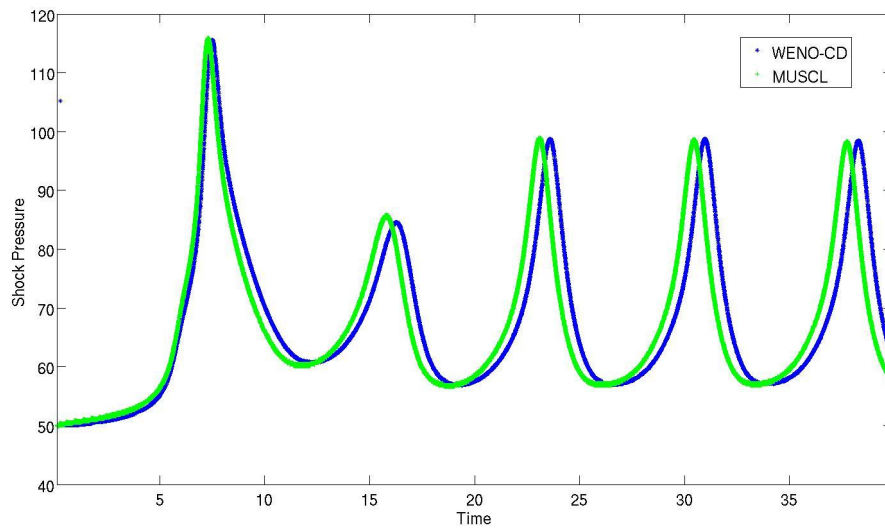
Figure 4.7: Preliminary unresolved axisymmetric laminar flame results

and overdrive  $f = 1.6$  is adopted to compare to the single mode period solutions found in (75) and (40). The initial condition is the same as that used by Hwang *et al.* (75), using a discontinuous ambient and post-detonation state. Deiterding (40) used the steady Zel'dovich, Von Neumann, and Doering (ZND) solution as the initial condition, yet, it was found that for the WENO method, the post-detonation solution is better suited as the initial nonperiodic solution decays faster. The shock pressure was determined two ways, first using a local maximum, and alternatively by detecting the shock position. Because shock-capturing, rather than shock-fitting, is used, there are oscillations in the shock pressure owing to the unavoidable errors of the shock moving back and forth across the grid (when the reference frame is determined by the known average shock velocity). The best results were found by detecting the time-dependent shock position and using this to calculate the pressure, which depends analytically on the shock velocity. This shock velocity was found by using second-order differentiation of the data points corresponding to the position of the local shock pressure peaks. Using this indirect extrapolation of the velocity leads to smoother data in figure 4.9 (50). This procedure has typically not been used by previous sources.

As shown in figure 4.8(a), after the initial transient relaxation, a periodic solution is reached. The features of interest, i.e., the period and amplitude of the pressure oscillation, agree, although the relaxation period is slightly different for each method.



(a) Uniform grid



(b) 4 levels of SAMR

Figure 4.8: Maximum shock pressure versus time. Uniform grid: Compares the WENO/CD solutions on a grid of 1,600 and 6,400 cells to a MUSCL solution with 16,000 cells. 4 levels: Comparing a WENO solution with 4 refinement levels (2, 2, 2, 2) and a base grid of 1600 cells to the highly resolved MUSCL solution with 16,000 cells. In each case the domain size is 80 and the final time is 40.

The magnitude and development of the initial start-up errors are grid resolution and method dependent, which is characteristic for this unstable problem (40). For a fairly coarse uniform grid, 20 and 80 cells per half-reaction-zone length,  $L_{\frac{1}{2}}$ , the WENO/centered difference hybrid scheme is fairly close and converges to a highly resolved MUSCL solution with 200 cells per  $L_{\frac{1}{2}}$ . In these tests a domain of size 80 was used. In figure 4.8(b), the dynamic mesh adaptation is tested by using a WENO solution with a base grid of 20 cells per  $L_{\frac{1}{2}}$  along with 4 refinement levels, which corresponds to 320 cells per  $L_{\frac{1}{2}}$  near the shock front.

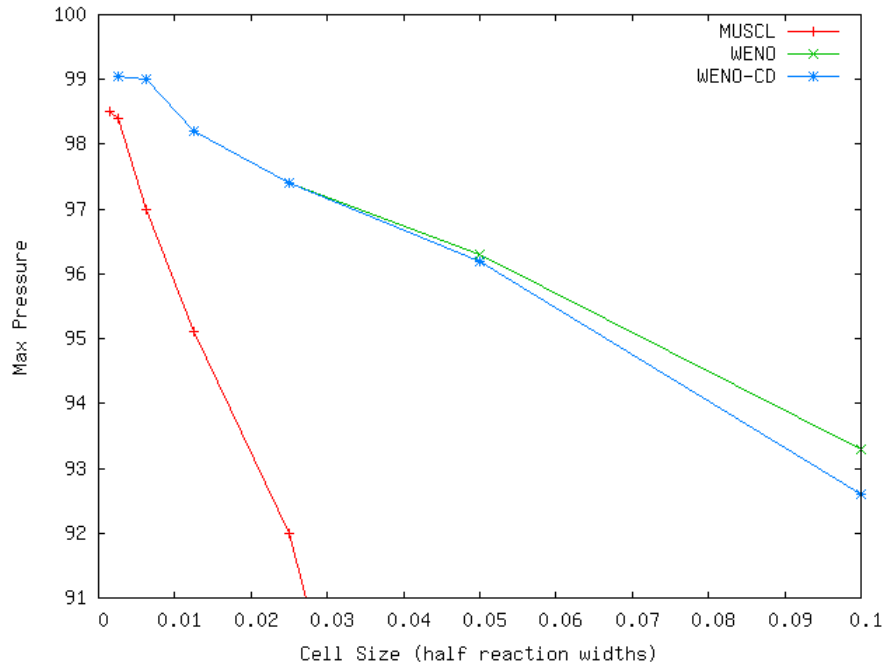


Figure 4.9: Convergence of the maximum pressure peak of  $\sim 99$  for the WENO/CD, WENO, and MUSCL methods.

In figure 4.9 and table 4.3, the convergence of the WENO/CD and pure WENO was compared in the uniform grid case to the convergence of the widely accepted MUSCL method as used by Deiterding (40). The method of Hwang *et al.* (75), a 3rd-order WENO scheme, also converges to a pressure of approximately 99. Here it is found that the WENO and WENO/CD solutions converge at similar rates to the maximum shock pressure. As expected, this is substantially higher than that of the 2nd-order MUSCL solution at the same resolution. Note that at least 10 cells per  $L_{\frac{1}{2}}$  are required to have an acceptable maximal pressure amplitude and period.



Cell Size (half reaction widths)	$L_{\frac{1}{2}}$	Cells	MUSCL Max Pressure	WENO Max Pressure	WENOCD Max Pressure
1.00E-001	10	160	-	93.3	92.6
5.00E-002	20	800	80.9	96.3	96.2
2.50E-002	40	1600	92.0	97.4	97.4
1.25E-002	80	3200	95.1	98.2	98.2
6.25E-003	160	6400	97.0	99.0	99.0
2.50E-003	400	16000	98.4	-	99.05
1.56E-003	641	25600	98.5	-	-

Table 4.3: Convergence of the maximum pressure peak for the one-dimensional, unstable two-species detonation problem. Values are shown for the MUSCL, WENO, and WENO/CD methods. The solution accepted by the detonation research community is  $\sim 99$  (40).

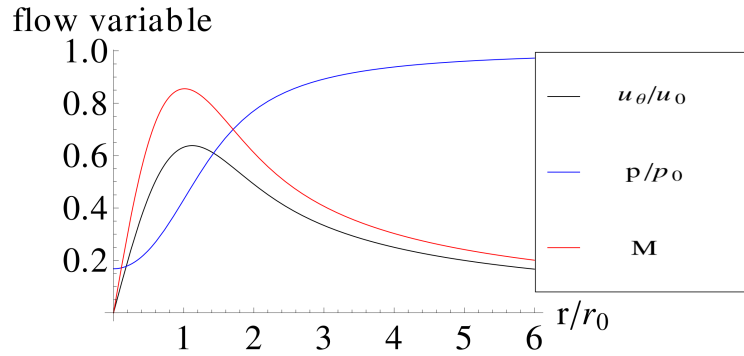


Figure 4.10: One-dimensional inviscid exact solution for the manufactured Lamb-Oseen vortex problem.

#### 4.1.6 Two-Dimensional Manufactured and Decaying Lamb-Oseen Vortex

For verification of the convergence properties of both the inviscid and viscous fluxes, a two-dimensional “manufactured solution” of the convecting Lamb-Oseen vortex (137) was constructed. Radial profiles for this exact solution, shown in figure 4.10, were obtained for a steady, inviscid vortex problem. An exact viscous, steady solution was then constructed by adding viscous fluxes together with analytically known source terms in both the momentum and energy equations to cancel them exactly. An order-verification via the manufactured solution procedure (OVMSP) (90) creates analytic solutions to the fully general differential equations solved by the code and uses a grid convergence study to confirm the order of accuracy. Fourth- and sixth-order, conservative (in each SAMR level) viscous fluxes were constructed and verified. A

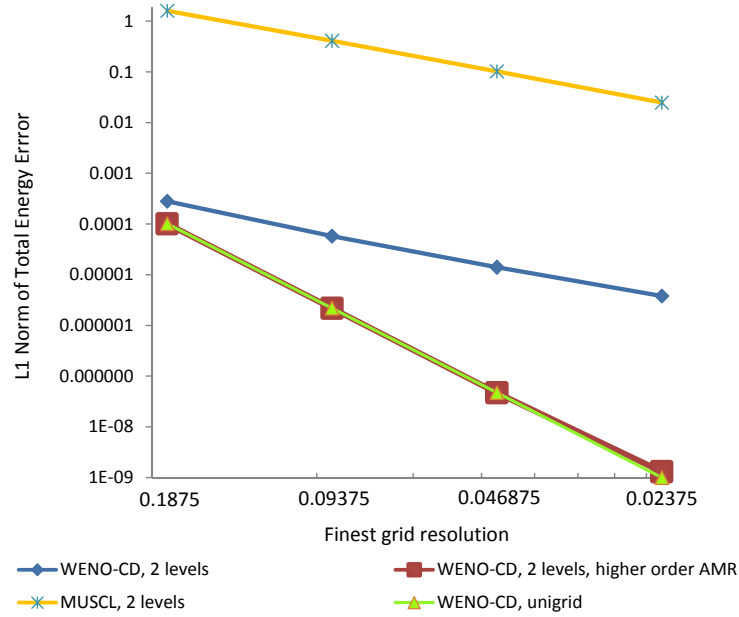
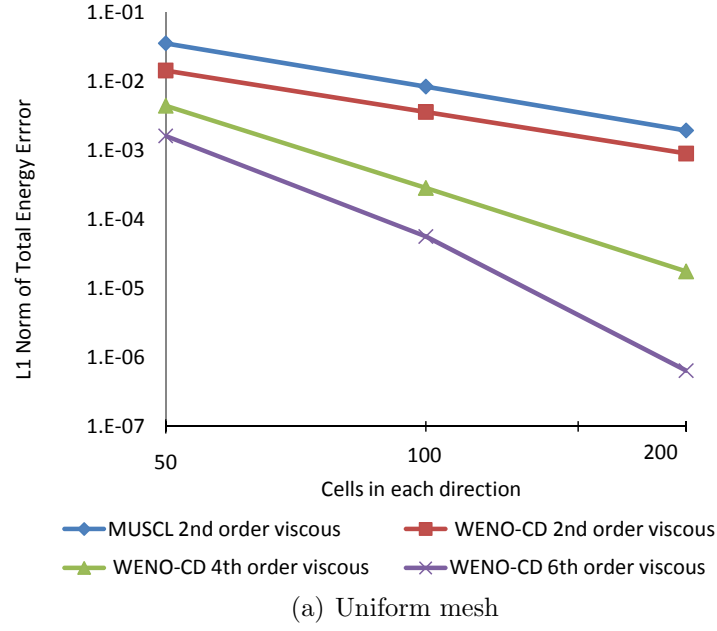


Figure 4.11: Convergence plot (log-log scale) for the manufactured Lamb-Oseen vortex solution (a) and the viscous decaying vortex (b). The convergence plots show the decrease of the  $L_1$ -error norm of the total energy as the resolution is doubled.

convergence study was conducted for a uniform and a two-level grid. When using first-order accurate prolongation and restriction, global 3rd-order spatial convergence was found for the two-level grid over a finite time for the 6th- and 4th-order methods. The uniform grid convergence results are shown in figure 4.11(a) and table 4.4.

Cells	MUSCL 2nd-order viscous $L_1$ -error	rate	WENO/CD 2nd-order viscous $L_1$ -error	rate	WENO/CD 4th-order viscous $L_1$ -error	rate	WENO/CD 6th-order viscous $L_1$ -error	rate
$50^2$	0.0355		0.0143		0.00442		0.00162	
$100^2$	0.00839	2.08	0.00359	1.99	0.000284	3.96	5.65E-05	4.84
$200^2$	0.00194	2.11	0.000899	2.00	1.76E-05	4.01	6.43E-07	6.46

Table 4.4: Convergence on uniform grids using the manufactured solution for the two-dimensional Lamb-Oseen vortex test, showing the error values of the  $L_1$ -norm of the total energy and the corresponding convergence rates for different methods with differing viscous flux stencils.

Further, a separate verification problem was constructed using a highly accurate simulation of the convecting, viscous, decaying Lamb-Oseen vortex. Here, the expected 6th-order convergence rate using the 5th-order prolongation and restriction was verified using the full compressible Navier-Stokes equations. For these test cases, a highly resolved  $4096 \times 4096$  mesh was used as reference result, and was compared to base meshes of  $64 \times 64$  to  $512 \times 512$  cells. This convergence test was carried out using two levels, a base grid with a static  $2 \times 2$  refinement mesh, centered in the vortex. In figure 4.11(b) and table 4.5, with 2 levels, 2nd-order convergence is found for all methods using the standard 1st-order accurate prolongation and restriction operators. With a uniform grid, 6th-order convergence is confirmed for WENO/CD. Lastly, with the new 5th-order accurate hybrid prolongation and restriction, overall 6th-order convergence is achieved even for the SAMR results. Note that in the SAMR case, the error is evaluated as the sum of the  $L_1$ -error norms on the domain  $\Omega_\lambda$  of level  $\lambda$  without higher refinement. Denoting by  $\Lambda$  the highest level available, the norm calculation reads

$$L_1(q) = L_1^e(\Delta x_\Lambda, \Delta y_\Lambda, \Omega_\Lambda) + \sum_{\lambda=0}^{\Lambda-1} L_1(\Delta x_\lambda, \Delta y_\lambda, \Omega_\lambda \setminus \Omega_{\lambda+1}), \quad (4.24)$$

where

$$L_1(\Delta x, \Delta y, \Omega) = \sum_{j,l} |q_{jl} - q_{jl}^r| \Delta x \Delta y \quad (4.25)$$

is the  $L_1$ -error norm on the domain  $\Omega$ , and where  $q_{jl}^r$  denotes the averaging projection

Finest grid resolution	WENO/CD 2 levels $L_1$ -error	rate	WENO/CD 2 levels higher-order SAMR $L_1$ -error	rate	MUSCL 2 levels $L_1$ -error	rate	WENO/CD unigrid $L_1$ -error	rate
0.1875	0.000282		0.000101		1.60		0.000102	
0.09375	5.80E-05	2.28	2.18E-06	5.53	0.409	1.97	2.19E-06	5.54
0.046875	1.40E-05	2.05	4.72E-08	5.53	0.103	1.99	4.75E-08	5.53
0.0234375	3.82E-06	1.87	1.31E-09	5.17	0.0248	2.05	1.01E-9	5.56

Table 4.5: Convergence results for the decaying (viscous) two-dimensional Lamb-Oseen vortex benchmark, showing the error values of the  $L_1$ -norm of the total energy and the corresponding convergence rates. Except for the MUSCL method, each WENO/CD test case uses 6th-order accurate viscous flux stencils, yet only the uniform grid and the multi-level test case using higher-order prolongation and restriction yields close to 6th-order convergence.

of the reference solution from the  $4096 \times 4096$  uniform mesh down to the desired mesh with step sizes  $\Delta x$ ,  $\Delta y$ .

## 4.2 Multi-Dimensional Unsteady Convergence Studies

Convergence studies for unsteady two-dimensional flow have been carried out to complete the verification process. By systematically increasing the complexity of the problem, convergence was tested for the nonreactive, two- and multi-component reactive shock reflection problems. For all of these cases, the initial conditions were selected such that the DMR type reflection was produced. See appendix B for more discussion on Mach reflections.

### 4.2.1 The Model Problem

Detonations are intrinsically three-dimensional; however, due to the complexity of the problem and the ability to easily extend an implementation from two to three space-dimensional, a two-dimensional model is used. The problem setup for a two-dimensional, shock-initiated detonation reflection is depicted schematically in figure 4.12(a). Two detonation waves travel symmetrically down inclined wedges of equal angle  $\theta_w$  and then collide. As depicted schematically in figure 4.12(b), the collision produces a symmetrical structure consisting of two triple points with Mach stems, reflected waves, and shear layers, one set for each incident shock wave. To reduce computational cost, the symmetry of the problem is utilized. For our pre-

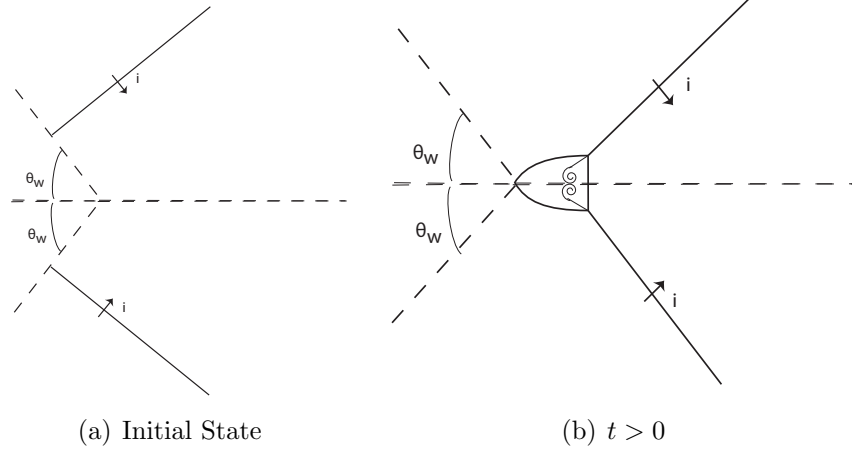


Figure 4.12: The model problem of two interacting planar shock waves

liminary results, one nonreacting, perfect gas species with constant specific heat was used. Later, one-step and multi-step reaction models involving multiple species were employed. Note that a Reynolds number,  $Re$ , for this flow can be defined by using the ambient density, speed of sound, and also the distance the incident shock has traveled along the bottom boundary,

$$Re = \frac{\rho_\infty a_\infty L(t)}{\mu_\infty}, \quad L(t) = d_{\text{shock}} \sin \theta_w t. \quad (4.26)$$

### 4.2.2 Initial and Boundary Conditions

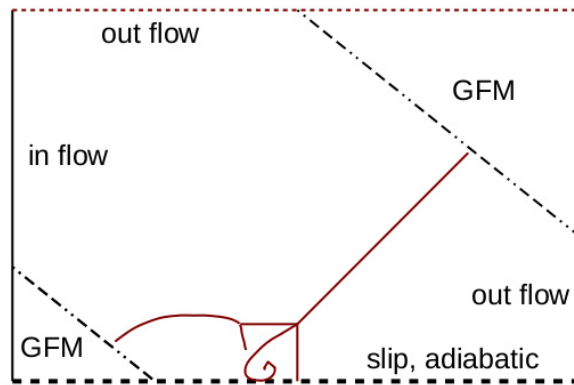


Figure 4.13: Boundary conditions for the reactive double Mach reflection problem. For the nonreactive problem, the top ghost-fluid-method (GFM) region is not needed and the exact shock solution is used at the upper boundary.

For the nonreactive simulations, the setup involves pre- and post-shock initial conditions throughout the domain. The boundary conditions include vanishing normal velocity, tangential stress and heat conduction on the inclined portions of the “wedge”; symmetry boundary conditions on the horizontal boundary with zero normal velocity, tangential stress, and heat conduction on the horizontal boundary, and simple zeroth-order inflow/outflow boundary conditions on the left and right boundaries, as shown in figure 4.13. Since this is a compressible supersonic flow, the boundary errors do not travel fast enough to interact with the solution area of interest. The inclined slip surface boundary is enforced using the level set implementation of the first-order accurate ghost fluid method (43). The exact traveling shock solution is prescribed along the top boundary. For this nonreactive case, the setup is similar geometrically to the wedge interaction problem studied by Vas Ilev *et al.* (76). However, we use different boundary conditions as our present interest is in shock-shock interactions rather than shock-solid boundary interactions. For the reactive case, the one-dimensional or planar ZND detonation wave solution was used as initial condition. This admits finite-rate chemical reactions and describes a detonation as an infinitely thin shock wave followed by a zone of exothermic chemical reaction. The shock travels with a speed given by the Chapman-Jouguet condition. The initial condition is found by numerically solving the one-dimensional, steady, reactive Euler equations using a numerical ordinary differential equation (ODE) solver. Also, in order to reduce boundary errors, the top boundary was angled and set to a solid slip boundary condition, as shown in figure 4.13. The initial and boundary conditions for the multi-component, detailed chemistry results are the same as in the two-component, one-step chemistry case, aside from a differing ZND solution due to the increased complexity in chemistry.

### 4.2.3 NonReactive Diffusive Double Mach Reflection

A fully resolved unsteady DMR simulation in air with  $\gamma = 1.4$  specific heat ratio was conducted. The initial conditions were selected to match the numerical and experimental results of Vas Ilev *et al.* (76), where a Mach number  $M = 4.5$ , inflow angle  $\theta_w = 36^\circ$ , and viscosity and thermal conductivity of  $\mu = 1.73 \cdot 10^{-5} \text{ Pa} \cdot \text{s}$  and  $k = 2.57 \cdot 10^{-2} \text{ W}/(\text{m} \cdot \text{K})$  were chosen. However, in order to gauge the performance of the code for detonation simulations, a slip boundary condition was applied, rather than the no-slip boundary condition proposed by Vas Ilev *et al.* (76). The constant viscosity and conductivity correspond approximately to the average values for the post-shock conditions for the ambient state with  $T = 300 \text{ K}$  and  $p = 2000 \text{ Pa}$ . Vas

Ilev et al. (76) was one of the first publications to look at 2D shock reflections with viscosity and thermal conductivity. They used the 2D Navier-Stokes equations with a single species perfect gas to look at the wall jetting effect of the slipstream in Mach reflections. They compare these computations to a self-similar viscous solution at different Reynolds number and also compared to their previous inviscid solution.

A nondimensionalization or scaling of the fluid dynamic equations was used and is detailed in §2.5. The maximum CFL parameter for automatic time step adjustment was 0.98 using the ten-step RK4 integration. Refinement criteria that capture the physics of each length scale in the problem were utilized. The density gradient is used to refine the convective length scale, the  $x$ - and  $y$ -velocity gradients are used for the viscous length scale, and the energy gradient for the conduction lengths. The viscous length scale is estimated by using the average density of the top and bottom flows of the shear layer  $\rho_{\text{avg}} = 0.1496 \text{ kg/m}^3$ . The shock speed and speed of sound used to calculate the Reynolds number are 1,566 and 348 m/s, respectively. Through experience, it has been found that for (2.32), using the time value at which the shear layer begins to become unstable is sufficient for calculating a viscous length scale  $\delta_{\text{visc}}$ . Note that this naturally applies only to resolved simulations, in which there are at least 10 to 100 cells within  $\delta_{\text{visc}}$  for our discretization approach. Therefore, despite our intention, the incident shock is marginally resolved.

table 4.6 summarizes runs performed for the nonreactive, diffusive double Mach reflection. For the result shown in table 4.6(D) the incident shock thickness (encompassing the high gradient part) is only slightly larger than  $\lambda_{\text{shock}} = \frac{8\mu}{5} \sqrt{\frac{2}{\pi\rho_{\infty}p_{\infty}}} \approx 3.2 \cdot 10^{-6} \text{ m}$ . This corresponds to approximately 100 cells across the shear layer (at finest grid resolution) immediately behind the triple point and some 10 cells across the incident shock.

In the absence of an exact solution and with the necessity of adaptive mesh refinement to resolve the scales, a standard convergence study is difficult. For the shear-layer portions of the flow, comparisons with free shear layer theory were used to study solution accuracy. Directly behind the triple point, the flow is laminar and stable; therefore, for constant viscosity, the thin-layer equations apply. The similarity solution, as shown in appendix D, obeys the Blasius ODE but with boundary conditions for the free-mixing layer. A demonstrative numerical result is shown in figure 4.14(a). Here, the growth and transition to instability (the initial inviscid mode) of the region dominated by vorticity is shown. The mixing thickness can also be obtained using the Von Kármán momentum-integral technique (15) as shown in appendix D. It is assumed that the flows on both sides of the shear layer are incompressible and that

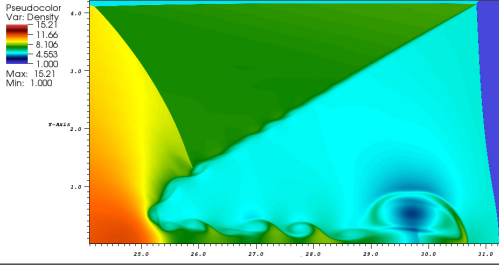
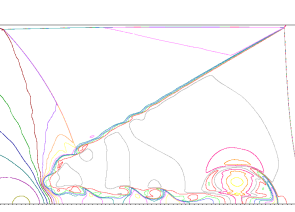
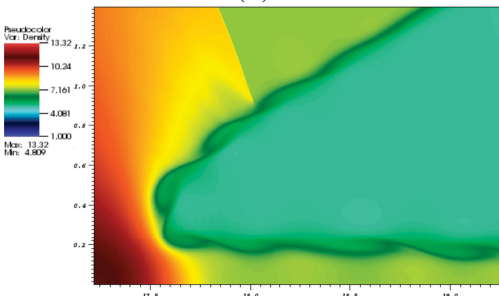
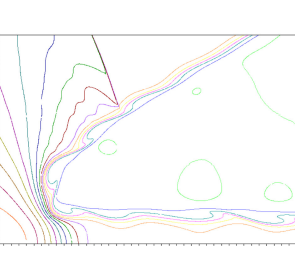
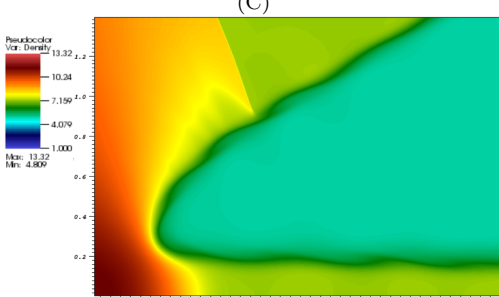
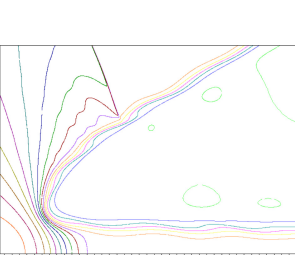
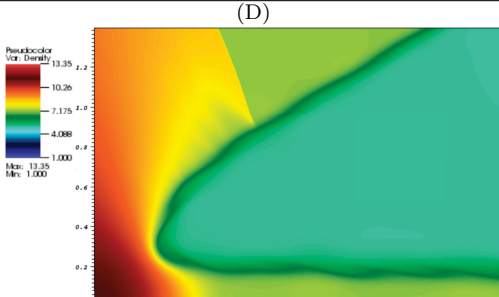
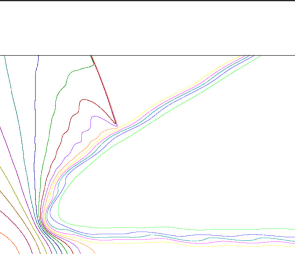
Density pseudo-color	Density contour	Method	Diffusion
(A) 		WENO/ CD-RK4 6 levels (2, 2, 2, 2, 2) base grid: 700 × 120 $x = [-1, 34]$ $y = [0, 6]$ $L_\infty = 0.001$ m	$\delta_{\text{visc}} = \sqrt{\frac{\mu t}{\rho}}$ $\approx 4.07$ $\cdot 10^{-5}$ m $\Delta x_{\text{min}} = 1.5625$ $\cdot 10^{-6}$ m $t = 5.0$ (nondim), $1.4368 \cdot 10^{-5}$ s $\text{Re} = 6,150$
(B) 		WENO/ CD-RK4 5 levels (2,2,2,4) base grid: 496 × 86 $x = [-0.8, 24]$ $y = [0, 4.3]$ $L_\infty = 0.001$ m	$\delta_{\text{visc}} \approx 3.57$ $\cdot 10^{-5}$ m $\Delta x_{\text{min}} = 1.5625$ $\cdot 10^{-6}$ m $t = 3.48$ (nondim), $9.298 \cdot 10^{-6}$ s $\text{Re} = 4,278$
(C) 		WENO/ CD-RK4 6 levels (2, 2, 2, 2, 4) base grid: 496 × 86 $x = [-0.8, 24]$ $y = [0, 4.3]$ $L_\infty = 0.001$ m	$\delta_{\text{visc}} \approx 3.57$ $\cdot 10^{-5}$ m $\Delta x_{\text{min}} = 7.8125$ $\cdot 10^{-7}$ m $t = 3.48$ (nondim), $9.298 \cdot 10^{-6}$ s $\text{Re} = 4,278$
(D) 		WENO/ CD-RK4 7-levels (2, 2, 2, 2, 2, 4) base grid: 496 × 86 $x = [-0.8, 24]$ $y = [0, 4.3]$ $L_\infty = 0.001$ m	$\delta_{\text{visc}} \approx 3.57$ $\cdot 10^{-5}$ m $\Delta x_{\text{min}} = 3.90625$ $\cdot 10^{-7}$ m $t = 3.48$ (nondim), $9.298 \cdot 10^{-6}$ s $\text{Re} = 4,278$

Table 4.6: Nonreactive diffusive double Mach reflection: pseudo-color density and contour plots of the DMR structure. figure (A) displays the long-term behavior and figures (B) to (D) demonstrate the convergence of the WENO/CD method in resolving the viscous processes in the shear layer, by showing a successive increase in resolution by a factor of 2 for three simulations. The approximate viscous scale and minimum cell size show the required resolution for convergence of the viscous DMR problem. *Note: For the electronic version, the zoom tool in the PDF reader can be used to study the details of the high-resolution plots.*



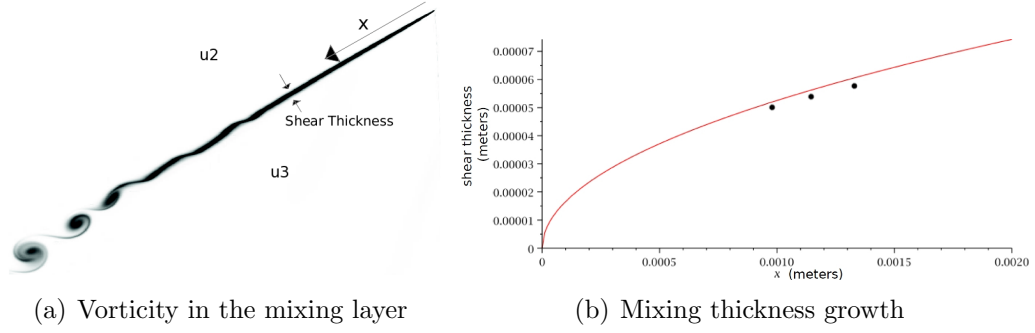


Figure 4.14: Vorticity in the mixing layer and the laminar mixing layer thickness as a function of distance from the triple point, Von Karman momentum-integral technique. The last black dot is from our numerical simulation for the approximate thickness at a distance of 1.35 mm behind the triple point. This thickness is in the laminar stable regime.

there is no pressure gradient along the layer. As assumed in Bendor (15), the upper and lower velocities,  $u_2$  and  $u_3$  as shown in figure 4.14(a), tangential to the interface are assumed to have a laminar profile and are approximated with third-order polynomials. The benefit of the Von Kármán integral method is that it approximates the effects of the density difference across the layer, unlike the Blasius method, for which an average density was used. Of equal importance is that it also allows for a viscosity variation: the lower fluid is much hotter than the upper fluid, yielding a physically nonnegligible change in viscosity. The total displacement thickness was calculated and is shown in figure 4.14(b). The dots on figure 4.14(b) show the comparison of the numerical and boundary layer theory results. Before conducting quantitative convergence calculations, the high-resolution results were compared to a simulation with one less refinement level, which supported visual convergence.

#### 4.2.3.1 Convergence Results

A series of simulations were conducted to investigate the influence of resolution and SAMR level distribution on the initial roll-up of the shear layer. Pseudo-color and contour plots of the density are presented in table 4.6 (B) to (D) for 3 different SAMR resolutions. Through this investigation, it was found that setting the refinement thresholds to enable adequate coverage of the shear layer and its surrounding region is vital for convergence because the interactions of the SAMR levels create grid-level disturbances that can influence the initially highly sensitive vortical roll-up. The region behind the shock wave close to the second triple point requires the highest

level of refinement (used similarly for the shear layer) because the roll-up first occurs behind this shock.

Levels	Density $L_1$ -error	rate	$y$ -velocity $L_1$ -error	rate	Total energy $L_1$ -error	rate
$t = 3.48$ , domain: [17.0, 24.0] $\times$ [0.0, 3.5]						
3	1.05458	-	0.429532	-	31.4198	-
4	0.675551	0.64	0.295575	0.54	20.6763	0.60
5	0.304157	1.15	0.131237	1.17	9.41859	1.13
6	0.223831	0.44	0.090042	0.54	6.35662	0.57
$t = 3.60$ domain: [17.0, 24.0] $\times$ [0.0, 3.5]						
3	1.11937	-	0.460977	-	33.0184	-
4	0.78734	0.51	0.340686	0.44	23.912	0.47
5	0.389708	1.01	0.164079	1.05	12.1556	0.98
6	0.284423	0.45	0.115549	0.51	8.31585	0.55
$t = 3.84$ domain: [18.5, 24.0] $\times$ [0.0, 3.5] (incident shock at edge of domain)						
3	1.24815	-	0.53609	-	37.1056	-
4	1.07438	0.22	0.46187	0.21	32.7679	0.18
5	0.576804	0.90	0.240978	0.94	17.843	0.88
6	0.413381	0.48	0.175842	0.45	12.3752	0.53

Table 4.7:  $L_1$ -error norms for some state variables using the 7-level case as the reference solution.

Base grid	Density $L_1$ -error	rate	Total energy $L_1$ -error	rate
$t = 3.84$ domain: [19.2, 24.0] $\times$ [0.0, 3.23] (incident shock at edge of domain)				
$62 \times 11$	1.17987	-	36.6927	-
$124 \times 22$	0.516237	1.19	15.7583	1.22
$248 \times 43$	0.289879	0.83	8.63115	0.87
$t = 3.84$ domain: [19.2, 23.55] $\times$ [0.0, 1.14] bottom jet (shocks are not included)				
$62 \times 11$	0.946061	-	29.9732	-
$124 \times 22$	0.418507	1.18	13.0559	1.20
$248 \times 43$	0.204751	1.03	6.27181	1.06

Table 4.8:  $L_1$ -error norms for some state variables using the 7-level case (with  $496 \times 86$  base grid) as the reference solution. Coarser solutions also have 7-levels, but use coarser base grids.

Using the highest resolved case as an approximate “exact” numerical solution, the convergence of the WENO/CD method was quantified. As an example, figure 4.15 shows the distribution of SAMR refinement levels for the 7-level case at a time of  $t =$

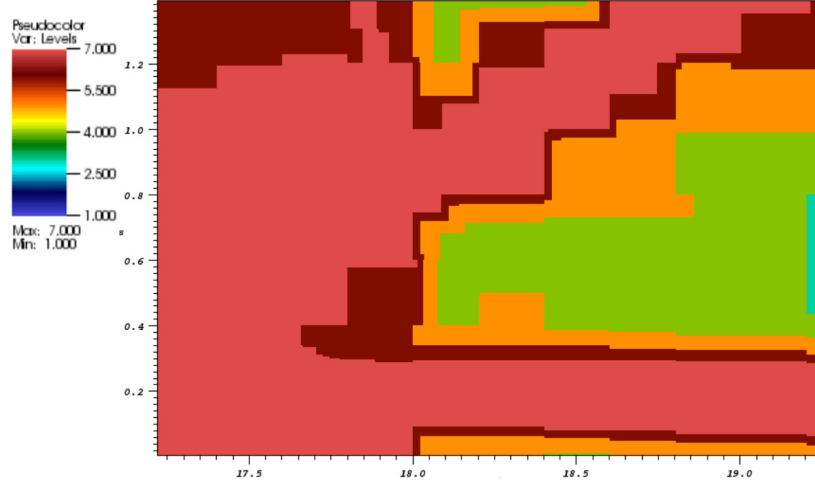


Figure 4.15: SAMR levels for the DMR convergence test. The domain corresponds to those of tests (B)-(D) of table 4.6.

3.48 (nondimensional). The  $L_1$ -error norms in table 4.7 demonstrate the convergence of the state variables density, momentum, and total energy. The computation of these norms utilized only the domain surrounding the shear layer. Here, convergence is demonstrated from the time the shear layer begins to roll up,  $t = 3.36$ , to the time at which half of the shear layer has left the domain,  $t = 3.84$ . For these norms, rates of convergence are calculated assuming that all levels are being refined, rather than just the finest level.

Also shown is table 4.8, where instead of changing the number of levels, the resolution of the base grid is halved in each direction. Here, because all grids are being refined/coarsened rather than just those coinciding with the finest grid, the convergence rates are slightly higher. Even higher rates are found when a domain excluding the shock waves is used for the norms. As an example, the rate of convergence for only the unstable jet at the bottom of the domain is shown. In this case the last rate for the density increases from 1.33 to 1.43 and for the total energy, from 1.35 to 1.44. Note that in all of these DMR test cases for tables 4.7 and 4.8, when comparing one result to another, all the coarse/fine grid boundaries do not exactly match up. This is unavoidable with our adaptive mesh refinement strategy, as the grid is being updated at every time step and its coverage depends on the local gradients of the solution.

The evaluation of the  $L_1$ -error norms is carried out as described at the end of §4.1.6, with the only difference that the reference solution  $q^r$  itself is now defined on a hierarchical SAMR mesh. The data on the highest locally available level of the reference solution is averaged onto the currently evaluated level of the present

approximation. Since the SAMR approach leads to refinement domains  $\Omega_\lambda$  that are always properly nested within the next coarser level domain  $\Omega_{\lambda-1}$  plus a buffer region of at least one layer of coarse level cells, it is safe to assume that for the cases considered here the reference solution is always significantly better resolved. We have implemented the used error norm computation for large-scale parallel adaptive simulations as a mere post-processing step reading the I/O files generated by AMROC into a separate single-processor program.

These quantitative measures and visual comparisons of the solution support that our method is converging. In our two highest resolutions shown in table 4.6, because the solutions visually look the same and the rates show convergence we can conclude that the diffusive processes are resolved.

#### 4.2.4 Double Mach Reflection Detonation

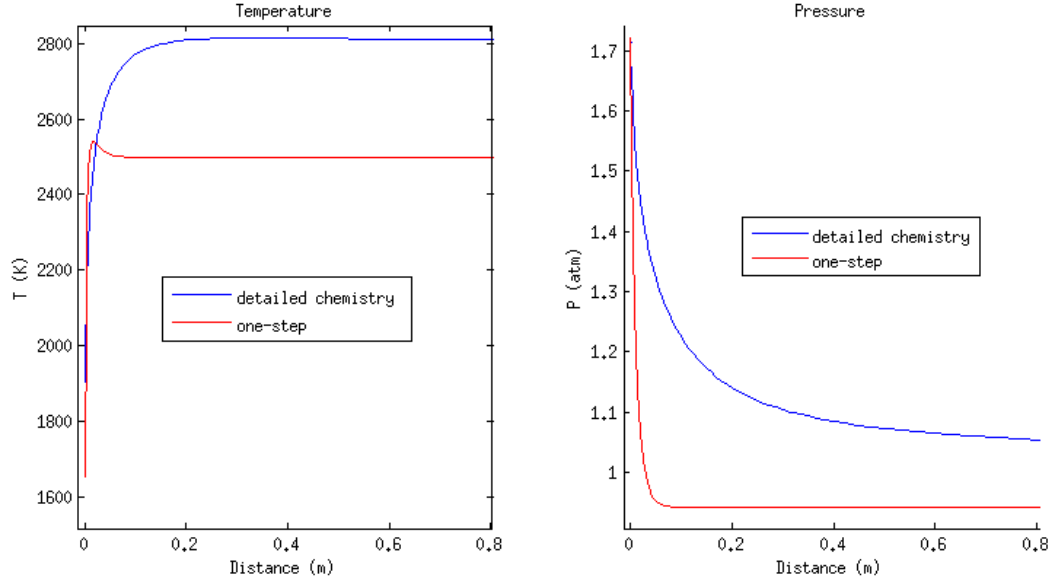
Demonstrative, fully-resolved, diffusive, detonation-reflection simulations have also been completed in two space-dimensions for a one-step, two-species, marginally stable detonation. The problem setup is similar to the nonreactive case, except for modifications of initial flow field and boundary conditions, required for an extension of a shock wave to a detonation. Simulations were conducted using the WENO/CD method and the robust MUSCL method for comparison. It was found that the accuracy of the flow was highly sensitive to the particular locations of the SAMR levels. A simple two-species, single-reaction model was used with temperature dependent transport properties. Because of the later goal of using multi-component detailed chemistry, the thermodynamical and transport properties of our model were selected and fitted to physical parameters for a  $\text{H}_2\text{-O}_2$  detonation initially at  $T = 300\text{ K}$  and  $p = 6,700\text{ Pa}$ . Using a high-temperature extension of the GRI30 mechanism in CANTERA and the SDToolbox<sup>2</sup>, the ZND solution was calculated with detailed chemistry and used to make an approximate chemistry and transport model with a single Arrhenius rate equation, constant specific heat, and temperature dependent transport. Feki *et al.* (52) is one of the earlier works which modeled species diffusion and viscosity in multidimensional reacting flows. Their formulation was applied to 1D detonations and 2D combustions flows. They also used an ENO formulation with 3rd order Runge-Kutta integration with time splitting for the stiff source terms.

The Arrhenius rate activation energy and pre-exponential, heat release, and specific heat ratio were chosen by matching the Chapman-Jouguet speed and the Von

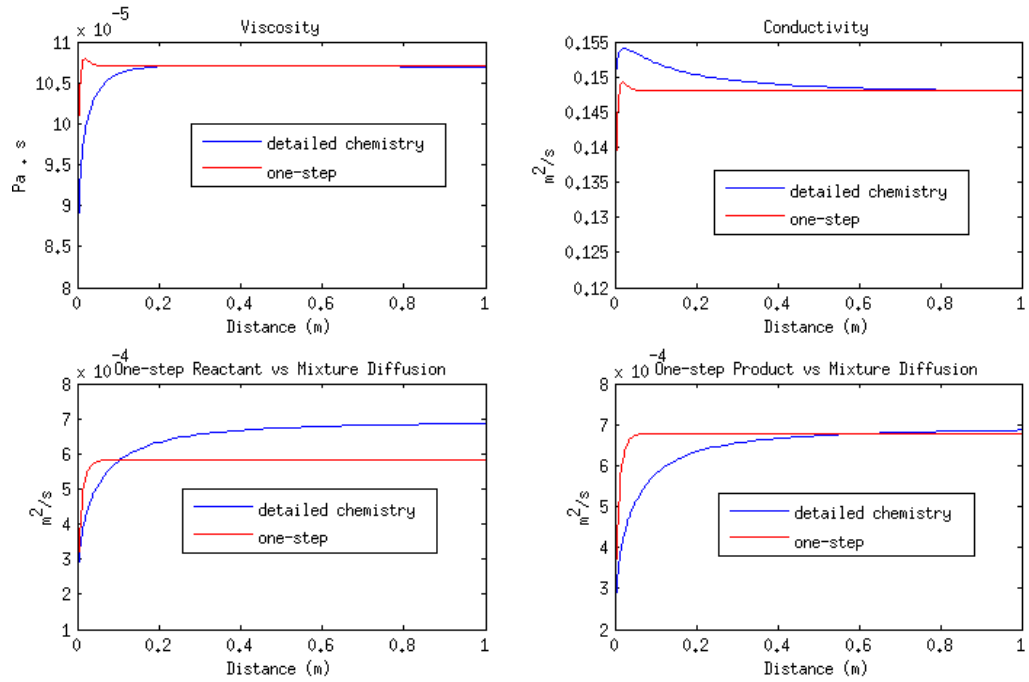
---

<sup>2</sup>[http://www.galci.caltech.edu/EDL/public/cantera/html/SD\\_Toolbox/index.html](http://www.galci.caltech.edu/EDL/public/cantera/html/SD_Toolbox/index.html)

Neumann (post-shock) pressure at the beginning of the ZND detonation, as shown in 4.16(a).



(a) ZND Initial Conditions: Temperature and Pressure



(b) Transport Properties: Viscosity, Conductivity, and Mass Diffusion

Figure 4.16: Comparing the initial conditions and transport properties of the one-step two-species with the detailed chemistry case. Reaction length is of the order of 1 meter for the full detailed chemistry, however, the induction length length is of the order of 1 mm for both the approximate one-step model and the detailed chemistry.

For this two-species, calorically perfect model we have

$$\gamma = \gamma_1 = \gamma_2, \quad p = \rho RT, \quad R = R_1 = R_2, \quad \text{and} \quad \rho = \rho_1 + \rho_2, \quad \rho_1 = \rho Y_1, \quad \rho_2 = \rho Y_2. \quad (4.27)$$

With the total energy defined by the heat release per unit mass parameter,  $q$ , the equation of state takes the explicit form

$$\rho e_t = \frac{p}{(\gamma - 1)} + \frac{1}{2}\rho(u^2 + v^2) + \rho_1 q, \quad \text{or} \quad e_t = \frac{p}{(\gamma - 1)\rho} + \frac{1}{2}(u^2 + v^2) + qY_1. \quad (4.28)$$

This is equivalent to having product and reactant enthalpies of the form

$$h_1 = h_0 + q + c_p T, \quad h_2 = h_0 + c_p T \quad \implies \quad h_2 - h_1 = h_{\text{prod}} - h_{\text{react}} = \Delta h_{\text{reaction}} = -q. \quad (4.29)$$

The mass fraction production rates are

$$\dot{\omega}_1 = -\rho Y_1 A \exp\left(\frac{E_a}{RT}\right), \quad \text{and} \quad \dot{\omega}_2 = \rho Y_1 A \exp\left(\frac{E_a}{RT}\right). \quad (4.30)$$

The thermodynamic parameters  $T_\infty = 300$  K,  $p_\infty = 6,670$  Pa,  $\rho_\infty = 0.077552$  kg/m<sup>3</sup>,  $\gamma = 1.29499$ ,  $W = 0.029$  kg/mol,  $q = 54,000$  J/mol,  $E_a = 30,000$  J/mol, and  $A = 6 \cdot 10^5$  s<sup>-1</sup> were used. This corresponds to a post-shock pressure of approximately 1.7 atm and detonation shock speed of  $d_{\text{shock}} = 1,587.84$  m/s. The viscosity, thermal conductivity, and mass diffusions were selected by matching general trends and the values at the end of the reaction zone of the one-step and detailed chemistry models encountered in their separate one-dimensional steady ZND solutions. In all of theses ZND configurations, the solution and parameters are described as a function of position or equivalently time. For the viscosity and conductivity, the Sutherland model was used,

$$\mu = \mu_{\text{ref}} \left(\frac{T}{T_{\text{ref}}}\right)^{\frac{3}{2}} \frac{T}{T_{\text{ref}}}, \quad k = k_{\text{ref}} \left(\frac{T}{T_{\text{ref}}}\right)^{\frac{3}{2}} \frac{T}{T_{\text{ref}}}. \quad (4.31)$$

A simple expression that includes the inverse dependence on pressure was used for the mass diffusion

$$D_1 = D_{1\text{ref}} \left(\frac{T}{T_{\text{ref}}}\right)^{\frac{3}{2}} \frac{T}{T_{\text{ref}}} \frac{p_{\text{atm}}}{p}, \quad D_2 = D_{2\text{ref}} \left(\frac{T}{T_{\text{ref}}}\right)^{\frac{3}{2}} \frac{T}{T_{\text{ref}}} \frac{p_{\text{atm}}}{p}. \quad (4.32)$$

At the end of the reaction zone, the temperature is approximately 2,500 K and the

pressure is  $\sim 1$  atm. This yields the following transport parameters for our one-step model:  $T_{\text{ref}} = 2,500$  K,  $\mu_{\text{ref}} = 1.07 \cdot 10^{-4}$  Pa s,  $k_{\text{ref}} = 0.148$  W/(mK),  $D_{1\text{ref}} = 5.5 \cdot 10^{-4}$  m<sup>2</sup>/s,  $D_{2\text{ref}} = 6.4 \cdot 10^{-4}$  m<sup>2</sup>/s. Note that for calculating a Reynolds number we use  $\mu_{\text{ref}}$  rather than  $\mu_{\infty}$  as  $\mu$  in this case is a function of temperature.

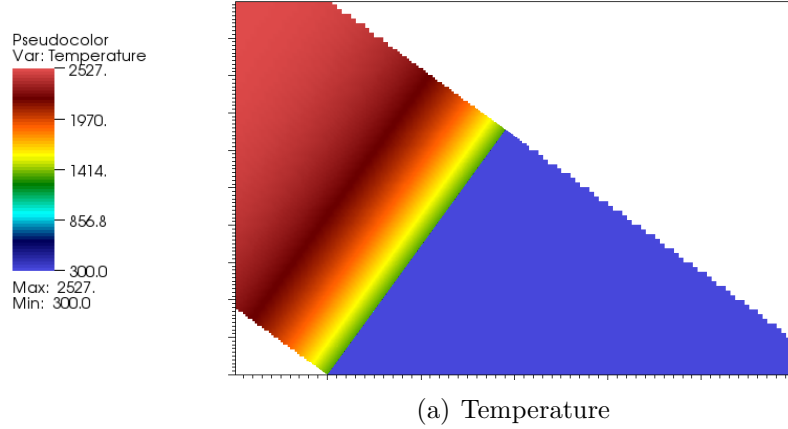


Figure 4.17: Temperature (K) pseudo-color plot for ZND initial condition with one-step chemistry.

#### 4.2.4.1 One-Step Chemistry

Results for the whole domain are presented in figures 4.17-4.18(a). For this simulation, the ZND planar steady detonation wave solution was used as initial condition. Using an average density,  $\rho \approx 0.60$  kg/m<sup>3</sup>, of the top and bottom portions of the shear layer directly behind the triple point, viscosity of  $5.95 \cdot 10^{-5}$  Pa s, thermal conductivity of  $0.847$  W/(mK), a mass diffusivity of  $1.57 \cdot 10^{-4}$  m<sup>2</sup>/s for the average temperature of  $2,000$  K, and a pressure of  $2$  atm the diffusive scales were estimated (see table 4.9(A)). Observe that the viscous scale is the smallest, and mass diffusion and heat diffusion scale are approximately 1.5 and 10 times larger, respectively.

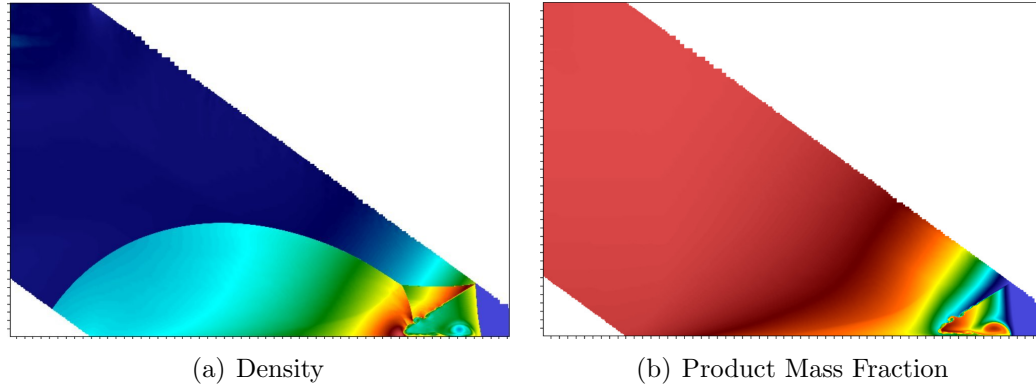


Figure 4.18: Pseudo-color plots for a fully-resolved marginally stable detonation with one-step chemistry.

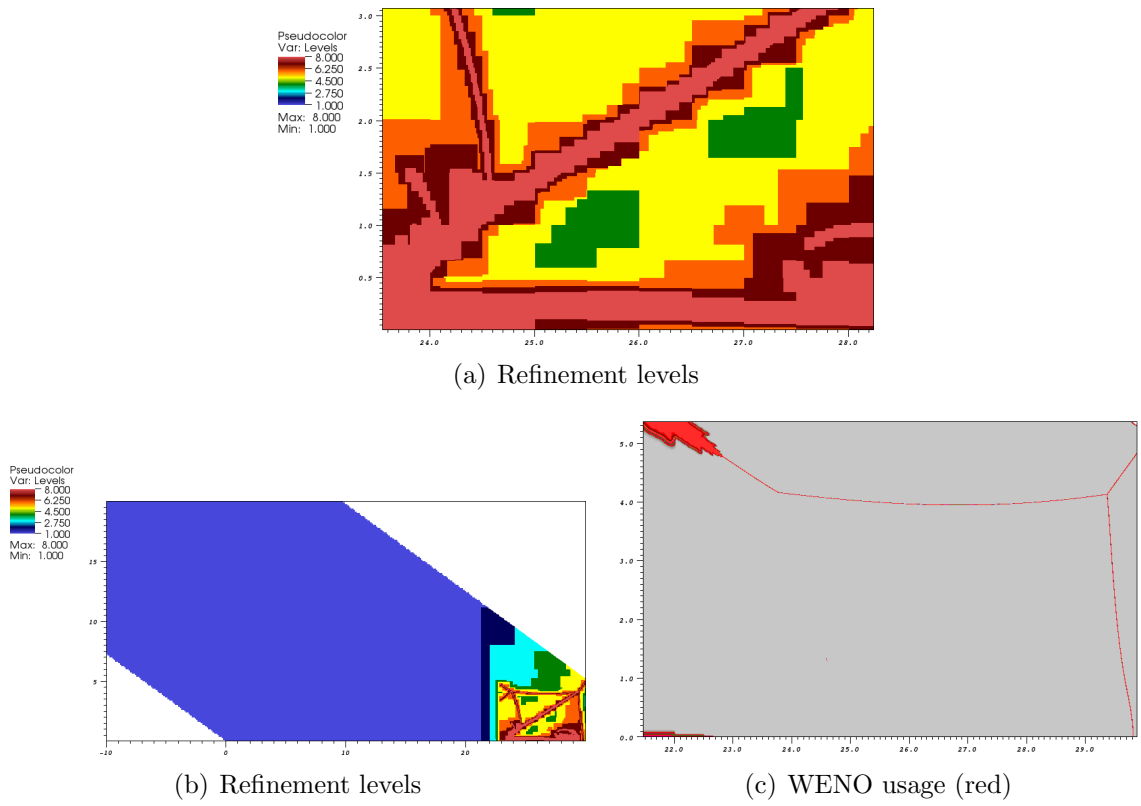


Figure 4.19: SAMR levels and WENO usage for the 8-level reactive DMR convergence test.



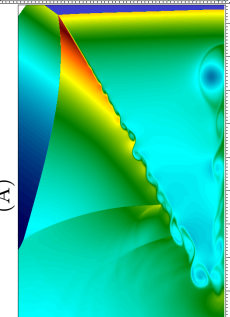
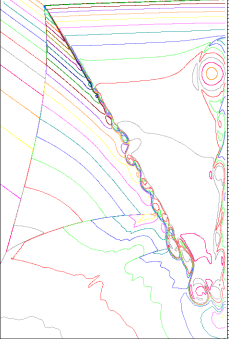
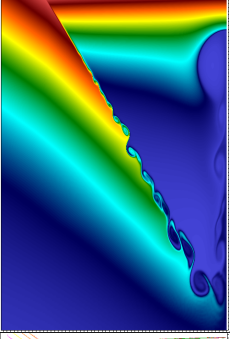
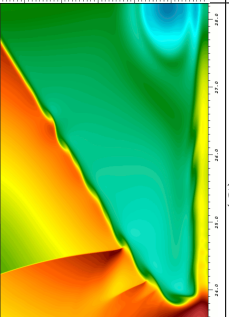
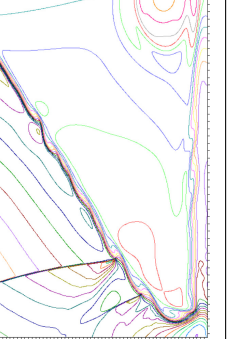
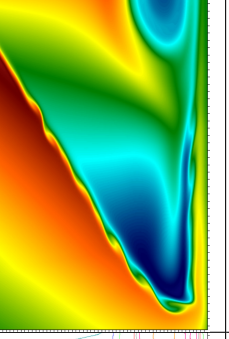
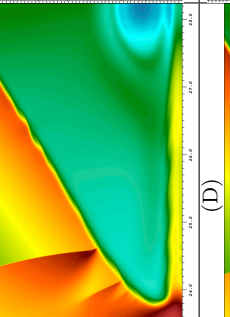
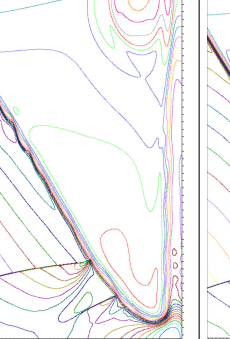
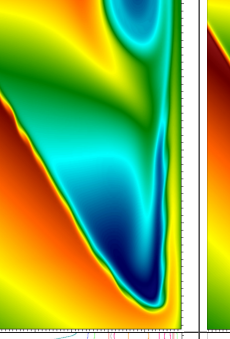
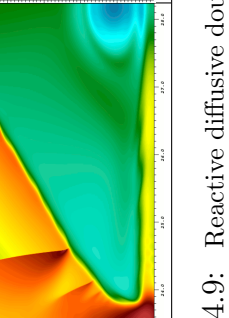
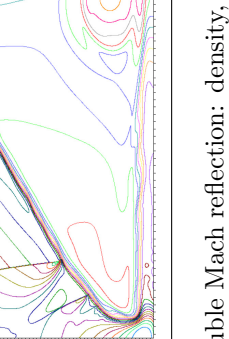
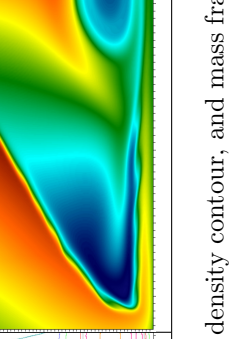
Density pseudo-color	Density contour	Mass fraction pseudo-color	Method	Diffusion
 <p>(A)</p>			WENO/CD- RK3/GRK4A 6 levels (2,2,2,2,2) base grid: 1080 × 675 $x = [-10, 70]$ $y = [0, 50]$ $L_\infty = 1 \text{ mm}$	$\Delta x_{min} = 2.31 \cdot 10^{-6} \text{ m}$ $\delta_{visc} \approx \sqrt{\frac{\mu}{\rho}}$ $= 5.44 \cdot 10^{-5} \text{ m}$ $\delta_{cond} \approx \sqrt{\frac{kt}{\rho c_v}}$ $= 2.08e-4 \text{ m}$ $\delta_{mass,1} \approx \sqrt{\frac{D_1 t}{\rho}}$ $= 8.84 \cdot 10^{-5} \text{ m}$ $t = 10 \text{ (nondim)},$ $2.996 \cdot 10^{-5} \text{ s, Re} = 6, 780$
 <p>(B)</p>			WENO/CD- RK3/GRK4A 6 levels (2,2,2,2,2) base grid: 320 × 160 $x = [-10, 30]$ $y = [0, 20]$ $L_\infty = 1 \text{ mm}$	$\Delta x_{min} = 3.91 \cdot 10^{-6} \text{ m}$ $\delta_{visc} \approx 3.57 \cdot 10^{-5} \text{ m}$ $\delta_{cond} \approx 1.36 \cdot 10^{-4} \text{ m}$ $\delta_{mass,1} \approx 5.81 \cdot 10^{-5} \text{ m}$ $t = 4.3 \text{ (nondim)},$ $1.2884 \cdot 10^{-5} \text{ s}$ $\text{Re} = 2, 910$
 <p>(C)</p>			WENO/CD- RK3/GRK4A 7-levels (2,2,2,2,2,2) base grid: 320 × 160 $x = [-10, 30]$ $y = [0, 20]$ $L_\infty = 1 \text{ mm}$	$\Delta x_{min} = 1.95 \cdot 10^{-6} \text{ m}$ $\delta_{visc} \approx 3.57 \cdot 10^{-5} \text{ m}$ $\delta_{cond} \approx 1.36 \cdot 10^{-4} \text{ m}$ $\delta_{mass,1} \approx 5.81 \cdot 10^{-5} \text{ m}$ $t = 4.3 \text{ (nondim)},$ $1.2884 \cdot 10^{-5} \text{ s}$ $\text{Re} = 2, 910$
 <p>(D)</p>			WENO/CD- RK3/GRK4A 8-levels (2,2,2,2,2,2,2) base grid: 320 × 160 $x = [-10, 30]$ $y = [0, 20]$ $L_\infty = 1 \text{ mm}$	$\Delta x_{min} = 9.77 \cdot 10^{-7} \text{ m}$ $\delta_{visc} \approx 3.57 \cdot 10^{-5} \text{ m}$ $\delta_{cond} \approx 1.36 \cdot 10^{-4} \text{ m}$ $\delta_{mass,1} \approx 5.81 \cdot 10^{-5} \text{ m}$ $t = 4.3 \text{ (nondim)},$ $1.2884 \cdot 10^{-5} \text{ s}$ $\text{Re} = 2, 910$

Table 4.9: Reactive diffusive double Mach reflection: density, density contour, and mass fraction pseudo-color plots of the DMR structure. Figure (A) demonstrates the long-term behavior and figures (B) to (D) demonstrate the convergence of the WENO/CD method in resolving the viscous processes in the mixing layer, by showing a  $2\times$  increase in resolution for 3 simulations. The approximate viscous scale and minimum cell size give the required resolution for convergence of the viscous DMR problem. Figures (E) to (F) show the convergence of a standard MUSCL scheme for the same problem. Figure (G) shows the details of the high-resolution simulation. *Note: For the electronic version, the zoom tool in the PDF reader can be used to study the details of the high-resolution plots.*

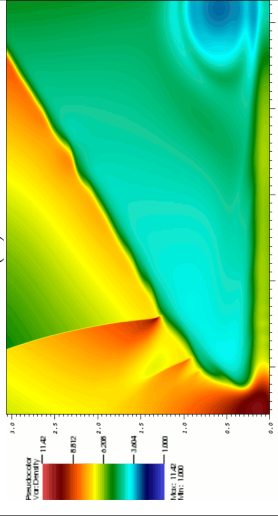
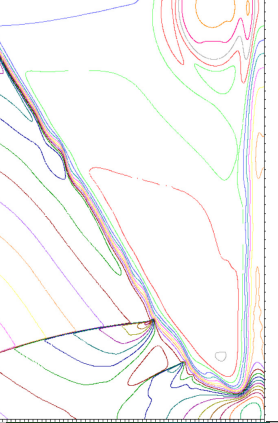
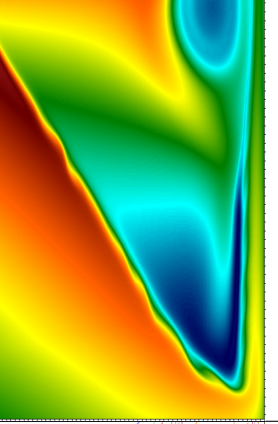
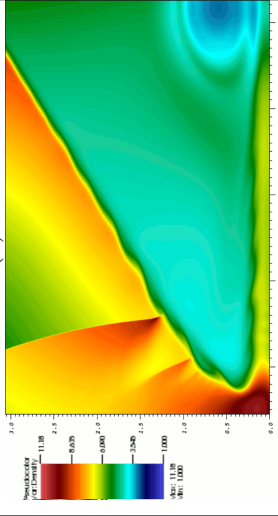
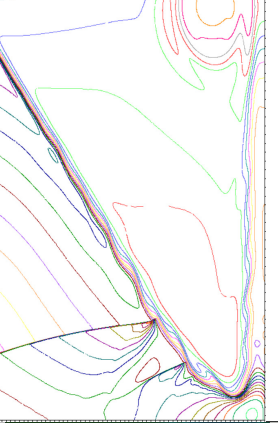
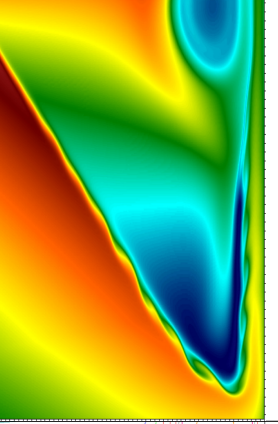
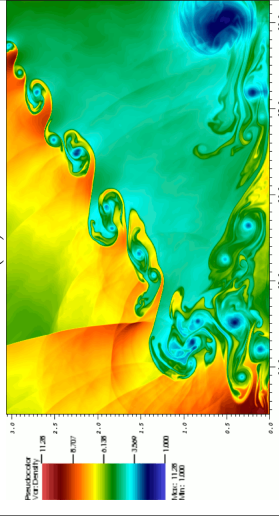
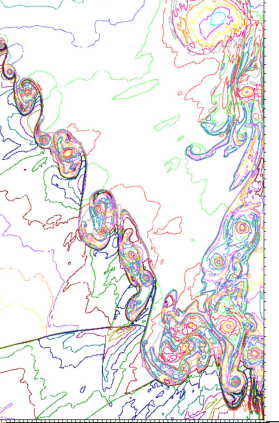
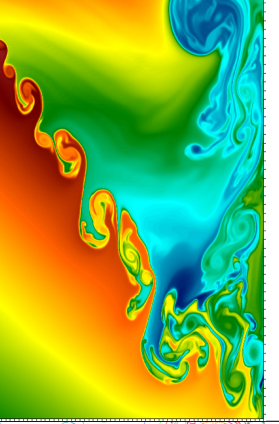
Density pseudo-color	Density contour	Mass fraction pseudo-color	Method	Diffusion
 <p>(E)</p>			MUSCL/ GRK4A 6 levels (2,2,2,2,2) base grid: $590 \times 352$ $x = [-10, 30]$ $y = [0, 22]$ $L_\infty = 1 \text{ mm}$	$\Delta x_{min} = 2.12 \cdot 10^{-6} \text{ m}$ $\delta_{visc} \approx 3.57 \cdot 10^{-5} \text{ m}$ $\delta_{cond} \approx 1.36 \cdot 10^{-4} \text{ m}$ $\delta_{mass,1} \approx 5.81 \cdot 10^{-5} \text{ m}$ $t = 4.3 \text{ (nondim)},$ $1.2884 \cdot 10^{-5} \text{ s}$ $\text{Re} = 2,910$
 <p>(F)</p>			MUSCL/ GRK4A 7-levels (2,2,2,2,2,2) base grid: $590 \times 352$ $x = [-10, 30]$ $y = [0, 22]$ $L_\infty = 1 \text{ mm}$	$\Delta x_{min} = 1.05 \cdot 10^{-6} \text{ m}$ $\delta_{visc} \approx 3.57 \cdot 10^{-5} \text{ m}$ $\delta_{cond} \approx 1.36 \cdot 10^{-4} \text{ m}$ $\delta_{mass,1} \approx 5.81 \cdot 10^{-5} \text{ m}$ $t = 4.3 \text{ (nondim)},$ $1.2884 \cdot 10^{-5} \text{ s}$ $\text{Re} = 2,910$
 <p>(G)</p>			MUSCL/ GRK4A 7-levels (2,2,2,2,2,2) base grid: $590 \times 352$ $x = [-10, 30]$ $y = [0, 22]$ $L_\infty = 1 \text{ mm}$	$\Delta x_{min} = 2.12 \cdot 10^{-6} \text{ m}$ $t = 4.3 \text{ (nondim)},$ $1.2884 \cdot 10^{-5} \text{ s}$

Table 4.10: Reactive diffusive double Mach reflection: density, density contour, and mass fraction pseudo-color plots of the DMR structure. Figure (A) demonstrates the long-term behavior and figures (B) to (D) demonstrate the convergence of the WENO/CD method in resolving the viscous processes in the mixing layer, by showing a  $2\times$  increase in resolution for 3 simulations. The approximate viscous scale and minimum cell size give the required resolution for convergence of the viscous DMR problem. Figures (E) to (F) show the convergence of a standard MUSCL scheme for the same problem. Figure (G) shows the equivalent inviscid simulation. *Note: For the electronic version, the zoom tool in the PDF reader can be used to study the details of the high-resolution plots.*

#### 4.2.4.2 Convergence Results

Using the nondimensional version of the equations and up to 8-levels of refinement, convergence of the method for the reactive DMR was verified as shown in tables 4.9 and 4.10 (B) to (D). For these simulations, the National Energy Research Scientific Computing Center (NERSC) machine “Carver” (quad-core Intel 5500 series) was used with 128 cores. Additionally, in order to increase the efficiency of the simulation and allow for higher resolution, a time-dependent coarsening region behind the DMR was utilized, as shown in figure 4.19(b). Three-step RK3 integration was used with a CFL time step parameter of 0.99 in conjunction with the time-split integration for the chemistry. As expected, it was found that when the induction length is larger than the viscous scales (as is for realistic physical parameters), a fully resolved simulation is limited by the viscous length scale. Shown in figure 4.19(c) is the use of the WENO scheme only at the strong shocks. At the highest resolution, the shock coming from the second triple point is not strong enough to activate the discontinuity flag and the centered difference method captures the shock satisfactorily. At these resolutions, the weak shocks are nearly resolved, yet the strong shocks remain under-resolved.

Levels	Density $L_1$ -error	rate	$Y_1$ $L_1$ -error	rate
$t = 4.300$ , domain: $[23.0, 30.0] \times [0, 5.0]$				
4	2.00432	-	0.216785	-
5	1.36915	0.55	0.160973	0.43
6	0.709029	0.95	0.0791281	1.03
7	0.329581	1.11	0.0360734	1.13
$t = 4.608$ domain: $[23.0, 30.0] \times [0, 5.0]$ (Mach stem/incident shock has left the domain)				
4	1.83941	-	0.226811	-
5	1.36174	0.44	0.170671	0.41
6	0.810797	0.75	0.104466	0.71
7	0.350756	1.21	0.0429677	1.28

Table 4.11:  $L_1$ -error norms for the state variables using the 8-level case as the reference solution.

Again, using the highest resolved 8-level case as a reference solution,  $L_1$ -error norms were calculated for the density and first species mass fraction to quantify the convergence of the reactive DMR problem. Quantitative results are given in table 4.11. Pseudo-color plots of the absolute value of the cell-wise difference between current and reference approximation are displayed in table 4.12. As previously shown for the nonreactive case, the solution is converging and accurately resolved. The latter statement is further supported by the visualization of the local errors in table 4.12,

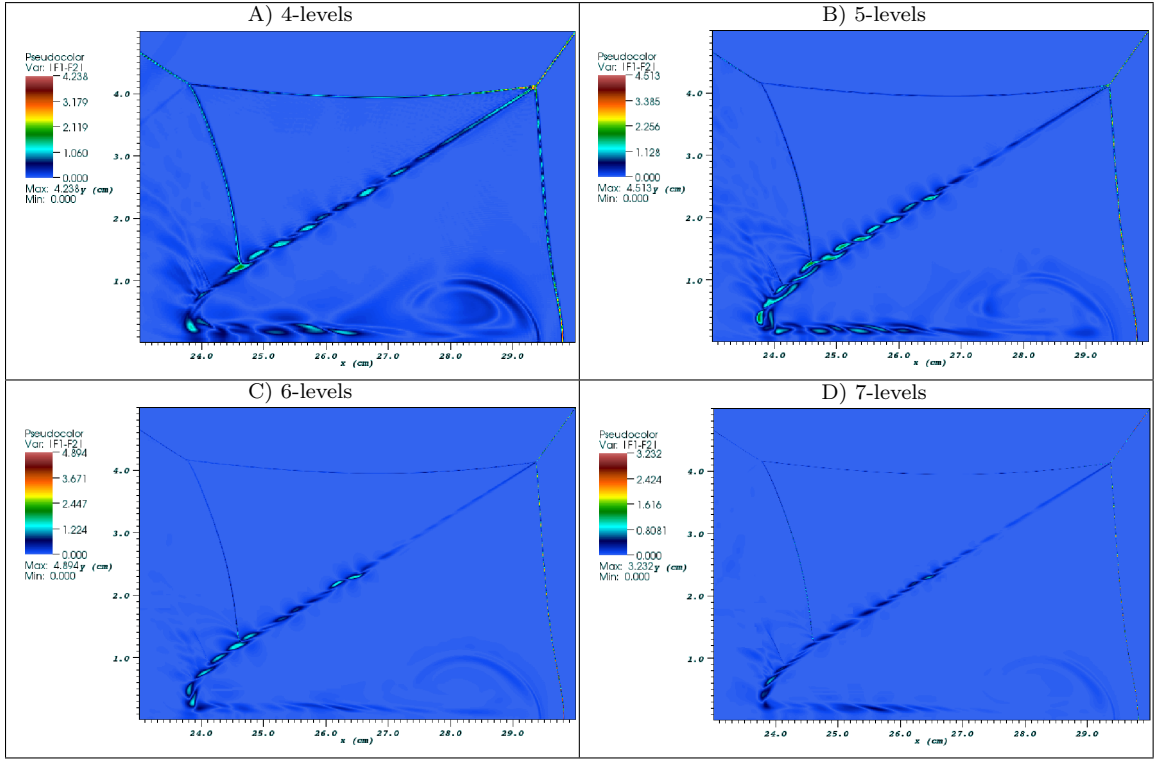


Table 4.12: Density errors calculated with a comparison to the highest resolved case (8-levels).

Scheme	Levels	Wall time	CPU time
MUSCL	6	$6.25 \cdot 10^3 \text{ s} = 1.74 \text{ h}$	55.6 h
MUSCL	7	$2.51 \cdot 10^4 \text{ s} = 6.97 \text{ h}$	233 h
MUSCL	8	$8.65 \cdot 10^4 \text{ s} = 24.0 \text{ h}$	769 h
WENO/CD	6	$1.74 \cdot 10^4 \text{ s} = 4.83 \text{ h}$	155 h
WENO/CD	7	$5.28 \cdot 10^4 \text{ s} = 14.7 \text{ h}$	470 h
WENO/CD	8	$1.78 \cdot 10^5 \text{ s} = 49.5 \text{ h}$	1590 h

Table 4.13: Comparison of run times for the MUSCL and WENO/CD methods using one-step, two-component chemistry for the DMR problem. Intel 5400 series, 32 cores,  $320 \times 160$  SAMR base grid,  $x = (-10, 30)$ ,  $y = (0, 20)$ , final time  $t = 4.91498476$ .



showing obvious visual convergence in the shear layer.

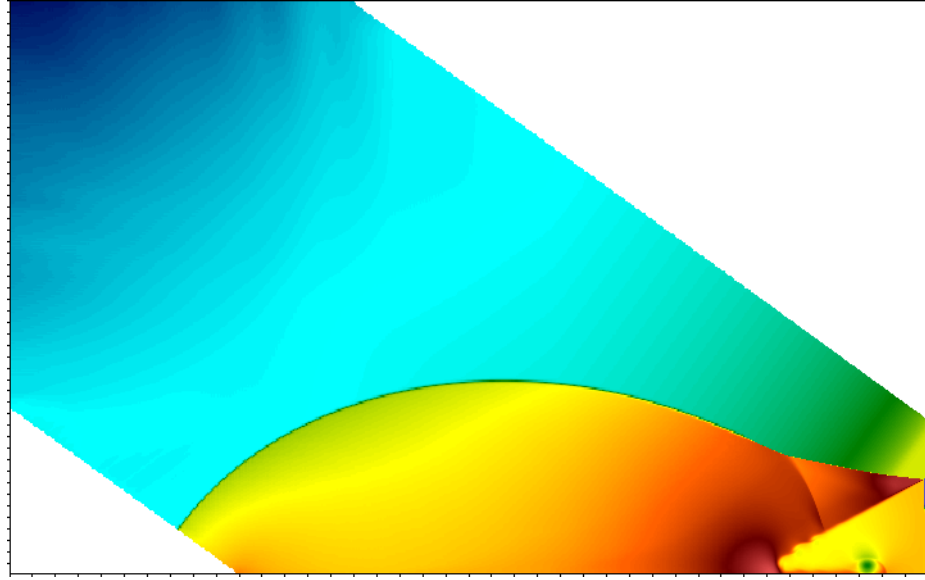
#### 4.2.4.3 Method Comparison

Using up to 7-levels refinement, the computation was repeated with the MUSCL method and second-order accurate finite differences for the diffusive terms. As shown in table 4.10 (E) to (F), the overall flow field is similar, including the position of the shock waves, the jet, and the mixing layer. However, not surprisingly, is the observed result that the roll-up of the shear layer occurs later, which is surmised to be from the additional numerical viscosity (from the spatial solver and temporal integrator) and from the second-order errors from linear interpolation across the SAMR levels. Also for comparison, an inviscid solution is shown in table 4.10(G). In this case, it is the numerical viscosity (which is a function of the resolution used) that dictates the roll-up of the mixing layer. This last case stresses the importance of including physical rather than numerical viscosity when simulating detonations as most detonation simulations use the reactive Euler equations as an approximation.

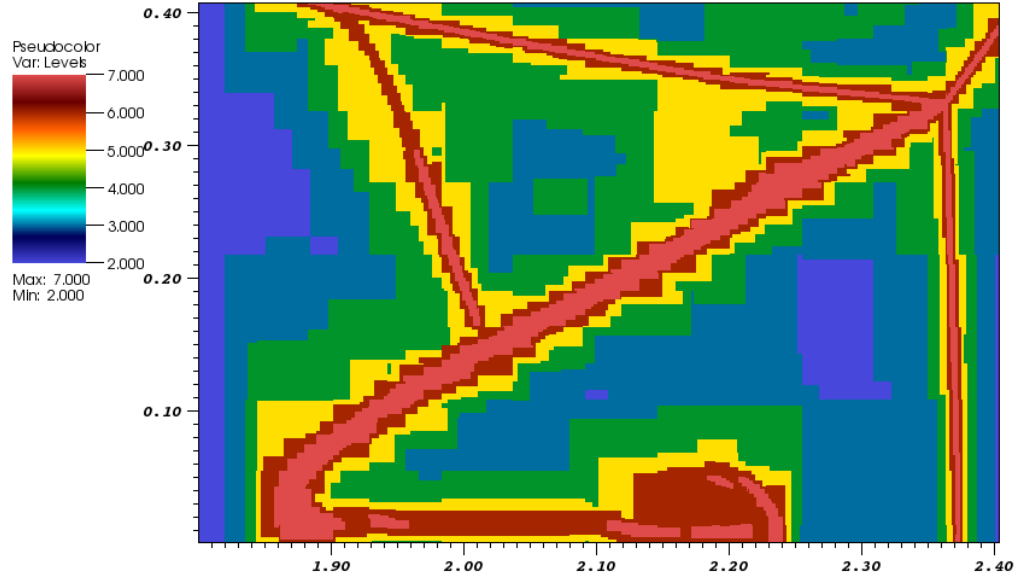
Also, as shown in table 4.13, is a comparison of the computational expense of the MUSCL and WENO/CD methods. Results are shown for 32 cores as actual wall time and total CPU hours. The WENO/CD method is approximately two times more expensive than MUSCL as the number of levels is increased while using the same base grid. Note that the wall times increase at a rate greater than linear as each level is added.

#### 4.2.5 H<sub>2</sub>-O<sub>2</sub>-Ar Multi-Component Chemistry

Using our simplified two-component one-step chemistry model as a basis for comparison, the results were further extended to realistic, multi-component, detailed chemistry. Adapted from Deiterding (40), detailed chemistry and transport of the diffusive DMR problem was modeled using a basic hydrogen-oxygen mechanism as extracted from the hydrocarbon mechanism by Westbrook (161). This mechanism consists of 9 species (O<sub>2</sub>, H<sub>2</sub>O, H, O, OH, H<sub>2</sub>, HO<sub>2</sub>, H<sub>2</sub>O<sub>2</sub>, Ar) and 34 Arrhenius-rate reactions. Due to the larger computational expense required by the additional species and chemistry terms, presently, the diffusive processes are two times less resolved than the previously presented two-component flow results. Because the reaction zone length scale is much larger than the diffusive scales, and we resolve the diffusive scales, the influence of the chemistry is completely resolved, as shown with the OH radical mass fraction field in table 4.14. Note that the two-component one-step case was



(a)



(b)

Figure 4.20: a) DMR density pseudo-color results with detailed chemistry and transport of an  $\text{H}_2\text{-O}_2\text{-Ar}$  detonation in a mixture of initial mole ratios of 2 : 1 : 7 and at  $T = 300\text{ K}$  and  $p = 6,700\text{ Pa}$ . The Chapman-Jouguet detonation speed is  $1,627\text{ m/s}$  and the induction length  $0.01875\text{ m}$ . Problem setup:  $[-0.010, 0.030]\text{ m} \times [0.0, 0.022]\text{ m}$ , 7 levels (2,2,2,2,2,2),  $590 \times 369$  base grid,  $\Delta x_{\min} = 1.06 \cdot 10^{-6}\text{ m}$ ,  $t = 1.2829 \cdot 10^{-5}\text{ s}$ . b) Refinement levels of the DMR at a time of  $t = 1.05386 \cdot 10^{-5}$ .

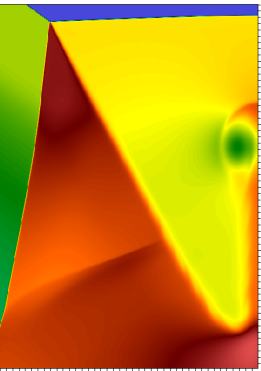


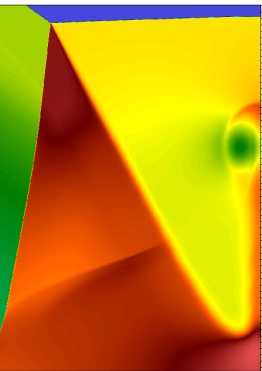

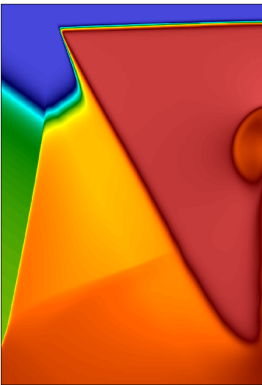
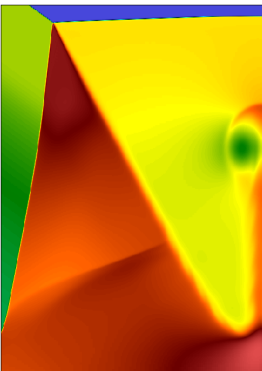

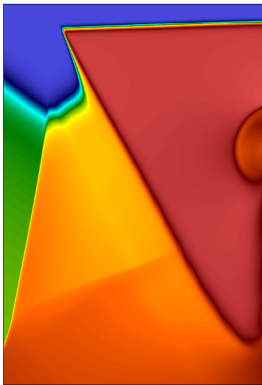
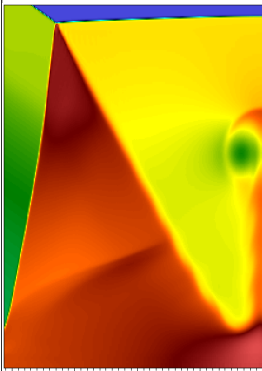

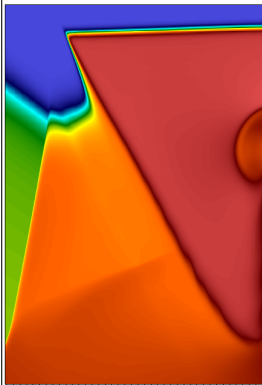
Density pseudo-color	Density contour	OH mass fraction pseudo-color	Method	Diffusion
 <p>(A)</p>			WENO/CD- RK3/GRK4A 4 levels (2,2,2) base grid: 590 × 369 $x = [-1 \text{ cm}, 3 \text{ cm}]$ $y = [0, 2.5 \text{ cm}]$	$\Delta x_{min} = 8.48 \cdot 10^{-6} \text{ m}$ $t = 1.05386 \cdot 10^{-5} \text{ s}$ Re = 2,910 (NERSC Carver) 128 cores: $7.7 \cdot 10^4 \text{ s} = 21 \text{ h}$ $\equiv 2,700 \text{ h CPU}$
 <p>(B)</p>			WENO/CD- RK3/GRK4A 5 levels (2,2,2,2) base grid: 590 × 369 $x = [-1 \text{ cm}, 3 \text{ cm}]$ $y = [0, 2.5 \text{ cm}]$	$\Delta x_{min} = 4.24 \cdot 10^{-6} \text{ m}$ $t = 1.05386 \cdot 10^{-5} \text{ s}$ Re = 2,910 (NERSC Carver) 128 cores: $2.3 \cdot 10^5 \text{ s} = 63 \text{ h}$ $\equiv 8,000 \text{ h CPU}$
 <p>(C)</p>			WENO/CD- RK3/GRK4A 6 levels (2,2,2,2,2) base grid: 590 × 369 $x = [-1 \text{ cm}, 3 \text{ cm}]$ $y = [0, 2.5 \text{ cm}]$	$\Delta x_{min} = 2.12 \cdot 10^{-6} \text{ m}$ $t = 1.05386 \cdot 10^{-5} \text{ s}$ Re = 2,910 (NERSC Carver) 256 cores: $5.2 \cdot 10^5 \text{ s} = 144 \text{ h}$ $\equiv 37,000 \text{ h CPU}$
 <p>(D)</p>			WENO/CD- RK3/GRK4A 7-levels (2,2,2,2,2,2) base grid: 590 × 369 $x = [-1 \text{ cm}, 3 \text{ cm}]$ $y = [0, 2.5 \text{ cm}]$	$\Delta x_{min} = 1.06 \cdot 10^{-6} \text{ m}$ $t = 1.05386 \cdot 10^{-5} \text{ s}$ Re = 2,910 millikan local Intel 5400 series 64 cores: $7.8 \cdot 10^6 \text{ s} = 2190 \text{ h}$ $\equiv 140,000 \text{ h CPU}$

Table 4.14: Reactive diffusive double Mach reflection with detailed chemistry: density, density contour, and mass fraction pseudo-color plots of the DMR structure.

Levels	density $L_1$ -error	rate	total energy $L_1$ -error	rate	OH mass fraction $L_1$ -error	rate
A)						
3	1.030E-6	-	3.531E+4	-	1.729E-4	-
4	7.445e-07	0.468	2.270E+4	0.637	1.589E-4	0.122
5	6.849e-07	0.124	2.037E+4	0.047	1.575E-4	0.013
6	6.723e-07	0.027	2.020E+4	0.004	1.565E-4	0.009
B)						
3	1.418E-6	-	4.447E+4	-	7.802E-5	-
4	1.306E-6	0.119	4.141E+4	0.103	6.899E-5	0.177
5	1.288E-6	0.020	4.013E+4	0.045	6.887E-5	0.003
6	1.276E-6	0.013	3.991E+4	0.008	6.778E-5	0.023

Table 4.15: Detailed chemistry convergence results:  $L_1$ -error norms for the state variables using the 7-level case as the reference solution: A) final time:  $t = 1.05386 \cdot 10^{-5}$  s, domain:  $[1.8, 2.4] \times [0, 0.4]$  cm, corresponding to when the mixing layer starts to roll up. B) final time:  $t = 1.1455 \cdot 10^{-5}$  s, domain:  $[2.026, 2.47] \times [0, 0.32]$  cm

modeled to correspond to the detailed chemistry simulations in terms of the reactive and diffusive length scales. Also, except for the 8-level case, the smallest cell sizes are the same, and the refinement criteria are similar. Therefore, a comparison of the simulations supports that this detailed chemistry result, being similar to the one-step result, is also resolved in the 7-level case shown in table 4.14. The expense of the highest resolved case was 140,000 h CPU, running 3 months continuously with 64 cores. An even further resolved simulation with 8-levels is currently infeasible for us. Also, note that at the current resolution, a nondimensionalization was unnecessary to avoid underflow errors.

Results are presented for the whole domain in figure 4.20 and for the area spanned by the DMR in table 4.14. Using the 7-level case as an “exact” solution, equivalent convergence rates were calculated and are shown table 4.15. The rates are significantly lower than for the previous configurations. Although the images in table 4.14 seem to suggest convergence, the quantitative analysis and visualizations of the local error similarly as in table 4.12 (not shown here) uncover that the computational resolution and refinement criterion were not yet sufficient. Two to four more times resolution is likely needed to show more convincing results. In the highest resolved detailed chemistry case, the thickness of the last refinement level around the shear layer is thinner than that used in the 7- and 8-level two-component one-step simulations. Our rates are calculated assuming that all levels are simultaneously made two times finer, where in practice just the finest level is refined. Therefore, the magnitude of the rates is dependent on the refinement criterion, specifically the efficiency parameter and error tolerances. The conclusive quantitative convergence results of the two-species



case support the validity of the multi-component results and also demonstrate some of the differences in a solution when choosing to model detailed chemistry. There are now multiple reactions scales, one of which, OH, is shown in table 4.14. These simulations were run only until the onset of instability in the shear layers, and a careful verification study was used to quantify our confidence in the validity of the results. Note that comparisons past the onset of the initial instability are problematic as the flow in the shear layer leaves the laminar regime.

The parameters selected for this case correspond to a *regular detonation* structure (142) with a nearly laminar reaction zone and periodically-spaced transverse waves. This corresponds to a weakly unstable mixture characteristic of low values of the effective activation energy (128) with a relative long energy release region compared to the induction zone length. The reaction zone fluctuations are quasi-steady (142) in weakly unstable waves, and the shear layers associated with the triple-points are primarily downstream of the induction zone. However, due to the subsonic (relative to the shock front) nature of the flow field, the dynamics of the mixing layers can influence the overall structure. In addition, there is clear experimental evidence (138) of jetting of relatively unreacted fluid into the reacted region in the weakly unstable case.

In the present simulations, the results show that there is a clear difference between simulations with and without diffusive transport in the region of the shear layers and jetting. As expected, the presence of diffusion dramatically affects the presence of the large-scale structures in the shear layer, features that are very prominent (134, 105) in inviscid simulations of detonations. However, without simulations of self-sustaining propagating detonations, it is unclear how diffusion will influence the qualitative and quantitative conclusions drawn from inviscid simulations. Of course, the role of diffusion will be strongly dependent on the characteristic Reynolds number associated with the shear flow. In the present case, a characteristic value of  $Re \sim 3000$  is representative of fuel-oxygen detonations at low pressure, similar to those examined in Radulescu *et al.* (134). Larger values are possible in fuel-air mixtures at high pressures. Extensive simulations of detonation structure with models of diffusive processes have been carried out in two and three space dimensions by the group at the Naval Research Laboratory, see for example, Kessler *et al.* (88). They simulated these flows using the reactive Navier-Stokes equations and one-step models with diffusive transport of a single species. The emphasis of these studies has primarily been on deflagration to detonation transition and comparisons of inviscid and viscous propagating detonation simulations are not presented.

The present study is most relevant to the simulation of *irregular detonations* which are characterized by a turbulent reaction zone and a large range of spatial scales both in the spacing of transverse waves, the associated shear layers and reaction fronts (7, 135). Motivated by the experimental observations, preliminary (4, 116) studies of diffusive reaction along shear layers have been carried out by previous authors. In particular, Massa *et al.* (116) carried out a two-dimensional simulation of the shear layer behind expected detonation triple points. Note that this is unlike our simulations in that it excludes all shock waves and symmetry boundary conditions which create the bottom jet. They investigated the role of vortical structures associated with Kelvin-Helmholtz (KH) instability in the formation of localized ignition using detailed chemical kinetics and transport. Their analysis indicates that the diffusive processes and KH instability play no role in ignition for low activation energy mixtures and have a modest role in ignition events for high activation energy mixtures. However, the model problem that Massa *et al.* examined was highly idealized and it is difficult to generalize the results to the structure of propagating detonations.

The present simulations are encouraging and demonstrate the feasibility of applying the computational method to the investigation of the mechanisms involved in the diffusive processes of irregular detonations. The goal is to study highly unstable mixtures for which major effects along the shear layers can be expected; e.g., unreacted pockets transported downstream or reaction behind highly fluctuating shock fronts. We apply these methods to two-dimensional simulations of irregular detonation problems with a reduced model of chemistry and transport. Even with the ongoing advances in computational capability, it seems unlikely that simulations which also resolve diffusive processes will be possible in the near term with realistic reaction mechanisms for hydrocarbon fuels in three-dimensional flows.

## Chapter 5

# Irregular, Diffusive Detonations

In this chapter, the direct numerical simulation (DNS) of irregular detonations is introduced and discussed in detail. For a direct numerical simulation, detailed multi-component chemistry, viscosity, heat conduction, and mass diffusion must be included in a multi-dimensional simulation in order to capture all physical processes. Past research has approached this problem by using various approximations that neglect one or more of these effects. This had made the problem more tractable and less computationally expensive. The only approximations in this work will be a two- rather than three-dimensional simulation in addition to the “pseudo DNS” capturing of strong the shocks.

Firstly in §5.1, the relevant past research in regard to irregular detonations and diffusive detonations is discussed. Then in §5.2, a reduced irregular mixture mechanism is developed, tested, and discussed. The descriptions and results of simulations with this mechanism begin in §5.3 where one-dimensional inviscid and viscous solutions at different resolutions are tested.

This chapter is a primer for simulation results that appear in the next two chapters. In the following chapter6, a small-scale double Mach reflection is studied in great detail. These simulations are run until instability arises in the initially steady wave. Moving on, in the next chapter7 this transition to instability of the steady ZND wave to a multi-dimensional front with characteristic cell sizes is simulated and studied. In these following two chapters in §6.6 and §7.3, a comparison of the simulated DMR structure and detonation cell length scales with those found for an experimentally studied detonation tube is conducted.

## 5.1 Background Research

Numerical studies of irregular detonations in the past have been challenging as detailed chemical kinetics alone dramatically increase the required computational expense. Many multi-dimensional simulations to date have included simple one-step chemistry, but progress was made in the late 90s when researchers began to use reduced detailed chemical kinetic models for the hydrogen-oxygen system as by Oran *et al.* (1), Inaba and Matsuo (77), and Eckett (49). Simulations in three-dimensions with detailed kinetics in hydrogen-oxygen-argon were first made in 2003 by Deiterding (40) and in 2004 a simplified ethylene-air model by Khoklov (89).

### 5.1.1 Recent Research on Unsteady Effects of Detonations

Only over the past 10 years have the effects of diffusion (mass, viscous, heat) in detonations been investigated. Diffusive/viscous processes are important in irregular detonations, but only because of their interactions with the highly unstable shock fronts. Because of their complexity and small size, these instabilities have been difficult to observe and quantify in both experiments and simulation. Some recent works which tackle these issues are discussed below.

Lee and Radulescu (99) describes the general contemporary theories for detonation propagation and structure. They explain the differences of three-dimensional stable and unstable detonations with the basic historical ZND theory and highlight its limitations. Between transverse wave collisions, the velocity of the leading shock generally fluctuates between 1.6 and 0.7 times the average velocity. They discuss how the highly variable flow is still related to an overall mean wave that moves close to the CJ speed.

Experiments of unstable (irregular) detonations have been carried out by multiple research groups. In Austin *et al.* (7, 6) experiments were conducted for various mixtures diluted with Ar (more stable) or N<sub>2</sub> (less stable). The regularity or irregularity (stability or instability) of the detonations was investigated with schlieren images and chemiluminescence of OH. Of their mixtures tested, detonations were found to be most unstable for propane-air. This seems to be the most unstable hydrocarbon studied experimentally in detonations to date. Haloua *et al.* (62) investigated experimentally unstable gaseous detonation of stoichiometric propane/oxygen mixtures, diluted or not with argon or helium. They identified four modes of unsteady propagation: stable detonation, stuttering mode, galloping mode, and fast flame. A comprehensive study was also undertaken by Pintgen *et al.* (128). Experiments, 2D Euler simulations, and

nonreactive 3 shock theory were compared for  $\text{H}_2/\text{O}_2/\text{Ar}$  diluted mixtures. Reasons were surmised for the possible existence of unburnt pockets behind the incident shock wave. These unburnt structures known as keystones show up in experiments when the fluorescence of OH is measured. OH is one of the radicals present in hydrocarbon-air reactive zones. Radulescu *et al.* (135) also experimentally investigated the gas ignition mechanism in typical irregular detonations. They have very clear high-resolution experimental photos of the unstable detonations. For systems with high activation energies and a sensitive dependence on temperature fluctuations, large portions of gas escape shock-induced ignition. The ignition of the remaining gas relies on turbulent mixing between burned and unburned gases.

Numerical studies on the unsteady effects of detonations have been conducted by many researchers. Notable ones are discussed below in chronological order. Gamezo *et al.* (55, 56) used a one-step reaction with different activation energies to study the appearance and nature of unreacted gas pockets downstream of the front, and the oscillation of the center-line velocity. Unstable detonations of ethylene- $\text{O}_2$  were examined by Khokhlov *et al.* (89). Their model consisted of the reactive Euler equations with Arrhenius kinetics, comparing the OH concentration to that found in experiments. They found the solutions to be sensitive to the adiabatic index (specific heat ratio) and the molecular weight. Higher specific heat ratios lead to higher post shock temperatures and more stability. Radulescu *et al.* (134) analyzes the cellular reaction zone structure of unstable methane-oxygen detonations, which are characterized by large hydrodynamic fluctuations and unreacted pockets with a fine structure. The quantitative comparison between experiment and numerics also permits identification of the current limitations of numerical simulations in capturing these effects. The flow fields were obtained from numerical solutions of the Favre-averaged Euler equations in time and space. They added artificial diffusion to the Riemann solver to suppress the entropy oscillations. The simulations revealed two important length scales, the first being associated with the chemical exothermicity and the second (the hydrodynamic thickness) with the slower dissipation of the hydrodynamic fluctuations, which govern the location of the average sonic surface. In the paper of Massa *et al.* (116), they state that three principal phenomena occur in the evolution of the triple-point shear layer: diffusion, the Kelvin-Helmholtz instability, and the auto-ignition of the shocked unreacted stream. They find that the chemical energy release at the transversal front is the dominant energetic contribution for high activation energy mixtures. The shear-layer instability appears to play no role in the formation of localized explosions. They find hot spots occurring in the high and medium activation energy

mixtures near the sonic-transition locus of the initially supersonic unreacted stream. Here, molecular diffusion heating is responsible for ignition supporting the localized and multidimensional nature of these irregular explosions.

### 5.1.2 Recent Research on Diffusive, Reactive Navier-Stokes

As discussed in Powers (131), viscosity, be it from physical or numerical errors, can have a large influence on detonation and reactive flow solutions in general. Singh et al. (146) considered both viscous and inviscid models and qualitatively measured the influences of both physical and numerical viscosity on two-dimensional detonation solutions. Here, the physical viscosity in the Navier-Stokes model was adjusted so that the viscous layers were roughly one-tenth the length of the induction length. Both the Euler and Navier-Stokes models were subjected to a grid-refinement study. In the Euler calculations, intrinsic numerical viscosity, which depends on the size of the grid and the details of the particular numerical method chosen, always played a role in the solution downstream of the shock. In the Navier-Stokes calculations at coarse resolutions, the same artificial viscosity dominates the physical viscosity, and the structures depend on the grid resolution. As the grid is refined for the Euler calculations, the artificial viscosity decreases, and fewer downstream instabilities, such as the Kelvin-Helmholtz instability, are suppressed. At coarse resolutions in the Navier-Stokes model predicts similar results as the Euler model. In this case, the inherent numerical viscosity of the method dominates the physical viscosity. However, as the grid is refined in the Navier-Stokes calculations, the physical viscosity dominates, and no finer-scale structures are apparent. We see these same effects in §6.2.

The first works including diffusion processes for a detailed chemistry and transport model began with a one-dimensional analysis. Singh *et al.* (147) used a wavelet based method to efficiently solve the one-dimensional reactive Navier-Stokes equations. In a paper by Arienti and Shepherd (5), simplified zero- and one-dimensional models were used to estimate the role of diffusion in detonations. From the triple points, there exist mixing layers of hot products and relatively colder unreacted reactants. The rate of mixing affects the time for which the colder flow ignites, and has more affect on the overall flow field if the detonation is highly unstable (in other words, sensitive or having a high activation energy). The zero-dimensional model assumes instantaneous mixing and the one-dimensional model assumes a one-dimensional laminarily diffusing flame. A study by Singh et al. (147) considered a one-dimensional Navier-Stokes model for a detailed  $\text{H}_2\text{-O}_2\text{-Ar}$  mixture and thus resolved shocks of

finite thickness. The viscous layer overlapped some of the finest reaction zone lengths but is distinct from the better understood induction zone. In another paper (145), they also examine the combustion modes possible behind shock waves through solutions of the one-dimensional, steady reactive Navier-Stokes (diffusive but nonviscous) equations with a detailed chemical reaction mechanism for stoichiometric methane-air mixtures.

Many researchers have simulated diffusion for two- and three-dimensional detonations, yet, almost all have neglected multi-component chemistry and/or have also neglected to resolve the diffusive scales. One work that stands out is that of the NRL group (88), which has modeled DDT (detonation to deflagration transition) in 2D and 3D. In their simulations they have used two-component chemistry. They found DDT to be very sensitive to the specific heat ratio.

The most recent and complex simulations to date that are relevant to this thesis are that of Massa *et al.* (116). In their two-dimensional simulations, also discussed in §1.1.6, they neglected the shock waves (which leaves out the main source of detonation instability) and simulated with detailed chemistry the shear layer behind detonation triple points. They investigated the role of vortical structures associated with Kelvin-Helmholtz instability in the formation of localized ignition.

## 5.2 Reactive Propane-Air Mechanism

Detonation for hydrocarbon fuels was simulated through the use of the multi-component model and a reduced mechanism. In order to control the computational expense in a simulation which includes detailed chemistry and transport, a custom reduced model which preserves the steady one-dimensional ZND solution was developed. This was matched for the expected range of detonation speeds in an unsteady multi-dimensional detonation. Propane is of high interest as it is one of the most unstable fuels for which detonations have been studied experimentally in labs to date (116).

### 5.2.1 Reduced Chemistry

The detailed hydrocarbon mechanism of Blanquart *et al.* (22, 21) was reduced from 161 species and 1055 reactions to 22 species and 53 reversible reactions, as shown in appendix E.1. This reduction is only for the  $\text{C}_3\text{H}_8\text{-5O}_2\text{-9N}_2$  mixture at an initial pressure of 20 kPa and temperature of 298 K and should only be trusted for overdrives of 0.8 to 1.4. In this reduction, molecules with greater than 3 carbon atoms were

neglected as were many nonessential reactions. After the initial reduction, a few of the rates for the subreactions of  $C_2H_5$  were tuned to rescale the induction times to match the experimental data.  $C_2H_5$  is a direct product of  $C_3H_8$  and therefore, tuning this reaction directly affects the induction time and only indirectly affects the exothermic energy release and long time relaxation reactions like  $CO_2$  and  $CO$ . The 22 species included in this mechanism are all essential, in that if any one species were to be removed, relatively large changes in at least one range of the overdrive solutions is affected. The species are  $C_3H_8$ ,  $O_2$ ,  $N_2$ ,  $H$ ,  $O$ ,  $OH$ ,  $H_2$ ,  $H_2O$ ,  $CO_2$ ,  $HO_2$ ,  $CO$ ,  $HCO$ ,  $CH_2$ ,  $CH_3$ ,  $CH_2O$ ,  $HCCO$ ,  $C_2H_2$ ,  $CH_4$ ,  $C_2H_3$ ,  $C_2H_4$ ,  $C_2H_5$ ,  $NC_3H_7$

### 5.2.1.1 Comparison to Detailed Chemistry

The detailed mechanism reduction was carried out by matching the induction times and the steady ZND solution profile as close as possible as shown in figures 5.1 and 5.2. The expected detonation wave speeds for the unsteady problem range from an overdrive,  $f = U/U_{CJ}$ , of 0.8 to 1.4. Therefore, throughout the reduction process, the steady ZND solution was matched as close as possible throughout this range. Shown in figures 5.3 and 5.4 are various properties of interest that were preserved in the reduction. The most difficult and important property to match is the thermicity, shown in figure 5.4. The location of the peak directly corresponds to the induction time/length. The shape and width of the peak directly corresponds to the exothermic pulse width. Thermicity describes the rate at which energy from chemical reactions is coupled to the fluid dynamics.

The thermicity term can be broken down into two parts, a dimensionless coefficient  $\sigma_i$  that depends on thermodynamic properties and the convective derivative of the species mass fractions,

$$\dot{\sigma} = \sum_{i=1}^{N_Y} \sigma_i \frac{DY_i}{Dt}. \quad (5.1)$$

As written, the coefficients  $\sigma_i$  in the thermicity term are difficult to compute since the necessary partial derivatives are not commonly available for a typical equation of state. Using thermodynamic identities, the following version can be obtained

$$\sigma_i = -\frac{1}{\rho} \frac{\partial \rho}{\partial Y_i} \bigg|_{P,T,Y_{k \neq i}} - \frac{\alpha_T}{c_P} \frac{\partial h}{\partial Y_i} \bigg|_{P,T,Y_{k \neq i}}. \quad (5.2)$$



Note that this relation is completely general and is independent of any assumptions about the equation of state or the reaction mechanism. The coefficient of thermal expansion is

$$\alpha_T = -\frac{1}{\rho} \left. \frac{\partial \rho}{\partial T} \right|_{P, \mathbf{Y}}. \quad (5.3)$$

For an ideal gas,

$$\sigma_i = \frac{\overline{W}}{W_i} - \frac{h_i}{c_P T}. \quad (5.4)$$

The entire coupling between the flow and the chemistry is contained with  $\dot{\sigma}$ . Thermicity measures the rate at which chemical energy is transformed into thermal energy and vice versa. The variation of the thermicity within the flow reflects the net effect of all chemical reactions taking place: bimolecular exchanges, recombination, and dissociation. The first term in Equation 5.2 is the effective energy release associated with changing the total number of moles of species per unit mass of the reacting mixture. The second term in Equation 5.2 is the normalized energy release associated with chemical bond breaking and formation.

Also, note that for the overdrive greater than one cases, there is an endothermic energy deposition in the early times which is described with a negative thermicity. For an overdrive less than one, the shape of the thermicity is very simple, it goes from practically zero to its final positive value very rapidly. In these cases the location of this rapid rise is important to match.

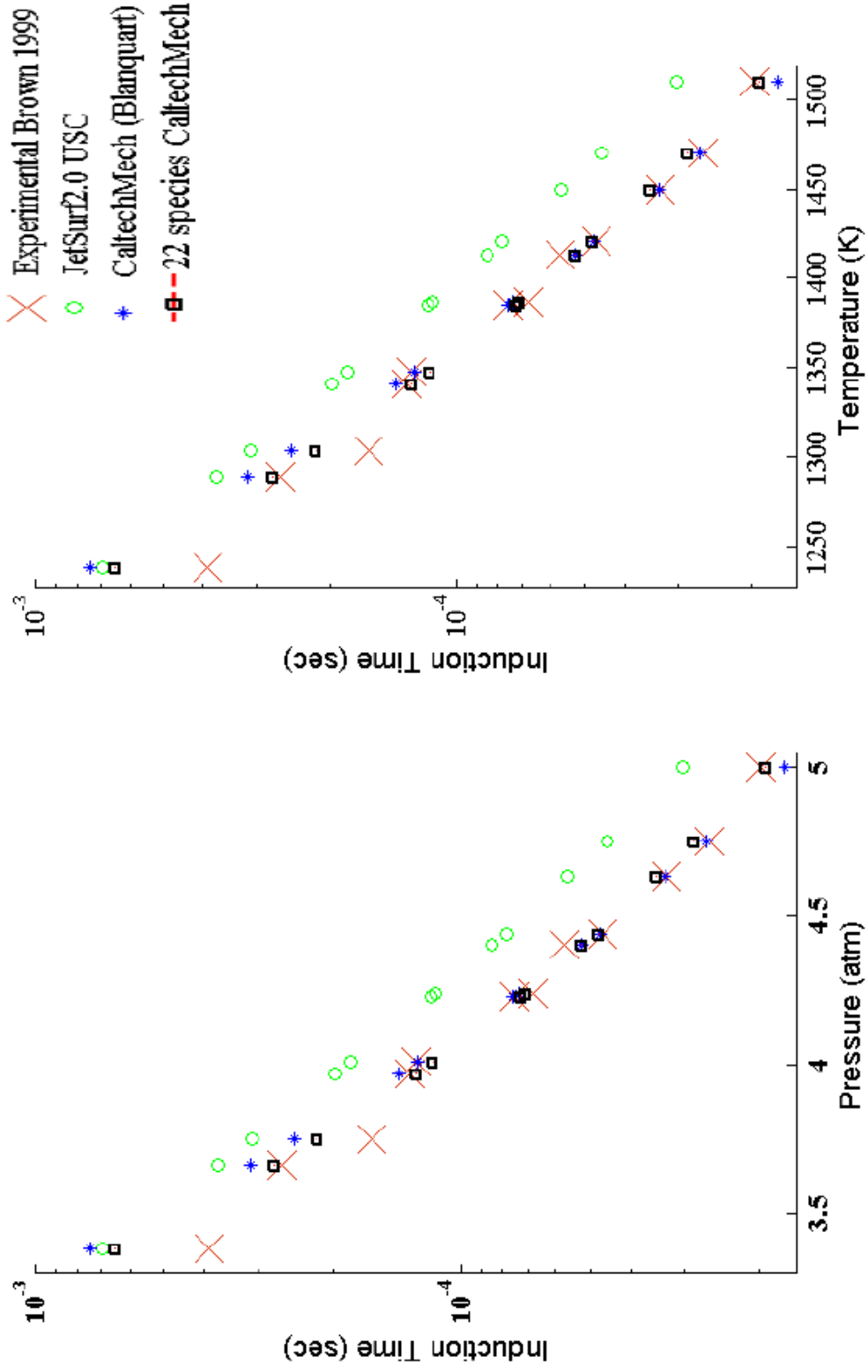


Figure 5.1: Detonation induction time comparisons for propane: comparing experimental vs. detailed (22, 21) and reduced mechanisms. The ambient conditions corresponds to  $T = 300$  K,  $P = 20$  kPa.

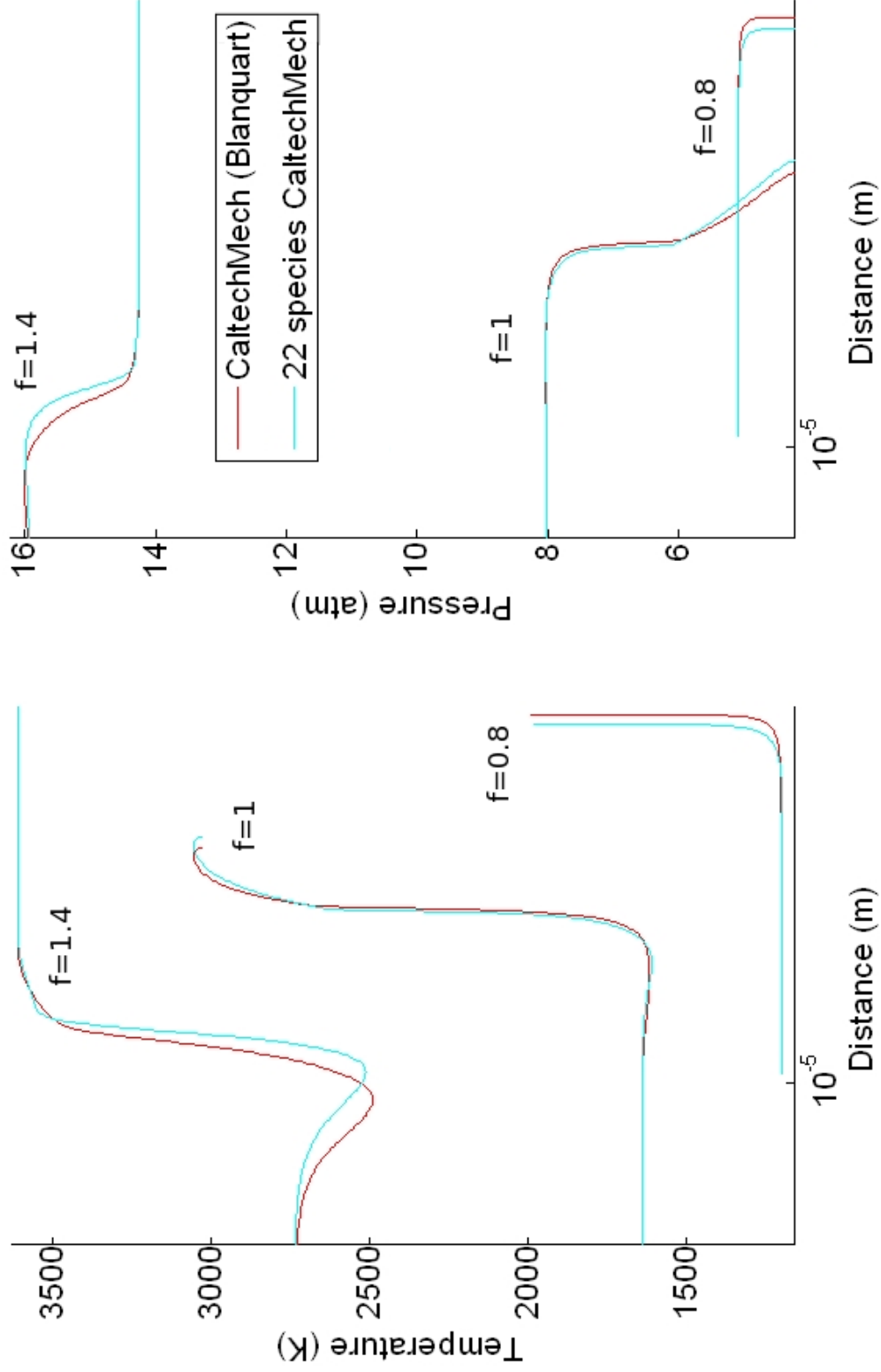


Figure 5.2: Comparing reduced and detailed mechanism (Blanquart) (22, 21) ZND solutions at different overdrives. The reduced propane mechanism neglects  $N_2$  chemistry and larger than C3 molecules to reduce 161 to 22 species and 1055 to 53 reactions. A few rates of subreactions for  $C_2H_5$  were hand tuned to re-scale induction times.

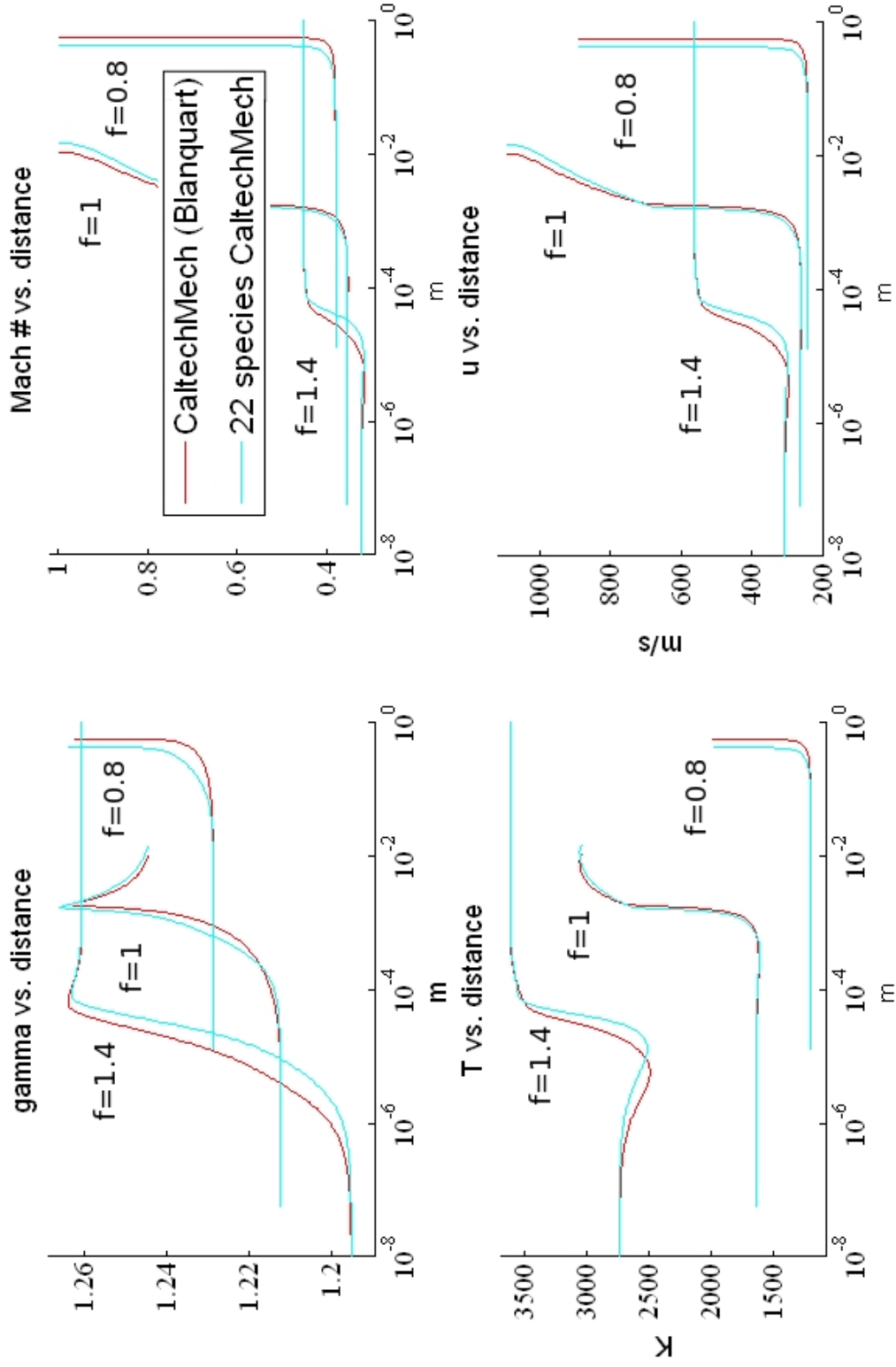


Figure 5.3: Comparing specific heats ( $\gamma$ ), Mach number, temperature, and velocities of the reduced (blue) and detailed (red) mechanisms at overdrives of 1.4, 1.0, and 0.8.

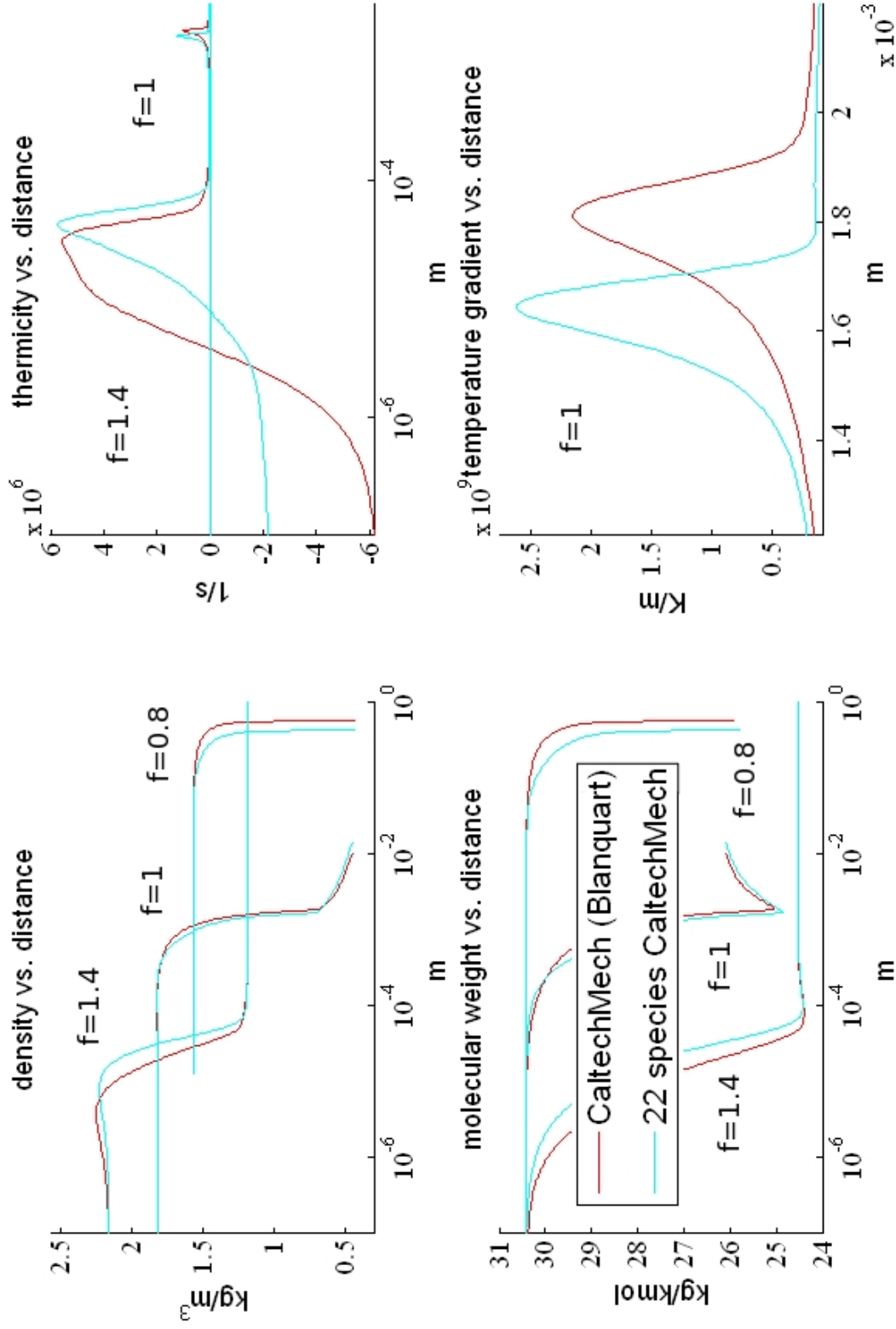


Figure 5.4: Comparing density, thermicity, molecular weights, and temperature gradients of the reduced (blue) and detailed (red) mechanisms at overdrives of 1.4, 1.0, and 0.8. The thermicity plot only shows the 1.4 overdrive case and the temperature gradient plot shows the 1.0 case.

### 5.2.1.2 Reduced Mechanism Chemistry

In figures 5.5, 5.6, and 5.7, as an example, using the CJ speed (overdrive = 1) case the change in composition through the detonation wave is shown. Note the distinct regions where the chain branching and relaxation zones begin. The relaxation involves the final formation of  $\text{CO}_2$  and  $\text{CO}$ .

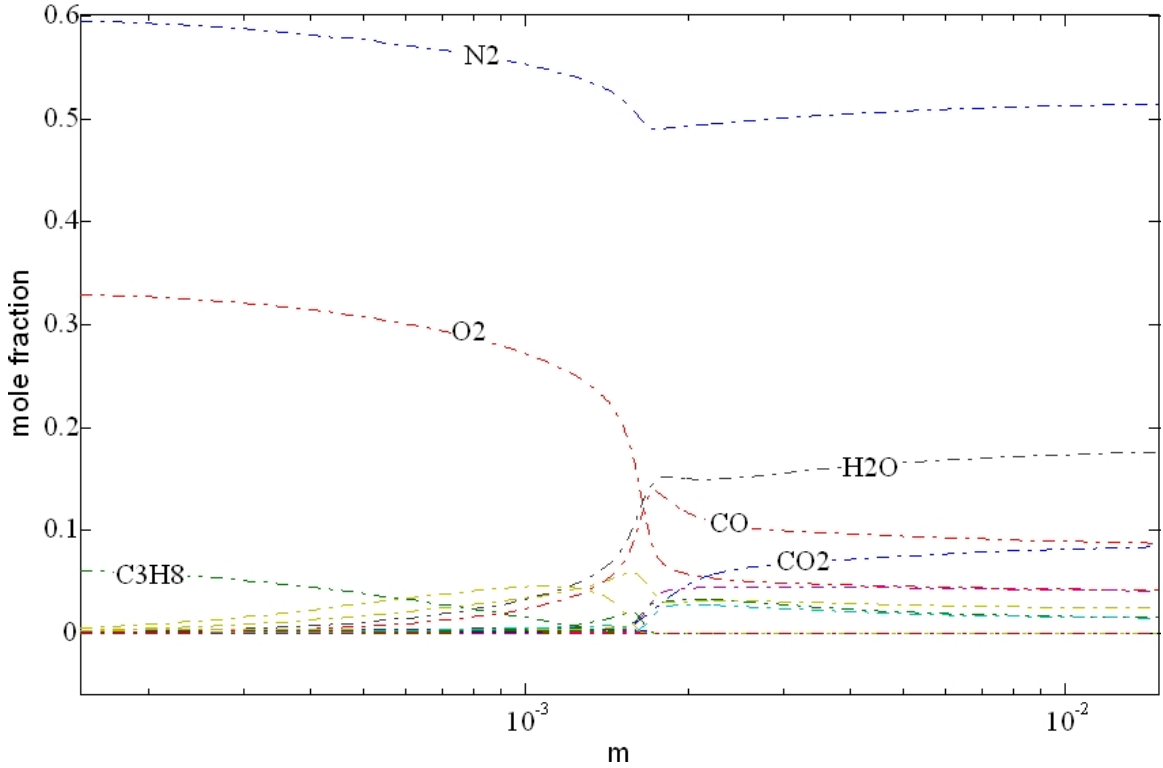


Figure 5.5: Mole fractions as a function of distance for each species for the reduced mechanism at an overdrive of 1.0 (CJ speed).

In figure 5.5, the species with the largest mole fractions are shown.  $\text{N}_2$  is a diluent and its mass (rather than mole) fraction is constant. All nitrogen-related reactions have been neglected in this reduction. This is a common practice for detonation hydrocarbon reductions. The rate at which  $\text{N}_2$  is made into  $\text{N}$ ,  $\text{NO}$ ,  $\text{NO}_2$ ,  $\text{N}_2\text{O}$ ,  $\text{NO}_3$ , etc. is very slow compared to the induction time and relaxation time for  $\text{CO}$  and  $\text{CO}_2$  formation. Therefore, the dynamics of the detonation are not affected. The only difference that would be seen if these reactions were included would be a slightly different final temperature far downstream of the detonation wave.

The induction length is clearly seen in figure 5.5 by looking for the rapid consumption of  $\text{O}_2$  and complete consumption of  $\text{C}_3\text{H}_8$ . The exothermic energy release

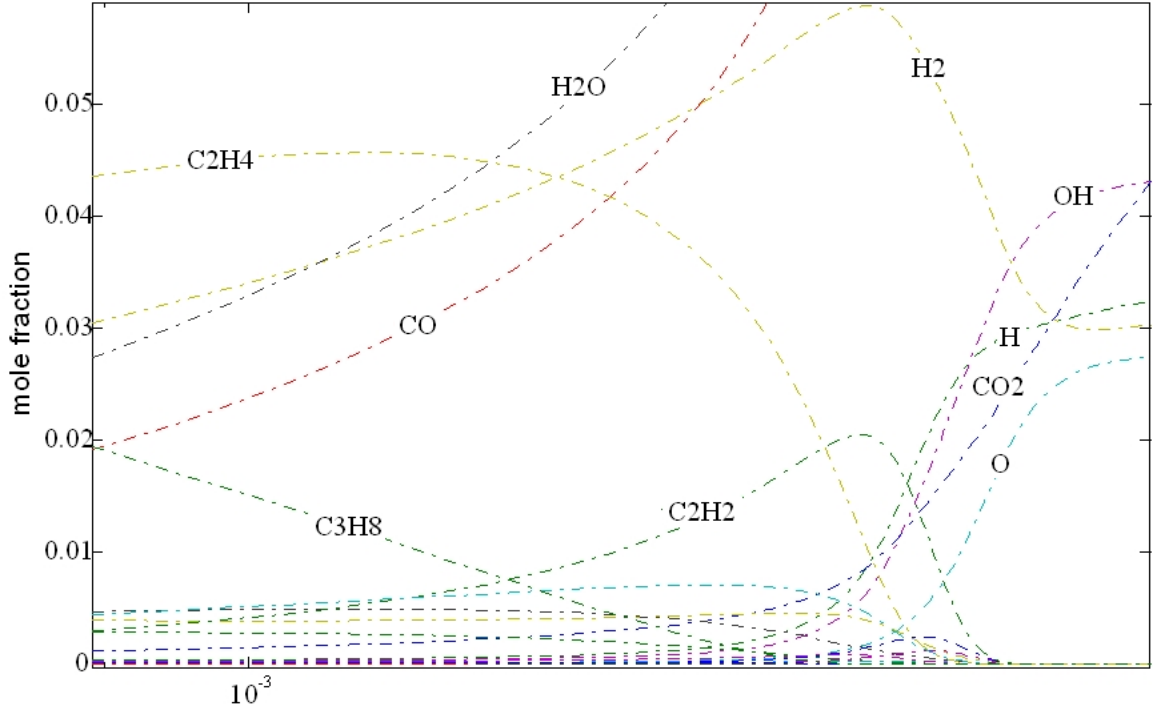


Figure 5.6: Zoomed in view of the mole fractions as a function of distance for each species for the reduced mechanism at an overdrive of 1.0 (CJ speed).

is seen by observing the rapid formation of  $\text{H}_2\text{O}$ . The chemical relaxation is mainly described by the formation of  $\text{CO}$  and  $\text{CO}_2$ .  $\text{HCO}$  which is in a relatively very small concentration shown in figure 5.7, is an important intermediate in this process.

In figure 5.6, the formation of the intermediate  $\text{H}_2$  and hydrocarbons  $\text{C}_2\text{H}_2$  and  $\text{CH}_4$  is observed. The formation of larger concentration radicals  $\text{OH}$ ,  $\text{H}$ , and  $\text{O}$  is also observed. In the next figure, 5.7, more chain branching intermediates are viewed more closely by zooming in. The formation and depletion of  $\text{CH}_2\text{O}$ ,  $\text{CH}_3$ ,  $\text{C}_2\text{H}_3$ ,  $\text{CH}_2$ ,  $\text{C}_2\text{H}_4$ ,  $\text{HCCO}$ , is observed. There are other species of smaller concentrations such as  $\text{C}_2\text{H}_5$ ,  $\text{C}_3\text{H}_7$ , and  $\text{CH}_2\text{O}$  which are also essential in the chain branching process. Also, essential at early times is the  $\text{HO}_2$  radical. Shown in figure 5.8, at an early time the small concentrations of  $\text{C}_3\text{H}_7$  and  $\text{C}_2\text{H}_5$  are formed and then consumed as they are broken down into smaller hydrocarbons.

Our numerical simulations investigate the mechanisms involved in the diffusive processes of irregular detonations. Here, the goal is to study a highly unstable mixture for which major effects along the shear layers can be expected; e.g., unreacted pockets transported downstream or highly irregular ignition. In this case, diffusive processes can be an integral part of the detonation mechanism.

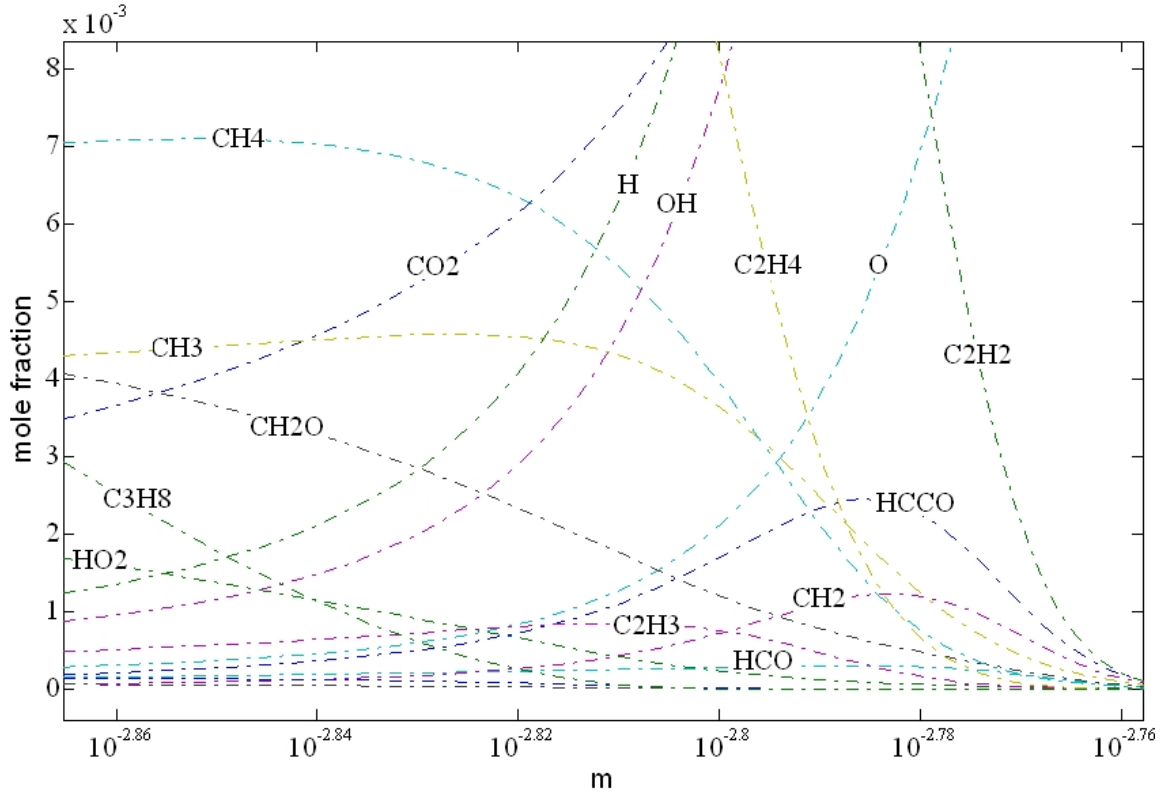


Figure 5.7: Highly zoomed in view of the mole fractions as a function of distance for each species for the reduced mechanism at an overdrive of 1.0 (CJ speed).

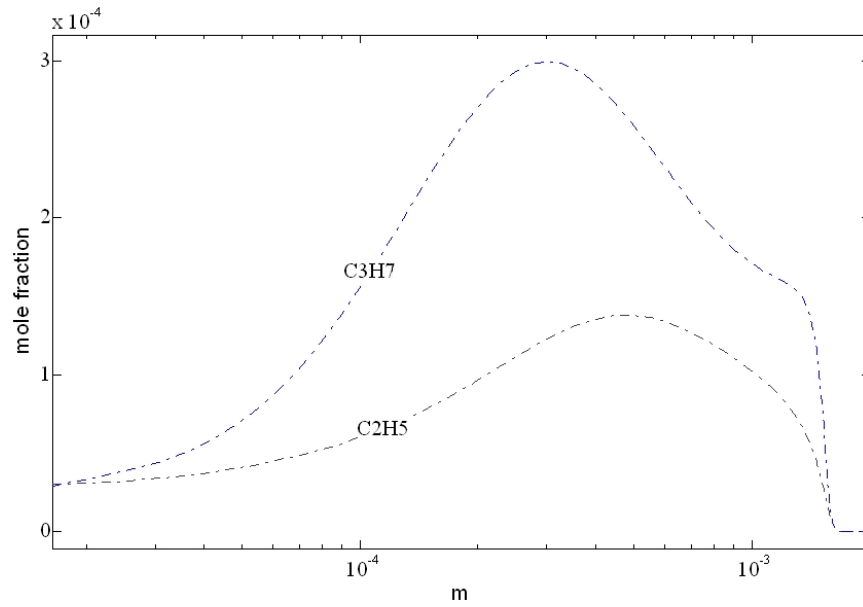


Figure 5.8: Zoomed in view of the mole fractions of  $\text{C}_3\text{H}_7$  and  $\text{C}_2\text{H}_5$  as a function of distance for each species for the reduced mechanism at an overdrive of 1.0 (CJ speed).



### 5.3 One-Dimensional Unsteady Results

Firstly, after the successful development of a reduced mechanism for the steady problem, a unsteady one-dimensional simulation was conducted. For this simulation, a uniform grid of 50,000 cells was used for a domain from -3 to 50 cm, with the smallest cell size equal to 10.6 micrometers. The ZND solution, at a speed slightly larger than the CJ case ( $\text{overdrive} = 1$ ) was used. As shown in figure 5.9(a), the detonation dies and does not self-propagate. The induction zone (where most of the rapid energy release is occurring) becomes separated from the leading shock. Soon after the separation process begins, there is an explosion in the induction zone and the flow locally speeds up and sends a strong pressure wave that runs up to the leading shock. However, this explosion was not strong enough and the induction zone continues to lag behind the leading shock, which without its support loses its strength. The separation of the induction zone is clearly seen by looking at the temperature in figure 5.9(b). The steep temperature rise marks the induction length.

This initial inviscid simulation was carried out at a coarse resolution which does not resolve all the length scales of the chemical reactions. Therefore, in order to test how well a coarse simulation performs, the simulation was repeated with a smallest cell size that was 10 times smaller. For this simulation, a base grid of 50,000 cells was used with 2 refinement levels (2x, 2x) for a domain from -3 to 20 cm, with the smallest cell size equal to 1.15 micrometers. The coarse- and fine-mesh simulations are compared in figures 5.10(a) and 5.10(b). Overall, the same pattern of a decoupled shock and reaction zone is found. The main difference for the simulations is the appearance of fine-scale oscillations which were previously damped out by numerical dissipation. Another large difference is that the simulation with higher resolution decouples at a later time than the lower resolution case. This is observed by seeing that the pressure rises less slowly initially and the is higher at a later time right when the decoupling begins.

Shown in figures 5.11(a) and 5.11(b) is a comparison between inviscid and viscous/diffusive simulations. As expected, at first glance, there is little difference between the two solutions. However, if one zooms in on the plots, it is seen that near the leading shock diffusion of heat has slightly raised the pressure and lowered the temperature for the viscous/diffusive case.

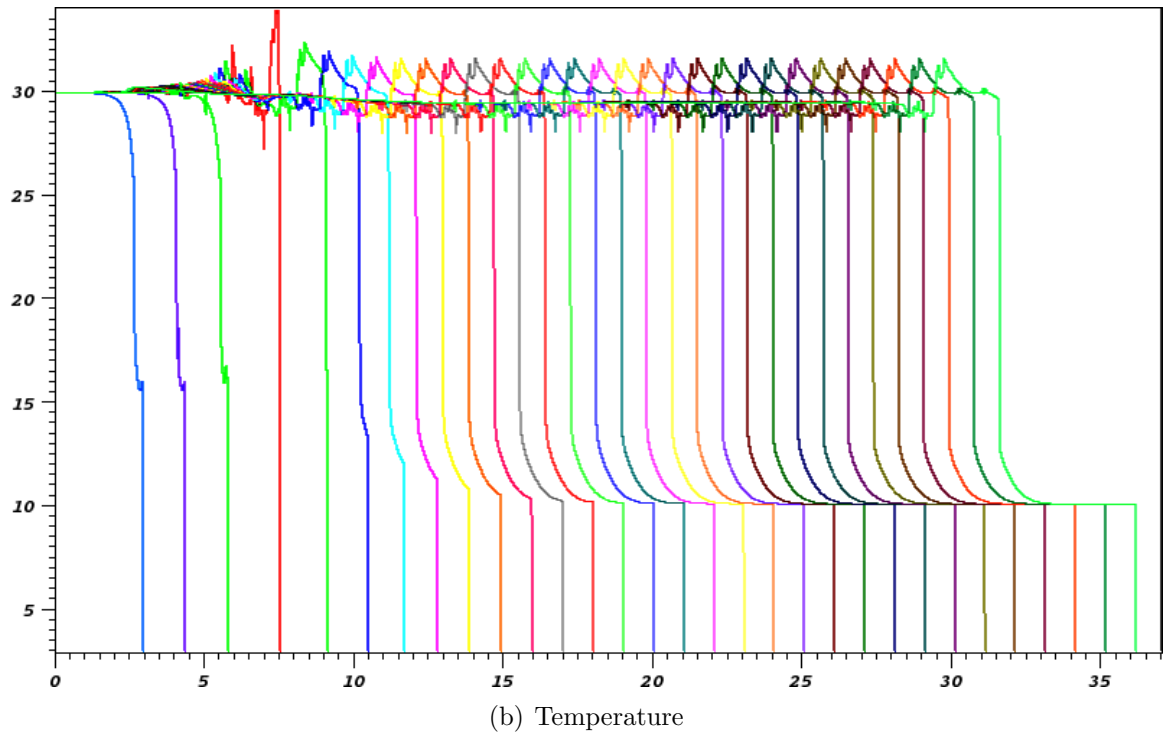
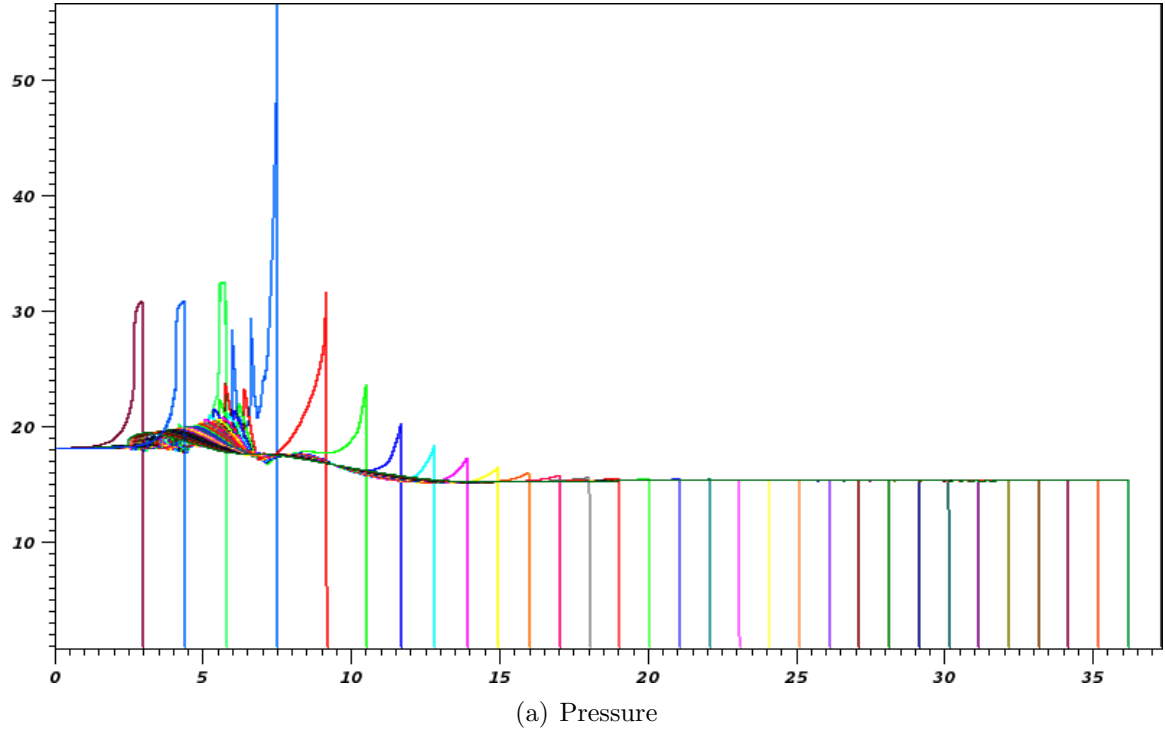


Figure 5.9: Time elapsed nondimensional pressure and temperature for the 1D inviscid case. The lines are plotted every  $t = 240 \text{ nodim} = 7.24 \cdot 10^{-6}$  seconds. The dimensions of the x-axis are cm.

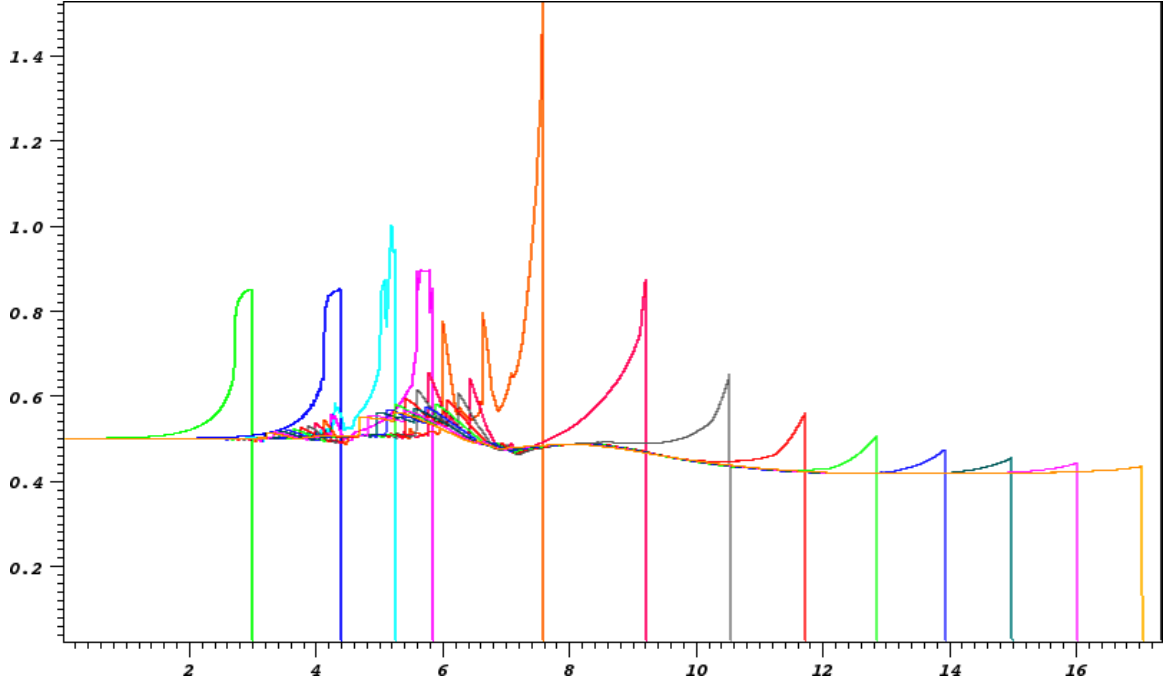
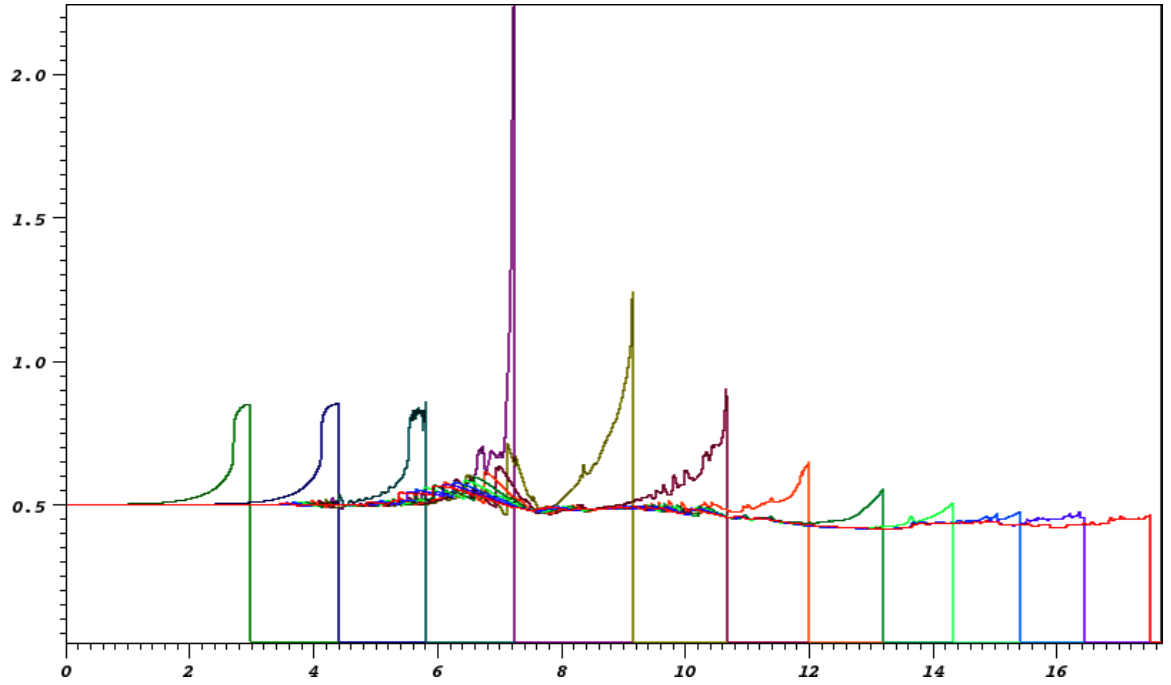
(a) Pressure:  $\Delta x_{min} = 10.6$  micrometers(b) Pressure:  $\Delta x_{min} = 1.15$  micrometers

Figure 5.10: Time elapsed nondimensional pressure for the 1D inviscid case. Comparing a coarse- and high-resolution simulations. The lines are plotted every  $t = 240$   $\text{nodim} = 7.24 \cdot 10^{-6}$  seconds for both simulations. The dimensions of the x-axis are cm.

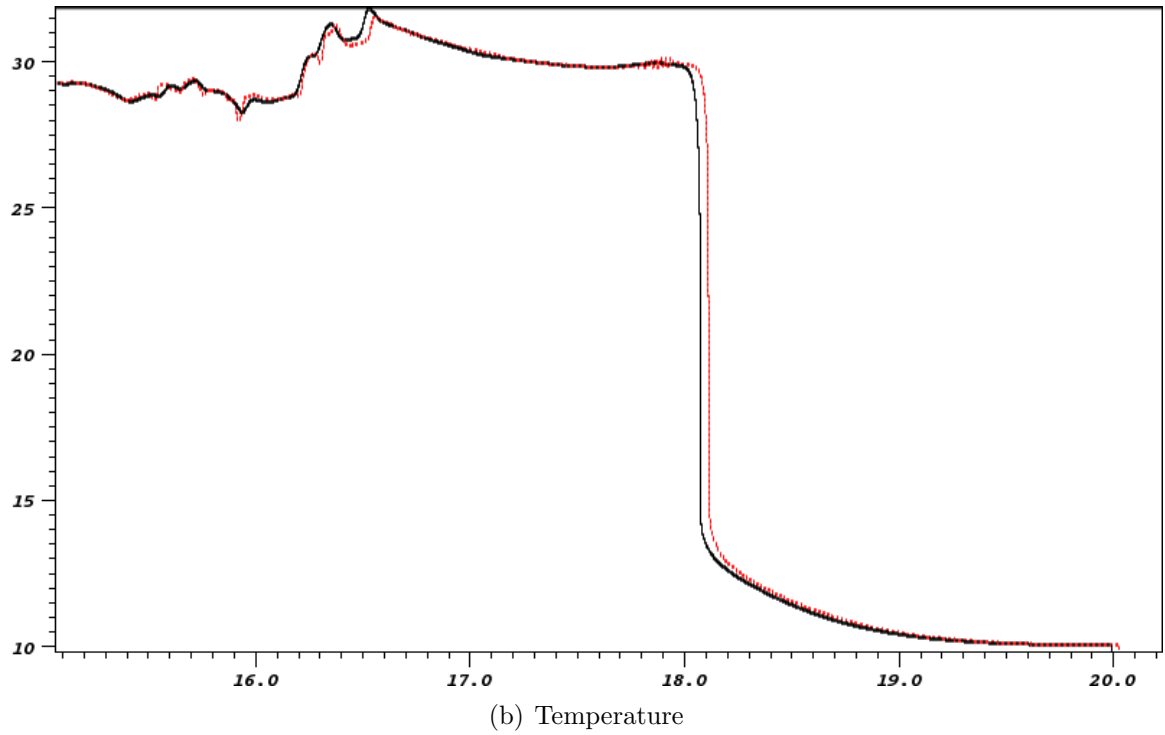
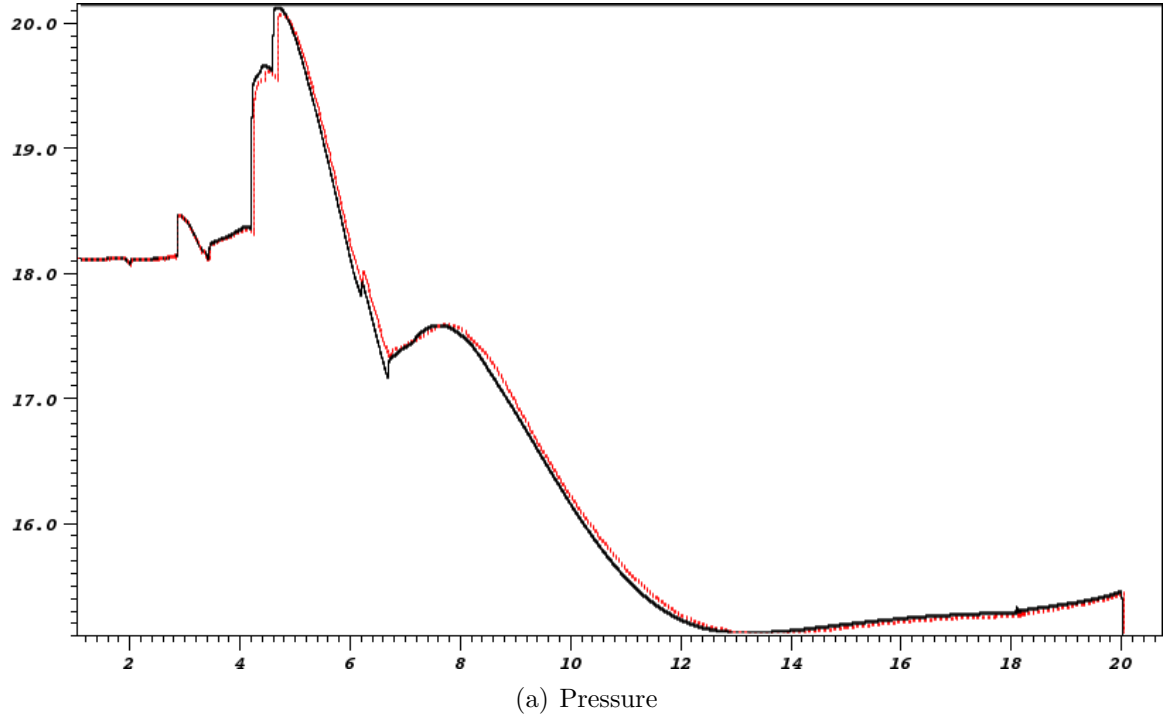


Figure 5.11: Non-dimensional pressure temperature for the 1D viscous (solid black) and inviscid (dotted red) cases at a time  $t = 1.08597 \cdot 10^{-4}$  seconds. The dimensions of the x-axis are cm.

## 5.4 Discussion

A reduced model was developed in order to simulate the most irregular detonation mixture experimentally studied to date. The full detailed hydrocarbon combustion mechanism of Blanquart (22, 21) was reduced to 22 species and 53 reversible reactions. The 22 species included in this mechanism are all essential, in that if any one species were to be removed, large changes in at least one range of the expected over- and underdriven solutions is affected. The shock von Neumann states, induction zones, and equilibrium states were all matched in addition to the location and shapes of the thermicity peak for the overdrives of 0.8 to 1.4.

Starting with a one-dimensional detonation failure test, as compared to all past detonation research, the first of its kind, multi-dimensional, unsteady, hydrocarbon, detonation simulations were begun. The next two chapters demonstrate these results in two-dimensions.

## Chapter 6

# Irregular Detonation Double Mach Reflection

The propane mechanism developed in chapter 5 was used extensively for a detonation double Mach reflection (DMR) simulation. In this chapter results from the diffusive and inviscid detonation DMR are shown and discussed. In §6.1, a time-elapsd, large-scale pressure and radical mass fraction visualization is shown. For each of these, the diffusive and inviscid results using WENO-CD are shown.

These results are from multiple simulations using domains of subsequently increasing size (multiples of 2). The first set corresponds to the smallest domain and the highest resolution using 6-levels (one base level and 5 refinement levels). All cases have a base grid of the same resolution. Figures 6.1-6.4 are of the pressure for only the 6-level simulation results. figures 6.12-6.20 are of the OH mass fraction and are organized as 6-, 5-, and 4-level cases. The time and Reynolds number, as defined by equation (4.26), are listed on each figure. The ambient dynamic viscosity, sound speed, and density used to calculate the Reynolds number were  $1.7501 \cdot 10^{-4}$  gm/cm·sec, 33,150 cm/sec, and  $2.46 \cdot 10^{-4}$  g/cm<sup>3</sup> (all in cgs units as used by CHEMKIN). In these computations, with these particular grids, the viscous solution was surprisingly only approximately two times more computationally expensive than the inviscid solution.

In §6.2, the influence of numerical viscosity as dependent on the grid resolution is studied. In §6.5 the diffusive and inviscid results for this irregular detonation DMR are compared. The influence of the diffusive terms is discussed. In §6.3 the inviscid and diffusive WENO-CD solutions are compared with an inviscid second-order accurate MUSCL solution. Lastly, in §6.4 the diffusive DMR of propane is described in detail qualitatively and quantitatively using traces. More detailed analysis is carried out in §6.4.1 where the flow directions of the DMR are studied by observing how the velocity vectors evolve in time. Various time steps and parameters are selected chronologically

and discussed in multiple figures. The appearance of new triple points from the convective-reactive instability is described.

## 6.1 Overview of Viscous and Inviscid DMR Simulations

In the following subsection, pseudo-color plots which show the complete range of physical processes are shown. The simulations begin with the initial, steady ZND solution reflecting off the bottom boundary where a DMR forms. The DMR firstly looks similar to the nonreactive case, but at later times the Mach stem and reflected and transverse waves which are within the induction zone go unstable and new triple points are formed. At a much later time the incident shock also goes unstable forming new triple points and interacting with the primary Mach stem.

Levels	x-dim (cm)	y-dim (cm)	final t (nondim)	final t (s)	final Re	$\Delta x_{min}$ (m)
3	-1, 8	0,6.8	792	$2.39 \cdot 10^{-5}$	328,000	$10.42 \cdot 10^{-6}$
4	-0.5, 4	0,3.4	336	$1.01 \cdot 10^{-5}$	139,000	$5.21 \cdot 10^{-6}$
5	-0.5, 2	0,1.7	204	$6.15 \cdot 10^{-6}$	93,000	$2.3 \cdot 10^{-6}$
6	-0.5, 1	0,1.2	108	$3.26 \cdot 10^{-6}$	46,500	$1.30 \cdot 10^{-6}$

Table 6.1: table of simulation runs for the detonation DMR.

Different domain sizes and resolutions were used, as shown in table 6.1. For the larger domains, fewer refinement levels and hence less resolution was used. This was done in order to keep the computational expense manageable. Note that all simulation results use a base grid of the same resolution. It is important to have a fine enough base grid, such that errors from the time prolongation when dealing with the sharp gradients in the species concentrations do not pollute the finer levels. For the 6-, 5-, and 4-level cases, the reflection was run up to  $x = 1, 2$ , and  $4$  cm. In this length/time range, the incident shock remains stable (no new triple points are formed). For the 3-level case, the reflection is run until  $x = 8$  cm. In these results, the incident shock is found to go unstable. Note that in all results, the Mach stem has new triple points forming, as does the reflected wave while it is still bounded by the induction length. In what follows, owing to the complexity of the graphical presentation, the reader should follow instructions where indicated, in order to view the visualizations. When this is completed, please move on to the descriptive text, starting in §6.4.

### 6.1.1 Pressure Psuedo-Color: 6-Levels, $x_{\max} = 1$ cm

Shown here in figures 6.1-6.4 are time-elapsed results of pressure for the highest resolved 6-level case. A 360x288 cell base grid spanning  $x=[-0.5,1]$  and  $y=[0,1.2]$  cm was used with 6-levels (base grid,2x,2x,2x,2x,2x) with smallest cell width =  $1.302083 \cdot 10^{-6}$  m. Viscous and inviscid results are compared. As discussed in §6.2, the numerical viscosity is found to be much smaller than the physical viscosity. In the first figure, 6.1, the DMR has traveled 3 mm along the bottom symmetry boundary. Instabilities have developed in the main reflected wave and in the next figure, 6.2, triple points have clearly formed. In figure 6.3, the Mach stem has also gone unstable and at least 4 triple points are clearly visible. Aside from the maximum pressure value which is larger for the viscous case, overall, the inviscid and viscous results for pressure appear to be very similar. If using a pdf reader, go to: view – > rotate – > clockwise 90 degrees. When finished viewing, rotate counterclockwise.



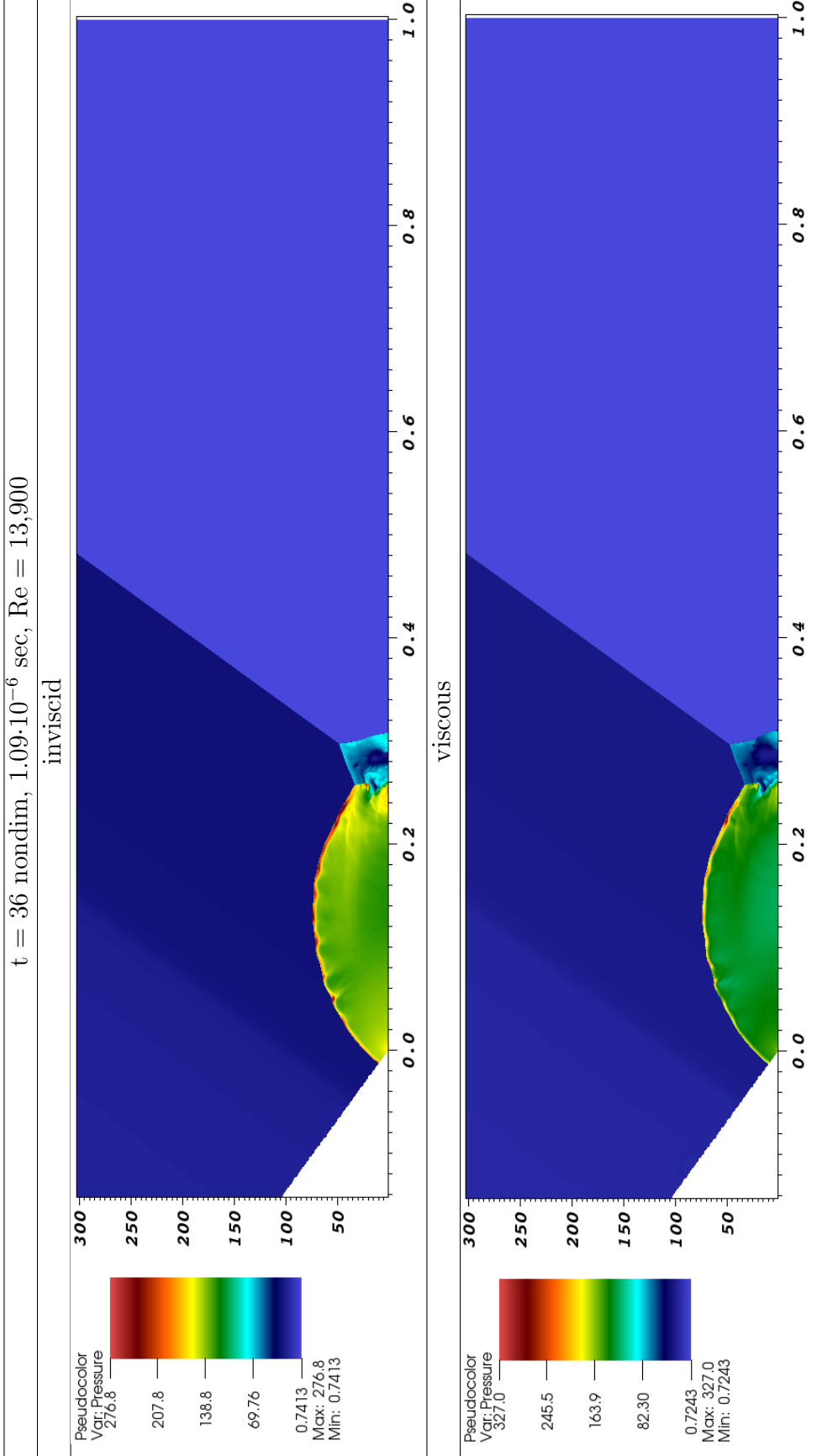


Figure 6.1: Pseudo-color pressure plot, 6-levels (base grid,2x,2x,2x,2x,2x) refinement with a 360x288 cell base grid spanning  $x=[-0.500,1]$  and  $y=[0,1.2]$  cm with smallest cell width =  $1.30208310^{-6}$  m, comparing inviscid and diffusive results.

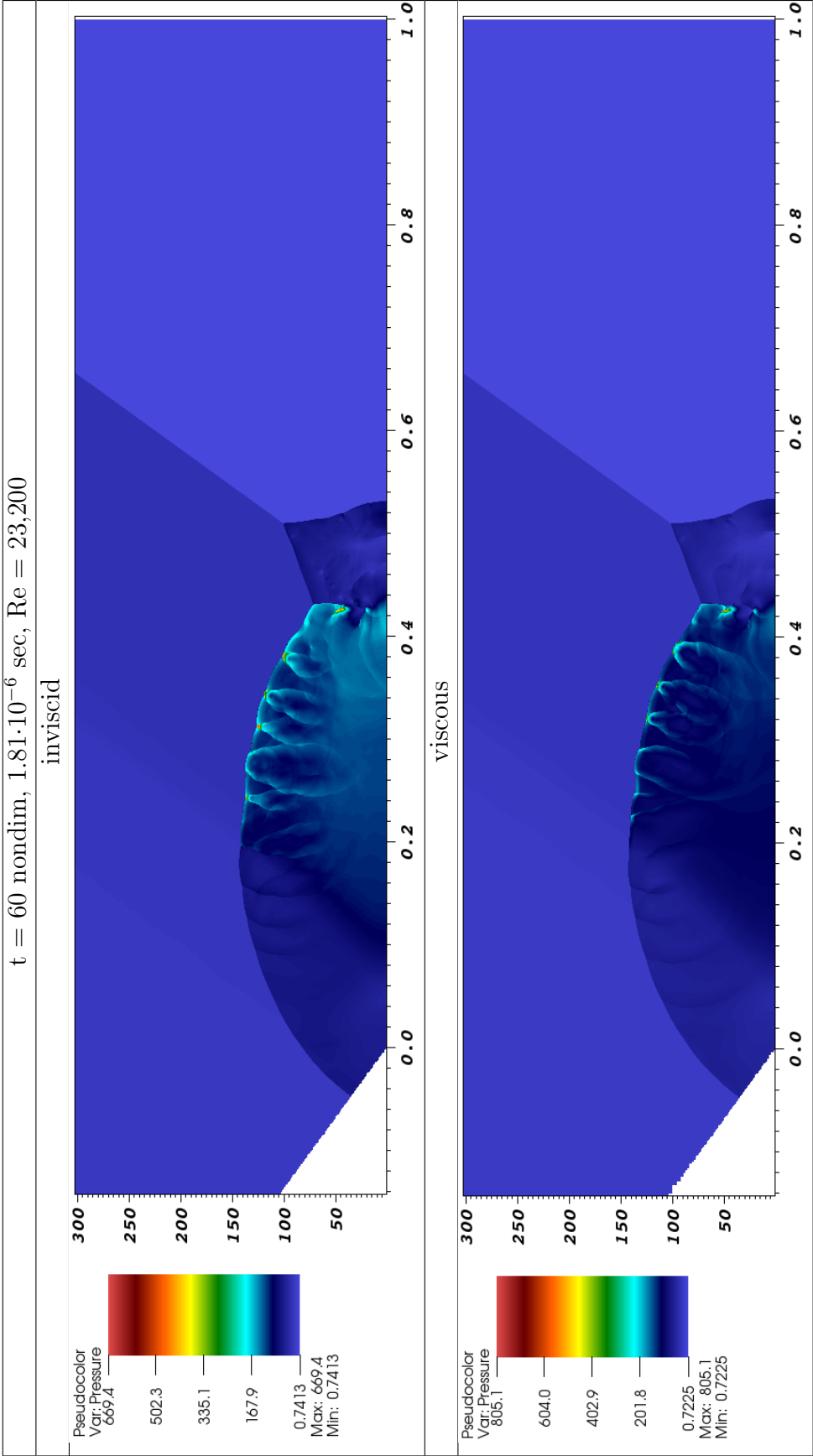


Figure 6.2: Pseudo-color pressure plot, 6-levels (base grid,2x,2x,2x,2x,2x) refinement with a 360x288 cell base grid spanning  $x=[-0.500,1]$  and  $y=[0,1.2]$  cm with smallest cell width =  $1.302083 \cdot 10^{-6}$  m, comparing inviscid and diffusive results.

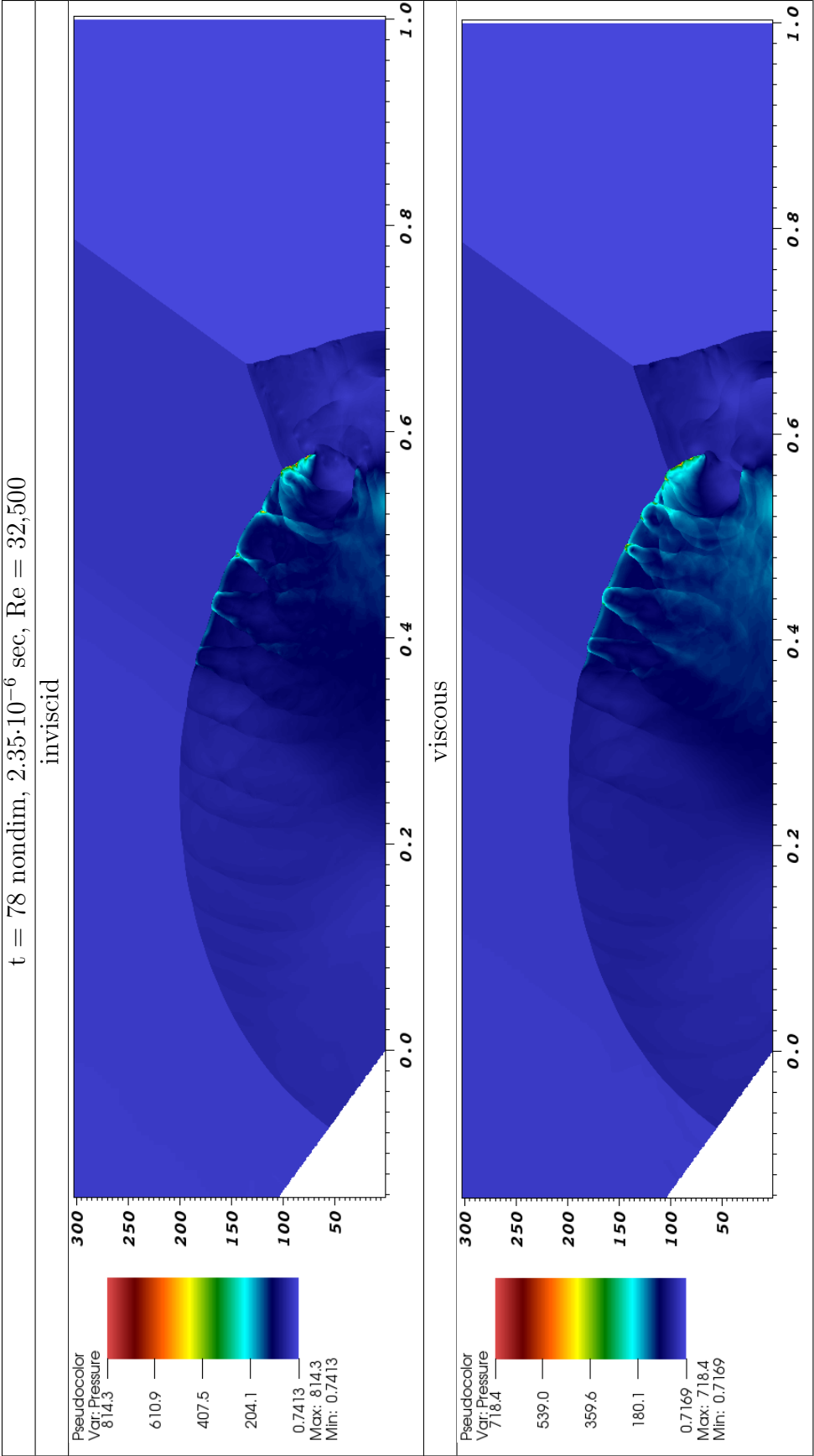


Figure 6.3: Pseudo-color pressure plot, 6-levels (base grid,2x,2x,2x,2x,2x) refinement with a 360x288 cell base grid spanning  $x=[-0.500,1]$  and  $y=[0,1.2]$  cm with smallest cell width =  $1.302083 \cdot 10^{-6}$  m, comparing inviscid and diffusive results.

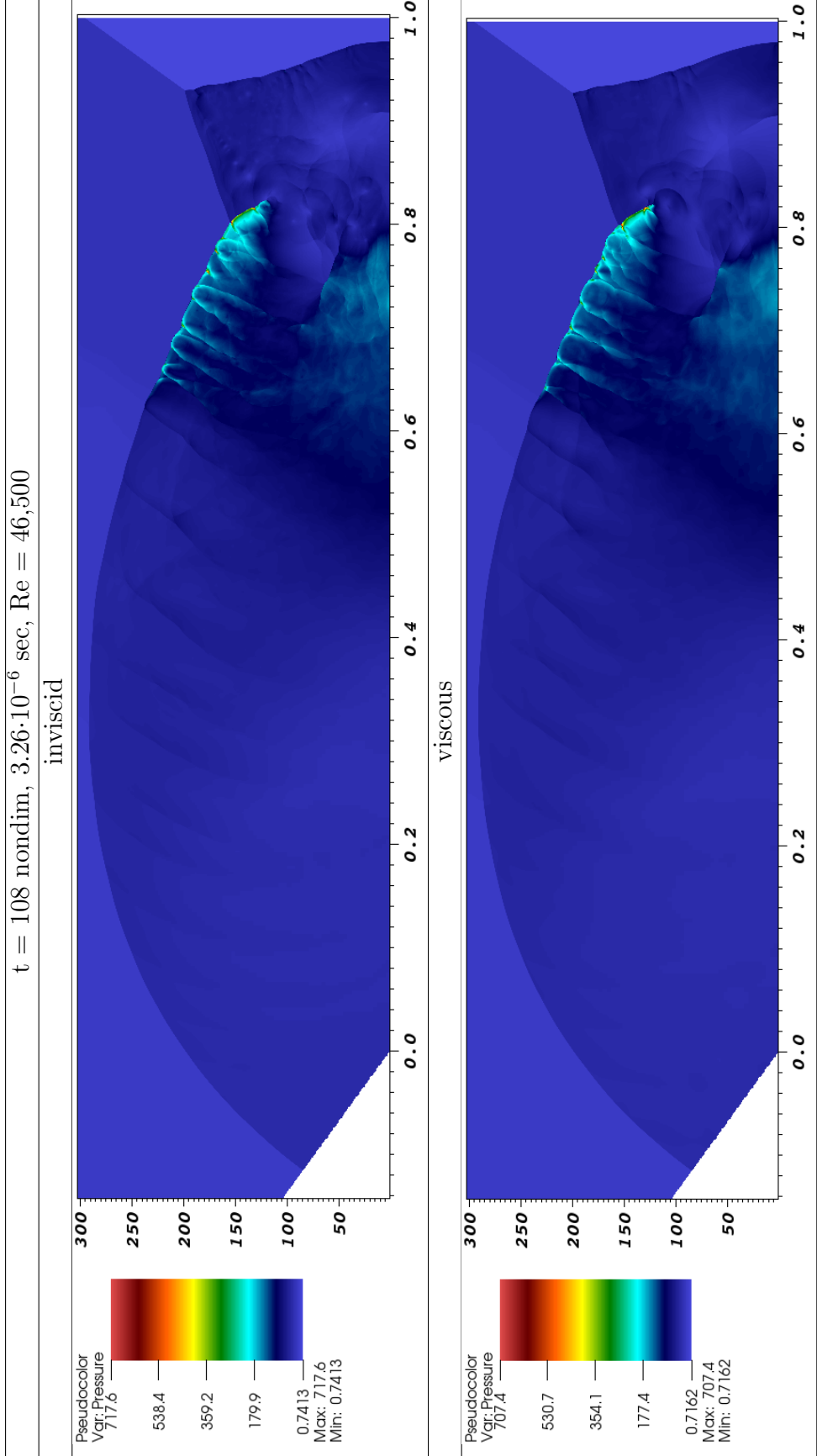


Figure 6.4: Pseudo-color pressure plot, 6-levels (base grid,2x,2x,2x,2x,2x) refinement with a 360x288 cell base grid spanning  $x=[-0.500,1]$  and  $y=[0,1.2]$  cm with smallest cell width =  $1.302083 \cdot 10^{-6}$  m, comparing inviscid and diffusive results.

### 6.1.2 Pressure Psuedo-Color: 3-Levels, $x_{\max} = 8$ cm

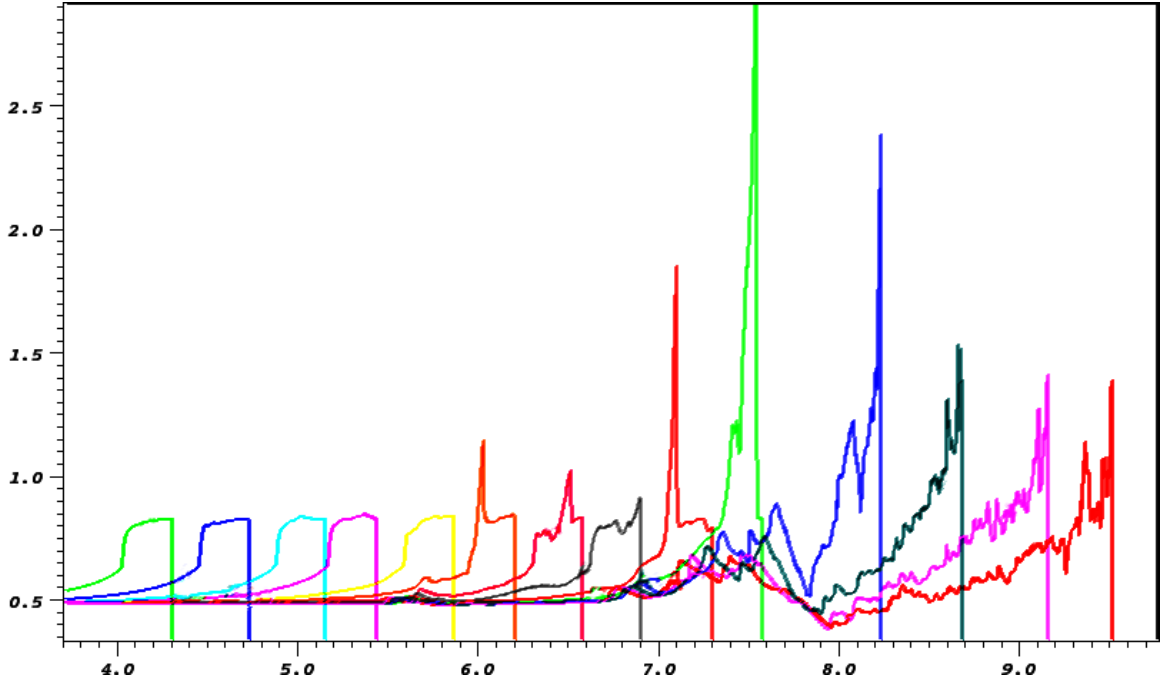


Figure 6.5: Incident shock pressure for the inviscid case. The green line peaks at about 4 MPa. The dimensions of the x-axis are cm and the y-axis are MPa.

Shown in figures 6.5-6.9 are time-elapsd results of pressure for a much less resolved case with 3-levels. A 2160x1624 cell base grid spanning  $x=[-1,8]$  and  $y=[0,6.8]$  cm was used with 3-levels (base grid,2x,2x) with smallest cell width =  $1.04167 \times 10^{-5}$  m, about 10 times larger than the previous case. Viscous and inviscid results are again compared. As discussed in §6.2, the numerical viscosity is found to be significantly larger than the physical viscosity at this resolution.

figure 6.5, shows a pressure trace through the incident shock. When comparing this result to the one-dimensional case in figure 5.9(a), it is seen that the introduction of another spatial dimension into the problem has allowed the reaction zone to stay coupled with the incident shock. In the 1D case, they become decoupled. However, in 2D, instabilities in the transverse direction of the flow have allowed chemical reactions to be accelerated and the incident shock to be supported by their energy release. A comparison of the 1D and 2D cases showing the propane mass fraction is shown later in figure 6.44

In the first figure below, 6.6, the DMR has traveled about 4 cm along the bottom symmetry boundary. The instabilities that are observed in figure 6.4 are still visible. Many more triple points are visible on the Mach stem which has grown in size,

however, now the secondary triple point of the DMR is no longer bounded by the induction length, and hence, there are no extra triple points around it as was observed in figure 6.4 when the DMR is much smaller. In figure 6.7, the incident shock is observed to have gone unstable. This is presumed to be due to the shock and the reaction zone decoupling as was seen for the one-dimensional results shown in §5.3. This instability also looks similar to that found on the main reflected shock shown in figure 6.1. In figure 6.9, new triple points are clearly visible on the incident shock. With these new instabilities formed, the reaction zone and shock are again coupled.

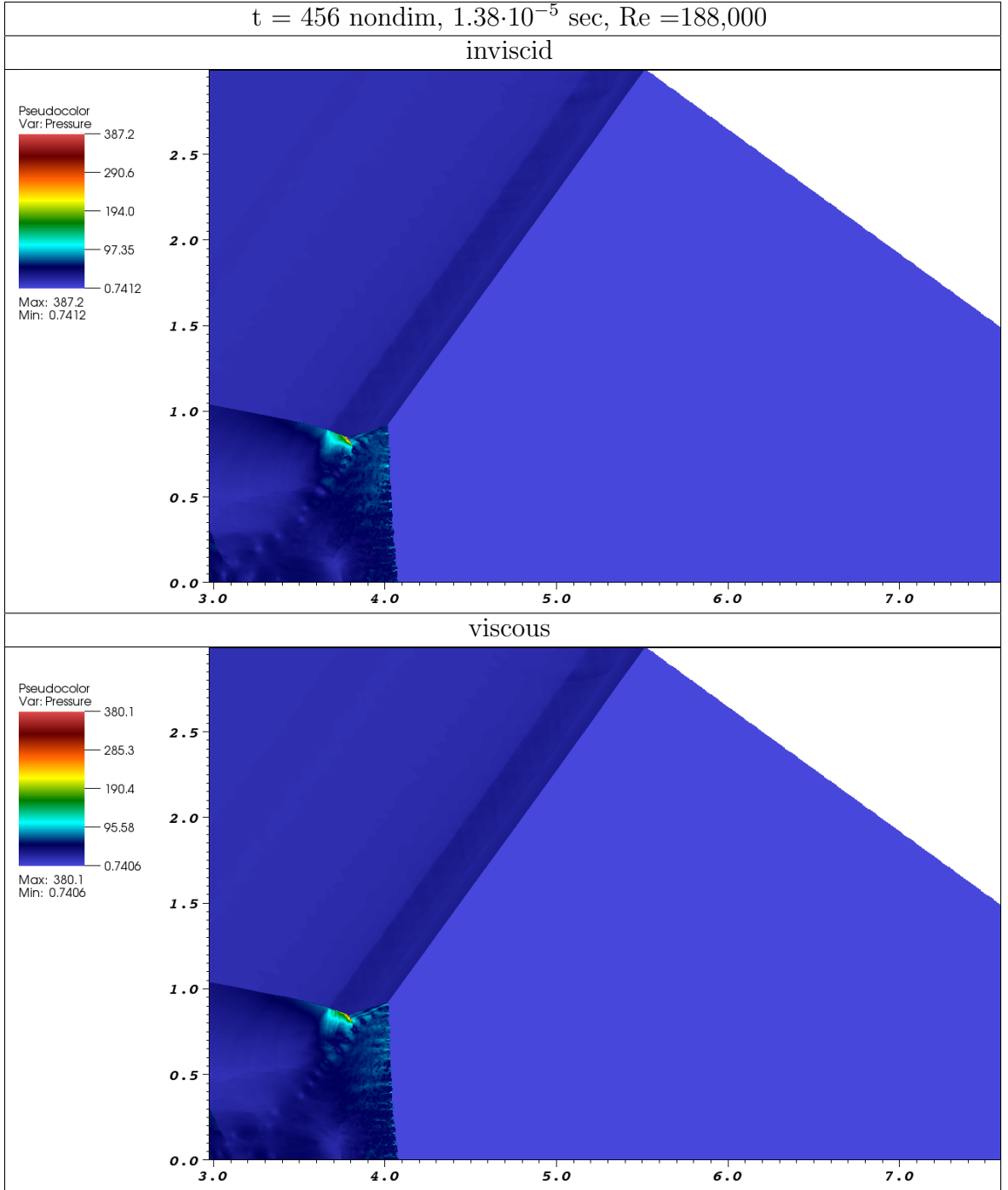


Figure 6.6: Pseudo-color plot of the pressure (Pa), 3-levels (base grid,2x,2x) refinement with a 2160x1624 cell base grid spanning  $x=[-1,8]$  and  $y=[0,6.8]$  cm with smallest cell width =  $1.0416710^{-5}$  m. Comparing inviscid and diffusive results.

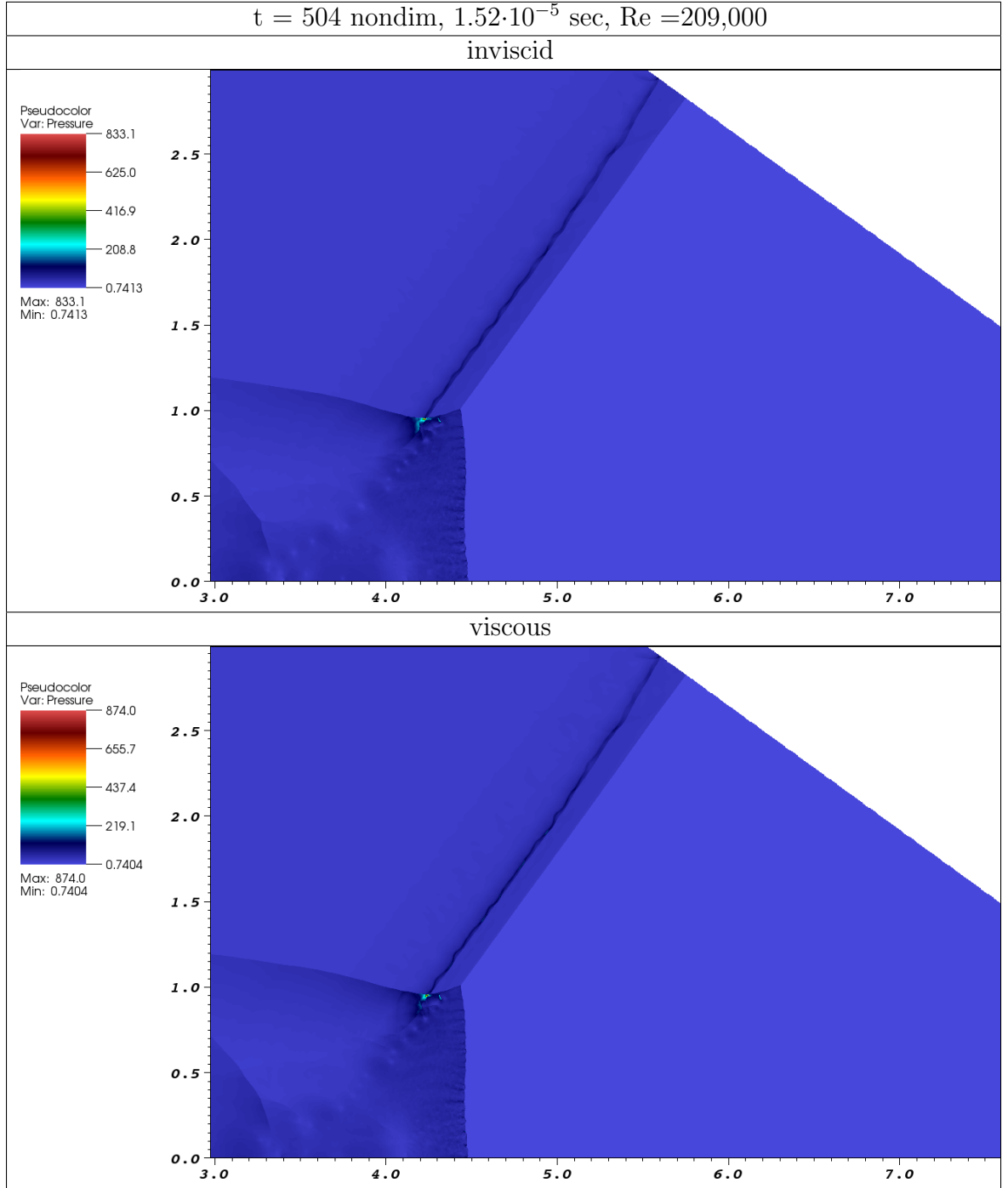


Figure 6.7: Pseudo-color plot of the pressure (Pa), 3-levels (base grid, 2x, 2x) refinement with a 2160x1624 cell base grid spanning  $x = [-1, 8]$  and  $y = [0, 6.8]$  cm with smallest cell width =  $1.04167 \cdot 10^{-5}$  m. Comparing inviscid and diffusive results.



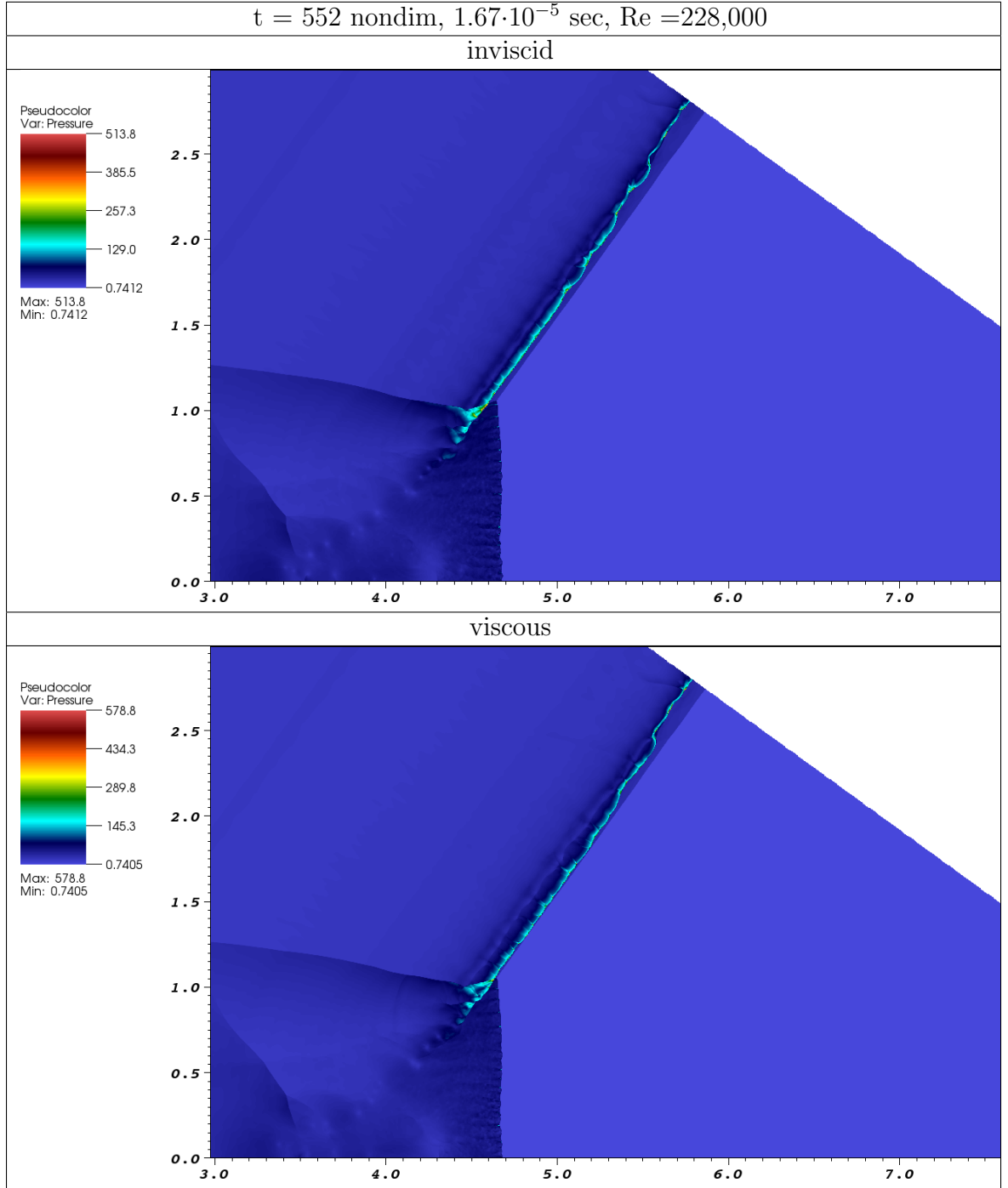


Figure 6.8: Pseudo-color plot of the pressure (Pa), 3-levels (base grid,2x,2x) refinement with a 2160x1624 cell base grid spanning  $x=[-1,8]$  and  $y=[0,6.8]$  cm with smallest cell width =  $1.04167 \cdot 10^{-5}$  m. Comparing inviscid and diffusive results.

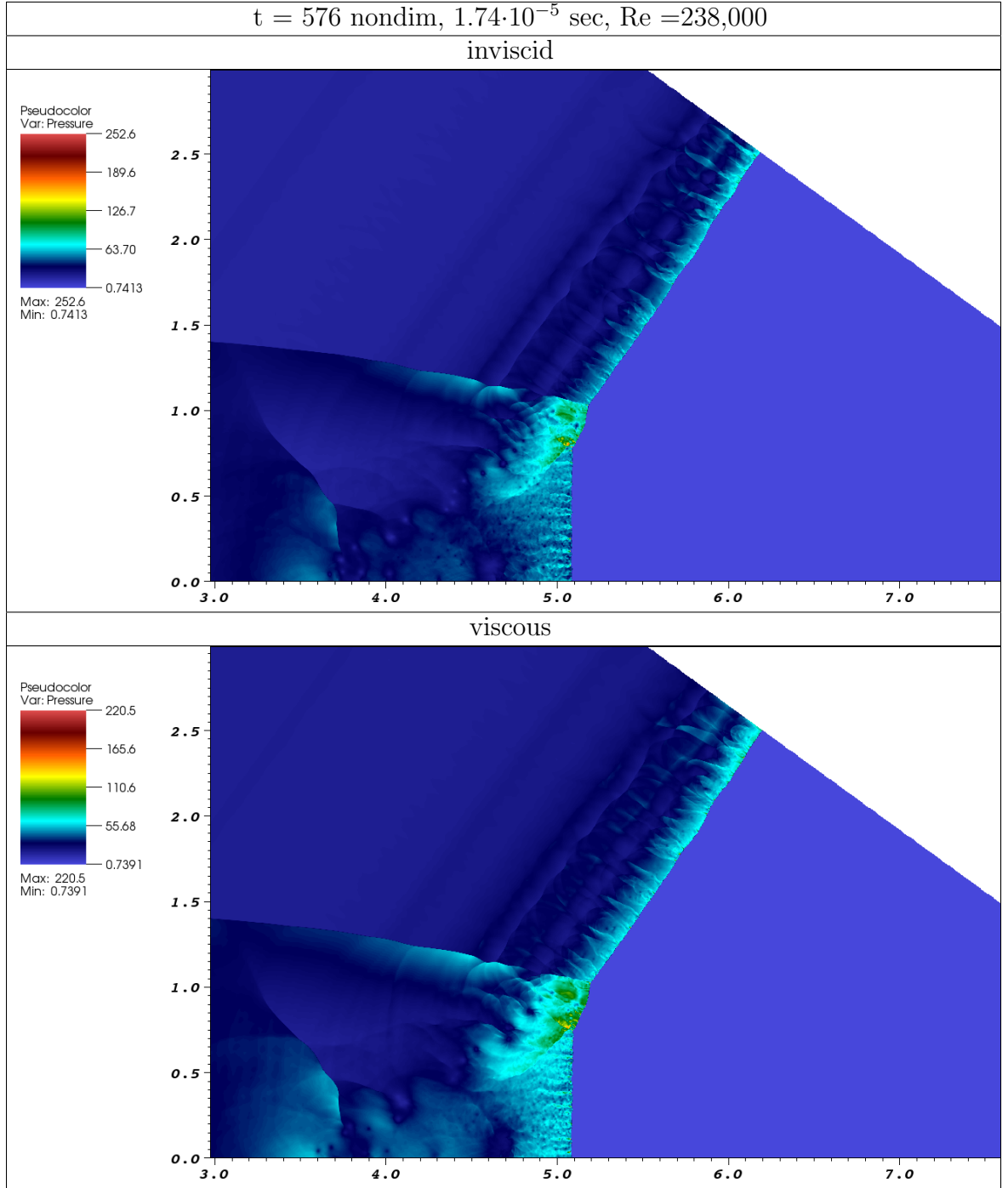


Figure 6.9: Pseudo-color plot of the pressure (Pa), 3-levels (base grid,2x,2x) refinement with a 2160x1624 cell base grid spanning  $x=[-1,8]$  and  $y=[0,6.8]$  cm with smallest cell width =  $1.04167 \cdot 10^{-5}$  m. Comparing inviscid and diffusive results.

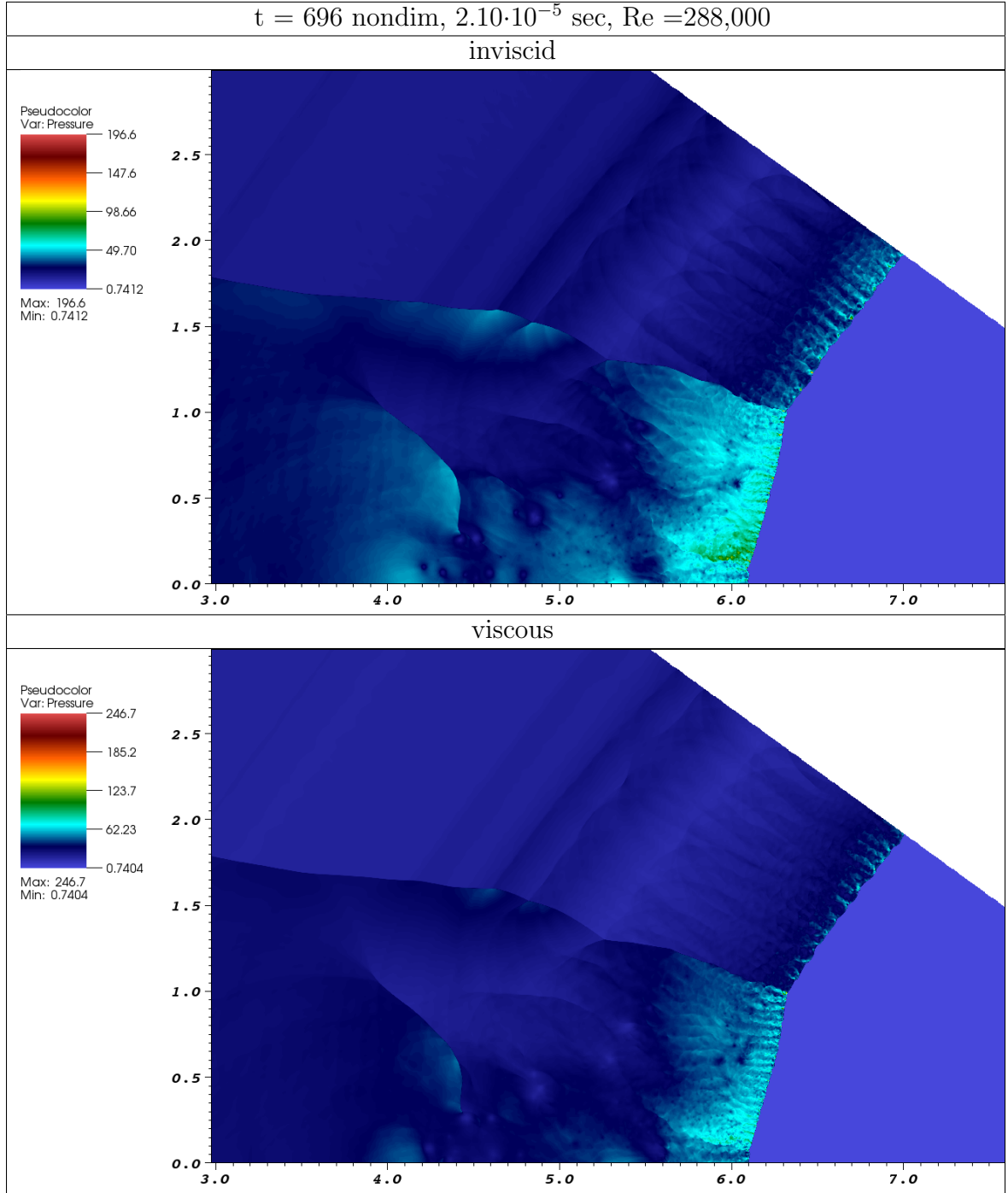


Figure 6.10: Pseudo-color plot of the pressure (Pa), 3-levels (base grid, 2x, 2x) refinement with a 2160x1624 cell base grid spanning  $x=[-1,8]$  and  $y=[0,6.8]$  cm with smallest cell width  $= 1.0416710^{-5}$  m. Comparing inviscid and diffusive results.

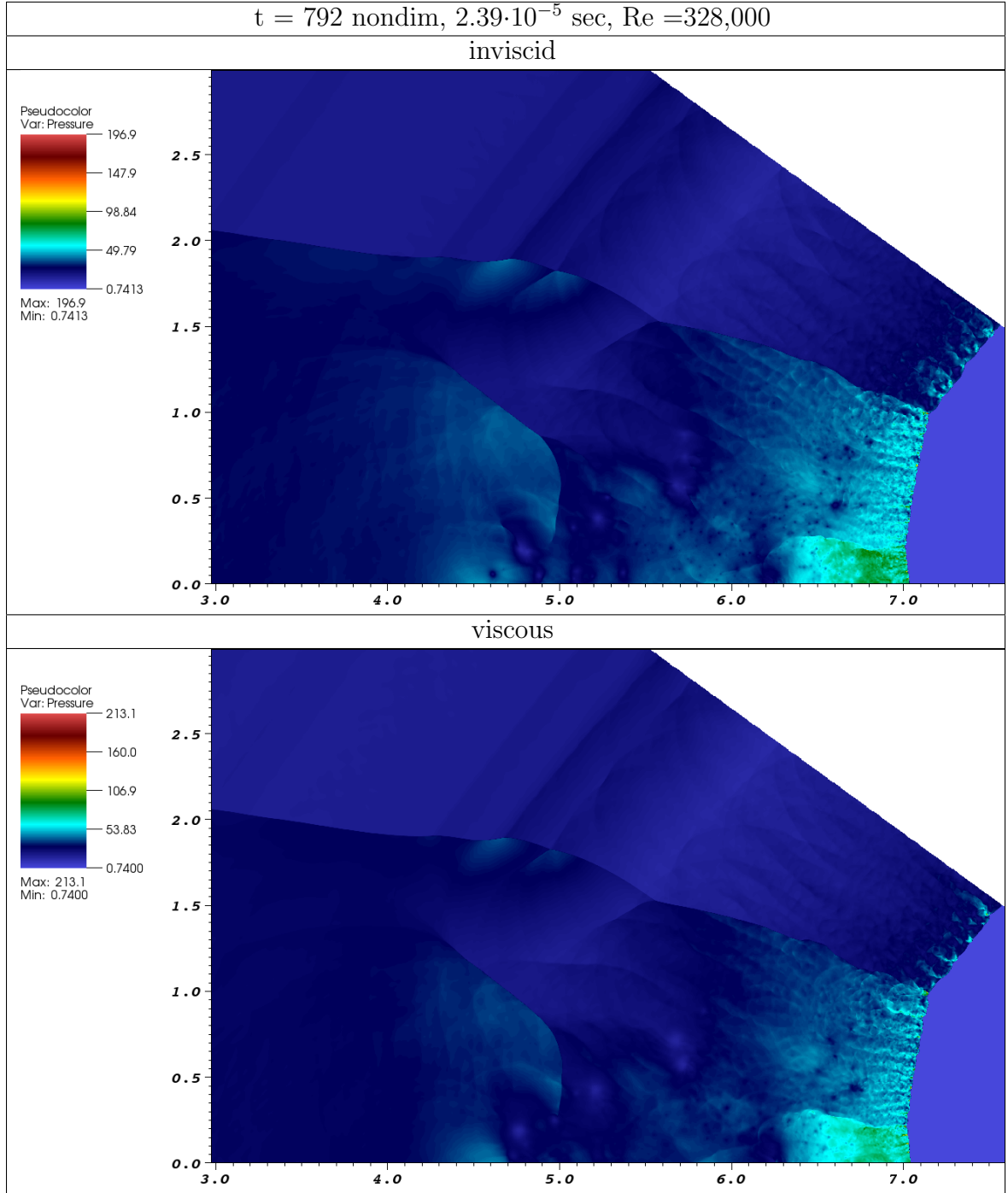


Figure 6.11: Pseudo-color plot of the pressure (Pa), 3-levels (base grid, 2x, 2x) refinement with a 2160x1624 cell base grid spanning  $x = [-1, 8]$  and  $y = [0, 6.8]$  cm with smallest cell width  $= 1.0416710^{-5}$  m. Comparing inviscid and diffusive results.

### 6.1.3 Radical Mass Fraction: 6-Levels, $x_{\max} = 1$ cm

Shown here in figures 6.12-6.15 are time-elapsd results of OH radical mass fractions for the highest resolved 6-level case. A 360x288 cell base grid spanning  $x=[-0.500,1]$  and  $y=[0,1.2]$  cm was used with 6-levels (base grid,2x,2x,2x,2x,2x) with a smallest cell width =  $1.30208310^{-6}$  m. Viscous and inviscid results are compared.

Each of these figures corresponds to the same time step as was shown in figures 6.1-6.4. In the first figure, 6.12, the DMR has again traveled 3 mm along the bottom symmetry boundary. By observing where the sharp gradient of the OH mass fraction occurs behind the incident shock, the induction length is observed. In this region, propane is firstly broken down into smaller hydrocarbons, and at the end radicals are rapidly produced and the large exothermic release (usually described with an exothermic pulse width) occurs. In figure 6.12, the whole DMR including the whole reflected shock wave is inside the induction zone. In the next figure, 6.13, only half of the reflected shock wave is in the induction zone and only half of the wave has triple points on it. However, the left half still has vortices inside of it from earlier formed triple points. In figures 6.14 and 6.15, less and less of the reflected shock has triple points. The induction length has not changed too much in size, however, the DMR structure is growing in time.

If using a pdf reader, go to: view – > rotate – > clockwise 90 degrees. When finished viewing, rotate counterclockwise.

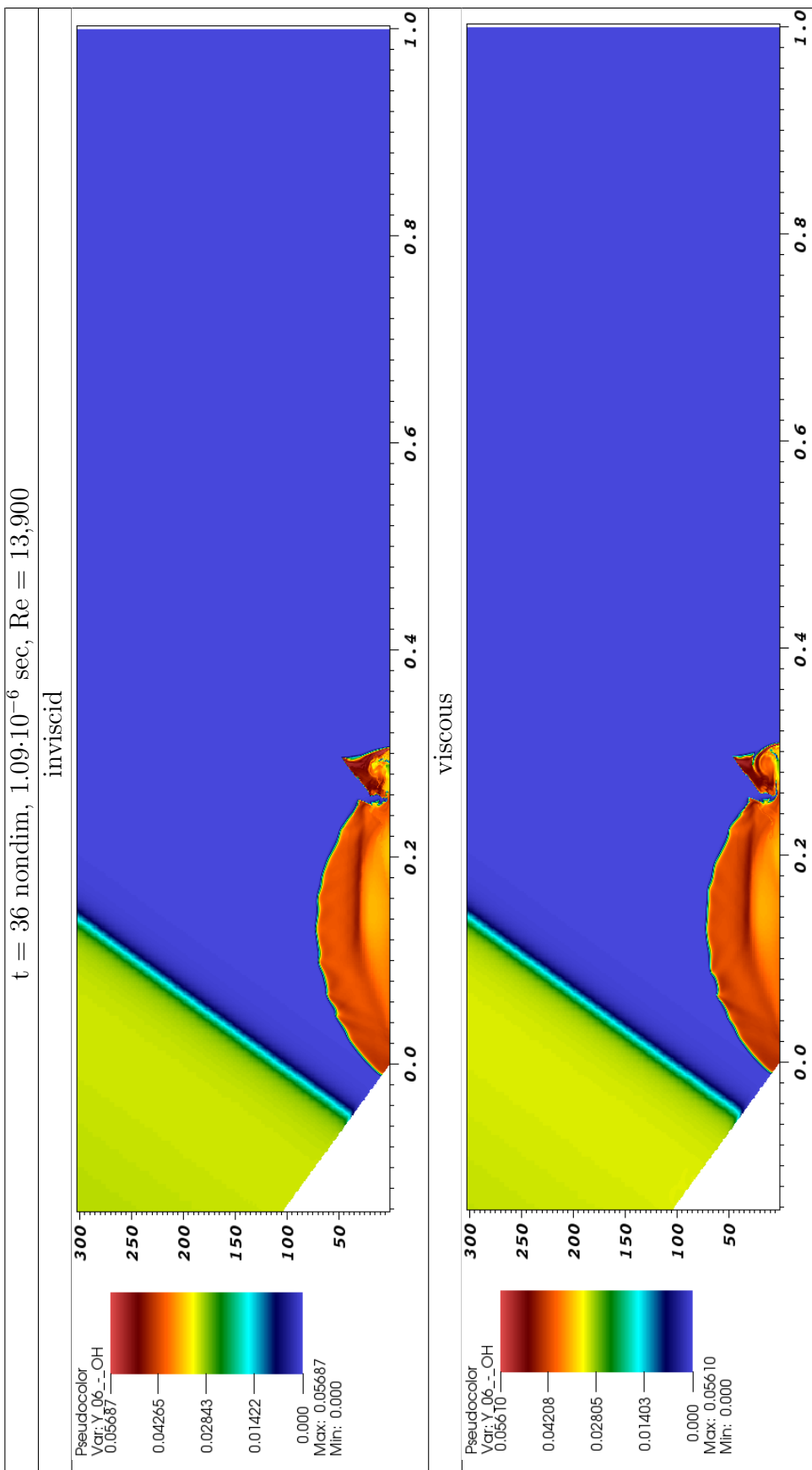


Figure 6.12: Pseudo-color plot of the OH radical mass fraction, 6-levels (base grid,2x,2x,2x,2x,2x) refinement with a 360x288 cell base grid spanning  $x=[-0.500,1]$  and  $y=[0,1.2]$  cm with smallest cell width  $= 1.30208310^{-6}$  m. Comparing inviscid and diffusive results.

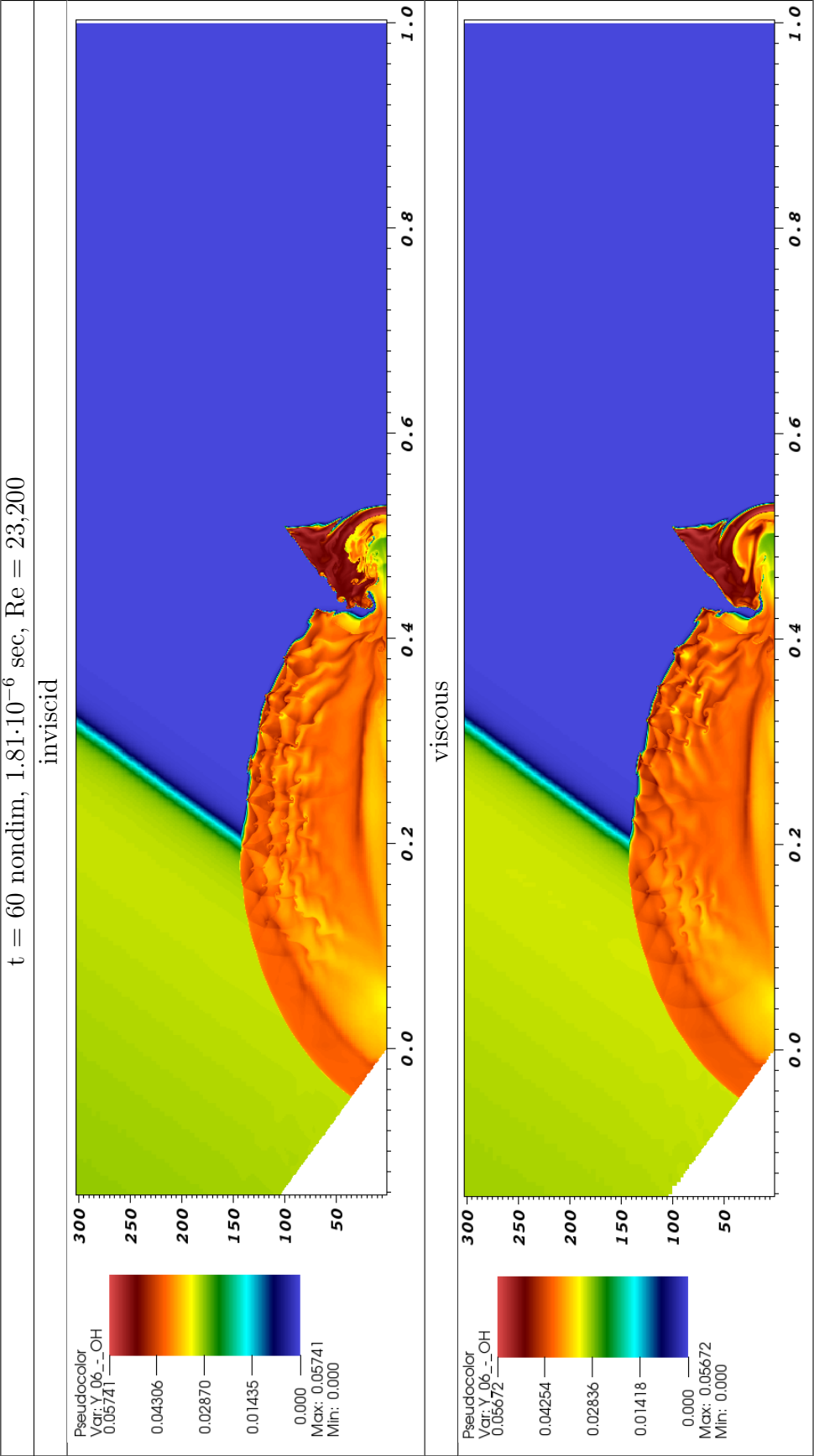


Figure 6.13: Pseudo-color plot of the OH radical mass fraction, 6-levels (base grid,2x,2x,2x,2x,2x) refinement with a 360x288 cell base grid spanning  $x=[-0.500,1]$  and  $y=[0,1.2]$  cm with smallest cell width  $= 1.30208310^{-6}$  m. Comparing inviscid and diffusive results.

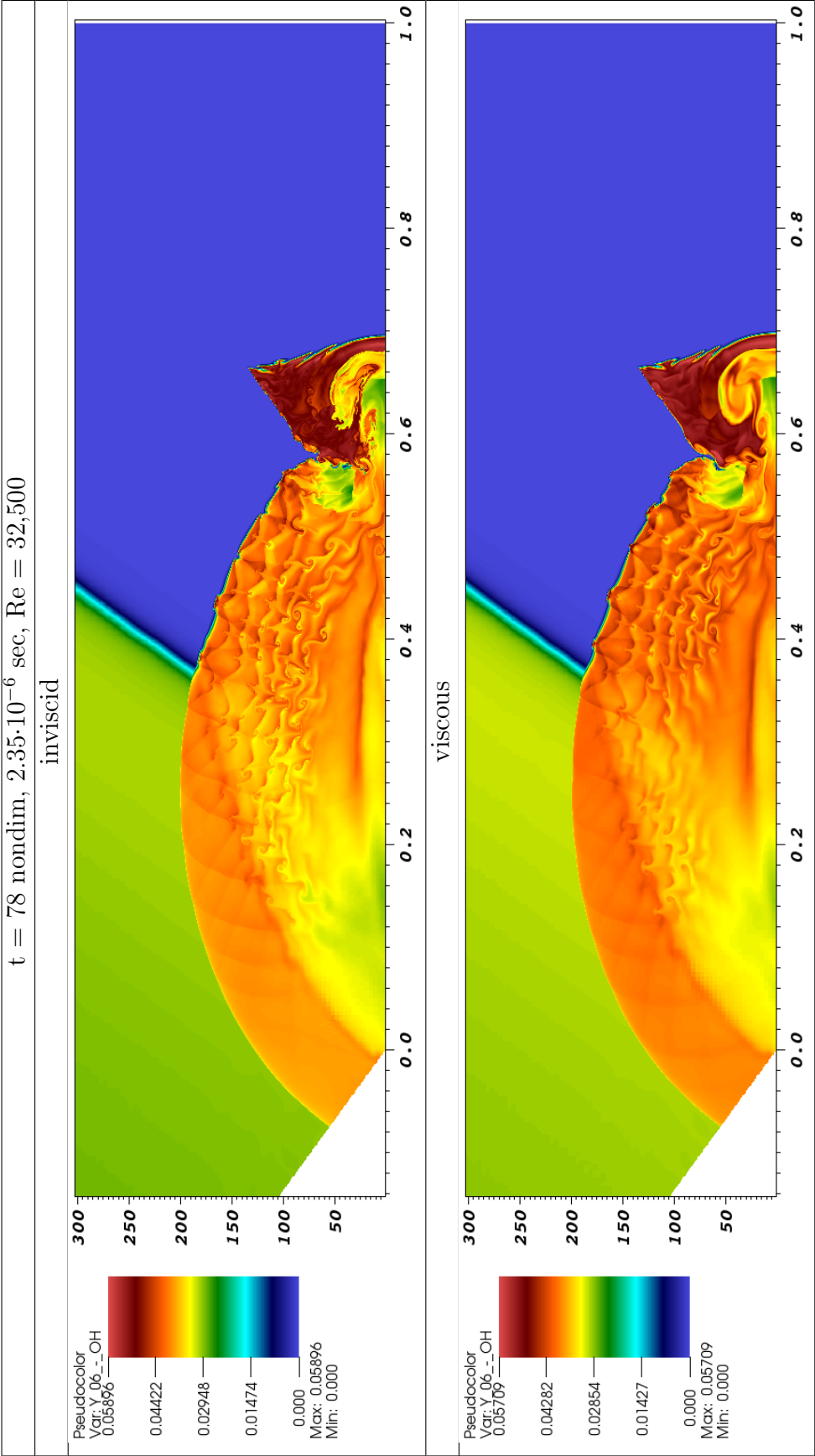


Figure 6.14: Pseudo-color plot of the OH radical mass fraction, 6-levels (base grid,2x,2x,2x,2x,2x) refinement with a 360x288 cell base grid spanning  $x=[-0.500,1]$  and  $y=[0,1.2]$  cm with smallest cell width  $= 1.30208310^{-6}$  m. Comparing inviscid and diffusive results.



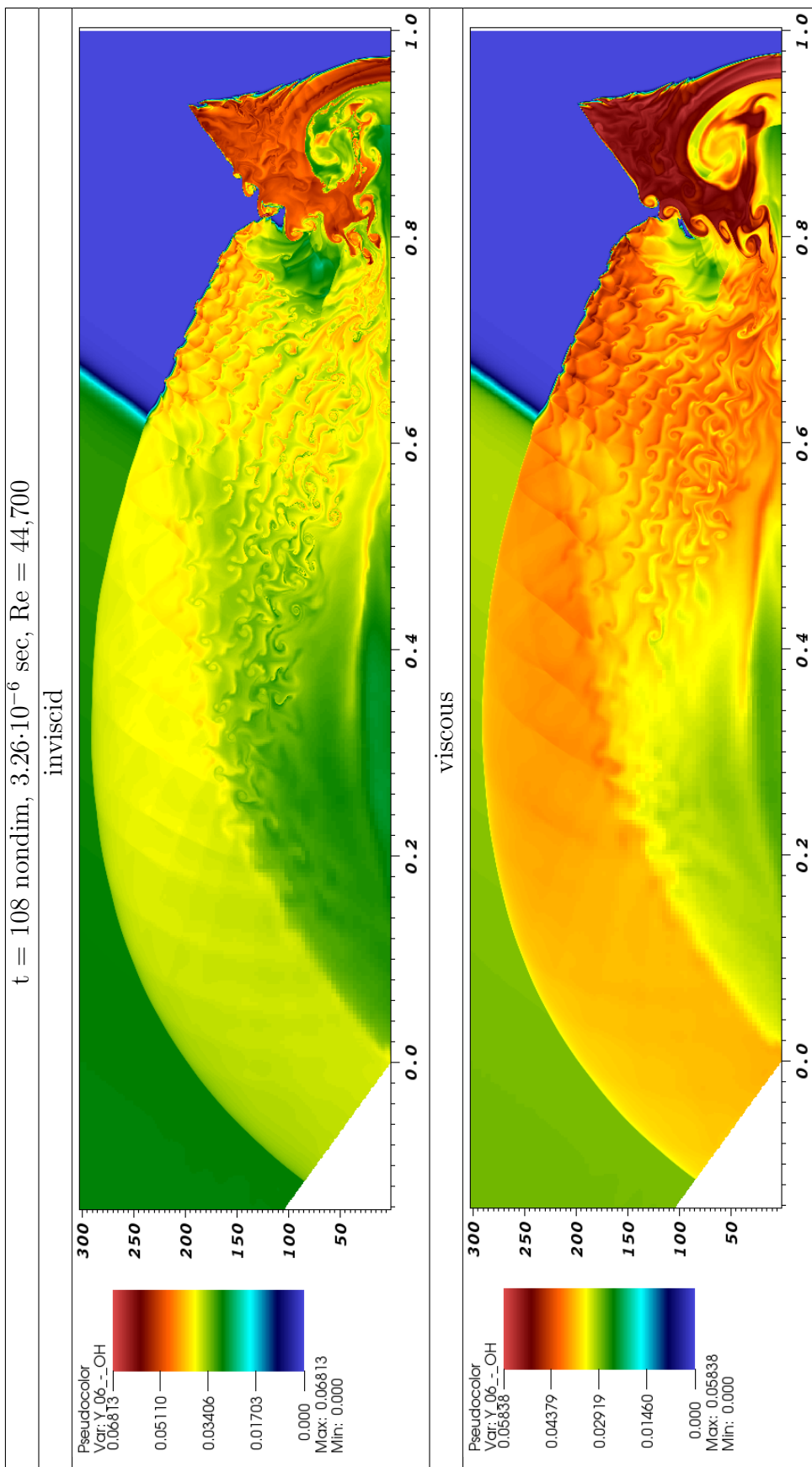


Figure 6.15: Pseudo-color plot of the OH radical mass fraction, 6-levels (base grid,2x,2x,2x,2x,2x) refinement with a 360x288 cell base grid spanning  $x=[-0.500,1]$  and  $y=[0,1.2]$  cm with smallest cell width  $= 1.30208310^{-6}$  m. Comparing inviscid and diffusive results.

#### 6.1.4 Radical Mass Fraction: 5-Levels, $x_{\max} = 2$ cm

Shown here in figures 6.16-6.18 are time-elapsd results of O radical mass fractions for the 5-level case. A 600x408 cell base grid spanning  $x=[-0.500,2]$  and  $y=[0,1.7]$  cm was used with 5-levels (base grid,2x,2x,2x,2x) with a smallest cell width =  $2.60416710^{-6}$  m. Note that the cell size of the base grid,  $4.1666710^{-5}$  m, is exactly that which was used in the 6-level case. Viscous and inviscid results are compared.

Here, even though we are now looking at the O rather than the OH radical mass fraction, the same trends are observed as was seen in figures 6.12-6.15. The numerical viscosity is still small enough to see differences in the inviscid and viscous solutions, however, only the small-scale vortices are affected. The larger scale structures are basically the same.

If using a pdf reader, go to: view – > rotate – > clockwise 90 degrees. When finished viewing, rotate counterclockwise.

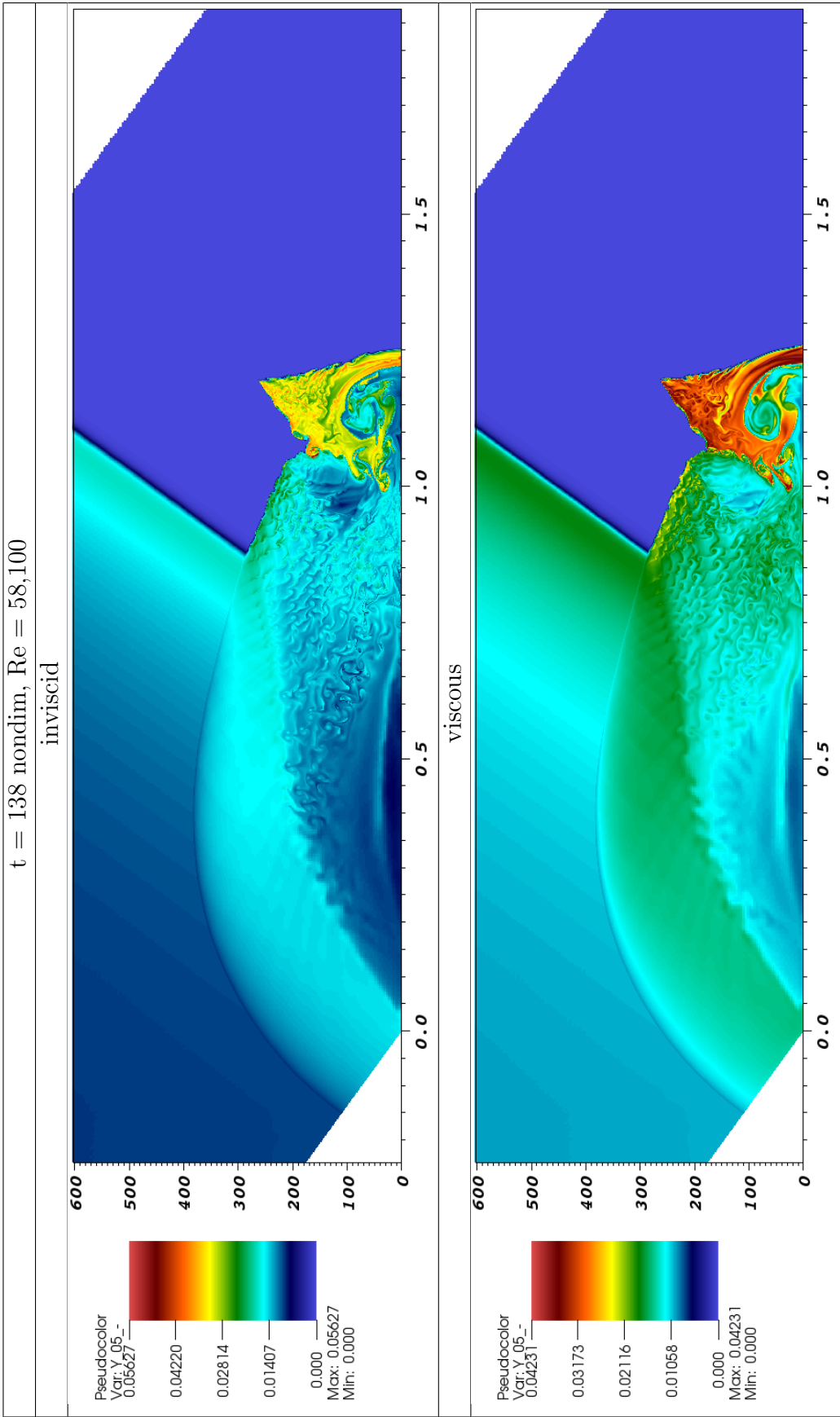


Figure 6.16: Pseudo-color plot of the O radical mass fraction, 5-levels (base grid,2x,2x,2x,2x) refinement with a 600x408 cell base grid spanning  $x=[-0.5,2]$  and  $y=[0,1.7]$  cm with smallest cell width  $= 2.604167 \cdot 10^{-6}$  m. Comparing inviscid and diffusive results.

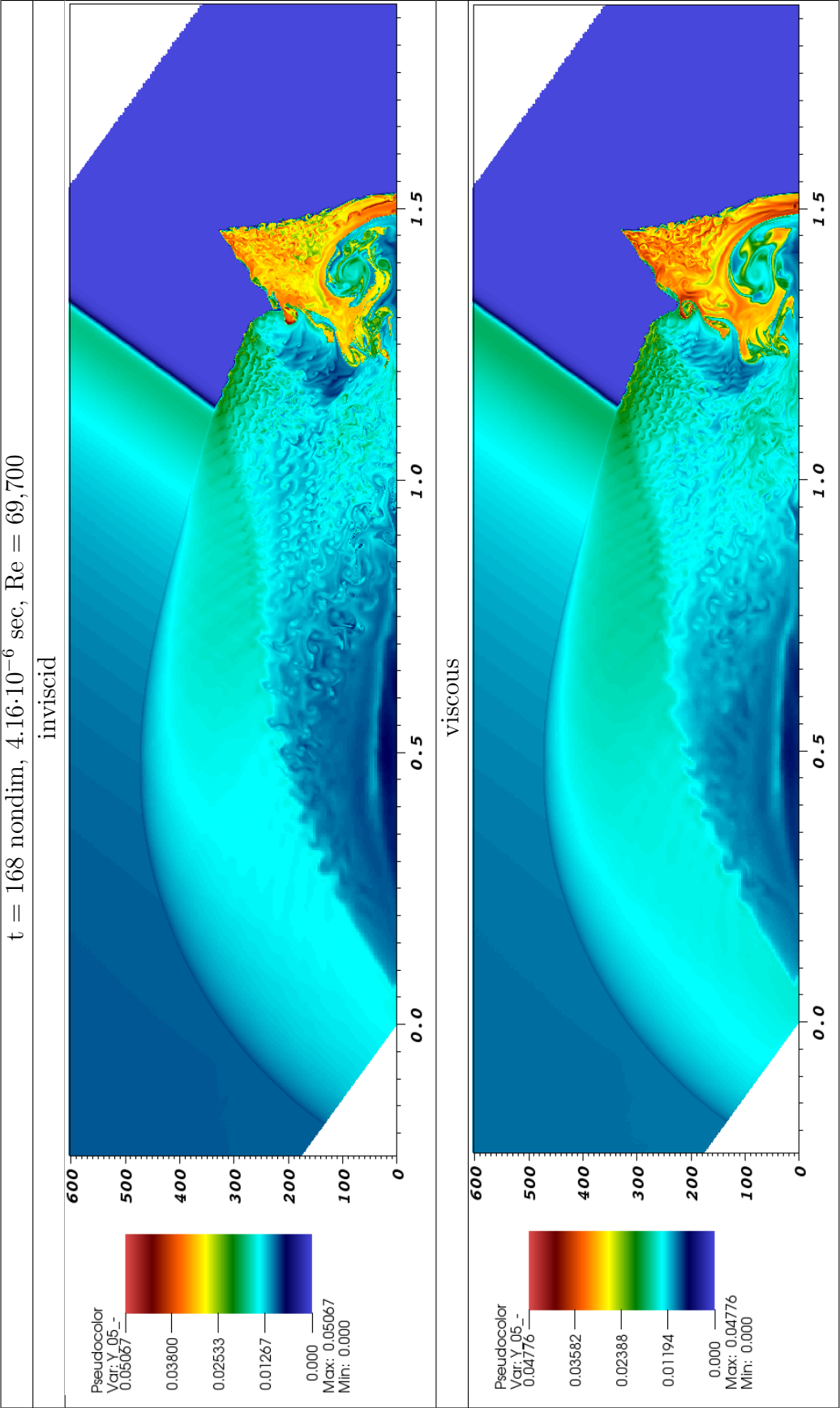


Figure 6.17: Pseudo-color plot of the O radical mass fraction, 5-levels (base grid, 2x, 2x, 2x, 2x) refinement with a 600x408 cell base grid spanning  $x=[-0.5, 2]$  and  $y=[0, 1.7]$  cm with smallest cell width  $= 2.60416710^{-6}$  m. Comparing inviscid and diffusive results.

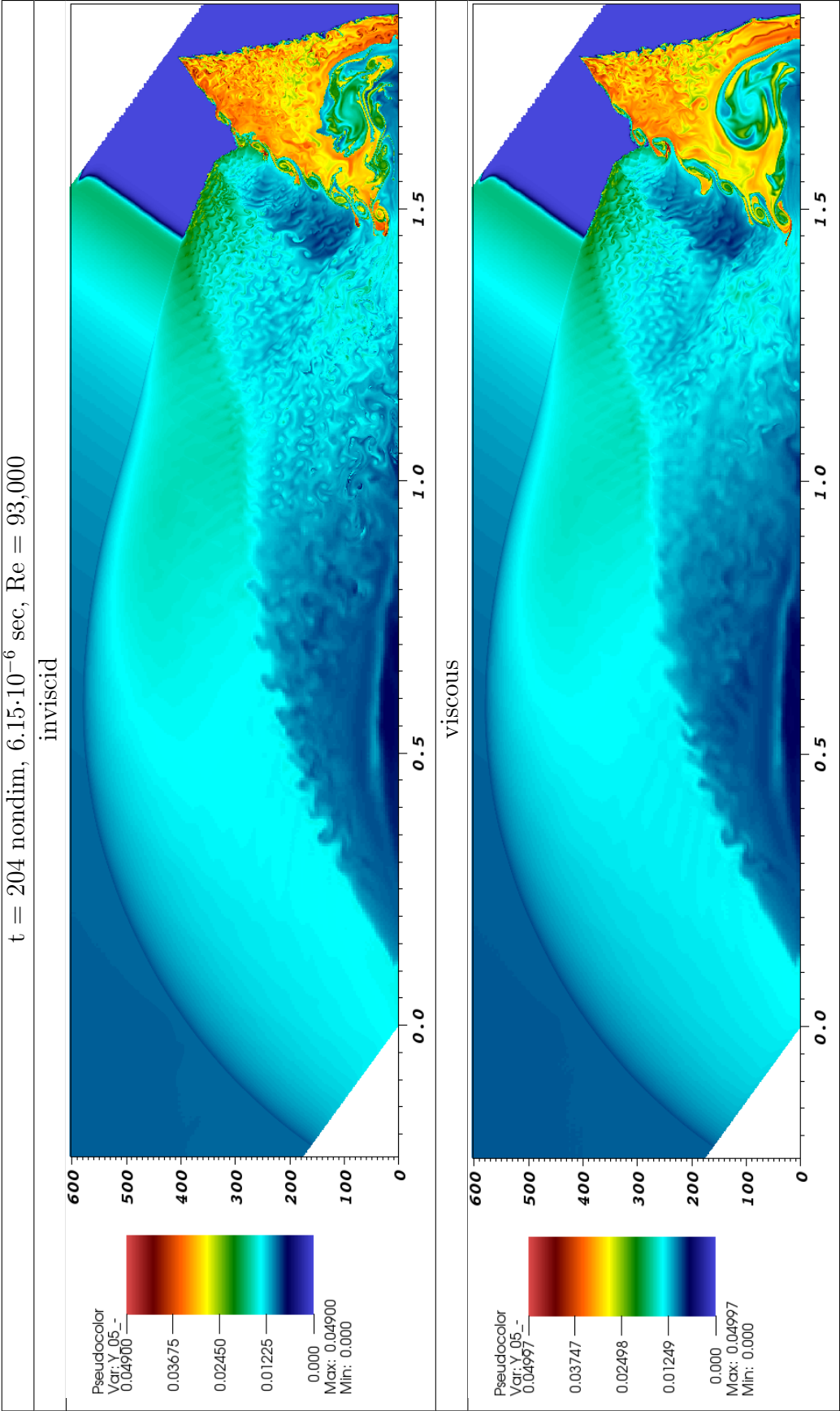


Figure 6.18: Pseudo-color plot of the O radical mass fraction, 5-levels (base grid,2x,2x,2x,2x) refinement with a 600x408 cell base grid spanning  $x=[-0.5,2]$  and  $y=[0,1.7]$  cm with smallest cell width  $= 2.60416710^{-6}$  m. Comparing inviscid and diffusive results.

### 6.1.5 Radical Mass Fraction: 4-Levels, $x_{\max} = 4$ cm

Shown here in figures 6.19 and 6.20 are time-elapsd results of O radical mass fractions for the 4-level case. A 1080x816 cell base grid spanning  $x=[-0.5,4]$  and  $y=[0,3.4]$  cm was used with 4-levels (base grid,2x,2x,2x) with a smallest cell width =  $5.2083310^{-6}$  m. Viscous and inviscid results are again compared.

Starting in figure 6.19, a transverse shock which is below and parallel to the main reflected shock has formed. In figure 6.20 it has grown in size, which is bounded by an interaction with the end of the induction zone and the location of the main shear/mixing layer coming from the primary triple point.

If using a pdf reader, go to: view – > rotate – > clockwise 90 degrees. When finished viewing, rotate counterclockwise.



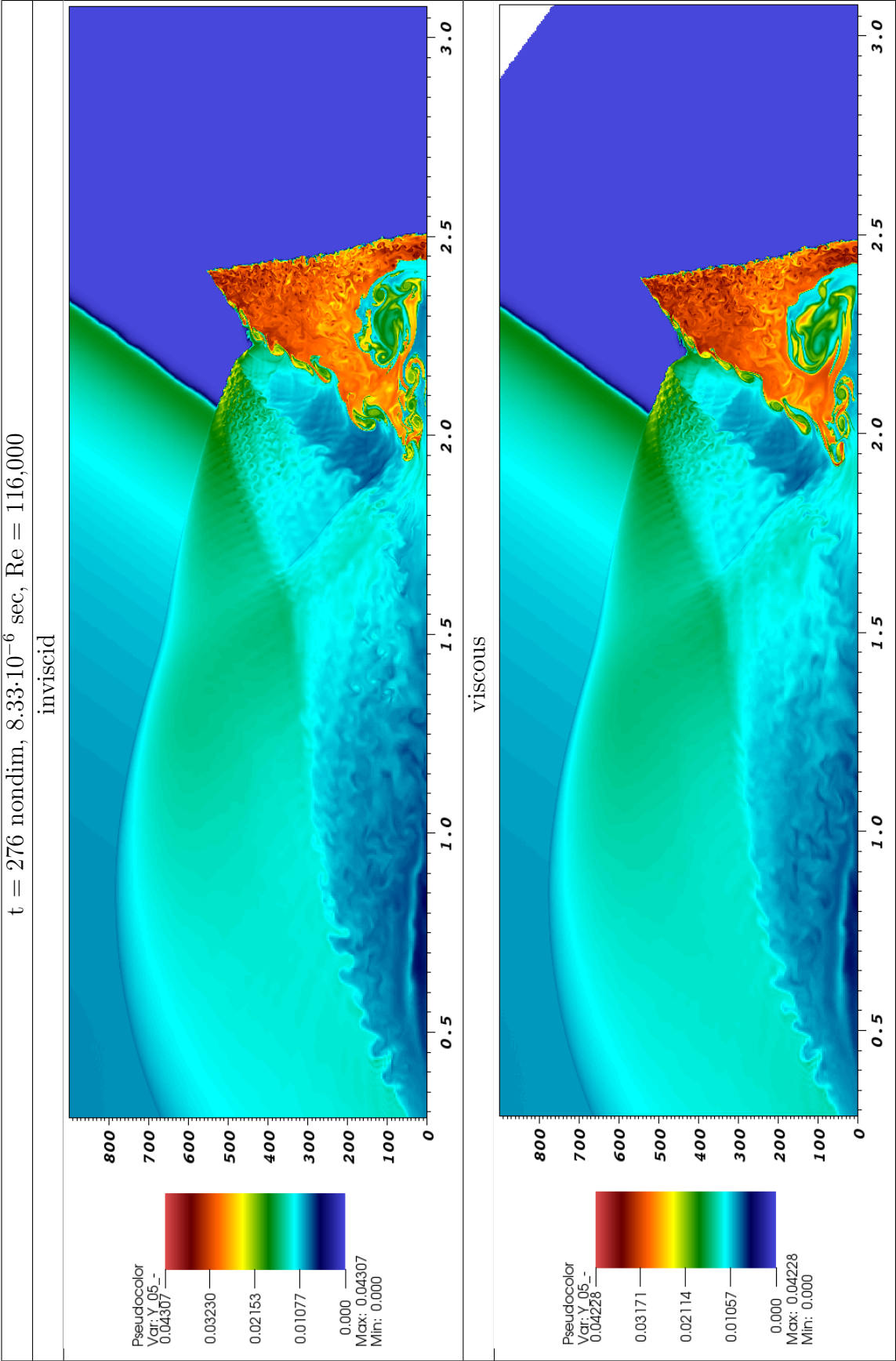


Figure 6.19: Pseudo-color plot of the O radical mass fraction, 4-levels (base grid, 2x, 2x, 2x) refinement with a 1080x816 cell base grid spanning  $x=[-0.5,4]$  and  $y=[0,3.4]$  cm with smallest cell width  $= 5.20833 \cdot 10^{-6} \text{ m}$ . Comparing inviscid and diffusive results.

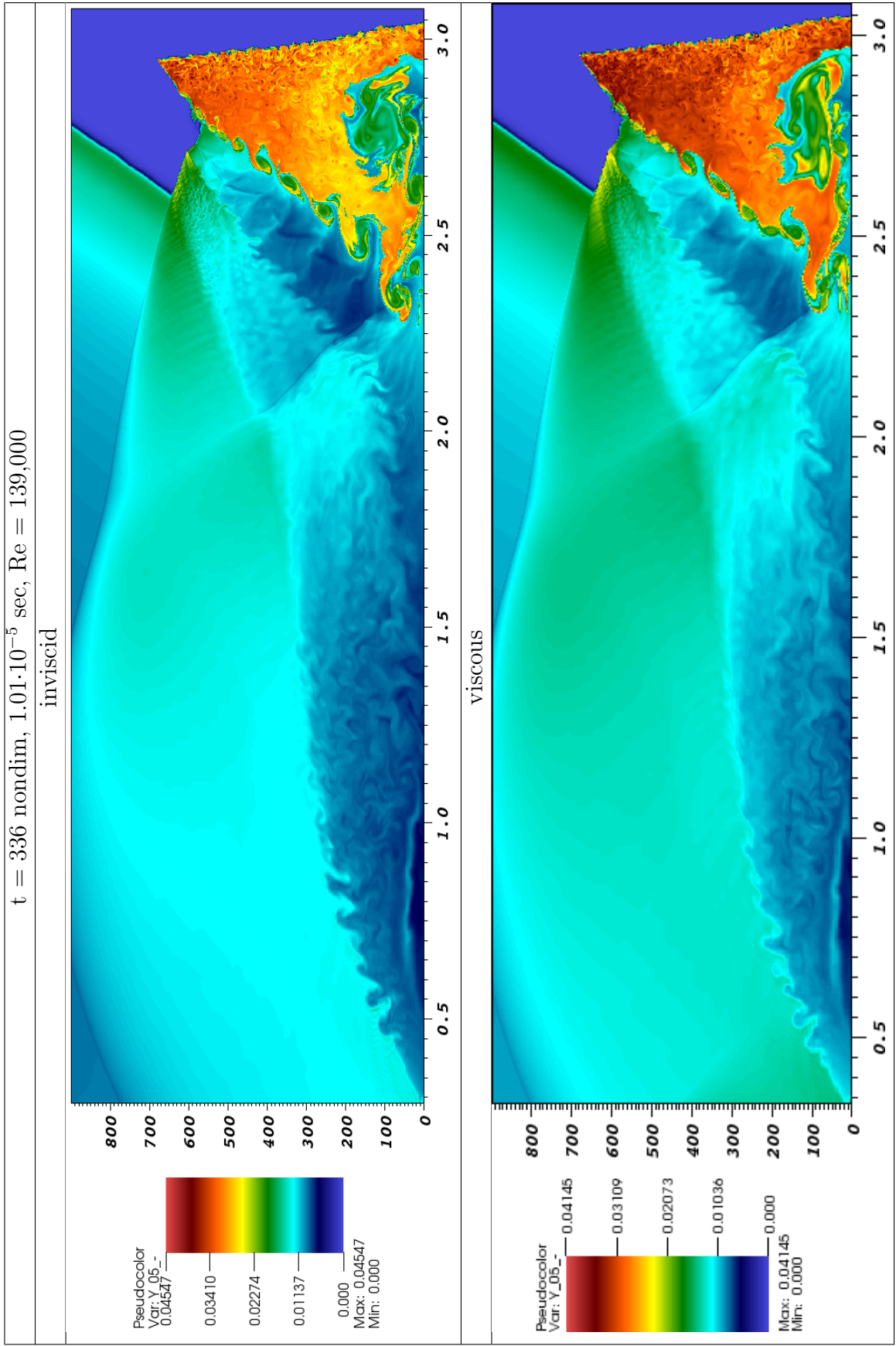


Figure 6.20: Pseudo-color plot of the O radical mass fraction, 4-levels (base grid,2x,2x,2x) refinement with a 1080x816 cell base grid spanning  $x = [-0.5, 4]$  and  $y = [0, 3.4]$  cm with smallest cell width  $= 5.20833 \cdot 10^{-6} \text{ m}$ . Comparing inviscid and diffusive results.



### 6.1.6 Radical Mass Fraction: 3-Levels, $x_{\max} = 3$ cm

Shown in figures 6.21-6.26 are time-elapsd results of OH radical mass fractions for the less resolved case with 3-levels. These results are from the same simulation which produced the results shown in figures 6.6-6.11. The 2160x1624 cell base grid spanning  $x=[-1,8]$  and  $y=[0,6.8]$  cm was used with 3-levels (base grid,2x,2x) with a smallest cell width =  $1.0416710^{-5}$  m. Viscous and inviscid results are again compared.

Starting in figure 6.24, a keystone like structure has formed from the incident shock accelerating into the Mach stem. Later in figure 6.26, this structure has grown such that it has interacted with the whole length of the Mach stem and a new reflected shock structure appears that is neither a DMR, SMR (single MR), or RR (regular reflection).

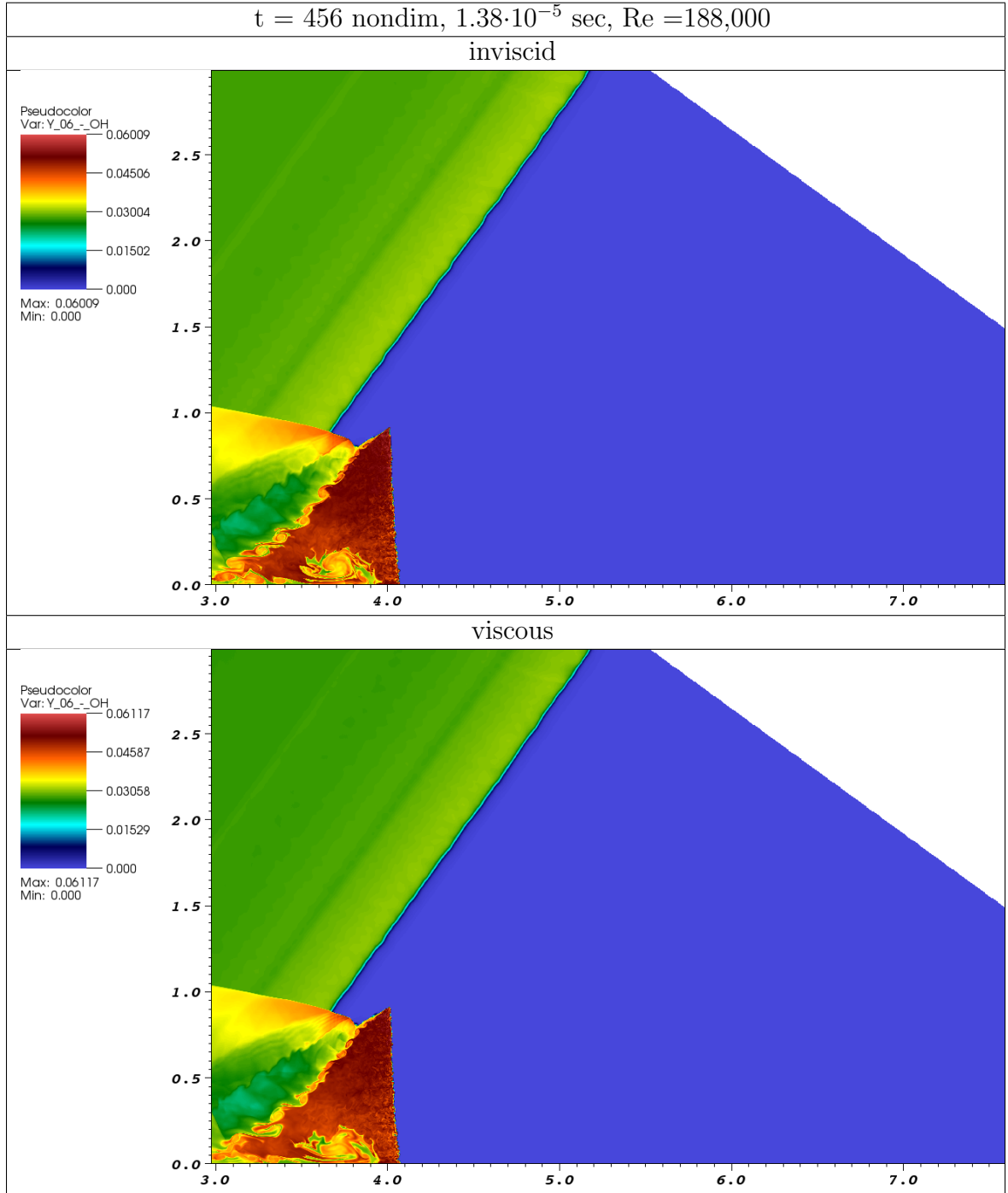


Figure 6.21: Pseudo-color plot of the OH radical mass fraction, 3-levels (base grid,2x,2x) refinement with a 2160x1624 cell base grid spanning  $x=[-1,8]$  and  $y=[0,6.8]$  cm with smallest cell width =  $1.0416710^{-5}$  m. Comparing inviscid and diffusive results.

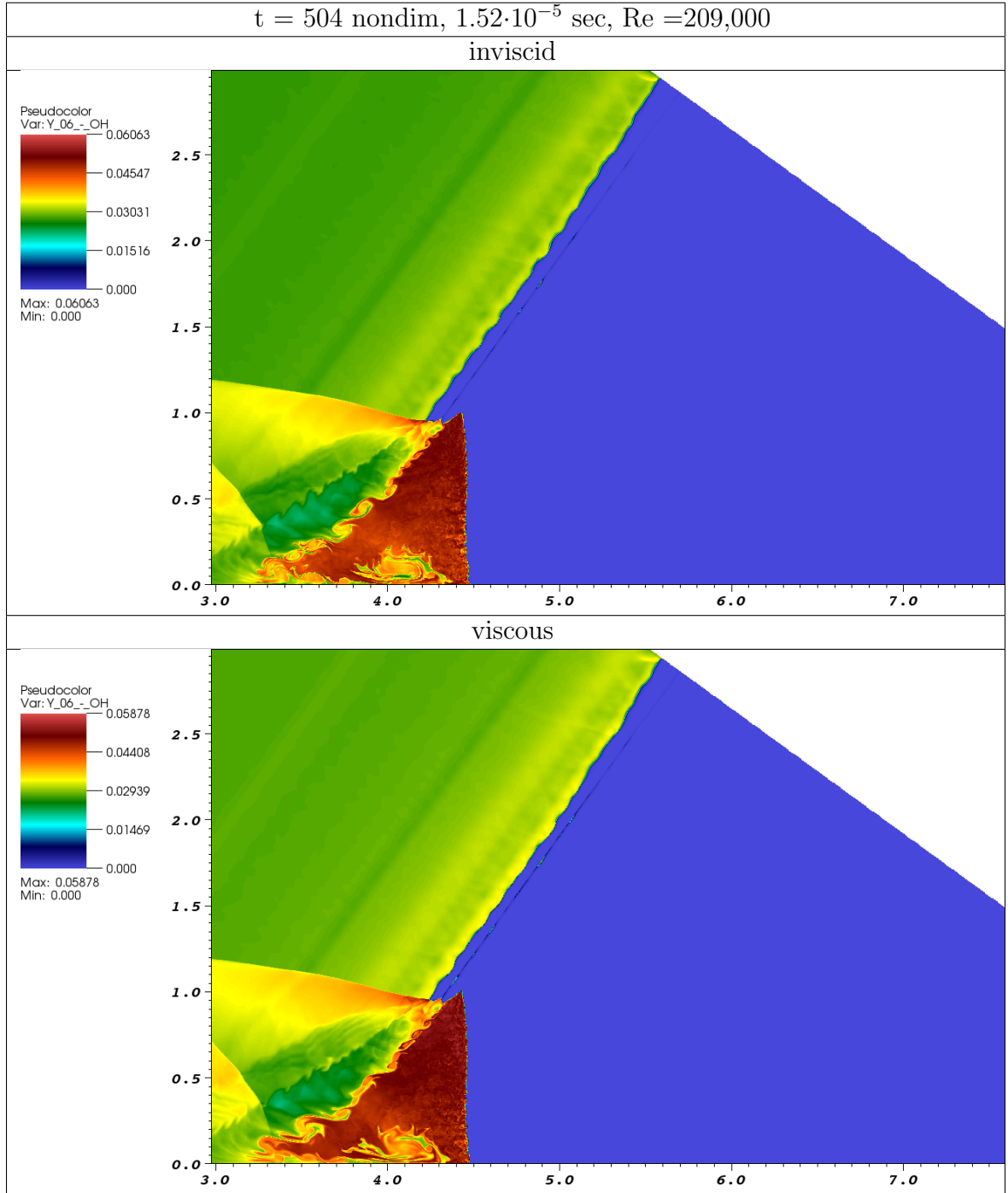


Figure 6.22: Pseudo-color plot of the OH radical mass fraction, 3-levels (base grid,2x,2x) refinement with a 2160x1624 cell base grid spanning  $x=[-1,8]$  and  $y=[0,6.8]$  cm with smallest cell width =  $1.0416710^{-5}$  m. Comparing inviscid and diffusive results.

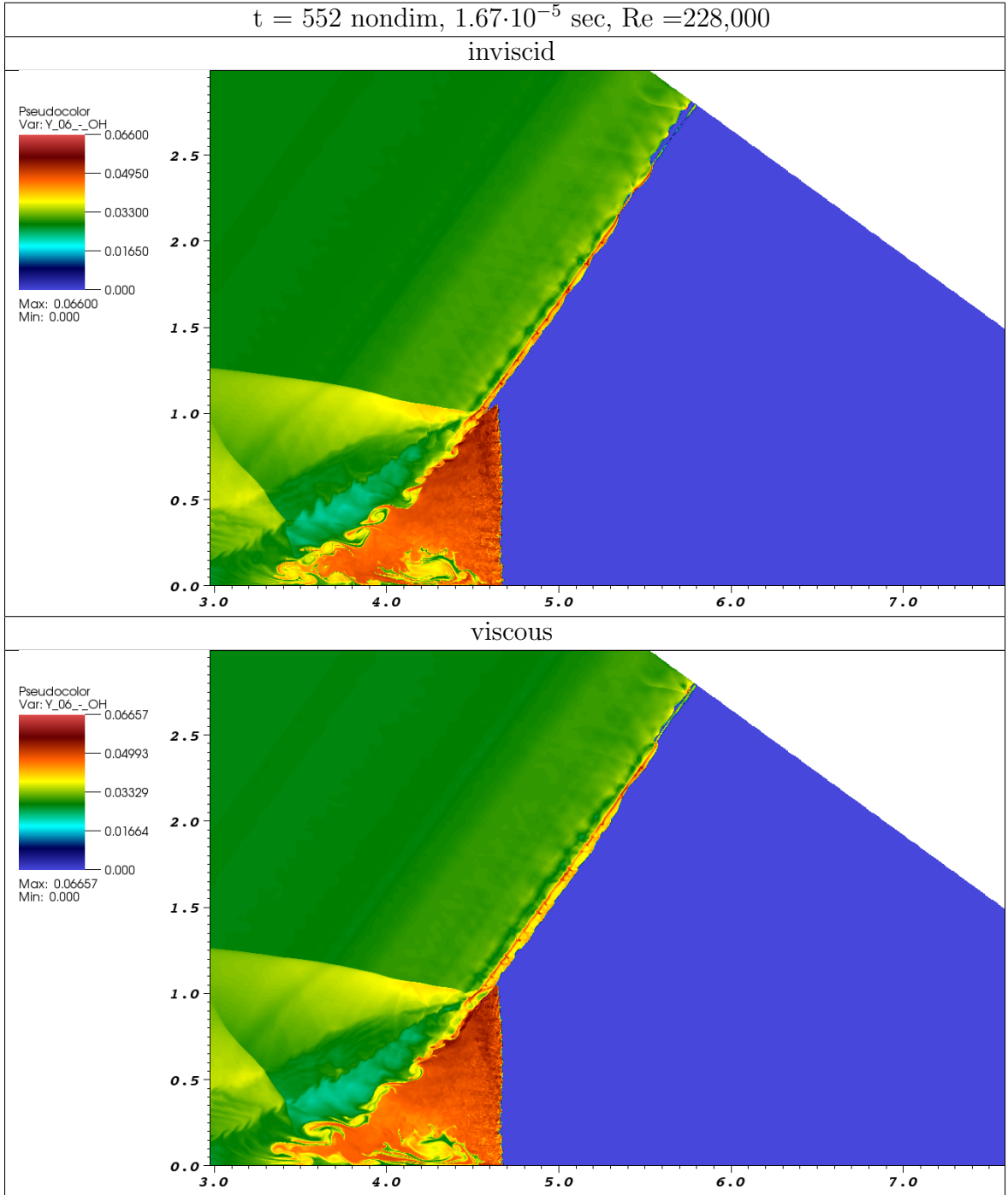


Figure 6.23: Pseudo-color plot of the OH radical mass fraction, 3-levels (base grid,2x,2x) refinement with a 2160x1624 cell base grid spanning  $x=[-1,8]$  and  $y=[0,6.8]$  cm with smallest cell width =  $1.0416710^{-5}$  m. Comparing inviscid and diffusive results.

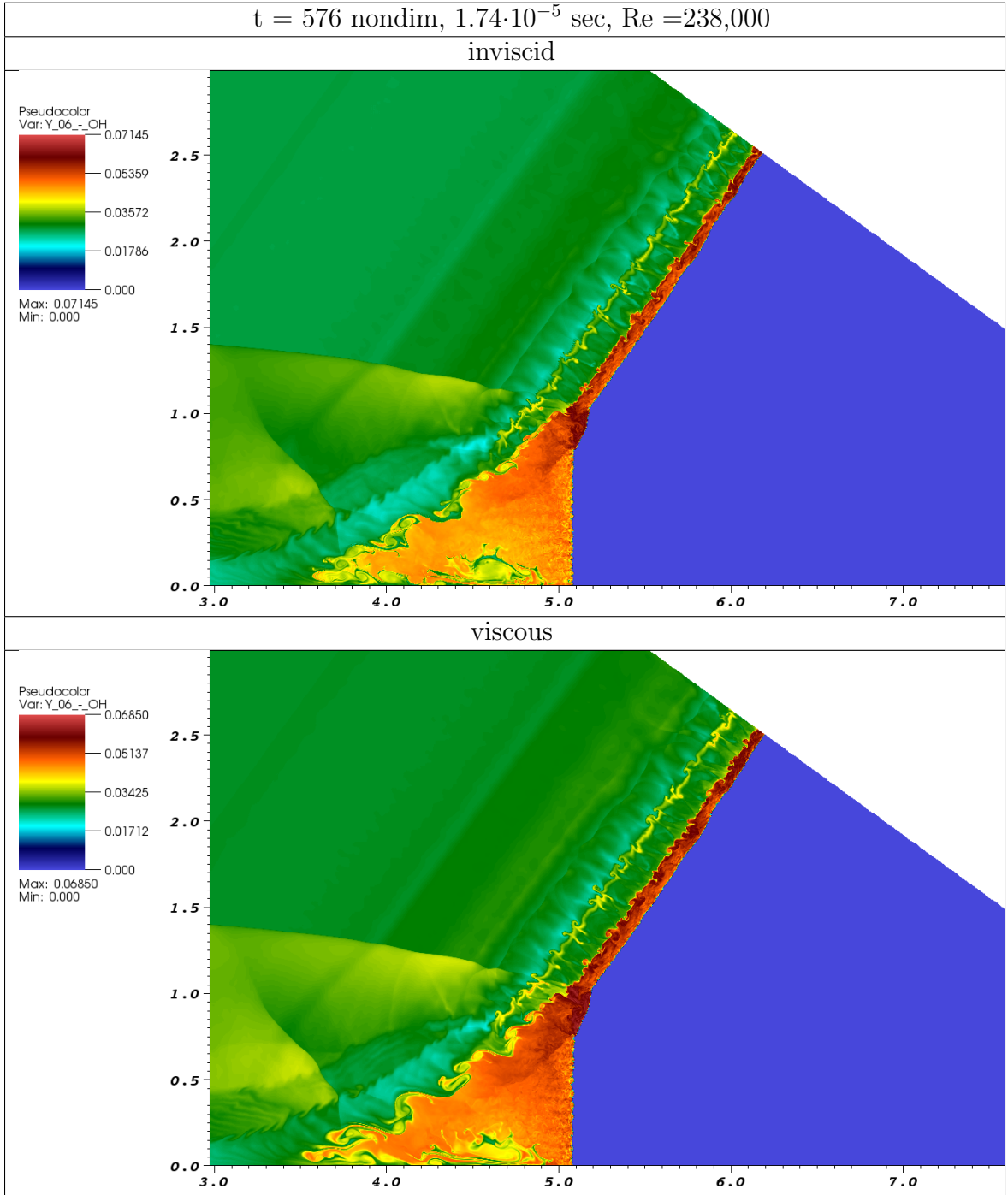


Figure 6.24: Pseudo-color plot of the OH radical mass fraction, 3-levels (base grid,2x,2x) refinement with a 2160x1624 cell base grid spanning  $x=[-1,8]$  and  $y=[0,6.8]$  cm with smallest cell width =  $1.0416710^{-5}$  m. Comparing inviscid and diffusive results.

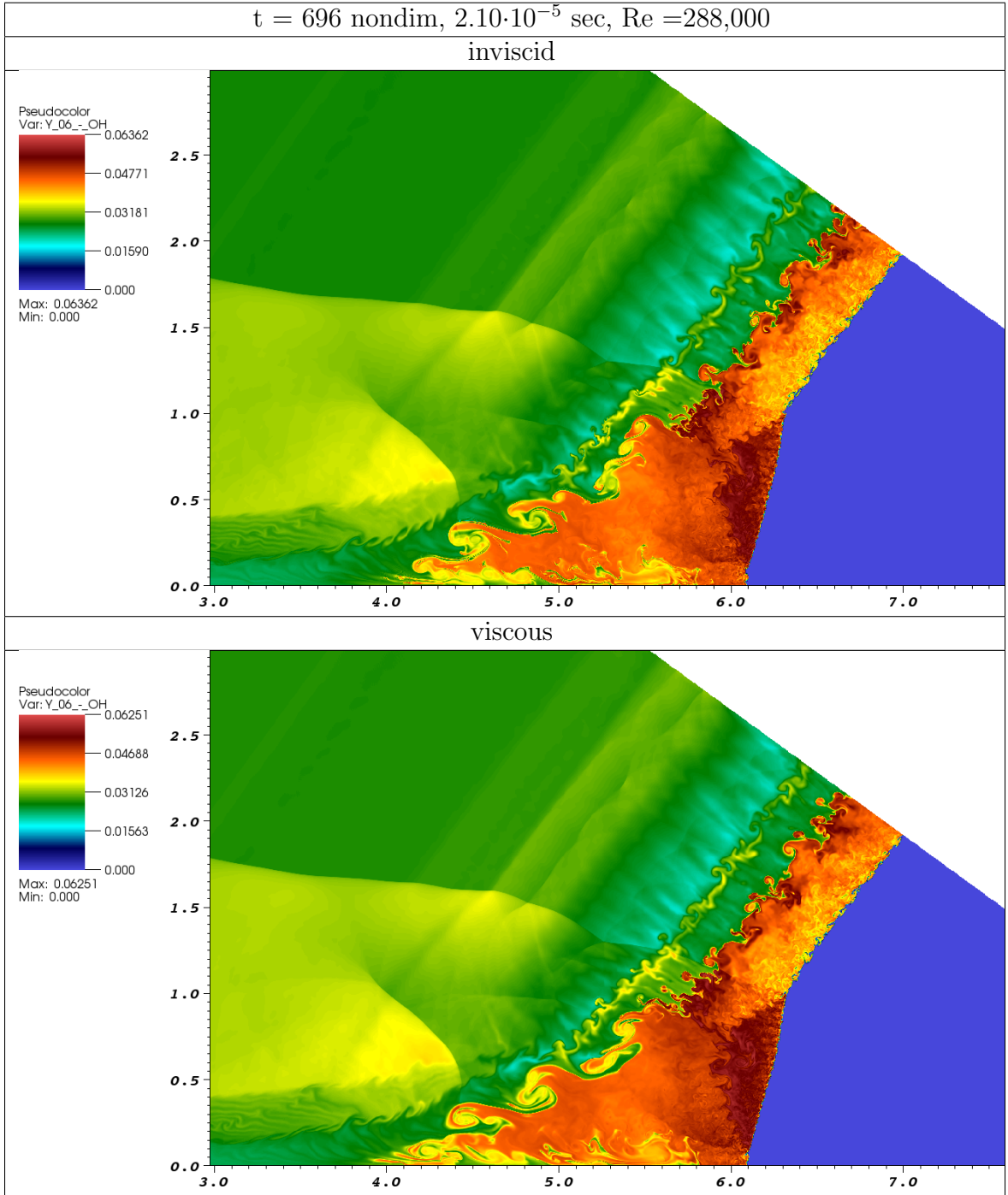


Figure 6.25: Pseudo-color plot of the OH radical mass fraction, 3-levels (base grid,2x,2x) refinement with a 2160x1624 cell base grid spanning  $x=[-1,8]$  and  $y=[0,6.8]$  cm with smallest cell width =  $1.0416710^{-5}$  m. Comparing inviscid and diffusive results.

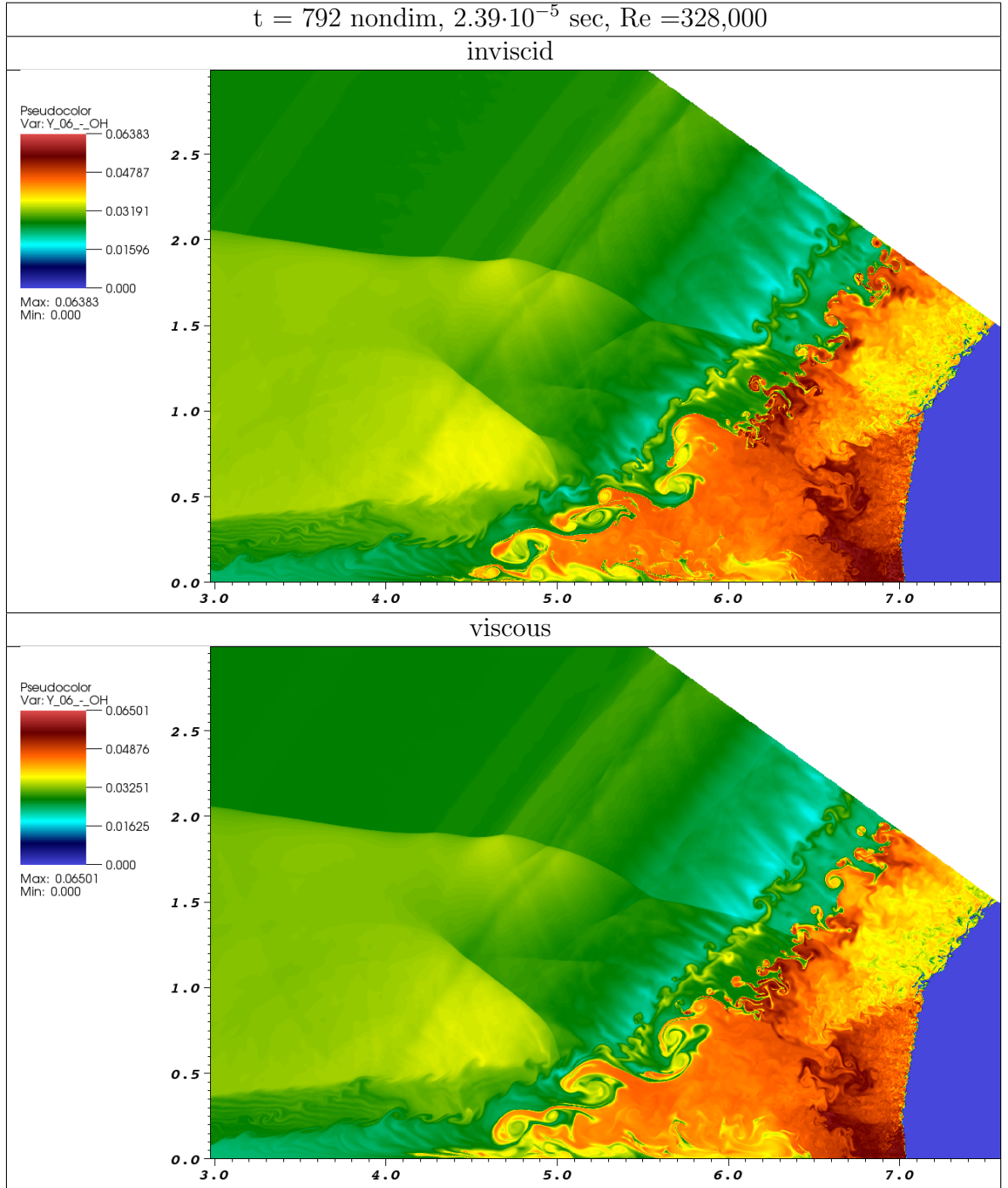


Figure 6.26: Pseudo-color plot of the OH radical mass fraction, 3-levels (base grid, 2x, 2x) refinement with a 2160x1624 cell base grid spanning  $x = [-1, 8]$  and  $y = [0, 6.8]$  cm with smallest cell width =  $1.0416710^{-5}$  m. Comparing inviscid and diffusive results.



## 6.2 Resolution Comparison

In this section, the influence of resolution and numerical viscosity is investigated by comparing solutions at the same time step, yet, with different grid resolutions. Shown in figures 6.27 and 6.28 are comparisons of the H mass fraction at different resolutions for inviscid and viscous/diffusive results. As levels are taken away from the highest resolved 6-level case, the influence of numerical viscosity and how it compares to the physical viscosity is clearly seen. In the 3-level case the numerical viscosity is clearly dominating the physical viscosity. For the 4-level case it appears that the numerical and physical viscosities are of similar magnitudes. This is based on the observation that the vortices are of very similar shape, but out of phase. Also, note that only when going to the resolution found in the 6- and 5-level cases (approximately 1.5 and 3.0 micrometers), does the unreacted pocket of hydrogen radicals appear in the main shear layer. Additionally, the number and the locations of new triple points appearing in the Mach stem and reflected wave are influenced by the numerical viscosity and resolution.

The influence of numerical viscosity is seen even more when using a lower order purely shock-capturing method such as the MUSCL method which is demonstrated in §6.3

## 6.3 MUSCL Comparison

An inviscid simulation was conducted using the second-order accurate CLAWPACK based MUSCL method of AMROC. Shown in figure 6.29 is a comparison of the temperature and pressure at the resolution used in the 5-level case. In figure 6.30 is a comparison of the O mass fraction. It is seen that the influence of numerical diffusion of the MUSCL result is very high at this particular resolution which yields marginally resolved results with a WENO-CD method. Also, the magnitudes of the pressure and temperature are different when compared to the WENO-CD result. An usually high maximum temperature and low maximum pressure is found. For the inviscid MUSCL result the maximum temperature is 4,647 K, the inviscid WENO-CD 4,399 K, and the diffusive WENO-CD 4,273 K. For the inviscid MUSCL result the maximum pressure is 14.28 MPa, the inviscid WENO-CD 18.34 MPa, and the diffusive WENO-CD 22.74 MPa.



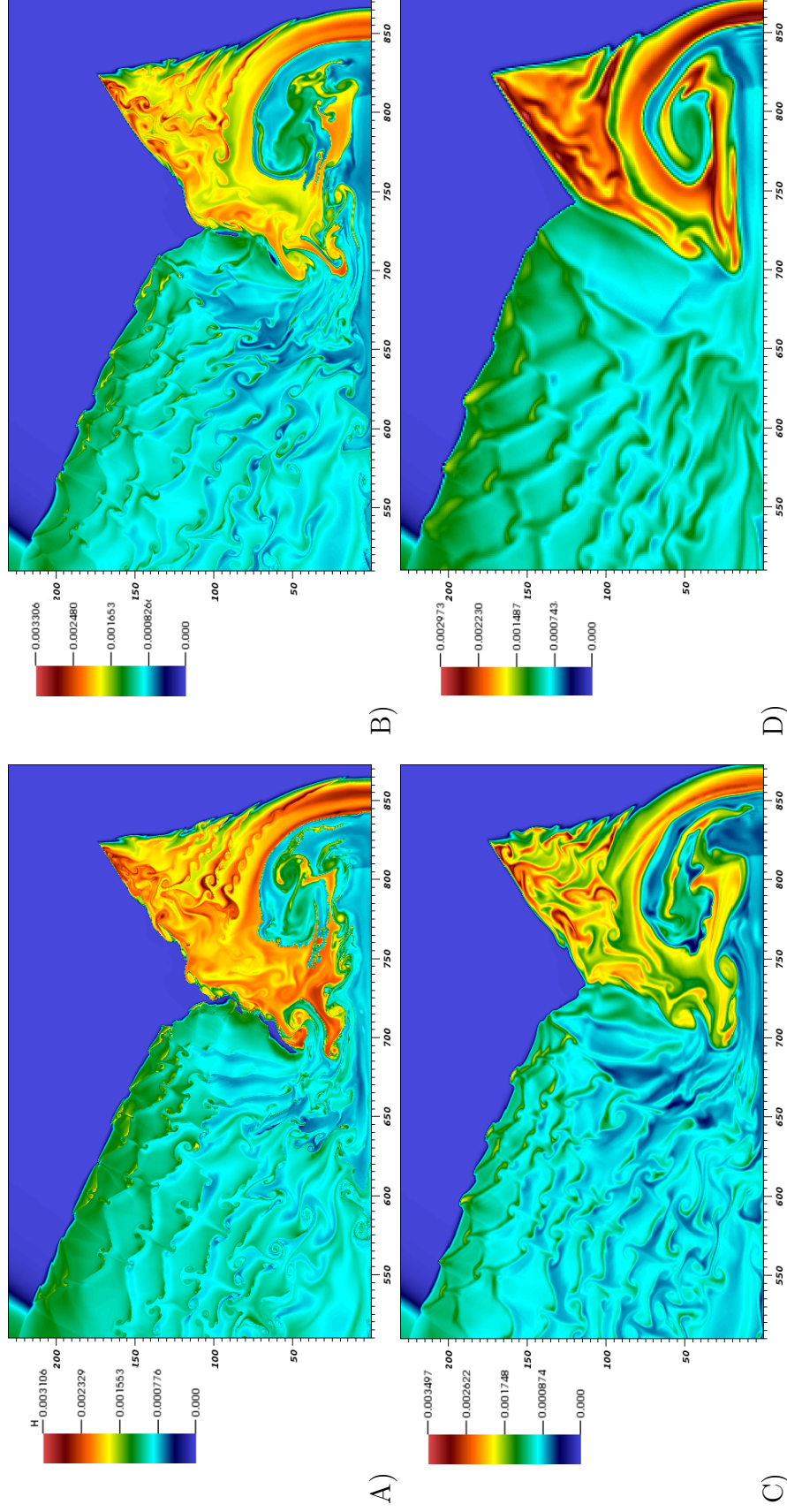


Figure 6.27: Inviscid solutions at a time of  $96 \text{ nondim} = 2.90 \cdot 10^{-6} \text{ s}$  for the 6 (A), 5 (B), 4 (C), and 3-level (D) cases. Showing the hydrogen radical mass fraction.

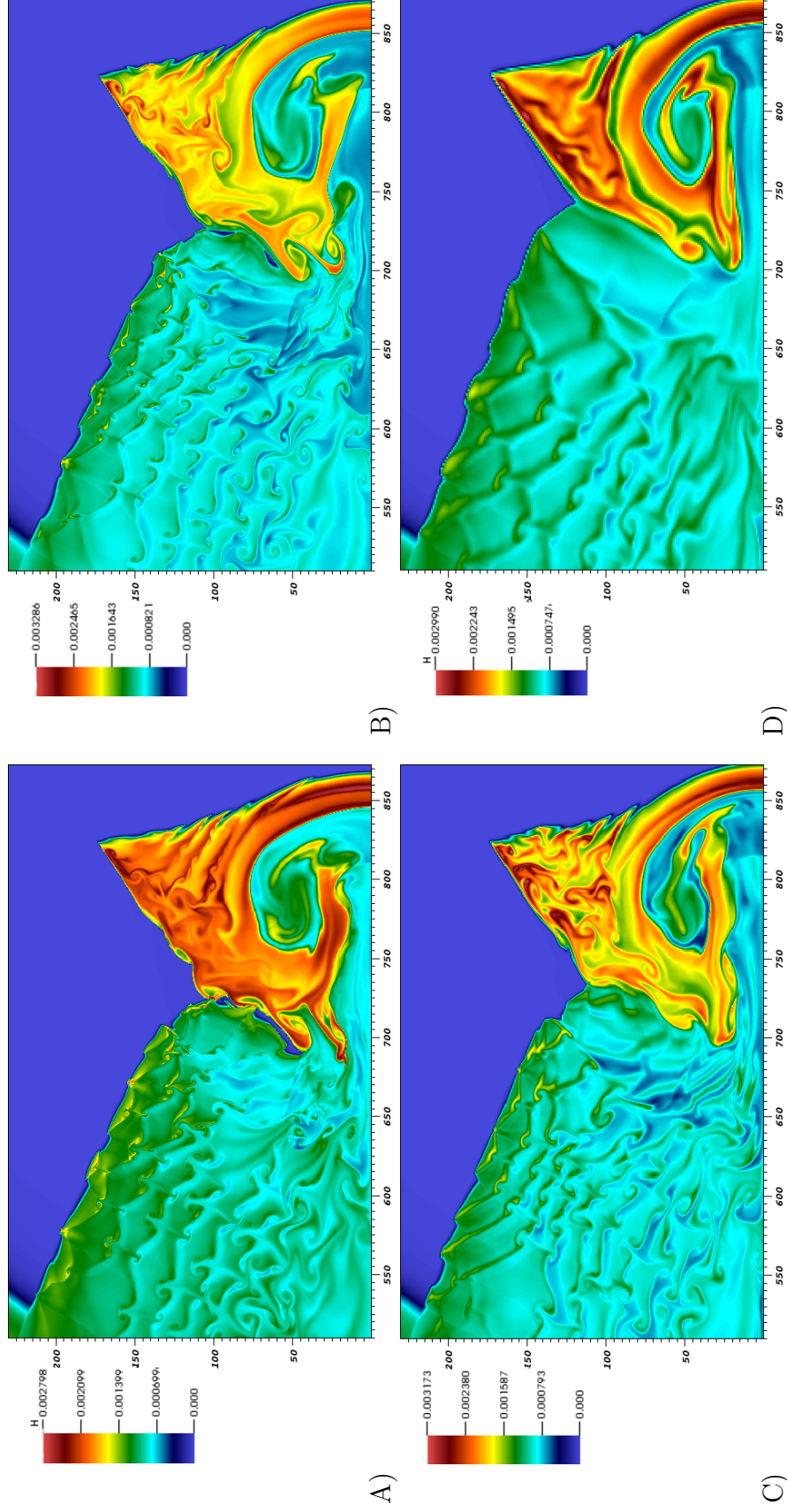


Figure 6.28: Viscous/diffusive solutions at a time of  $96 \text{ nondim} = 2.90 \cdot 10^{-6} \text{ s}$  for the 6, 5, 4, and 3-level cases. Showing the hydrogen radical mass fraction.

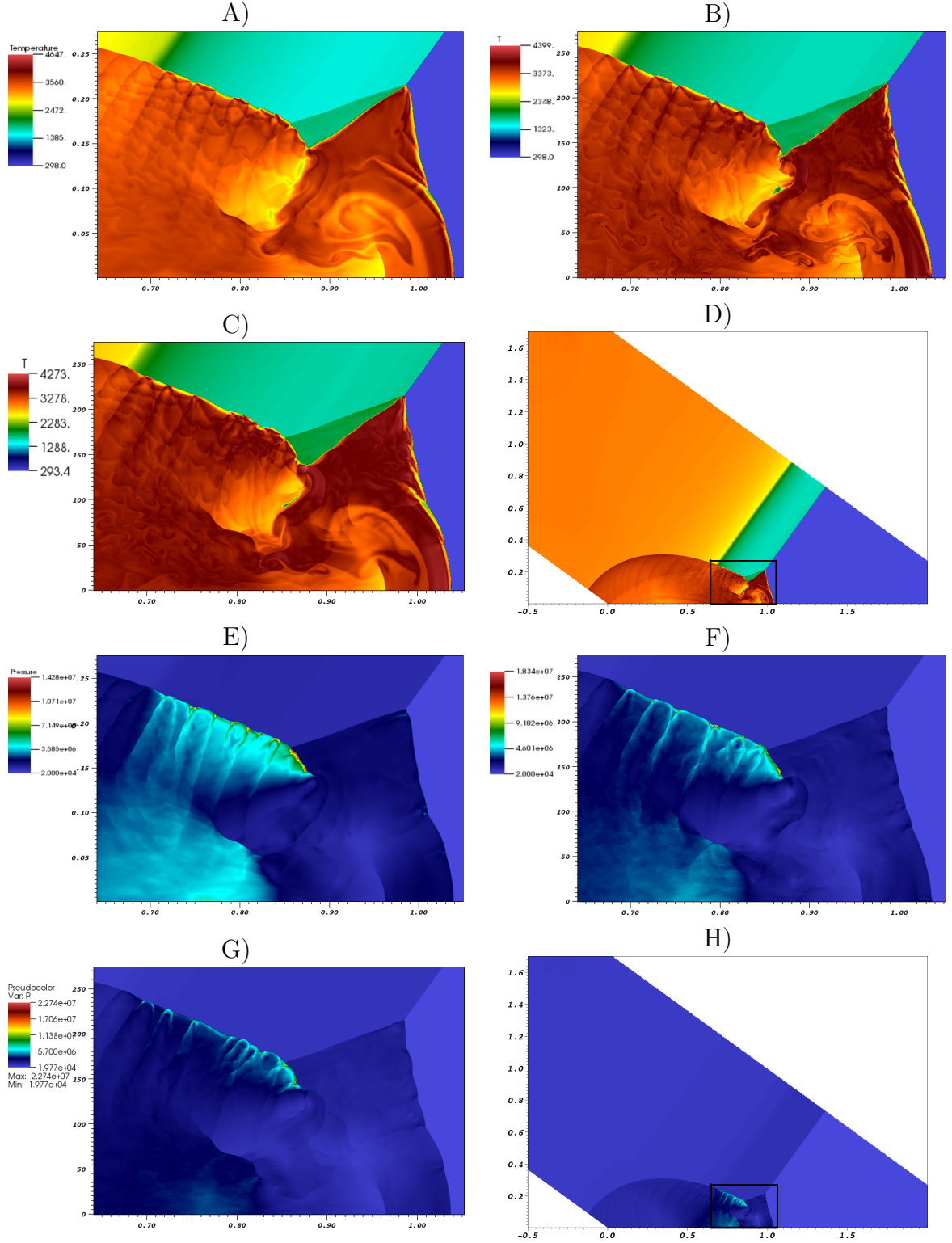


Figure 6.29: Comparing inviscid CLAWPACK (MUSCL) results to inviscid and viscous/diffusive WENO-CD results. All cases are for the same 5-level grid setup, at  $t=114$  nondim ( $3.44 \cdot 10^{-6}$  s),  $Re = 47,200$ . The first three are the temperature (K) for A) inviscid MUSCL, B) inviscid WENO-CD, and C) viscous/diffusive WENO-CD. D) is the whole inviscid WENO-CD solution. The next three, E), F), and G), are for the Pressure (Pa). H) is the whole inviscid WENO-CD solution. The units of the x- and y-axes are cm.



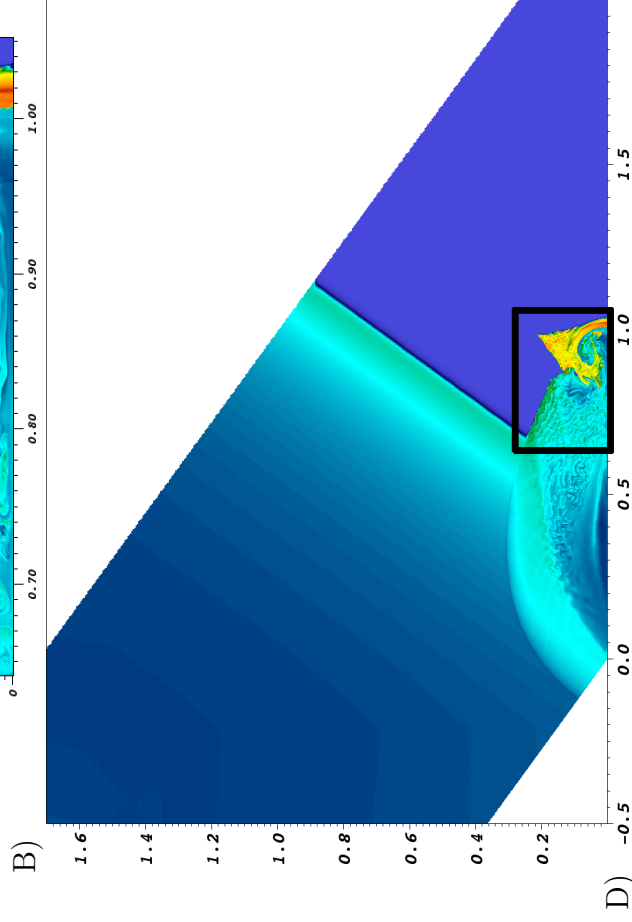
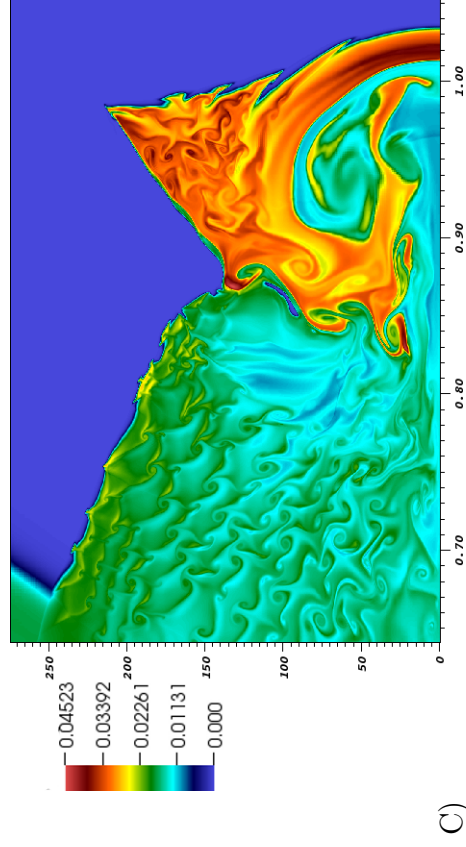
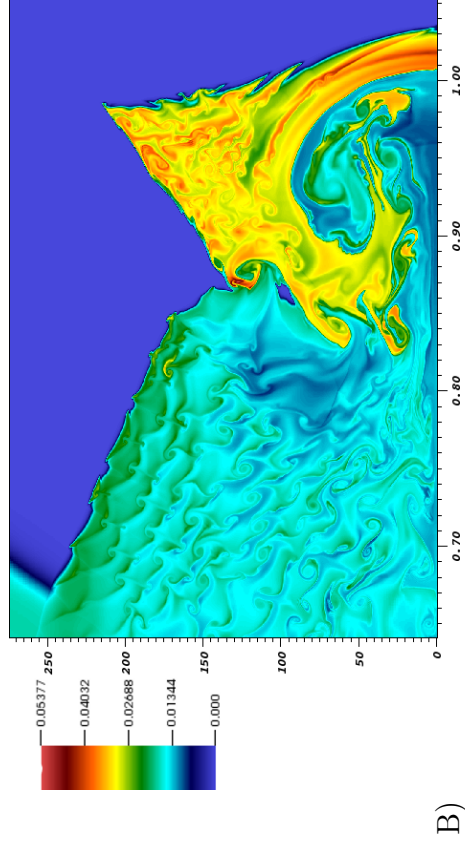
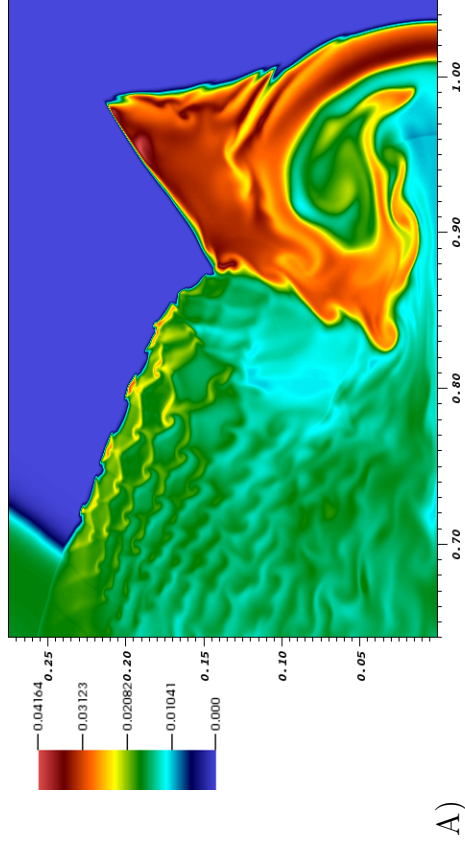


Figure 6.30: Comparing A) inviscid CLAWPACK (MUSCL) O mass fraction results to B) inviscid and C) viscous/diffusive WENO-CD results. D) is the whole inviscid WENO-CD solution. All cases are for the same 5-level grid setup, at  $t=114$  nondim ( $3.44 \cdot 10^{-6}$  s),  $Re = 47,200$ , with 5-levels. The units of the x- and y-axes are cm.

## 6.4 Diffusive, Detonation DMR Structural Details

In this section, the physical development of the diffusive double Mach reflection (DMR) is described in a chronological order as new features appear in the simulation, starting with figure 6.31 and ending with figure 6.46. The results shown come from multiple simulations. figures 6.31-6.38 are from the 6-level case, figure 6.39 the 5-level case, figure 6.40 the 4-level case, and figures 6.41-6.46 the 3-level case.

In the first figures, the DMR is seen to resemble a nonreactive DMR, with the primary and secondary triple points appearing with their respective, incident, reflected, and Mach stem shock waves. Very soon, the unstable nature of the chemistry starts to interact with these shocks. This interaction is observed to only occur within the induction (reaction) zone of the incident shock. The induction zone is described as the region from the main shock front to where the thermicity peak lies and similarly where the maximum temperature gradient lies. As the DMR structure grows in size, instabilities appear, and new transverse shocks and mixing layers/vortical structures appear. Eventually, the incident shock also goes unstable and interacts with the complex DMR structure. In what follows, each of the figures is described, noting important features as they appear in time.

Starting in figure 6.31, shortly after reflection, the DMR structure resembles the typical nonreactive case, except that the interaction of the shear layer jet and the Mach stem forms a triple point on the Mach stem. Then, in figure 6.32, instabilities of the chemical reactions begin to appear in the reflected shock. In figure 6.33, more reflected shocks have appeared within the DMR. Also, another triple point has formed near the primary one. Later in figure 6.34, multiple triple points have formed on the reflected shock. Also, looking at the main shear layer coming from the primary triple point, the above cooler fluid being entrained into the jet is not fully reacted. Now at a later time in figure 6.35, the newly formed triple points on the reflected shock are showing many new shear layers and other shear layers from shock reflections. Also, at this time, the secondary triple point (which also appears in the nonreactive DMR) has its shear layer rolling up as expected. Then, later in figure 6.36, the triple points formed on the main reflected shock have now had their reflected shocks and Mach stems reflect at least four times off each other forming at least four levels of shear layers. The main Mach stem is also becoming more unstable, showing the formation of new triple points. Even later in figure 6.37, at least five triple points are visible on the main Mach stem of the DMR. Also, very high pressures are appearing at the triple points on the main reflected shock.

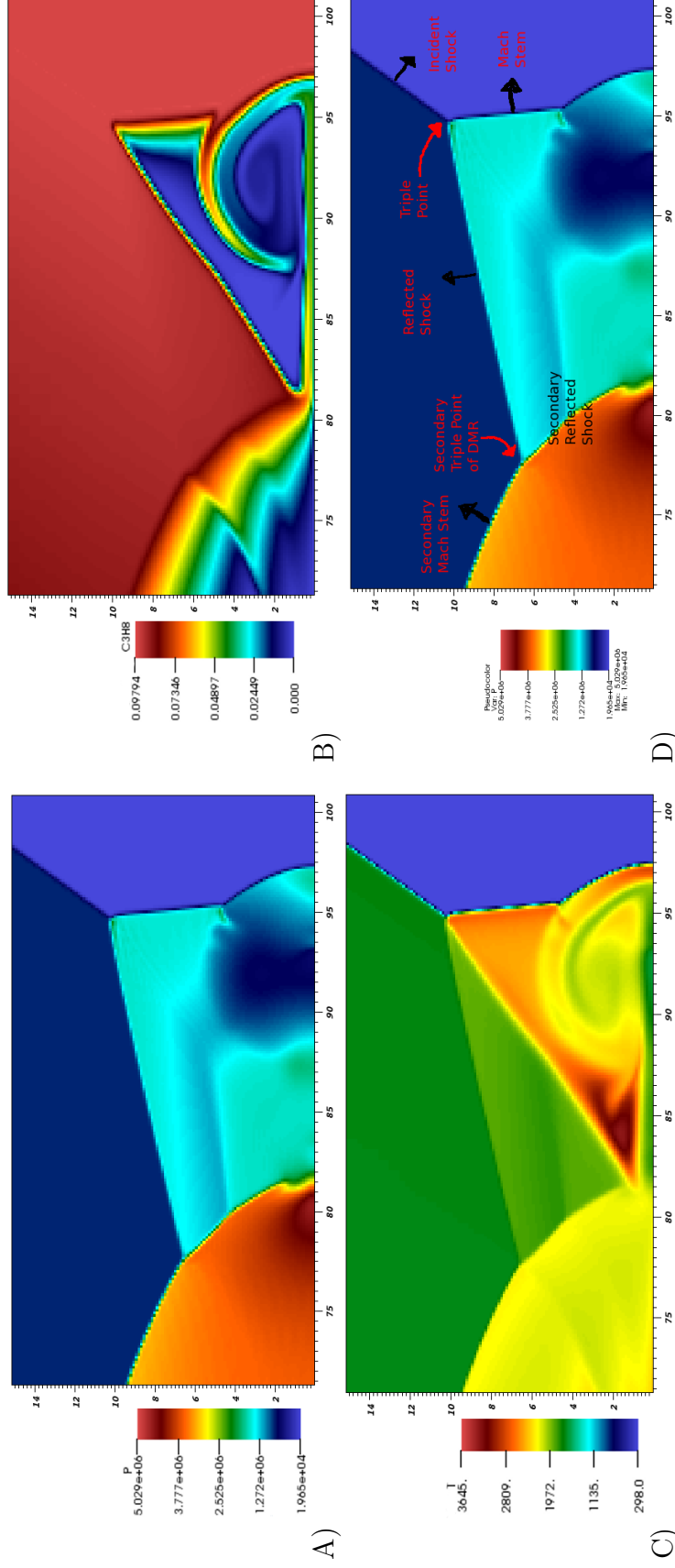


Figure 6.31: The interaction of the jet from the shear layer forms a triple point on the Mach Stem shortly after reflection. Showing diffusive results for A) and D) pressure (nondimensional), B) C<sub>3</sub>H<sub>8</sub> mass fraction, and C) temperature (K), at  $t = 12$  nondim ( $3.62 \cdot 10^{-7}$  s),  $Re = 4,960$ , with 6-levels. The units of the x- and y-axes are  $1 \cdot 10^{-3}$  cm.

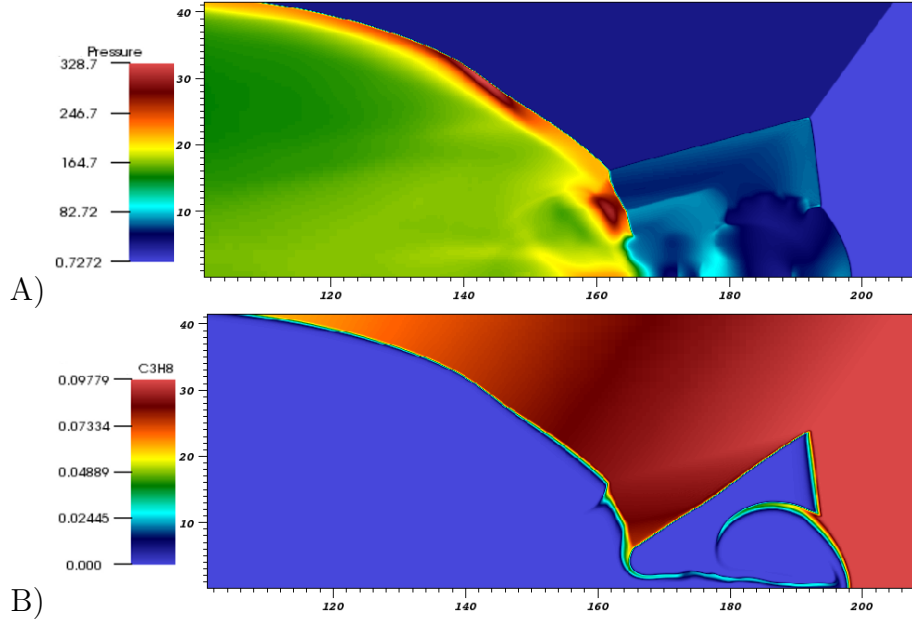


Figure 6.32: Instabilities of the chemical reactions first appearing in the reflected shock. Showing diffusive results for A) pressure (nondimensional) and B)  $C_3H_8$  mass fraction,  $t = 24$  nondim ( $7.24 \cdot 10^{-7}$  s),  $Re = 9,930$ , with 6-levels. The units of the x- and y-axes are  $1 \cdot 10^{-3}$  cm.

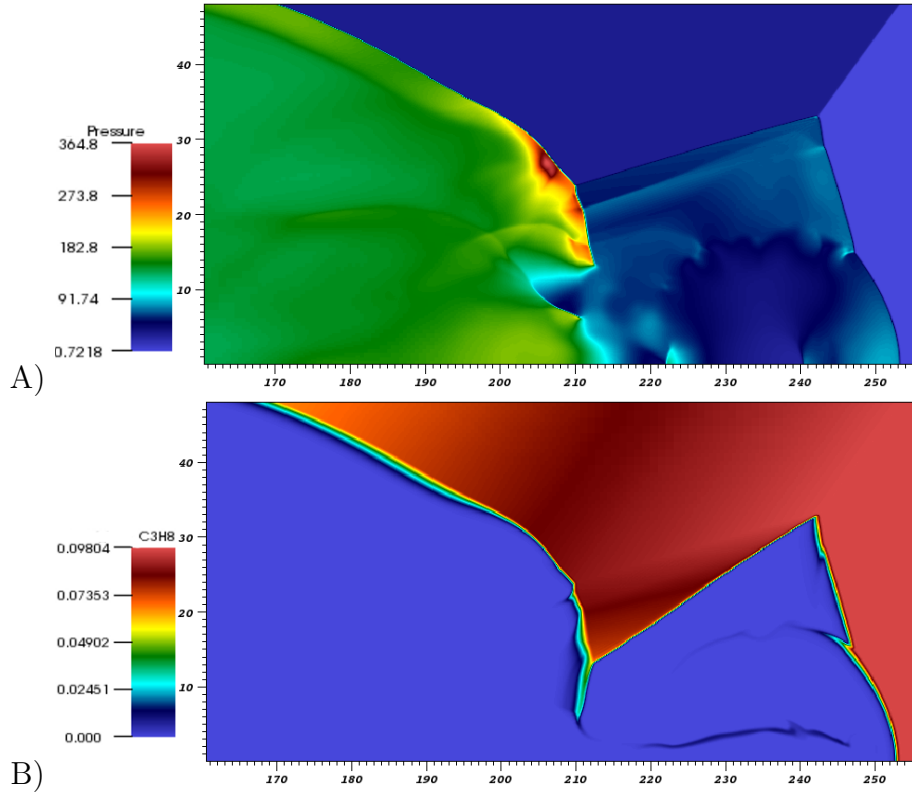


Figure 6.33: More reflected shocks have appeared within the DMR. Also, another triple point has formed near the primary one. Showing diffusive results for A) pressure (Pa) and B)  $C_3H_8$  mass fraction, at  $t = 30$  nondim ( $9.05 \cdot 10^{-7}$  s),  $Re = 12,400$ , with 6-levels. The units of the x- and y-axes are  $1 \cdot 10^{-3}$  cm.

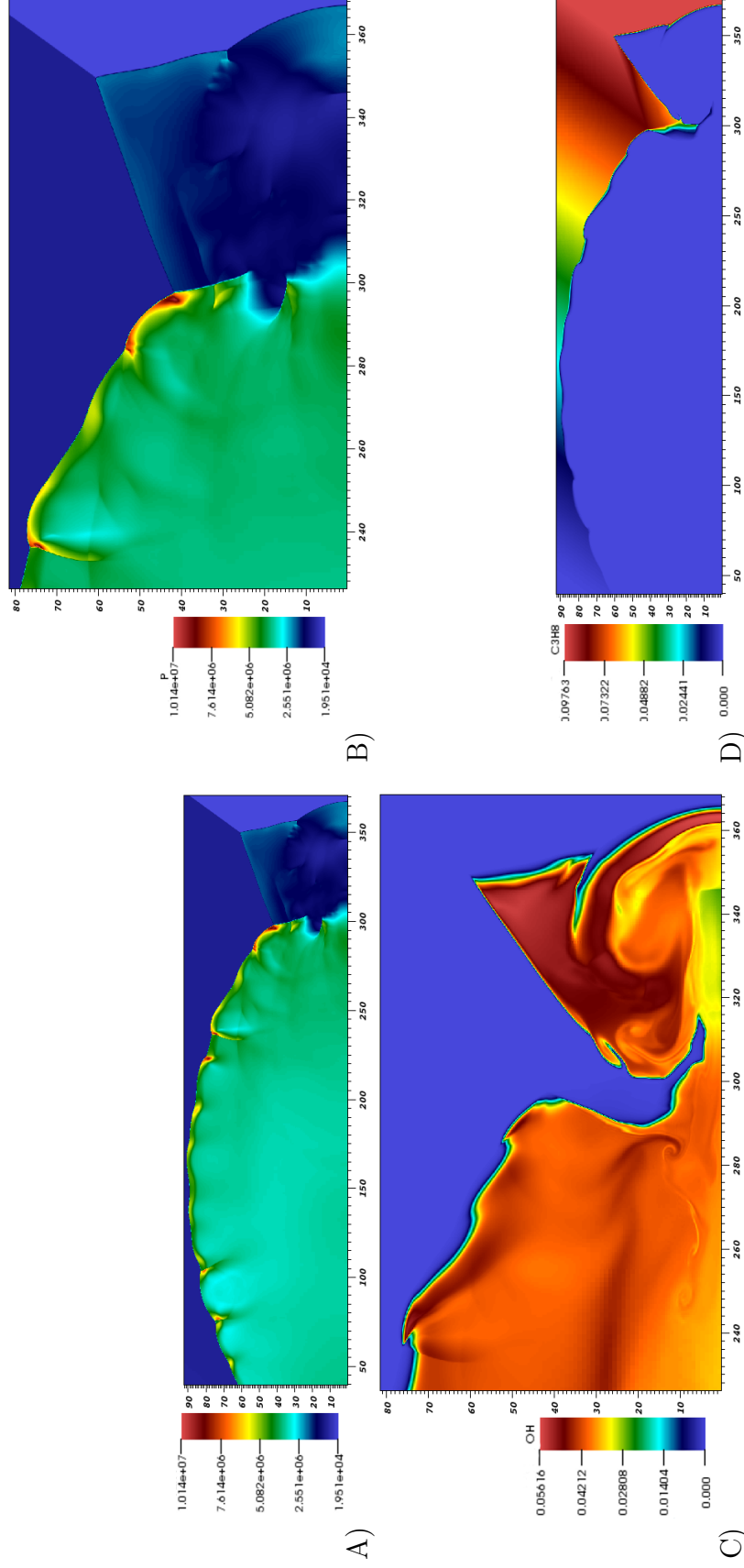


Figure 6.34: Showing diffusive results for A) pressure (Pa), B) zoomed in pressure view, C) OH mass fraction, and D)  $C_3H_8$  mass fraction, at  $t = 42$  nondim ( $1.27 \cdot 10^{-6}$  s),  $Re = 17,400$ , with 6-levels. The units of the x- and y-axes are  $1 \cdot 10^{-3}$  cm. Multiple triple points have formed on the reflected shock. Also, the fluid being entrained into the jet is not fully reacted.



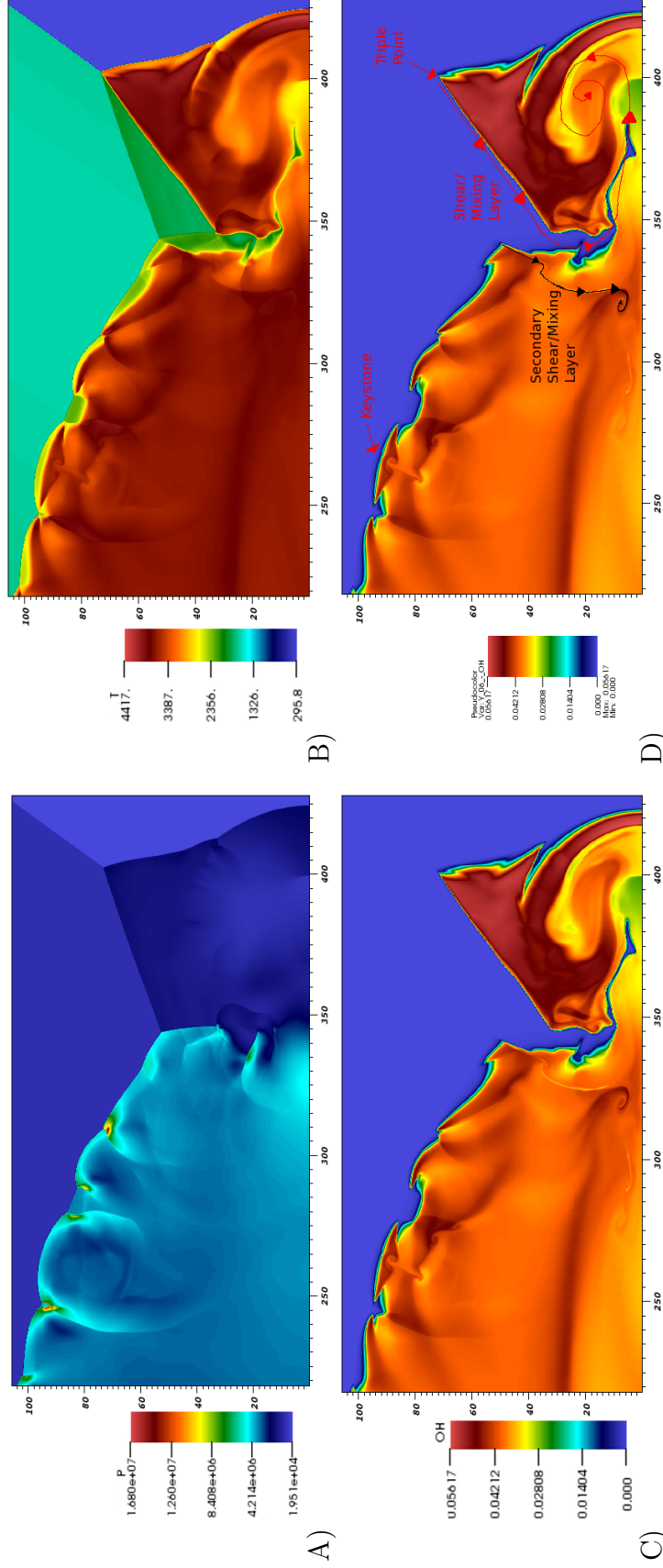


Figure 6.35: Showing diffusive results for A) pressure (Pa), B) temperature (K), and C) and D) OH mass fraction, at  $t = 48$  ns ( $1.45 \cdot 10^{-6}$  s),  $Re = 19,900$ , with 6-levels. The units of the x- and y-axes are  $1 \cdot 10^{-3}$  cm. The newly formed triple points on the reflected shock are showing many new shear layers and other shear layers from shock reflections. Also, the secondary triple point (which also appears in the nonreactive DMR) has its shear layer rolling up.

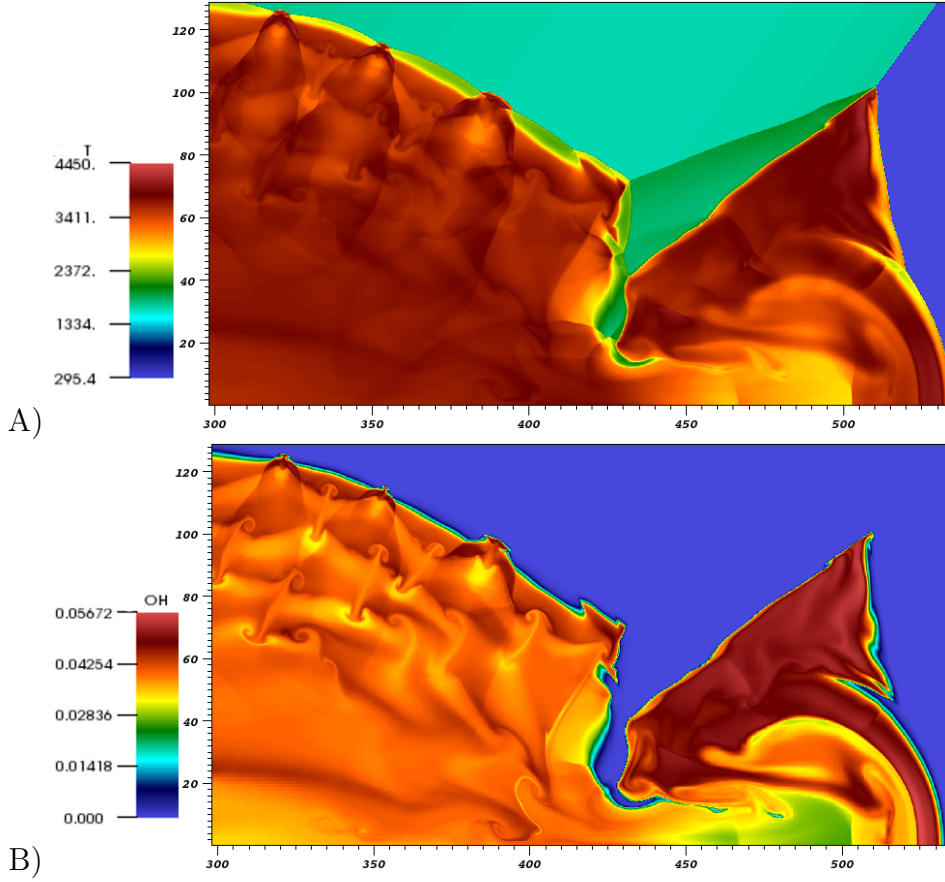


Figure 6.36: Showing diffusive results for A) temperature (K) and B) OH mass fraction, at  $t = 60$  nondim ( $1.81 \cdot 10^{-6}$  s),  $Re = 24,800$ , with 6-levels. The units of the x- and y-axes are  $1 \cdot 10^{-3}$  cm. The triple points formed on the main reflected shock have now had their reflected shocks and Mach stems reflect at least four times off each other forming at least four levels of shear layers. The main Mach stem is also becoming more unstable, showing the formation of new triple points.

Now, looking at later times, it is seen that the trend of more triple points and keystones forming and the resulting increase in mixing from their transverse shocks and shear layers continues. In figure 6.38 below, it is shown that there is now mixing occurring everywhere within the DMR. Keystone structures are seen on the main reflected shock. Also, the main shear layer emanating from the primary triple point is showing many roll-ups of vortices. A shock wave has also appeared within the main jet and traveled into the main shear layer. Multiple triple points have also appeared on the upper portion of the Mach stem, however, pronounced keystone structures do not yet appear. Note that the main incident shock is still very stable and has not yet shown any instabilities which will eventually lead to more triple points forming on it.

At a later time, now with 5-levels in figure 6.39, triple points are appearing uni-

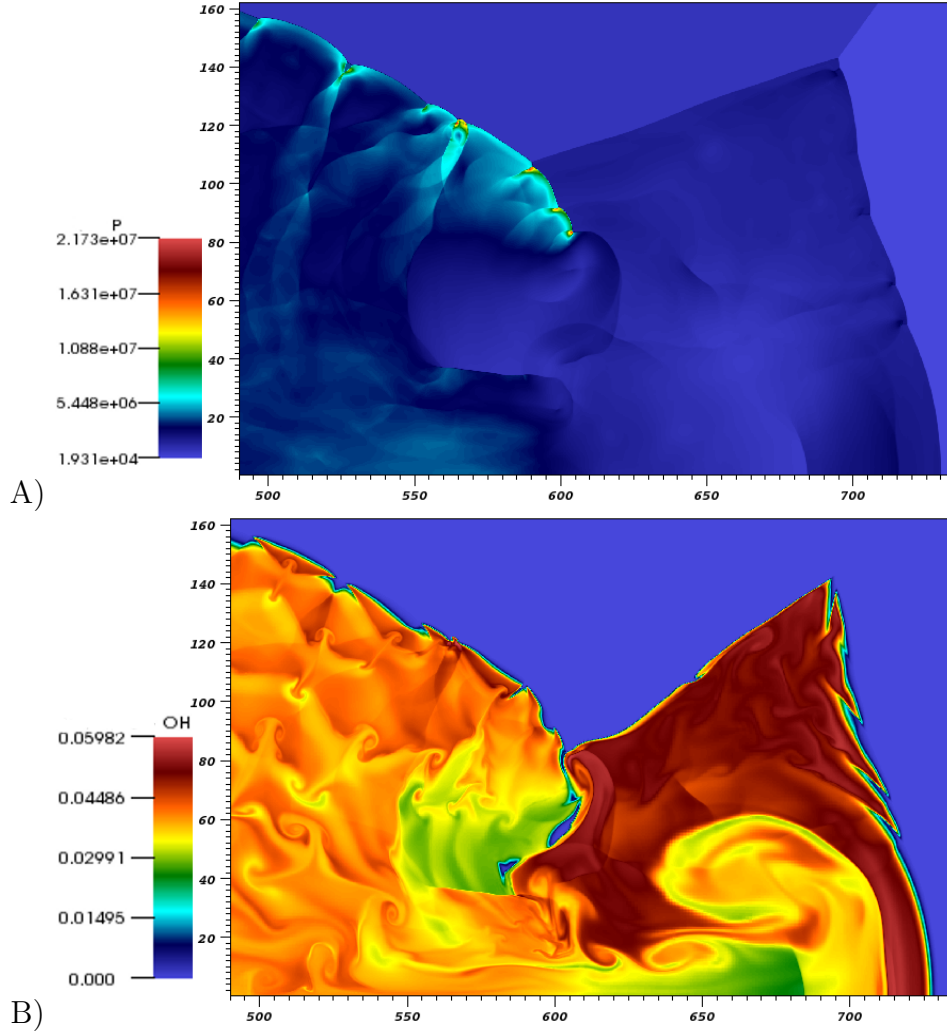


Figure 6.37: Showing diffusive results for A) Pressure (Pa) and B) OH mass fraction at  $t = 84$  nondim ( $2.53 \cdot 10^{-6}$  s),  $Re = 34,800$ , with 6-levels. The units of the x- and y-axes are  $1 \cdot 10^{-3}$  cm. At least five triple points are visible on the main Mach stem of the DMR. Also, very high pressures are appearing at the triple points on the main reflected shock.

formly along the main Mach stem. Keystone like structures are visible and the shear/mixing layer coming from the main triple point now shows inviscid instabilities all along its length. A small-scale cell pattern is also very visible when one looks at the y-component of the velocity in figure 6.39D).

At an even later time (and now with 4 rather than 5-levels) in figure 6.40, the occurrence of triple points and keystones in the Mach stem is very evident. Also, the region of the main reflected wave within the induction length is much smaller as compared to the relative size of the whole DMR structure. Now, with four times less resolution than the 6-level case, the vortices formed by the triple points on the

reflected shock are smeared with numerical viscosity. However, despite having less resolution, the growth and features of the DMR are as expected and similar to those at an earlier time step with 2x more resolution as shown in figure [6.39](#).

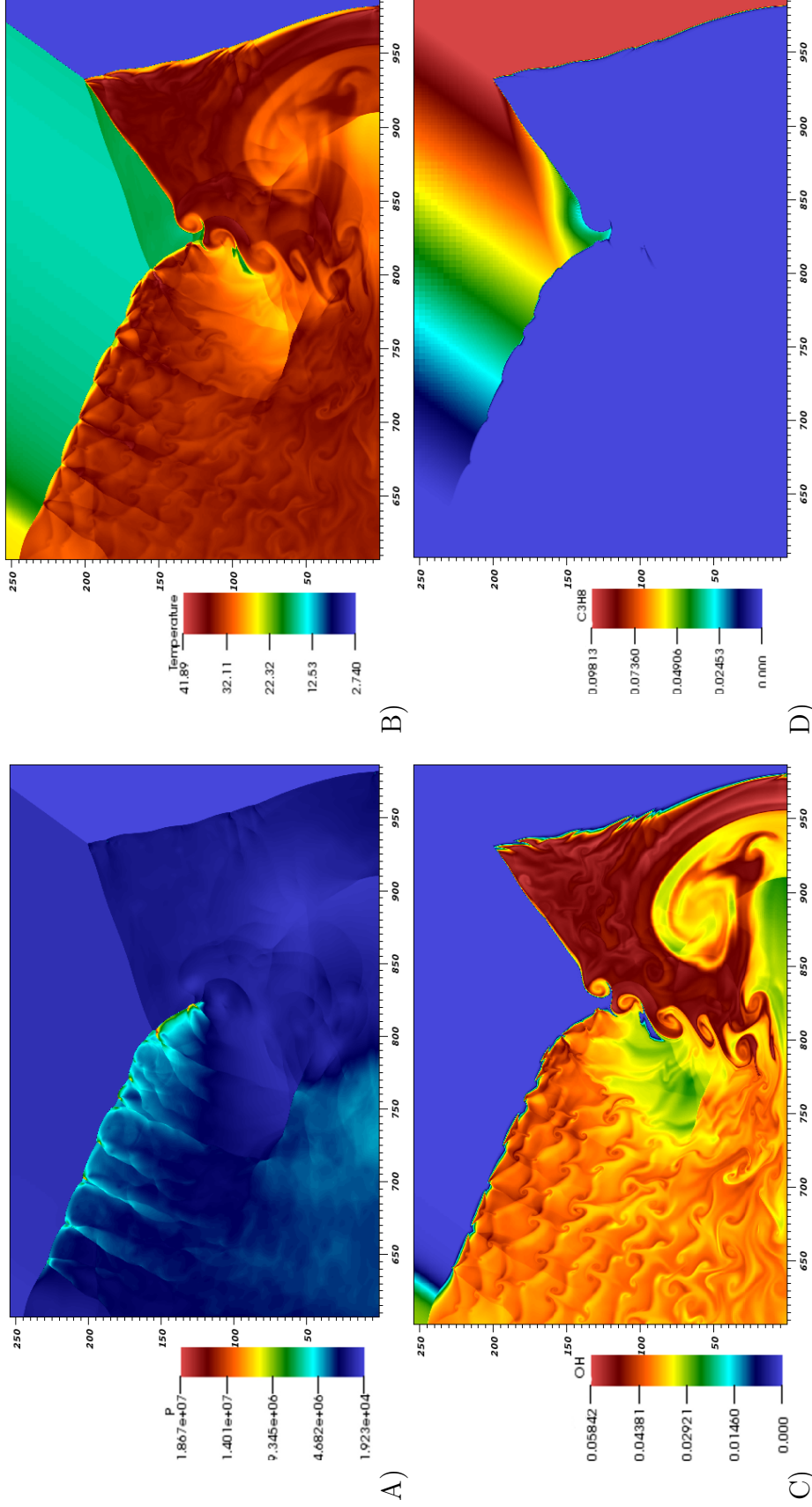


Figure 6.38: Showing diffusive results for A) pressure (Pa), B) temperature (K), C) OH mass fraction, and D)  $C_3H_8$  mass fraction at  $t = 108$  nondim ( $3.26 \cdot 10^{-6}$  s),  $Re = 44,700$ , with 6-levels. The units of the x- and y-axes are  $1 \cdot 10^{-3}$  cm. There is now mixing occurring every within the DMR. Keystone structures are seen on the main reflected shock. Also, the main shear layer emanating from the primary triple point is showing many roll-ups of vortices. A shock wave has also appeared within the main jet and traveled into the main shear layer. Many triple points have also appeared on the upper portion of the Mach stem, however, pronounced keystone structures do not yet appear. Note that the main incident shock is still very stable and has not yet shown any instabilities which will eventually lead to more triple points forming.



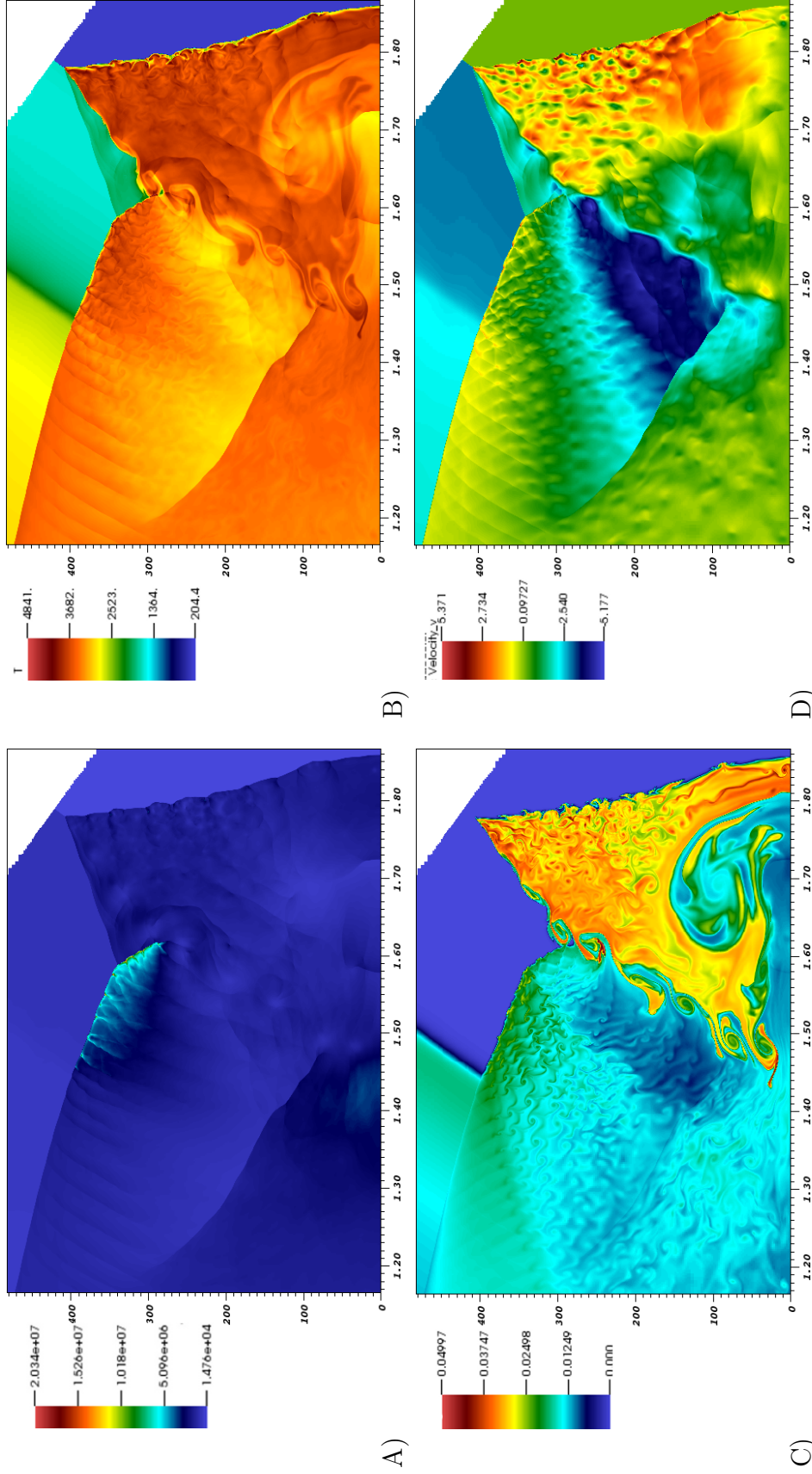


Figure 6.39: Showing diffusive results for A) pressure (Pa), B) temperature (K), C) OH mass fraction, and D) nondimensional y-component velocity at  $t = 204$  nondim ( $6.15 \cdot 10^{-6}$  s),  $Re = 84,400$ , with 5-levels. The units of the x- and y-axes are cm. Now triple points are appearing uniformly along the main Mach stem. Keystone like structures are visible. The shear/mixing layer coming from the main triple point now shows inviscid instabilities all along its length. A small-scale cell pattern is also visible when one looks at the y-component of the velocity. Note that the resolution of this simulation result is two times lower than that in the previous figure 6.38.

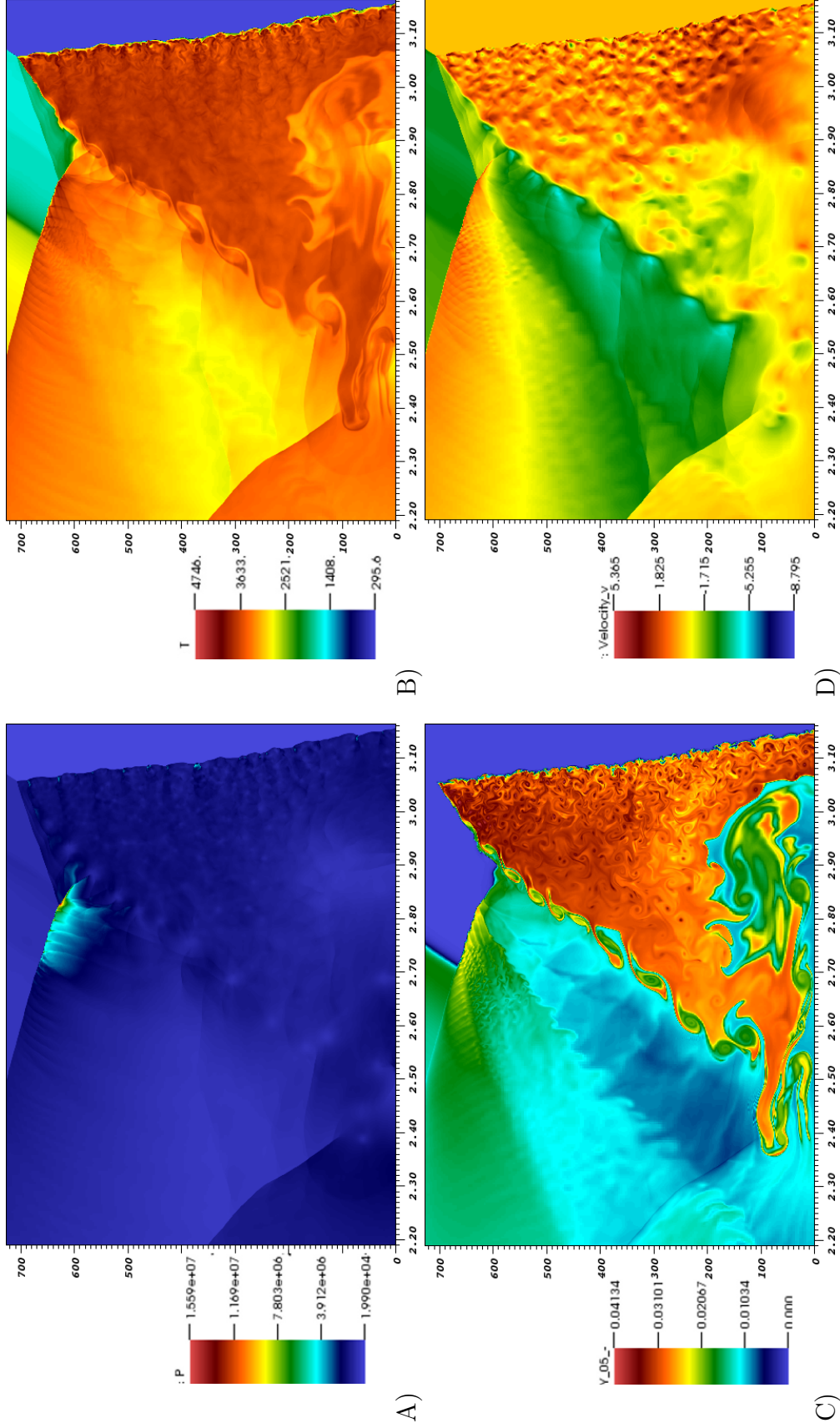


Figure 6.40: Showing diffusive results for A) pressure (Pa), B) temperature (K), C) OH mass fraction, and D) nondimensional y-component velocity at  $t = 348$  nondim ( $1.05 \cdot 10^{-5}$  s),  $Re = 144,000$ , with 4-levels. The units of the x- and y-axes are cm. Note that the resolution of this simulation result is two times lower than that in the previous figure 6.39.

Now, in the figures 6.41-6.46, the unstable decoupling and recoupling of the reaction zone of the incident shock is investigated in detail. In figure 6.41, by looking at the product  $\text{H}_2\text{O}$  mass fraction one sees that the reaction zone has become decoupled from the incident shock front for a long enough time to allow diffusive multi-dimensional mixing to create instabilities leading to a deflagration that grows and eventually accelerates into the shock front.

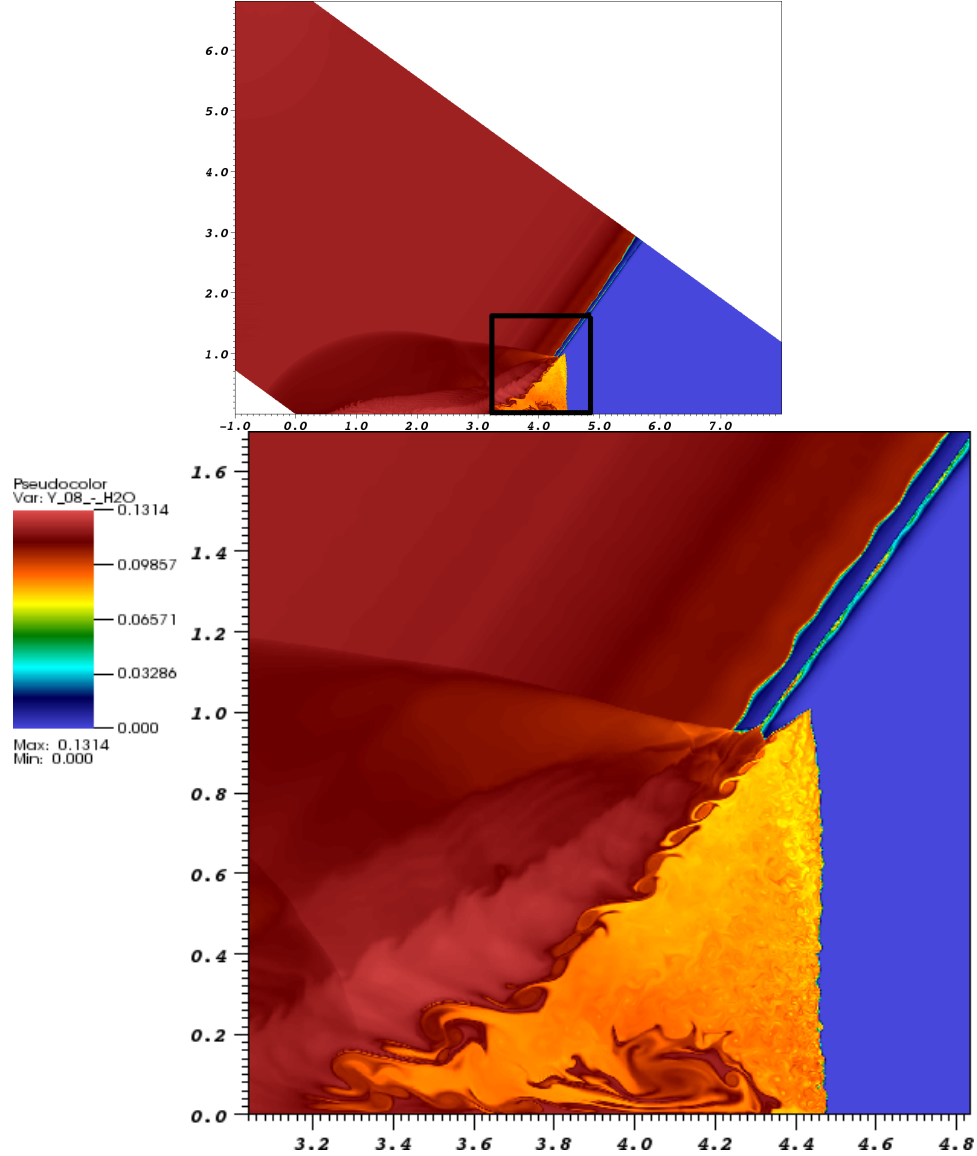


Figure 6.41: At a time of  $t = 504 \text{ nondim} = 1.52 \cdot 10^{-5}$  seconds, the incident shock/detonation has gone unstable. The original induction zone is showing transverse oscillations and ahead of it a local explosion is developing. Showing diffusive results for the  $\text{H}_2\text{O}$  mass fraction. The units of the x- and y-axes are cm.



Also, for the same time value shown in figure 6.42A), the localized unstable deflagration is seen by looking at the creation of the H radical. In figures 6.42B)-D), very rapidly, the deflagration has grown and collided with the shock front, creating a dynamic reaction zone length characteristic of a pulsating detonation. In figure 6.43, the same domains and time values are shown again, but now for the pressure. It is seen that the localized deflagration has created a pressure wave (seen as a pressure spike in a 1D cut). This nonuniform wave travels upstream raising the temperature and pressure of the flow in a nonuniform way which leads to more diffusive mixing and an acceleration of the energy release. In figure 6.43, the formation of new triple points is observed on the incident wave. Also, observe that in all of these time steps of figure 6.43, the pressure waves created by the ignition have propagated into the DMR and have largely influenced its structure. Note that the formation of these deflagration and subsequent keystone structures is a chaotic multi-dimensional process, which was influenced by small but fairly uniform errors created by the interaction of the grid with the numerical scheme.

In figure 6.44 is comparison of the 1D solution, a), with the 2D planar solution, b). The fuel mass fraction in the reaction zone behind the incident shock is shown sequentially. The initial decoupling of the shock and reaction zone (seen by observing the increase in length of this zone) is seen in both the 1D and 2D cases. However, in the 2D case a thinner reaction zone is established and the detonation becomes overdriven.

In figure 6.45, the whole DMR/incident detonation interaction is shown at a later time value. At this time the incident detonation has interacted with all of the primary Mach stem. Mixing is now occurring at a much larger scale. There is a range of scales observed from the largest scale occurring near the end of the main reflected wave to the smaller scales of the triple point separation distance (related to cell size) and mixing scales behind the incident shock, the large keystone, and the remaining Mach stem close to the bottom boundary. In figure 6.46, the interaction of the incident shock and the DMR and shown in detail. The growth of a large scale keystone like structure is seen as the incident shock accelerates into the Mach stem and primary mixing layer.

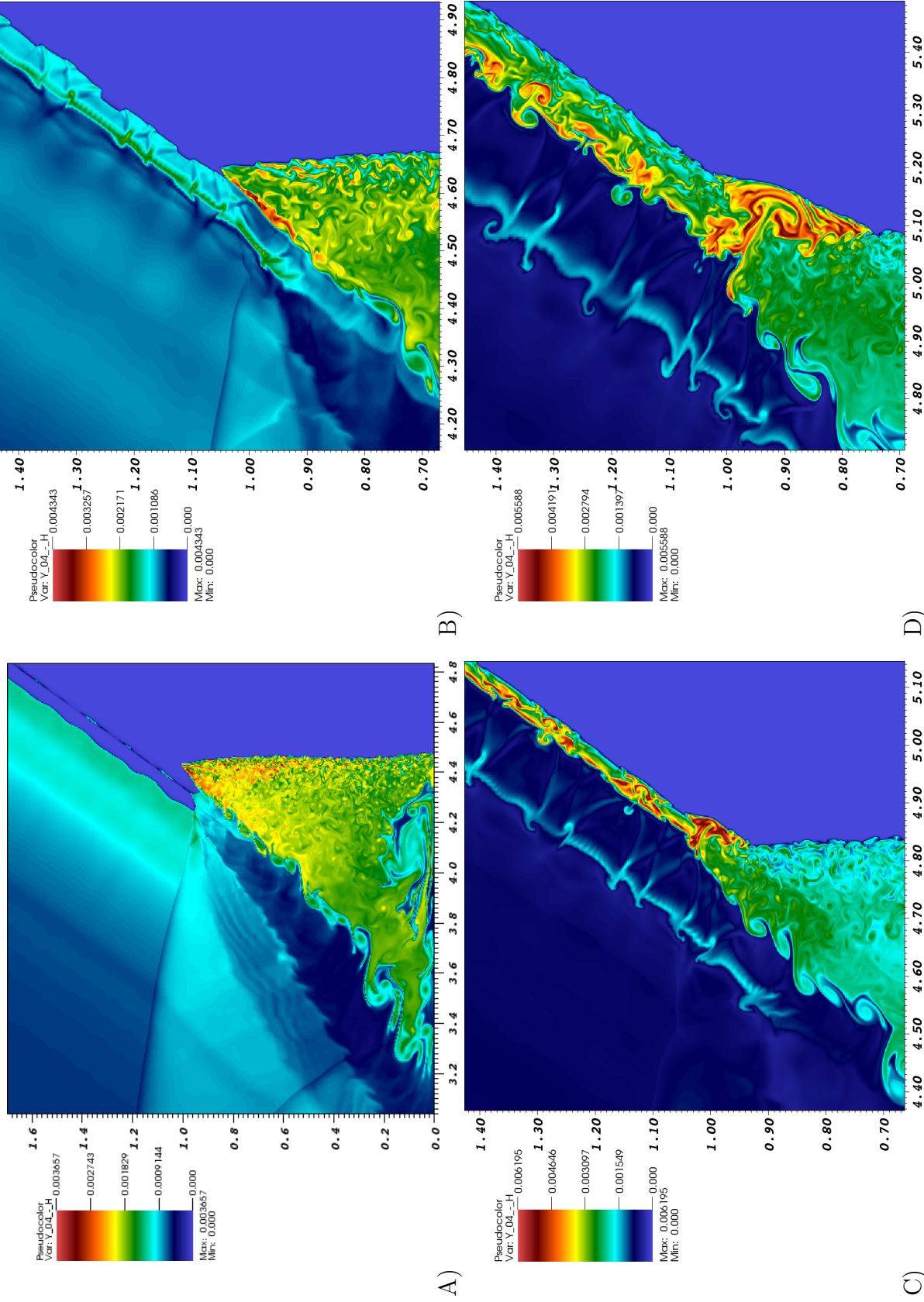


Figure 6.42: Showing diffusive results for the H mass fraction at subsequent time values of A)  $t = 1.66 \cdot 10^{-5}$  sec, B)  $1.59 \cdot 10^{-5}$  sec, C)  $1.73 \cdot 10^{-5}$  s, and D)  $1.52 \cdot 10^{-5}$  s. In B) the explosion has propagated forward, reaching and accelerating the incident shock wave. At this point the incident shock wave also goes unstable showing the typical unsteady and chaotic keystone structure and triple points. Also, observed is incident shock/detonation wave accelerating into the mach stem, engulfing the main primary triple point and creating a large scale keystone like structure. The units of the x- and y-axes are cm.

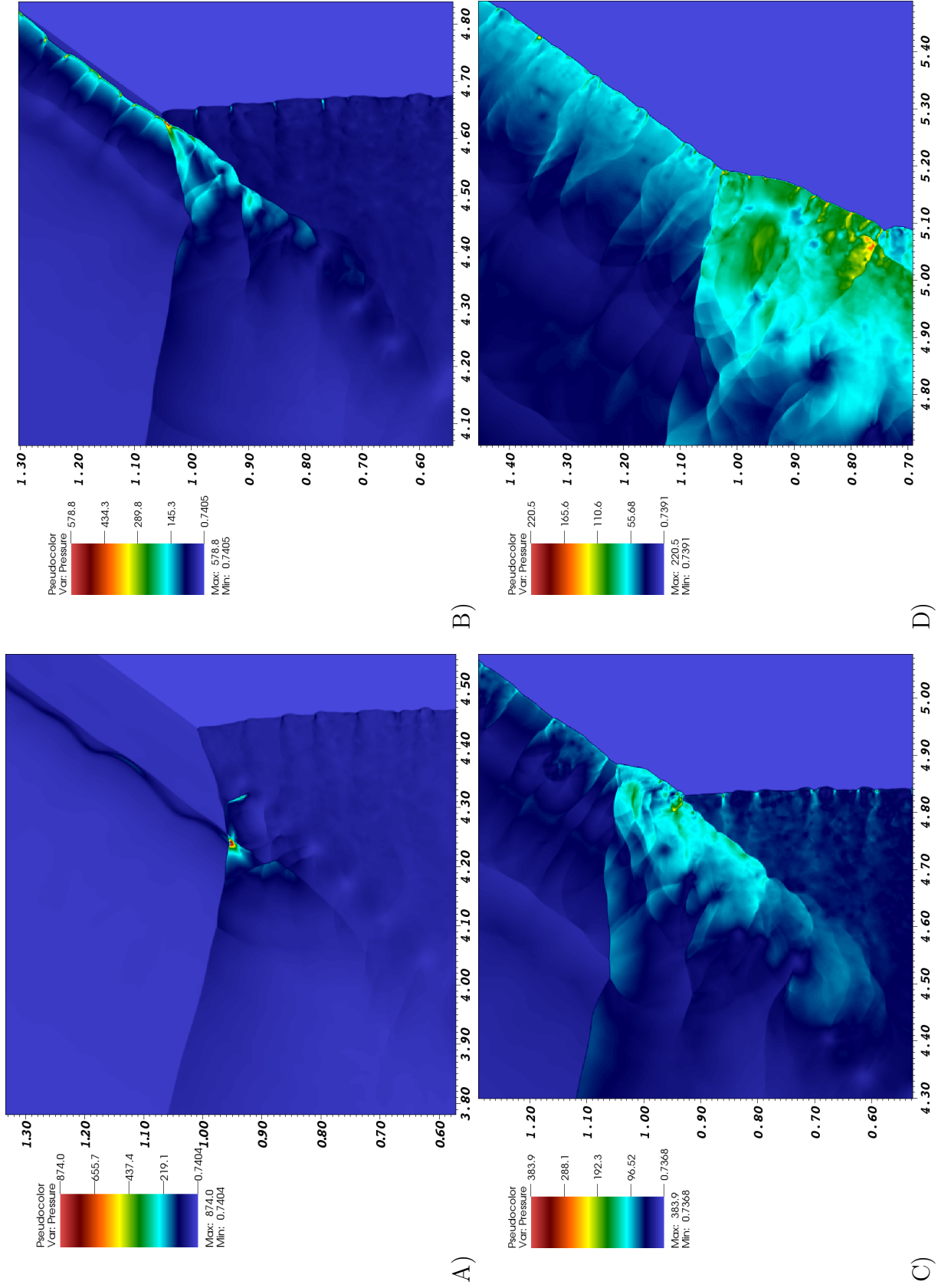


Figure 6.43: Showing diffusive results for pressure at subsequent time values, which correspond to the times in figure 6.42. In B) the appearance of new triple points is observed. Also observed is the creation and reflection transverse waves along the accelerated incident front. The units of the x- and y-axes are cm.

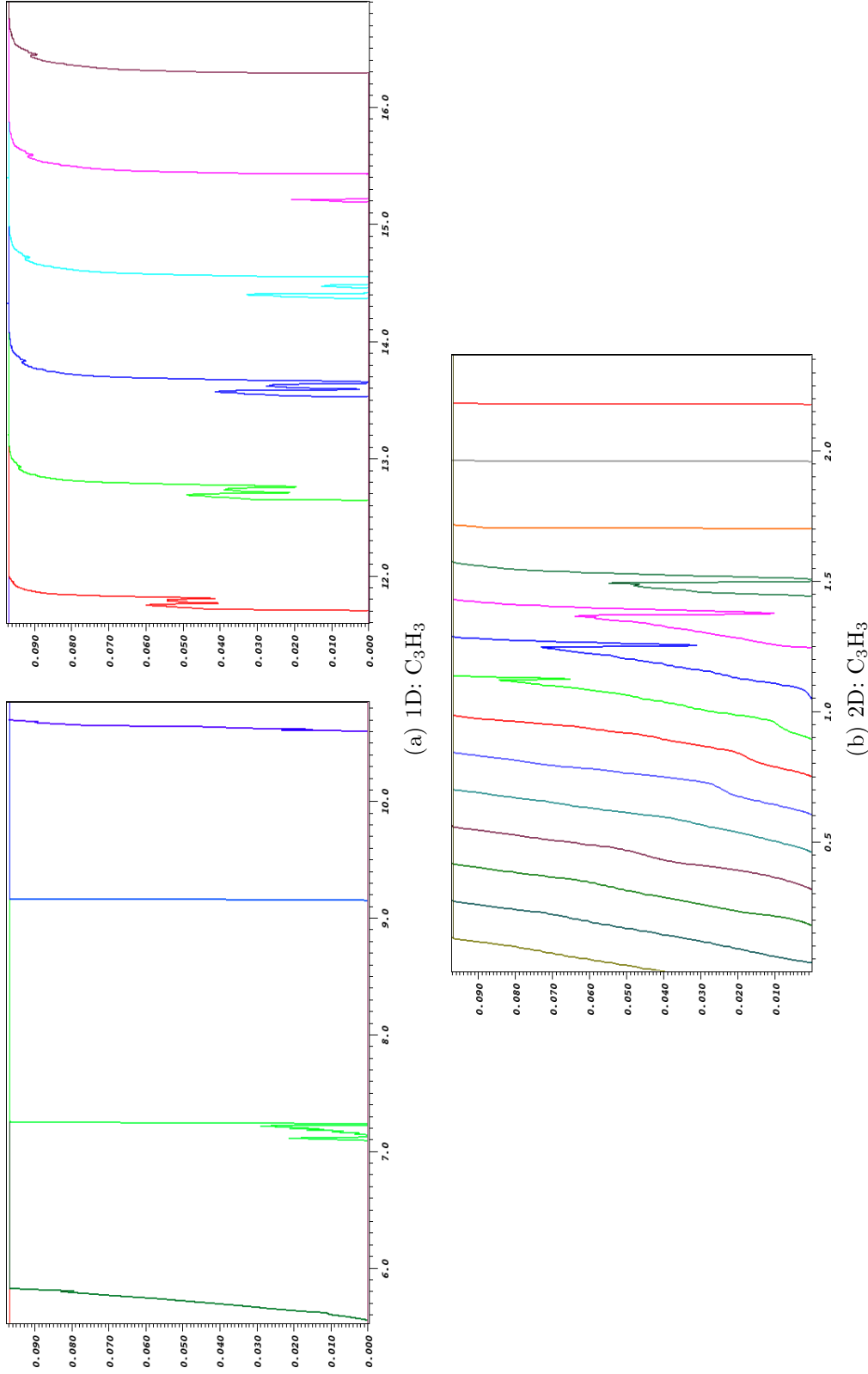


Figure 6.44: Shown is a comparison of the failure of the detonation for the 1D case in a) and an acceleration of the detonation for the 2D case in b). In each sub-figure, the propane mass fraction is plotted as through the incident (initially planar and steady for both cases) shock/detonation front is plotted at subsequent time values, where each color represents a different time. In a) for the 1D case, it is observed that the reaction zone lags behind and becomes decoupled from the shock front. Shown is the propane fuel mass fraction, which continues to be consumed but at a distance farther and farther from the shock wave. In b) for the 2D case, the same process starts initially. That is, the reaction zone starts to lag behind the shock front more and more, however, a new reaction zone due to diffusive mixing and the interaction with transverse shock waves begins to form ahead of the initial reaction zone. This new zone goes in size and is accelerated forward, propelling the incident shock forward. The units of the x- and y-axes are cm. For a) they correspond to absolute distances and for b) are relative distances.

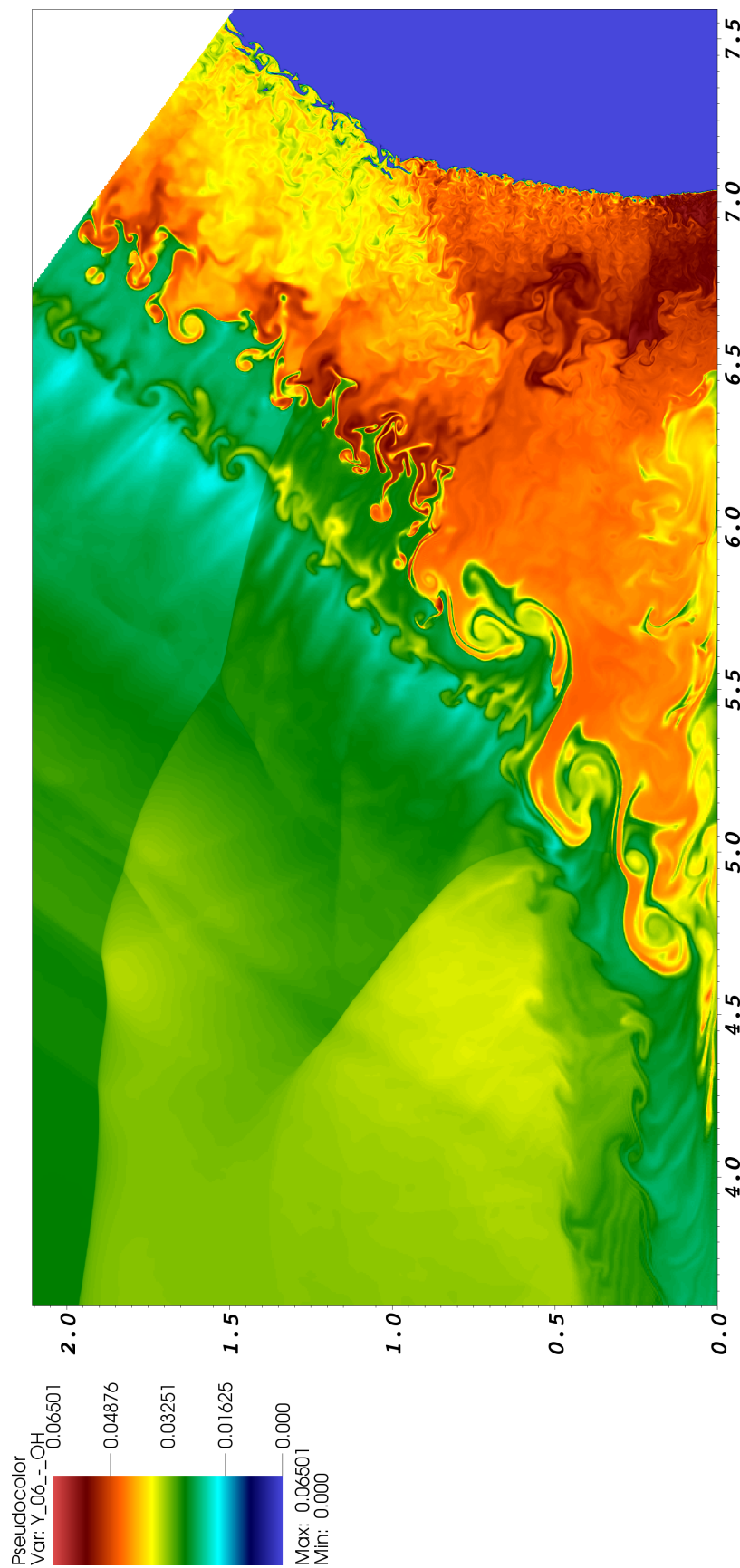


Figure 6.45: Showing diffusive results for the OH mass fraction at a time of  $t = 2.39 \cdot 10^{-5}$  s. At this time the incident detonation has interacted with all of the primary Mach stem. Lots of mixing is occurring everywhere and there is a range of scales observed from the largest scale occurring near the end of the main reflected wave to the smaller scales of the triple point separation distance (cell size) and mixing scales behind the incident shock, the large keystone, and the remaining Mach stem close to the bottom boundary. In figure 6.46 zoomed in views of the keystone structure at earlier time values are shown.



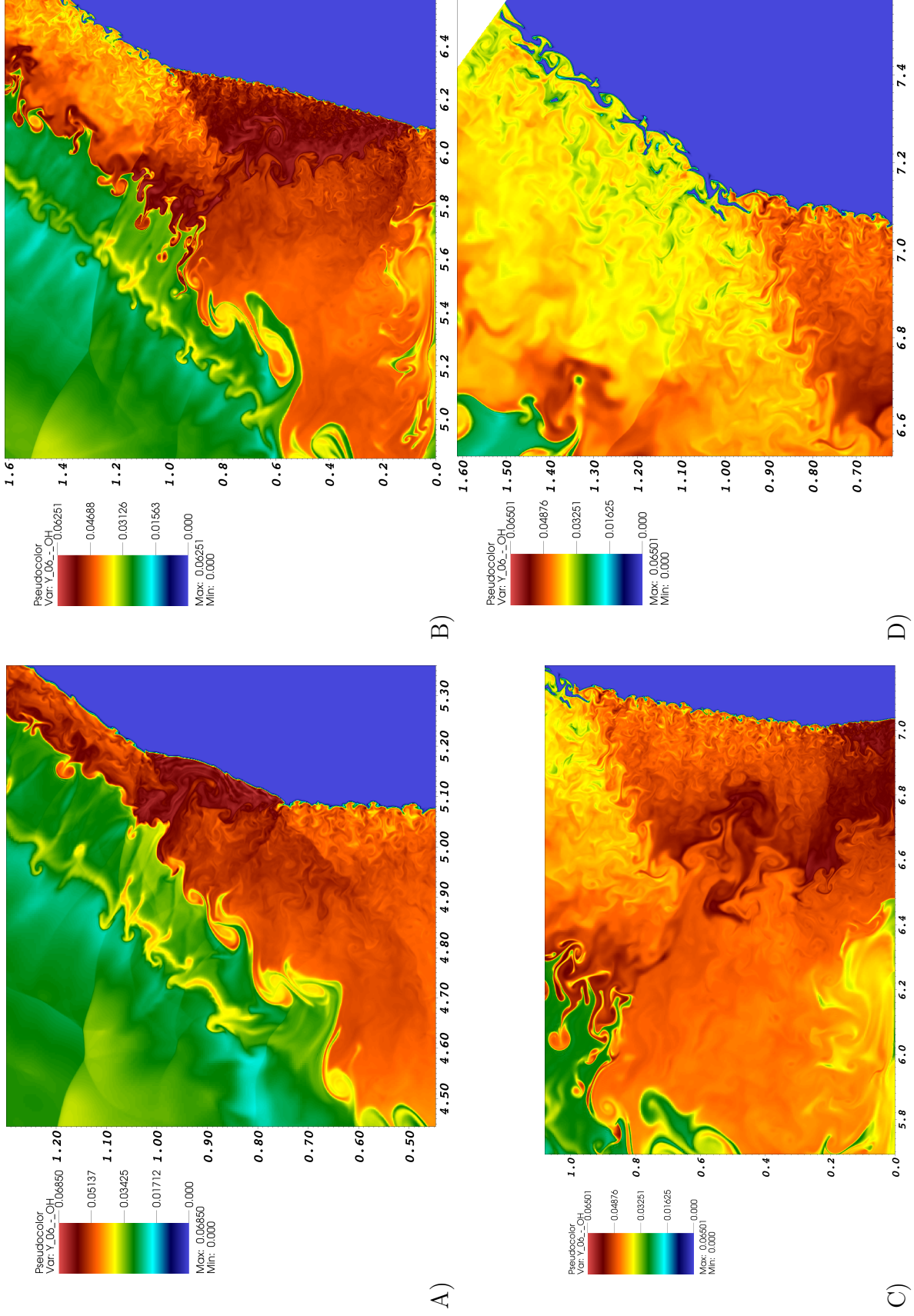


Figure 6.46: Showing zoomed in views of the development of the keyhole like structure created when the incident shock accelerates into the Mach stem. Showing diffusive results of the OH mass fraction at A)  $t = 1.73 \cdot 10^{-5}$  sec, B)  $t = 2.06 \cdot 10^{-5}$  sec, and C) and D) where  $t = 2.06 \cdot 10^{-5}$  s. The units of the x- and y-axes are cm.

### 6.4.1 Velocity Vector Visualizations

In this subsection, velocity vectors are visualized on top of pseudo-color plot of such quantities as pressure. The changes in flow direction is clearly seen as the flow passes through multiple shocks waves. In figures 6.47 and 6.48 close ups for the 6-level case are shown. In figure 6.49, results for the 3-level large domain case are shown.

Starting with figure 6.47A) and B), one can observe two processes that change the flow direction, shock waves, and shear layers. The function of the shock waves is to turn the flow such that it is parallel to the bottom boundary, a consequence of the no-slip boundary condition. the shear layer results from a mismatch in magnitude and flow direction of the flow (in the reference frame of the primary triple point) which has passed through the Mach stem or the incident shock and then the reflected shock. Note that this reflected shock serves as the incident shock for the secondary triple point, as is labeled in figure 6.31D). The transverse shock (which is the reflected shock of the secondary triple point) interacts with the shear layer, turning the flow and creating the jet that has moved its way into the main Mach stem. The collision of the shear layer with this shock and its symmetrical shear layer mirrored on the other side of the boundary pushes the flow forward at a relatively large velocity, as seen in the visualization of figure 6.47, where the magnitude of the velocity is proportional to the arrow size. In figure 6.47C), at a later time, the complexity of the flow is seen by the growth in instability of the shear layer. Also, a growing region where the shear layer has destroyed the transverse shock is observed. Then, in figure 6.47D), at an even later time, the creation of triple points on the main reflected shock (technically the mach stem of the secondary triple point), is observed. These triple points each have their own incident and reflected shocks, but share a Mach stem, just as the main Mach stem has a mirror image which is modeled with the symmetry boundary condition. The reflected shocks of these triple points are referred to as transverse shocks when discussing their influence on the whole flow field.

Now, later in figure 6.48A) and B), the interaction of the triple points' transverse shocks is observed, with multiple collisions and reflections having occurred. In figures 6.48C) and D), the very slight influence of the shear layers of the triple points occurring on the main reflected shock on the overall flow field velocity is observed. Also observed is the the beginnings of triple points on the Mach stem. This is seen by the appearance of shear layers, kinks in the Mach stem, and also slightly different flow directions near the Mach stem shock wave.

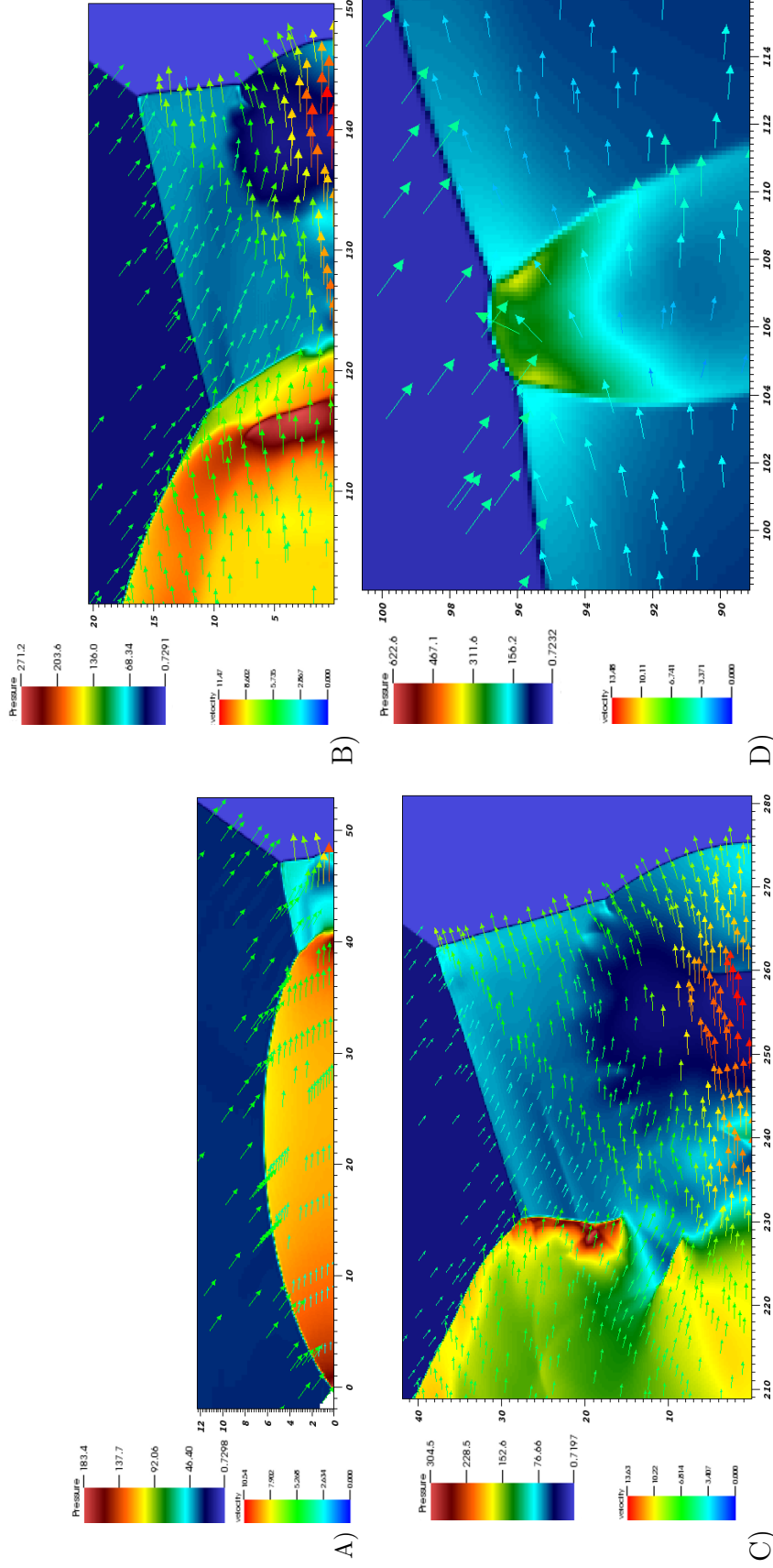


Figure 6.47: Showing velocity vectors superimposed on pressure pseudo-color plots at subsequent time values for the highest resolved 6-level case. In A)  $t = 6$  nondim =  $1.81 \cdot 10^{-7}$  sec, B)  $t = 18$  nondim =  $5.43 \cdot 10^{-7}$  sec, C)  $t = 32.3425$  nondim =  $9.76 \cdot 10^{-7}$  sec, and D)  $t = 48$  nondim =  $1.45 \cdot 10^{-6}$  s. D) shows a zoomed in view of triple points which have formed on the main reflected wave of the DMR.



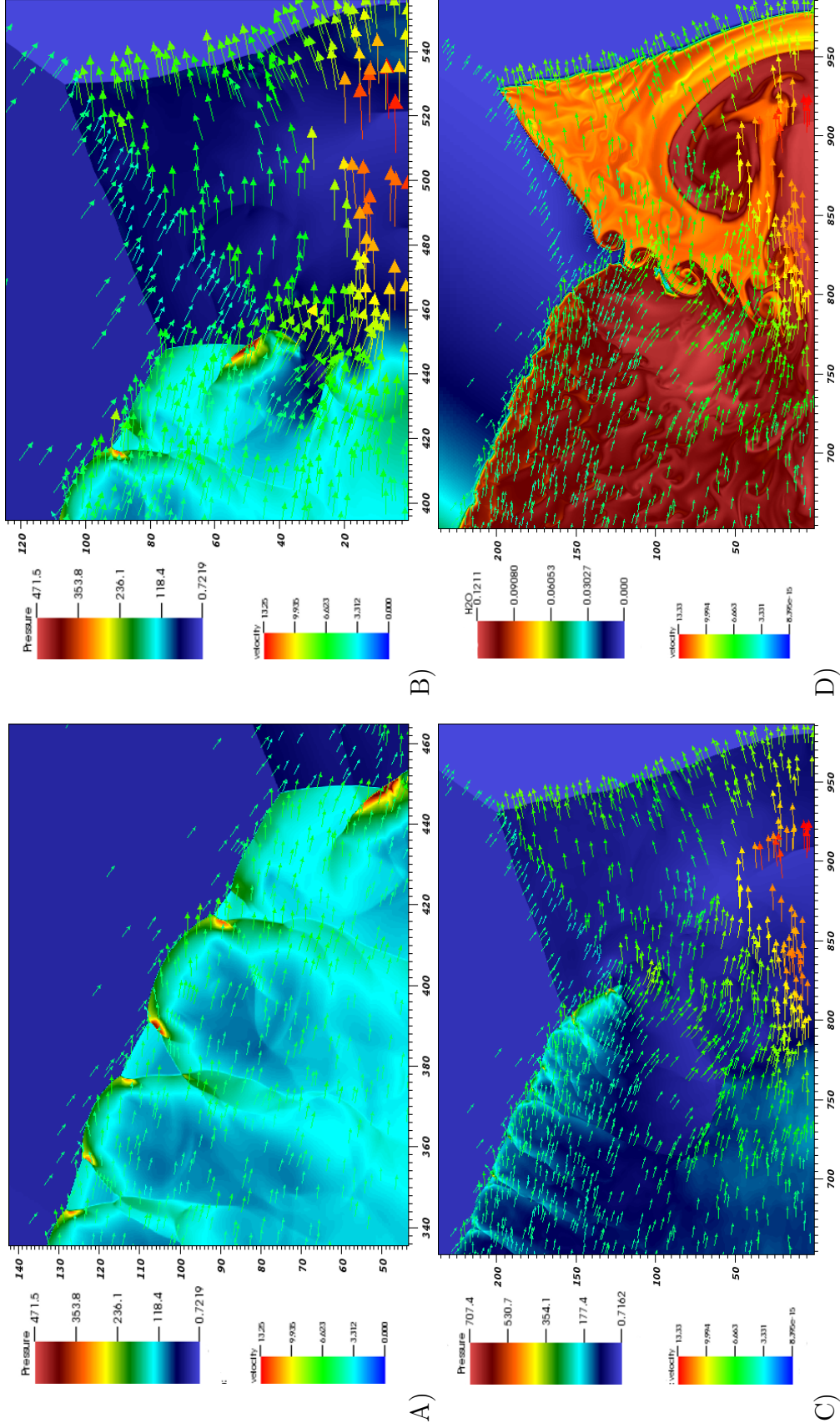


Figure 6.48: Showing velocity vectors superimposed on pressure pseudo-color plots ( A, B, and C ) at subsequent time values for the highest resolved 6-level case. D) shows a pseudo color mass fraction plot of  $\text{H}_2\text{O}$ . In A) and B)  $t = 62.2126$  nondim  $= 1.88 \cdot 10^{-6}$  sec, C) and D)  $t = 108$  nondim  $= 3.26 \cdot 10^{-6}$  s.

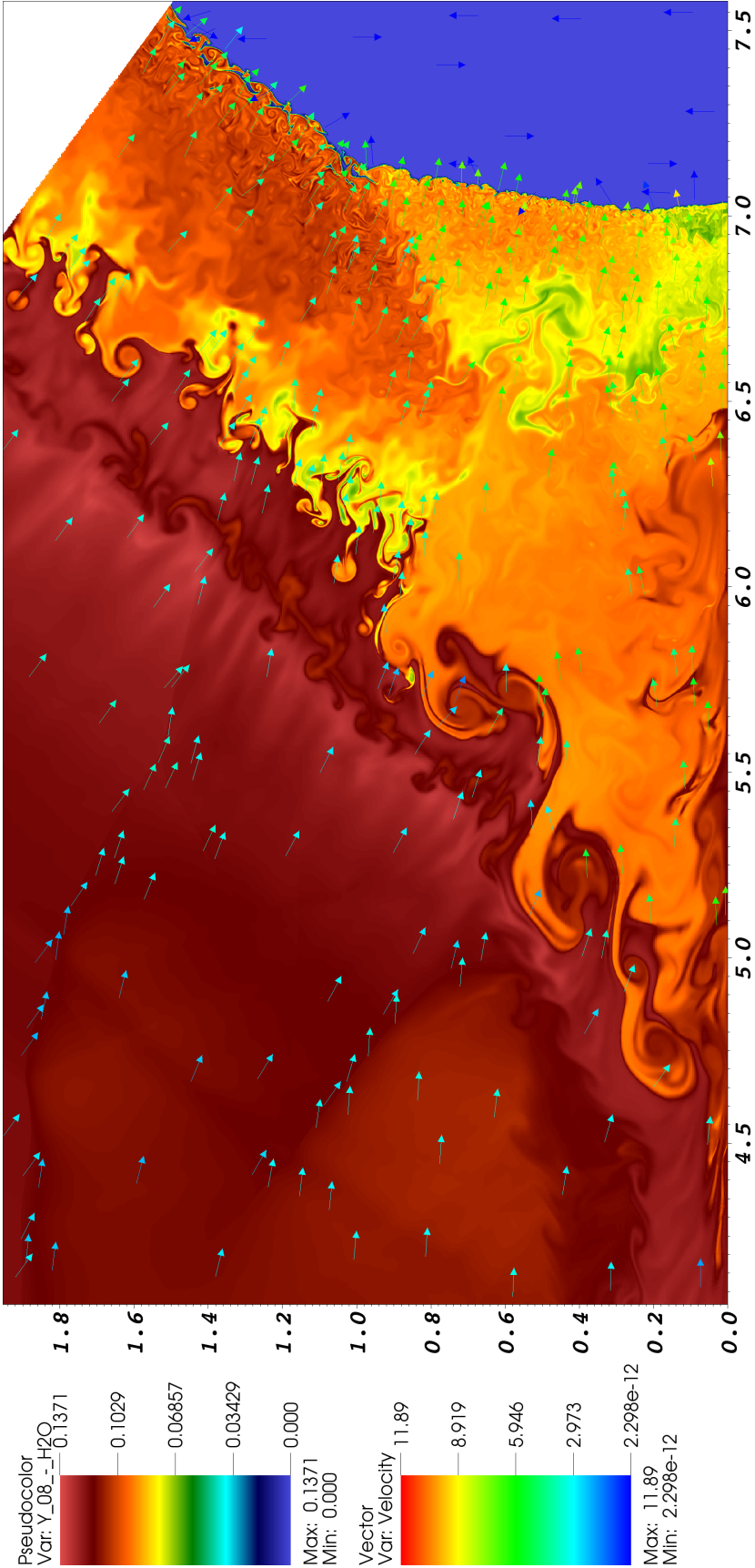


Figure 6.49: Showing velocity vectors superimposed on a pseudocolor plot of the H<sub>2</sub>O mass fraction at the final time of  $t = 2.39 \cdot 10^{-5}$  s. Note that this figure is a very high-resolution image. It is recommended that one uses the zoom tool of the pdf viewer to zoom in and view at the smaller scale structures.

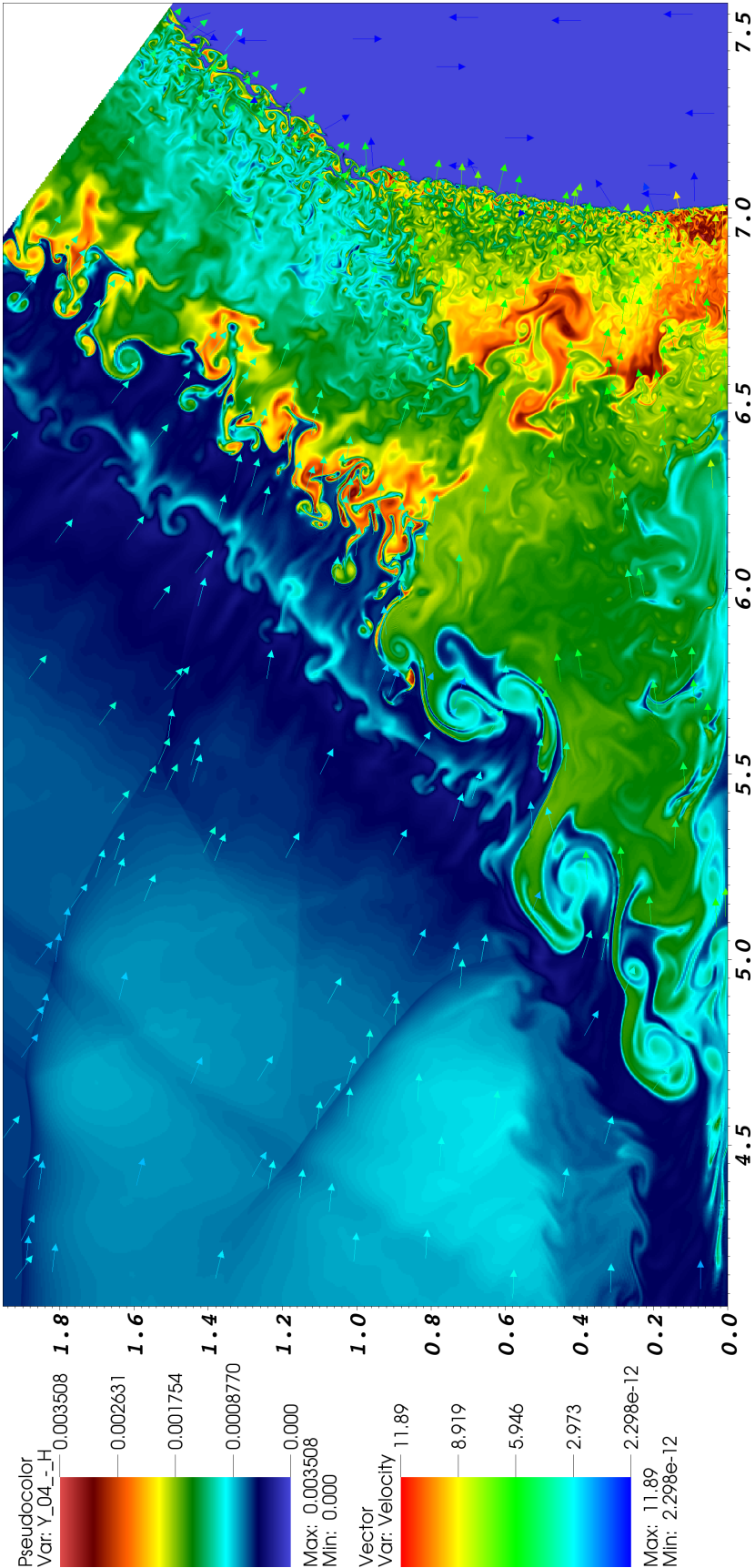


Figure 6.50: Showing velocity vectors superimposed on a pseudo-color plot of the H mass fraction at the final time of  $t = 2.39 \cdot 10^{-5}$  s. Note that this figure is a very high-resolution image. It is recommended that one uses the zoom tool of the pdf viewer to zoom in and view at the smaller scale structures.

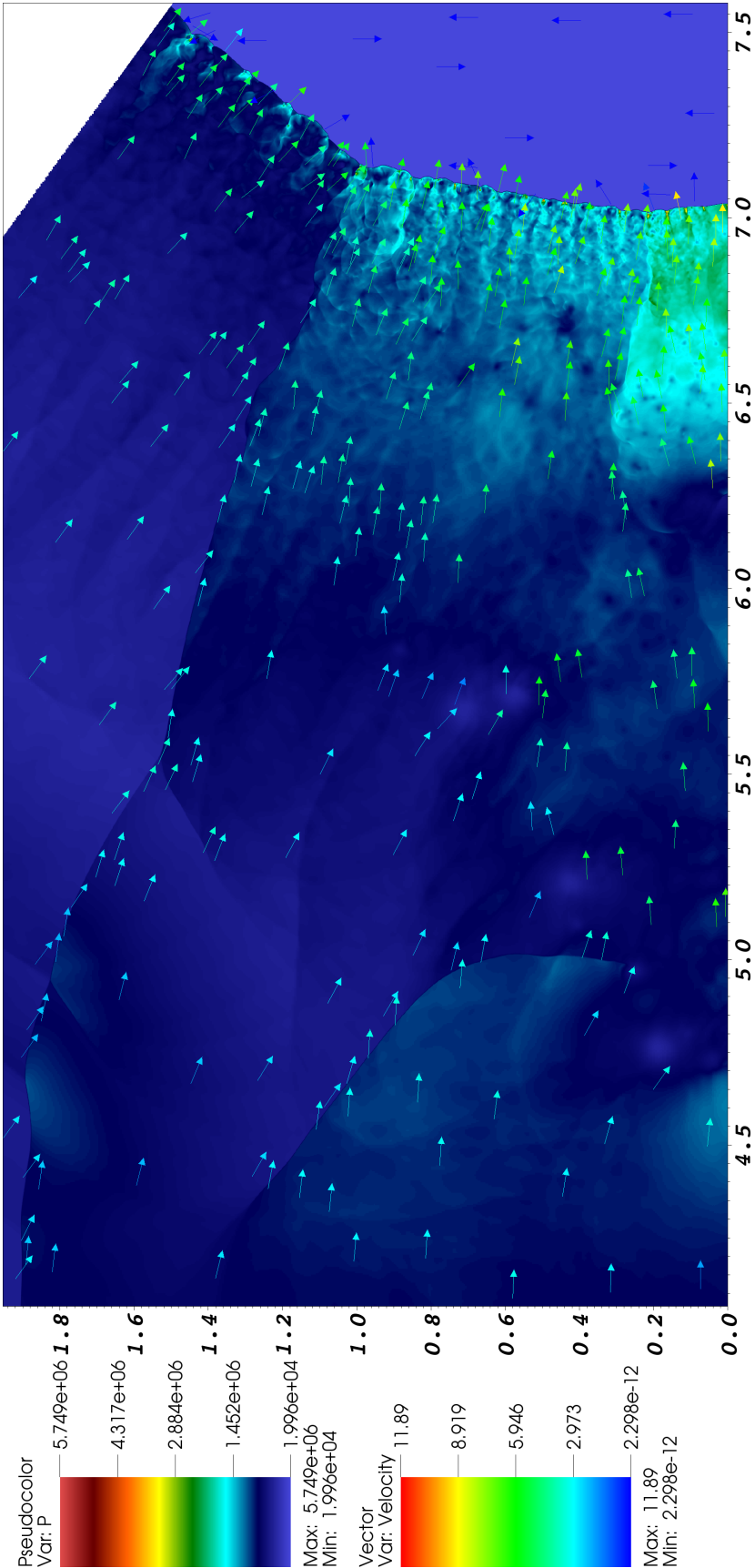


Figure 6.51: Showing velocity vectors superimposed on a pseudo-color plot of the pressure at the final time of  $t = 2.39 \cdot 10^{-5}$  s. Note that this figure is a very high-resolution image. It is recommended that one uses the zoom tool of the pdf viewer to zoom in and view at the smaller scale structures.



At a much later time in figures 6.49, 6.50, and 6.51, the differing transverse flow directions around the triple points/keystones is more visible and pronounced. By looking at the pressure in figure 6.51, one sees that within what was a DMR (whose size is observed by looking at the location of the primary triple point, which is now about 1 cm above the bottom boundary) has become a chaotic mixture of transverse waves and shear layers.

## 6.5 Detailed Inviscid/Viscous Comparison

An inviscid simulation was conducted for each diffusive simulation in order to measure the influence of the viscous, heat, and mass diffusion terms in the reactive Navier-Stokes equations. In figure 6.52 the results are directly compared, and in figures 6.53, and 6.54, inviscid results are shown which correspond to the diffusive results shown in figures 6.38 and 6.39. The largest difference in the results is seen by comparing the mass fractions of an intermediate radical species such as H, O, or OH.

As shown in figure 6.52, there are large differences between the two solutions. The viscous/diffusive terms have largely contributed towards the shape of the jet at the bottom of the the DMR. In the viscous case, the jet has moved farther up stream and has interacted with the Mach stem, forming a triple point. In the viscous case, the jet is farther back and is interacting less with the Mach stem, and a triple point is not clearly seen. Also, looking at the H radical, the influence of diffusion on reacting the partially burnt pockets is observed. Note that with even higher resolution and smaller numerical viscosity, more and more incompletely reacted pockets in the unstable shear layer would be observed. In these inviscid simulations, these partially reacted pockets are predominately combusted due to the chemical mechanism rather than also with diffusion as is the case for the viscous simulation.

In figures 6.53 and 6.54, a slight influence of diffusion is seen in the shear layer for the visualization of  $C_3H_8$ . Differences are also seen in the magnitudes of the pressure and temperature. The maximum temperature of the diffusive simulation is lower and its maximum pressure is higher. Heat diffusion cools the hot gases by mixing them with the cooler cases, most notably at the shear layers, where in the perfectly inviscid solution with no numerical viscosity, there is a discontinuous jump in temperature and velocity.

As was demonstrated in §6.2 the numerical viscosity has dominated the physical viscosity in the 3-level case and is the same order of magnitude in the 4-level case. Therefore, only the sensitivity of the solution to small changes in viscosity can be

deduced. In the 3-level case there is virtually no observable change. In the 4-level case there is only a visible change in the phase (location not size) of the vortices.

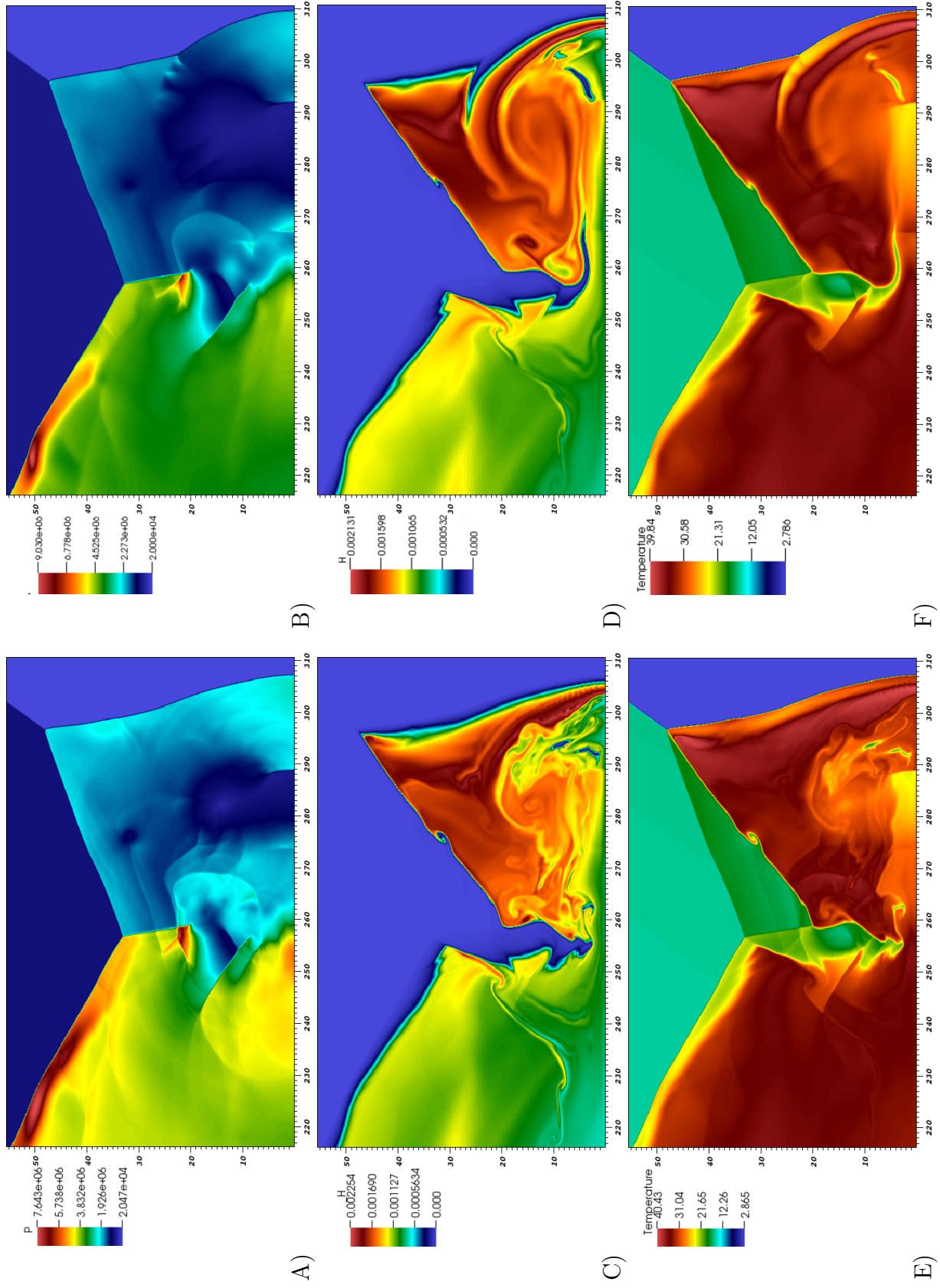


Figure 6.52: Comparing inviscid (left side) and viscous (right side) solutions of the DMR problem at a time of  $t = 36$  nondim.  $= 1.09 \cdot 10^{-6}$  s. Showing pseudo-color results for A) and B) pressure (Pa), C) and D) H radical mass fraction, and E) and F) nondimensional temperature. The units of the x- and y-axes are  $1 \cdot 10^{-3}$  cm.

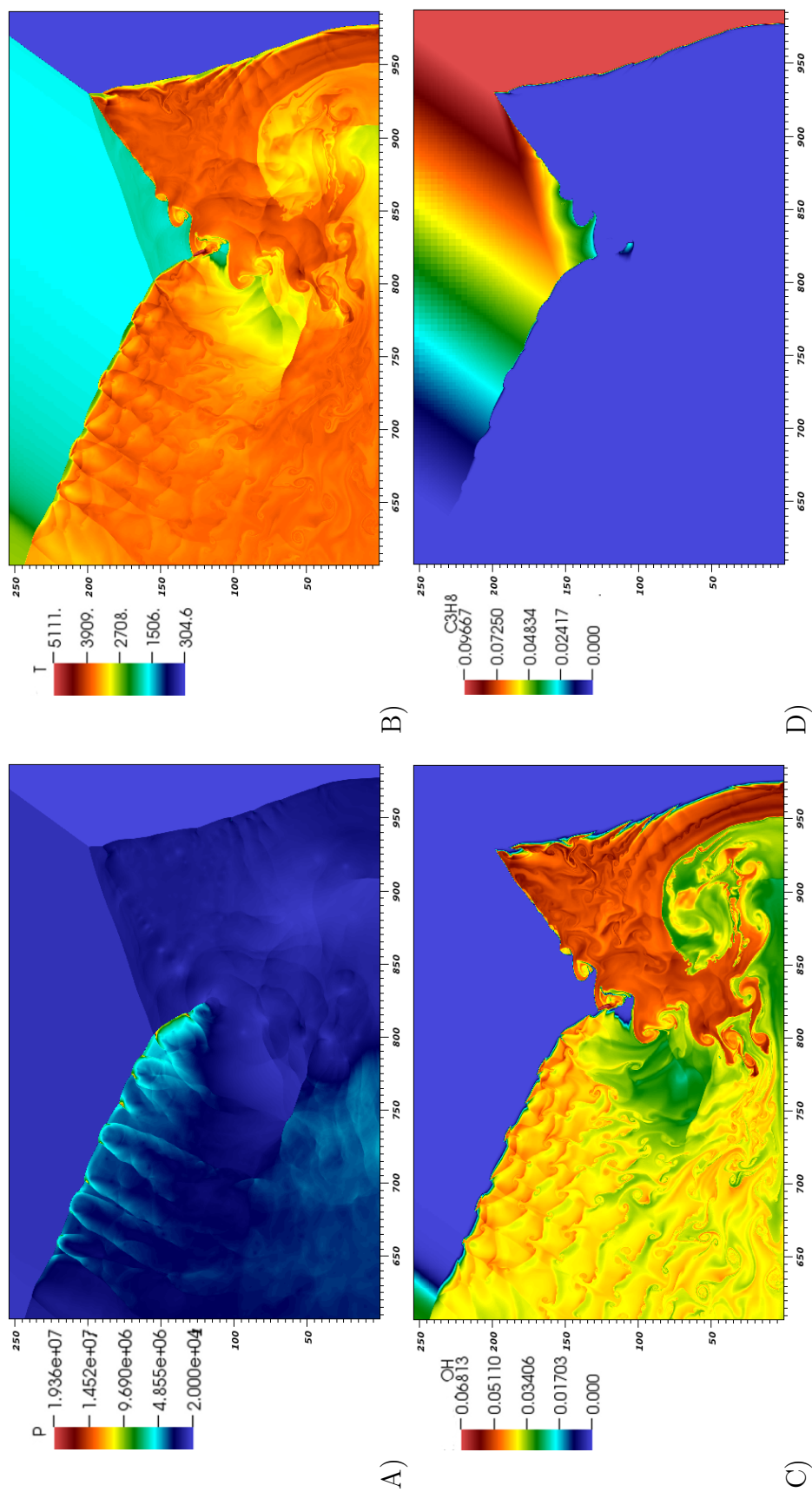


Figure 6.53: Inviscid results of A) pressure (Pa), B) temperature (K), C) O mass fraction, and D)  $C_3H_8$  mass fraction at the same time step,  $t=108$  nondim ( $3.26 \cdot 10^{-6}$  s), with 6-levels as in figure 6.38. The units of the x- and y-axes are  $1 \cdot 10^{-3}$  cm.



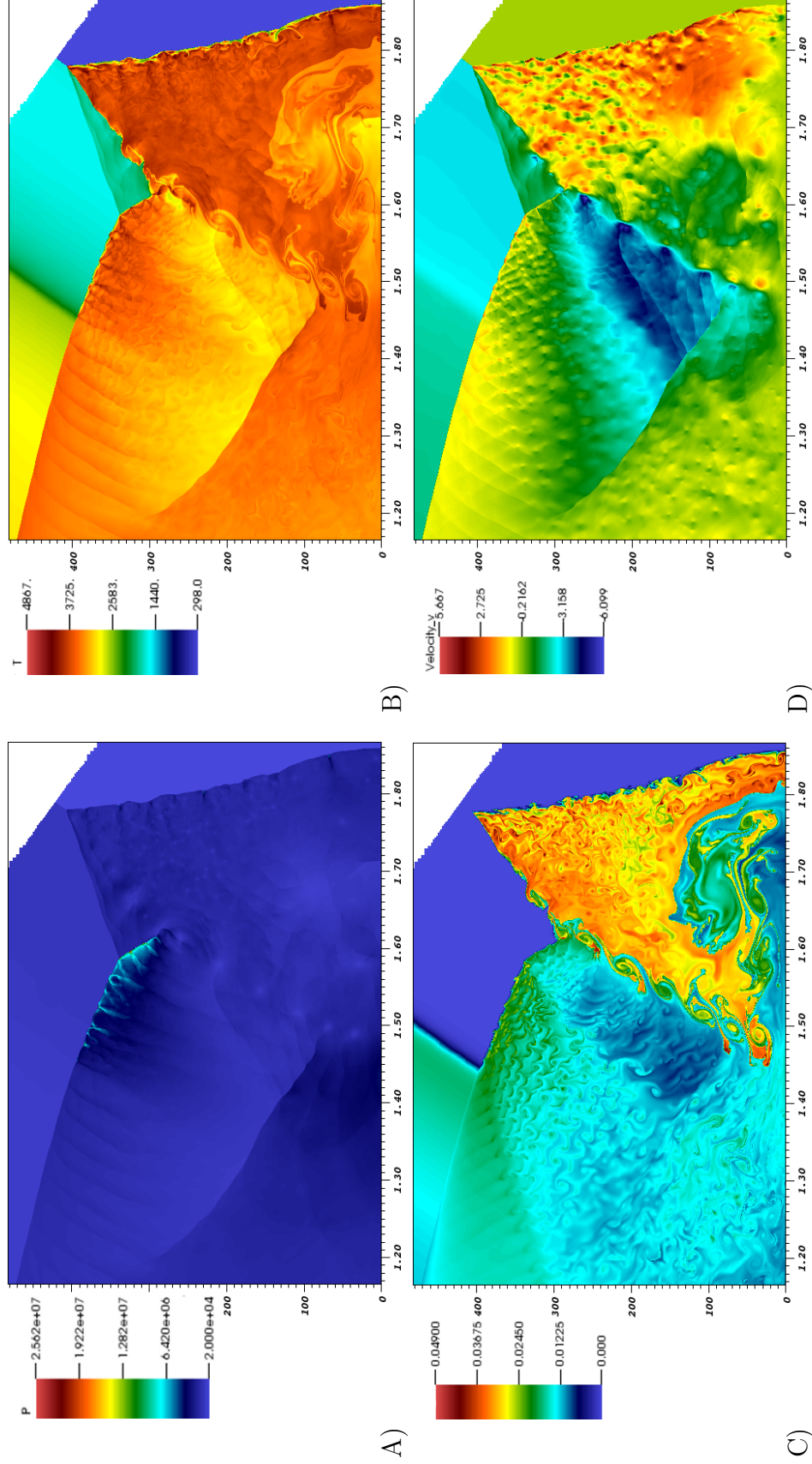


Figure 6.54: Inviscid results of A) pressure (Pa), B) temperature (K), C) O mass fraction, and D) y-component of the nondimensional velocity at the same time step,  $t = 204$  nondim ( $6.15 \cdot 10^{-6}$  s),  $Re = 84,400$ , with 5-levels as in figure 6.39. The units of the x- and y-axes are cm.

### 6.5.1 Product Traces

In the previous section, the viscous and inviscid solutions were compared using pseudo-color plots. These visualizations are useful for comparing qualitatively the difference in the solutions, particularly identifying features of the flow such as shock waves and shear layers. They are also useful for comparing minimum and maximum values of the solution. However, in order to better appreciate a quantitative comparison of solutions, different visualization methods must be employed, such as one-dimensional cuts.

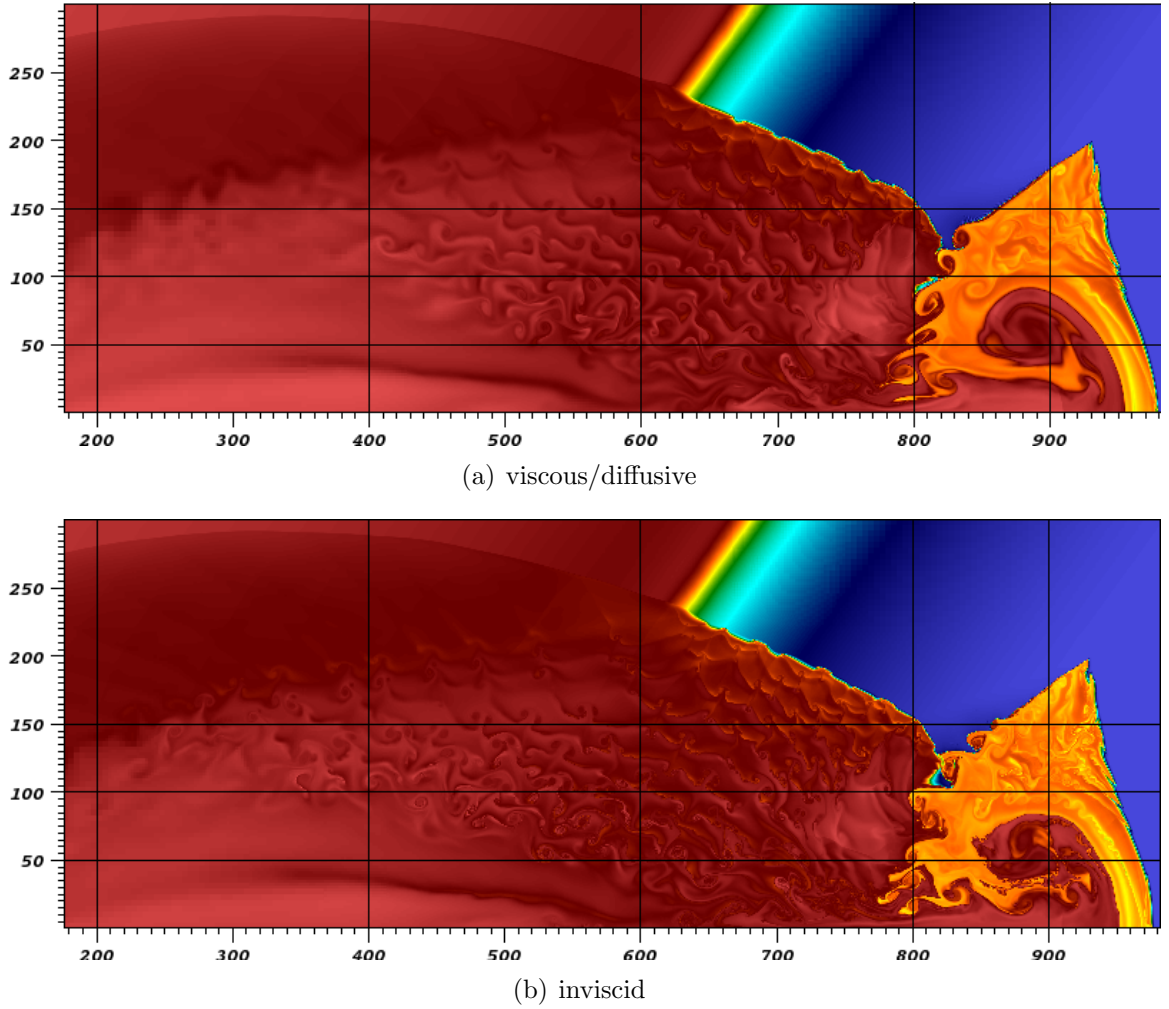


Figure 6.55: Key showing traces used without output from the case shown in figure 6.15 is used.

Shown in figure 6.55 are the viscous and inviscid solutions at the final time step for the highest resolved 6-level case. Also shown is a grid overlaying the solutions. This

grid corresponds to the 1D cuts of the product  $\text{H}_2\text{O}$  mass fraction. The horizontal cuts start at  $y = 0.05$  cm and then  $y = 0.1$  and  $0.15$  cm, as displayed in figures 6.56-6.58. Also used are vertical cuts at  $x = 0.2, 0.4, 0.6, 0.8$ , and  $0.9$  cm, as displayed in figures 6.59-6.63.

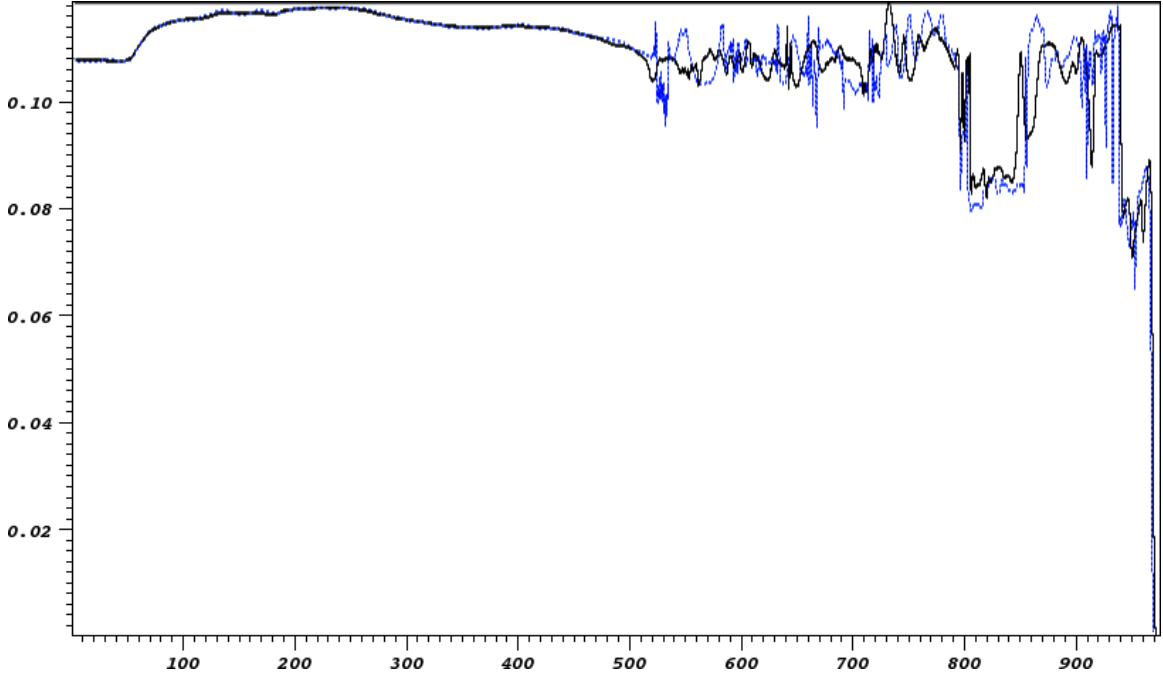


Figure 6.56:  $\text{H}_2\text{O}$  mass fraction traces starting at  $(x,y) = (0,0.05)$  and going to  $(0.975,0.05)$  cm. Solid black is viscous/diffusive and dotted blue is inviscid. Output from the 6-level case shown in figure 6.15 is used.

In these horizontal cuts, a small-scale cell-like pattern is observed by looking at the average wavelength the peaks in the product mass fraction. These oscillations which show an average wavelength are due to the shear layers and transverse shocks which are produced by the triple points on the main reflected shock. Both the inviscid and viscous solutions show this pattern, however, the inviscid solution shows lower valleys and high peaks, and also shows some higher frequency oscillations. These differences in the inviscid solution are dependent on the numerical viscosity, which is dependent on the resolution of the grid. The amplitude of these patterns will increase and more high frequency oscillations will increase as the grid is made finer. These plots also shown the change in the product  $\text{H}_2\text{O}$  due to the shear layers on the Mach stem, the main shear layer from the primary triple point, and the transverse shock. In figure 6.63, there also a huge dip in the mass fraction as the cut passes through the part of the flow which has only passed through the incident shock.

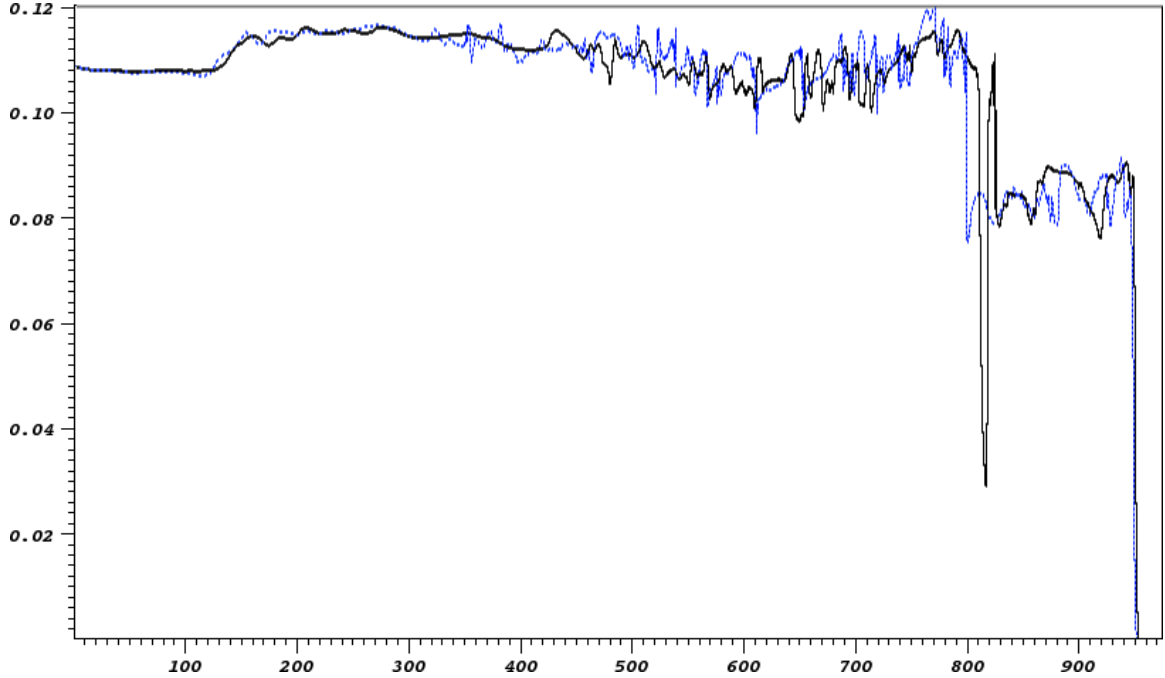


Figure 6.57:  $\text{H}_2\text{O}$  mass fraction traces starting at  $(x,y) = (0,0.1)$  and going to  $(0.975,0.1)$  cm. Solid black is viscous/diffusive and dotted blue is inviscid. Output from the 6-level case shown in figure 6.15 is used.

In the vertical cuts the same general conclusions are made. In the left most cut shown in figure 6.59, the viscous and inviscid solutions are very similar. In this region physical and numerical dissipation has smoothed out the vortices. This is most likely due to numerical viscosity because less refinement levels were purposefully used here to speed the computation. In the next cut, shown in figure 6.60, more resolution is used and also the local Reynolds number of the flow is higher, therefore the shear layers are less dissipated. The inviscid solution is oscillating at a slightly higher frequency than the viscous solution. In the next cut, figure 6.61, at  $x = 0.6$  cm, the frequencies of the solutions are much closer. However; then looking at the next cut at  $x=0.8$  cm, , figure 6.62, the inviscid solution is seen to have many more high frequency oscillations. This is now because the cut is going through the unstable main shear layering coming from the primary triple point. In the last vertical cut, figure 6.63, the jet is passed through, for which the solutions are very different, but then after passing through the jet and entering the region behind the mach stem which does not contain the shear layer, the solutions are again similar.

Regarding information gained from the previous traces, there is motivation to attempt to measure a characteristic small-scale from the triple points and shear layers

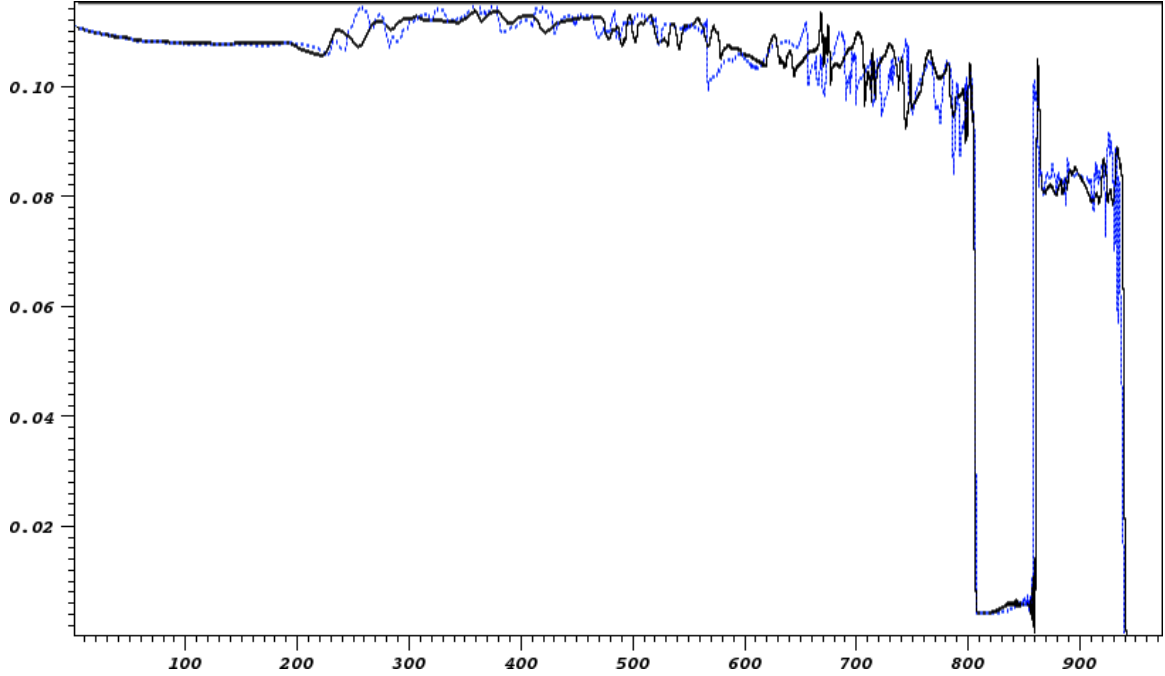


Figure 6.58:  $\text{H}_2\text{O}$  mass fraction traces starting at  $(x,y) = (0,0.15)$  and going to  $(0.975,0.15)$  cm. Solid black is viscous/diffusive and dotted blue is inviscid. Output from the 6-level case shown in figure 6.15 is used.

occurring on the main reflected shock wave. In figure 6.64, shown is a cut that is reasonably parallel to the triple points. Looking only at the trace from  $x$  (on the trace plot) = 75 to 175, a pattern that repeats three times is observed for both solutions, while being slightly different for each. The wavelength of this oscillation is approximately 0.03 cm ( $3 \cdot 10^{-4}$  m).

In figure 6.66, shown is a cut that is reasonably perpendicular to the triple points. In this case it is harder to identify a pattern with just the eye. Also the inviscid and viscous solutions are very out of phase, and many high frequency oscillations in the viscous solution have been damped out, appear in the inviscid solution. Using “double peak” pattern for the viscous solution a wavelength of approximately 0.02 cm ( $3 \cdot 10^{-4}$  m) is observed.

Now in figure 6.68, product traces are employed on the final time step of the 5-level simulation results for the inviscid and viscous WENO-CD solution and also the second-order accurate MUSCL method. For the trace going through the triple point shear layers in figure 6.69, the WENO-CD solution is shown and in figure 6.70. As expected the viscous and inviscid WENO-CD solutions are similar. Also, one can compare these to a similar trace at an earlier time using the 6-level solution

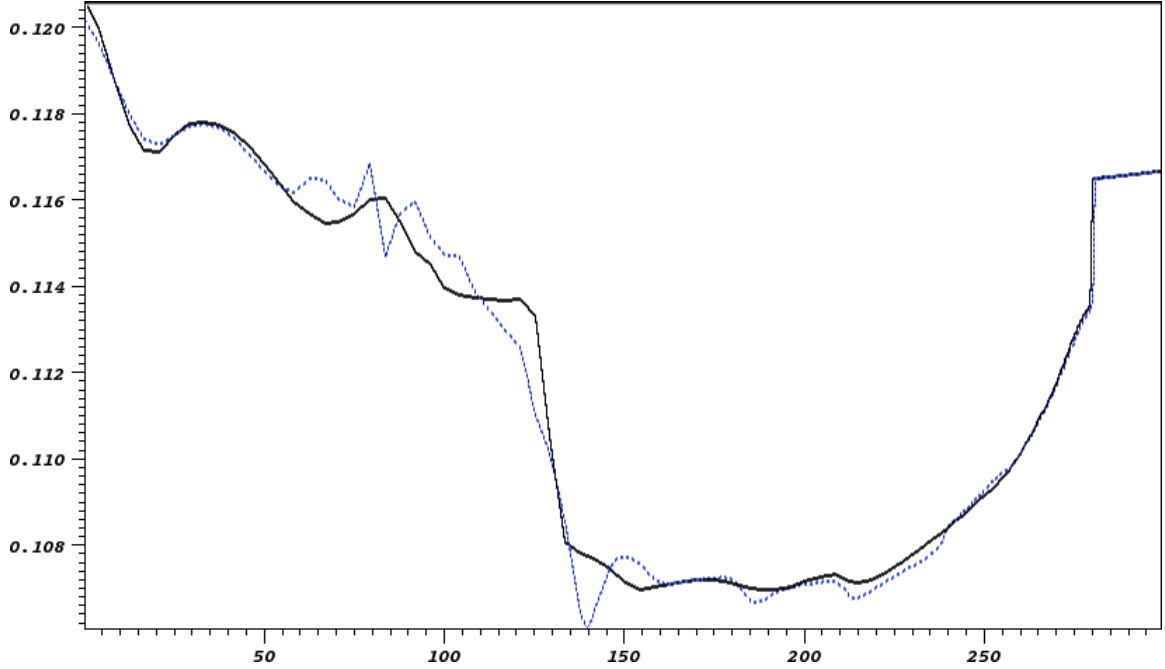


Figure 6.59:  $\text{H}_2\text{O}$  mass fraction traces starting at  $(x,y) = (0.2,0)$  and going to  $(0.2,0.32)$  cm. Solid black is viscous/diffusive and dotted blue is inviscid. Output from the 6-level case shown in figure 6.15 is used.

(figure 6.61). No particular patterns for this 5-level case are observed, as is observed in the 6-level solution. This is most likely due to the larger Reynolds number, due to the time step being approximately 2 times later. The numerical and physical viscosity has had more time to create instabilities and increase the chaos of the flow. However, still with this 5-level result, using the distance between the single large peaks in the mass fraction, an average wavelength can be determined, which is approximately 0.025 cm ( $2.5 \cdot 10^{-4}$  m), which is the same scale which was measured in the 6-Level simulation at an earlier time step.

Now, looking at figure 6.70, one sees a very different result for the MUSCL method. It captures the mean properties of the mass fraction, however, almost all of the small-scale oscillations have been damped out by numerical viscosity.

Now in figures 6.71 and 6.72, a product trace through the shear layers created by triple points on the Mach stem is shown for the 3 solutions. The inviscid and viscid WENO-CD solutions are very different. This trace touches the right-most portion of the large jet and then travels through shear layers created by triple points on the Mach stem and then gets closer and closer to the triple points (due to the fact the the Mach stem is curved). The portion of the trace which travels through the triple point

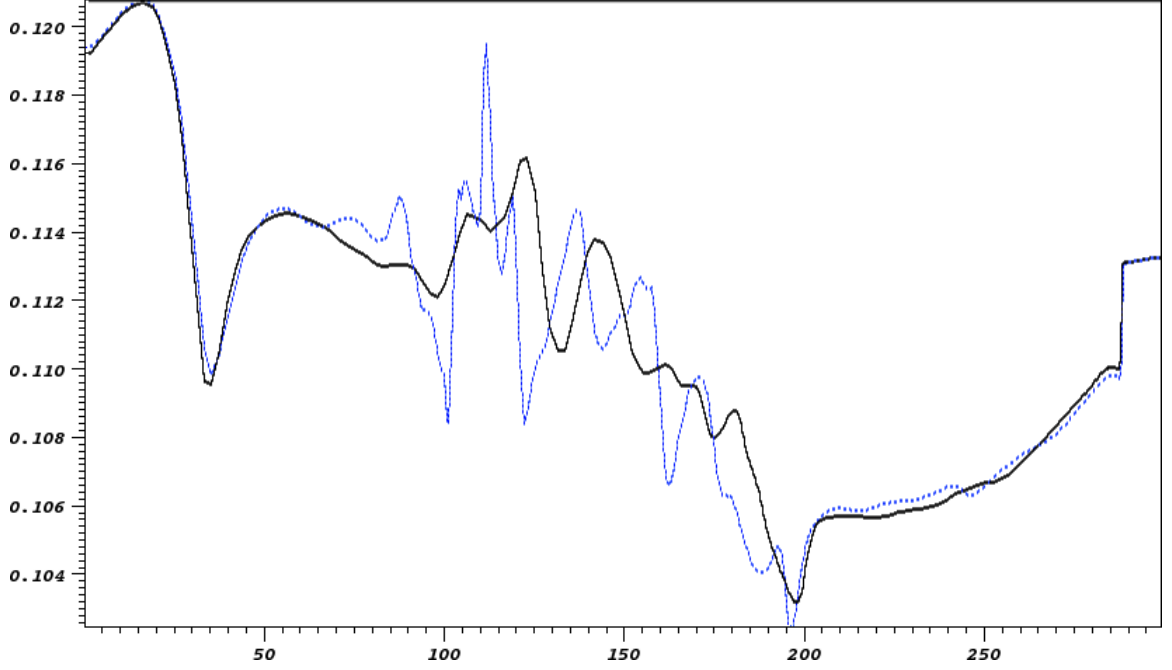


Figure 6.60:  $\text{H}_2\text{O}$  mass fraction traces starting at  $(x,y) = (0.4,0)$  and going to  $(0.4,0.32)$  cm. Solid black is viscous/diffusive and dotted blue is inviscid. Output from the 6-level case shown in figure 6.15 is used.

shear layers is different due to the different positions and times of creation of the triple points for the inviscid and viscous flows. Also, compared again is the inviscid MUSCL solution, which has overwhelmed the solution with numerical viscosity.

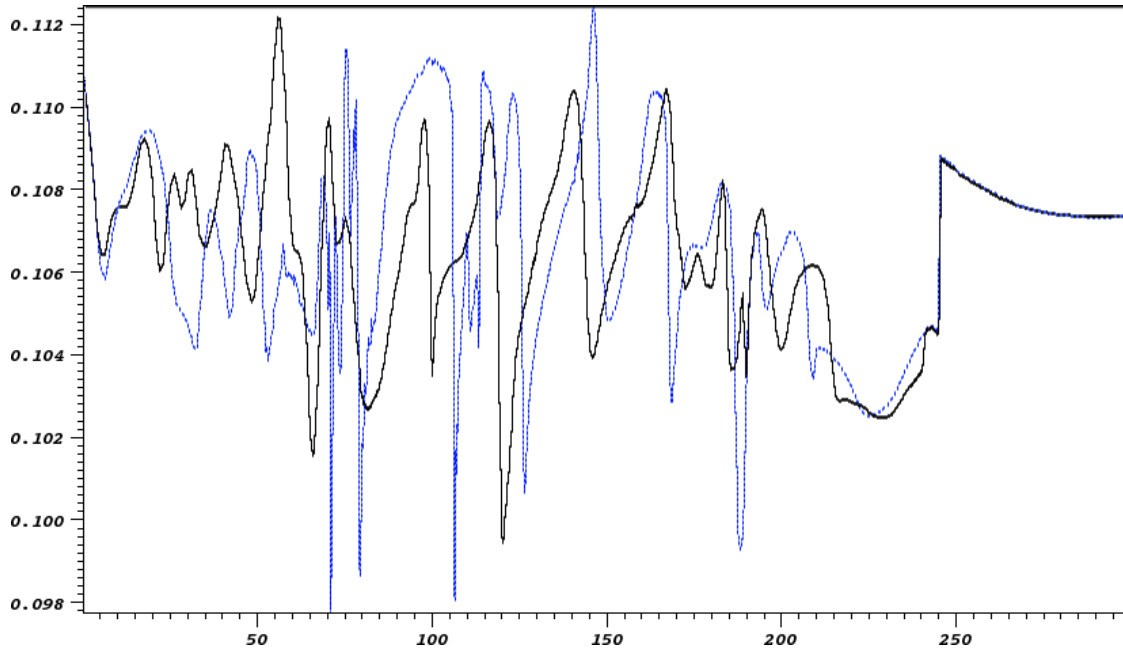


Figure 6.61:  $\text{H}_2\text{O}$  mass fraction traces starting at  $(x,y) = (0.6,0)$  and going to  $(0.6,0.32)$  cm. Solid black is viscous/diffusive and dotted blue is inviscid. Output from the 6-level case shown in figure 6.15 is used.

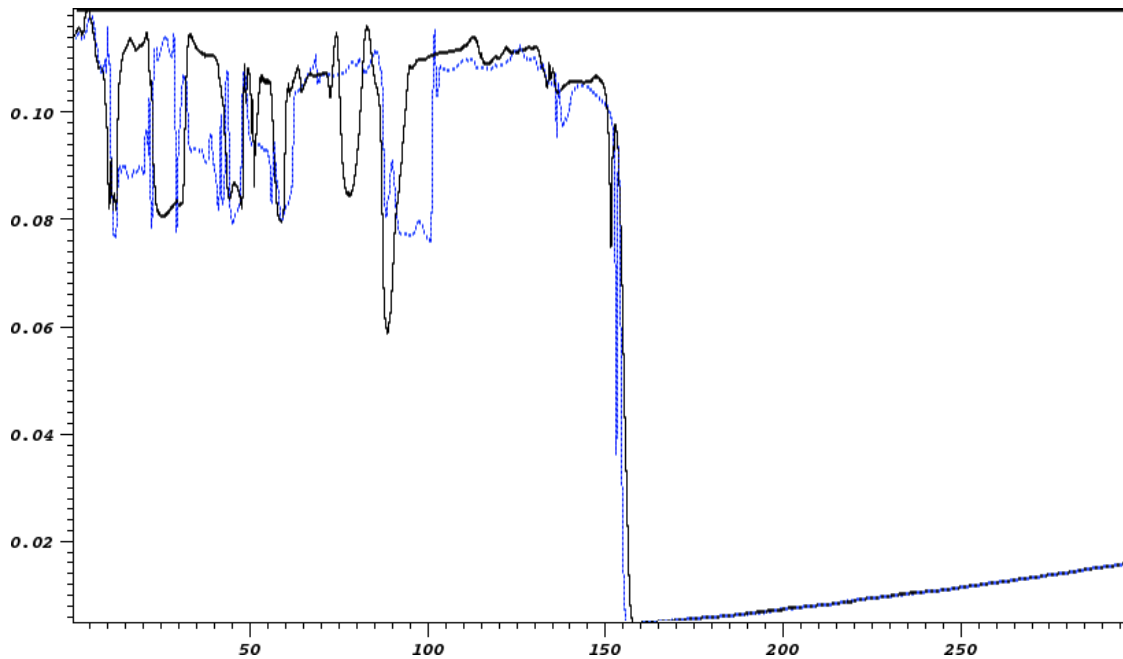


Figure 6.62:  $\text{H}_2\text{O}$  mass fraction traces starting at  $(x,y) = (0.8,0)$  and going to  $(0.8,0.32)$  cm. Solid black is viscous/diffusive and dotted blue is inviscid. Output from the 6-level case shown in figure 6.15 is used.



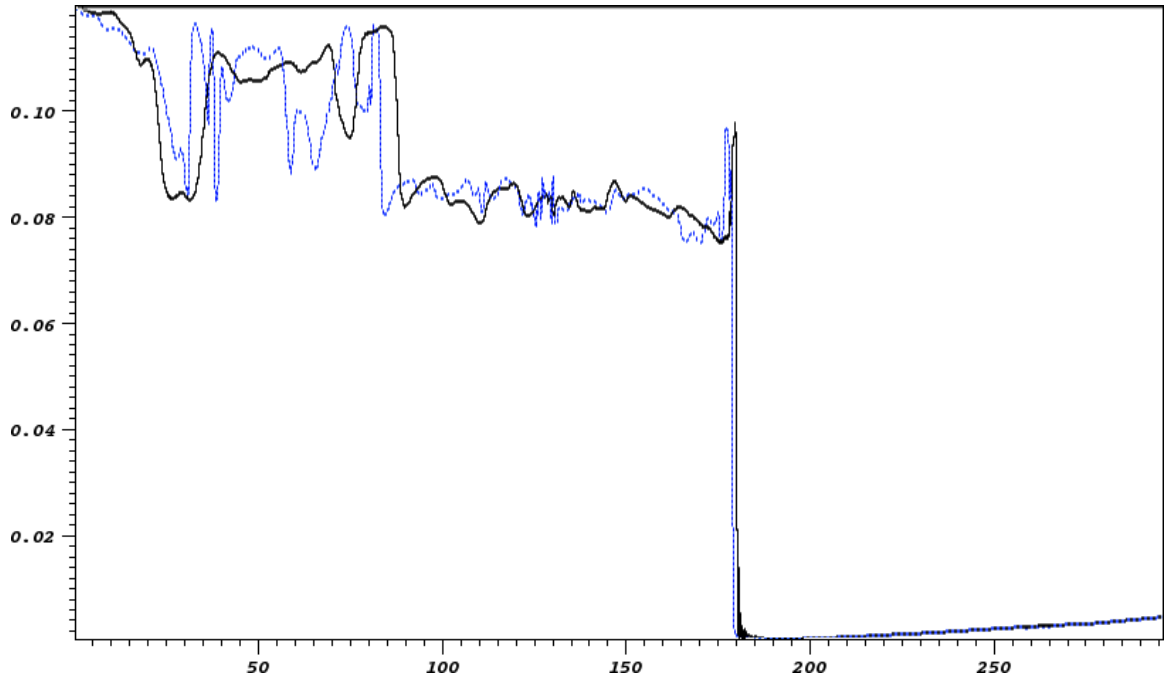


Figure 6.63:  $\text{H}_2\text{O}$  mass fraction traces starting at  $(x,y) = (0.9,0)$  and going to  $(0.9,0.32)$  cm. Solid black is viscous/diffusive and dotted blue is inviscid. Output from the 6-level case shown in figure 6.15 is used.

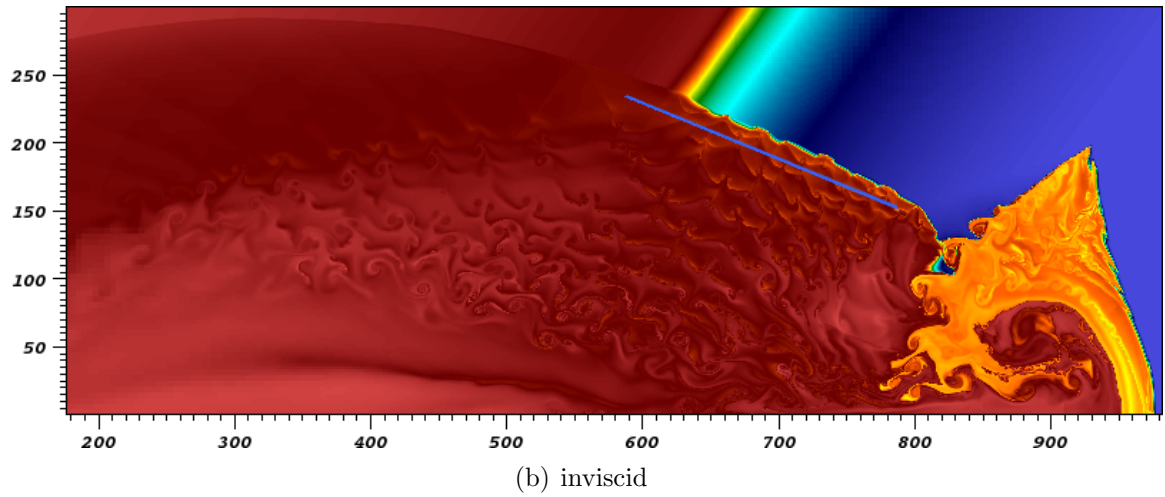
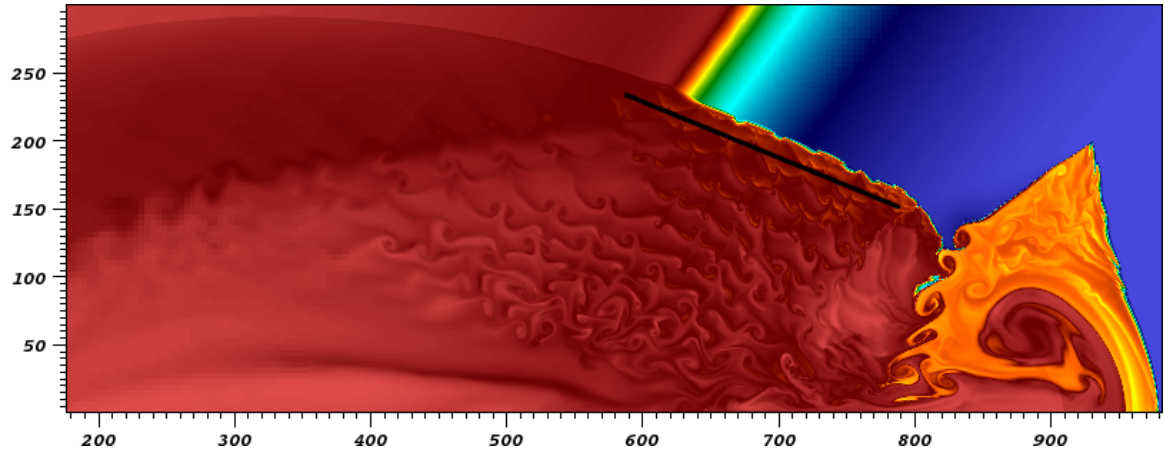


Figure 6.64:  $\text{H}_2\text{O}$  mass fraction traces starting at  $(x,y) = (0.58683, 0.232936)$  and going to  $(0.789084, 0.15026)$  cm. Output from the 6-level case shown in figure 6.15 is used.

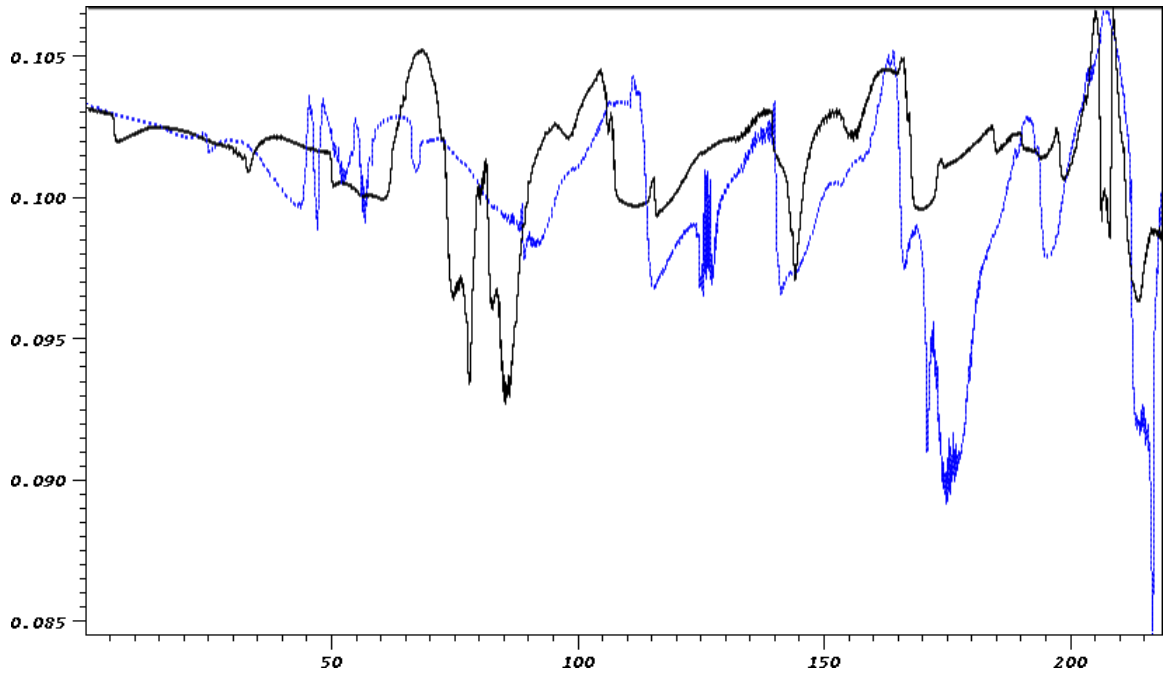
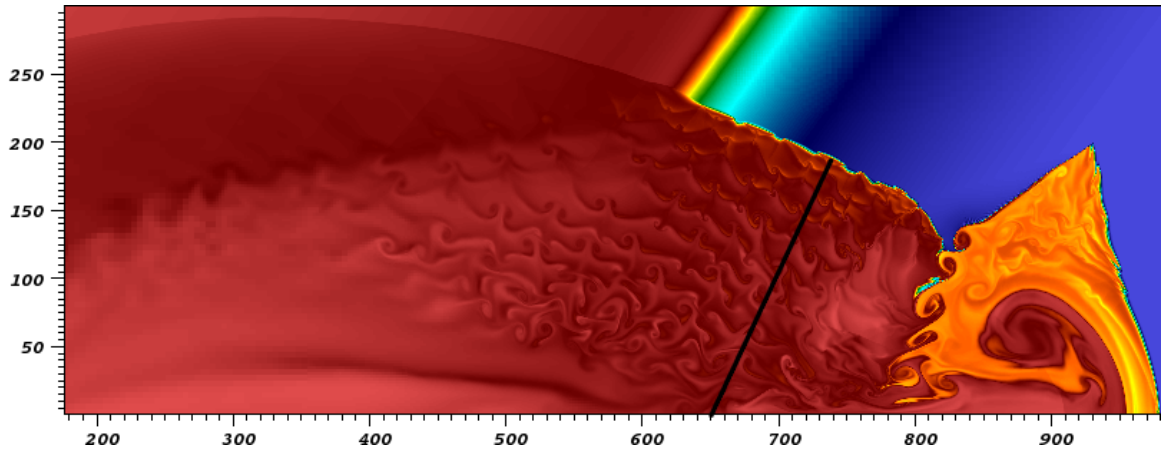
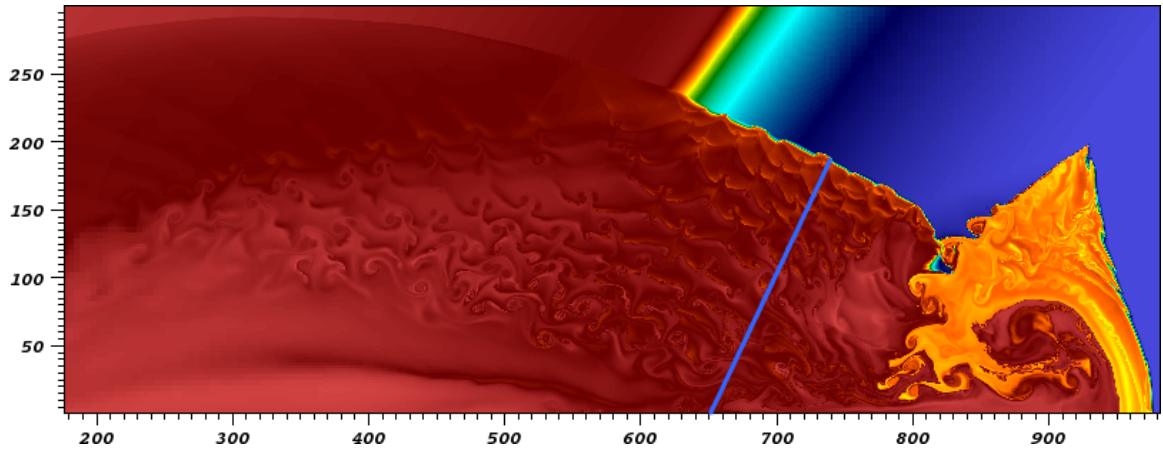


Figure 6.65:  $\text{H}_2\text{O}$  mass fraction traces starting at  $(x,y) = (0.58683, 0.232936)$  and going to  $(0.789084, 0.15026)$  cm. Solid black is viscous/diffusive and dotted blue is inviscid. Output from the 6-level case shown in figure 6.15 is used.



(a) viscous/diffusive



(b) inviscid

Figure 6.66:  $\text{H}_2\text{O}$  mass fraction traces starting at  $(x,y) = (0.73852, 0.18615)$  and going to  $(0.651474, 0.288406)$  cm. Output from the 6-level case shown in figure 6.15 is used.

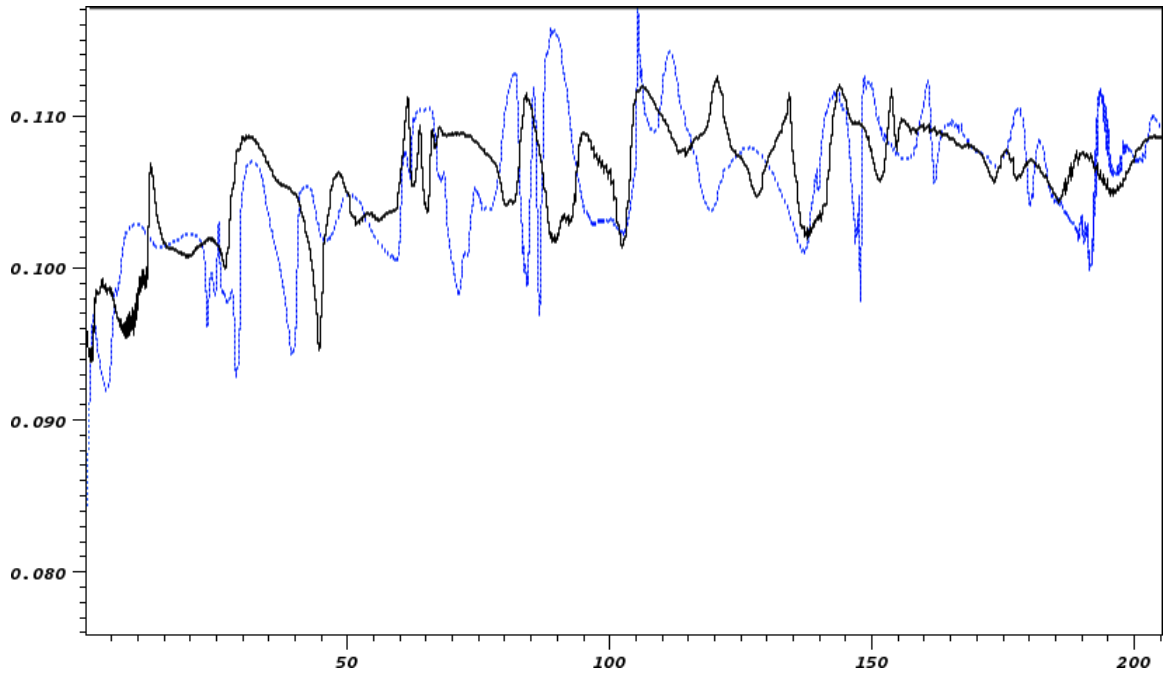
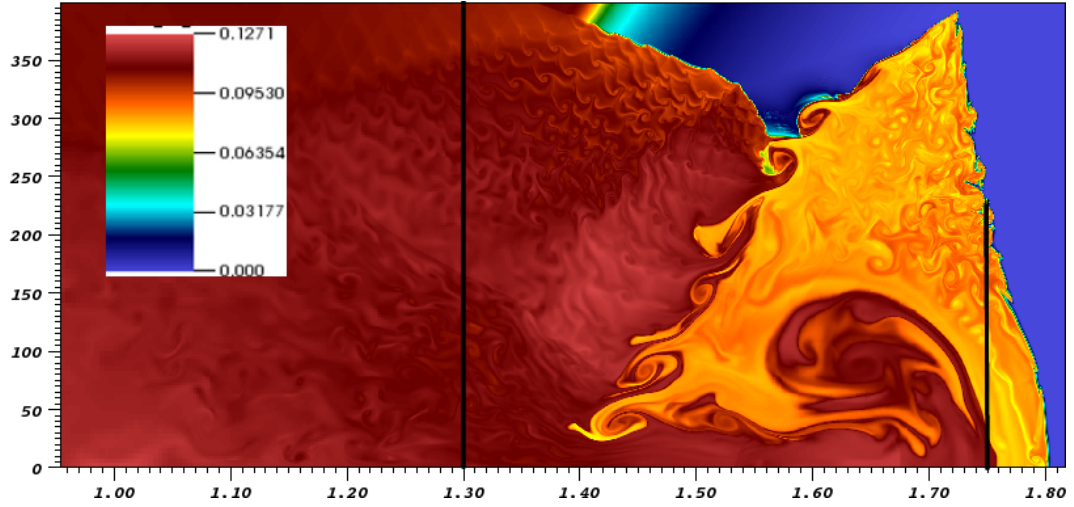
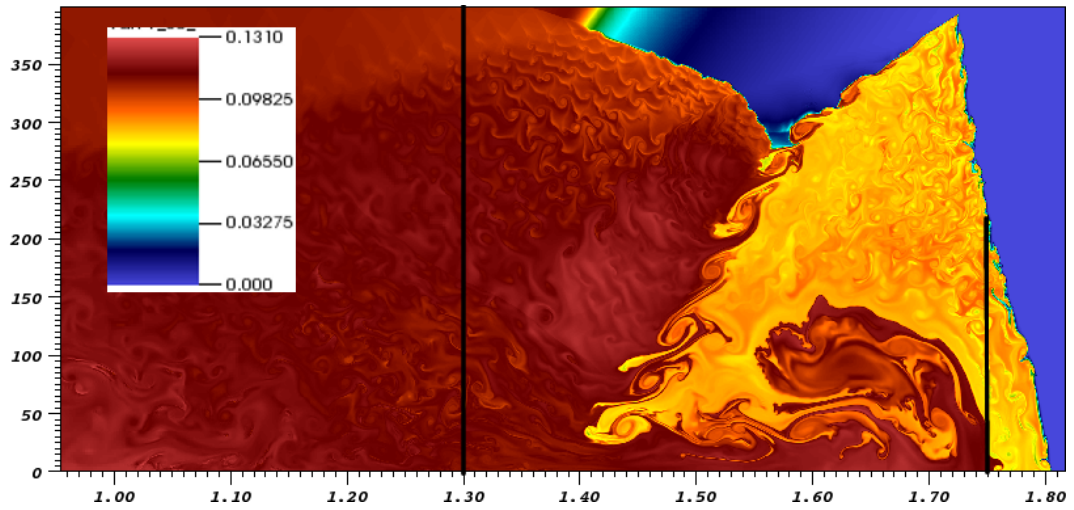


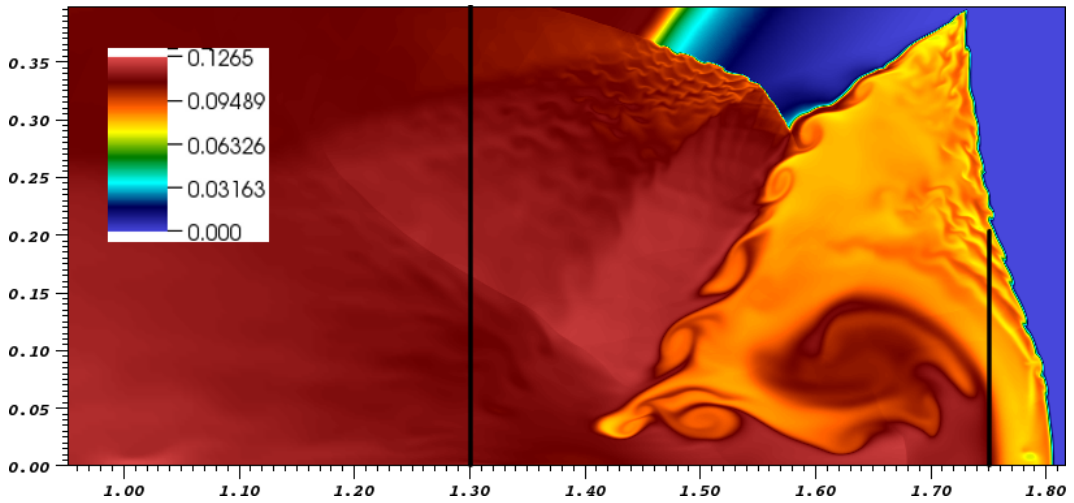
Figure 6.67:  $\text{H}_2\text{O}$  mass fraction traces starting at  $(x,y) = (0.73852, 0.18615)$  and going to  $(0.651474, 0.288406)$  cm. Solid black is viscous/diffusive and dotted blue is inviscid. Output from the 6-level case shown in figure 6.15 is used.



(a) viscous/diffusive



(b) inviscid



(c) inviscid MUSCL

Figure 6.68: Key showing traces used with output from the 5-level case shown in figure 6.18

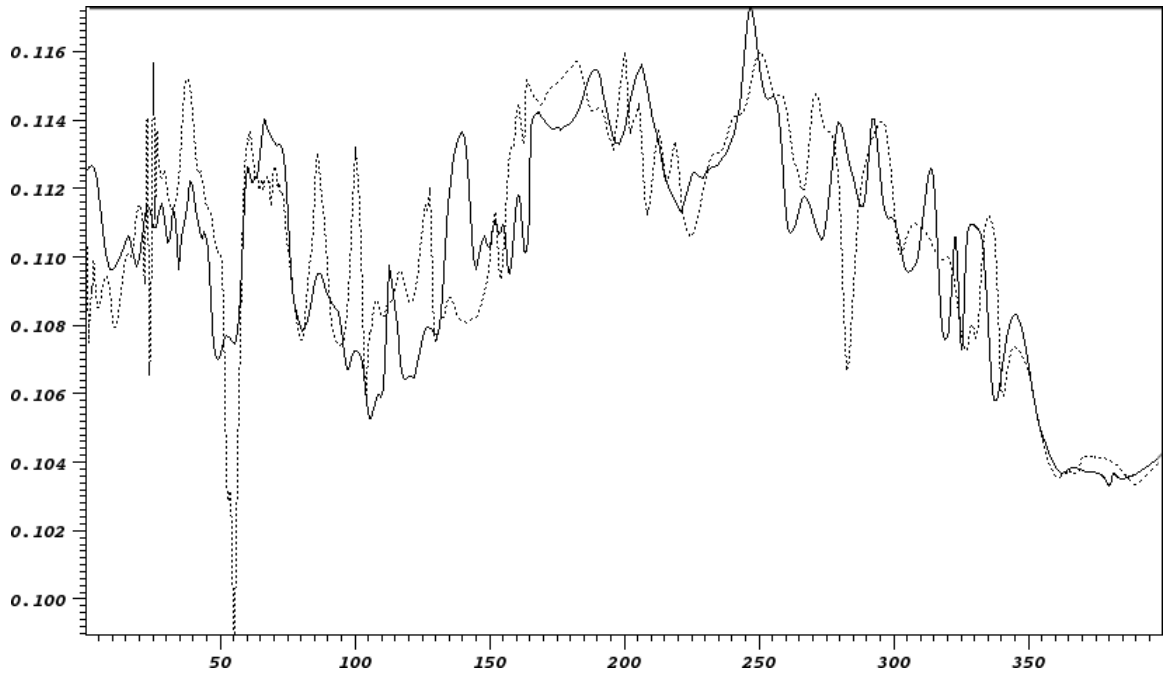


Figure 6.69:  $\text{H}_2\text{O}$  mass fraction traces starting at  $(x,y) = (1.3,0)$  and going to  $(1.3,0.4)$  cm. Solid is viscous/diffusive and dotted is inviscid. Output from the 5-level case shown in figure 6.18 is used.

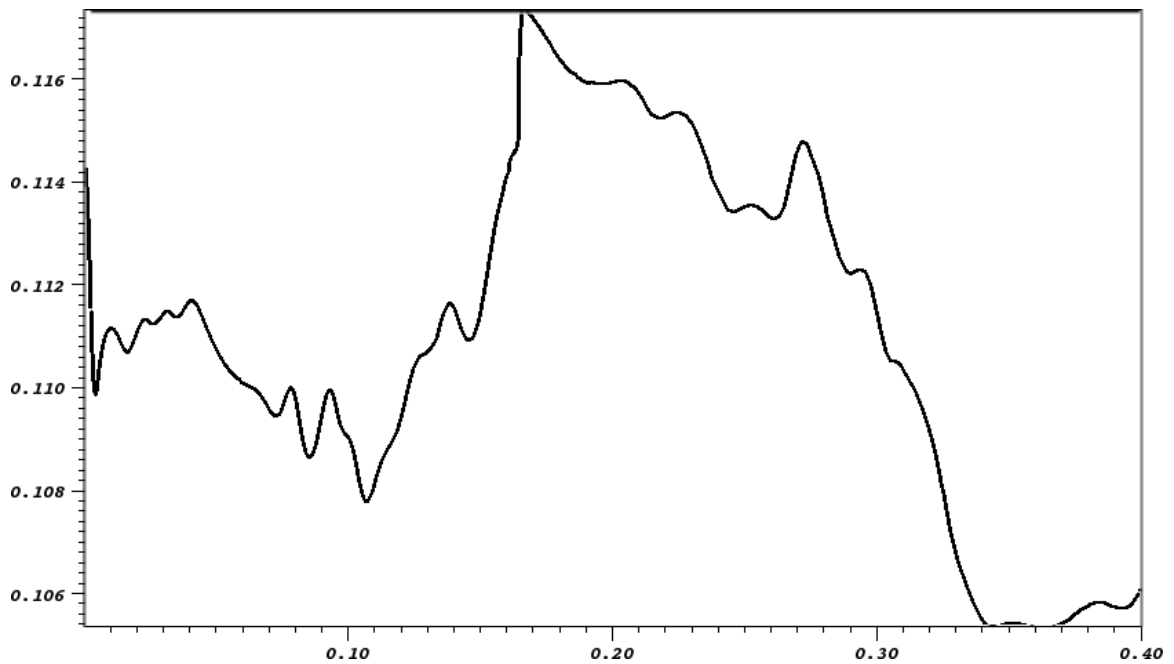


Figure 6.70:  $\text{H}_2\text{O}$  mass fraction traces starting at  $(x,y) = (1.3,0)$  and going to  $(1.3,0.4)$  cm. Solid black MUSCL with 5-levels.

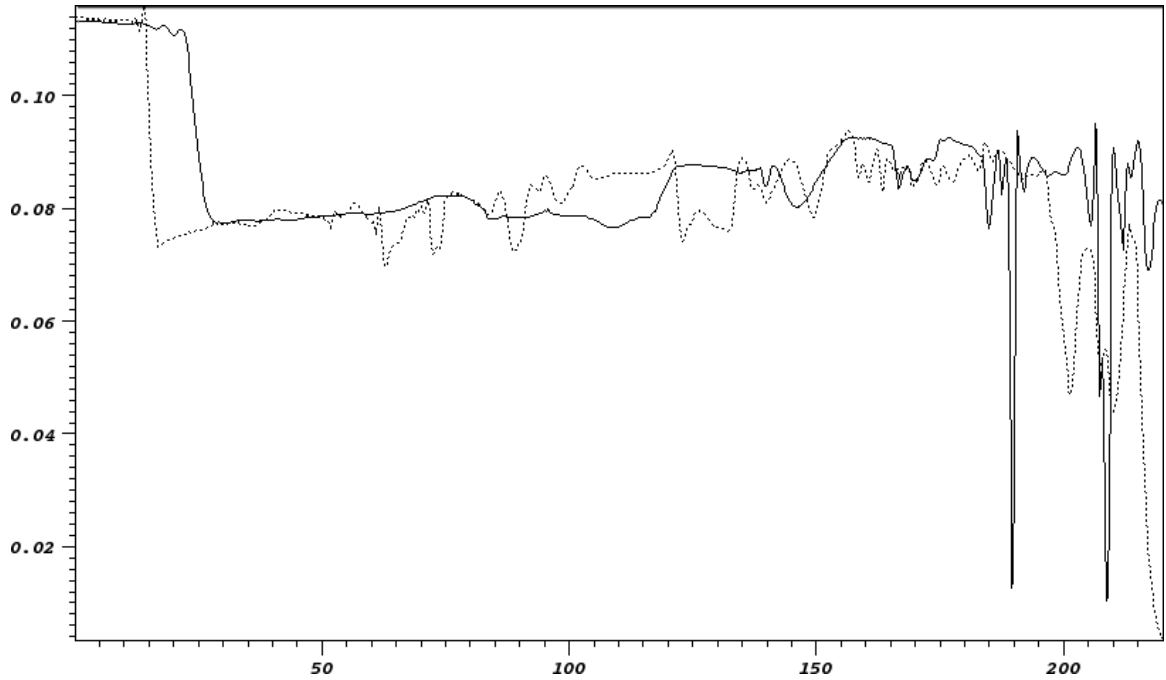


Figure 6.71:  $\text{H}_2\text{O}$  mass fraction traces starting at  $(x,y) = (1.3,0)$  and going to  $(1.75,0.22)$  cm. Solid is viscous/diffusive and dotted is inviscid. Output from the 5-level case shown in figure 6.18 is used.

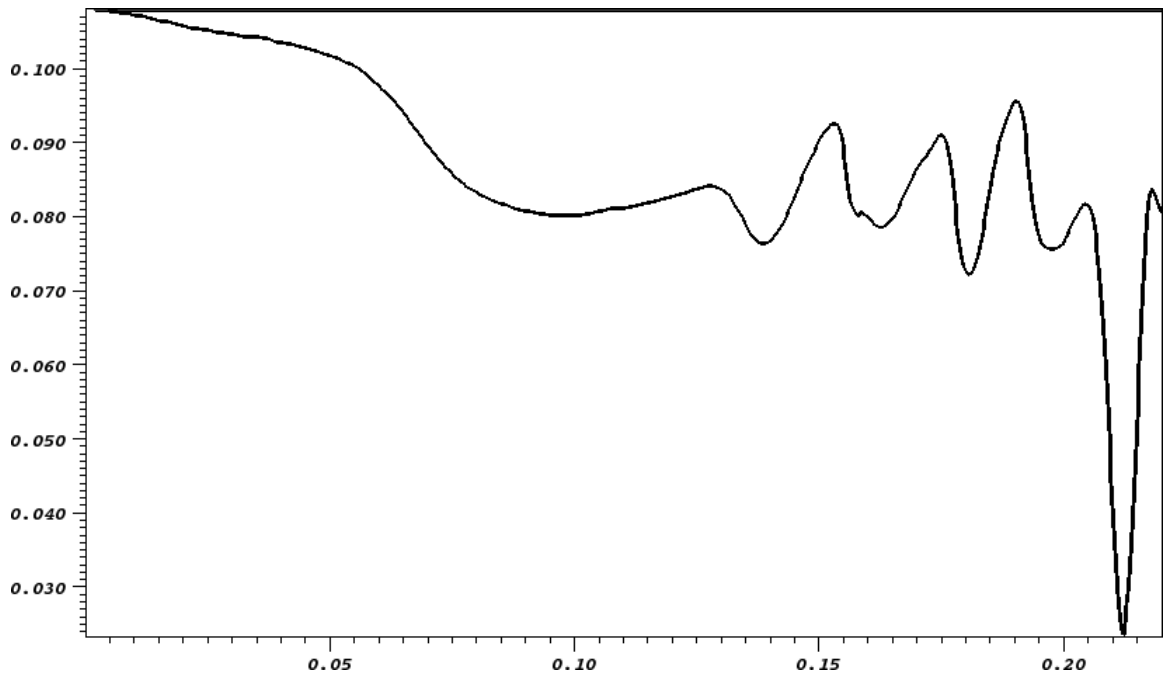


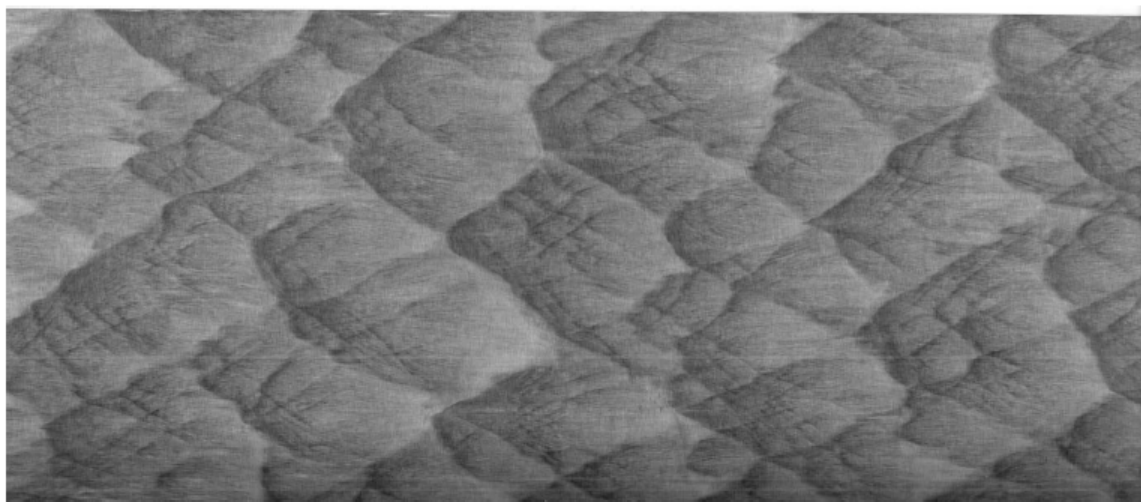
Figure 6.72:  $\text{H}_2\text{O}$  mass fraction traces starting at  $(x,y) = (1.75,0)$  and going to  $(1.75,0.22)$  cm for MUSCL with 5-levels.



## 6.6 Soot Foil Length Scales

In experiments conducted by Austin (6), this exact propane mixture ( $\text{C}_3\text{H}_8\text{-5O}_2\text{-9N}_2$  at ambient temperature and 20 kPa) was detonated and visualized using a rectangular narrow tube (150x18 mm cross section) where one dimension was smaller than the dominate cell size. One must note that the cellular structure of a detonation wave is three-dimensional and dependent on the confining geometry due to shock reflections off the solid structure's walls. In a rectangular channel as used in Austin's experiments, the propagation direction of transverse waves is ideally in two orthogonal planes orthogonal to one another. In round and exactly square tubes the three-dimensional complexity of the front makes visualization difficult because one is integrating through the flow field. In these experiments, the instability was suppressed in the plane where the tube dimension is on the order of the detonation cell width. These narrow channel detonations are different from unsuppressed detonations, where in particular, the track angle and the calculated transverse wave strength is larger.

Using soot foils, Austin found a range of length scales of cellular instability from the dominant cell width of  $45 \pm 8$  mm to the smaller observable scales of 10 mm, as shown in figure 6.73.



Shot 47:  $\text{C}_3\text{H}_8\text{-5O}_2\text{-9N}_2$

Figure 6.73: Soot foil in propane detonation mixture,  $\text{C}_3\text{H}_8\text{-5O}_2\text{-9N}_2$  20 kPa, showing the range of cell sizes found in experiment with a narrow tube with a 15x1.8 cm cross section. Reprinted with permission from Austin (6).

### 6.6.1 Small-Scale DMR Comparisons

On the soot foil, scales smaller than approximately 1 mm are unresolvable. In §6.5.1 for the DMR simulations, the scale which was measured in the product traces through the shear layers of the reflected wave was an average value of 0.25 mm, which is unfortunately below this scale. However, the triple points found on the unstable incident and Mach stem shocks also form length scales. By measuring the average distance between the triple points on these waves, and also by looking at the pressure peaks in a trace just behind these waves, a length scale can be measured. For the 3-level DMR simulation, the last time step was used for this purpose. The traces used on the incident and Mach stem waves are shown in figures 6.74 and 6.76. By dividing the length of this trace by the number of triple points, a scale of 0.55 mm is found on the incident shock, and a scale of 0.3 mm is found on the Mach stem. Also, a slightly less crude method is to look at the actual major pressure peaks along these waves, as is shown in figures 6.74 and 6.76. Dividing the length by the number of peaks in this case yields a length scale of 1.1 mm on the incident shock, and a scale of 0.5 mm on the Mach stem.

The intermittent small cell scales shown on the soot foil are of the order of 1 cm. Even the scales measured on the unstable incident waves at these early times of instability in the DMR simulations are 10 times smaller than this. It is presumed that a larger domain and longer in time simulation could show this 1 cm scale. There is another obvious scale shown in the soot foil, the average dominate cell size of 4.5 cm. The domain used in the DMR simulation is unfortunately not large enough to show this scale.

figure 6.78B), reprinted from Austin (6), shows a plot of the normalized cell width as a function of the overdrive. From this result, we can conclude that because the scales are of order of 1 mm, which is much smaller than the dominant cell size of 4.5 cm, the detonation must be highly overdriven at the end of the 3-level DMR simulation. When a larger domain is used, the detonation eventually becomes underdriven and the triple point spacing increases to a size which is observable in experiment.

Shown below in figure 6.79 is a schlieren visualization of this detonation mixture. The dominate cell size is clearly seen. Also observed is the prospect of comparing the simulated DMR result to one of these many Mach stem/incident shock interactions. Albeit, formed from a different process, the DMR is physically similar to the triple point collisions in a self-propagating unsteady multi-dimensional detonation. Shown in figure 6.80 is a particular schlieren image that will be used in a comparison. The

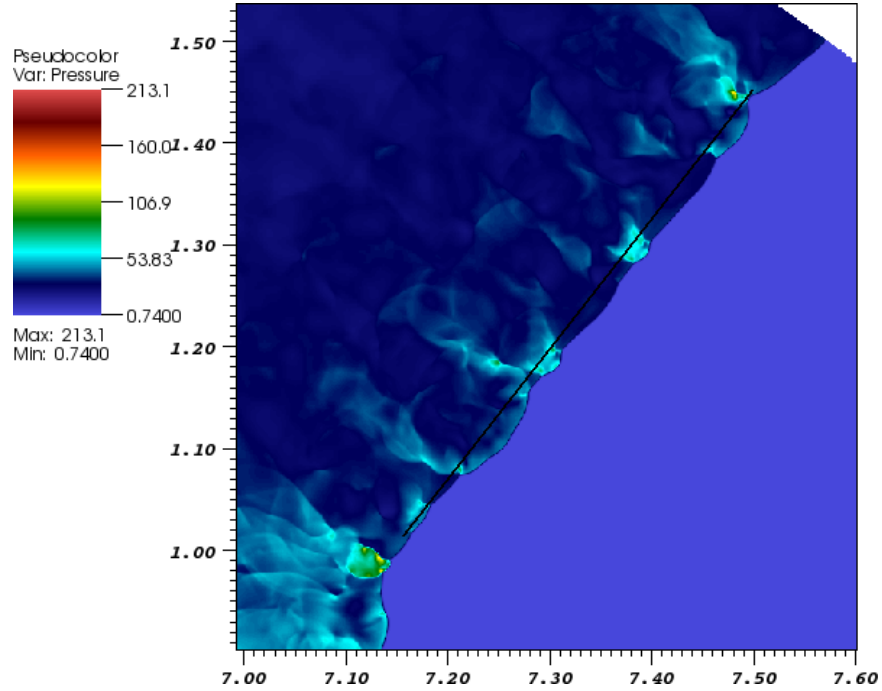


Figure 6.74: Pseudo-color pressure plot at  $t=2.39 \cdot 10^{-5}$  seconds showing the trace used to estimate a small-scale cell size for the simulated incident wave.

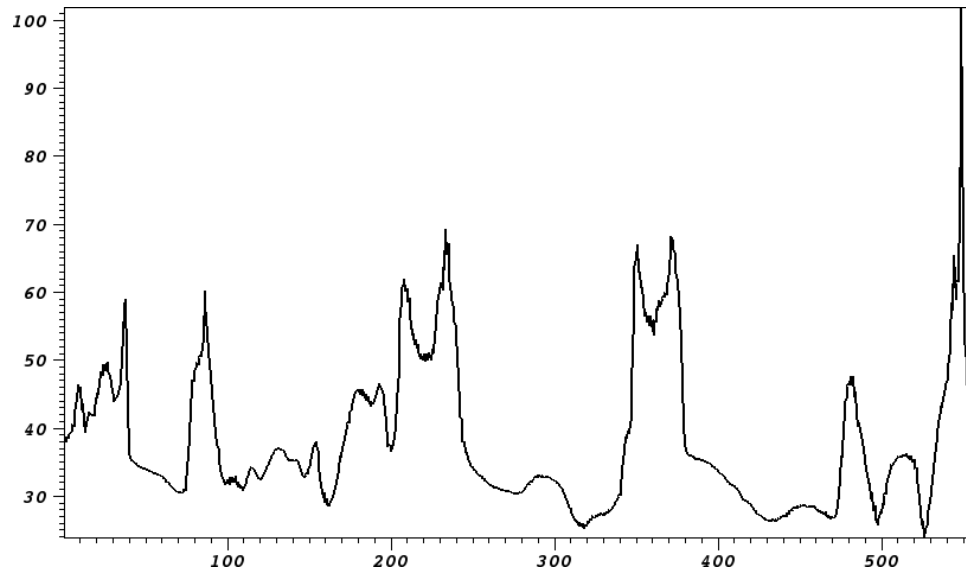


Figure 6.75: Pressure trace through the incident wave as shown in figure 6.74.

exact region to be compared is boxed out and shown with a zoomed in view in figure 6.81a).

The first simulation comparison, figure 6.81b), shows the reflection of the incident

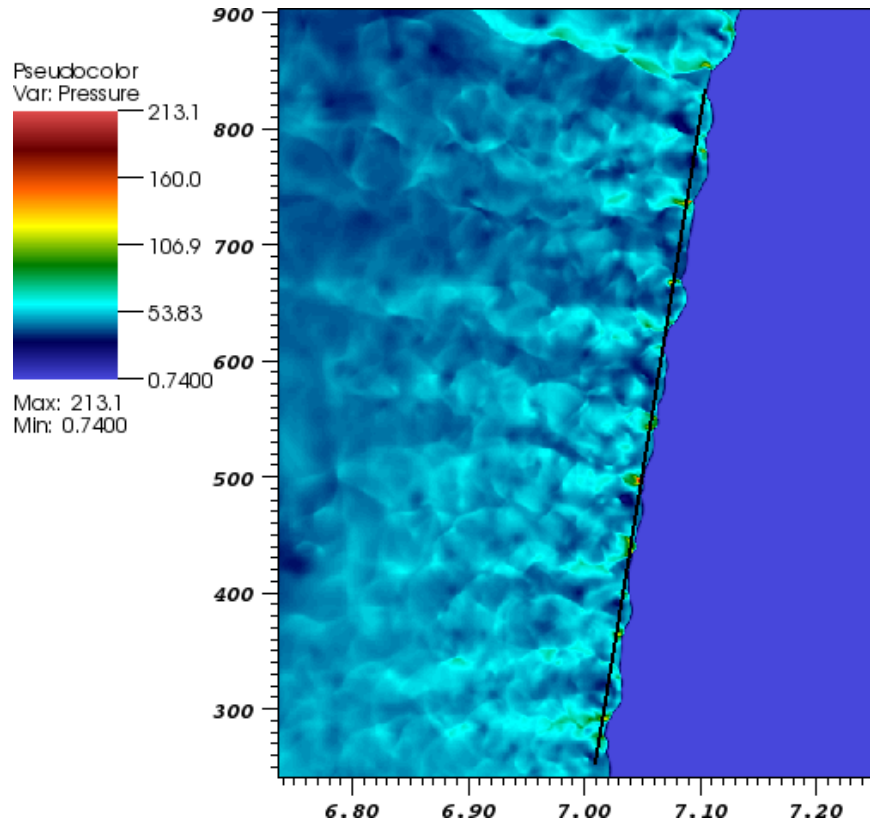


Figure 6.76: Pseudo-color pressure plot at  $t=2.39 \cdot 10^{-5}$  seconds showing the trace used to estimate a small-scale cell size for the simulated “Mach stem” wave.

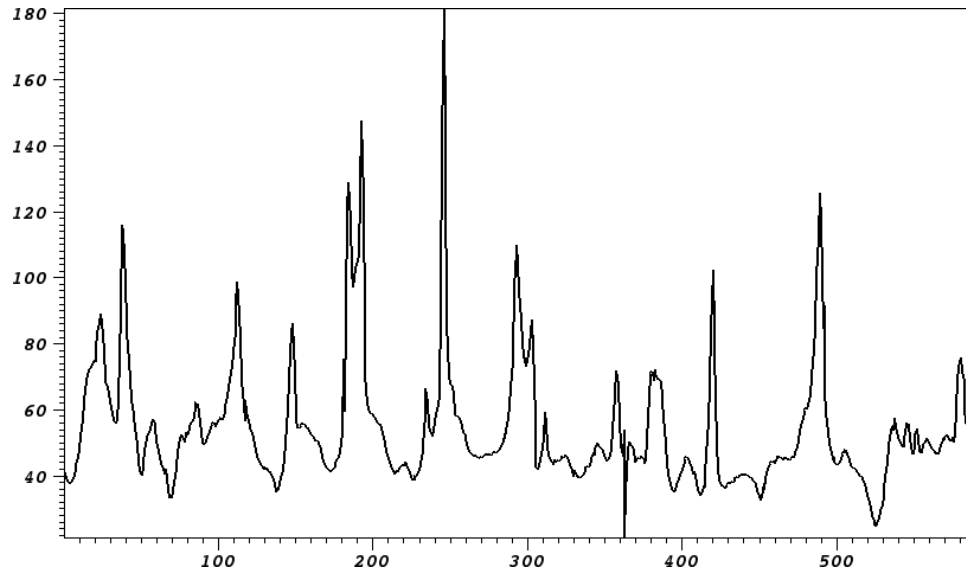


Figure 6.77: Pressure trace through the “Mach stem” wave as shown in figure 6.76.

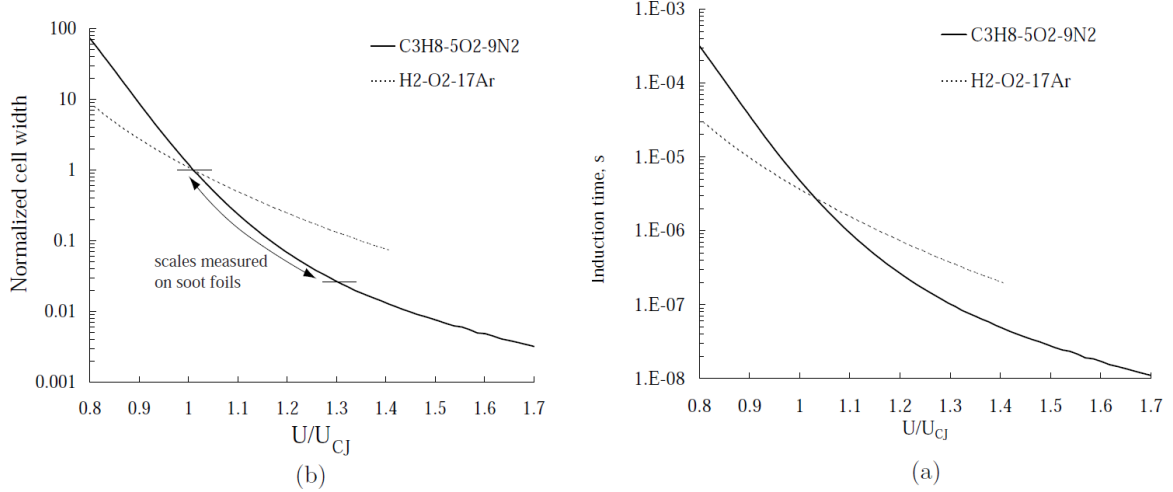


Figure 6.78: (a) Induction time calculated as a function of lead shock strength using a zero-dimensional constant volume approximation and the detailed kinetics mechanism of Konnov (1998). (b) Estimation of substructure cell width as a function of lead shock strength. The range of fine-scale cells observed on a soot foil in this mixture is also shown. The lower bound is set by the resolution at which cells may be detected by eye, about 1 mm. Reprinted with permission from Austin (6).

shock instability. When the incident shock first went unstable, it propagated past the main DMR triple point into the Mach stem. This wave traveled all the way to the bottom symmetry boundary where it reflected and is now traveling back upwards. The second simulation comparison, figure 6.81c), shows the whole incident/Mach stem combination. Similarities include a curvature on the Mach stem and a straight incident shock. A difference is the scale of the experimental image, which is about 4 cm high. The main Mach stem in the simulation is approximately 1 cm high. With greater future computational resources, the DMR problem could be run longer to show a comparison at the same scale.

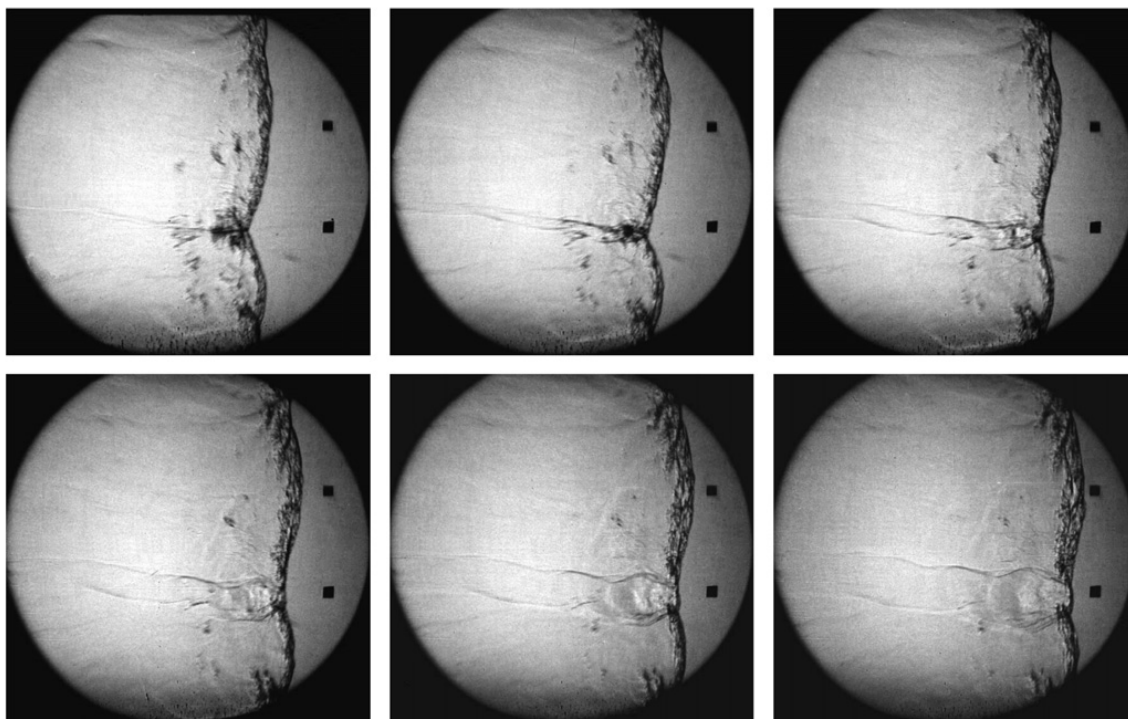


Figure 6.79: Time-resolved shadowgraph images of a detonation propagating in  $\text{C}_3\text{H}_8\text{-5O}_2\text{-9N}_2$  in the narrow channel. Time between frames is 1.6 micros. Field of view is about 138 mm. Reprinted from Austin *et al.* (7).

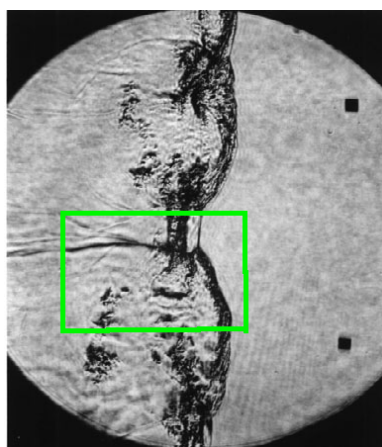
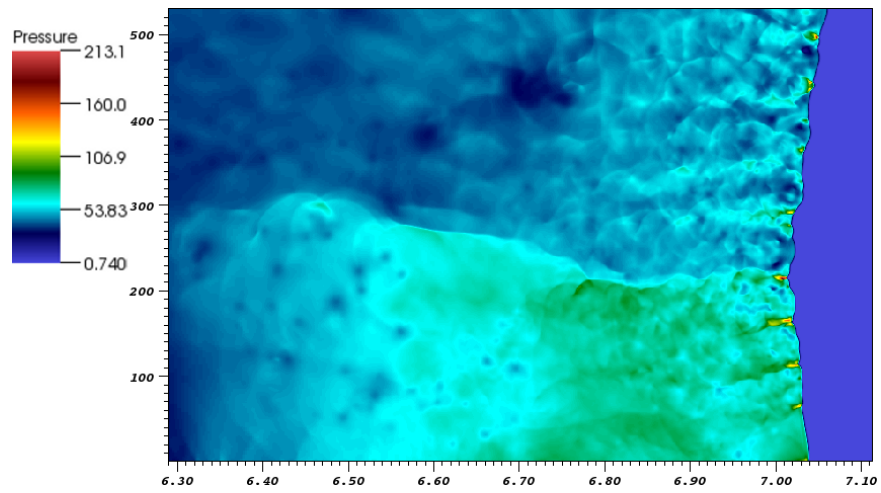


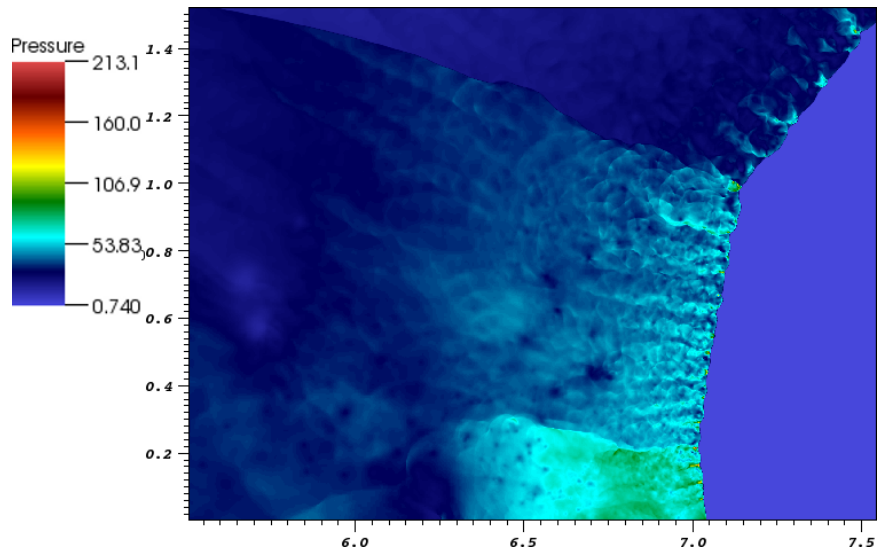
Figure 6.80: Image of a detonation propagating in  $\text{C}_3\text{H}_8\text{-5O}_2\text{-9N}_2$ . Reprinted with permission from Massa *et al.* (116). Field of view is about 138 mm and the channel is 150 mm wide. The green box is used for a comparison to the DMR structure in figure 6.81.



(a)



(b)



(c)

Figure 6.81: Image of a dominate scale incident shock/Mach stem combination compared to the 3-level simulation result. The schlieren image is from figure 6.80.

## 6.7 Discussion

The reduced propane mechanism was used to simulate a double Mach reflection (DMR) in a DNS fashion resolving all the diffusive scales (except the strong shocks). Also simulated were marginally unresolved and generally unresolved inviscid and viscous simulations. By also simulating a range of resolutions and comparing the viscous solution to the inviscid solution, the amount the numerical viscosity that pollutes the solution was estimated. With these comparisons, evidence was shown supporting the case that the 6- and 5-level simulations of the DMR were resolved and the 4-level case was marginally resolved.

Also studied was the process in which the incident initially steady shock goes unstable. This is a multi-dimensional process which only occurs when more than one dimension is simulated. This unstable incident shock/Mach stem combination found in the DMR has a direct similarity to the triple points of real detonations which move across the front and collide with each other creating the detonation cell pattern. Using soot foils, the range of resolvable (with soot) scales has been measured for irregular detonations. In these resolved and unresolved DMR simulations, the numerically measured scales were found to be below the experimentally (visually) resolvable limit. In the next chapter, larger domains and time scales are used to make this direct comparison to the experimentally resolvable scales.



## Chapter 7

# Irregular Detonation Cell Structure

In §6.4 in the previous chapter, the transition of the initially steady incident wave of a detonating double Mach reflection to an unsteady multi-dimensional wave was realized. In these simulations, the domain was of insufficient size to fully understand this phenomena. In this chapter, the transition to and the long term behavior of a two-dimensional unsteady irregular detonation is studied.

These simulations were conducted using the same initial conditions that were used in the 1D case for the propane mixture in §5.3. The detonation was propagated in different-sized rectangular domains with periodic boundary conditions on the top and bottom boundaries.

Firstly, as was done for the DMR simulations, the detonation was simulated in the lab frame, allowing the wave to propagate across the mesh. A large number of cells was required for this simulation, and therefore, the transverse size of the domain and running time was limited. Transition from the steady ZND solution to an unsteady chaotic detonation solution was observed at multiple resolutions and for the inviscid and viscous/diffusive models.

Secondly, the detonation was simulated in the average velocity (CJ) frame. A smaller parallel distance for the domain was required, and hence, a larger transverse confinement was feasible. The influence of the channel width and numerical and physical viscosity were studied. With these simulations in §7.3, a comparison to the experimental soot foil results, introduced in §6.6, was made matching the dominant cell size. The statistical stationarity of the results was also confirmed and is discussed in §7.3.4.

## 7.1 Thin Channel, Lab Frame Results

In the lab frame, the initially steady detonation was propagated through a thin (smaller than the expected cell size) periodically confined geometry. Both unresolved, in terms of the diffusive properties, and marginally resolved simulations were conducted.

### 7.1.1 Two Levels, Unresolved

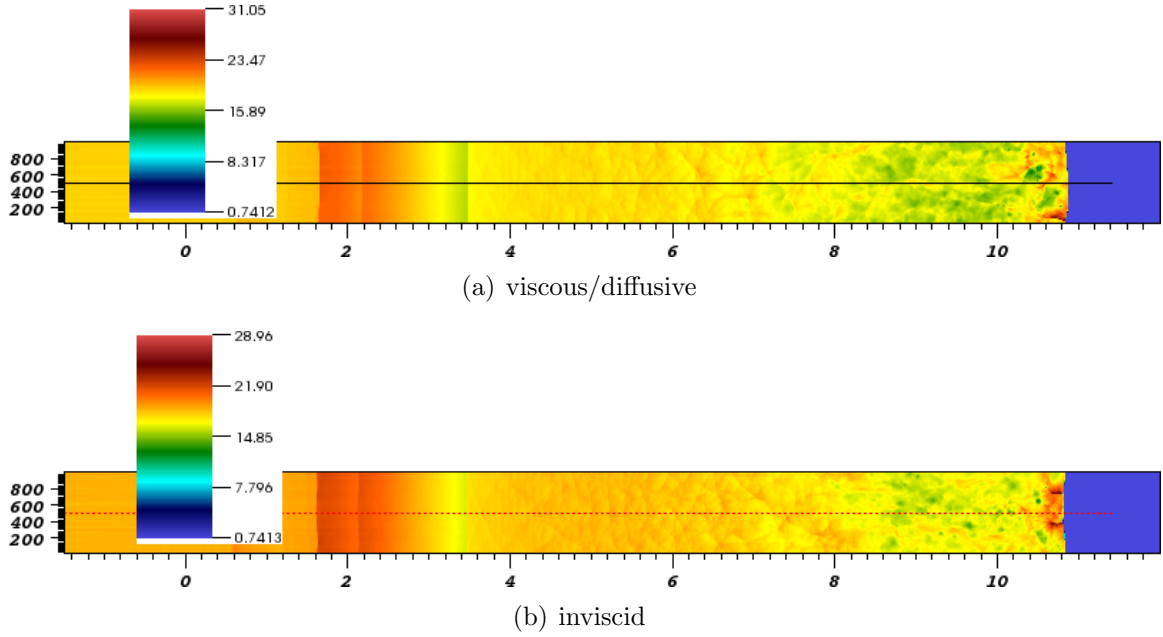


Figure 7.1: Pressure (kPa) traces at  $y=0.5$  cm. Output from the 2-level case with a channel width of 1 cm, base grid cell size of  $41.67 \mu\text{m}$ , smallest cell size  $20.8 \mu\text{m}$ .

Shown in figures 7.1 and 7.3 are results from a demonstrative unresolved simulation. For these results, two-levels (base grid plus one refinement level, 2x finer) were used with the base grid having  $3240 \times 240$  cells for a domain  $x=(-3,12)$  and  $y=(0,1)$  cm. In figures 7.2 and 7.4 the influence of physical viscosity is observed by comparing the pressure and temperature traces for the inviscid and viscous solutions. The pressure for the viscous case is larger throughout the whole domain. Also, for this particular time step ( $t = 1800$  nondim) the temperature for the inviscid case is slightly lower near the leading shock. One would postulate that with low-enough numerical viscosity for the inviscid case, this trend could continue causing the detonation to fail. Also, note that the average leading shock speed in the inviscid case is slightly lower

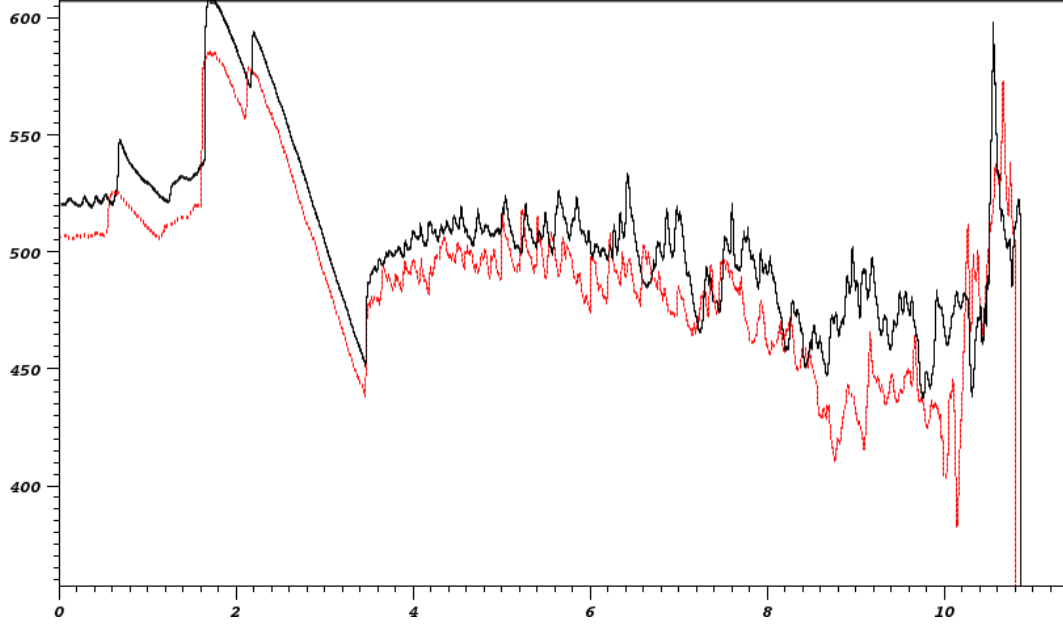


Figure 7.2: Pressure (kPa) traces at  $y=0.5$  cm. Solid black is viscous/diffusive and dotted red is inviscid. Output from the 2-level case shown in figure 7.1 used.

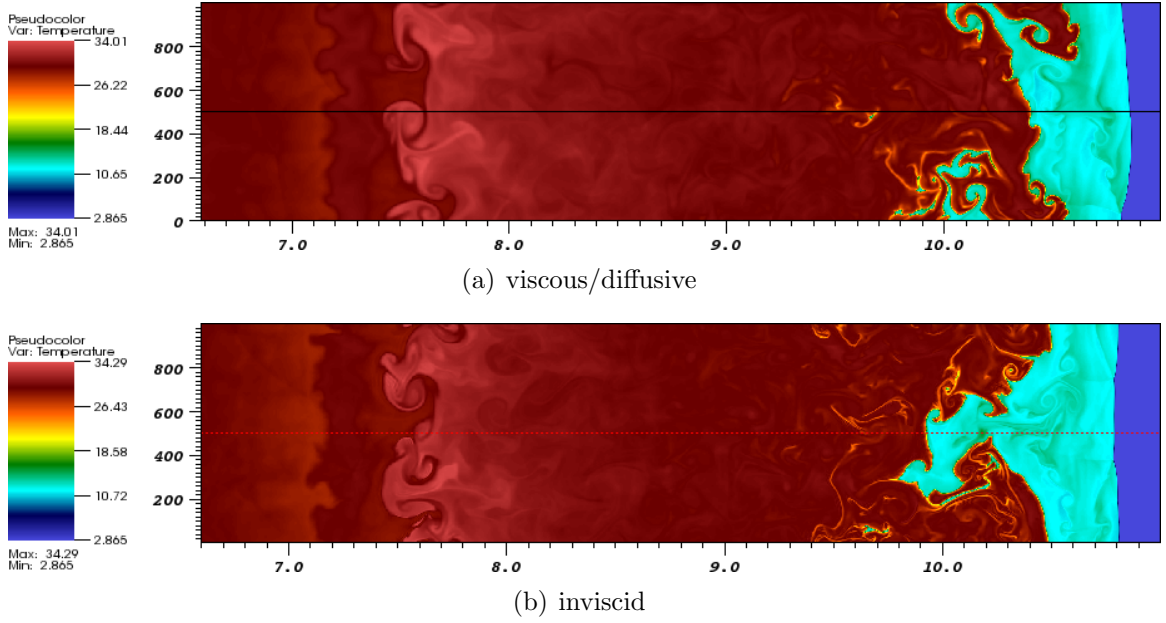


Figure 7.3: Temperature (K) traces at  $y=0.5$  cm. Output from the 2-level case with a channel width of 1 cm, base grid cell size of  $41.67 \mu\text{m}$ , smallest cell size  $20.8 \mu\text{m}$ .

than the viscous case. This is observed by seeing a lag in the shock position.

Also observed are the effects of the transverse periodic confinement. Only one

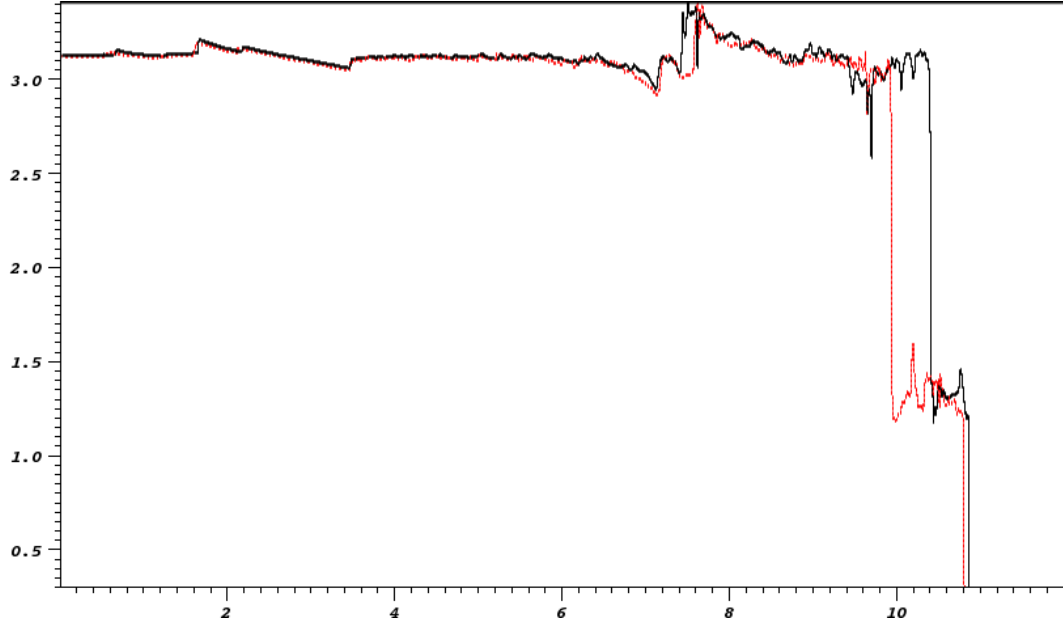


Figure 7.4: Temperature (K) traces at  $y=0.5$  cm. Solid black is viscous/diffusive and dotted red is inviscid. Output from the 2-level case shown in figure 7.3 used.

to two triple points are able to exist in this 1 cm channel. Due to the increase in transverse shock reflections, the flow appears different from the relatively unconfined unsteady shock which was observed when the incident wave of the DMR went unstable. There, in the early times of instability, quite uniform triple points and shear layers are observed across the front as is shown in figures 6.21-6.26.

### 7.1.2 Four Levels, Marginally Resolved

The thin channel simulation of §7.1.1 was repeated with two more refinement levels. To keep up with the increased computational expense, a channel 2x thinner in the  $y$ -direction was used. This creates even more nonphysical transverse shock reflections, however, the influence of a decrease in numerical viscosity from using higher resolution can still be observed.

Shown in figure 7.5 are the nondimensional temperature results. For these results, 4 levels (3 refinement levels, 2x finer each) were used with a base grid of 3240x120 cells for a domain  $x=(-3,12)$  and  $y=(0,0.5)$  cm. In figures 7.6 and 7.7 the influence of physical viscosity is again observed. Even though this is at an earlier timestep than that observed in the previous 2-level case, the same trends are observed when comparing the viscous and inviscid cases. The only difference is that at this particular

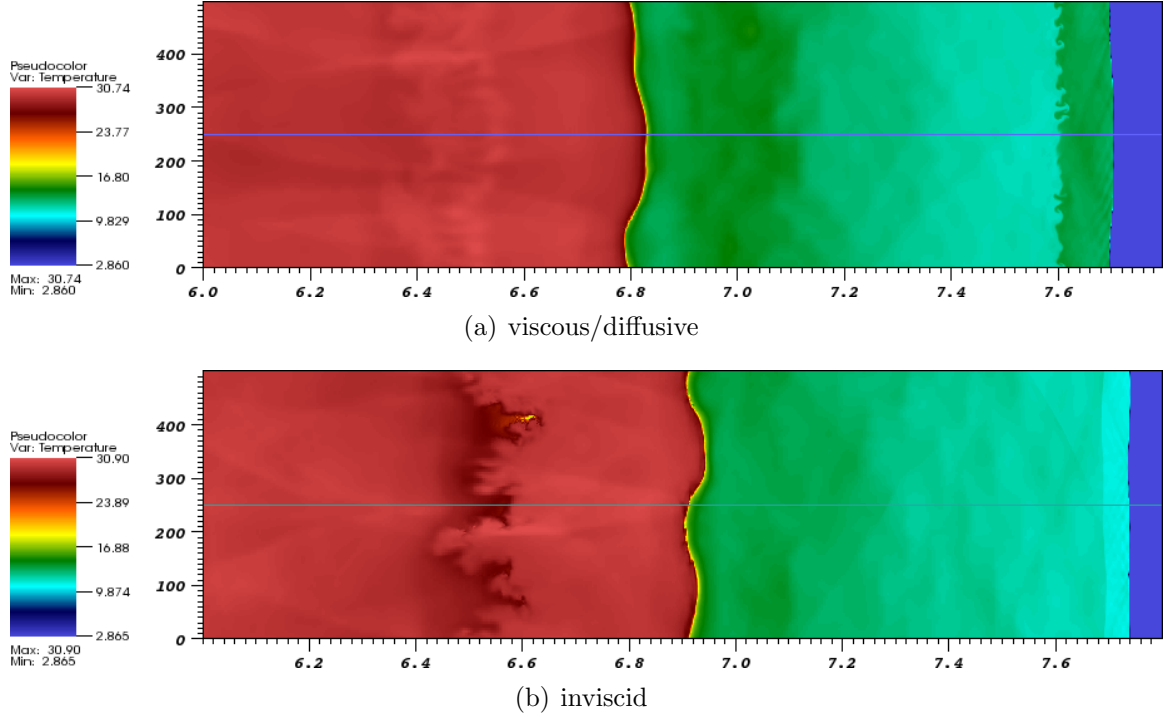


Figure 7.5: Non-dimensional temperature traces at  $y=0.5$  cm. Output from the 4-level case with a channel width of 0.5 cm, base grid cell size of  $41.67 \mu\text{m}$ , smallest cell size  $5.21 \mu\text{m}$ .

timestep and  $y$ -location, at the leading shock, the inviscid solution has a high peak. It still lags behind the inviscid solution.

One can also compare the startup process (ZND to unsteady detonation) for the inviscid and viscous cases. By looking at the visualization of the nondimensional temperature in figure 7.5b), cauliflower-like instabilities are observed in the inviscid solution. This is from the interaction of the grid with the natural chemical and Kelvin-Helmholtz instabilities and unnatural low viscosity.

Shown in figure 7.8 are the nondimensional pressure results, at a slightly later time. For these results, the leading shock has moved from approximately  $x=7.7$  cm to 8.6 cm. The centerline traces of nondimensional pressure and temperature are shown in figures 7.9 and 7.10. The trends that were observed at the previous time step are now backwards. The viscous solution is lagging behind the inviscid solution, proof the two solutions are now out of phase.

Comparing to the 2-level thin channel solution, the appearance of triple points on the leading shock has been even more suppressed, due to the thin channel, which through the use of the periodic boundary conditions, has not allowed the transverse

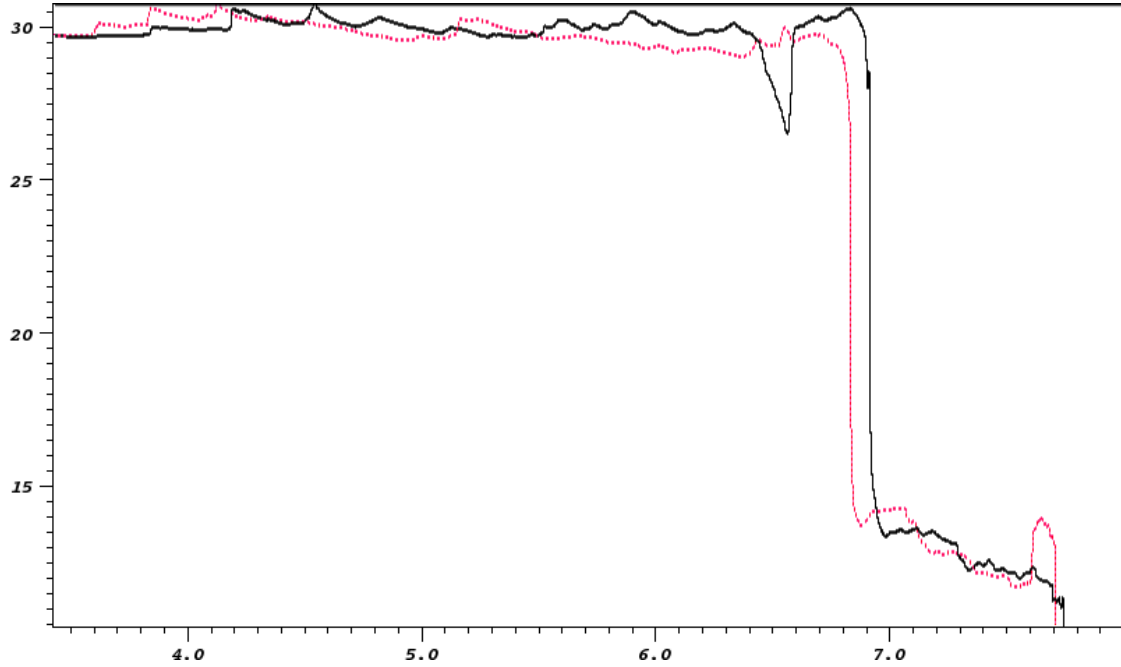


Figure 7.6: Non-dimensional temperature traces at  $y=0.5$  cm. Solid black is viscous/diffusive and dotted red is inviscid. Output from case shown in figure 7.5.

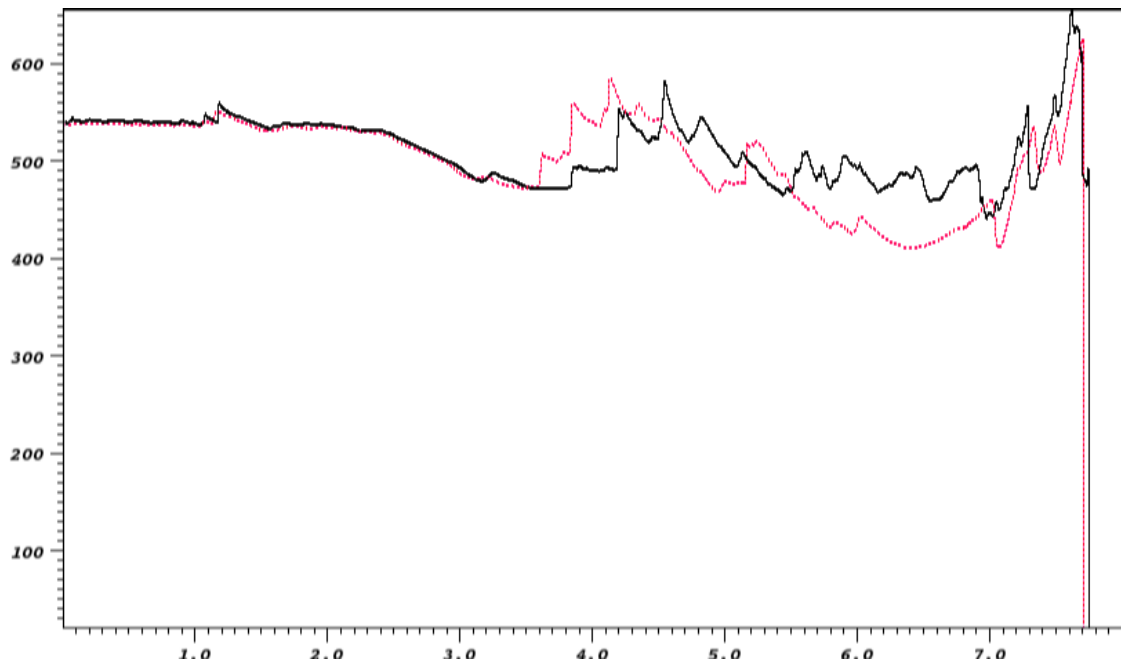
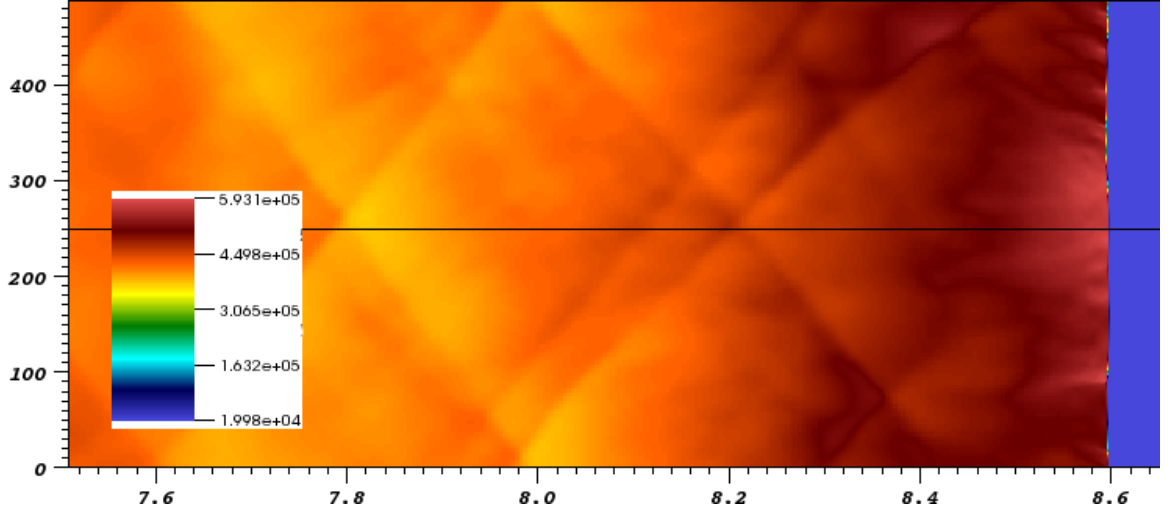
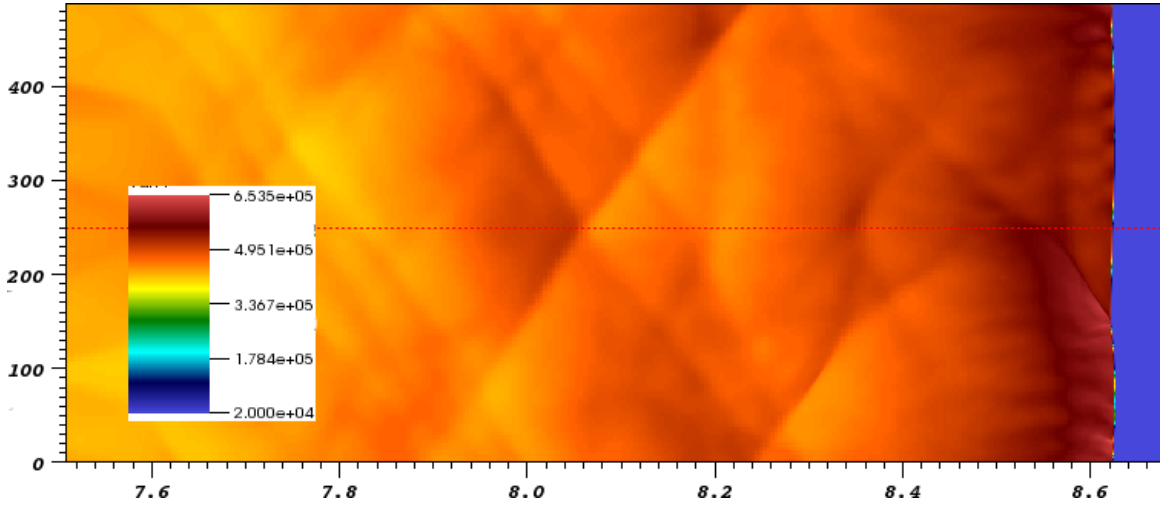


Figure 7.7: Non-dimensional pressure traces at  $y=0.5$  cm. Solid black is viscous/diffusive and dotted red is inviscid. Output from case shown in figure 7.5.

shocks to travel very far before reshocking the flow. This phenomena also occurs experimentally with solid boundary conditions when the tube spacing is on the order or smaller than the cell size ( $45 \pm 8$  mm for this mixture and IC) as is discussed in §6.6. Therefore, in order to truly understand the formation of triple points in an unsteady multi-dimensional detonation, a domain wider than the cell size is required. Due to the increased domain size, this creates difficulties in resolving the viscous/diffusive scales.



(a) viscous/diffusive



(b) inviscid

Figure 7.8: Non-dimensional pressure traces at  $y=0.5$  cm. Output from the 4-level case with a channel width of 0.5 cm, base grid cell size of  $41.67 \mu\text{m}$ , smallest cell size  $5.21 \mu\text{m}$ .

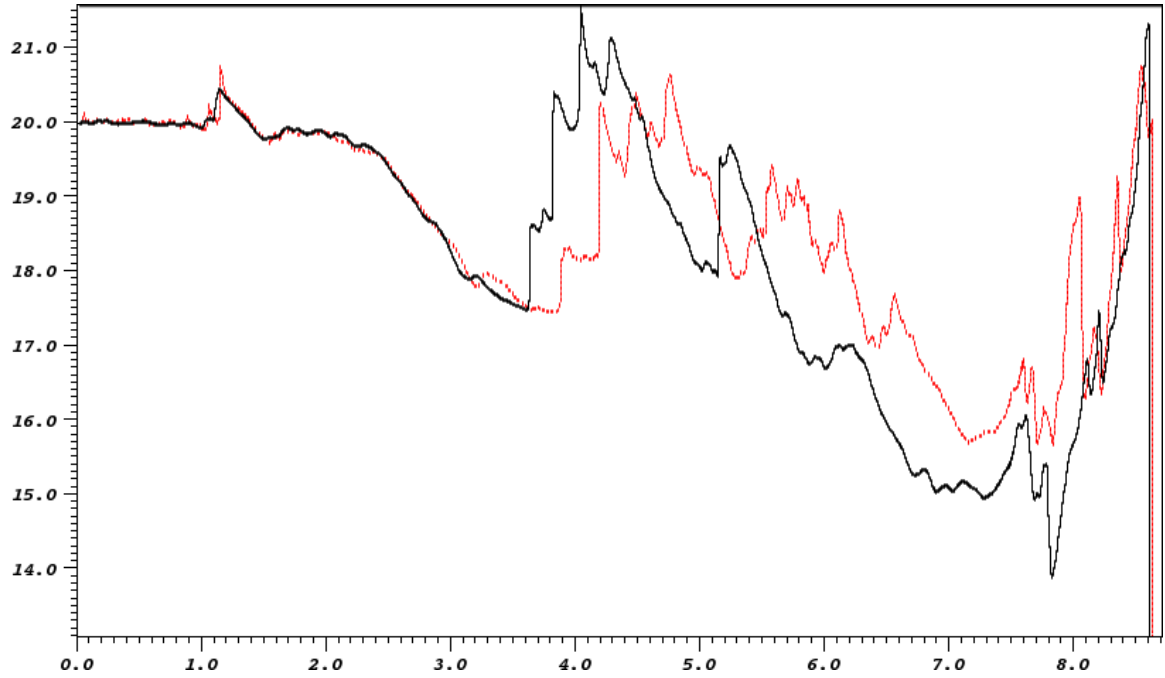


Figure 7.9: Pressure traces at  $y=0.5$  cm. Solid black is viscous/diffusive and dotted red is inviscid. Output from the 4-level case shown in figure 7.8 used.

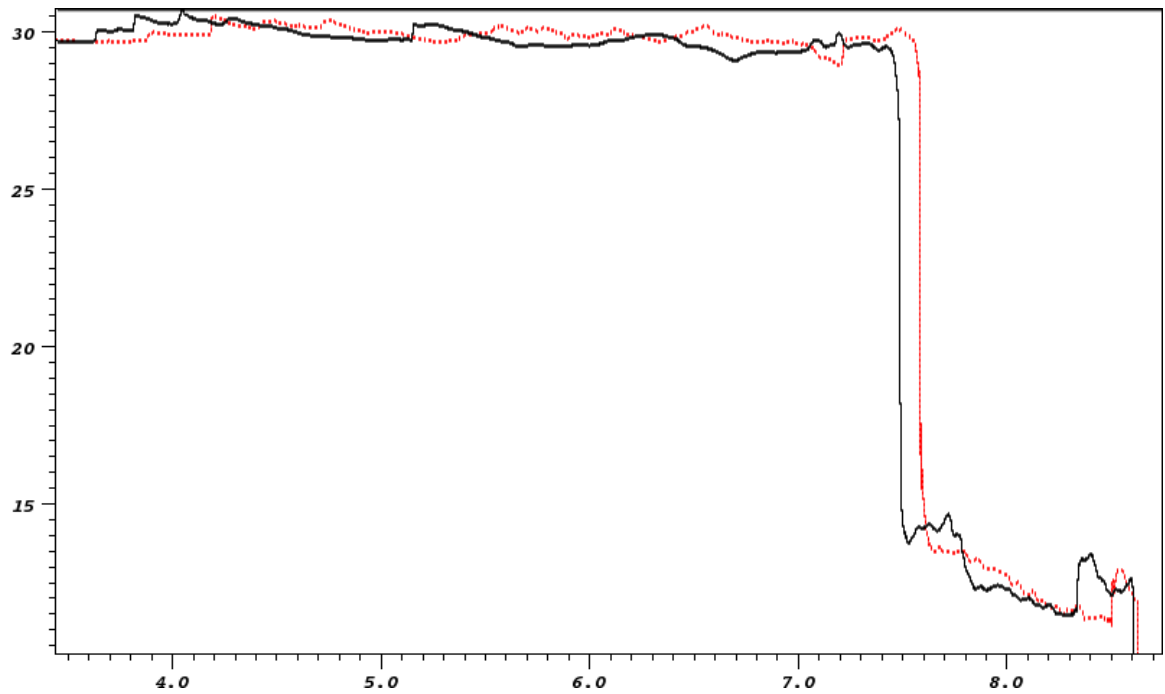


Figure 7.10: Non-dimensional temperature traces at  $y=0.5$  cm. Solid black is viscous/diffusive and dotted red is inviscid. Output from the 4-level case shown in figure 7.10 used.



## 7.2 Wide Channel, CJ Frame Results

As the next step, the planar detonation was simulated using a much larger domain, approximately 2 to 4 times larger than the experimentally determined cell size. 8 cm and 16 cm wide domains were used for simulations in the CJ reference frame with a horizontal domain size of -6 to 3 cm with the ZND wave initially centered at  $x = 0$ . Two different resolutions were tested, a 2-level and a 3-level case. The 2-level case is the lowest resolution ( $\Delta x = 7.407407 \cdot 10^{-5}$  m) which will support the formation of triple points and a self-propagating detonation. Below this resolution, no triple points form and the detonation dies as the shock speed decays.

Because the ultimate goal of these wide channel simulations is to reproduce the experimentally observed detonation cells, some analysis of the detonation length scales and properties encountered is warranted. In order to ensure a self-propagating detonation in all simulations, a slightly overdriven initial condition has been used. The initial condition is for a shock speed of 1950 m/s, which when compared to the CJ speed of 1933.215 m/s yields an overdrive of  $f = 1.008683$  ( $U/U_{CJ}$ ) or  $f = 1.01441$  ( $[U/U_{CJ}]^2$ ), depending on the notation used. Shown in table 7.1 is a summary of the properties of the initial state and the CJ speed solution (which it is theorized that the unsteady solution will approximately oscillate around).

$U_{shock}$	$f = U/U_{CJ}$	$p_{equil}$	$T_{equil}$	$l_{ind}$	$t_{ind}$
1950 m/s	1.00893	18.11 (nondim) = $4.89 \cdot 10^5$ Pa	3106.3 K	1.424 mm	$4.71 \cdot 10^6$ sec
1933.22 m/s	1.0	15.48 (nondim) = $4.18 \cdot 10^5$ Pa	3024.9 K	1.643 mm	$5.45 \cdot 10^6$ sec

Table 7.1: Comparing the chosen initial condition with the CJ solution for the T=298 K, P = 20kPa detonation.

Of great note is that for the CJ detonation, the CJ length (where chemical equilibrium is reached and the Mach number equals one when the overdrive equals one), is 1.49 cm in length. This length is 4.02 times smaller than the domain (6 cm) used to start a self-propagating unsteady detonation in the CJ frame. In preliminary simulations, a domain of 3 cm was first used, and it was found that the detonation died, failing to self-propagate. A 6 cm equilibrium length corresponds to an underdriven detonation 84.7 percent slower than the CJ detonation. For  $f = 0.847$ , the von Neumann state is  $p = 5.796$  Pa and  $T = 3025$  K. Most likely in the multi-dimensional unsteady detonation simulation and in experiments, there are portions of the detonation which are even more underdriven and could require more than a 6 cm length to

model the influence with the main shock front. However, in these simulations 6 cm was found to be adequate for self-propagation and the formation of detonation cells when the transverse domain size was large enough, as is discussed in §6.6.

Also of importance is the induction length, where the rapid heat release occurs. For the CJ solution this length is 36.6 times shorter than the domain of 6 cm used model the unsteady detonation problem. The induction length for the overdriven initial condition is 42.1 times smaller than 6 cm.

For a 2-level case with  $x = [-6, 3]$  cm and  $y = [0, 8, \text{ or } 16]$  cm and a base grid of 1080x960 and 1080x1920 for the 8 and 16 cm wide cases, the solution was studied in detail and found (despite the low resolution) to match the experiments of Austin as is discussed in §6.6. Here, the smallest cell size is  $\Delta x = 7.464 \cdot 10^{-5}$  m.

A 3-level simulation was also conducted. Due to the increased computational expense, this simulation was run for shorter time. In figures 7.11-7.14, the start-up phenomena (now in the CJ frame) for a 16 cm wide channel shown. In these simulations a domain with  $x = [-6, 3]$  and  $y = [0, 16]$  cm was used with 2 refinement levels and a base grid of size 1080x1920. The smallest cell size in this case is  $\Delta x = 3.703704 \cdot 10^{-5}$  m.

From a time of  $t = 1036.7$  to 1368 (nondim) the influence of a Kelvin-Helmholtz instability on heating the fluid is observed by looking at the temperature psuedo-color plot. Then, at a time of  $t = 1440$ , a vertical sliver of hot gas is observed near the main shock/detonation front. This sliver rapidly grows, turning into a local explosion, which propagates into the main front pushing it forward overdriving the detonation as is seen at a time of  $t = 1517.38$  onward. At  $t = 1656$ , triple points with a nonuniform spacing of an approximate average of 0.08 cm have formed. At  $t = 1800$  the spacing has decreased to approximately 0.05 cm and the detonation has accelerated. Note that as was found for the resolved DMR simulation, the spacing of the triple points depends on the resolution and is possibly smaller than these values for a resolved simulation, which for this base grid, would require at least 5 to 6 levels total.

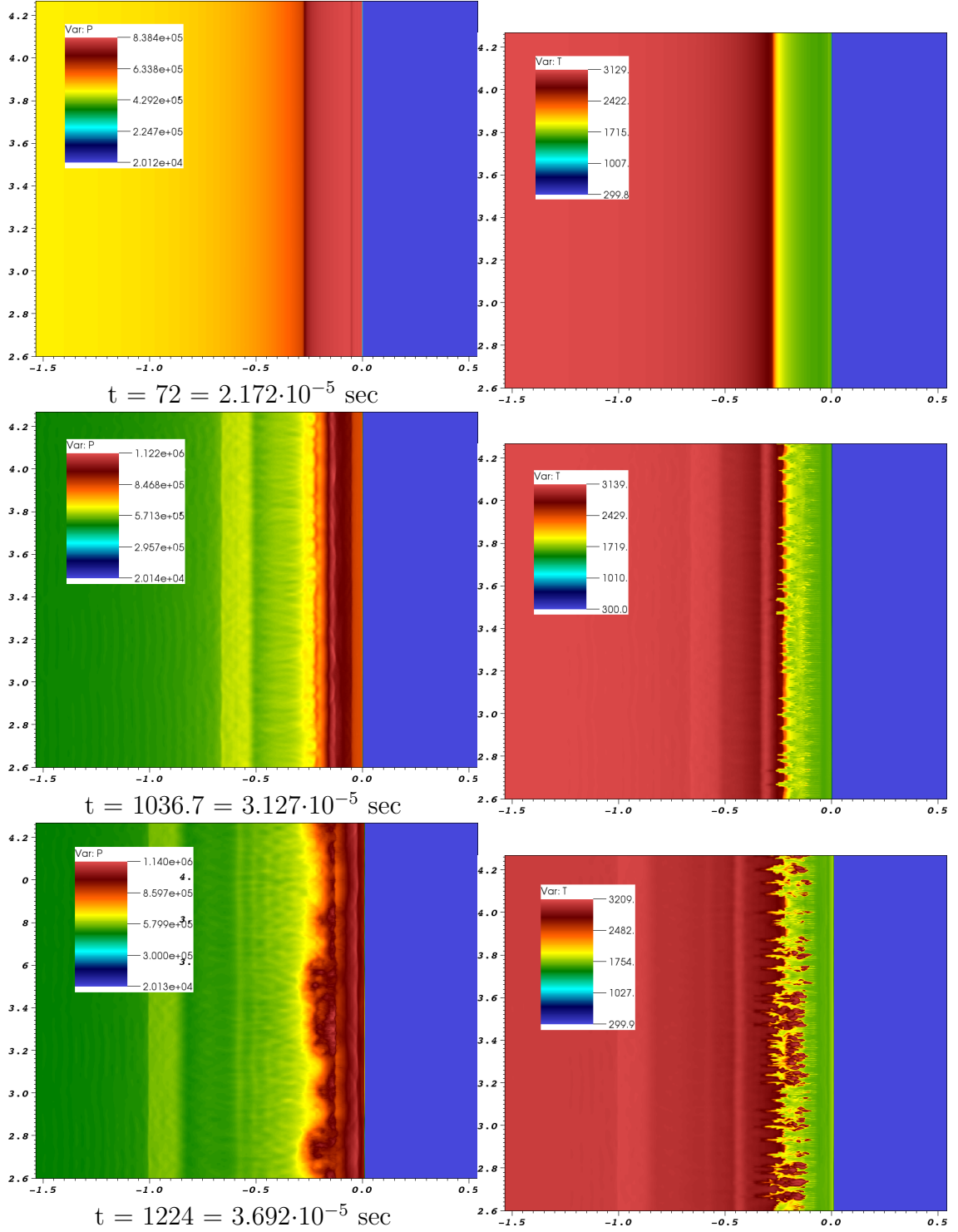


Figure 7.11: Psuedo-color pressure(Pa) and temperature(K) results, showing transition from a steady ZND wave to an unsteady overdriven detonation. 3-levels with  $\Delta x_{min} = 1.04167 \cdot 10^{-5}$  m.

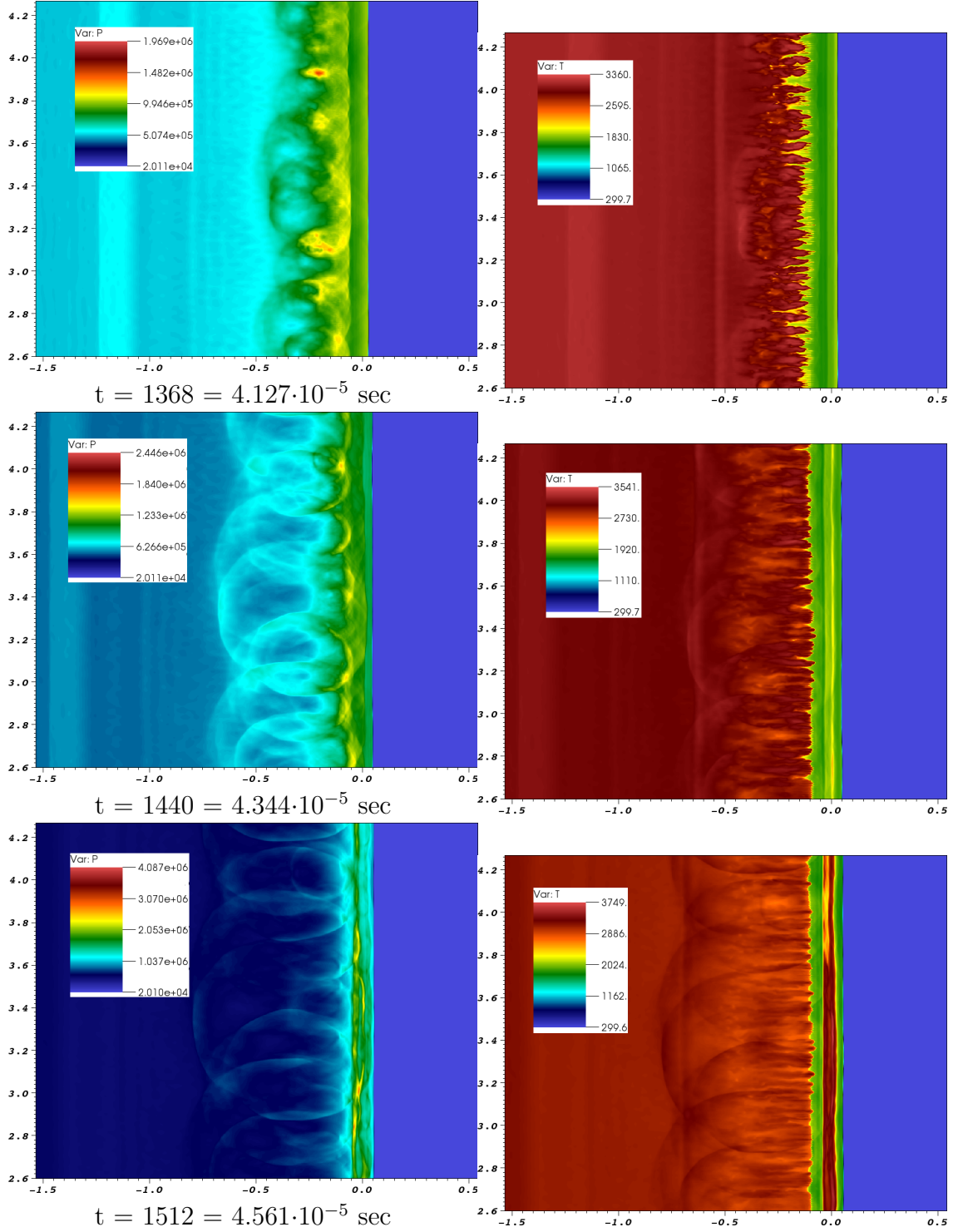


Figure 7.12: Psuedo-color pressure(Pa) and temperature(K) results, showing transition from a steady ZND wave to an unsteady overdriven detonation. 3-levels with  $\Delta x_{min} = 1.04167 \cdot 10^{-5}$  m.

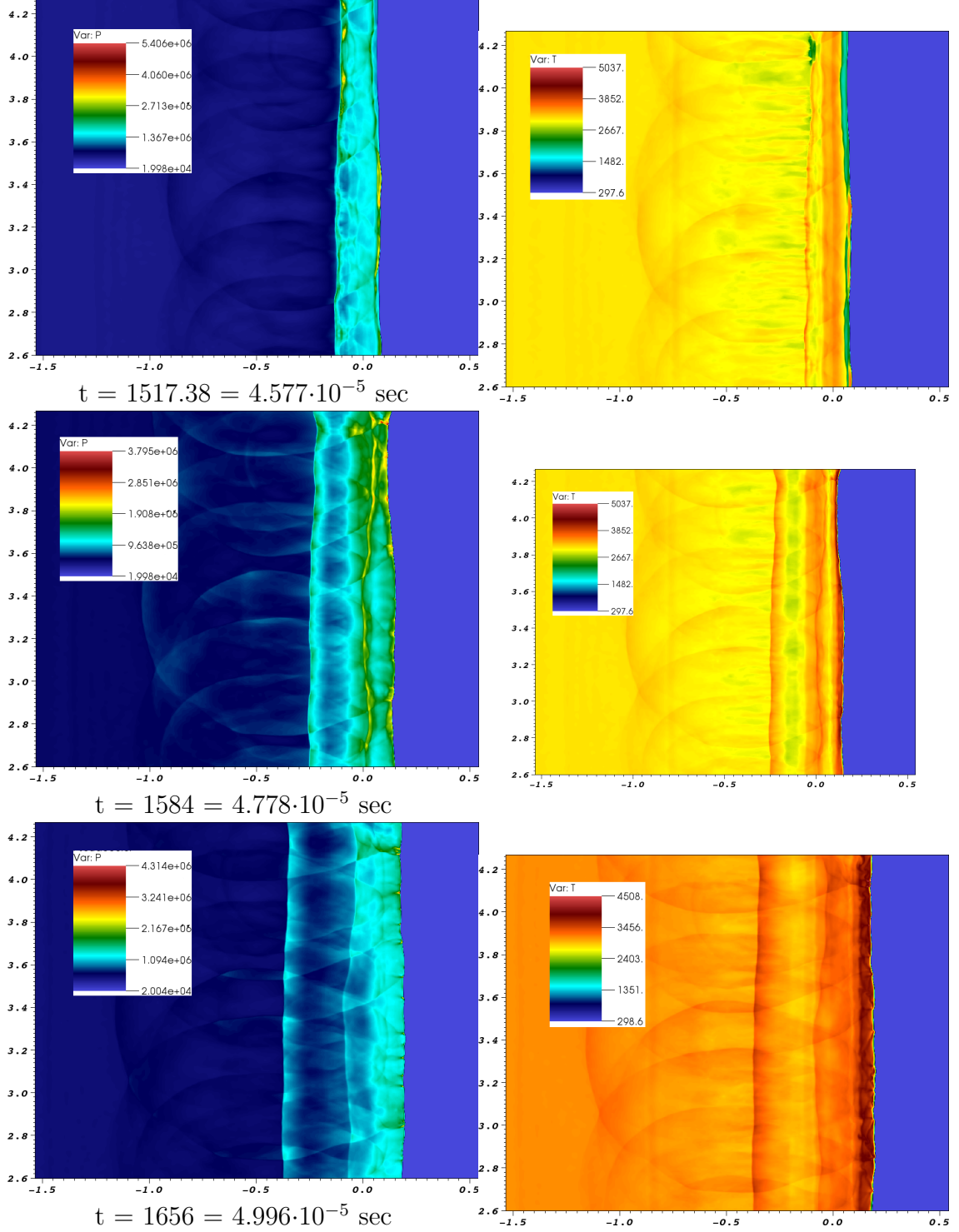


Figure 7.13: Psuedo-color pressure(Pa) and temperature(K) results, showing transition from a steady ZND wave to an unsteady overdriven detonation. 3-levels with  $\Delta x_{min} = 1.04167 \cdot 10^{-5} \text{ m}$ .

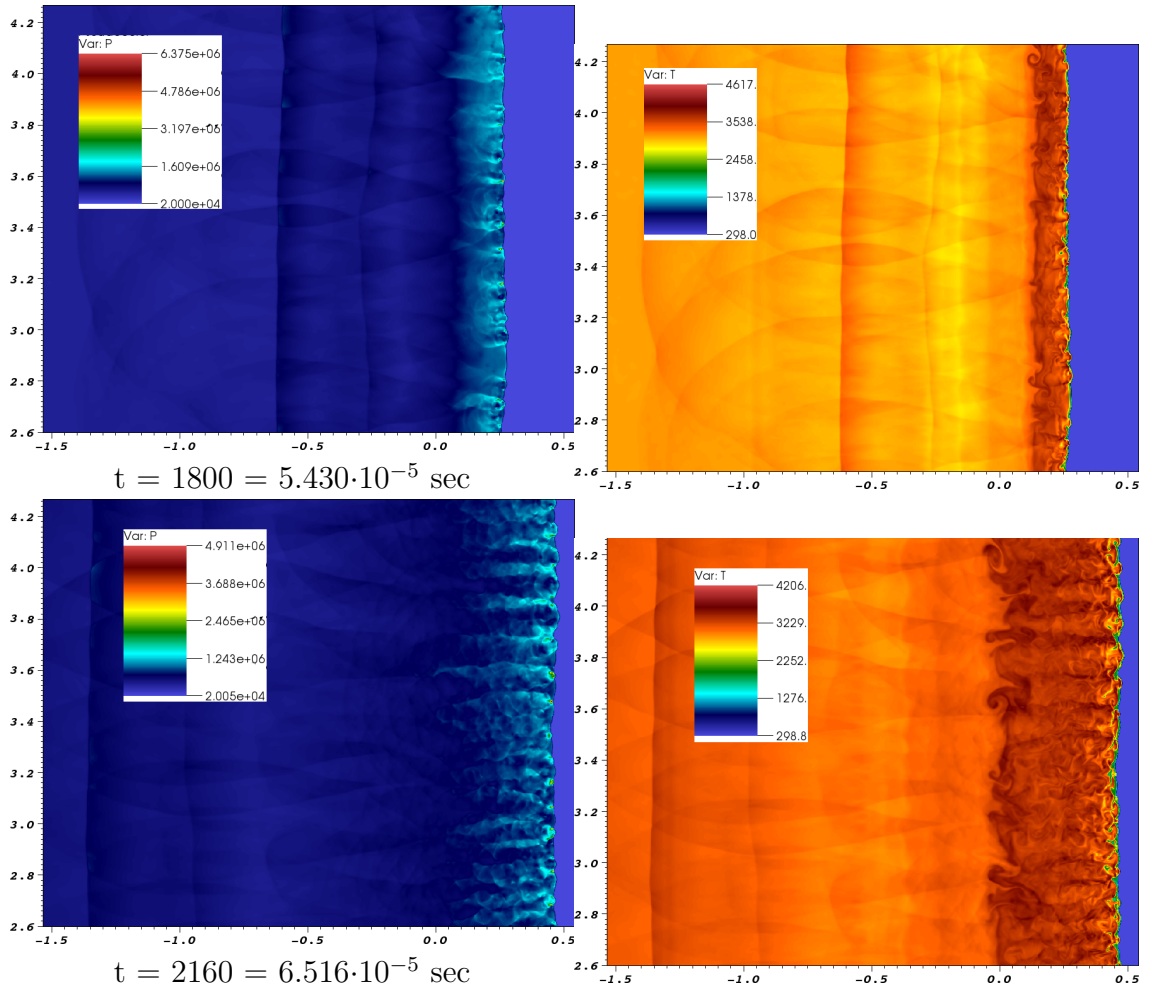


Figure 7.14: Psuedo-color pressure(Pa) and temperature(K) results, showing transition from a steady ZND wave to an unsteady overdriven detonation. 3-levels with  $\Delta x_{min} = 1.04167 \cdot 10^{-5}$  m.



## 7.3 Dominant Cell Size Comparison

Real detonations studied in experiments are a multi-dimensional and multiscale phenomena. However, there is one scale, the dominant cell size, which can be observed in schlieren images and on soot foils. In the past, this cell size has been observed in two- and three-dimensional simulations with periodic and solid boundary conditions. However, all these simulations used much smaller mechanisms and many ignored detailed diffusive transport. Fortunately, resolving the viscous/diffusive scales is not required in order to demonstrate the large-scale detonation cells.

In order to accomplish this, two channel simulations slightly smaller than 4 and 8 detonation cells in the transverse direction were carried out. A two-level mesh was utilized with domain of size  $x = [-6, 3]$  cm and  $y = [0, 8 \text{ or } 16]$  cm and a base grid of 1080x960 or 1080x1920 for the 8 and 16 cm wide cases. Here, the smallest cell size is  $\Delta x = 7.464 \cdot 10^{-5}$  m.

### 7.3.1 Eight cm Channel Width

In order to determine a dominant cell size, the motion of the triple points on the main shock front must be tracked. This shows a full range of scales, however, determining a dominant scale from the triple point spacing is difficult because there are many triple points, and only the strongest ones contribute to a dominant pattern. This is also complicated by the fact that there is a finite transition from the steady ZND solution to a fully developed statistically stationary cell pattern. In this transition region the flow becomes overdriven, but initially nonchaotic in the transverse direction. As was shown in §7.2, a fairly uniform distribution of triple points very closely (0.05 cm) spaced develops. The number of triple points decreases rapidly and reaches a statistically stationary (but still changing) value. This change is demonstrated in figure 7.15, where the number is shown to decrease from 50 to approximately 10 for the 8 cm wide channel. As the simulation is run farther, the number increases as overdriven portions of flow are created, and then decreases as these fast-moving portions slow to underdriven states. This is demonstrated in figure 7.16, which is a tally of the number of triple points during the output time range that is used for a dominant cell size comparison.

Despite the difficulties of having so many triple points, if one runs the 8 cm wide channel long enough, one can still see some cells while ignoring the triple point strengths. This can be seen by comparing the experimental soot foil with the simulation's triple points in figures 7.17 and 7.18. At around time step 20 in figure 7.18, a

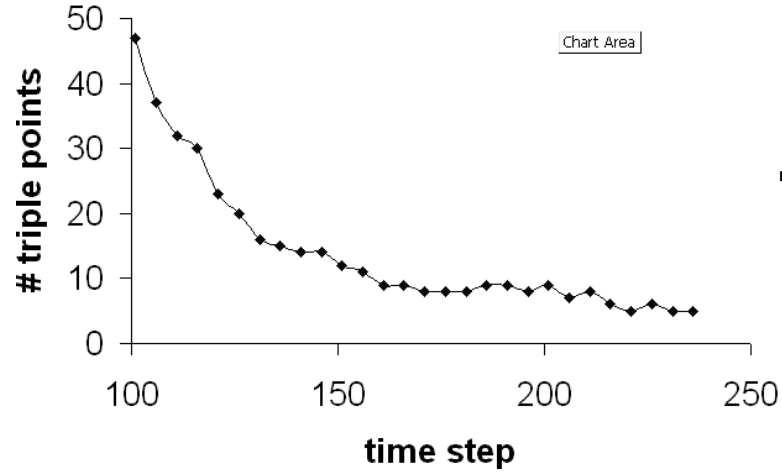
**# triple points**

Figure 7.15: Triple point count during the transition from steady ZND to unsteady detonation cells. Time  $t = 756$  (nondim) =  $2.28054375 \cdot 10^{-5}$  sec to  $t = 2916$  (nondim) =  $8.79638302 \cdot 10^{-5}$  sec. The output steps are every 16 (nondim) time units.

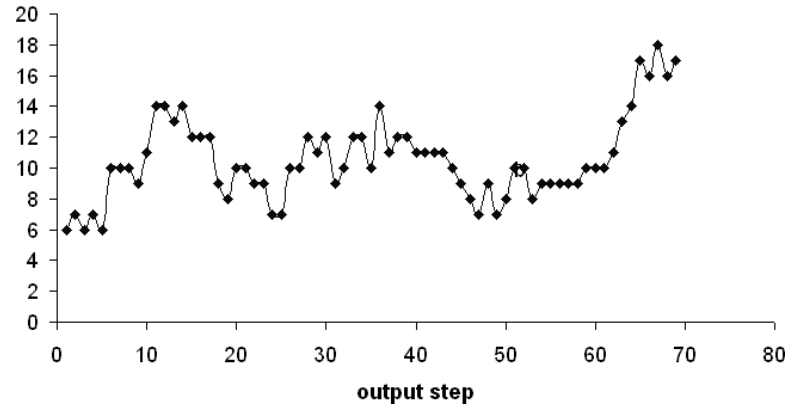
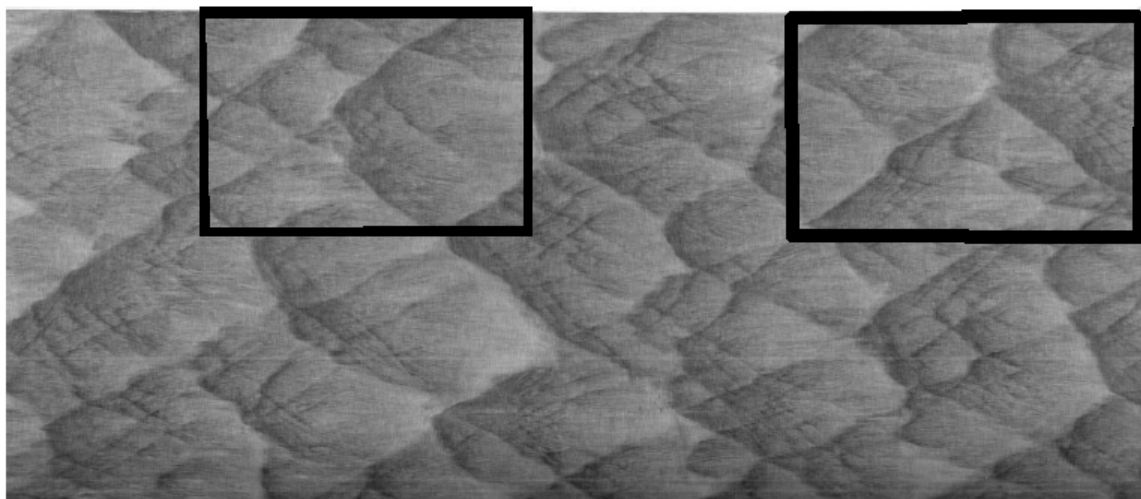
**Number of Triple Points**

Figure 7.16: 8 cm channel triple point count. Points correspond with data in figure 7.18.

dominant size of approximately 5 cm is observed. However, also at the last time step shown, a collision of two triple points (and later other triple points in the domain too) has led to a very large cell that practically covers the whole domain width of 8 cm. This is larger than the 4.5 cm expected from the soot foil, and attributed to the transverse domain not being wide enough. Therefore, to obtain the proper cell size the domain width was doubled to 16 cm, and the simulation was repeated.





Shot 47:  $\text{C}_3\text{H}_8\text{-5O}_2\text{-9N}_2$

Figure 7.17: Soot foil (15 cm wide) in the propane detonation mixture,  $\text{C}_3\text{H}_8\text{-5O}_2\text{-9N}_2$  at 298 K and 20 kPa, showing a similar region as is shown with the triple point tracks in figure 7.18

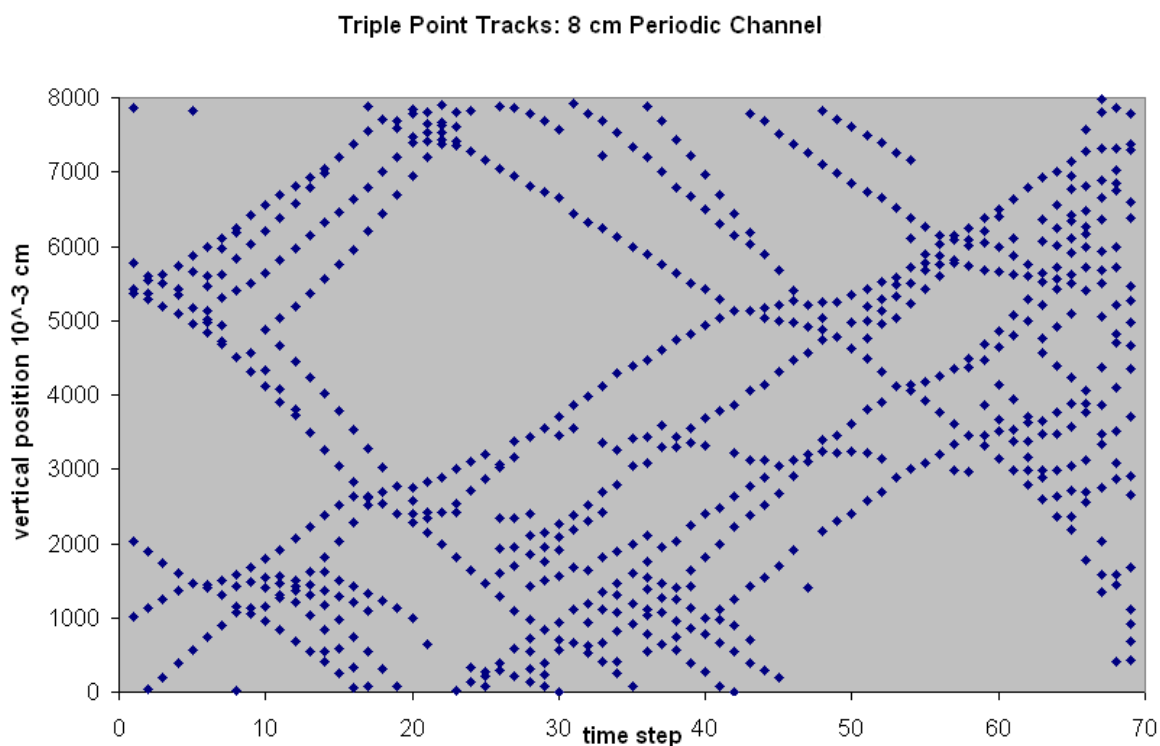
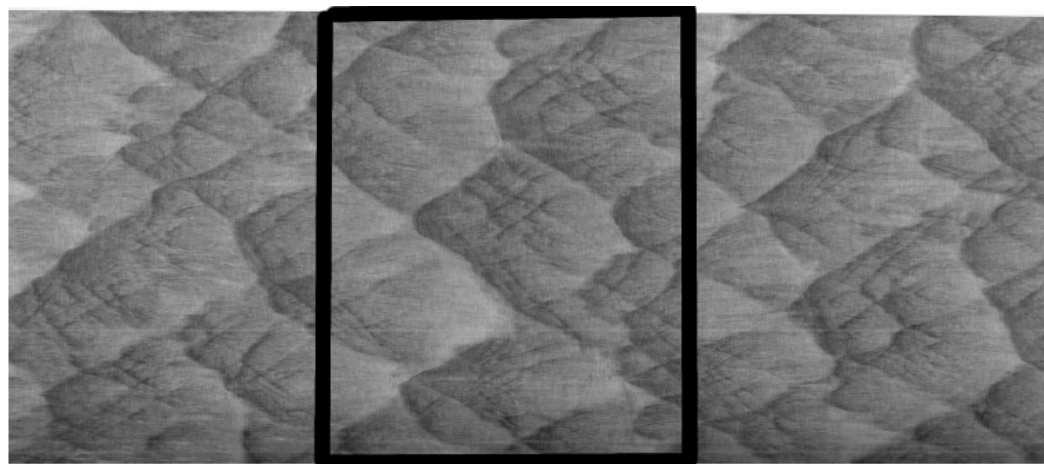


Figure 7.18: 8 cm periodic channel triple point tracks from  $t = 4896$  (nondim) =  $1.47692357 \cdot 10^{-4}$  sec to  $t = 7488$  (nondim) =  $2.25882428 \cdot 10^{-4}$  sec. A similar region in the soot foil is shown in figure 7.18.

### 7.3.2 Sixteen cm Channel Width



Shot 47:  $\text{C}_3\text{H}_8\text{-5O}_2\text{-9N}_2$

Figure 7.19: Soot foil (15 cm wide) in the propane detonation mixture,  $\text{C}_3\text{H}_8\text{-5O}_2\text{-9N}_2$  at 298 K and 20 kPa, showing a similar region as is shown with the triple point tracks in figure 7.20

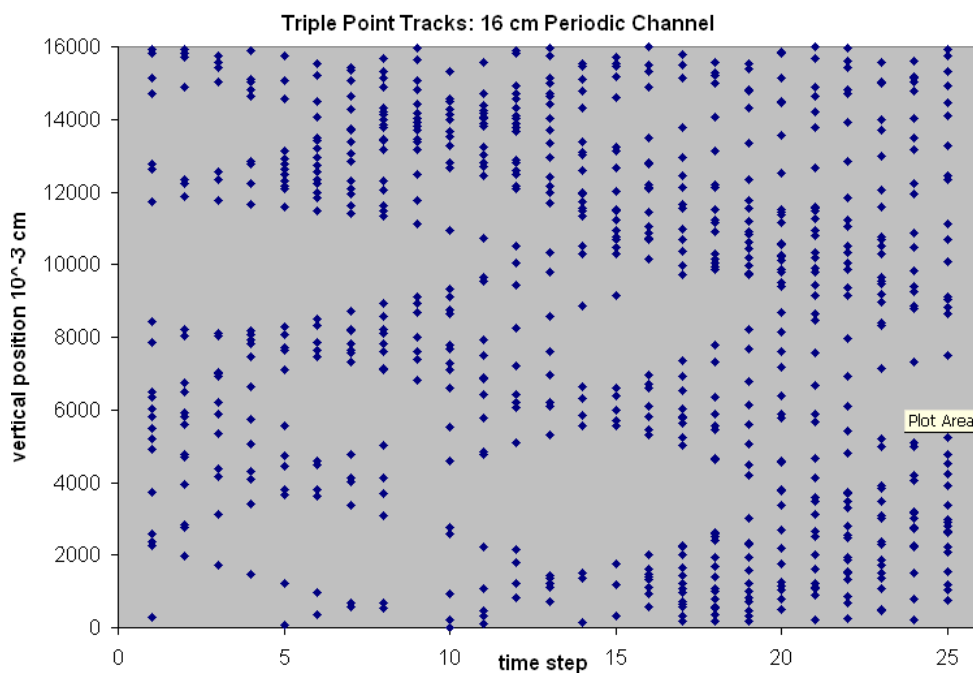


Figure 7.20: 16 cm periodic channel triple point tracks for the last 25 output steps from  $t = 6,984$  (nondim)  $= 2.106792 \cdot 10^{-4}$  sec to  $t = 8712$  (nondim)  $= 2.62805517 \cdot 10^{-4}$  sec. A similar region in the soot foil is shown in figure 7.20.

Now, with a larger transverse domain of 16 cm (one cm wider than the experimental channel), the triple points were tracked as shown in figure 7.20 which can be compared to the boxed out region on the soot foil in figure 7.19. Analyzing the large spaces between the triples points, very clearly, 3 to 4 cells can be seen in different regions across the domain. This agrees with the experimentally measured cell size of  $4.5 \pm 0.5$  cm which would create 3.5 cells on average across the domain. This was a very computationally expensive simulation, utilizing 3072 cores on the order of a week on the DOE LBNL NERSC Hopper supercomputing system.

Again, the total number of triple points across the main shock front verses time is plotted in figure 7.21. From these results it is seen that with an average value of 30, the number oscillates from 19 to 41. This leads to an average spacing of 0.53 cm with a maximum local average of 0.84 cm and a local minimum average of 0.39 cm.

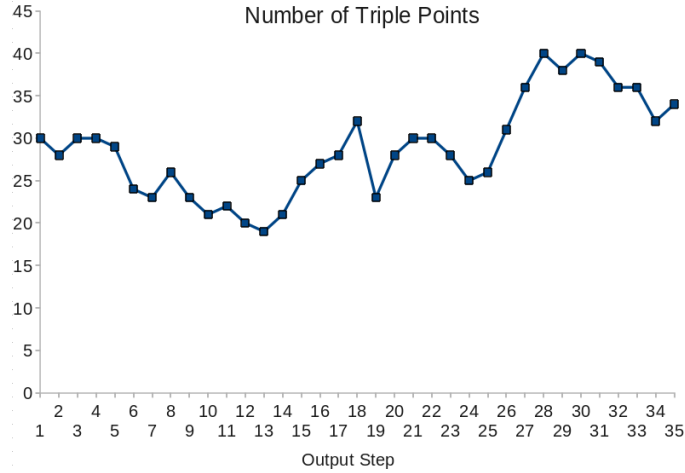


Figure 7.21: 16 cm channel triple point count for the last 35 output steps for  $t = 6336$  (nondim)  $= 1.91131285 \cdot 10^{-4}$  sec to  $t = 8712$  (nondim)  $= 2.62805517 \cdot 10^{-4}$  sec. The last 25 points correspond with the data in figure 7.20.

The dominant cell size is even more clearly seen by looking at the actually 2D psuedo-color simulation results. Results of nondimensional pressure,  $H_2O$  mass fraction,  $OH$  mass fraction, and temperature are shown in figures 7.22-7.29. Dominant cells are observed by looking at the curvature of the main shock front and the regions of high/low pressure and temperature existence of products or reactants and extra high/equilibrium values of radicals. Note that in these figures, the maximum of the psuedo-color scale was fixed so that all subsequent output steps used similar coloring.

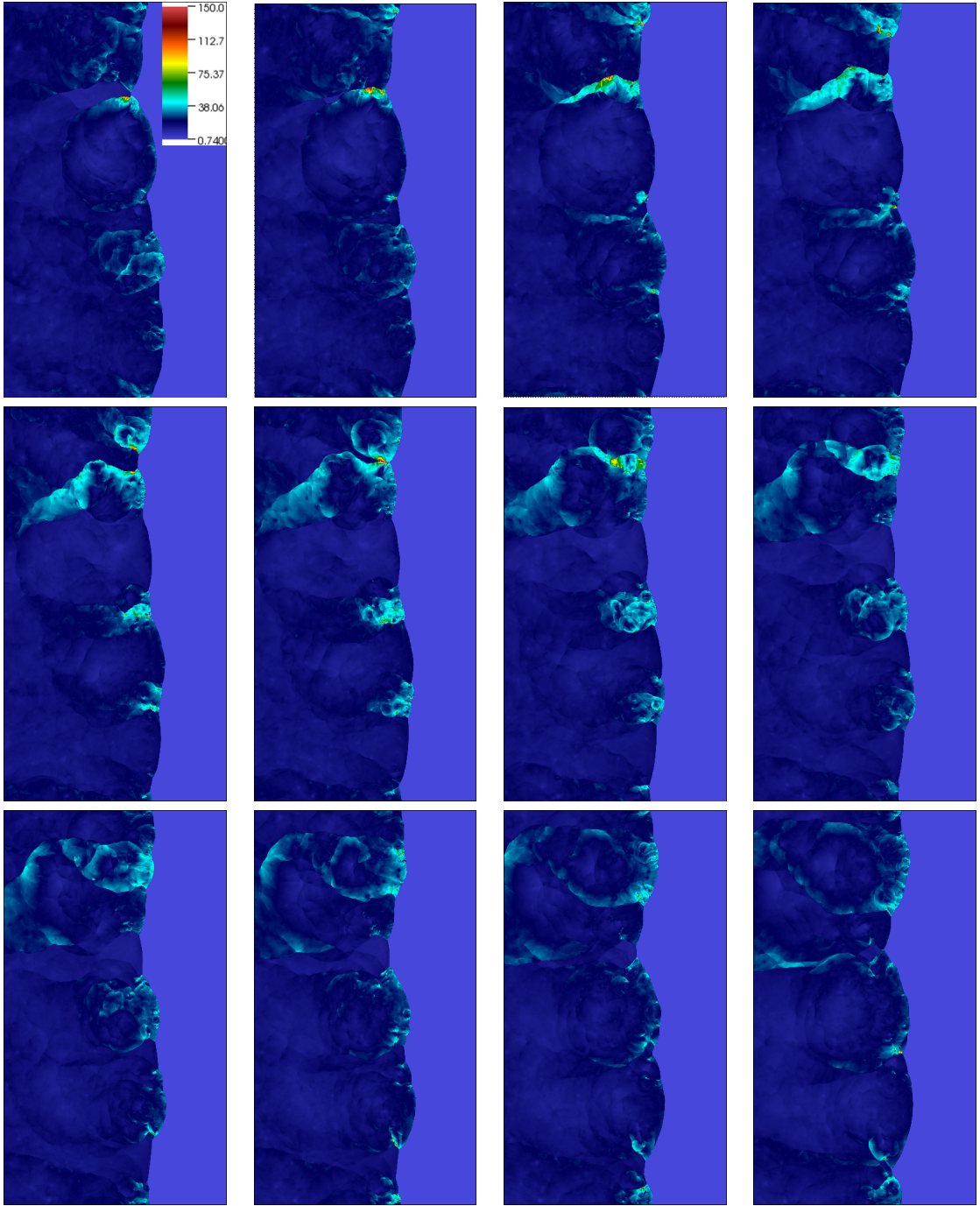


Figure 7.22: Psuedo-color nondimensional pressure results starting at  $t = 6984$  (nondim)  $= 2.106792 \cdot 10^{-4}$  sec with each result at a subsequent  $\Delta t = 72$  (nondim)  $= 2.172 \cdot 10^{-6}$  sec. Note that the maximum pressure shown has been fixed at  $p = 150$ .



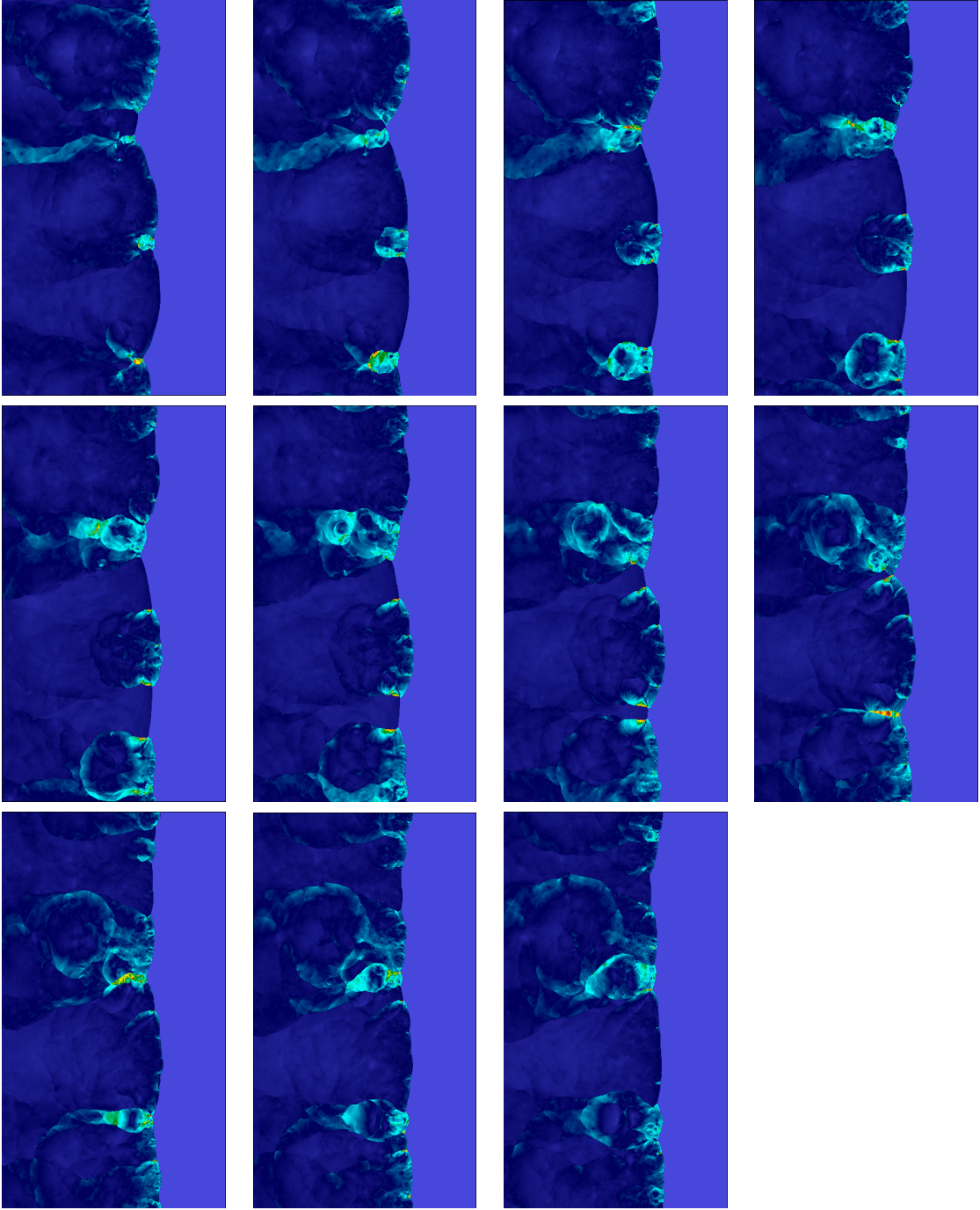


Figure 7.23: Psuedo-color nondimensional pressure results starting at  $t = 7848$  (nondim)  $= 2.367432 \cdot 10^{-4}$  sec with each result at a subsequent  $\Delta t = 72$  (nondim)  $= 2.172 \cdot 10^{-6}$  sec. Note that the maximum pressure shown has been fixed at  $p = 150$ .

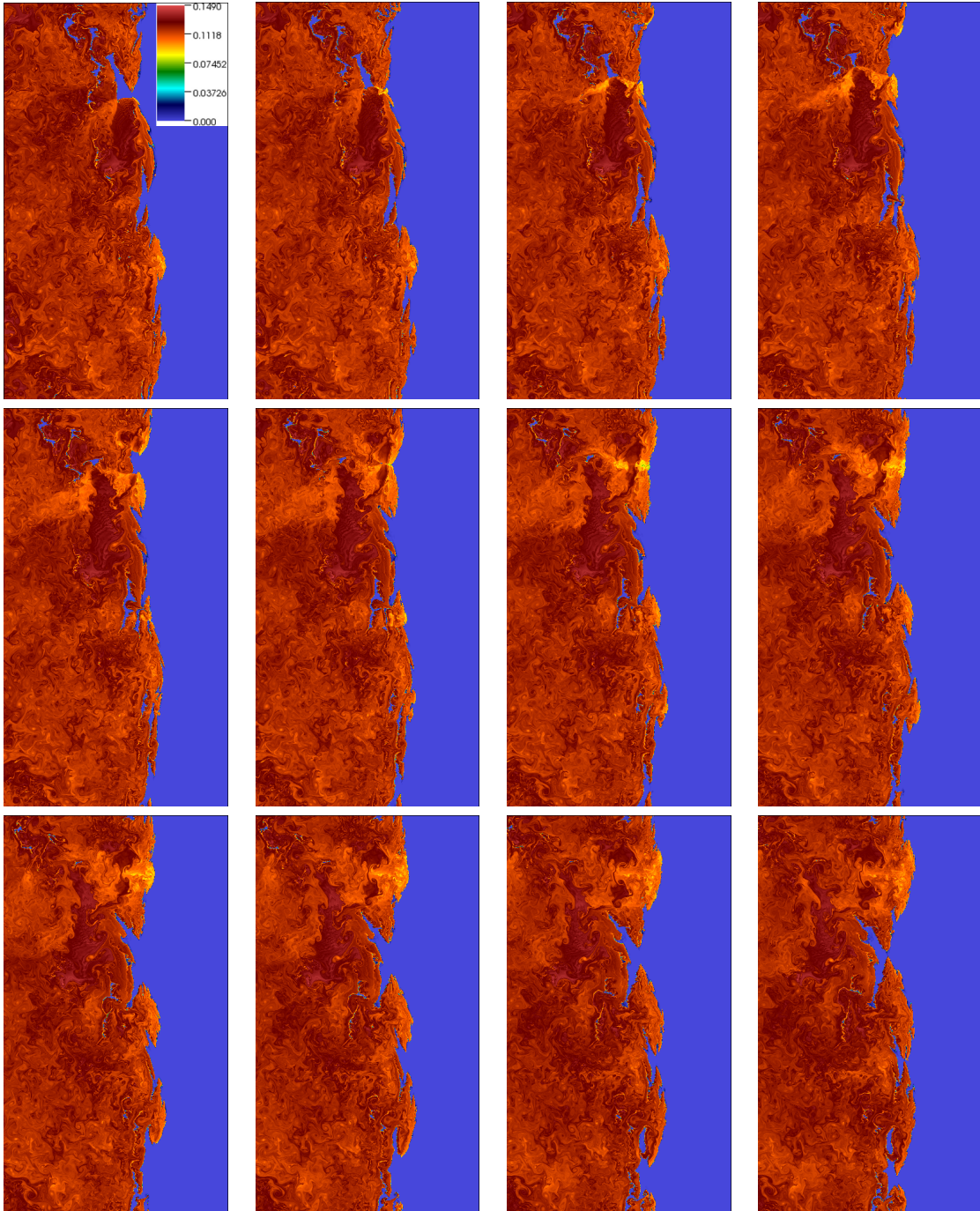


Figure 7.24: Psuedo-color  $\text{H}_2\text{O}$  mass fraction results starting at  $t = 6984$  (nondim) =  $2.106792 \cdot 10^{-4}$  sec with each result at a subsequent  $\Delta t = 72$  (nondim) =  $2.172 \cdot 10^{-6}$  sec. Note that the max fraction has be shown has been fixed at  $Y_i = 0.1490$ .



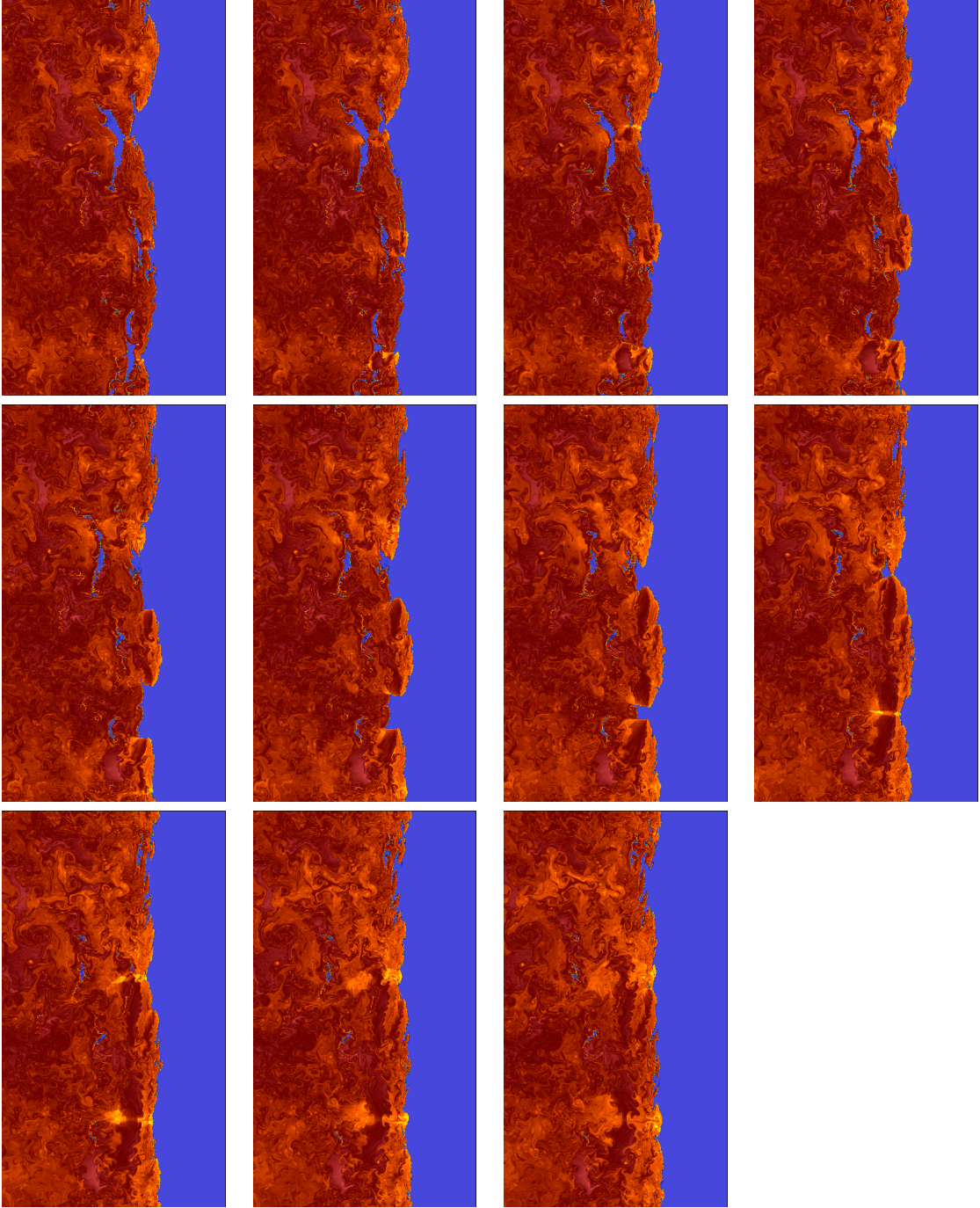


Figure 7.25: Psuedo-color  $\text{H}_2\text{O}$  mass fraction results starting at  $t = 7848$  (nondim) =  $2.367432 \cdot 10^{-4}$  sec with each result at a subsequent  $\Delta t = 72$  (nondim) =  $2.172 \cdot 10^{-6}$  sec. Note that the max fraction has be shown has been fixed at  $Y_i = 0.1490$ .

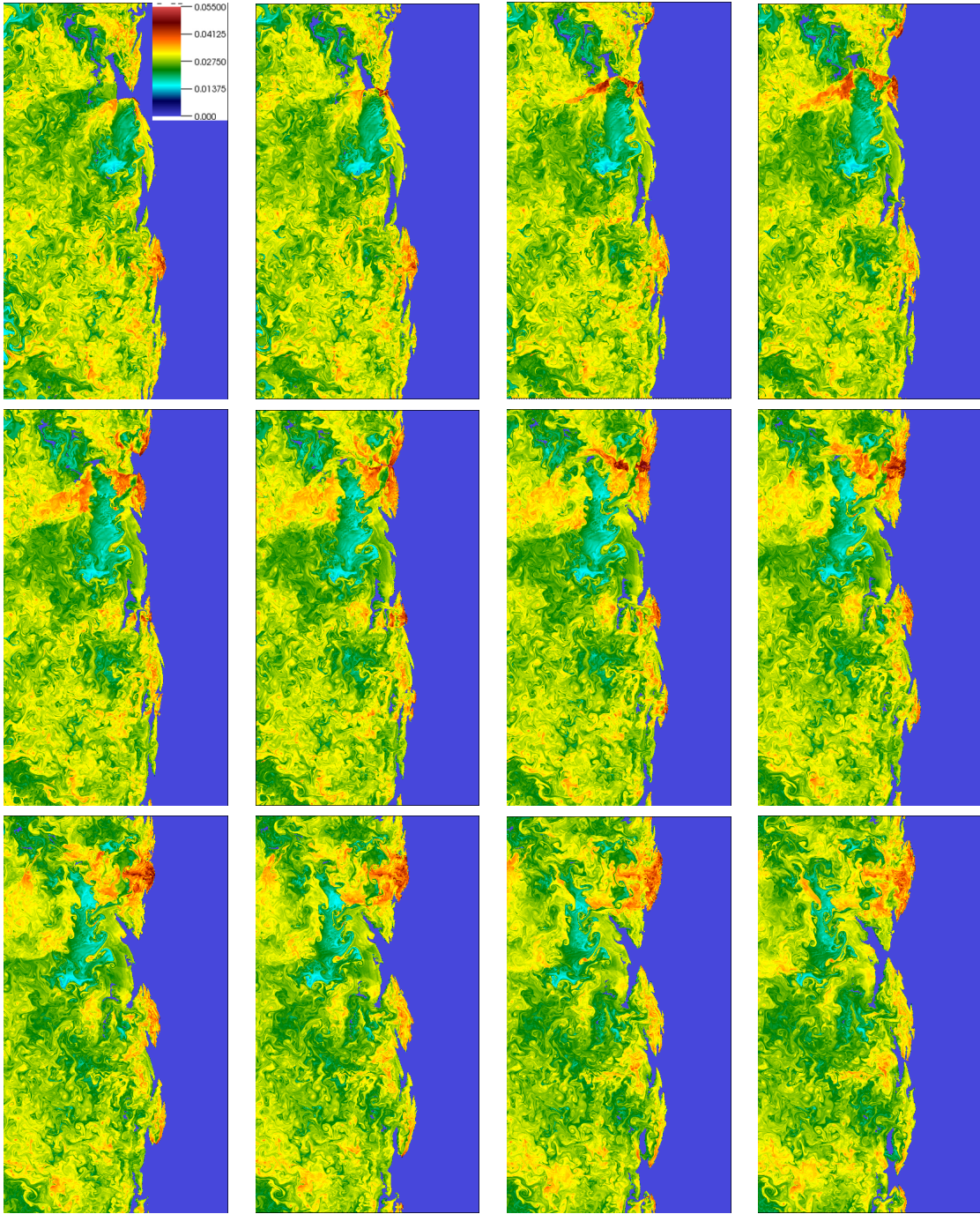


Figure 7.26: Psuedo-color OH mass fraction results starting at  $t = 6984$  (nondim) =  $2.106792 \cdot 10^{-4}$  sec with each result at a subsequent  $\Delta t = 72$  (nondim) =  $2.172 \cdot 10^{-6}$  sec. Note that the max fraction has be shown has been fixed at  $Y_i = 0.055$ .



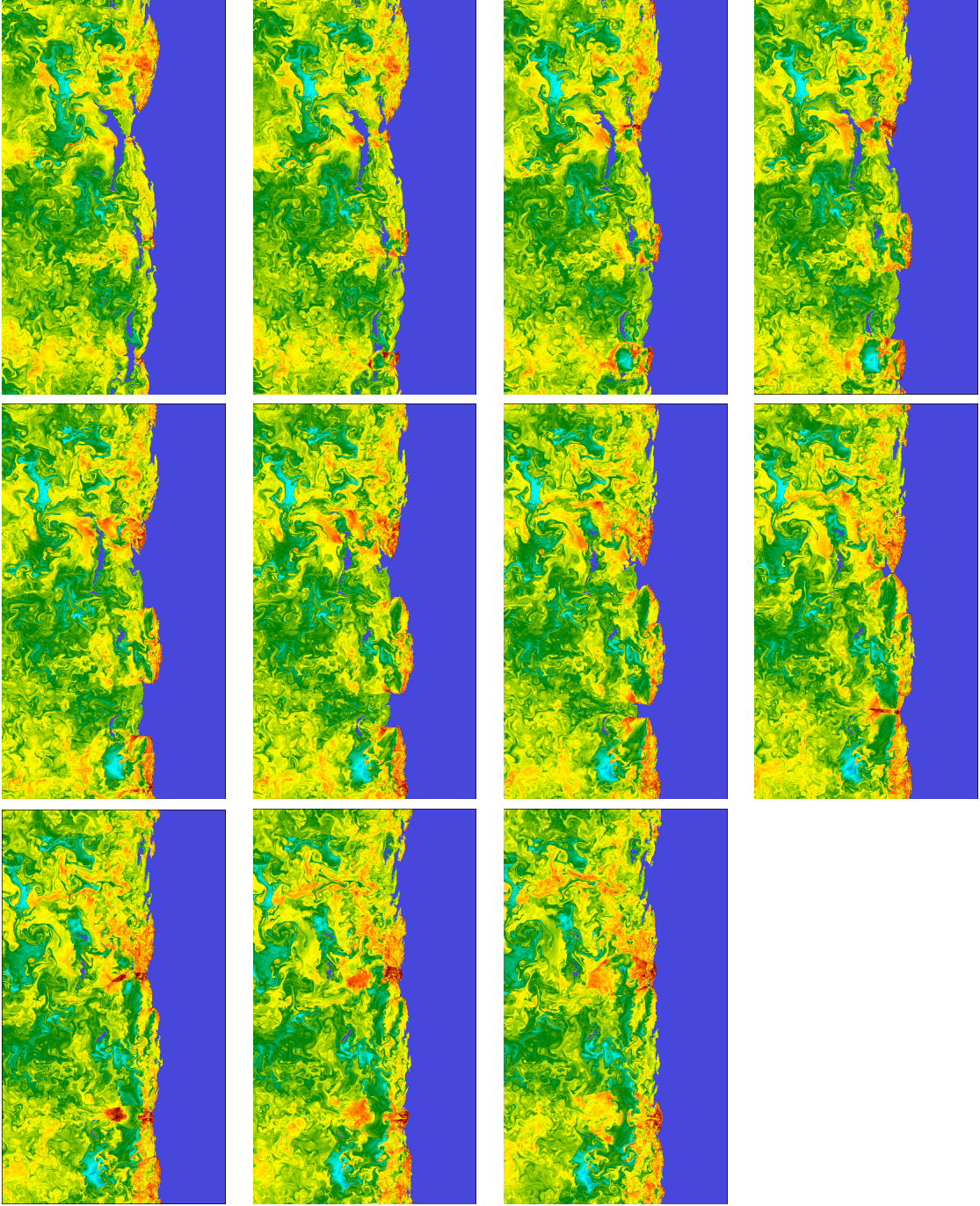


Figure 7.27: Psuedo-color OH mass fraction results starting at  $t = 7848$  (nondim) =  $2.367432 \cdot 10^{-4}$  sec with each result at a subsequent  $\Delta t = 72$  (nondim) =  $2.172 \cdot 10^{-6}$  sec. Note that the max fraction has be shown has been fixed at  $Y_i = 0.055$ .

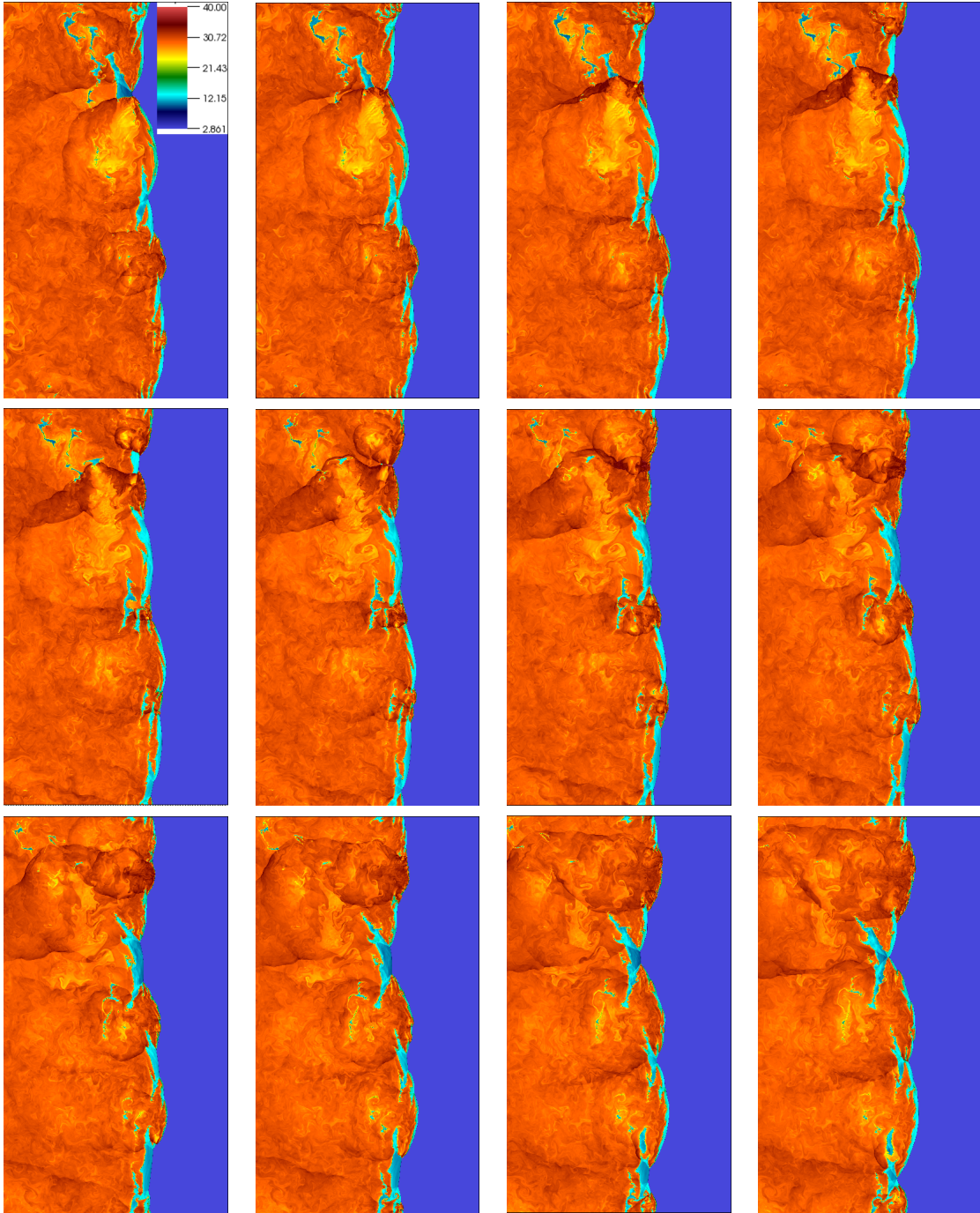


Figure 7.28: Psuedo-color nondimensional temperature results starting at  $t = 6984$  (nondim)  $= 2.106792 \cdot 10^{-4}$  sec with each result at a subsequent  $\Delta t = 72$  (nondim)  $= 2.172 \cdot 10^{-6}$  sec. Note that the maximum temperature has be shown has been fixed at  $T = 40$ .



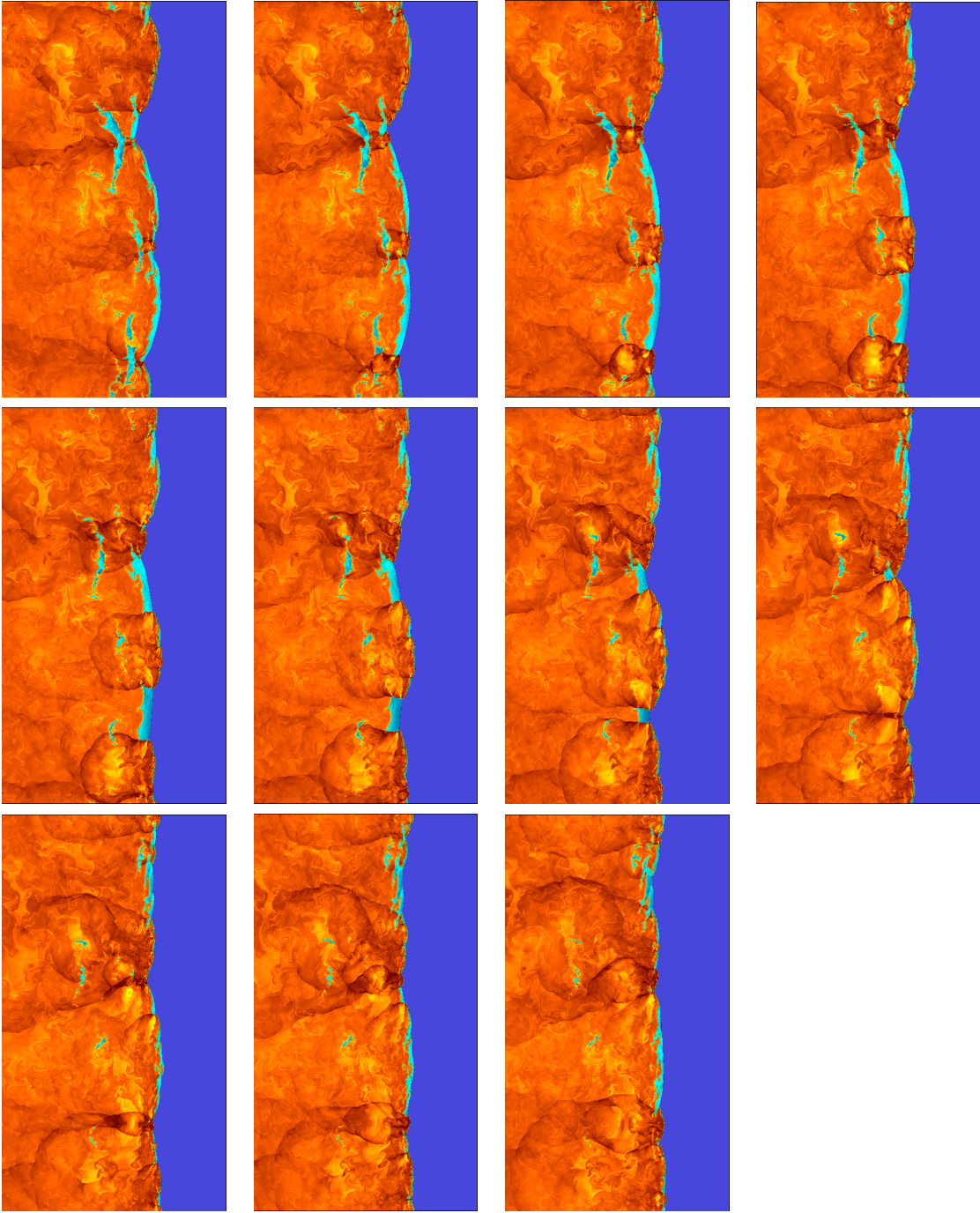


Figure 7.29: Psuedo-color nondimensional temperature results starting at  $t = 7848$  (nondim)  $= 2.367432 \cdot 10^{-4}$  sec with each result at a subsequent  $\Delta t = 72$  (nondim)  $= 2.172 \cdot 10^{-6}$  sec. Note that the maximum temperature has be shown has been fixed at  $T = 40$ .

As an example, two output steps are shown in figures 7.30 and 7.31. In figure 7.30, 5 detonation cells are clearly observed. In figure 7.31, depending on the interpretation, either 3, 4, or 5 cells exist. Looking at where the outer brackets point to, 3 fairly large cells are clearly observed. However, within the upmost cell, another cell with very strong pressure and temperature values is rapidly growing.

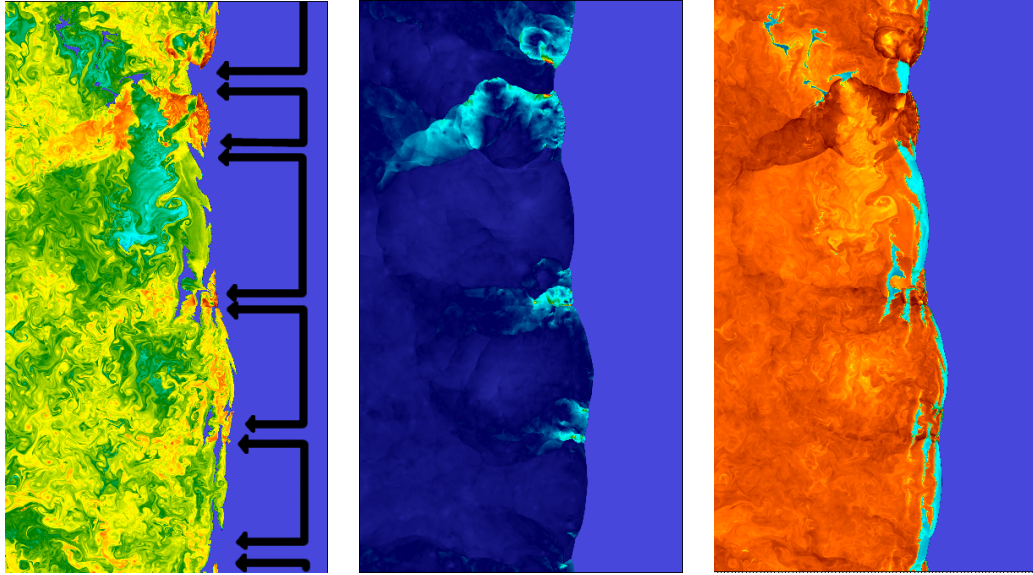


Figure 7.30: Psuedo-color OH mass fraction, pressure, and temperature. Five detonation cell regions are labeled.

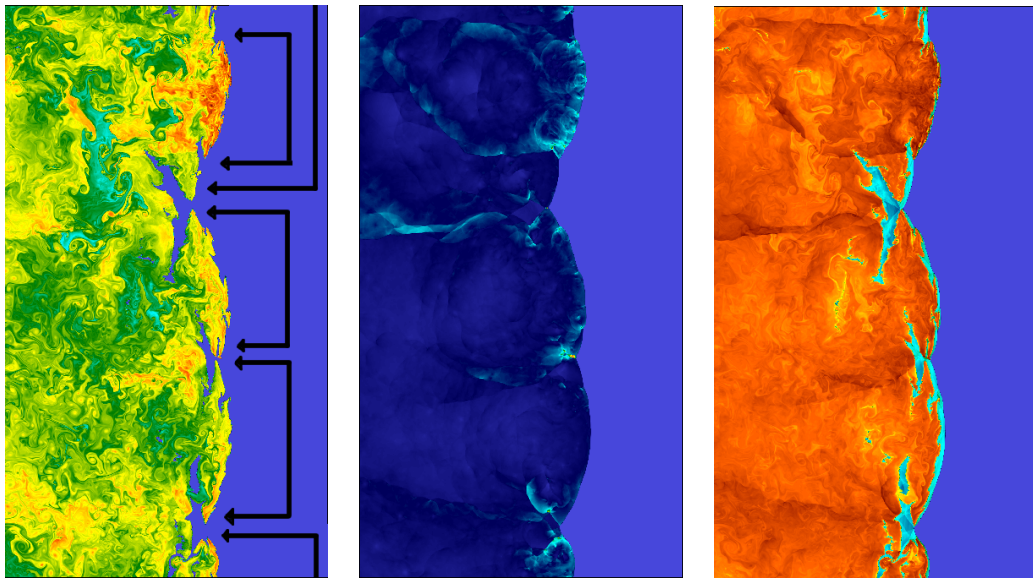


Figure 7.31: Psuedo-color OH mass fraction, pressure, and temperature. Four detonation cell regions are labeled. The top-most cell has a cell within a cell.

### 7.3.3 Chemiluminescence Comparison

A experimental comparison of another variety can also be made by considering the OH radical concentrations/temperature. Austin experimentally measured the chemiluminescence of the OH radical near the detonation front. These chemiluminescence images, some of which are shown in figure 7.32, show regions of high fluorescence intensity or hot spots where high temperature radicals are found. Comparing these to the simultaneous schlieren images indicate that the hot spots occur in the vicinity of triple-point shear layers near the end of the cell cycle. A comparison to the simulation shown in figure 7.33 is made by looking where the highest concentrations of OH are found and matching the shear layers and triple points. These high temperatures and radical concentrations occur when two strong triple points collide, engulfing a region of underdriven unreacted gas. As this gas quickly reacts from the high temperatures created by the collision and subsequent reaction, more high temperature radicals are formed into the keystone shape.

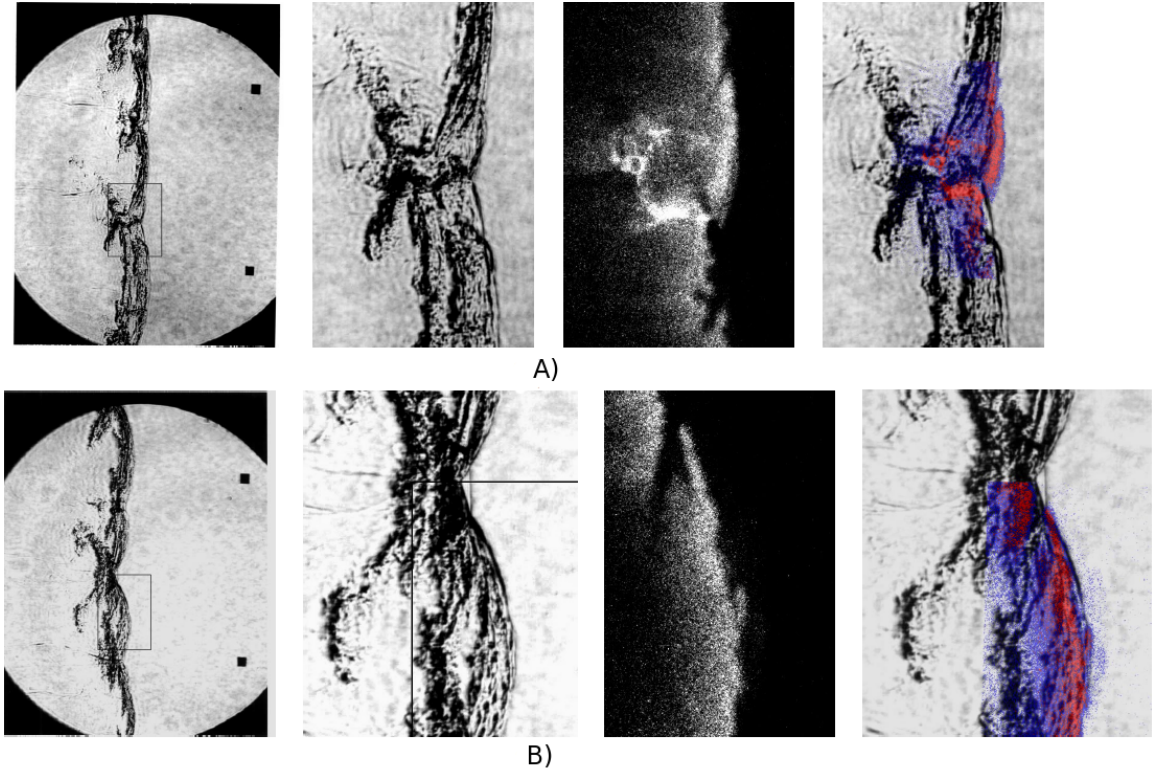


Figure 7.32: OH chemiluminescence images in figure 7.32 found in experiment by Austin (6). These can be compared to the OH mass fraction results shown in figure 7.33.



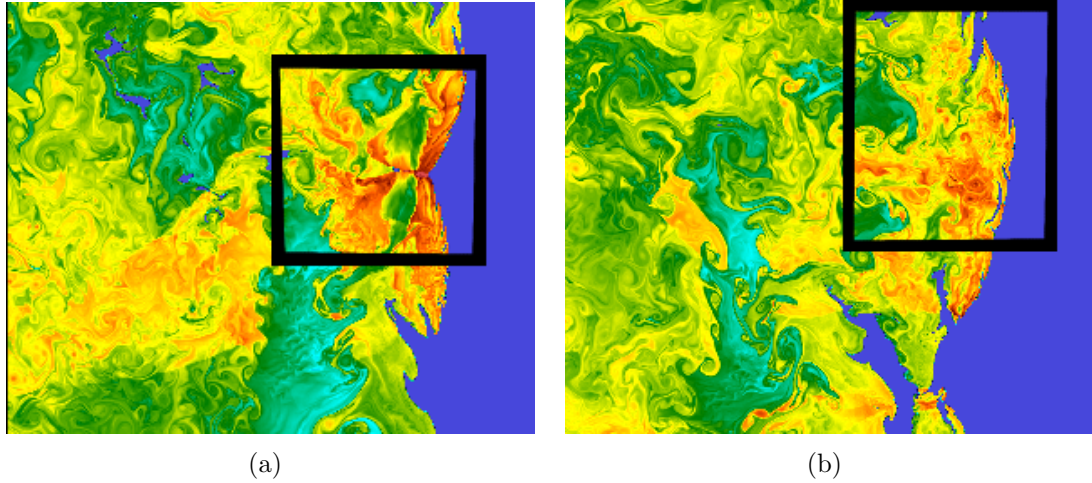


Figure 7.33: Comparing OH radical mass fraction results to the OH chemiluminescence images in figure 7.32 found in experiment by Austin (6).

### 7.3.4 Statistical Analysis

A statistical analysis of the detonation cell simulation was also carried out. By using horizontal cuts of pressure, shown in figure 7.34, at different output steps, a distribution of all encountered pressures was produced. In figure 7.35, the distribution shows the underdriven equilibrium pressures in the range of 12.5 to 15.48 (nondim). Also shown are the overdriven equilibrium pressures and the von Neumann (immediately post-shock) pressures, which range up to 200 (nondim) in the 2D pseudocolor plots. By fitting this distribution with a generalized extreme value (GEV) distribution, along the  $y = -8$  cm cut it is found to be centered at a pressure of 18.06 which is approximately equal to the equilibrium pressure, 18.111 of the initially overdriven ZND detonation. In figure ??, the distribution is centered at a slightly higher pressure of 18.4. However, looking at the range of pressures found in the distribution it is observed that the maximum pressures are much higher, showing that for this position and time range the cut travels closer through a triplepoint and/or an overdriven portion of the cell cycle.

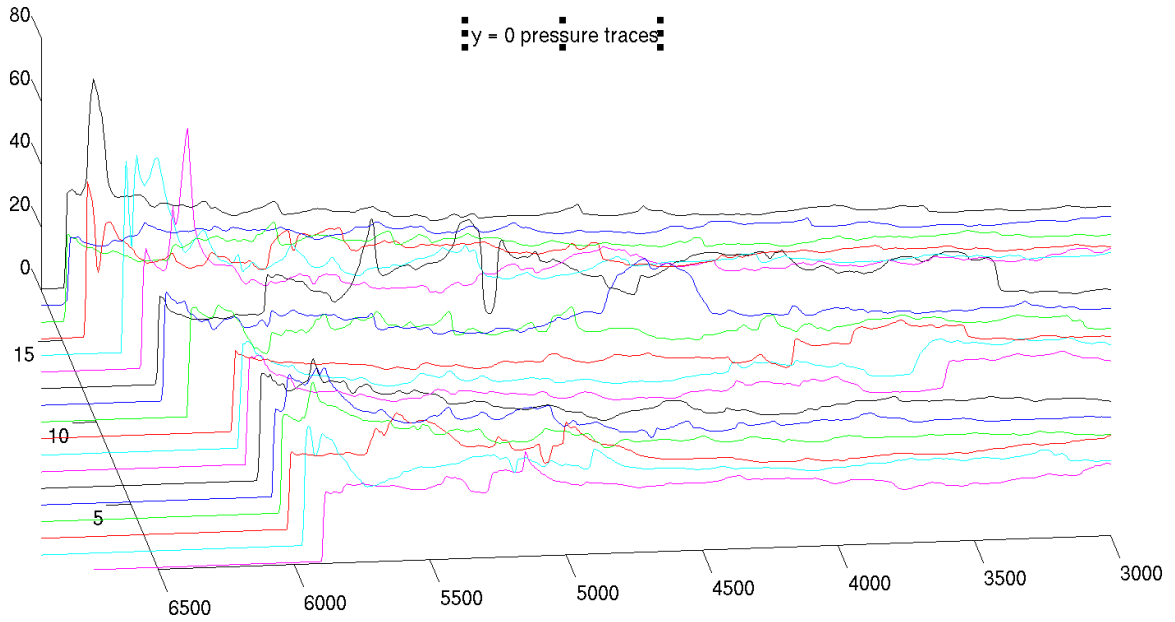


Figure 7.34: Nondimensional pressures along the  $y = 0$ ,  $x = [-6000, 3000] \cdot 10^{-3}$  cm cut for the last 18 output steps in the 16 cm wide detonation channel simulation.

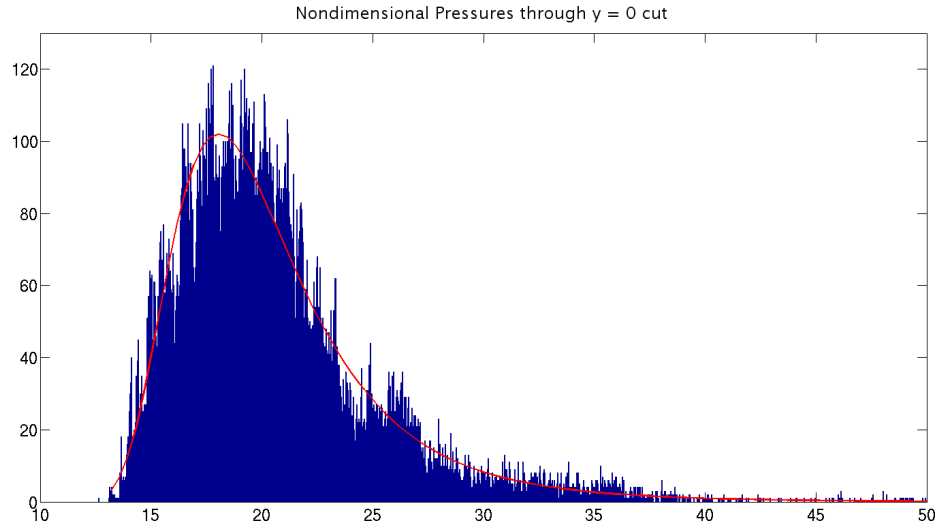


Figure 7.35: Distribution of all pressures (shown in figure 7.34) along the  $y = -8$  cm cut for the last 18 output steps in the 16 cm wide detonation channel simulation. The distribution is centered at a nondimensional pressure of 18.06 which is approximately equal to the initial overdriven ( $U/U_{CJ} = 1.008683$ ) equilibrium pressure of 18.111. The dimensional equivalents are  $4.8442 \cdot 10^5$  and  $4.8863 \cdot 10^5$  Pa.

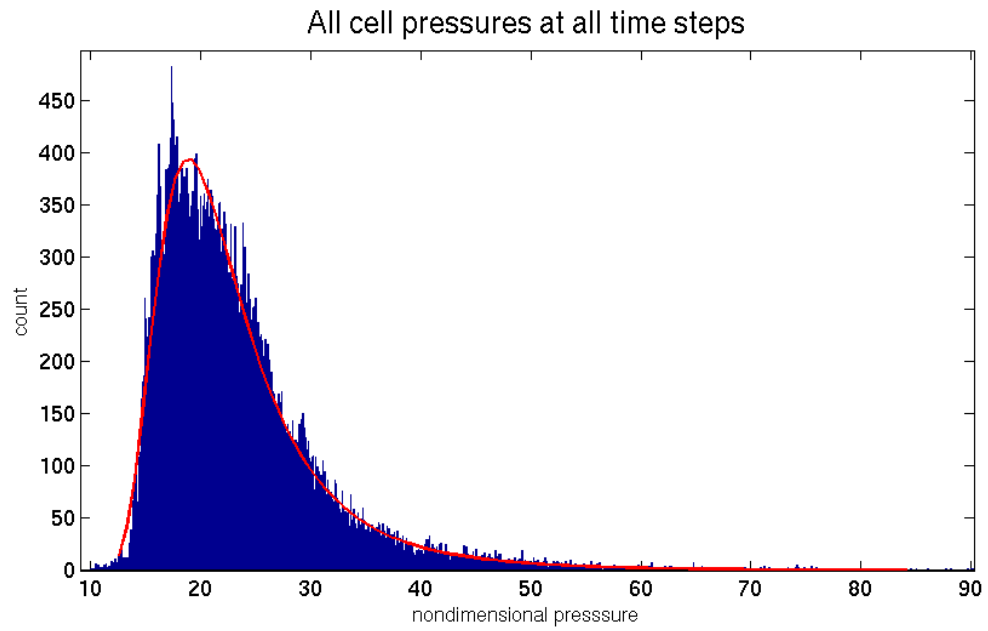


Figure 7.36: Distribution of all pressures along the  $y = 0$  cm cut for the last 18 output steps in the 16 cm wide detonation channel simulation. The distribution is now centered at a nondimensional pressure of 18.4.



## 7.4 Discussion

Simulated and compared to experiments of Austin (6) was the transition from a steady, planar, transversely periodic, ZND solution to a fully developed chaotic irregular detonation cell pattern. By comparing soot foils, schlieren, and chemiluminescence images, quantitative agreement with the experimentally dominant cell size of 45 mm was found, in addition to the qualitative comparison of the density/pressure gradients and radical concentrations.

The statistical stationarity of the multi-dimensional unsteady solution was also investigated. By “binning” and then fitting the pressure traces at different times to a probability distribution, the data was observed to be clearly centered at the equilibrium pressure of the initially slightly overdriven steady ZND solution. While having wild oscillations in pressure throughout the solution, the results on average oscillate around this pressure and hence there is an average speed for this self-sustained chaotic irregular detonation.

## Chapter 8

# Detonation Shock Bifurcation

### 8.1 Motivation

Previous researchers have investigated the interaction of reflected shock waves with boundary layers in the context of shock tube performance and it has been observed (114, 124) that interaction with the boundary layer may cause the reflecting shock wave to bifurcate into an unaffected normal shock wave and a leading shock wave or foot that travels along the tube wall. Mark developed a simple model for predicting conditions under which bifurcation will occur. However, no analogous theory has been developed for detonations and the possible role of the boundary layer in detonation reflection has received relatively little attention in past research (143). The goal of the present study is to obtain some insights into the effects of shock wave boundary layer interaction on detonation reflection in order to make more realistic models of pressure loads for structural response in finite-element simulations as well as single degree of freedom models such as used by Karnesky *et al.* (84).

Using the available experimental data for comparison at the time of 1969, Davies and Wilson (36), improved on Mark's theory of the 1950s (114). This led to a  $x^{\frac{3}{4}}$  dependence for the laminar case and a  $x^{\frac{9}{10}}$  for the turbulent case. In experiment, all cases followed a  $x^1$  dependence, therefore, the laminar theory was proven deficient.

Significant 2D simulations for a perfect gas conducted by Weber *et al.* in 1995 (159) confirmed the experimental findings in (36) for a linear dependence of foot growth, but also suggested a nonlinear dependence at greater distances from the end wall (7 cm and more). These results were conducted on a stretched grid with a second-order accurate flux-corrected transport (FCT) method. The resolution used yielded resolved results when the shock was closest to the end wall. The resolution in the vertical direction was increased by 10.5 percent with each  $\Delta x$  cell traversed

from the end wall. Therefore, their data, which was for bifurcations occurring up to 11 cm from the end wall, had a decrease in resolution from being completely resolved to extremely unresolved. Yet, some confidence was gained knowing the unresolved simulation results were started from a more resolved condition.

More recently, in the experimental work of Petersen and Hanson (124), the initial linear dependence was reconfirmed and at the close distance of 2 cm, the bifurcation process was studied in detail. One finding was that the size and duration of the bifurcated region do not depend on the test pressure for the range of pressures and mixtures of their study.

A similar problem in two-dimensions was simulated by Gamezo et al in 2001 (57) for shock-bifurcation induced DDT (deflagration to detonation transition). More recent (2005) work by Gamezo *et al.* (87) has simulated this phenomena (but in a steady frame) in three dimensions using one-step chemistry. The main 3D effect they observed in their steady RSBs (reactive shock bifurcations) attached to a 3D rectangular channel was from the presence of the second no-slip wall in a 3D rectangular channel. The two RSBs that form at adjacent walls interact with each other and produce an oblique Mach stem between two oblique shocks, when then interacts with a central Mach stem creating a hot-spot that leads to a detonation initiation.

The effects of a nonsteady shock wave boundary layer interaction on a detonation (rather than shock) reflection have had yet to be investigated for gases mixtures which require the use of detailed thermodynamics, chemistry, and transport. Also, the current mentioned simulations, while gaining basic insights, have failed to fully resolve the viscous and diffusive scales in the boundary and shear layers at scales which are comparable to experiments.

## 8.2 Ideal Detonation Reflection Model

If we are only interested in the shock for times soon after the detonation reflects, then it is possible to make some simplifying assumptions and thereby create a model for the amplitude of the reflected wave as done by Karnesky (83). One-dimensional numerical simulations of the reflecting shock (see §8.6) predict that there is a very small pressure gradient between the reflected shock and the end wall until the shock reaches the tail of the expansion. Based on this observation, we made the approximation that there is zero pressure gradient behind the reflected shock so that the pressure just behind the shock is equal to the pressure at the end wall for all times. This approximation is only valid for sufficiently short times following reflection when the shock is still in

the Taylor wave. For later times, an expansion wave will develop behind the reflected shock, and the pressure gradient cannot be neglected (35).

Assuming that the pressure  $P_R$  behind the reflected shock is known, we can use the shock jump relations (154) to find the speed,  $U_R$ , of the reflected shock. The result is

$$U_R(t) = -u(x, t) + c(x, t) \sqrt{\frac{\gamma + 1}{2\gamma} \left[ \frac{P_R(t)}{P(x, t) - 1} \right] + 1}, \quad (8.1)$$

where  $u(x, t)$ ,  $P(x, t)$ , and  $c(x, t)$  are the velocity, pressure, and sound speed just upstream of the shock, as determined by the Taylor wave solution. To use this method of computation, the pressure-time history of the shock must be known from either experimental measurement or simulation. Using the zero-pressure gradient assumption discussed above, the present results approximate the reflected shock pressure as the measured pressure history at the end wall. The pressure history is fit to a simple exponential decay of the form

$$P_R(t) = (P_{CJ,ref} - P_3) \exp\left(-\frac{t - t_{ref}}{\tau}\right) + P_3. \quad (8.2)$$

The decay constant  $\tau$  is found by fitting the measured pressure trace to equation 8.2. Combining this solution for the reflected wave with the previous analytical solution for the Taylor wave, the pressure  $P(x, t)$  within the tube is entirely specified (35).

### 8.3 Experimental Setup

Gauge distance from reflecting end, m	<b>P1</b>	<b>P2</b>	<b>P3</b>	<b>P4</b>	<b>P5</b>	<b>P6</b>	<b>P7</b>
	1.686	1.559	1.432	1.305	0.133	0.121	0.108
	<b>P8</b>	<b>P9</b>	<b>P10</b>	<b>P11</b>	<b>P12</b>	<b>P13</b>	
	0.095	0.070	0.057	0.044	0.032	0.000	

Table 8.1: Pressure gauge locations

The later numerical simulations using one-step and detailed chemistry are compared to the experimental results of Damazo (35, 84). For the purposes of examining the dynamics of the reflected waves, the specimen tube is outfitted with thirteen pressure gauges. A complete list of gauge locations is given in table 8.1. Before each experiment, the tube assembly is evacuated before being filled with stoichiometric ethylene-oxygen via the method of partial pressures to an initial total pressure of 50

kPa. Following ignition, we observe a well-formed detonation has already developed when the combustion wave reaches pressure gauge P1, indicating DDT occurs prior to any pressure measurements (35).

## 8.4 Experimental Results

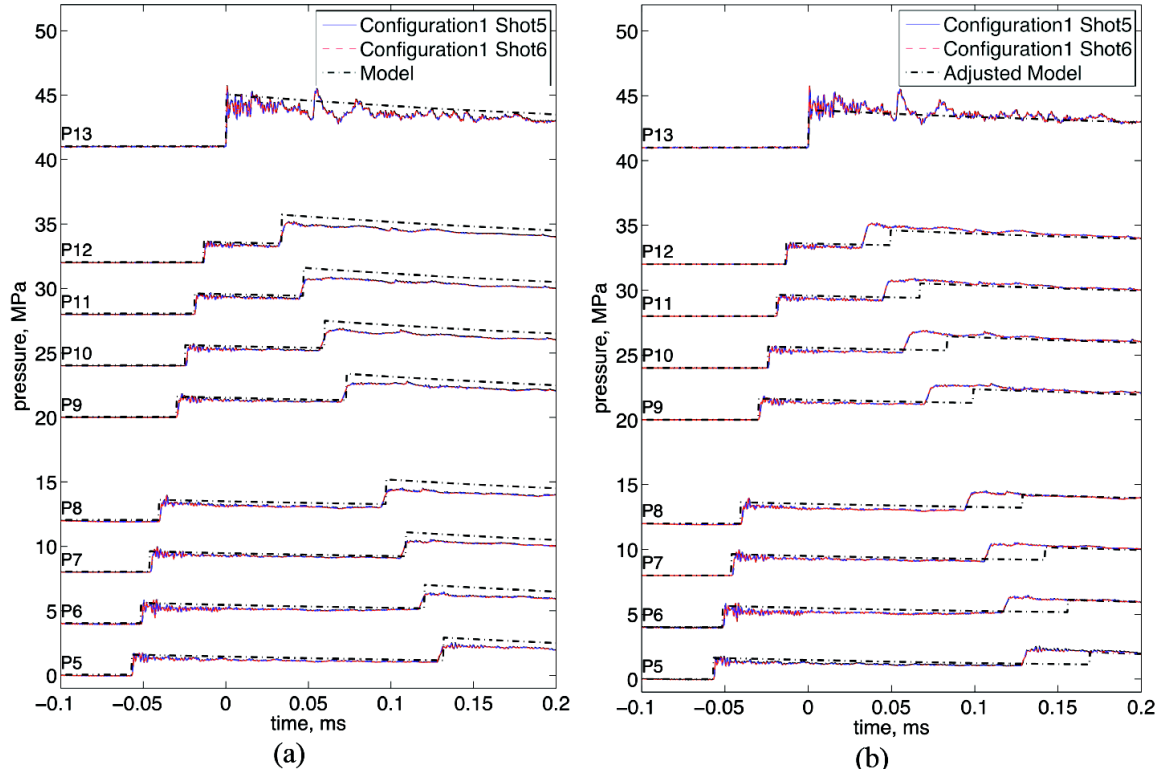


Figure 8.1: Pressure data compared to model results using two different end-wall pressure histories. Vertical offsets are proportional to the physical separation of the gauges. Reprinted from Damazo and Ziegler *et al.* (35).

figure 8.1 illustrates the typical pressure profiles observed in an experiment. The initial rise in pressure for gauges P5 through P12 marks the arrival time of the detonation. From these measurements, we can extract the detonation wave speed to be  $U_{det} = 2,348$  m/s. The theoretical CJ velocity is 2,339 m/s. Gauges P5 through P12 then track the reflecting shock wave as it travels away from the reflecting end (35).

Although we are accurately predicting the shock speed, we observe that the measured wall pressure is approximately 20 percent below that predicted by one-dimensional theory. In other words, the speed of the reflected shock wave is inconsistent with the pressure data measured at the wall of the tube. If we vary the

parameters of peak and plateau pressure to more accurately fit the recorded shock amplitudes, we get the profiles shown in figure 8.1(b). Now the pressures are accurately predicted, but the shock speed is not. It is also noteworthy that the measured rise time of the pressure of the reflected shock is slower than expected, four times longer than the rise time of the incident detonation wave (35).

These discrepancies suggest that the pressure is not uniform across the tube and the shock waves are not one-dimensional. One possible reason for these discrepancies is the viscous boundary layer that will be present at the tube wall. The reflected shock wave may be interacting with the boundary layer to create a multi-dimensional wave front near the reflected end. Such effects have been observed in shock tubes where interaction of the reflected shock wave with the boundary layer set up by the incident shock results in separated flow with an oblique shock in the boundary layer leading the main reflected wave (114, 124).

## 8.5 Reflected Shock Wave-Boundary Layer Interaction

A sketch of reflected shock wave-boundary layer interaction is shown in figure 8.2. The incident detonation induces a velocity in the fluid. The no-slip condition requires the velocity to be zero at the wall and thus a boundary layer is created. The reflected shock wave propagates into the flow outside the boundary layer in an essentially one-dimensional fashion. Near the wall, the combination of low-speed fluid in the boundary layer and the pressure rise across the reflected shock wave can result in the separation of the flow. A system of oblique shocks is created to equilibrate the pressures in the region next to the end wall. The leading portion of the reflected shock wave that passes through the boundary layer (shock wave O in figure 8.2 is an oblique wave and a reflected wave (R) is observed where this joins the normal (N) shock wave. This configuration resembles the shock bifurcation or lambda shock observed in the more familiar process of shock wave-boundary layer interaction in supersonic steady flow. Experiments in nonreacting flow show that boundary layer separation and oblique shocks only occur under certain conditions. Mark (114) developed a simple criterion for when shock waves bifurcate. He theorized that bifurcation will occur if the stagnation pressure in the boundary layer in the shock-fixed frame is less than the pressure behind the normal shock. When using this criterion, it is necessary to determine the Mach number of the reflecting shock wave in the boundary

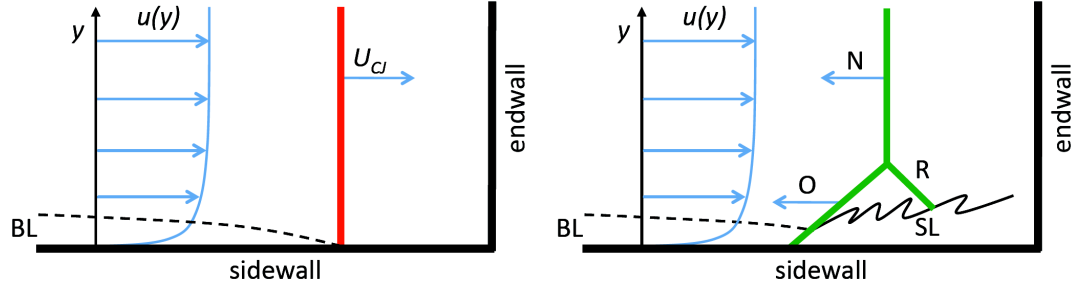


Figure 8.2: Schematic of flow for bifurcated shock wave. Reprinted from Damazo and Ziegler *et al.* (35).

layer. When we attempt to apply this to reflecting detonations, we encounter a serious difficulty because of the temperature dependence of the sound speed and the Mach number with distance from the wall. Mark considered relatively weak shock waves and assumed that the sound speed within the boundary layer remains constant. However this assumption is not valid in the case of reflecting detonations due to the large temperature variations within the boundary layer. To resolve this issue and investigate the conditions under which boundary layer separation occurs for detonation reflection, it is necessary to consider the unsteady interaction of the reflected shock wave with a compressible viscous flow, described in the following two sections.

In the first §8.6, a two-component perfect gas model of the reactive Navier-Stokes was used with temperature dependent transport properties. This model helped gain some basic insights for the detonation bifurcation problem. In the next §8.7 a reduced mechanism was used to simulate the detonation bifurcation problem with detailed chemistry and transport. Also simulated were shock bifurcation problems with isothermal boundary conditions.

## 8.6 Computational Results: Simple Two-Component

In the simplified preliminary simulations, two types of simulations were performed. A nonreactive, one-dimensional Euler (inviscid) simulation was carried out in order to have a reference solution for comparison to experiments and the full two-dimensional, viscous simulations. The main simulations were two-dimensional viscous compressible reactive computations of an incident detonation wave reflecting from a planar end wall and also setting up a boundary layer on the sidewall. No-slip adiabatic boundary



conditions were used on the bottom and right walls, inflow conditions on the left, and outflow on the upper right boundary. At  $t = 0$ , the fluid adjacent to the wall has a nonzero velocity, and thus there were start up errors from causing the boundary layer to form in this manner. It is assumed that these errors are small enough to be neglected and do not overly influence the general bifurcation structure. Both simulations used simplified models of the chemical reaction process and considered idealized detonation waves with reaction zones, but using parameters that did not result in unstable detonation fronts. Although highly idealized, we believe that these models do provide insight into the key physical processes.

A simple thermo-chemical mechanism was designed to model a  $\text{H}_2$ ,  $\text{O}_2$ , Ar detonation with mole ratios of 2, 1, and 7 at a state with a pressure and temperature of 50 kPa and 298 K. Using a high temperature extension of the GRI30 mechanism in CANTERA and the [Shock and Detonation Toolbox](#), a ZND solution was calculated with detailed chemistry. A fitting procedure was used together with this solution to determine approximate parameters for a one-step Arrhenius model with simple depletion rate for the modeled chemical reaction. For this two-species model, the total energy is defined by the heat release per unit mass parameter,  $q$ . Viscosity, conductivity, and mass diffusion were calculated by the Sutherland model (162).

The approximate two-species mechanism properties were fitted to match the detailed mechanism's ZND solution properties at one-half the reaction length. The gas and chemistry parameters used are given below in table 8.2. These values correspond to a post shock von Neumann pressure of approximately 1.42 MPa and detonation shock speed of  $U_{shock} = 1774$  m/s. The reference values for viscosity, thermal conductivity, and mass diffusion were selected by matching values at the end of the reaction zone. This yields the following reference properties:  $T_{ref} = 2700$  K,  $\mu_{ref} = 1.07 \cdot 10^{-4}$  Pa·s,  $k_{ref} = 0.148$  W/(m·K),  $D_{ref} = 6 \cdot 10^{-4}$  m<sup>2</sup>/s.

$T_{amb}$ , K	$P_{amb}$ , kPa		$W$ , kg/mol	$q$ , J/mol	$E_a$ , J/mol	$A$ , s <sup>-1</sup>
298	50	1.4333	0.031	43000	30000	125000

Table 8.2: Gas and chemistry parameters used in computations.

Shown in figure 8.3 is the comparison between the 1D reactive Euler simulations and the approximate analytic pressure model. As assumed in the simple model, the gradient in pressure between the shock and the end wall is extremely small and the model approximations are reasonable. Overall, the agreement of the model and the one-dimensional inviscid calculations are reasonable. As found with the experimental results, both the reflected shock speed and the reflected shock amplitude could not

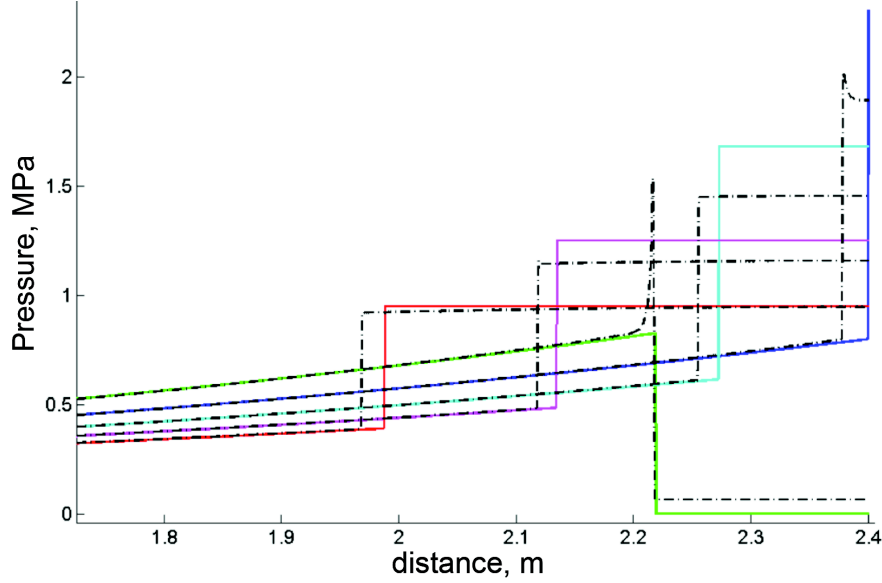


Figure 8.3: Comparison of the approximate pressure model,  $P_R(x)$  to the 1D reactive Euler simulation of the TZ wave for a tube of length 2.4 meters with  $\tau = 3000$ , and a reflected shock pressure of 2.45 MPa, the approximate reflected value for the CJ post detonation state (the reflected von Neumann state is 8.86 MPa).

be exactly matched.

The 2D simulations were carried out using the ZND initial condition starting in a domain of 40x40 mm. Four mesh refinement levels were used, for which case the smallest cell size was  $7.8 \cdot 10^{-3}$  mm. These results were not fully resolved, however, enough cells were used across the boundary layer to gain insight into the overall flow properties.

figure 8.4 clearly shows that the boundary layer separates and a bifurcated reflected shock wave develops. The basic structures discussed earlier in connection with nonreactive shock waves are clearly visible. These include the oblique shock propagating ahead of the main wave that is slightly curved and a reflected oblique wave extending from the triple point nearly to the wall. A series of vortices are visible near the wall and appear to be the result of the rolling up of the vortical boundary layer fluid. A number of weak shock waves can be observed propagating away from the interaction region toward the center of the flow.

As shown in figure 8.5 the pressure at the wall is significantly different than either the pressure in the center of the flow or the reference inviscid solution. The pressure at the wall clearly shows the lower amplitude oblique shock wave propagating ahead of the normal shock in the core flow. A series of pressure oscillations are visible which

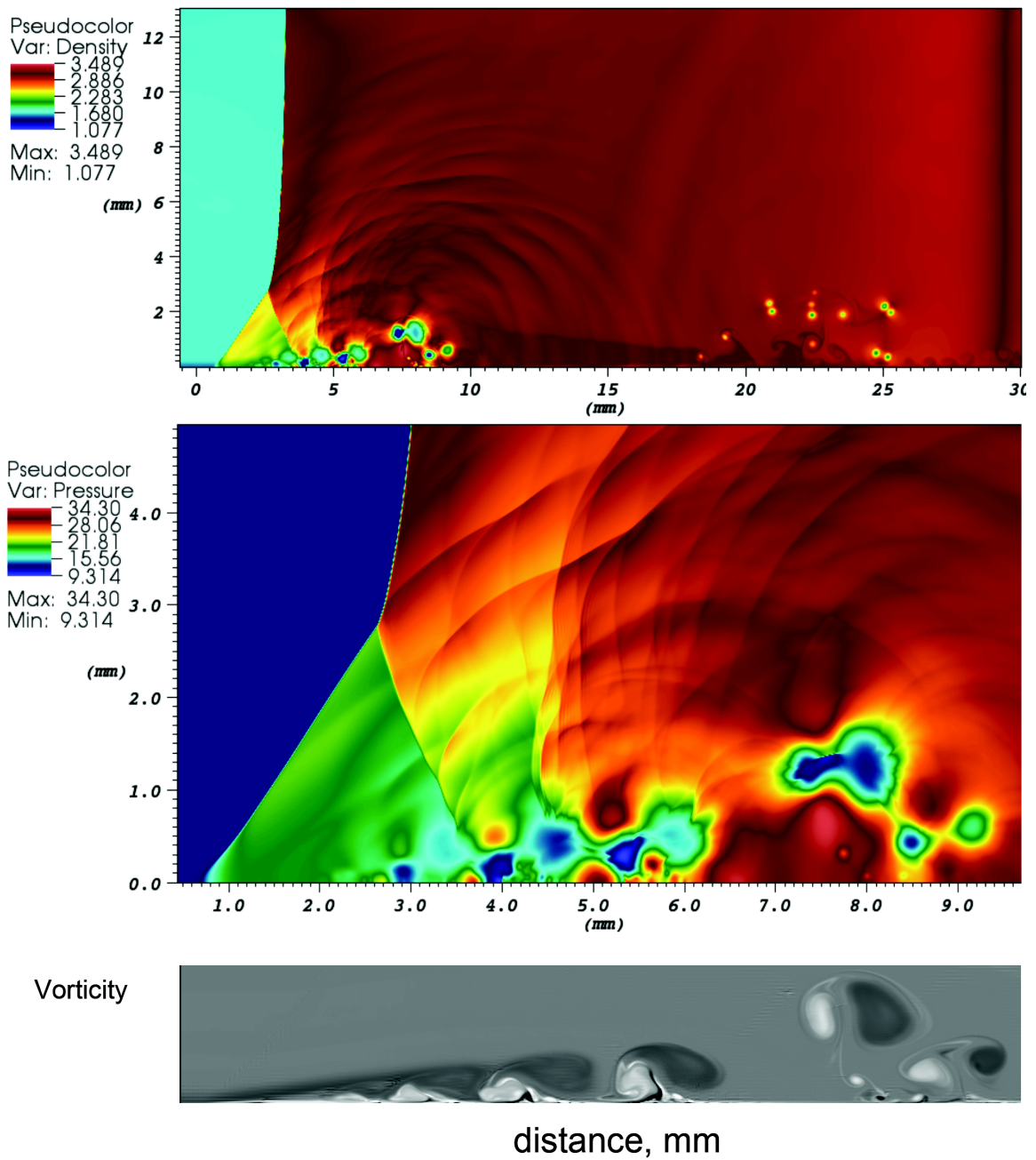


Figure 8.4: 2D reflected detonation: Density, pressure, and vorticity pseudo-color plots (nondimensional units) of the shock bifurcation from a detonation reflection at 50 kPa initial pressure. The reflecting end wall is at  $x=30$  mm.

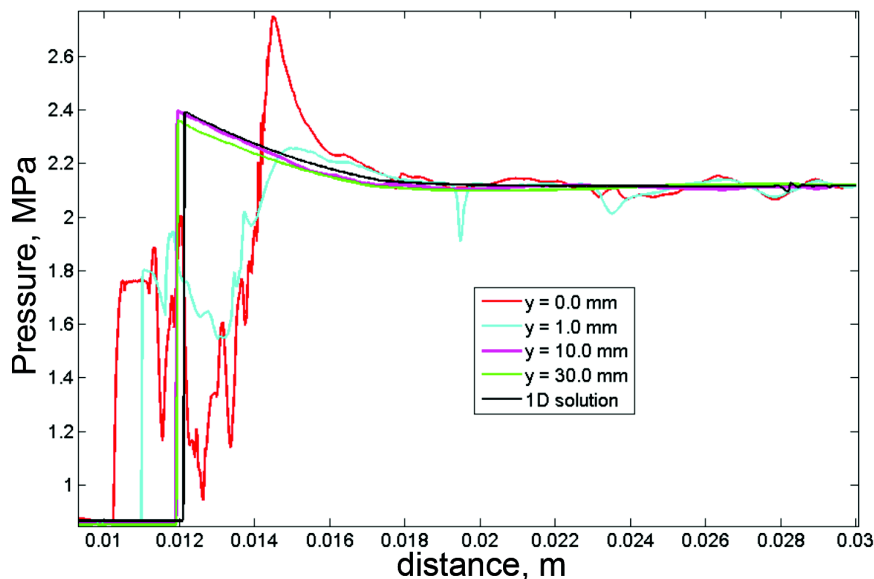


Figure 8.5: Pressure traces at the heights of 0, 1, 10, and 30 mm from the wall  $2.56 \cdot 10^{-5}$  s after reflection.

appear to be associated with the vortices moving along the wall and are terminated by a sharp rise associated with the reflected shock wave of the triple point. The amplitude and timing of the one-dimensional inviscid solution is in good agreement with the wave form in the core of the two-dimensional viscous flow. This indicates that at this particular time, the viscous effects are still confined to the walls. The pressure traces shown in figure 8.1 confirm our speculations regarding the potential effects of reflected shock-boundary layer interaction on side wall pressure histories.

## 8.7 Computational Results: Detonation and Shock Bifurcation with Detailed Chemistry and Transport

Comparison's between simulations and experiments of Damazo were conducted for  $\text{H}_2\text{-N}_2\text{O}$  detonation and shock reflections. The purpose of this study was to demonstrate how different sizes and shapes of bifurcations result for different mixtures. The mechanism used is a reduced version of the original 1989 Miller-Bowman  $\text{H}_2\text{-N}_2\text{O}$  mechanism and is listed in appendix E.2. This reduced mechanism has 14 species ( $\text{H}_2$ ,  $\text{N}_2\text{O}$ ,  $\text{O}$ ,  $\text{O}_2$ ,  $\text{OH}$ ,  $\text{H}_2\text{O}$ ,  $\text{HO}_2$ ,  $\text{N}$ ,  $\text{H}$ ,  $\text{NO}$ ,  $\text{HNO}$ ,  $\text{N}_2$ ,  $\text{NH}$ ,  $\text{N}_2\text{H}$ ) and 19 reversible reactions. It has been matched to a range of induction times and temperatures found

in ZND solutions at overdrives 0.8 to 1.4.

In experiments of Damazo, shock bifurcations were compared for 3 different cases: a  $\text{H}_2\text{-N}_2\text{O}$  detonation, a  $\text{N}_2\text{O}$  shock wave at an incident Mach number of 2.7, and an air shock wave at Mach number of 2.2. Experimental/numerical comparisons of these are shown in figures 8.6, 8.7, and 8.8. The detonation simulation is an initially underdriven steady ZND wave, matching the same speed found in the experiment, 15 kPa. The initial detonation Mach number is 5.9 (underdriven, incident speed 1670 m/s, which is 7 percent below the CJ speed of 1804 m/s).

These cases are summarized in table 8.3 below.

mixture	ambient p (kPa)	Mach #	$\rho_{vN}$ (kg/m <sup>3</sup> )	$p_{vN}$ (Pa)	$T_{vN}$ (K)	$u_{vN_{fluid}}$ (m/s)
Air	25	2.2	0.868	137,500	550	256
$\text{N}_2\text{O}$	15	2.7	1.183	123,000	550	163
mixture	ambient p (kPa)	Mach #	$\rho_{vN}$ (kg/m <sup>3</sup> )	$p_{vN}$ (Pa)	$T_{vN}$ (K)	$u_{shock}$ (m/s)
$\text{H}_2\text{-N}_2\text{O}$	15	5.9	2.08	609,300	1,403	1,670 m/s

Table 8.3: Summary of bifurcation simulations.

In the next §8.7.1, schieren images for each of these three cases is compared to unresolved simulations with two different solid wall boundary conditions, isothermal and adiabatic. In the following §8.7.2, large-scale temperature and pressure results are dicussed in detail. Next, in §8.7.3, resolved smaller scale simulations of all the cases are shown and discussed. In this results the viscous/diffusive scales range from be completely resolved to marginally resolved as the bifurcation process is analyzed from immediate reflection to cm sized scales. In §8.7.4, the exact geometry of the feet from the simulations is analyzed, plotted, and compared to Mark's original three-shock theory for shock bifurcations. Lastly, in §8.7.5 pressure traces through the large-scale bifurcations are analyzed and their influenced on experimental pressure measurements is discussed.

### 8.7.1 Schlieren vs. Multi-Component Simulation Comparisons

In figures 8.6-8.8, large-scale simulations (2D psuedo-color density plots) are compared with schlieren images from experiments of Damazo. In these simulations for the nonreactive shock cases, two different wall boundary conditions were used, adiabatic and isothermal. As suspected, the isothermal results agree better with experiment. For the reactive detonation case, only the adiabatic wall condition was used, however, agreement with experiment was still found. It must be noted that in all of these large-

scale simulations, the viscous/diffusive scales are very unresolved. This simulations used on the order of 50 cores for a week at a time. To even marginally resolve one of these large scale simulations, a supercomputer using on the order of 1000 cores running for the same time would required.

Starting with the air comparison in figure 8.6, the foot shape and size in the isothermal simulation matches that found in experiment. A slight difference is the convex curvature in the reflected shock of the simulation. It is surmised that this is due to two different effects, possibly the vertical domain isn't large enough and the pressure wave from the boundary layer is reflecting off the upper boundary, and/or there is not enough resolution in the simulation. A simulation result using the adiabatic wall boundary condition is also shown, and for this case the size and shape of the foot is found to be vastly different from the simulation result. However the noncurvature of the reflected shock has been restored.

In the next comparison for  $N_2O$  shown in figure 8.7, excellent agreement is again found for the isothermal wall case. The height of the foot and the angle of the foot are similar to the experimental image. Also, in both images curved pressure waves and a shear layer are seen emanating from the foot. The foot in this case now resembles the foot found for air's adiabatic wall case. For the  $N_2O$  adiabatic wall case, the foot is massive, being two times larger than the isothermal case in height and in length. The angle of the foot is also markedly smaller.

For the last case shown in figure 8.8, the  $H_2$ - $N_2O$  detonation bifurcation is similar to the experimental image. The feet in both images are small, however, they have a different shape, for example, the simulation result has a much larger foot angle and a shorter foot height. Yet, interpretation of the experimental image in this case is difficult as either the foot has a very large angle and a relatively large height, or what seems to be the foot could actually just be the curved reflected shock, and the actual foot is very small and in the boundary layer region where the schlieren shows too dark of a contrast to pick out features.

One would expect that with an isothermal boundary condition, the trend which was found for the nonreactive shocks would continue, with the result being that the foot angle would increase and the height of the triple point would also decrease. Unfortunately, simulating a detonation along an isothermal solid wall is beyond the current implementation AMROC and the ghost fluid boundary condition. This is due to the difficulty of having both extremely large temperature and density gradients and the requirement of 6 ghost cells cells when using 6th-order diffusive stencils. This problem is made even more difficult when detailed thermodynamics is used as

most thermodynamic enthalpy polynomials are only defined to  $T = 300$  K, and lower temperatures are needed when using a symmetry boundary condition with ghost cells. Despite these difficulties some insight can still be gained by studying the Adiabatic wall case.

### 8.7.2 Temperature and Pressure Results: Large-Scale Bifurcations

More results, now for the temperature and pressure are shown in figures 8.9, 8.11, and 8.13.

For the air and  $N_2O$  case the isothermal and adiabatic cases can be compared in even more detail. One obvious difference is that the maximum temperature and pressure is about 20 percent higher in adiabatic case. The viscous dissipation of the boundary layer heats the fluid and this heat stays in the fluid in the adiabatic case.

For the detonation case, in figure 8.13c), the mass fraction of  $H_2O$  is shown. Here, one finds for the detonation case that behind the reflection and in the boundary layer, chemical equilibrium has still not been reached. However, in the top part of the foot, due to the high temperatures from passing through the shock, there are more products. It is presumed that these different compositions influence the shape of the bifurcation.

In these large-scale (approximately 5 cm from reflection) simulations, the initial boundary layer is only marginally resolved, and there are start-up errors which bounce across the domain. We assume that these are small and do not change the overall solution. To remove these errors one would have to use a recirculating boundary layer, where a solution point is recycled and used on the left boundary. Also, the Taylor waves (due to the velocity being zero at the left tube end) behind the detonation and shock waves have been neglected. An additional effect that makes the simulations and experimental results different is three dimensionality. The shocks and shear layers are fuzzy because they are integrated (by the camera) across the tube. There are also shocks and boundary layers on the outer sides (windows) of the tube.



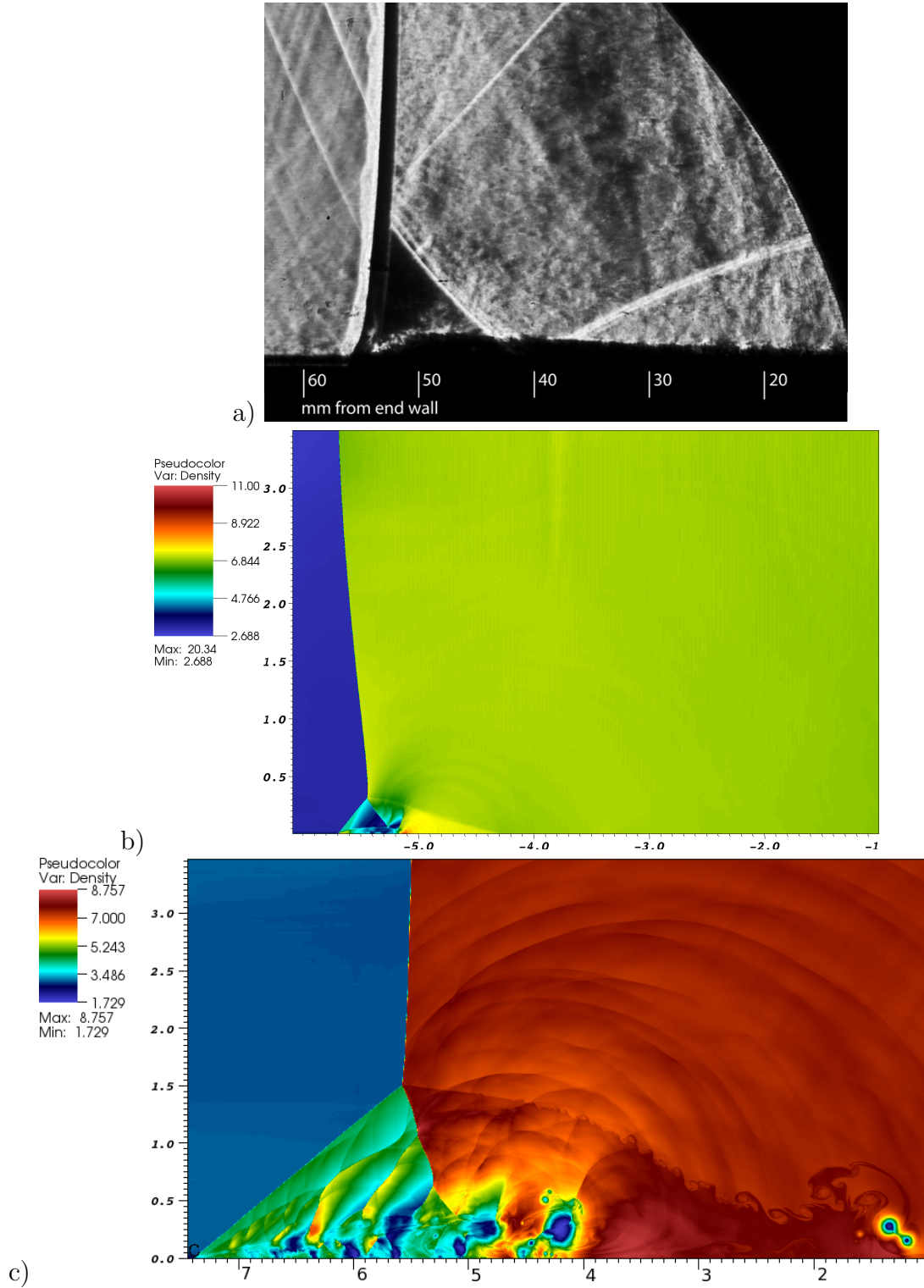


Figure 8.6: Air at 25 kPa. Mach number is 2.2. a) is a schlieren image. b) (isothermal BC) and c) (adiabatic BC) is a pseudo-color plot of the nondimensional density at the same scale and distance from the end wall. Here the end wall is at  $x=0$  cm. For this simulation the shock wave was started at  $x = 7$  and the domain is of size  $x = (14, 0)$  cm and  $y = (0, 7)$  cm. There were 3 refinement levels (2,2,2) (4 levels total) with a base grid of size [800,400] cells.

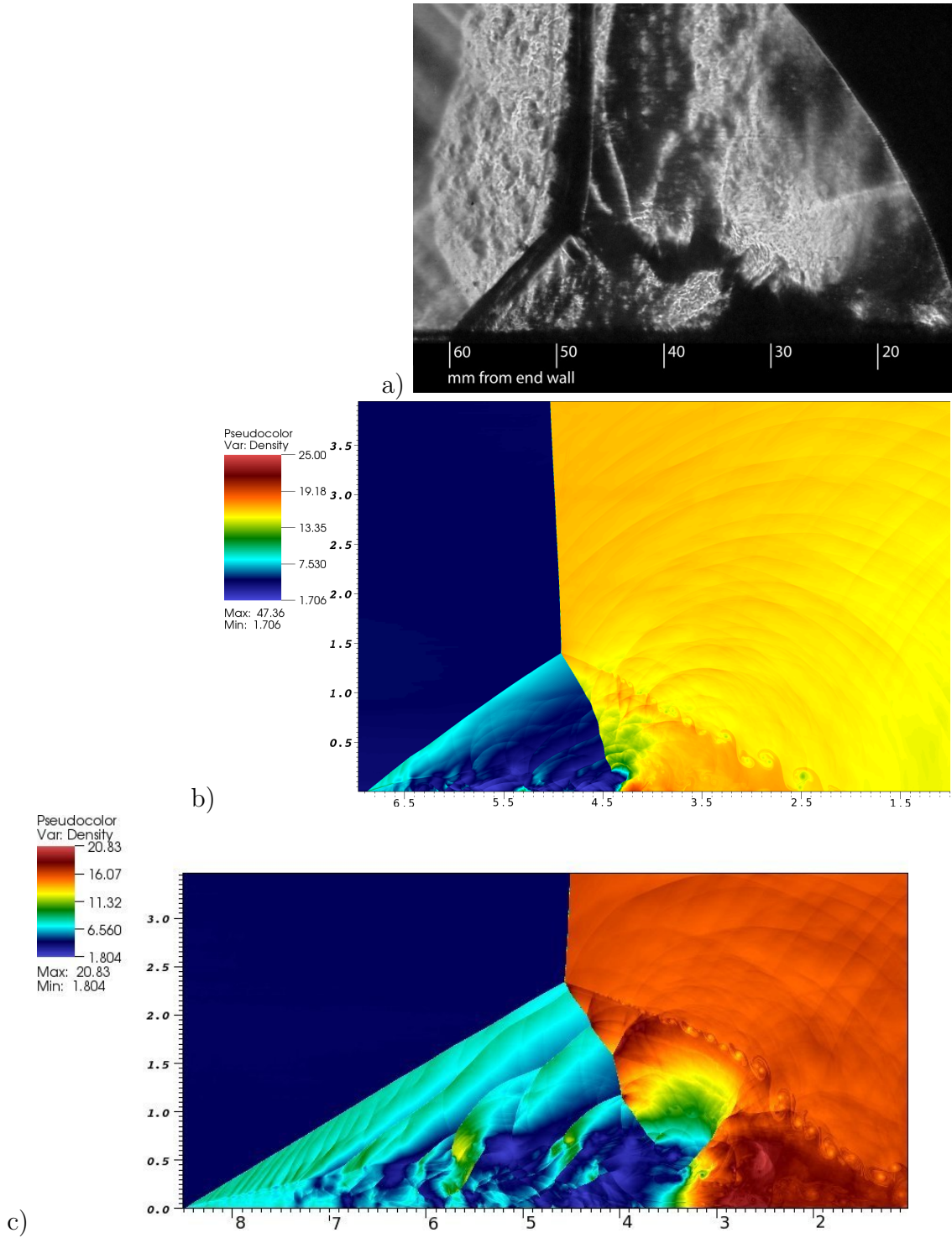


Figure 8.7:  $\text{N}_2\text{O}$  at 15 kPa. Mach number is 2.7. a) is a schlieren image. b) (isothermal BC) and c) (adiabatic BC) is a pseudo-color plot of the nondimensional density at the same scale and distance from the end wall. Here the end wall is at  $x=0$  cm. For this simulation the shock wave was started at  $x = 7$  and the domain is of size  $x = (14, 0)$  cm and  $y = (0, 7)$  cm. There were 3 refinement levels (2,2,2) (4 levels total) with a base grid of size  $[800, 400]$  cells.

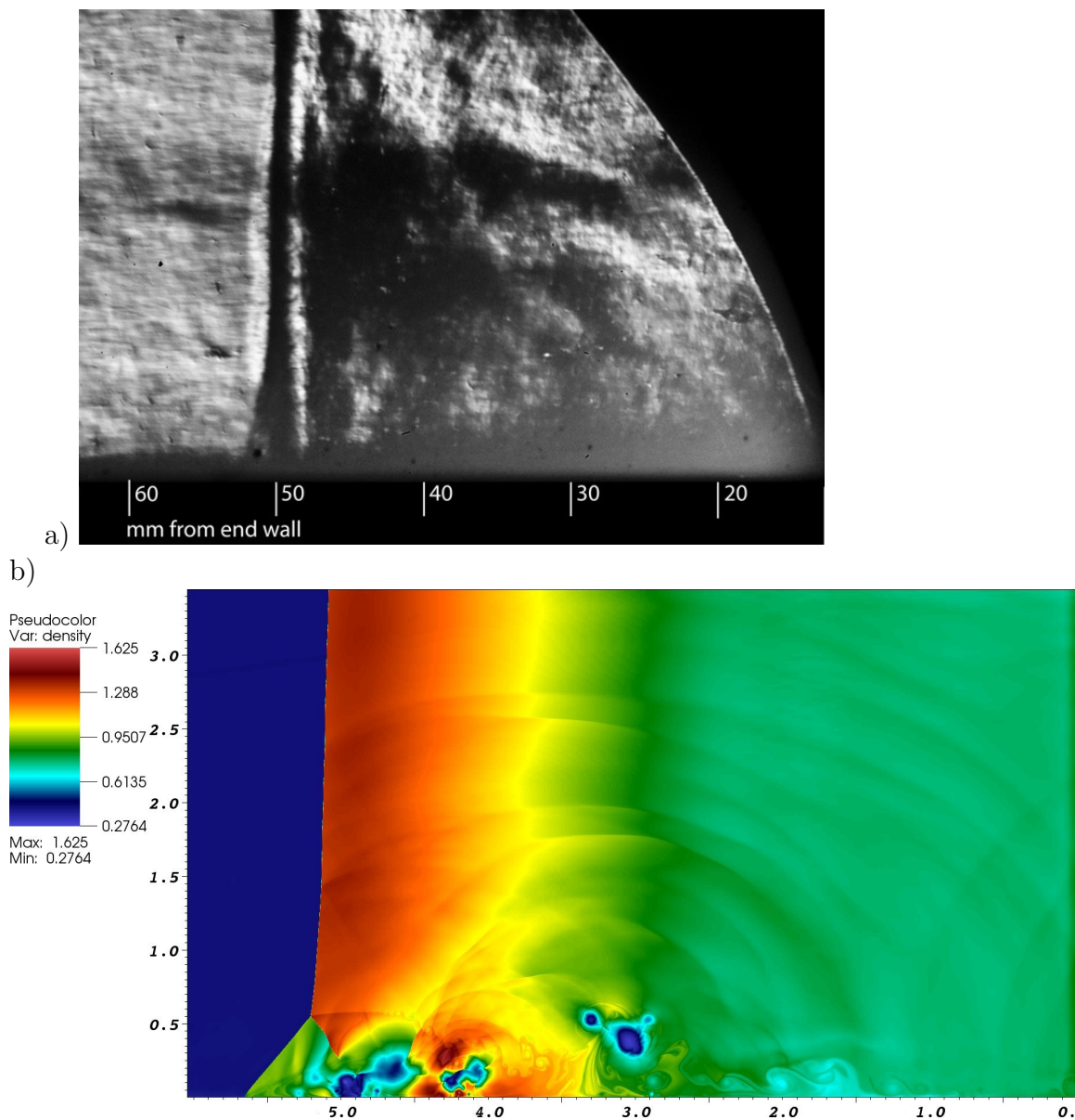


Figure 8.8: 9:H<sub>2</sub>, 1:N<sub>2</sub>O by mole fraction at 15 kPa. The initial detonation Mach number is 5.9 (underdriven, incident speed 1670 m/s, which is 7 percent below the CJ speed of 1804 m/s). Figure a) is the experimental result. figure b) is a pseudocolor plot of the nondimensional density at the same scale and distance from the end wall. Here the end wall is at  $x=0$  cm. For this simulation the shock wave was started at  $x = 7$  and the domain is of size  $x = (14, 0)$  cm and  $y = (0, 7)$  cm. There were 3 refinement levels (2,2,2) (4 levels total) with a base grid of size [800,400] cells.

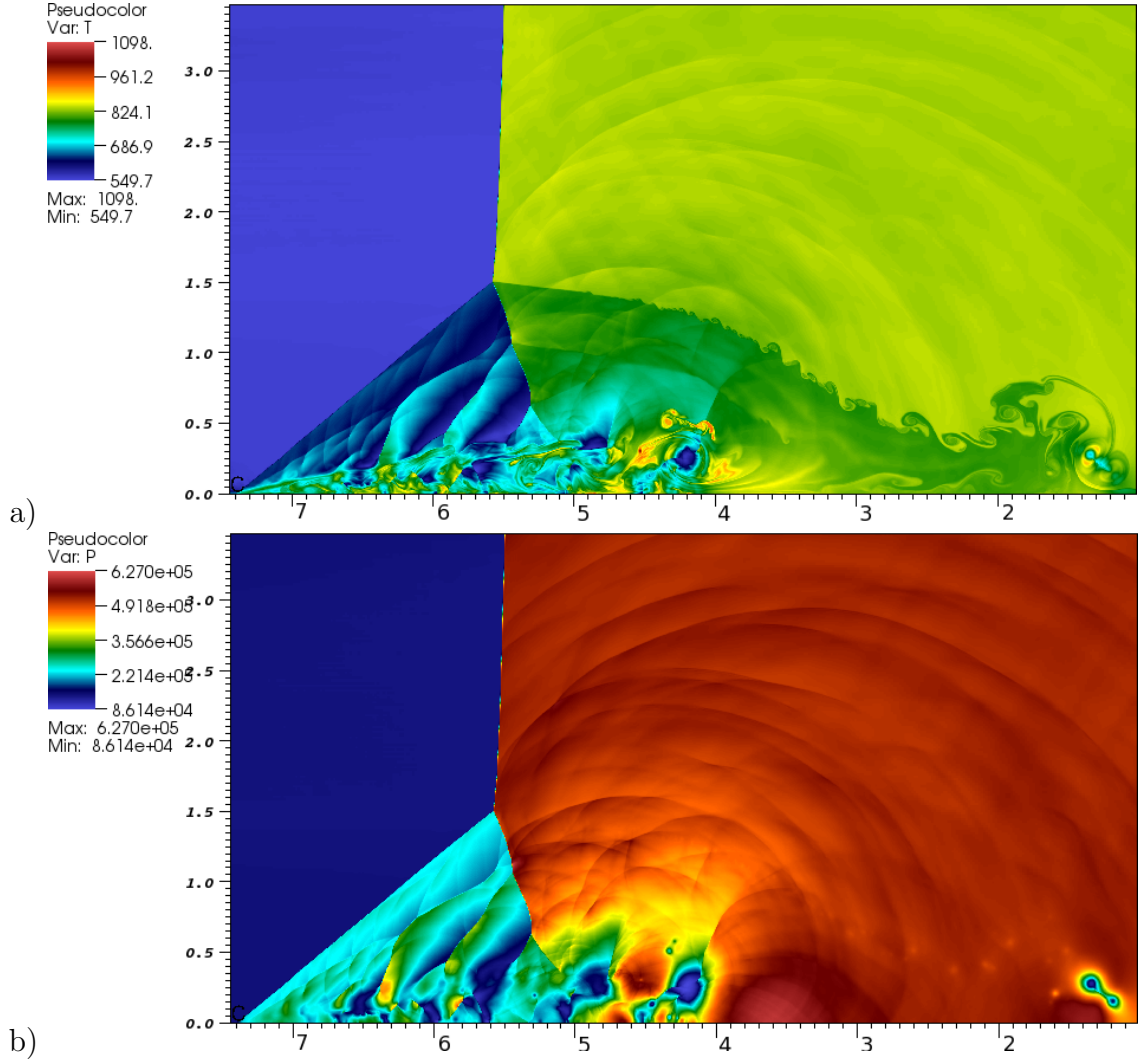


Figure 8.9: Adiabatic case: Air at 25 kPa with Mach number 2.2. a) and b) are pseudo-color plots of the temperature (K) and pressure (Pa) at the same scale and distance from the end wall. Here the end wall is at  $x=0$  cm. For this simulation the shock wave was started at  $x=0$  and the domain is of size  $x = (14, 0)$  cm and  $y = (0, 7)$  cm. There were 3 refinement levels (2,2,2) (4 levels total) with a base grid of size  $[800, 400]$  cells.

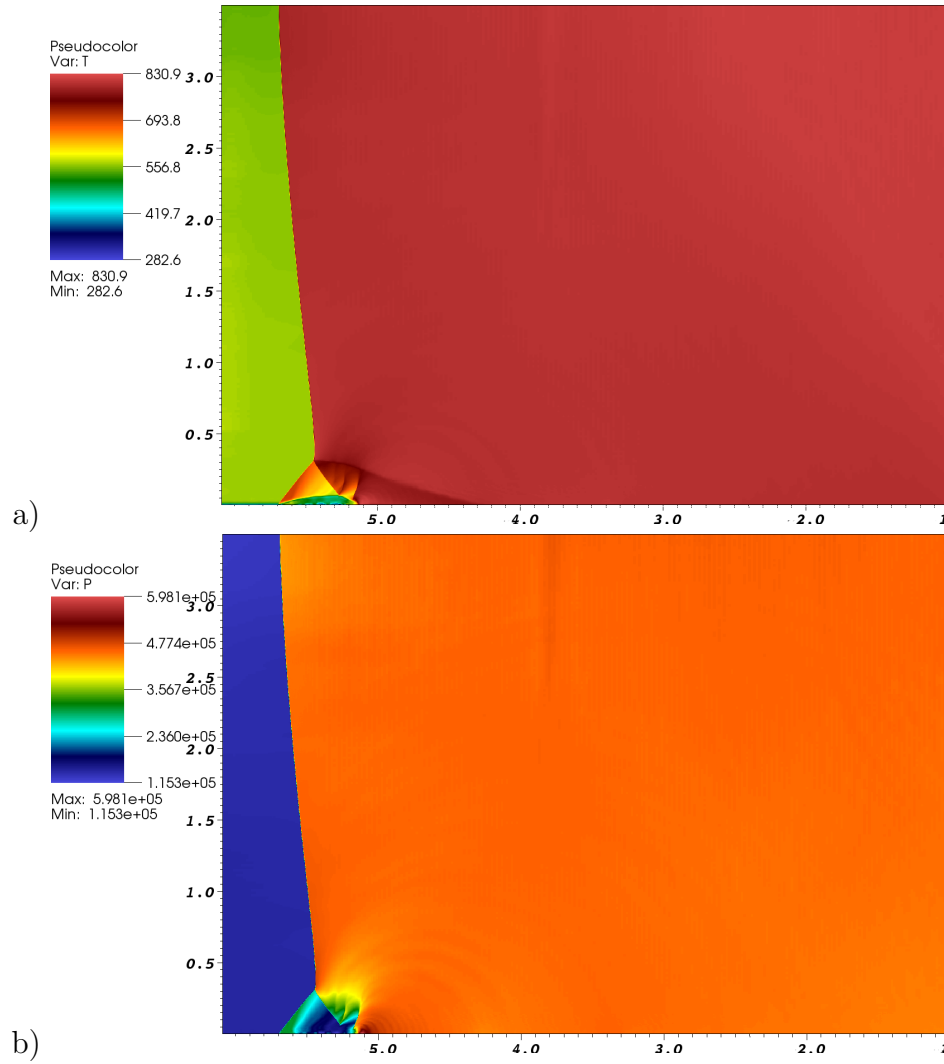


Figure 8.10: Isothermal case: Air at 25 kPa with Mach number 2.2. a) and b) are pseudo-color plots of the temperature (K) and pressure (Pa) at the same scale and distance from the end wall. Here the end wall is at  $x=0$  cm. For this simulation the shock wave was started at  $x = 7$  and the domain is of size  $x = (14, 0)$  cm and  $y = (0, 7)$  cm. There were 3 refinement levels (2,2,2) (4 levels total) with a base grid of size [800,400] cells.



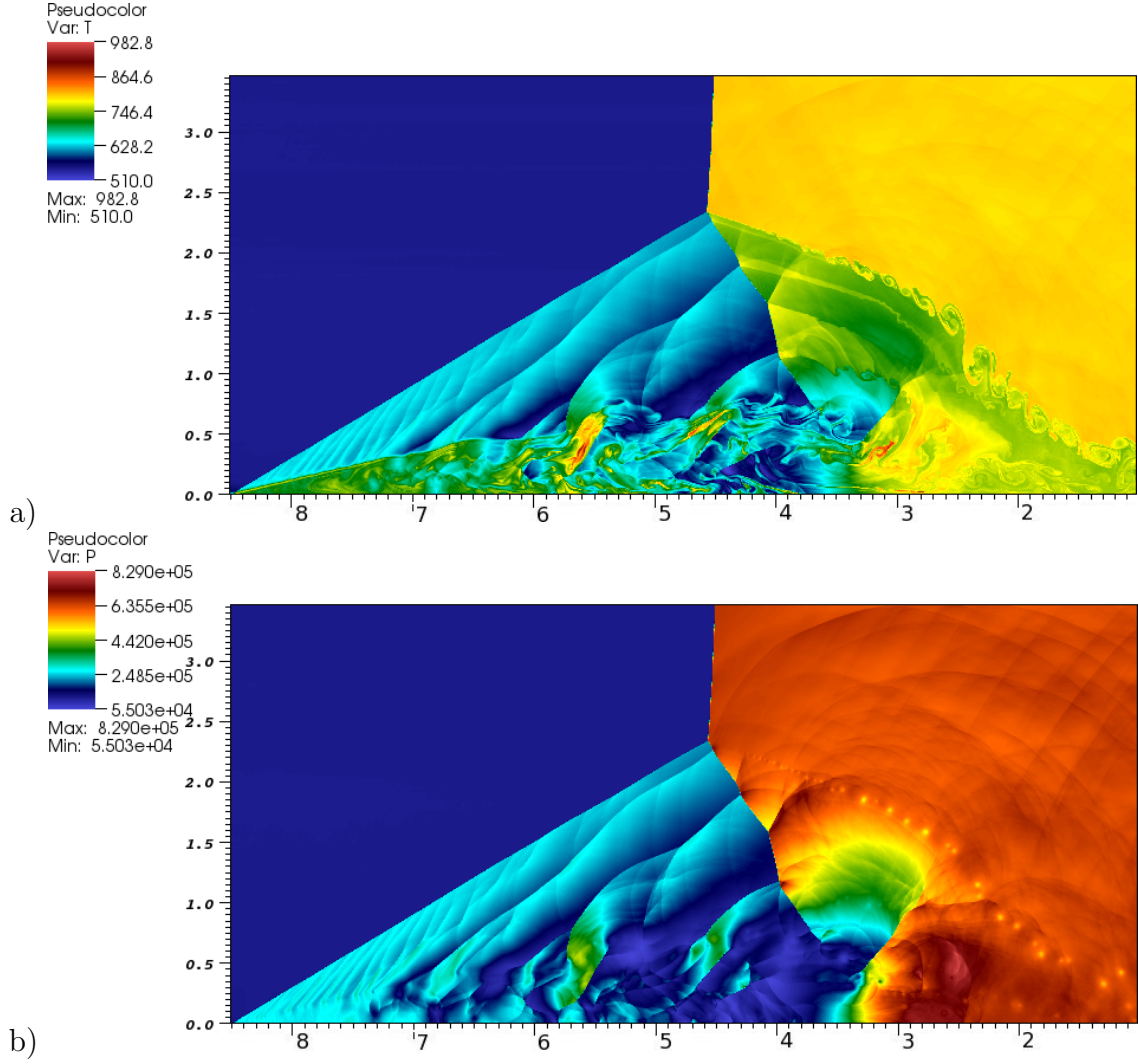


Figure 8.11: Adiabatic case:  $N_2O$  at 15 kPa. Mach number is 2.7 a) and b) are pseudo-color plots of the temperature (K) and pressure (Pa) at the same scale and distance from the end wall. Here the end wall is at  $x=0$  cm. For this simulation the shock wave was started at  $x = 7$  and the domain is of size  $x = (14, 0)$  cm and  $y = (0, 7)$  cm. There were 3 refinement levels (2,2,2) (4 levels total) with a base grid of size  $[800, 400]$  cells.

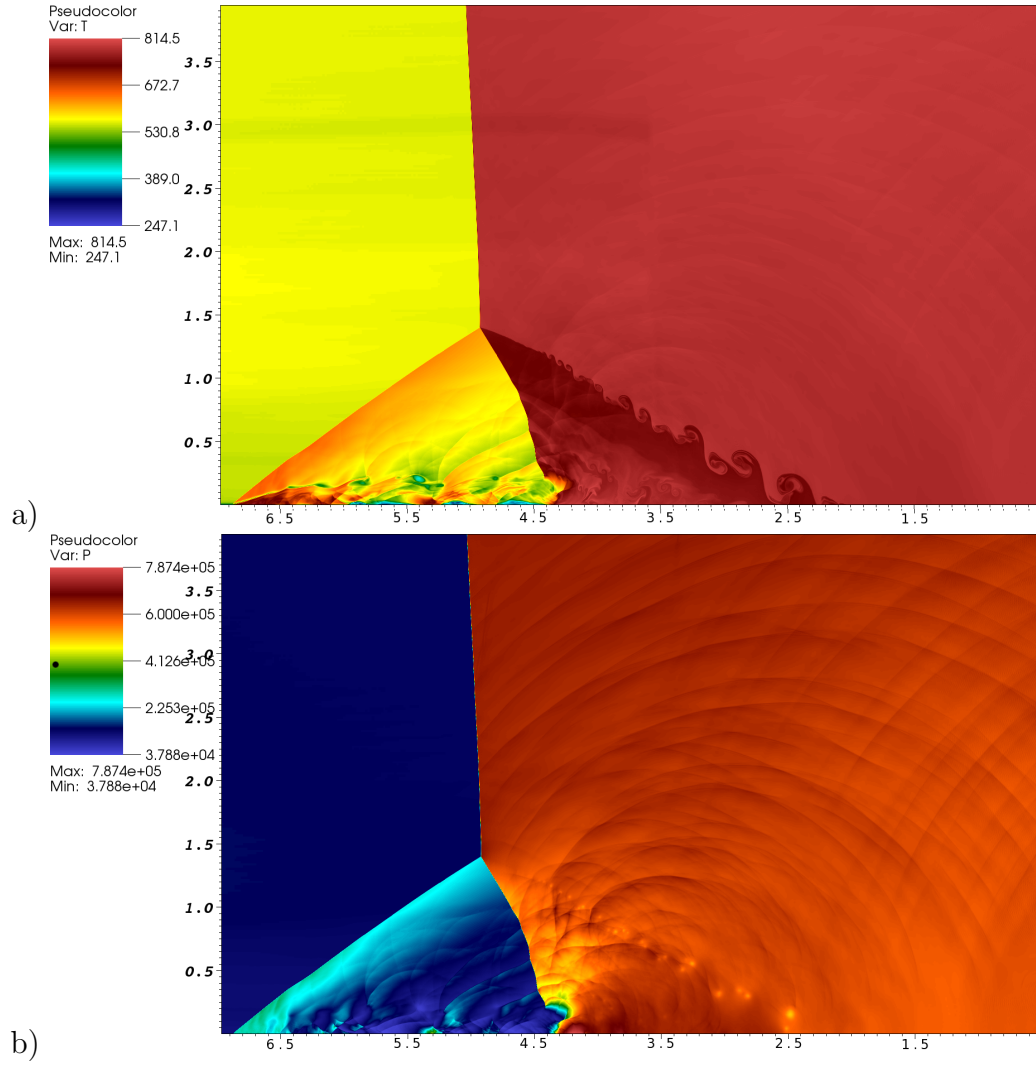


Figure 8.12: Isothermal case: N<sub>2</sub>O at 15 kPa. Mach number is 2.7 a) and b) are pseudo-color plots of the temperature (K) and pressure (Pa) at the same scale and distance from the end wall. Here the end wall is at  $x=0$  cm. For this simulation the shock wave was started at  $x = 7$  and the domain is of size  $x = (14, 0)$  cm and  $y = (0, 7)$  cm. There were 3 refinement levels (2,2,2) (4 levels total) with a base grid of size [800,400] cells.



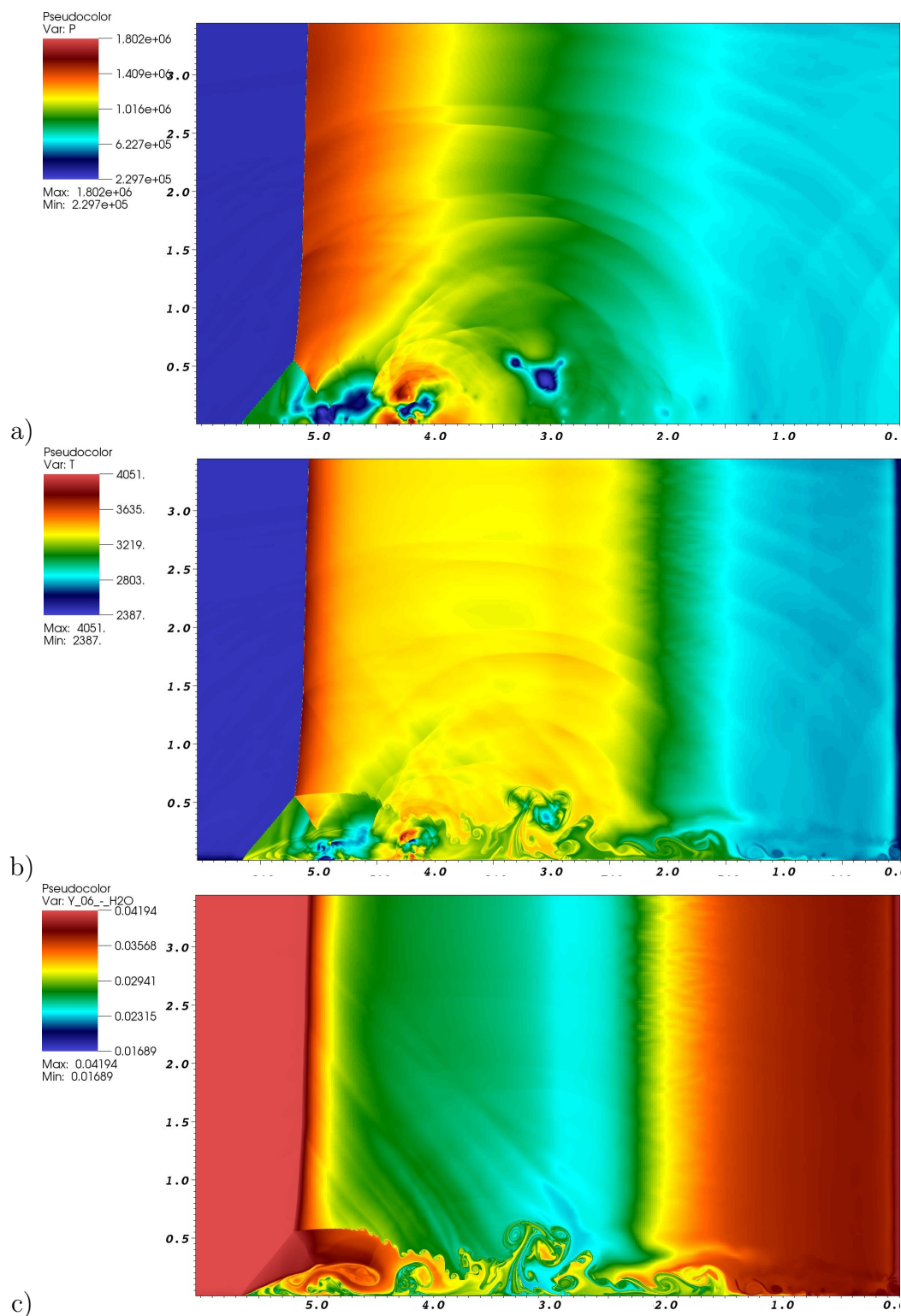


Figure 8.13: 9:H<sub>2</sub>, 1:N<sub>2</sub>O by mole fraction at 15 kPa. Mach number is 5.9 (underdriven, incident speed 1670 m/s, which is 7 percent below the CJ speed of 1804 m/s). Figure a), b), c) are pseudocolor plots of the pressure (Pa), temperature (K), and H<sub>2</sub>O mass fraction. Here the end wall is at  $x = 0$  cm. For this simulation the ZND detonation solution was started at  $x = 3.5$  and the domain is of size  $x = (10.5, 0)$  cm and  $y = (0, 7)$  cm. There were 3 refinement levels (2,2,2) (4 levels total) with a base grid of size [800,400] cells.

### 8.7.3 Resolved Small-Scale Bifurcations

In order to understand how bifurcations form and the flow properties inside, resolved simulations of the 3 mixtures were conducted at the early times of reflection. For the simulation results with the bifurcation closest to the wall, a very high resolution with  $\Delta x_{min} = 4 \cdot 10^{-8}$  m, was used to fully resolve the boundary layer. For other results with increasing distances from the wall, lower resolutions, 2 to 8 times coarser, were used as labeled in each figure. For the higher resolution simulations, the domain was smaller, and hence, the shock or detonation was started closer to the end wall.

In all nonreactive cases, regardless of the mixture or boundary condition, immediately after reflection (approximately  $30 \cdot 10^{-6}$  m), all bifurcations are of about the same shape. With these small foot sizes, only the viscous/diffusive effects are influencing the bifurcation. This is shown in figures 8.16, 8.20, 8.23, and 8.28. At later times and distances from the wall, the top triple point of the foot materializes and the foot grows, now at different rates and with different shapes for each mixture and boundary condition. Another similarity of all the results is that above the triple point, there is a concave curvature of the main reflected wave. It is surmised that this is due to the pressure waves that are created by the initial compressible boundary layer. In figure 8.14, this pressure wave is seen by visualizing the boundary layer of the incident shock. Also shown in figure 8.15 are traces through the boundary layer after it has become established, at a time four times later than the result shown in figure 8.14. Here, location of the pressure wave and its affect on the temperature profile is observed.

For the reactive case, even more immediately after reflection ( $10 \cdot 10^{-6}$  m) as shown in figure 8.32, the foot takes a different shape. It is longer (smaller angle), possibly due to the heating and reactions of the mixture near the bottom wall. As discussed later, the complexity of the foot is increased due to the nonconstant temperatures, and the evolving reaction progress, behind the incident wave, reflected wave, and behind the foot. Even another factor is the inherent instability of the detonation, which causes additional triple points and shear layers to appear on the reflected wave and inside the foot.

#### 8.7.3.1 Air: Isothermal BC

Now, for just considering air for the isothermal case, in the second result, figure 8.17, comparing to the previous figure 8.16, one can see that the curved section of the shock on the foot is about the same size, yet, the straight portion of the shock leading to

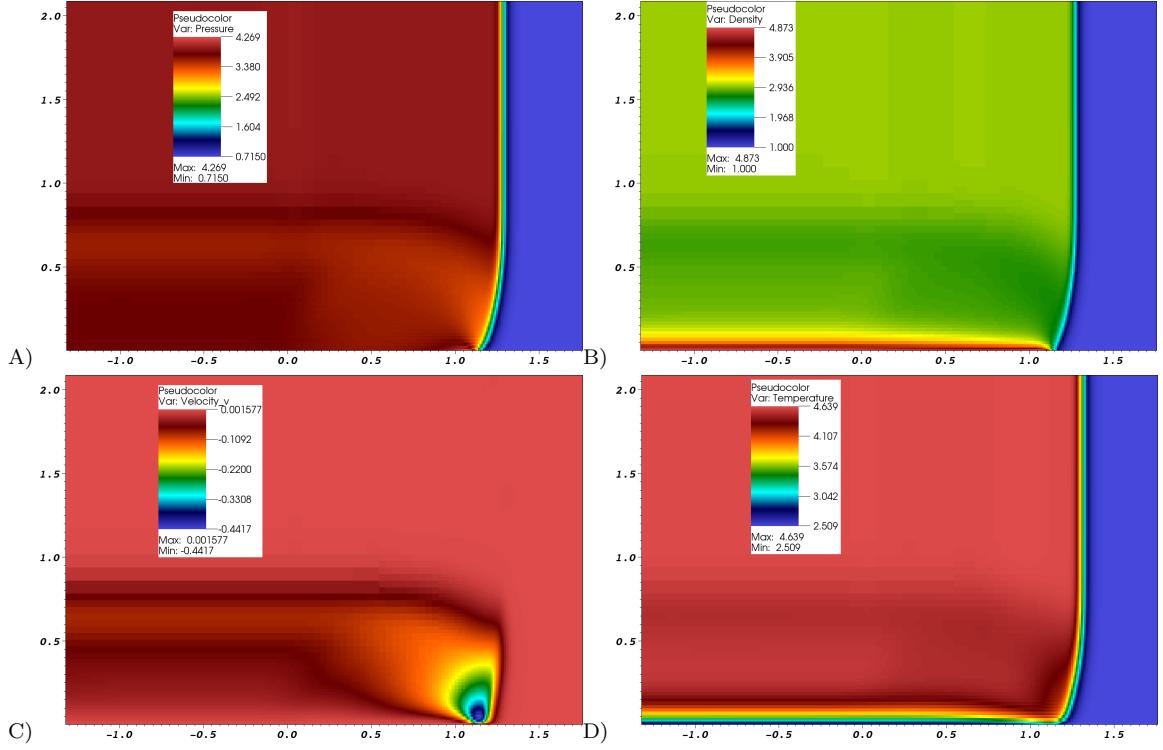


Figure 8.14: Air, isothermal BC case: Incident shock boundary layer. Showing results for nondimensional A) pressure, B) density, C) y-velocity, and D) temperature (K). In these figures the incident shock has traveled approximately  $1.25 \cdot 10^{-3}$  cm. The x and y units are  $10^{-3}$  cm.  $\Delta x_{min} = 4.88 \cdot 10^{-8}$  m. Note that the blurry/blocky region shows where there exists the coarser refinement regions.

what is now a clear triple point is markedly larger. By looking at the vorticity (plot C in the two figures), one can determine what part of the upper flow is passing through the straight shock, and where the boundary layer is passing through the curved shock. At a later time in figure 8.18, the third shock emanating from the triple point is now more visible. As by three-shock theory, this is labeled as a reflected shock. Also, by looking at the temperature in figure 8.18D), one observes that just now the shear layer behind the foot is going unstable. In the last isothermal air figure 8.19, the instabilities in the shear layer have grown, and also shocklets that emanate from the newly formed vortices are visible. In figure 8.6, the experimental image, most likely due to the small size of the foot, fails to show these shocklets. However, for the  $N_2O$  experimental case shown in figure 8.7, the foot is much larger and its stronger shocklets are visible.

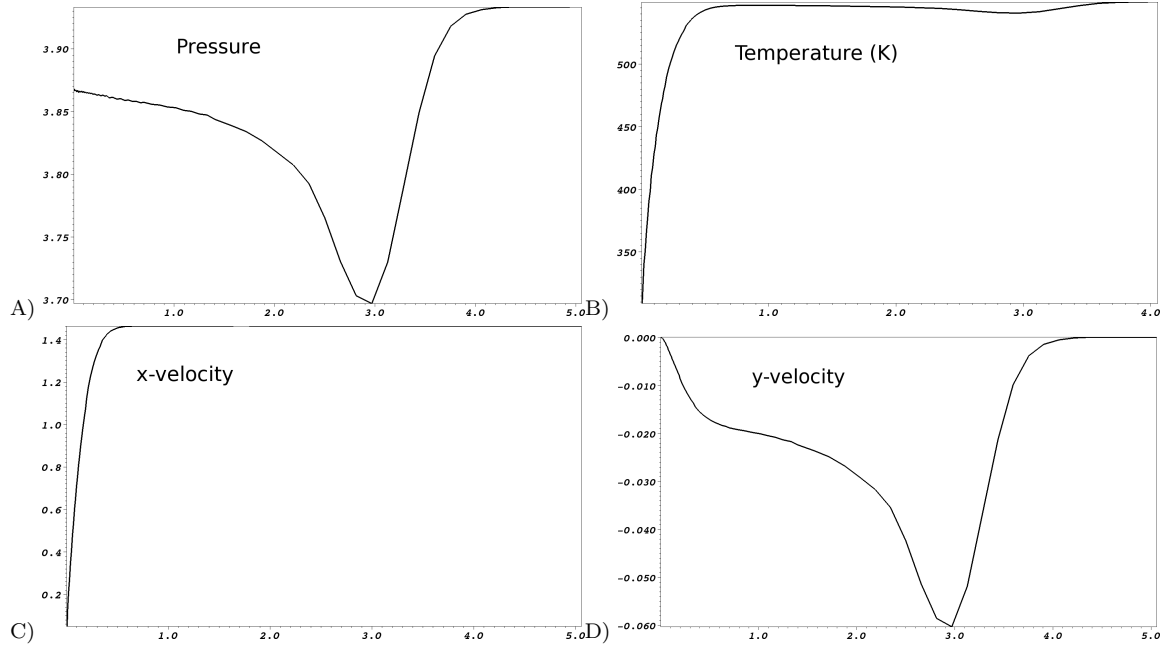


Figure 8.15: Air, isothermal BC case: Incident shock boundary layer traces at a time of  $t = 2.5$  (nondim) =  $7.2 \cdot 10^{-8}$  sec. Showing results for A) temperature (K), nondimensional B) pressure, C) x-velocity, and D) y-velocity. In these figures the incident shock has traveled approximately  $1.25 \cdot 10^{-3}$  cm. The x and y units are  $10^{-3}$  cm.  $\Delta x_{min} = 4.88 \cdot 10^{-8}$  m. Note that the straight lines show where there exists the coarser refinement regions.

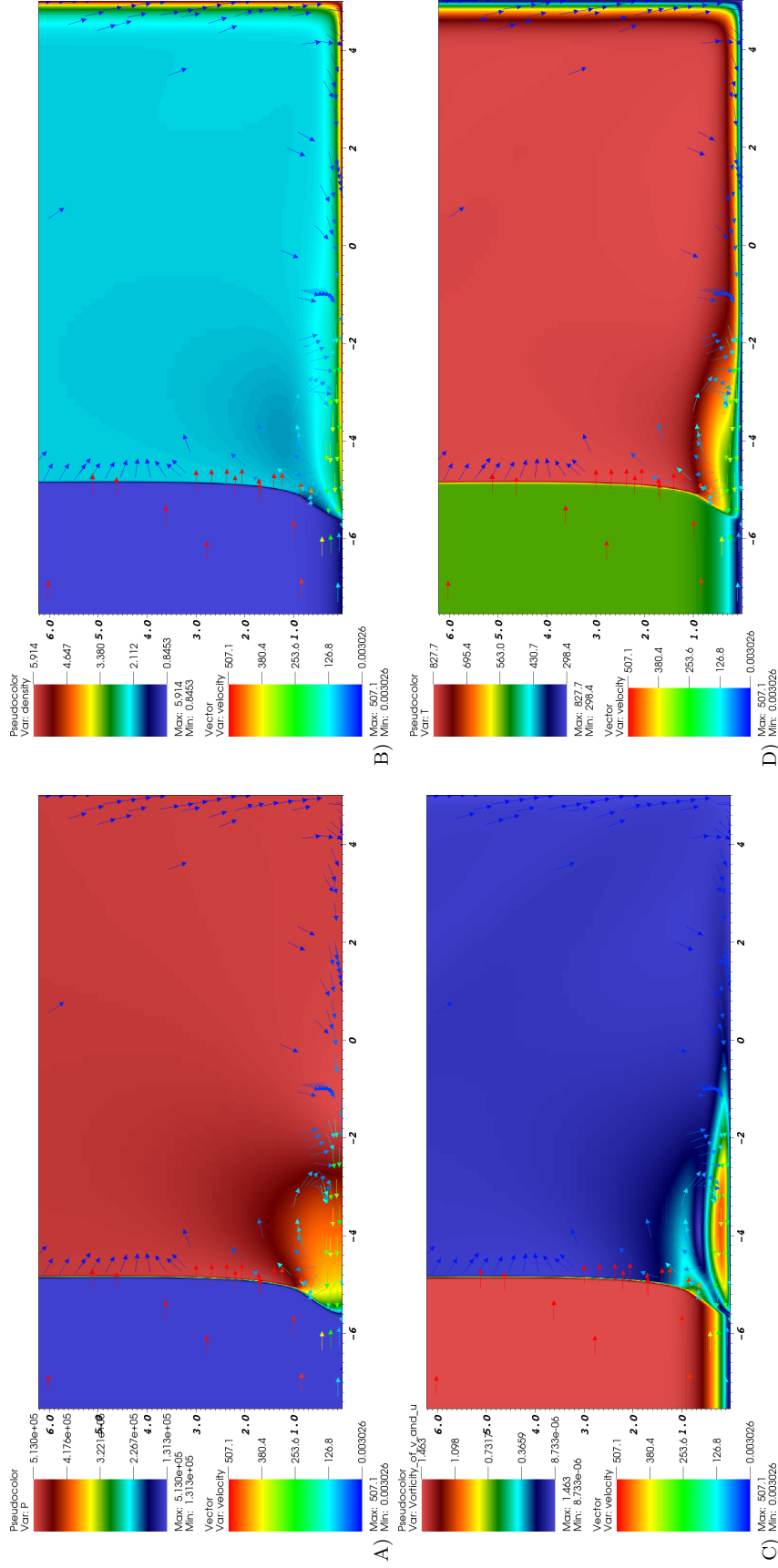


Figure 8.16: Isothermal BC case: Velocity vectors superimposed on pseudo-color plots of various quantities for the air shock-bifurcation case with detailed chemistry and transport. Showing results for A) pressure (Pa), B) density ( $\text{kg/m}^3$ ), C) nondimensional vorticity, and D) temperature (K). In these figures the shock is approximately  $10 \cdot 10^{-3}$  cm from the wall. The x and y units are  $10^{-3}$  cm.  $\Delta x_{min} = 4.88 \cdot 10^{-8}$  m.

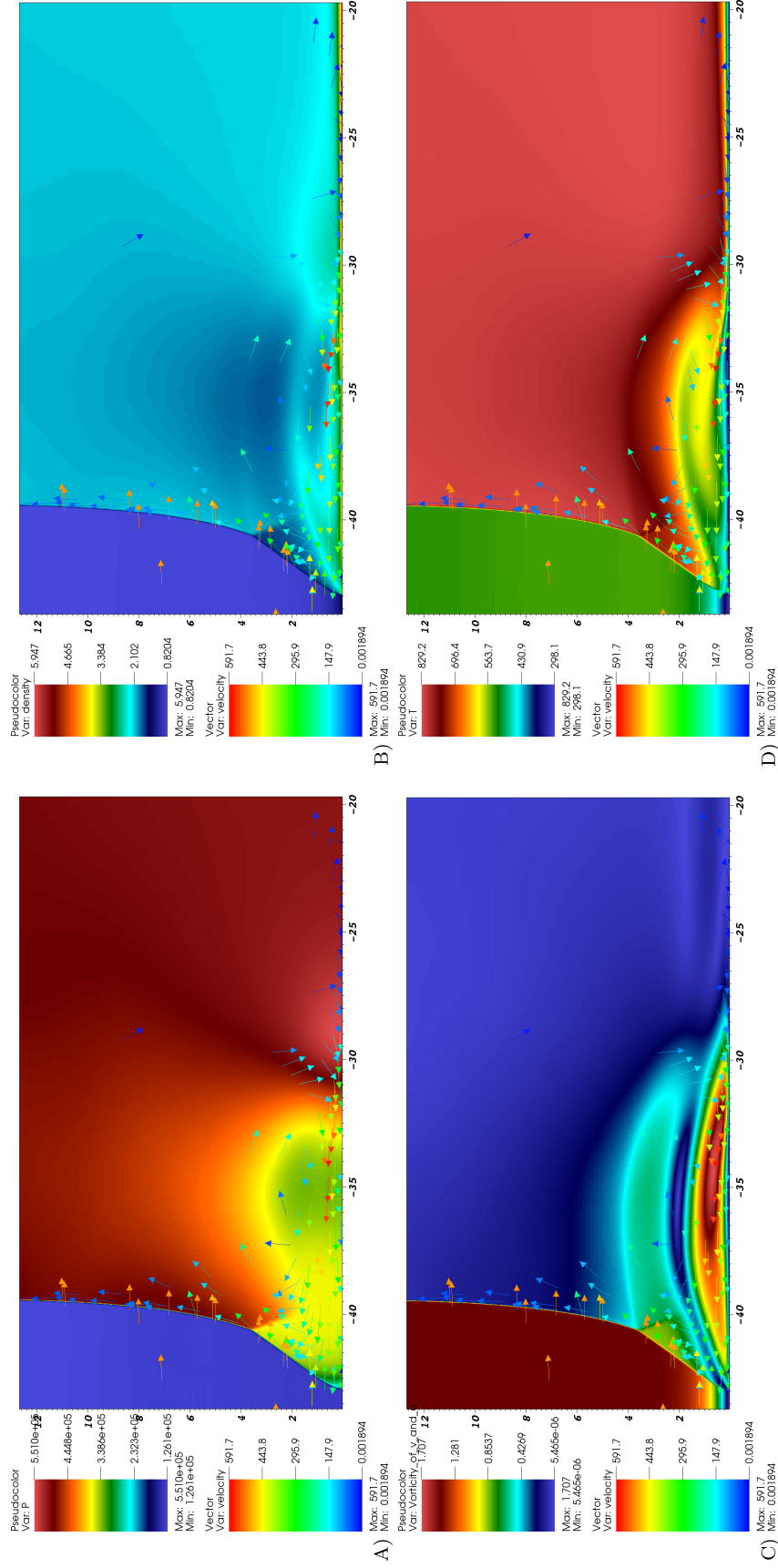


Figure 8.17: Isothermal BC case: Velocity vectors superimposed on pseudo-color plots of various quantities for the air shock-bifurcation case with detailed chemistry and transport. Showing results for A) pressure (Pa), B) density ( $\text{kg/m}^3$ ), C) nondimensional vorticity, and D) temperature (K). In these figures the shock is approximately  $45 \cdot 10^{-3}$  cm from the wall. The x and y units are  $10^{-3}$  cm.  $\Delta x_{min} = 4.88 \cdot 10^{-8}$  m.

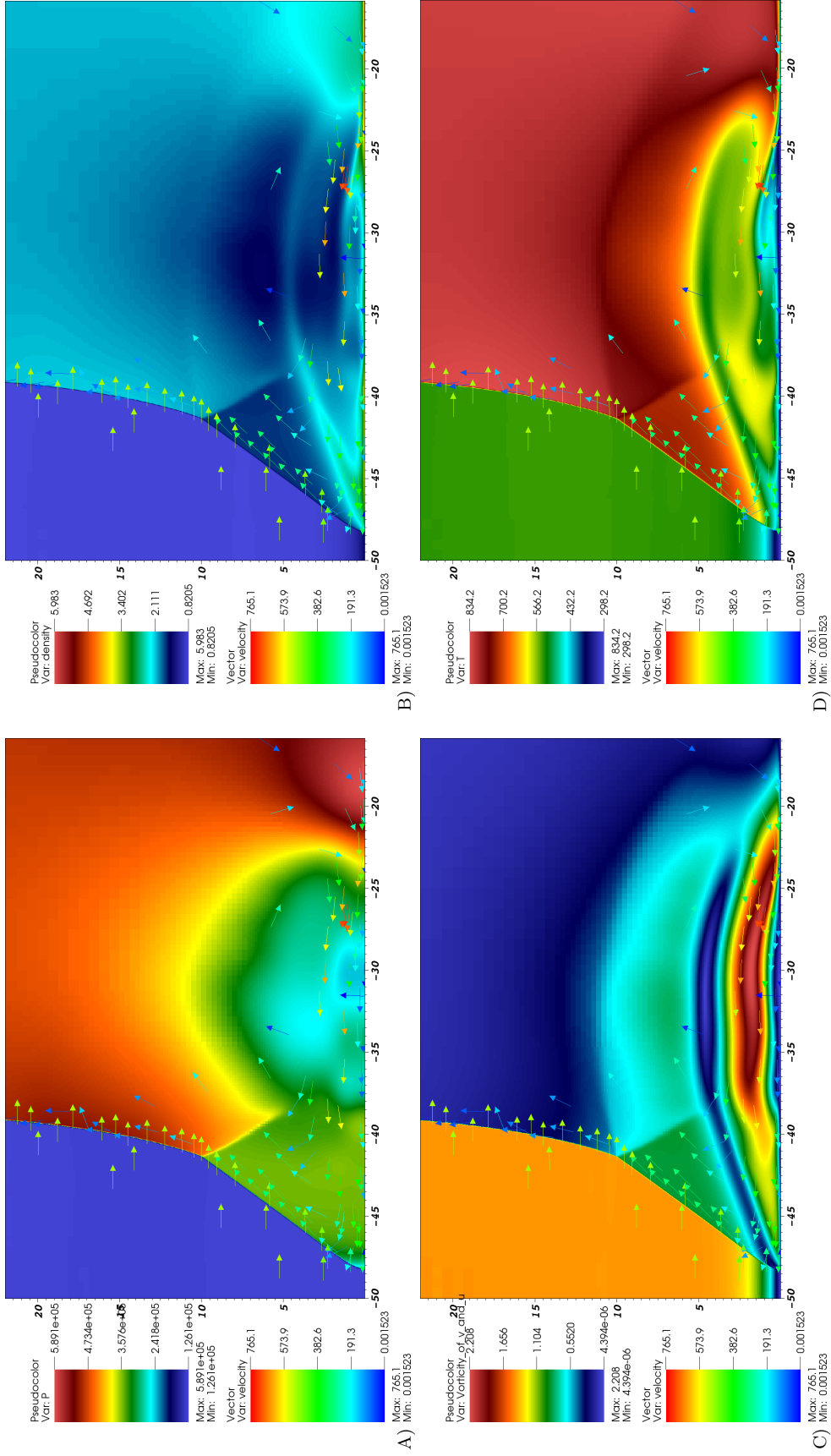


Figure 8.18: Isothermal BC case: Velocity vectors superimposed on pseudo-color plots of various quantities for the air shock-bifurcation case with detailed chemistry and transport. Showing results for A) pressure (Pa), B) density (kg/m<sup>3</sup>), C) nondimensional vorticity, and D) temperature (K). In these figures the shock is approximately 90·10<sup>-3</sup> cm from the wall. The x and y units are 10<sup>-3</sup> cm.  $\Delta x_{min} = 9.77 \cdot 10^{-8}$  m.



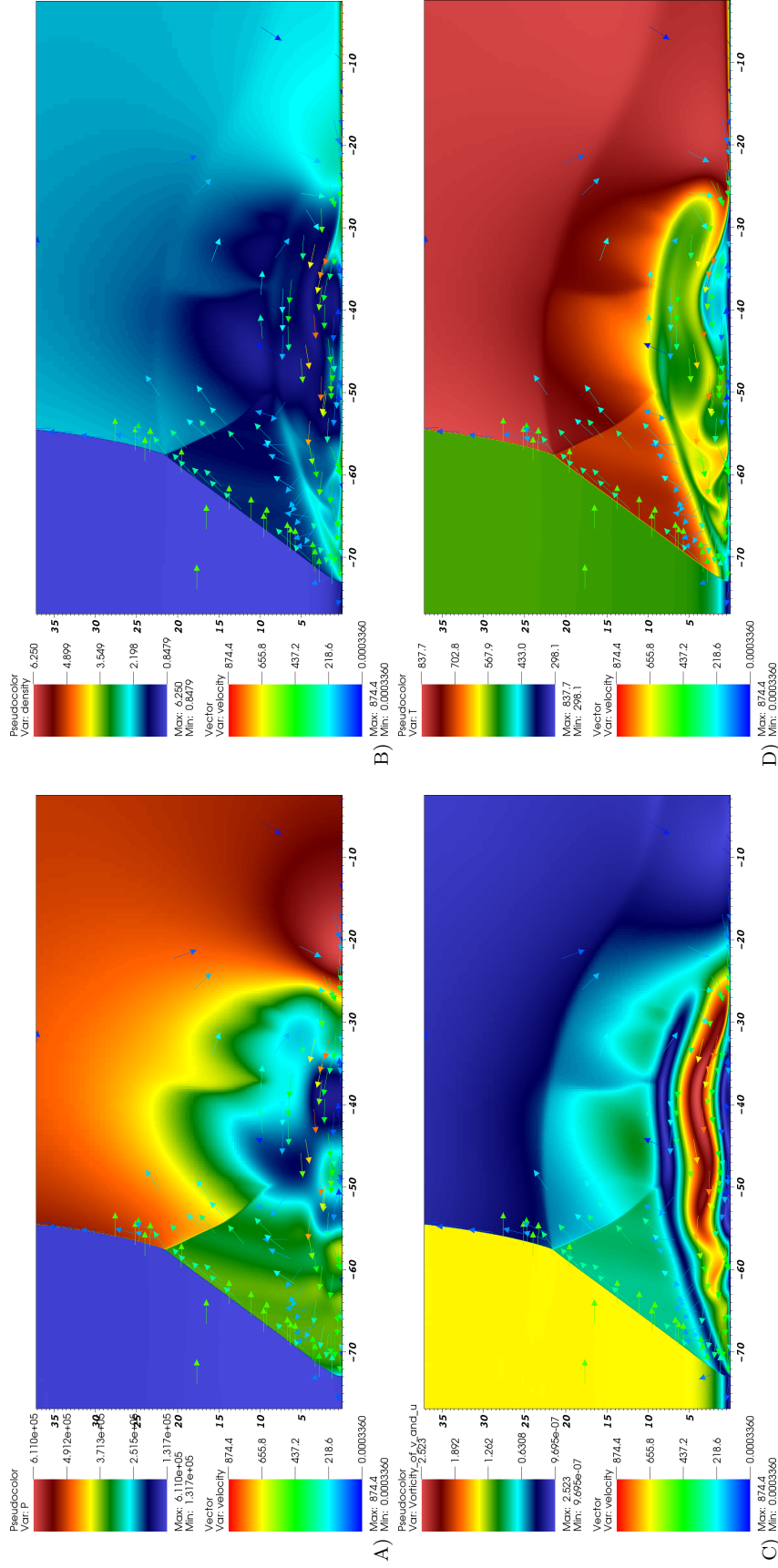


Figure 8.19: Isothermal BC case: Velocity vectors superimposed on pseudo-color plots of various quantities for the air shock-bifurcation case with detailed chemistry and transport. Showing results for A) pressure (Pa), B) density ( $\text{kg/m}^3$ ), C) nondimensional vorticity, and D) temperature (K). In these figures the shock is approximately  $155 \cdot 10^{-3}$  cm from the wall. The x and y units are  $10^{-3}$  cm.  $\Delta x_{\min} = 1.95 \cdot 10^{-7}$  m.

### 8.7.3.2 Air: Adiabatic BC

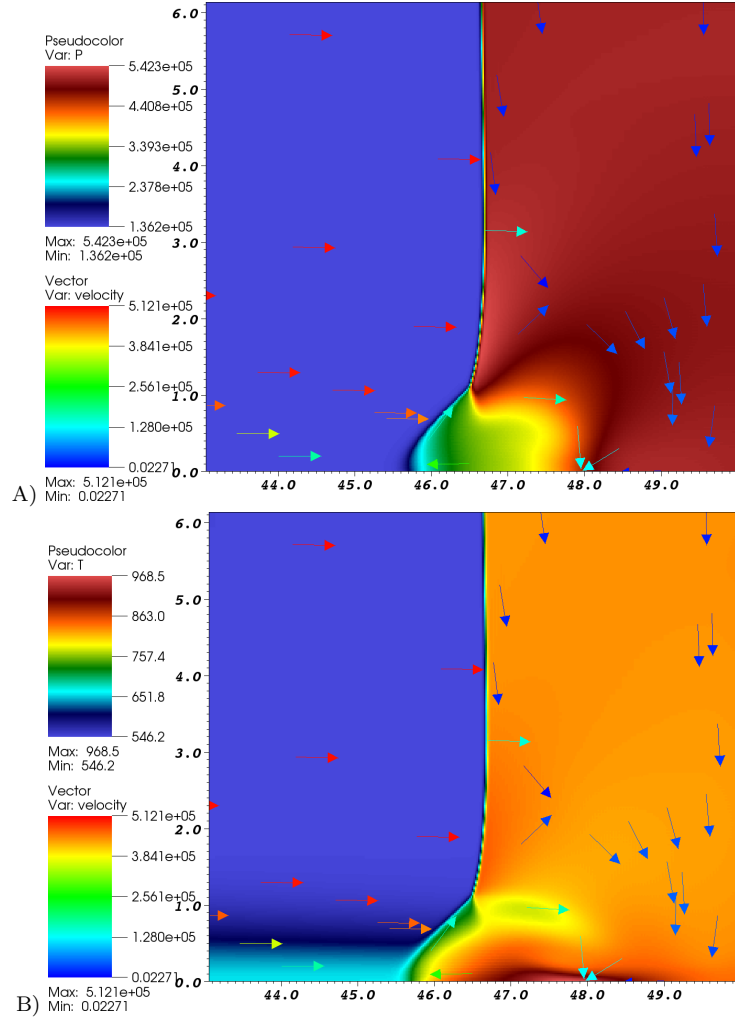


Figure 8.20: Adiabatic BC case: Velocity vectors superimposed on pseudo-color plots of pressure (Pa) and temperature (K) for the air shock-bifurcation case with detailed chemistry and transport. In these figures the shock is approximately  $3 \cdot 10^{-3}$  cm from the wall. The x and y units are  $10^{-3}$  cm.  $\Delta x_{min} = 1.95 \cdot 10^{-7}$  m.

Starting with figure 8.20, one may compare the initial foot start-up of the adiabatic case with that of the isothermal case. Here, the reflected wave has only traveled  $30 \cdot 10^{-6}$  m and already its height is  $10 \cdot 10^{-6}$  m. For the isothermal case, a height of  $10 \cdot 10^{-6}$  m is not reached until the reflected wave has traveled  $100 \cdot 10^{-6}$  m. Despite this, the shapes of the feet are the same. The reasons for these differences, is influenced by the sizes of the boundary layers. For the adiabatic case the thermal boundary layer is much thicker (less steep gradients). Also, unlike the isothermal case, there is not a pronounced density gradient.

Moving on to the next result, figure 8.21, the reflected shock has now traveled  $450 \cdot 10^{-6}$  m. As for the isothermal case in figures 8.18 and 8.19, the same trends of a triple point, an unstable shear layer, and shocklets appearing are found.

In the last result, a zoomed in view of the large-scale foot from figure 8.6 is shown. Looking at the temperature, density, and vorticity, the shear layer just above the wall, and emanating from the triple point can be identified. Both of these layers have gone unstable. The shear layer near the wall has many strong vortical structures where create a chaotic combination of shocklets throughout the foot that propagate into the domain behind the main reflected shock.

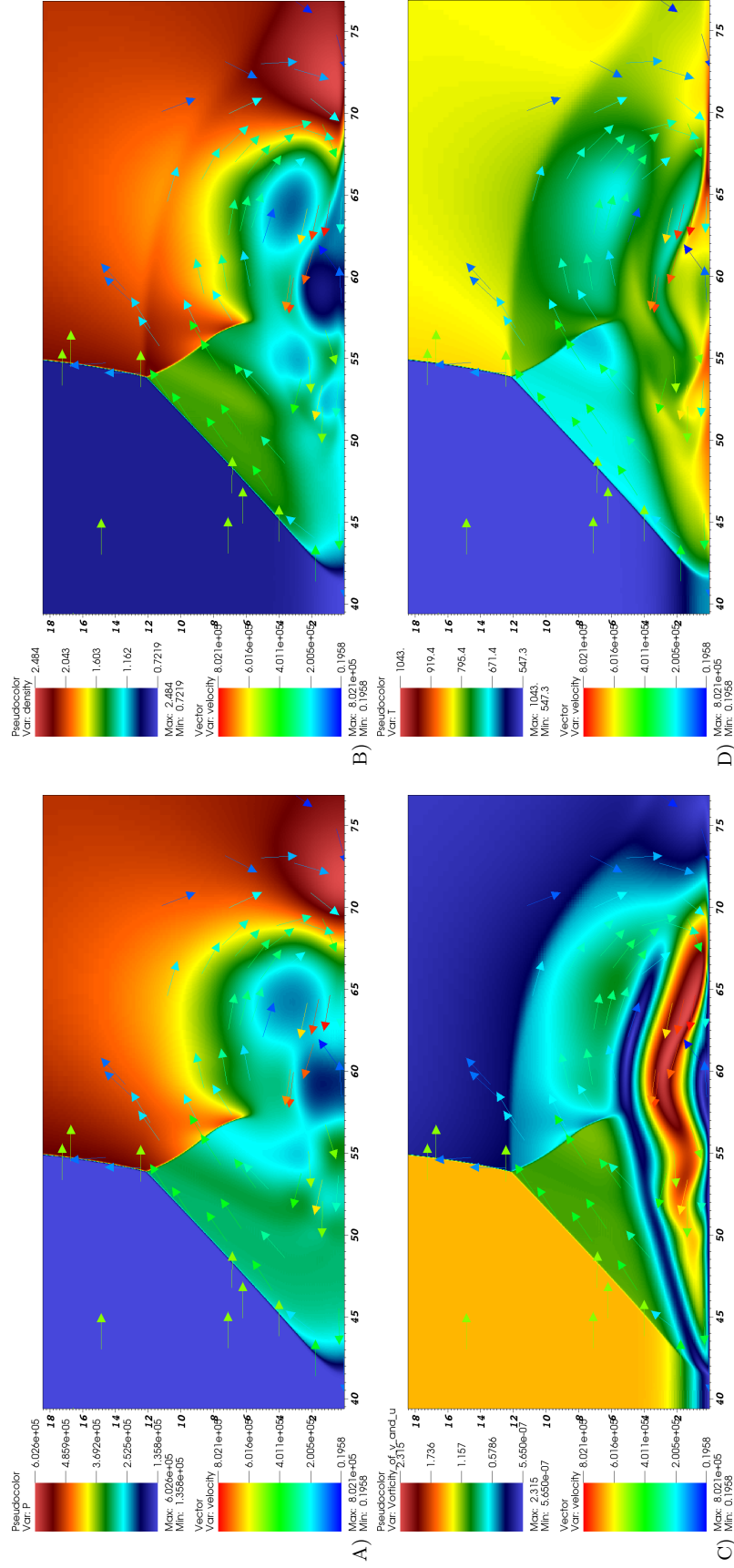


Figure 8.21: Adiabatic BC case: Velocity vectors superimposed on pseudo-color plots of various quantities for the air shock-bifurcation case with detailed chemistry and transport. Showing results for nondimensional A) pressure, B) density, C) vorticity, and D) temperature. In these figures the shock is approximately  $45 \cdot 10^{-3}$  cm from the wall. The x and y units are  $10^{-3}$  cm.  $\Delta x_{min} = 3.91 \cdot 10^{-7}$  m.

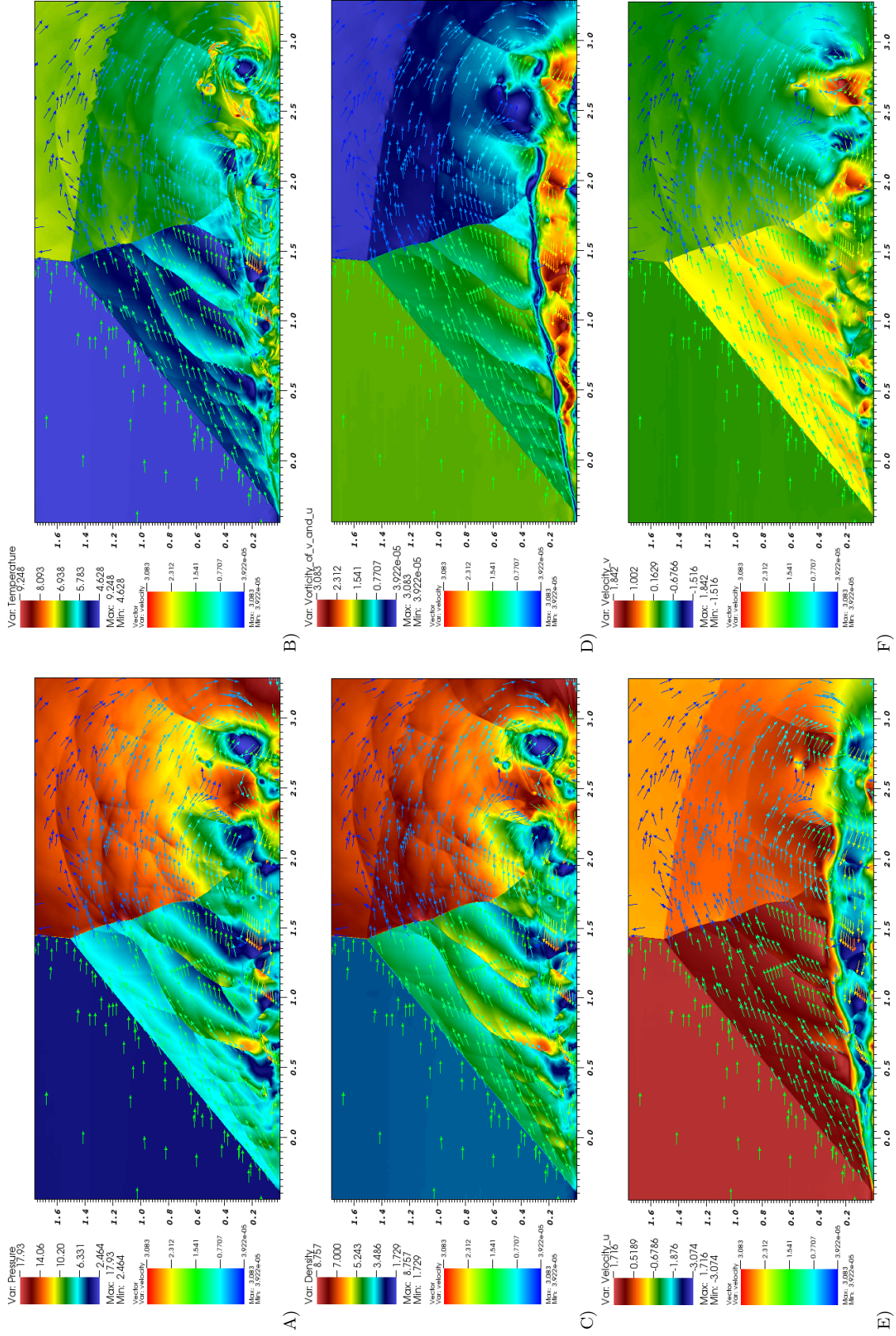


Figure 8.22: Adiabatic BC case: Velocity vector pseudo-color plots for the air shock-bifurcation case with detailed chemistry and transport. Showing results for nondimensional A) pressure, B) density, C) temperature, D) vorticity, and E) and F) the x and y velocities. The shock is approximately  $5.5 \cdot 10^{-3}$  cm from the wall. The x and y units are cm.  $\Delta x_{min} = 2.19 \cdot 10^{-5}$  m.

### 8.7.3.3 N<sub>2</sub>O: Isothermal BC

A first look the N<sub>2</sub>O results with an isothermal wall shows many similarities to the air case with an adiabatic wall. At the same distance from the wall, approximately  $30 \cdot 10^{-6}$  m, the height of the foot is only 40 percent smaller as is seen in figure 8.23. As we find later for the adiabatic case, the height of the foot for the adiabatic N<sub>2</sub>O case is the largest foot of all cases. For the isothermal case, as is seen in figures 8.23, 8.24, 8.25, 8.26, and 8.27 the same trends continue, appearance of a triple point and reflected wave, and shear layers which go unstable forming shocklets from the layers just above the wall. Some of the vorticies near the wall are also lifted up, creating a chaotic flow behind the foot in the large-scale results. A “medium-scale” result is also shown in figure 8.27. At this time when the reflected shock is  $1.850 \cdot 10^{-3}$  m from the wall, many shocklets have formed near the front of the foot in addition to the shocks that first appear in the rear of the foot as is seen in figure 8.25.



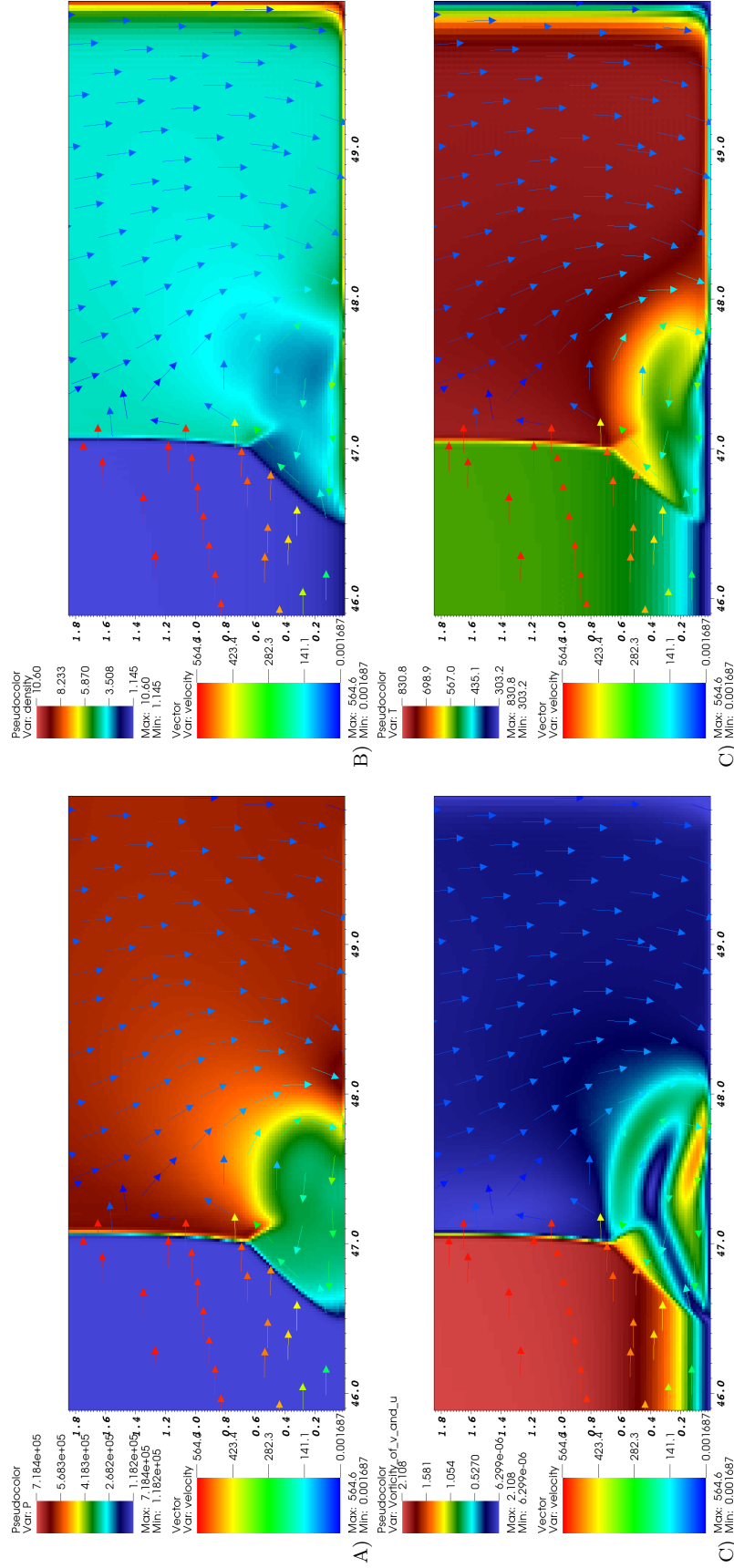


Figure 8.23: Isothermal BC case: Velocity vectors superimposed on pseudo-color plots of various quantities for the  $N_2O$  shock-bifurcation case with detailed chemistry and transport. Showing results for nondimensional A) pressure (Pa), B) density ( $kg/m^2$ ), C) nondimensional vorticity, and D) temperature (K). In these figures the shock is approximately  $3 \cdot 10^{-3}$  cm from the wall. The x and y units are  $10^{-3}$  cm.  $\Delta x_{min} = 9.77 \cdot 10^{-8}$  m.



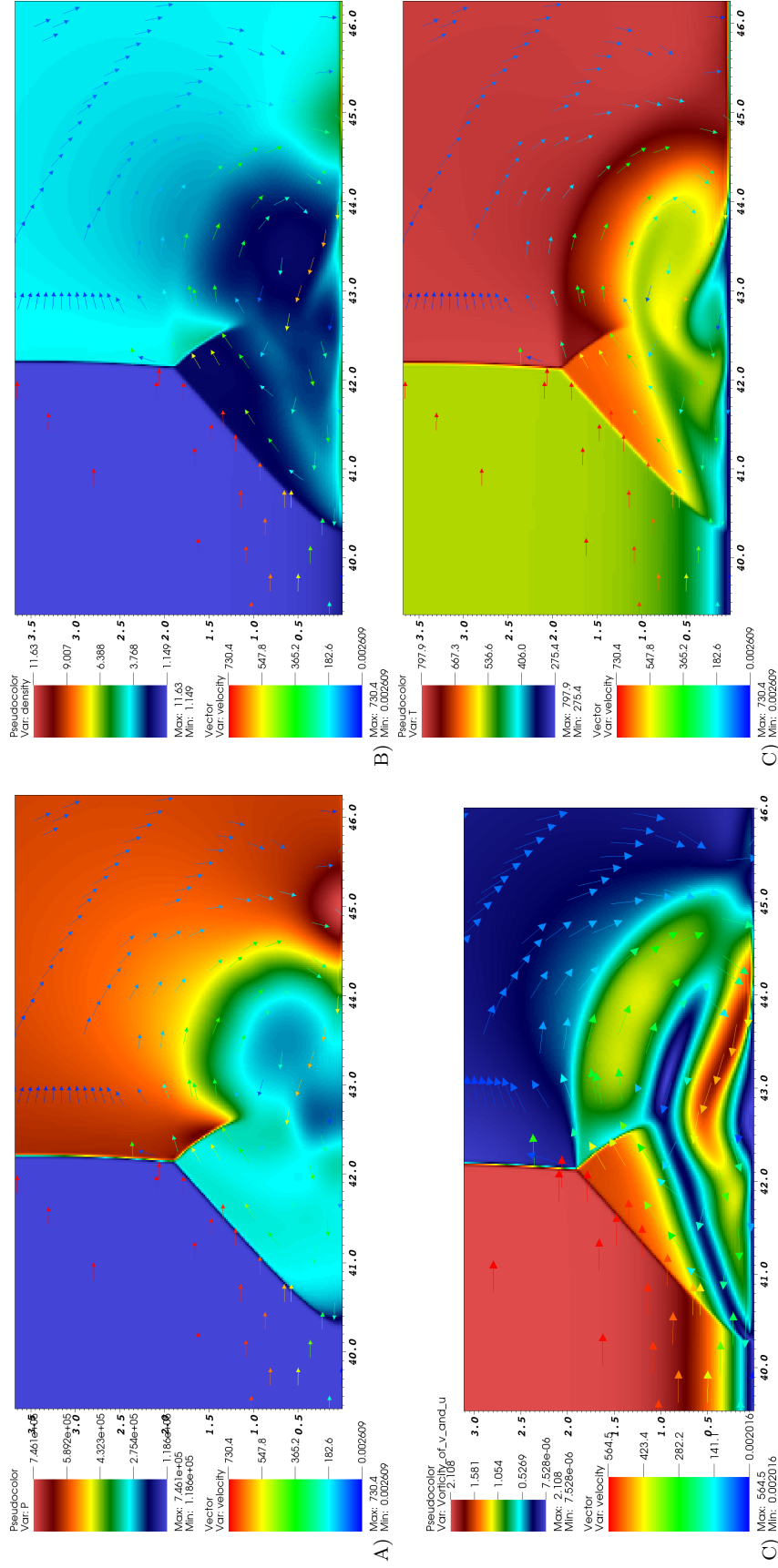


Figure 8.24: Isothermal BC case: Velocity vectors superimposed on pseudo-color plots of various quantities for the  $\text{N}_2\text{O}$  shock-bifurcation case with detailed chemistry and transport. Showing results for nondimensional A) pressure (Pa), B) density ( $\text{kg/m}^3$ ), C) nondimensional vorticity, and D) temperature (K). The shock is approximately  $8 \cdot 10^{-3}$  cm from the wall. The x and y units are  $10^{-3}$  cm.  $\Delta x_{\min} = 9.77 \cdot 10^{-8}$  m.

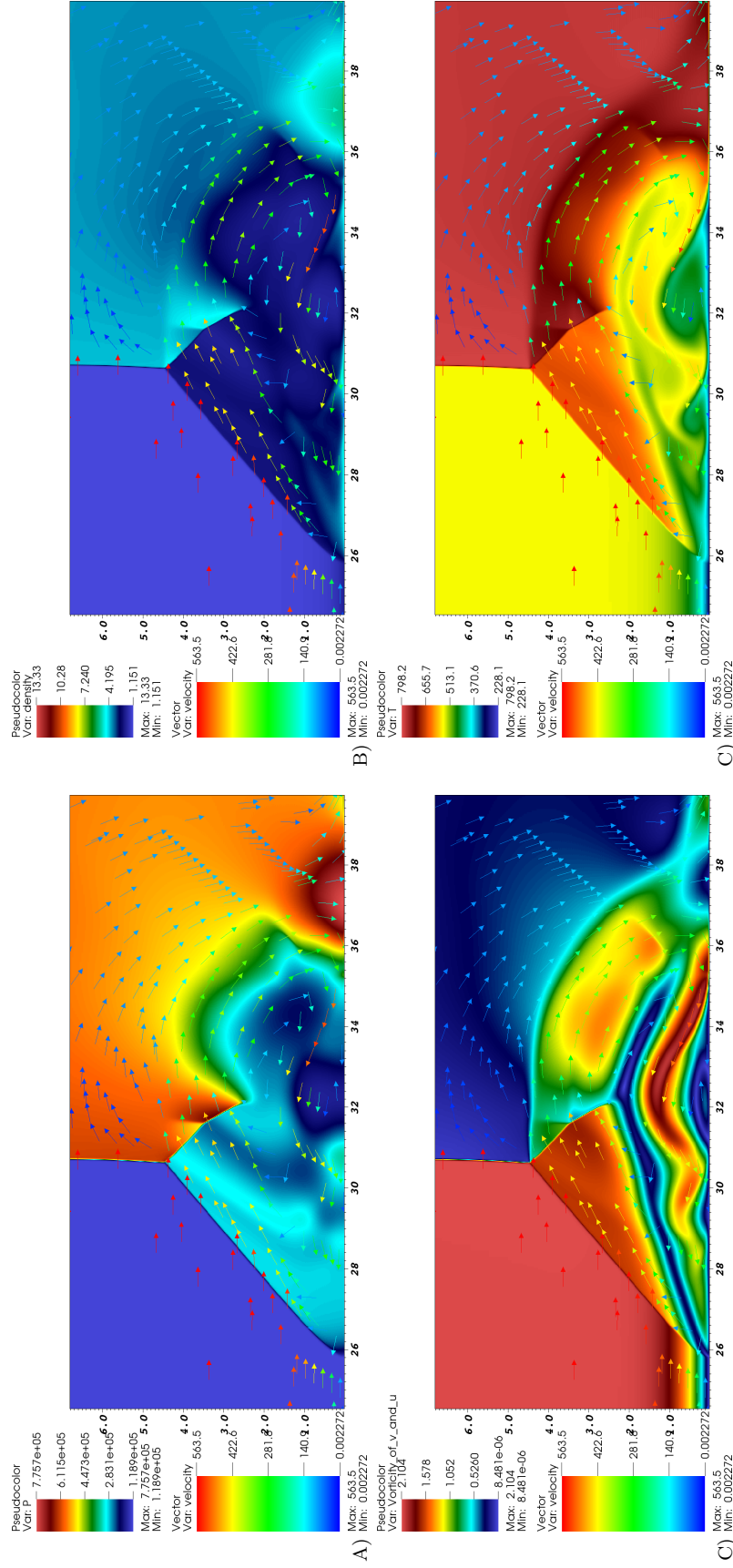


Figure 8.25: Isothermal BC case: Velocity vectors superimposed on pseudo-color plots of various quantities for the  $N_2O$  shock-bifurcation case with detailed chemistry and transport. Showing results for nondimensional A) pressure (Pa), B) density ( $kg/m^3$ ), C) nondimensional vorticity, and D) temperature (K). In these figures the shock is approximately  $20 \cdot 10^{-3}$  cm from the wall. The x and y units are  $10^{-3}$  cm.  $\Delta x_{min} = 9.77 \cdot 10^{-8}$  m.

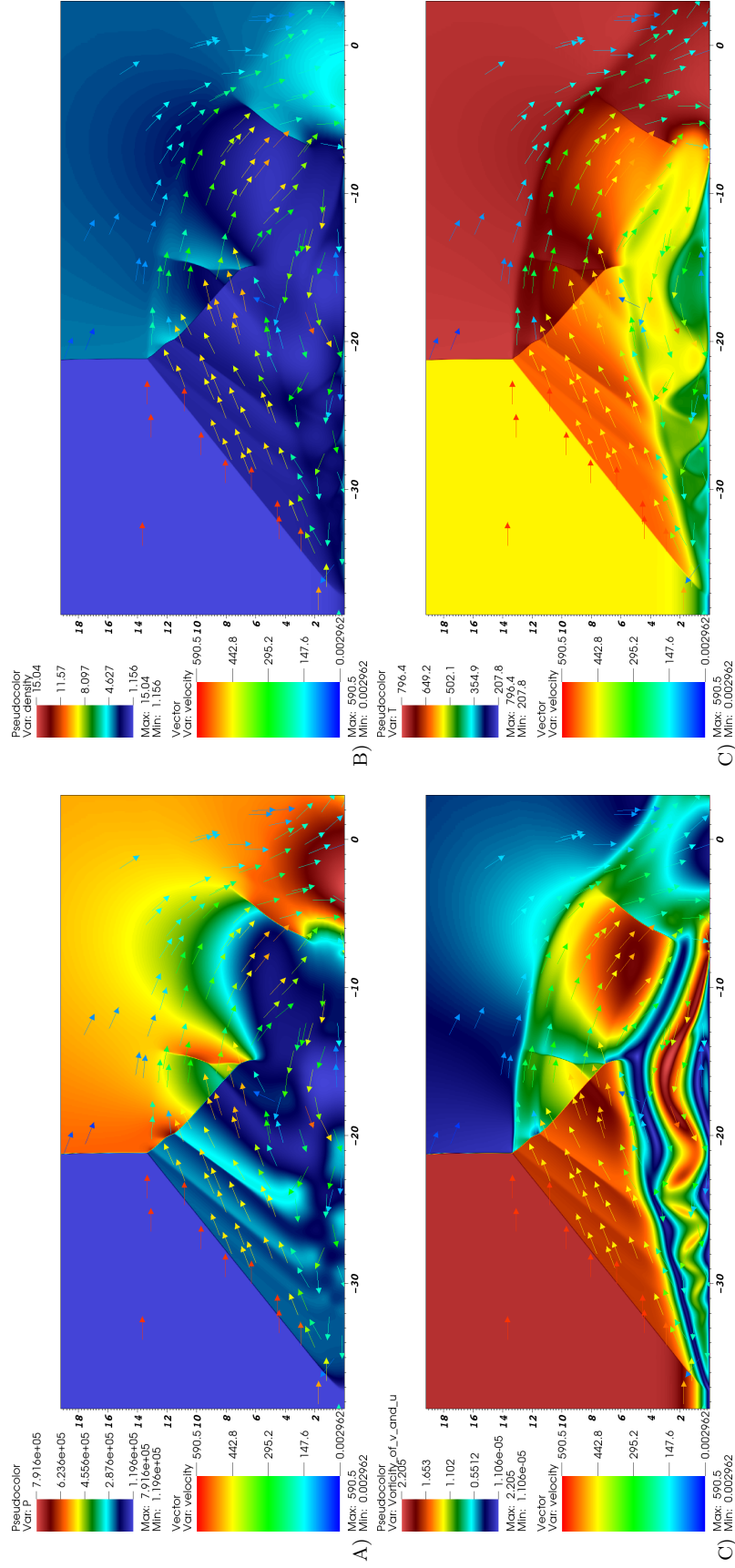


Figure 8.26: Isothermal BC case: Velocity vectors superimposed on pseudo-color plots of various quantities for the  $\text{N}_2\text{O}$  shock-bifurcation case with detailed chemistry and transport. Showing results for nondimensional A) pressure (Pa), B) density ( $\text{kg/m}^3$ ), C) nondimensional vorticity, and D) temperature (K). In these figures the shock is approximately  $70 \cdot 10^{-3}$  cm from the wall. The x and y units are  $10^{-3}$  cm.  $\Delta x_{\min} = 9.77 \cdot 10^{-8}$  m.

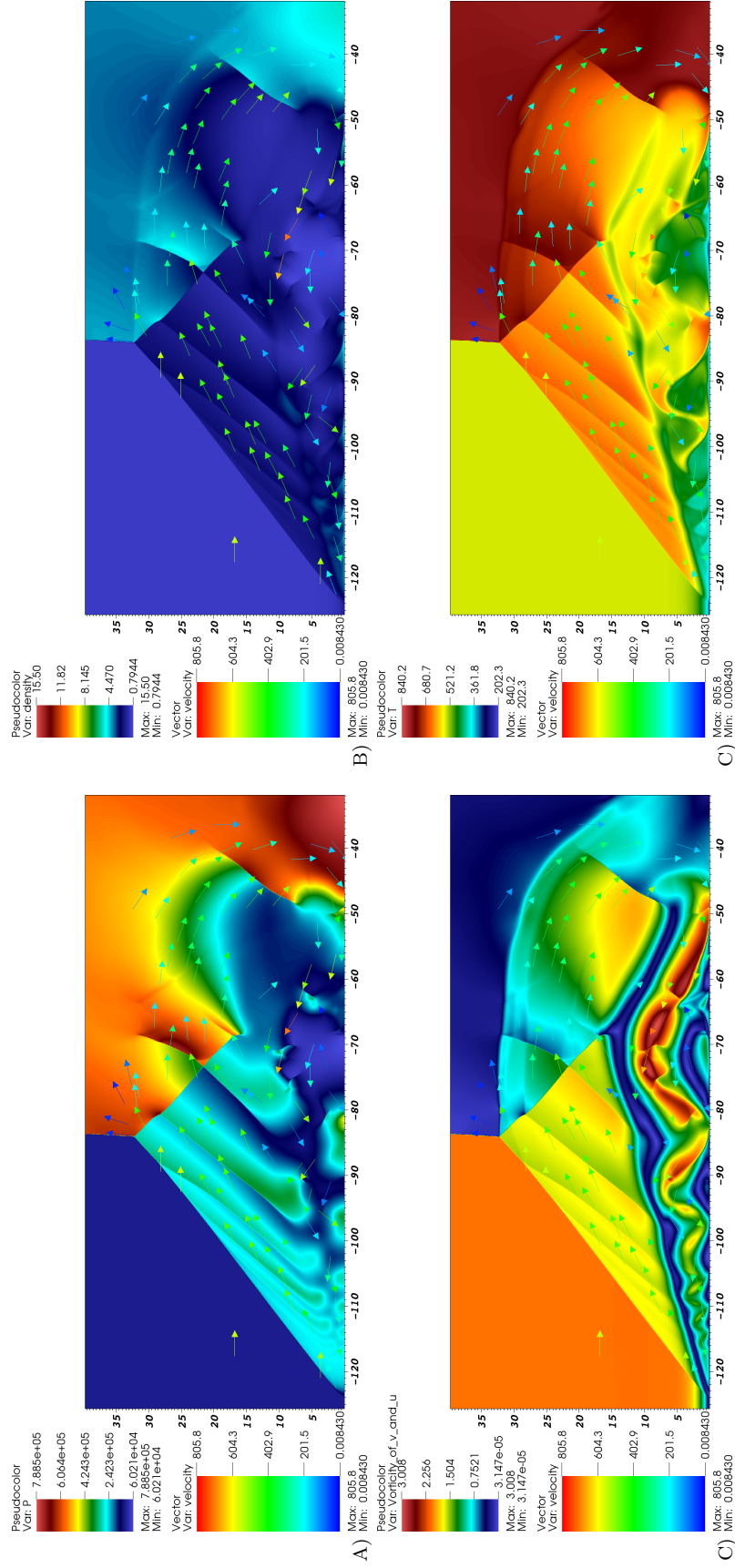


Figure 8.27: Isothermal BC case: Velocity vectors superimposed on pseudo-color plots of various quantities for the N<sub>2</sub>O shock-bifurcation case with detailed chemistry and transport. Showing results for nondimensional A) pressure (Pa), B) density (kg/m<sup>3</sup>), C) nondimensional vorticity, and D) temperature (K). In these figures the shock is approximately  $185 \cdot 10^{-3}$  cm from the wall. The x and y units are  $10^{-3}$  cm.  $\Delta x_{min} = 1.95 \cdot 10^{-7}$  m.

### 8.7.3.4 N<sub>2</sub>O: Adiabatic BC

Firstly, looking at figure 8.28, as compared to the air adiabatic case, for N<sub>2</sub>O the foot is already 50 percent larger in height. In the next figure 8.29 at a distance of  $75 \cdot 10^{-6}$  m, a shocklet is forming behind the foot, the earliest of all results discussed so far. Another shocklet is also forming just below the triple point. In the last figure 8.30, the massive 4 cm long foot used in the experimental comparison is zoomed in on, showing the chaotic flow and large number of shocklets.

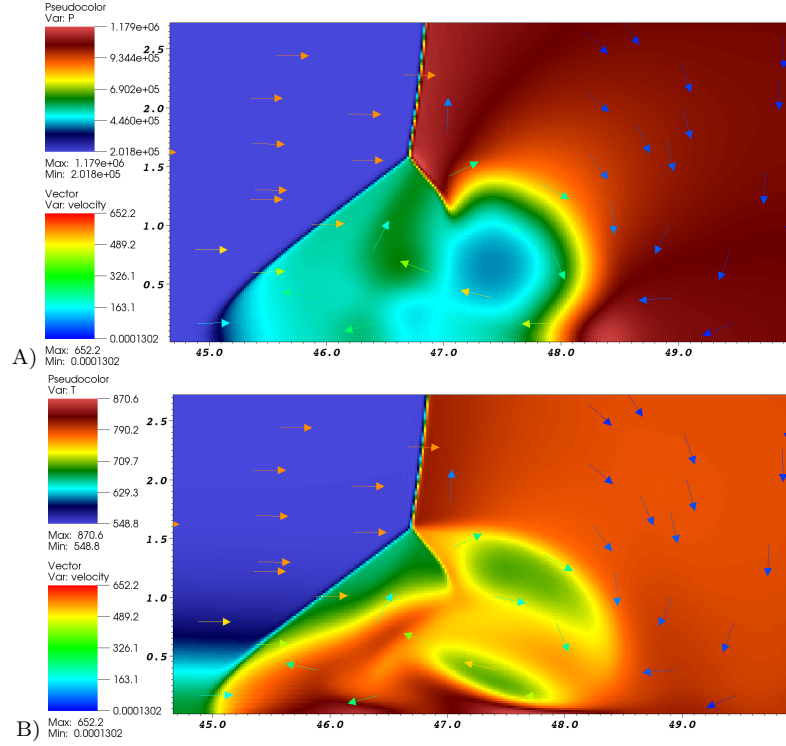


Figure 8.28: Adiabatic BC case: Velocity vectors superimposed on pseudo-color plots of various quantities for the N<sub>2</sub>O shock-bifurcation case with detailed chemistry and transport. Showing results for nondimensional A) pressure (Pa), and B) temperature (K). In these figures the shock is approximately  $3 \cdot 10^{-3}$  cm from the wall. The x and y units are  $10^{-3}$  cm.  $\Delta x_{min} = 4.88 \cdot 10^{-8}$  m.

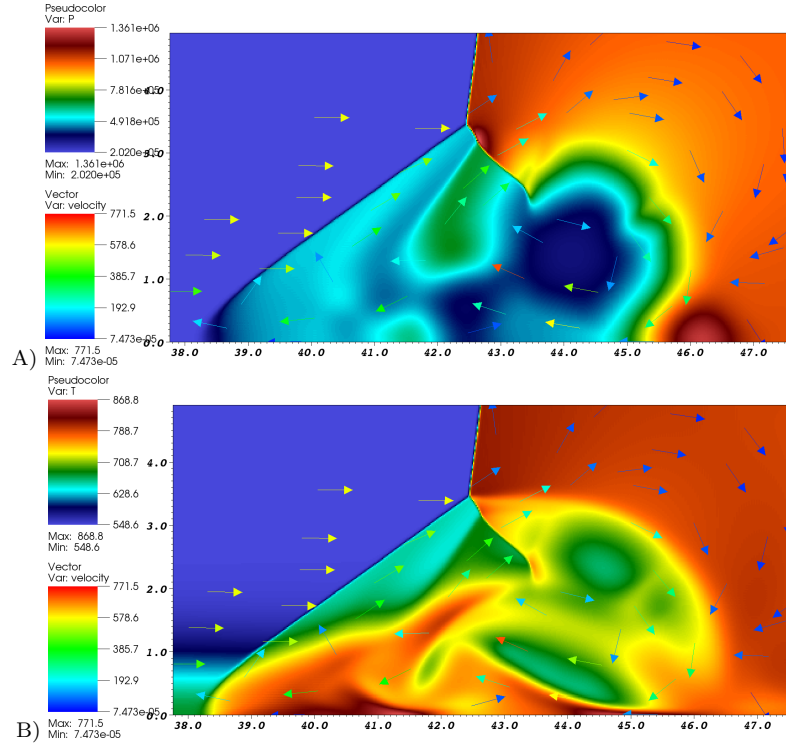


Figure 8.29: Adiabatic BC case: Velocity vectors superimposed on pseudo-color plots of various quantities for the  $N_2O$  shock-bifurcation case with detailed chemistry and transport. Showing results for nondimensional A) pressure (Pa), and B) temperature (K). In these figures the shock is approximately  $7.5 \cdot 10^{-3}$  cm from the wall. The x and y units are  $10^{-3}$  cm.  $\Delta x_{min} = 4.88 \cdot 10^{-8}$  m.



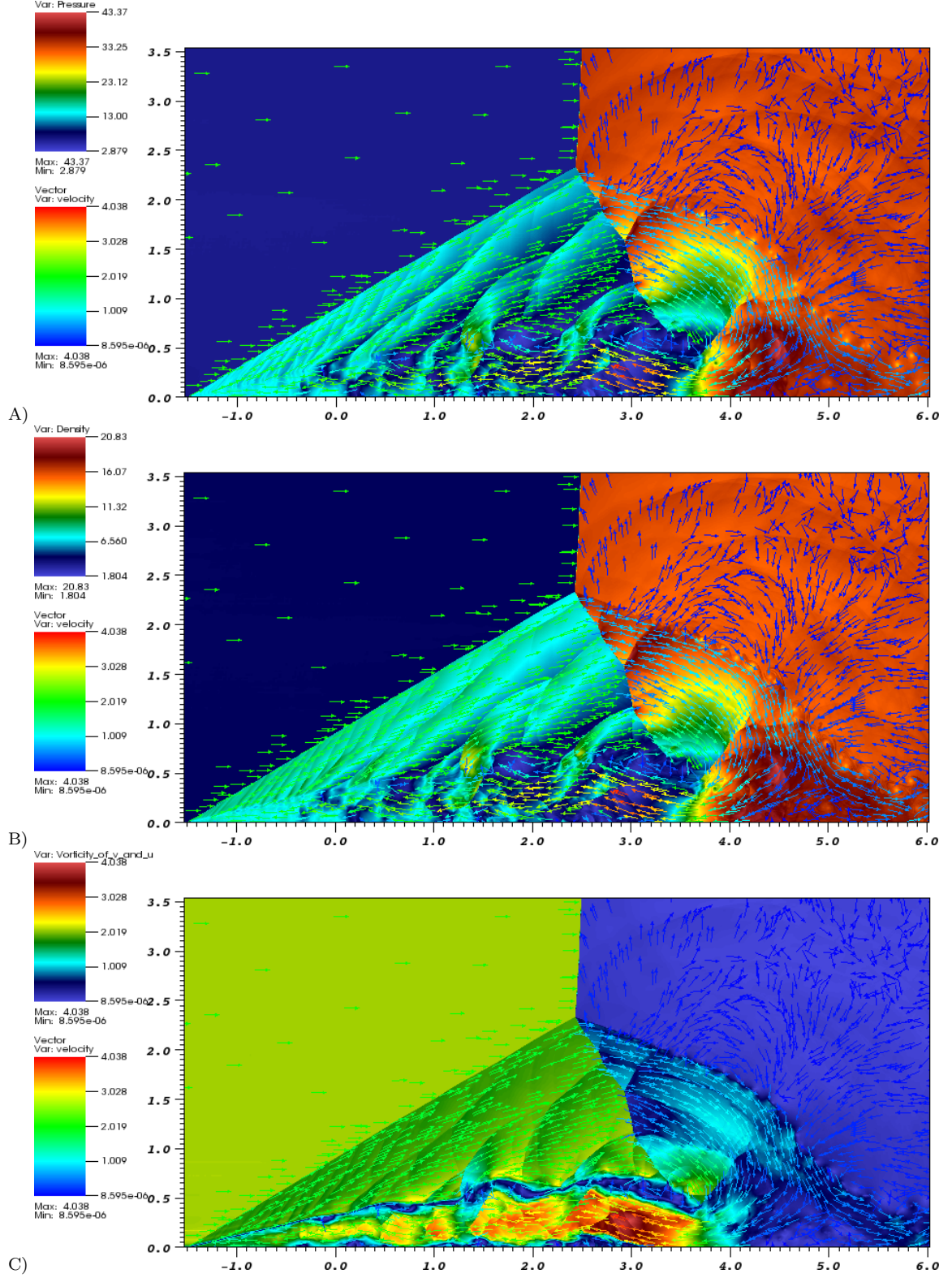


Figure 8.30: Adiabatic BC case: Velocity vectors pseudo-color plots for the  $\text{N}_2\text{O}$  shock-bifurcation case with detailed chemistry and transport. Showing results for nondimensional A) pressure, B) density, and C) vorticity. In these figures the reflected shock is approximately 4.5 cm from the wall. The x and y units are cm.  $\Delta x_{\min} = 2.19 \cdot 10^{-5}$  m.



### 8.7.3.5 H<sub>2</sub>-N<sub>2</sub>O: Adiabatic BC

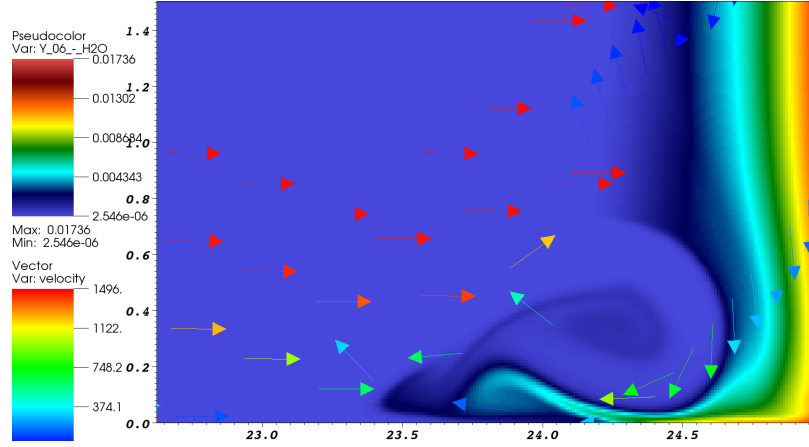


Figure 8.31: Velocity vectors superimposed on a pseudo-color plot of H<sub>2</sub>O mass fraction. In this figure the shock is approximately  $1 \cdot 10^{-3}$  cm from the wall. The x and y units are  $10^{-3}$  cm.  $\Delta x_{min} = 3.91 \cdot 10^{-8}$  m.

As was previously mentioned, for the reactive case, immediately after reflection in figure 8.32, the foot is already at a large size in length and height. This is presumed to be due to the accelerated rate of chemical reaction due to the heating of the fluid from the formation of the reflected shock and also from this shock interacting with the already preheated boundary layer from the adiabatic wall boundary condition. In figure 8.31, the pseudo-color plot of the H<sub>2</sub>O mass fraction shows the high concentrations near the right end wall, and also at the bottom wall where already one vortex is rolling up. Because of the enhanced temperature and pressure of the reflected wave, the induction length of the initially underdriven wave has been shortened and the detonation is now overdriven.

In the next set of results shown in figure 8.33, the foot has grown, the bottom vortices have gone even more unstable, and a local explosion of the right most vortex has occurred. This is identified by observing the appearance of two triple points in the pressure plot 8.33B) and the bubble of hot (red) fluid in the temperature plot 8.33D). Also, of note, is that the bottom vortices are much larger relative to the foot than those that were found in the nonreactive bifurcations. This again is due to the expansion of the fluid due to the chemical heat release.

In the next figure 8.34, at a later time where the reflected shock has traveled from  $70 \cdot 10^{-6}$  to  $240 \cdot 10^{-6}$  m and with two times less resolution, the same effects are seen. However, the previously, very individualized vortices have all diffused into each other. Also, the reflected shock has now gone unstable, forming triple points

which will eventually lead to a detonation cell pattern. Each of these triple points creates a shear layer, and these are observed in addition to the shear layer emanating from the main triple point of the foot. Note, that in the experiment, there was already a detonation cell pattern propagating behind the incident shock. In these simulations this was approximated with a steady ZND solution. However, because the induction length of the reflected shock/detonation is much larger than that for the incident shock/detonation, there is a finite region where accelerated reaction will take place. This region lasts all the way until the reflected reaches the end of the reaction zone of the incident detonation. Because the incident detonation is underdriven, the induction length and full reaction zone length are close to each other and are approximately equal to 0.716 and 1.66 cm. As a comparison, for the reflected overdriven detonation, the induction zone length is equal to approximately  $2.4 \cdot 10^{-6}$  m, and its full reaction length is approximately  $60 \cdot 10^{-6}$  m.

In the next figure 8.35, the same trends discussed continue. However, now the shape of the foot has changed. The angle of the foot has increased and the height of the foot is now about the same size as the length of the foot. Also, the region of the foot which is not occupied by vortices has increased in size. This change in geometry of the foot is presumed to be from the acceleration of reaction and the appearance of triple points below the main triple point.

In the last figure 8.36, where shock has traveled 2 cm, the triple points on the main reflected shock no longer exist. This is not due to the influence of numerical viscosity, as if one looks at the early times of reflection as in figure 8.35, even at this coarse resolution, the main reflected wave still goes unstable. However, after the wave has propagated approximately 1 cm from the end wall, the triple points on the main reflected wave disappear due to the pre-shocked consumption of fuel behind the incident detonation.

Another feature shown in figure 8.36 that does not appear in the nonreactive cases is a lifting of the rear-most wall vortex. This vortex has moved high enough such that it has pushed up the shear layer which emanates from the main triple point of the foot.

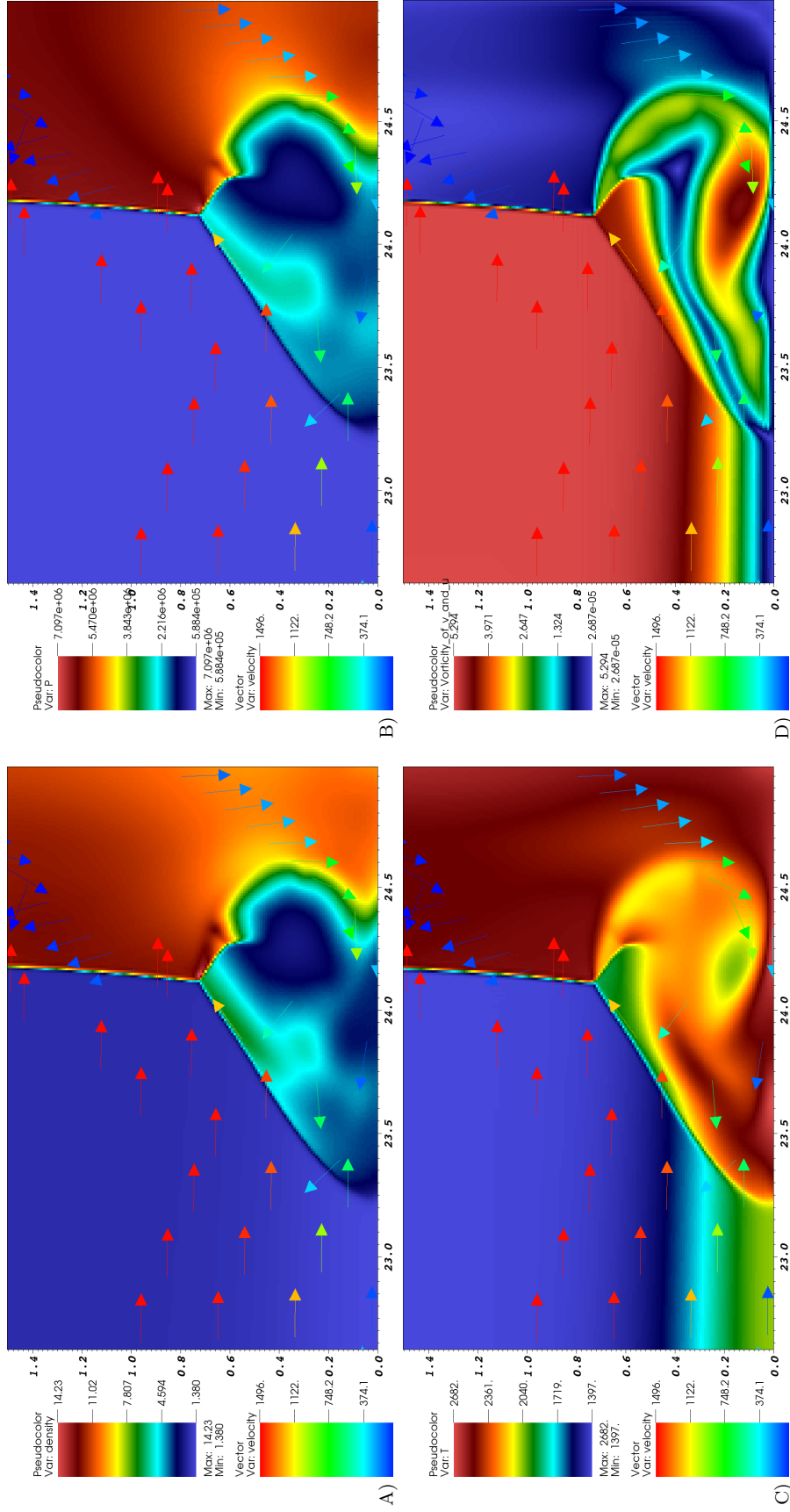


Figure 8.32: Velocity vectors superimposed on pseudo-color plots of various quantities for the detonation shock-bifurcation case with detailed chemistry and transport. Showing results for A) density ( $\text{kg/m}^2$ ), B) pressure (Pa), C) temperature (K), and D) nondimensional vorticity. In these figures the shock is approximately  $1 \cdot 10^{-3}$  cm from the wall. The x and y units are  $10^{-3}$  cm.  $\Delta x_{\min} = 3.91 \cdot 10^{-8}$  m.

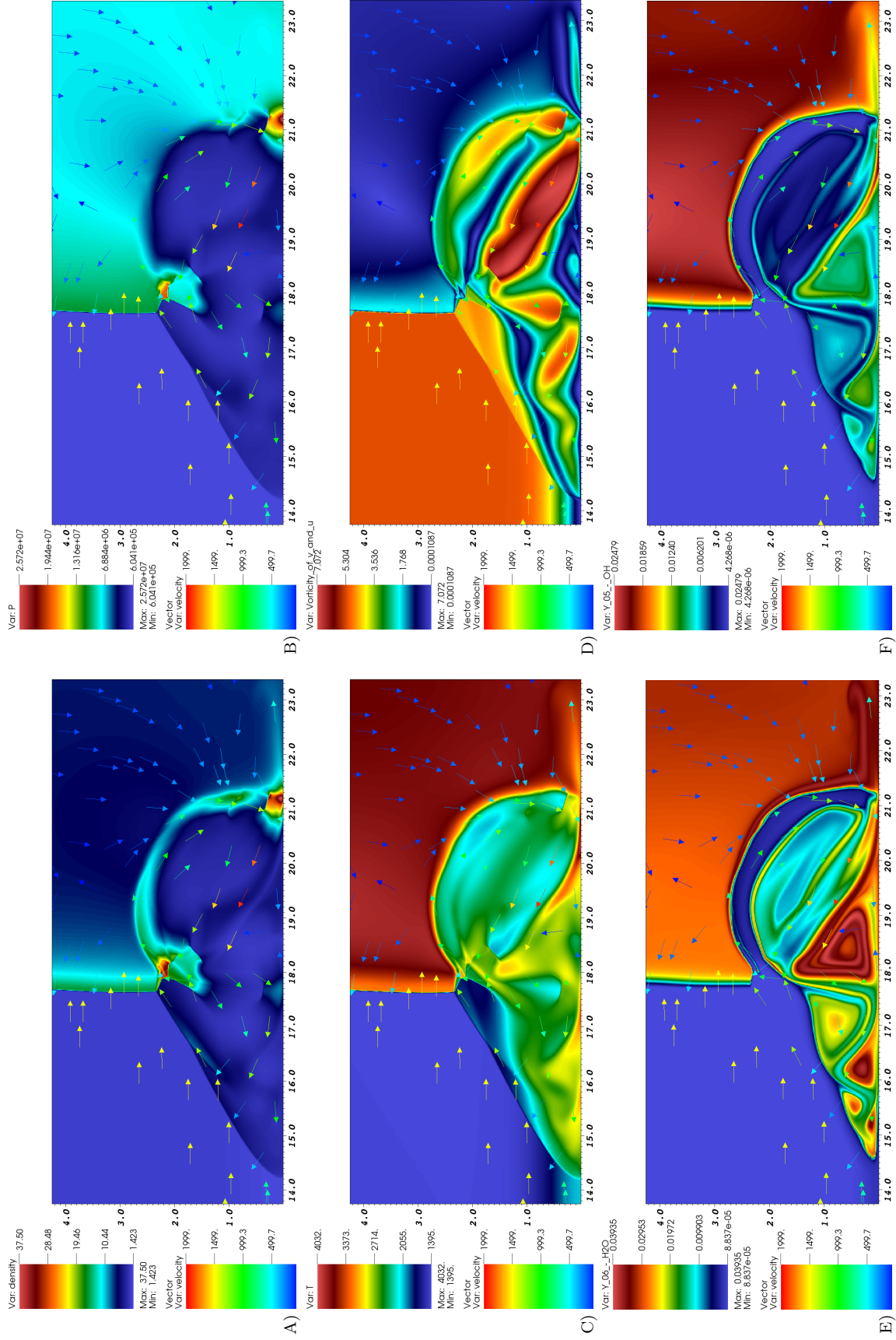


Figure 8.33: Velocity vectors superimposed on pseudo-color plots of various quantities for the detonation shock-bifurcation case with detailed chemistry and transport. Showing results for A) density (kg/m<sup>3</sup>), B) pressure (Pa), C) temperature (K), D) nondimensional vorticity, E) H<sub>2</sub>O mass fraction, and F) OH mass fraction. In these figures the shock is approximately 7·10<sup>-3</sup> cm from the wall. The x and y units are 10<sup>-3</sup> cm.  $\Delta x_{min} = 3.91 \cdot 10^{-8}$  m.

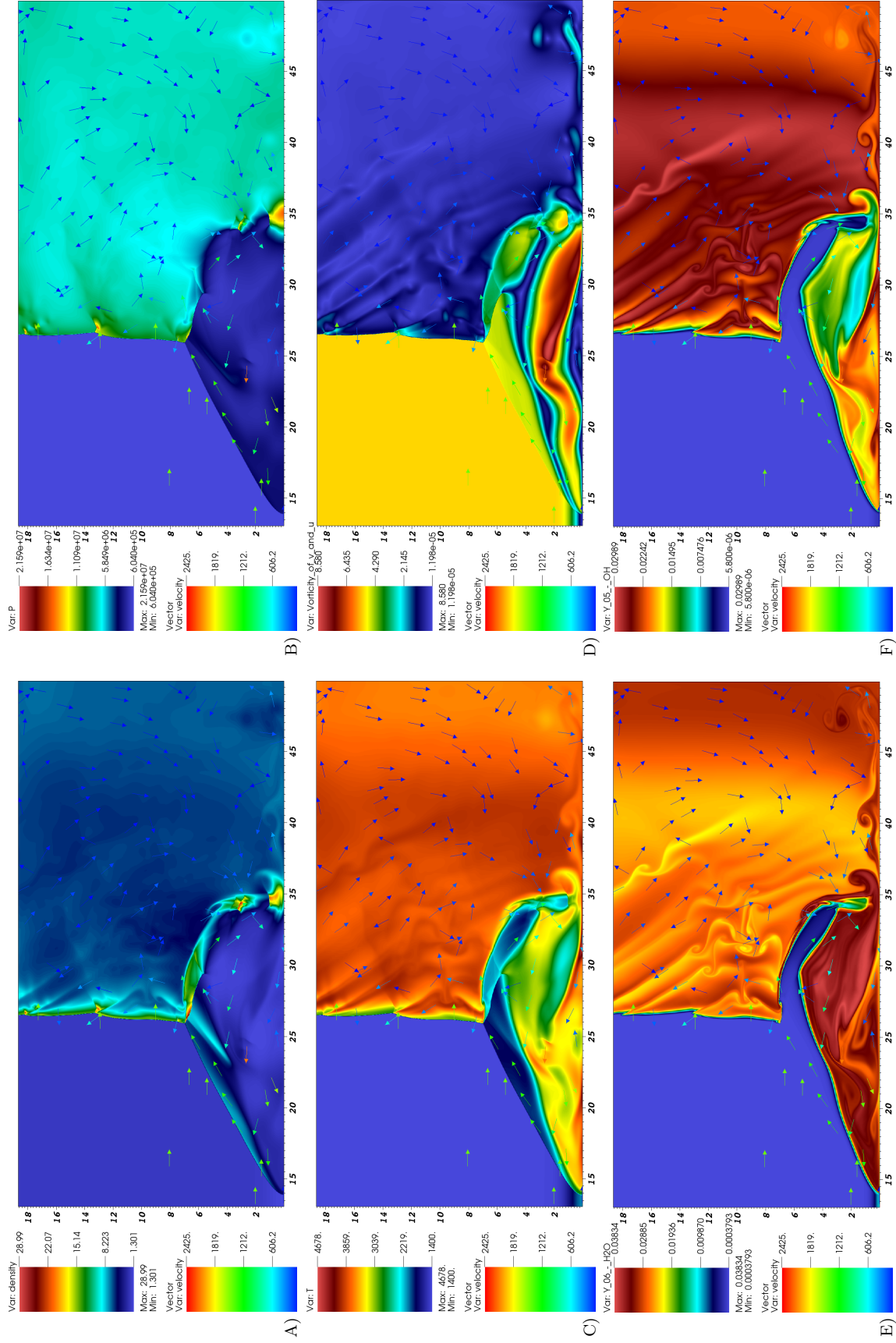


Figure 8.34: Velocity vectors superimposed on pseudo-color plots of various quantities for the detonation shock-bifurcation case with detailed chemistry and transport. Showing results for A) density (kg/m<sup>3</sup>), B) pressure (Pa), C) temperature (K), D) nondimensional vorticity, E) H<sub>2</sub>O mass fraction, and F) OH mass fraction. In these figures the shock is approximately  $24 \cdot 10^{-3}$  cm from the wall. The x and y units are  $10^{-3}$  cm.  $\Delta x_{min} = 7.81 \cdot 10^{-8}$  m.



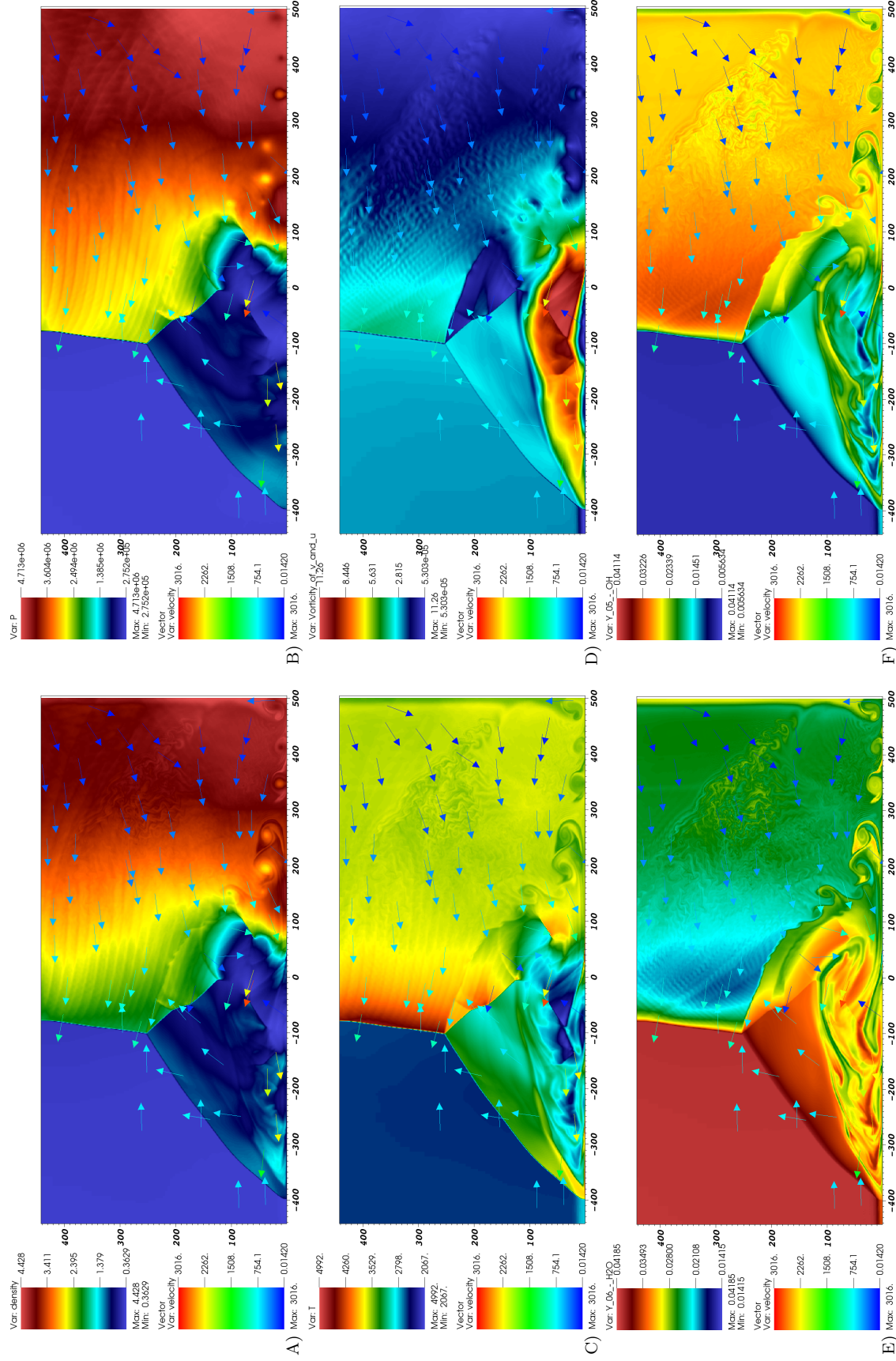


Figure 8.35: Velocity vectors superimposed on pseudo-color plots of various quantities for the detonation shock-bifurcation case with detailed chemistry and transport. Showing results for A) density ( $\text{kg/m}^3$ ), B) pressure (Pa), C) temperature (K), D) nondimensional vorticity, E)  $\text{H}_2\text{O}$  mass fraction, and F) OH mass fraction. In these figures the shock is approximately  $600 \cdot 10^{-3}$  cm from the wall. The x and y units are  $10^{-3}$  cm.  $\Delta x_{\min} = 1.09 \cdot 10^{-5}$  m.

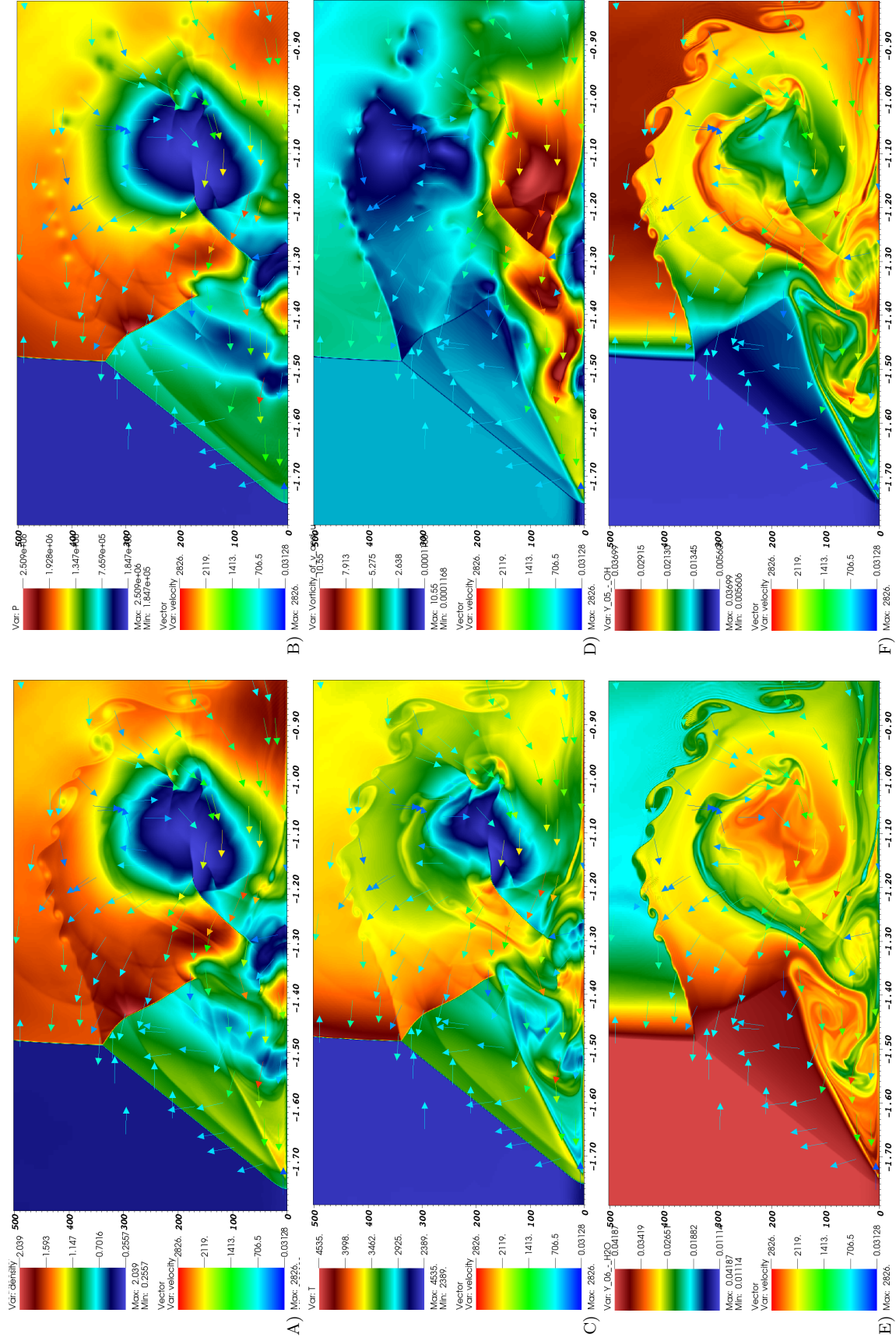


Figure 8.36: Velocity vectors superimposed on pseudo-color plots of various quantities for the detonation shock-bifurcation case with detailed chemistry and transport. Showing results for A) density ( $\text{kg/m}^3$ ), B) pressure (Pa), C) temperature (K), D) nondimensional vorticity, E)  $\text{H}_2\text{O}$  mass fraction, and F) OH mass fraction. In these figures the shock is approximately 2 cm from the wall. The x and y units are cm.  $\Delta x_{\min} = 1.09 \cdot 10^{-5}$  m.



### 8.7.3.6 Specific Heat Ratio

Also of possible influence on the size and existence of a foot is the specific heat ratio,  $\gamma$ . Mark found that for perfect gases, increasing the specific heat increases the region of existence of a bifurcated foot when considering all possible incident shock speeds. Shown in figure 8.37 is a comparison of the specific heats for air for the isothermal and adiabatic wall boundary cases. For the isothermal case, due to the temperature being lower, near the wall the specific heat has a maximum value of 1.398, whereas for the adiabatic wall, the value is slightly less than 1.37 near the wall. This could have a contribution to foot angle.

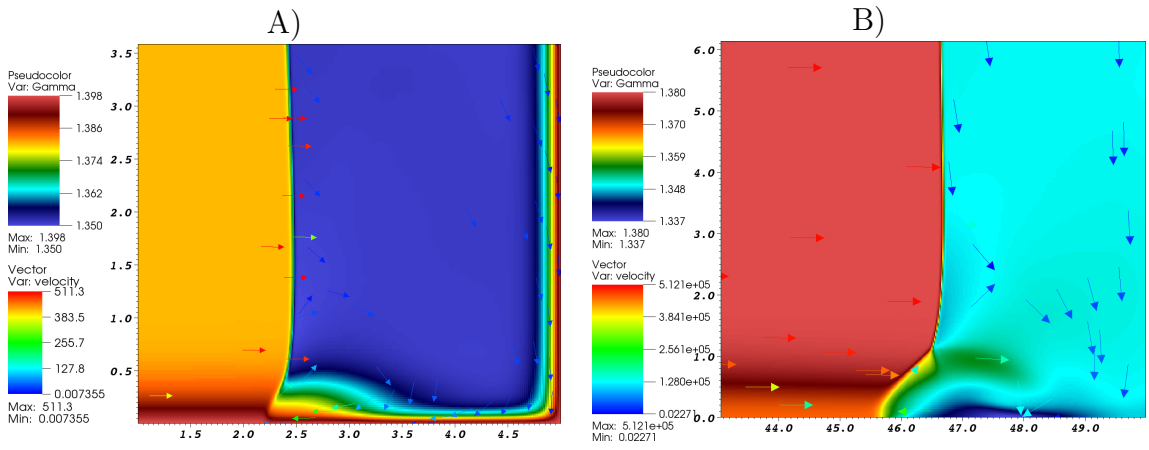


Figure 8.37: Specific heat,  $\gamma$  A) isothermal wall case, B) adiabatic wall case. A) velocity is in m/s and the wall is at  $x = 5 \cdot 10^{-3}$  cm, B) velocity is in mm/s and the wall is at  $x = 50 \cdot 10^{-3}$  cm.

### 8.7.4 Foot Geometry

The applicability of Mark's bifurcation theory to multi-component thermodynamics, detailed chemistry and transport was studied. For each of the three mixtures and for each of the two possible wall boundary conditions, whether a bifurcation should be expected and the angle  $\alpha$  that the foot creates was calculated. In figure 8.38, a diagram labeling the fluid states and foot geometry angles is shown. Note that this is a simplified, but still different convention of that used by Mark (114).

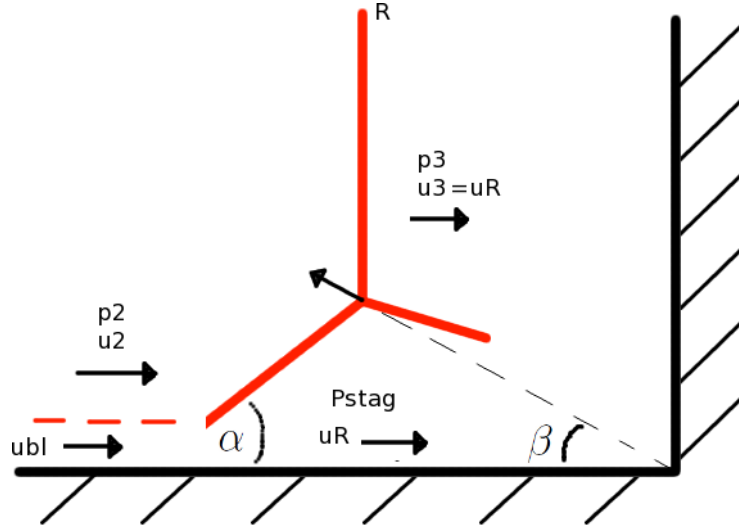


Figure 8.38: Schematic of the flow field after shock reflection from the tube end, in the reference frame of the reflected shock's triple point. The triple point connected to the reflected wave,  $R$ , moves at a nonconstant velocity  $\mathbf{u}_{triplepoint}$  traveling at a nonconstant angle  $\beta$ . The post incident shock state is state 2 and the post reflected shock state is state three. The boundary layer is approximated to be fixed to the wall and travel at a speed  $u_R$  with respect to the reflected shock. The foot formed by the reflect shock boundary layer interaction forms an angle  $\alpha$  with the wall and the triple point. Behind the foot, the flow speed is approximately zero in the reflected shock frame, leading to a stagnation pressure of  $p_{stag}$ .

As a first step, whether a bifurcation (a “foot”) appears in the flow is determined by calculation the stagnation pressure of the boundary layer and comparing this to the reflected shock pressure. If the stagnation pressure is lower, then a foot appears. The stagnation pressure depends on the pressure, density, and speed of the boundary layer with respect to the foot's speed which is approximately the same speed as the reflected shock,

$$p_{stag} = p_{bl} + \rho_{bl} u_R^2. \quad (8.3)$$

However, the density of the boundary layer is different depending on the boundary condition. In the case of an adiabatic wall, there is no heat loss and the temperature and density is that of the post incident shock,

$$\rho_{bl} = \frac{RT_2}{p_2}. \quad (8.4)$$

In the other case, for an isothermal wall, the boundary layer is approximated to have a constant temperature which is equal to the ambient state,

$$\rho_{bl} = \frac{RT_1}{p_2}, \quad (8.5)$$

where  $T_1$  is the ambient temperature. In reality, there is a solid/gas heat conduction problem which governs the nonlinear nonconstant boundary layer temperature, however, approximating the wall as isothermal is the more realistic choice of the two. In shock and detonation cases simulated, a foot was predicted by Mark's theory.

By making an assumption about the angle  $\beta$  at which the triple point travels, the angle  $\alpha$ , that the foot makes with the wall can also be computed. It is theorized that the post shock pressure behind the foot must be equal to the stagnation pressure of the boundary layer. This post shock pressure is calculated by transforming the problem in the reference frame of the foot which moves at the same velocity of the triple point above it. The triple point is traveling at an unknown angle, and therefore, this angle was either assumed to be zero or equal the average value found in the simulations. The velocity of the triple point depends on the angle  $\beta$  in the following fashion,

$$\mathbf{u}_{triplepoint} = u_R \cdot \mathbf{i} + u_R \tan \beta \cdot \mathbf{j}. \quad (8.6)$$

This leads to a velocity in state 2 of the flow where its normal component depends on both the angles  $\alpha$  and  $\beta$ ,

$$u_N = [(u_2 + u_R) + u_R \tan \beta] \sin \alpha. \quad (8.7)$$

With this relation, the **Shock and Detonation Toolbox** was used to reverse engineer a post shock pressure based on the angle  $\alpha$ . The angle  $\alpha$  which leads to a pressure equal to the stagnation pressure is the solution.

The described calculation was carried out for each of the three mixtures, for each of the two wall boundary conditions, and  $\beta$  approximated as zero or as the average simulation value. Additionally, for the detonation case, the post shock state

was assumed to be for both state 2 and the region behind the foot to be either “frozen” with no chemical reactions, or “equilibrium” with all chemical reactions going to completion. The results are organized in table 8.4 below. Mark’s theory

Mixture	Wall BC	Empirical $\beta$ input	$P_{stagnation}$	$\alpha$ output (theory)	$\alpha$ (simulation)
Air	adiabatic	0	$2.41 \cdot 10^5$ Pa	44.7	39-47
Air	adiabatic	14	$2.41 \cdot 10^5$ Pa	39.7	39-47
Air	isothermal	0	$3.29 \cdot 10^5$ Pa	54.2	49-57
Air	isothermal	5	$7.94 \cdot 10^5$ Pa	45.0	49-57
N <sub>2</sub> O	adiabatic	0	$1.78 \cdot 10^5$ Pa	32.8	31-44
N <sub>2</sub> O	adiabatic	25	$1.78 \cdot 10^5$ Pa	28.7	31-44
N <sub>2</sub> O	isothermal	0	$2.25 \cdot 10^5$ Pa	37.2	35-51
N <sub>2</sub> O	isothermal	14	$2.25 \cdot 10^5$ Pa	33.3	35-51
9H <sub>2</sub> -N <sub>2</sub> O frozen chem.	adiabatic	0	$9.47 \cdot 10^5$ Pa	27.8	29-56
9H <sub>2</sub> -N <sub>2</sub> O frozen chem.	adiabatic	20	$9.47 \cdot 10^5$ Pa	25.3	29-56
9H <sub>2</sub> -N <sub>2</sub> O frozen chem.	isothermal	0	$2.85 \cdot 10^6$ Pa	51.8	-
9H <sub>2</sub> -N <sub>2</sub> O frozen chem.	isothermal	20	$2.85 \cdot 10^6$ Pa	46.1	-
9H <sub>2</sub> -N <sub>2</sub> O equil. chem.	adiabatic	0	$7.94 \cdot 10^5$ Pa	33.0	29-56
9H <sub>2</sub> -N <sub>2</sub> O equil. chem.	adiabatic	20	$7.94 \cdot 10^5$ Pa	29.7	29-56
9H <sub>2</sub> -N <sub>2</sub> O equil. chem.	isothermal	0	$2.70 \cdot 10^6$ Pa	77.8	-
9H <sub>2</sub> -N <sub>2</sub> O equil. chem.	isothermal	20	$2.70 \cdot 10^6$ Pa	62.7	-

Table 8.4: Table of parameters comparing results from DNS and Mark’s Theory using three-shock theory and the **Shock and Detonation Toolbox** for detailed thermodynamics and chemistry. Mark’s theory has two input parameters, the incident shock Mach number and an optional triple point vertical displacement angle  $\beta$ . The output from the theory is the angle  $\alpha$ , which describes the size of the foot. This angle is compared to the DNS values for the two wall boundary conditions, isothermal and adiabatic.

does surprisingly well predicting the angle  $\alpha$  given the complexity involved in the simulations. Even more importantly, the theory predicts the trends of the angle when changing the mixture type and using the adiabatic or isothermal boundary condition. In all cases, a smaller angle  $\alpha$  is predicted when an adiabatic boundary condition is used. Also predicted is that for the air case, the angle  $\alpha$  is larger, leading to a shorter foot as was observed in the simulations. Another trend that the theory predicts is the increasing the angle  $\beta$  always decreases the angle  $\alpha$ . For just the reactive case, the equilibrium chemistry leads to a larger  $\alpha$  which better matches the simulations. Also, by looking at the isothermal detonation result with equilibrium chemistry, very large  $\alpha$  angles (63-78 degrees) are predicted. This better matches the very short foot which was found in experiment and shown in figure 8.8.

Of important note, is that in the simulations, the angles  $\alpha$  and  $\beta$  change with time and also with the different resolutions used in each simulation. These changes are plotted and discussed in §8.7.4.1 and §8.7.4.2.

#### 8.7.4.1 Bifurcation Shock Geometry

For each of the nonreactive shock mixtures and for both boundary conditions, the geometrical properties of foot length and triple point height,  $\delta$ , and the angles  $\alpha$  and  $\beta$  as labeled in figure 8.2 were studied. Also, studied was the effect of grid resolution on these properties.

In figures 8.39-8.42, these properties are plotted with respect to the distance,  $x$ , the reflected shock has traveled past the wall. The first two plots of each for the triple point height and the foot length are on a log-log scale. The last two plots of each are on a log scale only for the  $x$ -axis.

For all nonreactive cases, the foot length and triple point height grow at similar polynomial rates. On a log-log plot these growth rates appear as linear with a slope of approximately one. In all nonreactive cases, the angle  $\alpha$  begins at a value of approximately 50 degrees, and then decreases linearly on a  $x$ -log plot. The angle  $\beta$  appears to be the most sensitive of all parameters. For the adiabatic air case and for both  $N_2O$  cases, a general trend of slowly decreasing and then slowly increasing angle as the foot moves farther from the wall is found. Gaining insight on trends for the isothermal air case is more difficult as the affect of resolution on the results is found to be relatively large.

The air case with an isothermal wall has the smallest foot length and height out of all the nonreactive cases studied. Not surprisingly is the result that with a smaller scale, the viscous effects of numerical viscosity are much larger. In the plots of the foot growth, triple point height, and  $\beta$  change in figure 8.39, each resolution has a largely different starting value. Despite this, the curves over all have the same general shapes.

Another factor that could be affecting the results when simulated at different resolution is the starting distance for the incident shock. Due to domain size constraints, for each resolution the incident shock and hence initial boundary layer was started at different distances from the end wall. Ideally, to get the best results for an experimental comparison, the shock should be started at a distance equal to the length of the tube. However, this is obviously too expensive to simulate for a resolved simulation.

Other trends of note, are a comparison of the isothermal to adiabatic results. For the angle  $\beta$ , the adiabatic results yields a larger result, and a taller foot. For the angle  $\alpha$ , the adiabatic results yields a smaller result and hence a longer foot. For  $N_2O$ , the slopes of the log-log foot-length and foot-height plots are similar for the isothermal and adiabatic wall. For air, the isothermal wall slope is slightly steeper.

### Comparisons to Past Works

Using the available experimental data for comparison at the time of 1969, Davies and Wilson (36), improved on Mark's theory of the 1950s (114). They used the boundary layer models of Mirels to calculate the growth rate of the bifurcated foot from shock reflection. Two growth rate models were constructed, one for laminar and one for turbulent boundary layers. The laminar theory was based on the Blasius equation and the turbulent theory was based on an empirical model of the boundary layer thickness. To obtain a foot height, the mass flow rate equations of the boundary layers were integrated (with some additional approximations based on experimental findings) and with the knowledge of a foot temperature, the foot volume was found, which led to a calculated foot height based on the distance from the end wall. This led to a  $x^{\frac{3}{4}}$  dependence for the laminar case ( $\delta = \delta_L(M_s)x^{\frac{3}{4}}p_{amb}^4$ ), and a  $x^{\frac{9}{10}}$  dependence for the turbulent case ( $\delta = \delta_T(M_s)x^{\frac{9}{10}}p_{amb}^{10}$ ). In experiment, all cases followed a  $x^1$  dependence, therefore, the laminar theory was proven deficient. Their theoretical models are also only valid up to Mach numbers of 3.6.

Our simulation results also show a linear trend agreeing with experiment for the foot height growth rate. Ignoring the unresolved large-scale results, polynomial fits were constructed for each of the test cases:

$$\text{N}_2\text{O (isothermal): } \delta = 0.18x^{0.95}$$

$$\text{N}_2\text{O (adiabatic): } \delta = 0.38x^{0.98}$$

$$\text{Air (isothermal): } \delta = 0.12x^{1.06}$$

$$\text{Air (adiabatic): } \delta = 0.27x^{1.01}$$

These agree very with the experimental rate of approximately  $x^1$ , considering the larger  $x$  values used in the fits are only marginally rather than fully resolved, especially for the isothermal wall air test case.

In the previous simulations of Weber *et al.* (159), a similar trend was found. In these simulations, the bifurcation was simulated for a shock in air which had traveled up to approximately 10 cm. Three Mach numbers were tested: 2.6, 5.0, and 10.0. They used different incident shock conditions than our tests (Mach number of 2.6 and initial pressure of 0.02 atm = 2,026.5 Pa) and a single component perfect gas model. A linear foot growth rate was found, but only up to 9 cm of foot travel where the rate leveled off to practically zero. This trend agrees with experiments of Matsuo *et al.* where the rate decreased rapidly at a distance of 7 cm. This led to Weber's simulations overestimating the growth by 20 percent at  $x = 11$  cm. However, up to approximately 6 cm the results agreed very well with experiment. This discrepancy is surmised to be due to a lack of grid resolution which is needed to simulate the

turbulent shear and boundary layers that are most likely present at this distance. These results were for the isothermal wall case. Similarly to our approach, they also simulated the adiabatic wall and found a significantly larger foot and a loss of linearity at approximately  $x = 6$  cm.

The evidence for a lack of resolution in Weber's simulations is supported by a result in which they decreased the cell size by 50 percent and found the foot angle  $\alpha$  to decrease by 1 percent and the foot height to decrease by 4.2 percent. This trend suggests that using more resolution would produce a result that would better match experiment. Weber et al. also simulated a resolved case with a very low pressure of 206.5 Pa and (with now a larger bifurcation for  $x$  up to 12 cm) and found a more convincing trend that is shown by experiments in general. However, no experimental data at this low pressure existed at the time. Unlike the unresolved result, when the linearity of the growth rate stopped, a slow increase rather than a practically lack of growth was found.

In our simulations, due to the much higher initial pressures tested, our bifurcations showed no approach to linearity in the range  $x = 0$  to 5 cm for the reflected shock. Our large-scale simulations with the 14 cm sized domain are, like Weber's results, unresolved. However, except for our even less resolved isothermal air case, the shock-bifurcation results at high and low resolutions exhibit basically the same trends. Also, of important note is the improvement of our numerical method over the high numerical viscosity creating low (second rather than sixth) order FCT method.



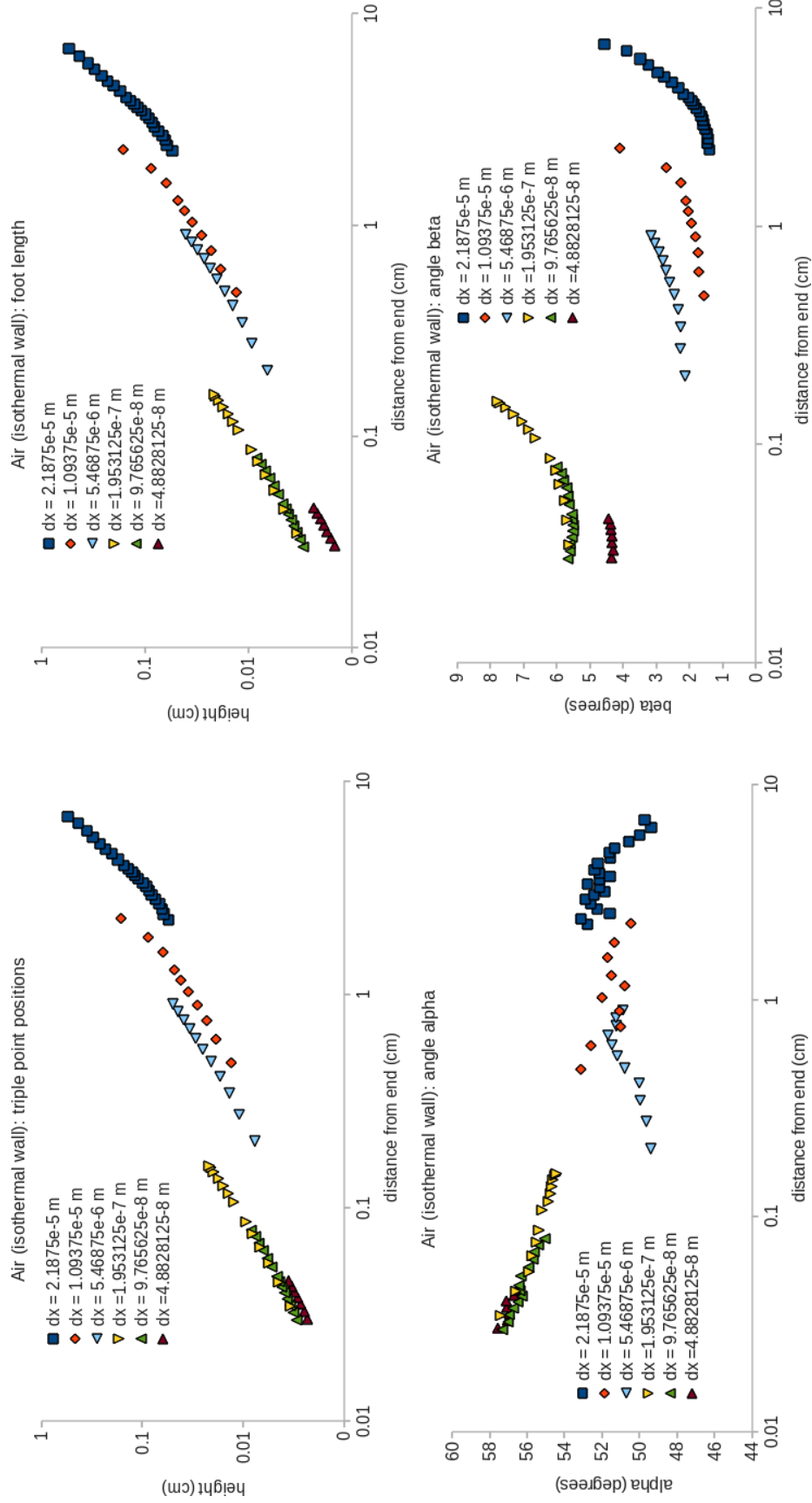


Figure 8.39: Air: isothermal wall results. Showing the evolution of triple point height, angle  $\alpha$ , and angle  $\beta$  as the triple point moves a horizontal distance from the end wall.

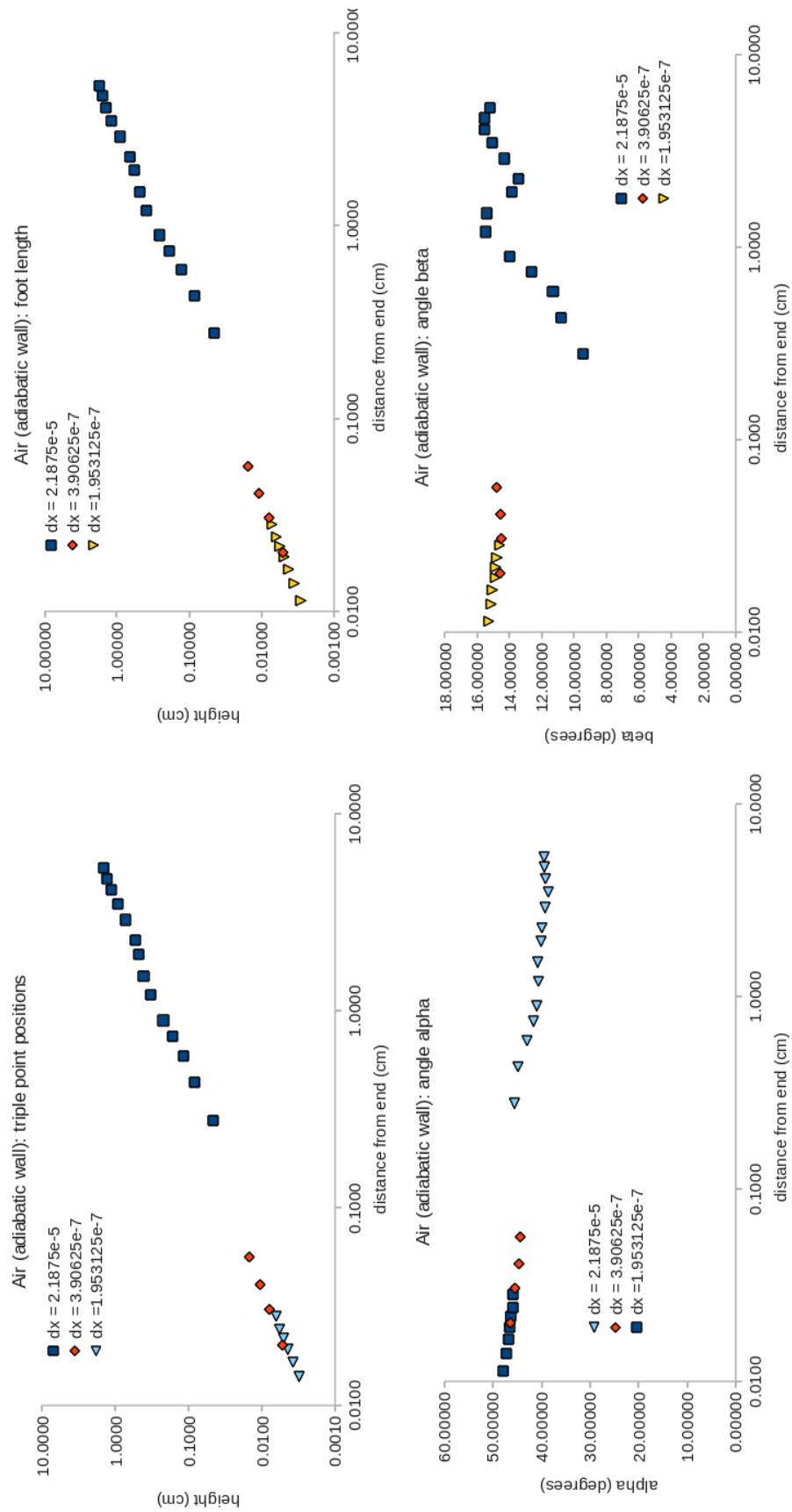


Figure 8.40: Air: adiabatic wall results. Showing the evolution of triple point height, angle  $\alpha$ , and angle  $\beta$  as the triple point moves a horizontal distance from the end wall.

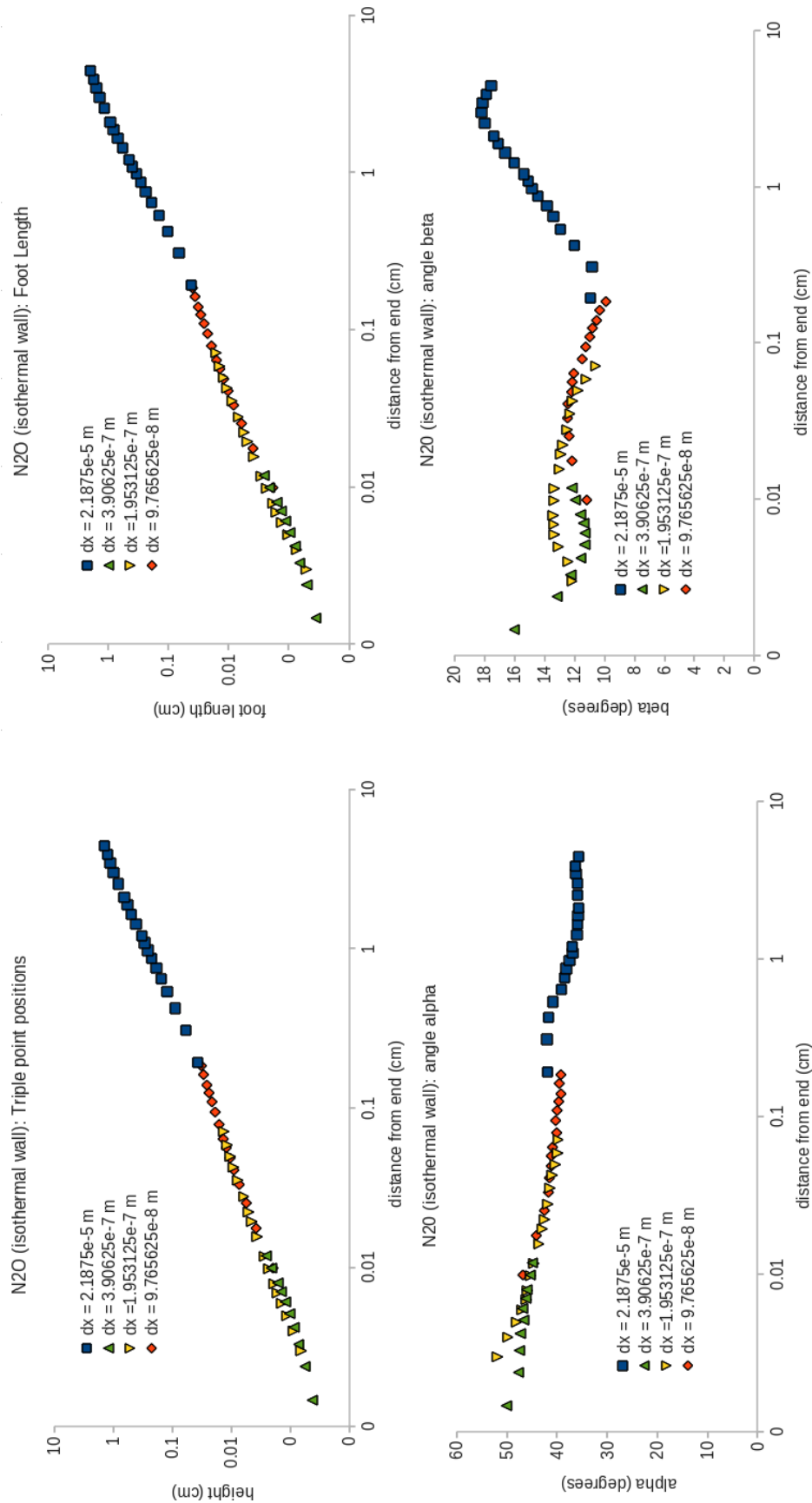


Figure 8.41: N<sub>2</sub>O: isothermal wall results. Showing the evolution of triple point height, foot length, angle  $\alpha$ , and angle  $\beta$  as the triple point moves a horizontal distance from the end wall.

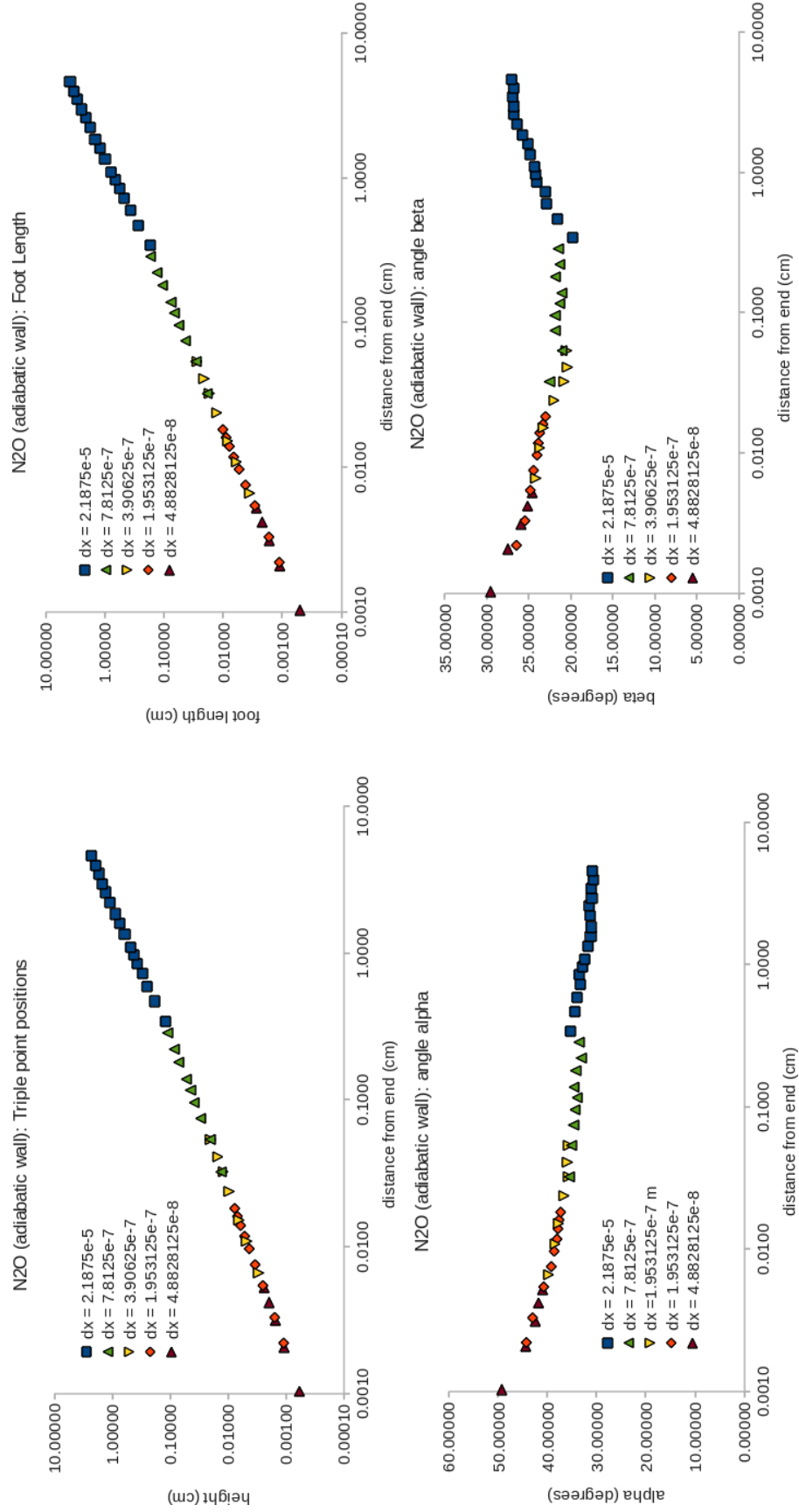


Figure 8.42:  $N_2O$ : adiabatic wall results. Showing the evolution of triple point height, foot length, angle  $\alpha$ , and angle  $\beta$  as the triple point moves a horizontal distance from the end wall.

#### 8.7.4.2 Bifurcation $\text{H}_2\text{-N}_2\text{O}$ Detonation Geometry

In figure 8.43, the geometrical parameters of the detonation with an adiabatic boundary are shown over the range of resolutions and distances from the end wall. Except for the coarsest resolution where numerical viscosity is influencing the solution, the different curves of resolution match up very closely.

At the early times of reflection, the foot length and height are increasing linearly (on a log-log plot) and the angles  $\alpha$  and  $\beta$  are both decreasing with  $\beta$  decreasing at a greater rate. This translates into the foot length growing proportionally faster than the foot height. Then a farther distance from the wall, for all properties, but most obviously for the angle  $\beta$  there is a trend change. Specifically the curvature on the plots reverse at  $x = 0.01$  cm. The foot length and height growth temporarily go to zero before increasing again, and the angle  $\alpha$  stop decreasing and start to increase and then decrease again. As discussed in §8.7.3.5, this is surmised to be due to a local explosion occurring in the rear-most vortex of the foot. This vortex with its two triple points and pressure rise slightly raises the main triple point.

For the parameters in the figure, yet another, clear change in inflection and trend occurs when the induction length of the incident wave (0.716 cm, as discussed in §8.7.3.5) has been passed. For the foot height/triple point y-position, the growth completely stops until a horizontal distance of 4 cm has been reached. For the foot length, the opposite trend results with the lengthening of the foot accelerating until approximately 4 cm of travel has been reached. Because the foot height has become temporarily constant, this translates into the angle  $\alpha$  also growing rapidly and the angle  $\beta$  decreasing rapidly.

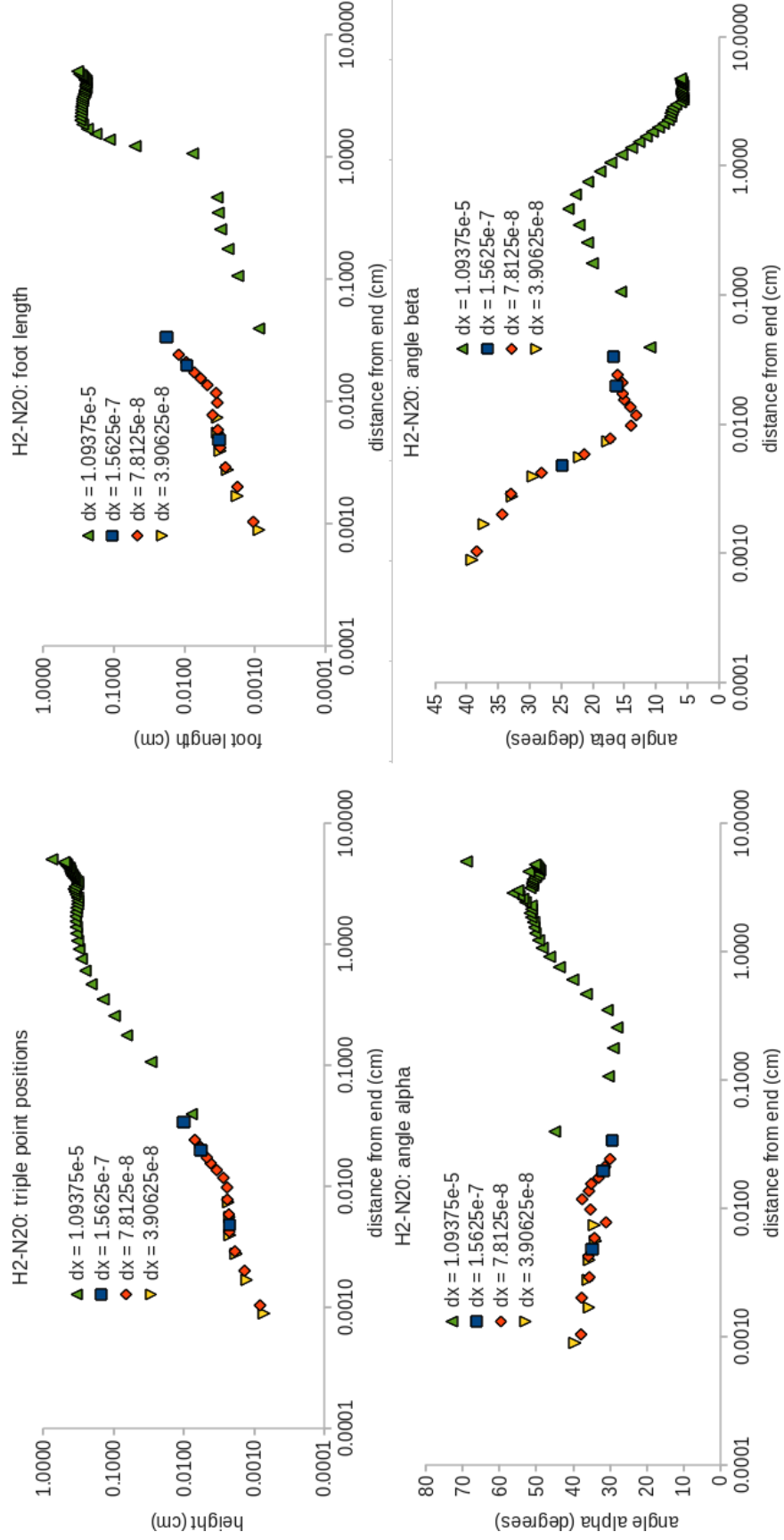


Figure 8.43:  $H_2-N_2O$ : adiabatic wall results. Showing the evolution of triple point height, foot length, angle  $\alpha$ , and angle  $\beta$  as the triple point moves a horizontal distance from the end wall.

### 8.7.5 Pressure Traces

Now, as was done for the simplified two-component model in § 8.6, the pressure traces at different times and heights about the bottom wall of the tube are plotted. These are plotted with the earliest time trace at the bottom and the later time traces piled on top sequentially. The experimental results for a detonation in figure 8.1 are plotted verses time, but with pressure gauges at farther distances from the end wall stacked on top of the previous sequentially. Results are shown for the shock cases with the isothermal wall in figures 8.44-8.46 for air and figures 8.47-8.49 for  $\text{N}_2\text{O}$ . The adiabatic wall detonation results are shown in figures 8.50-8.52.



## 8.7.5.1 Air

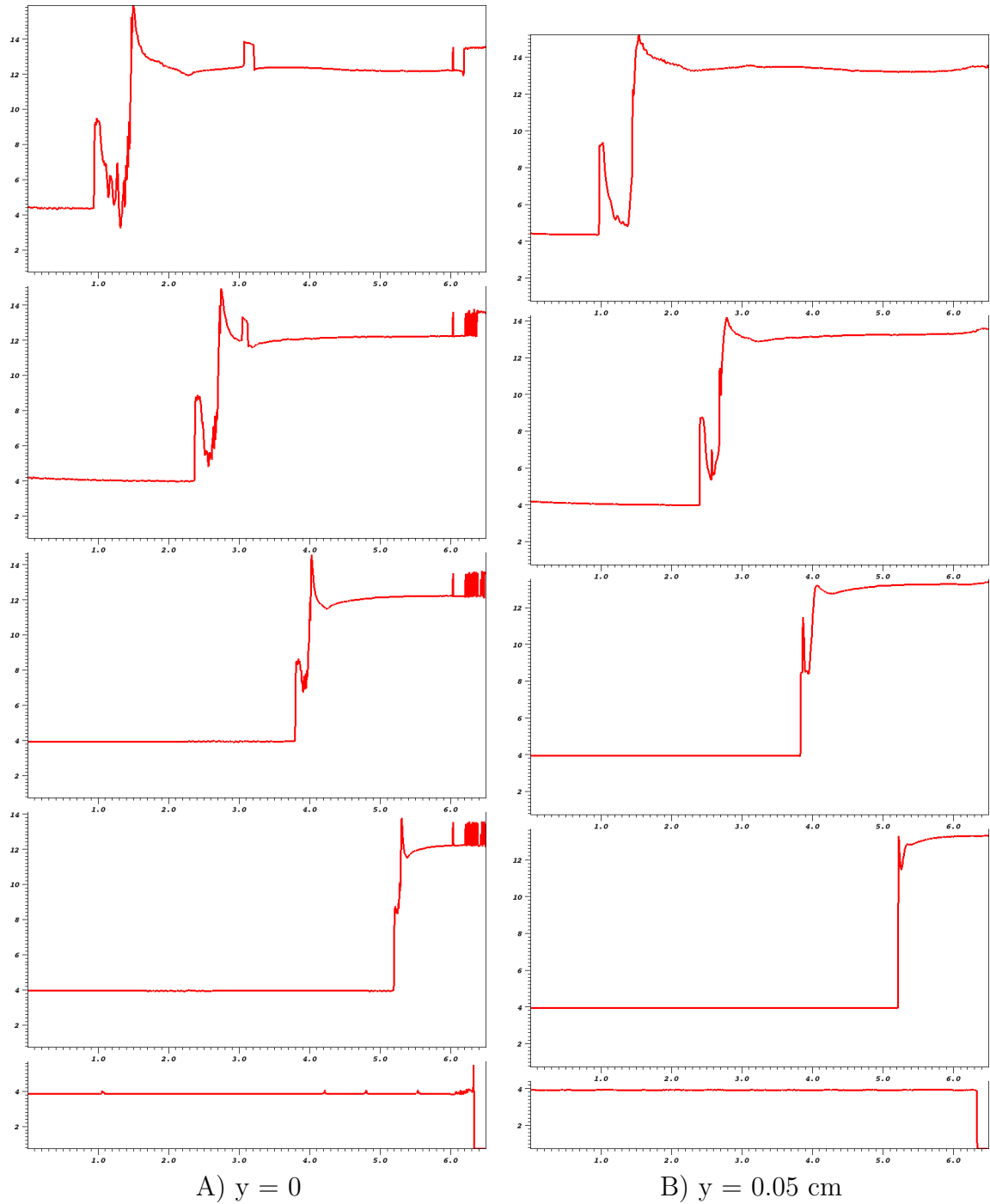


Figure 8.44: Air: Pressure (MPa) traces. The x-axis is cm and the tube end is at  $x = 6.5 \text{ cm}$ . Showing traces at times  $t = 150, 1650, 3150, 4650, 6150$  (nondim) which is equivalent to  $t = 4.328 \cdot 10^{-6}, 4.761 \cdot 10^{-5}, 9.089 \cdot 10^{-5}, 1.342 \cdot 10^{-4}, 1.775 \cdot 10^{-4} \text{ sec}$ .

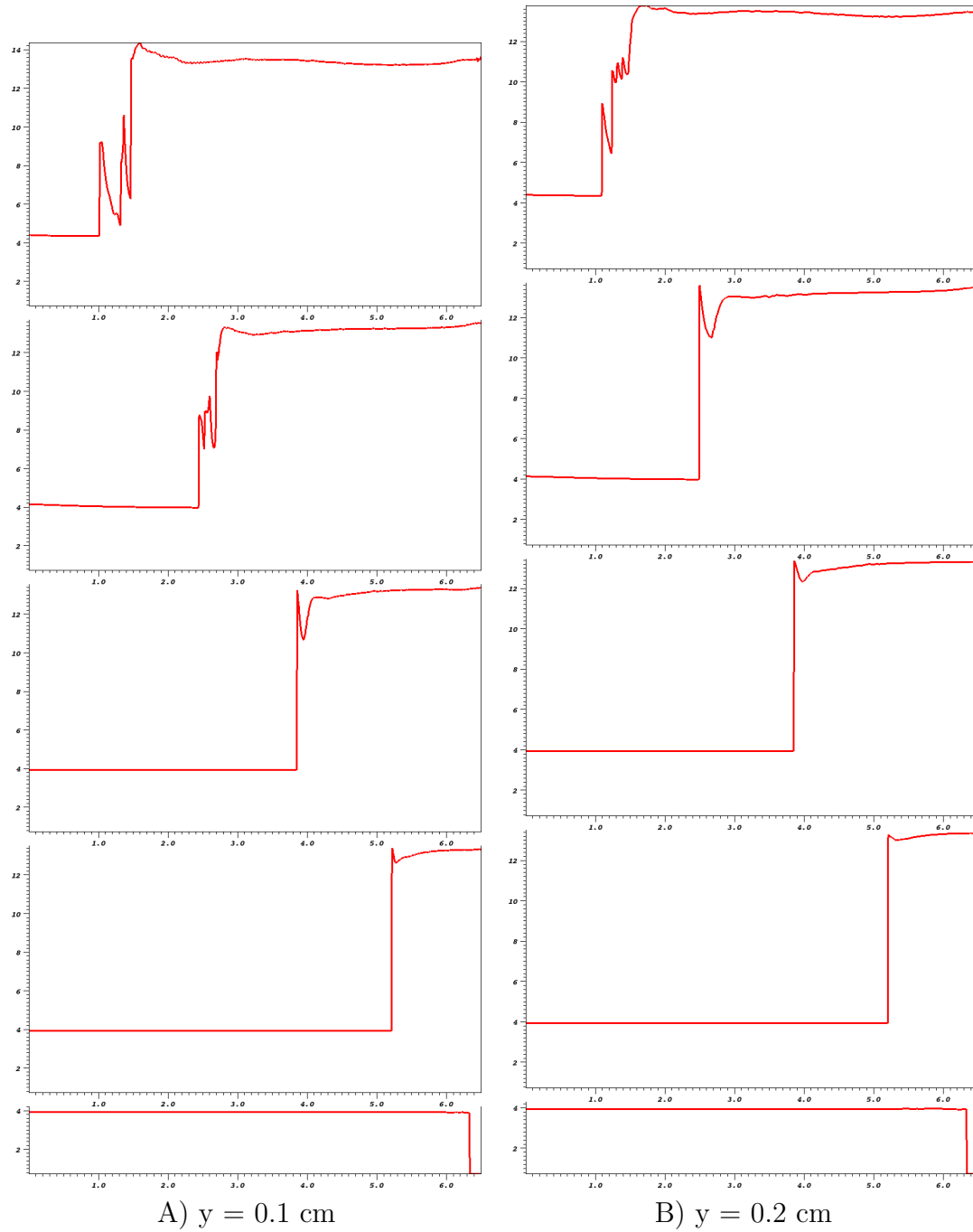


Figure 8.45: Air: Pressure (MPa) traces. The x-axis is cm and the tube end is at  $x = 6.5$  cm. Showing traces at times  $t = 150, 1650, 3150, 4650, 6150$  (nondim) which is equivalent to  $t = 4.328 \cdot 10^{-6}, 4.761 \cdot 10^{-5}, 9.089 \cdot 10^{-5}, 1.342 \cdot 10^{-4}, 1.775 \cdot 10^{-4}$  sec.

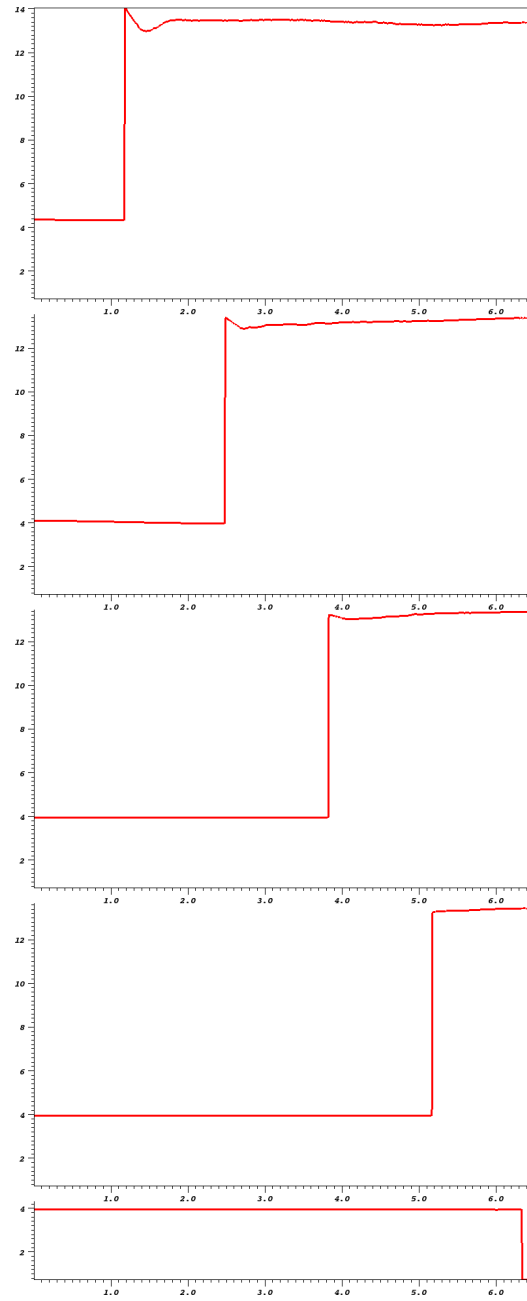


Figure 8.46: Air:  $y = 0.5$  cm pressure (MPa) trace. The x-axis is cm and the tube end is at  $x = 6.5$  cm. Showing traces at times  $t = 150, 1650, 3150, 4650, 6150$  (nondim) which is equivalent to  $t = 4.328 \cdot 10^{-6}, 4.761 \cdot 10^{-5}, 9.089 \cdot 10^{-5}, 1.342 \cdot 10^{-4}, 1.775 \cdot 10^{-4}$  sec.

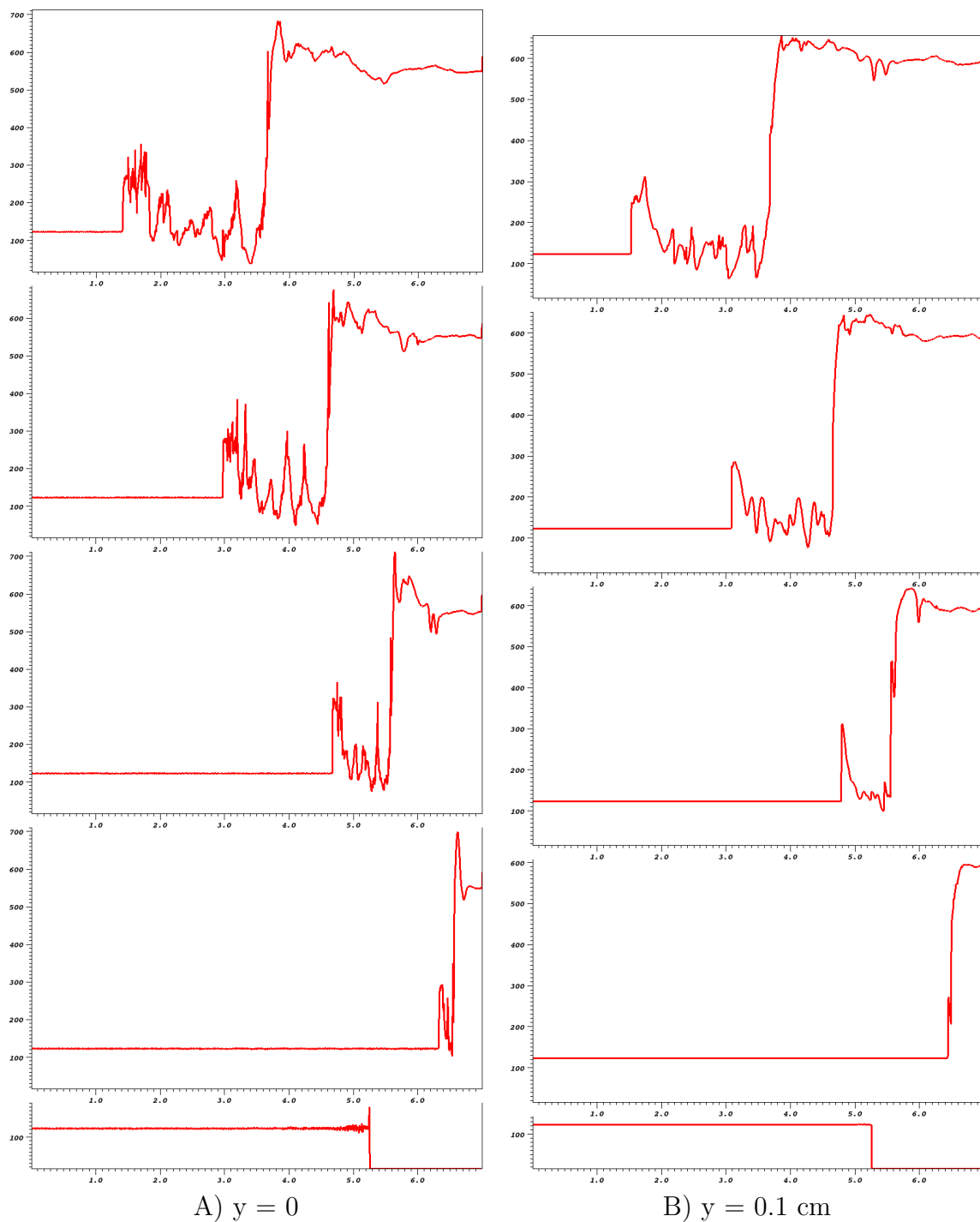
8.7.5.2 N<sub>2</sub>O

Figure 8.47: N<sub>2</sub>O: Pressure (KPa) traces. The x-axis is cm and the tube end is at  $x = 7 \text{ cm}$ . Showing traces at times  $t = 2100, 3600, 5100, 6600, 8100$  (nondim) which is equivalent to  $t = 7.841 \cdot 10^{-5}, 1.344 \cdot 10^{-4}, 1.904 \cdot 10^{-4}, 2.464 \cdot 10^{-4}, 3.024 \cdot 10^{-4} \text{ sec}$ .

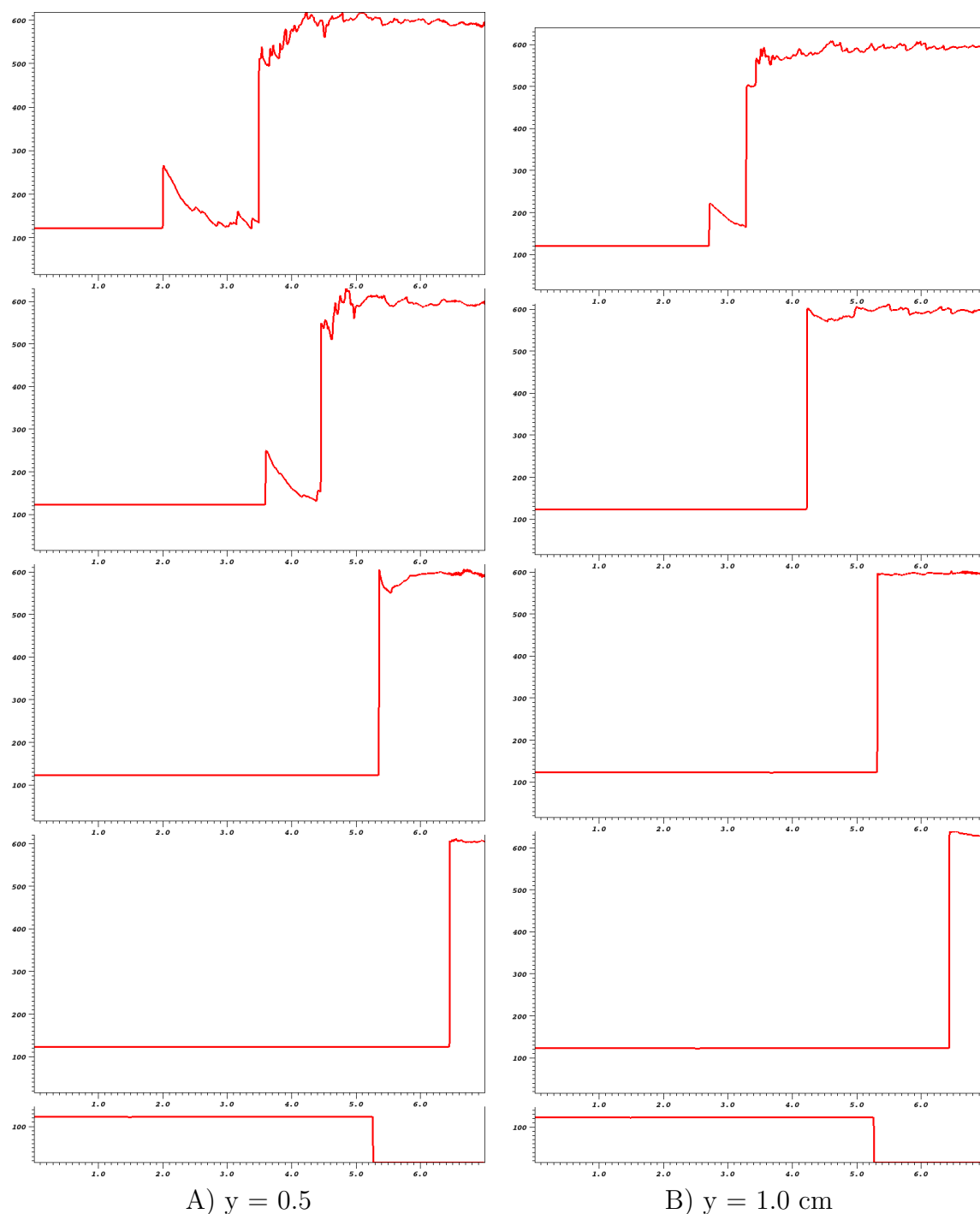


Figure 8.48:  $\text{N}_2\text{O}$ : Pressure (KPa) traces. The x-axis is cm and the tube end is at  $x = 7 \text{ cm}$ . Showing traces at times  $t = 2100, 3600, 5100, 6600, 8100$  (nondim) which is equivalent to  $t = 7.841 \cdot 10^{-5}, 1.344 \cdot 10^{-4}, 1.904 \cdot 10^{-4}, 2.464 \cdot 10^{-4}, 3.024 \cdot 10^{-4} \text{ sec}$ .

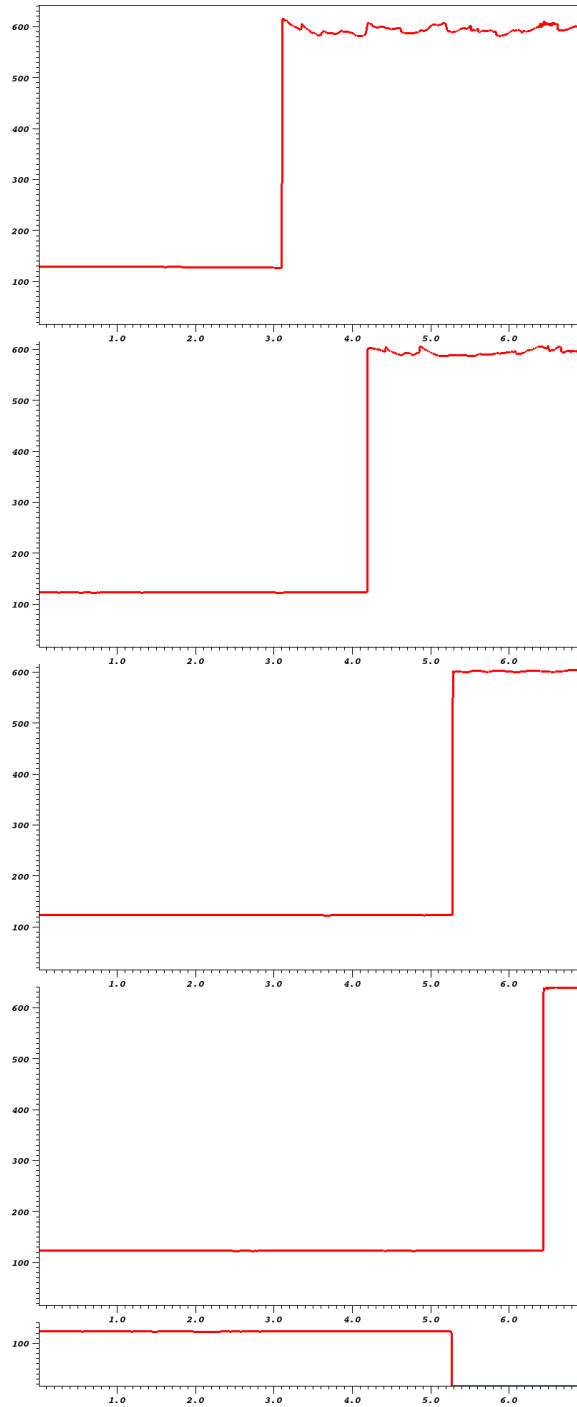


Figure 8.49:  $y = 1.5$  cm pressure (kPa) trace. The x-axis is cm and the tube end is at  $x = 7$  cm. Showing traces at times  $t = 2100, 3600, 5100, 6600, 8100$  (nondim) which is equivalent to  $t = 7.841 \cdot 10^{-5}, 1.344 \cdot 10^{-4}, 1.904 \cdot 10^{-4}, 2.464 \cdot 10^{-4}, 3.024 \cdot 10^{-4}$  sec.

### 8.7.5.3 H<sub>2</sub>-N<sub>2</sub>O

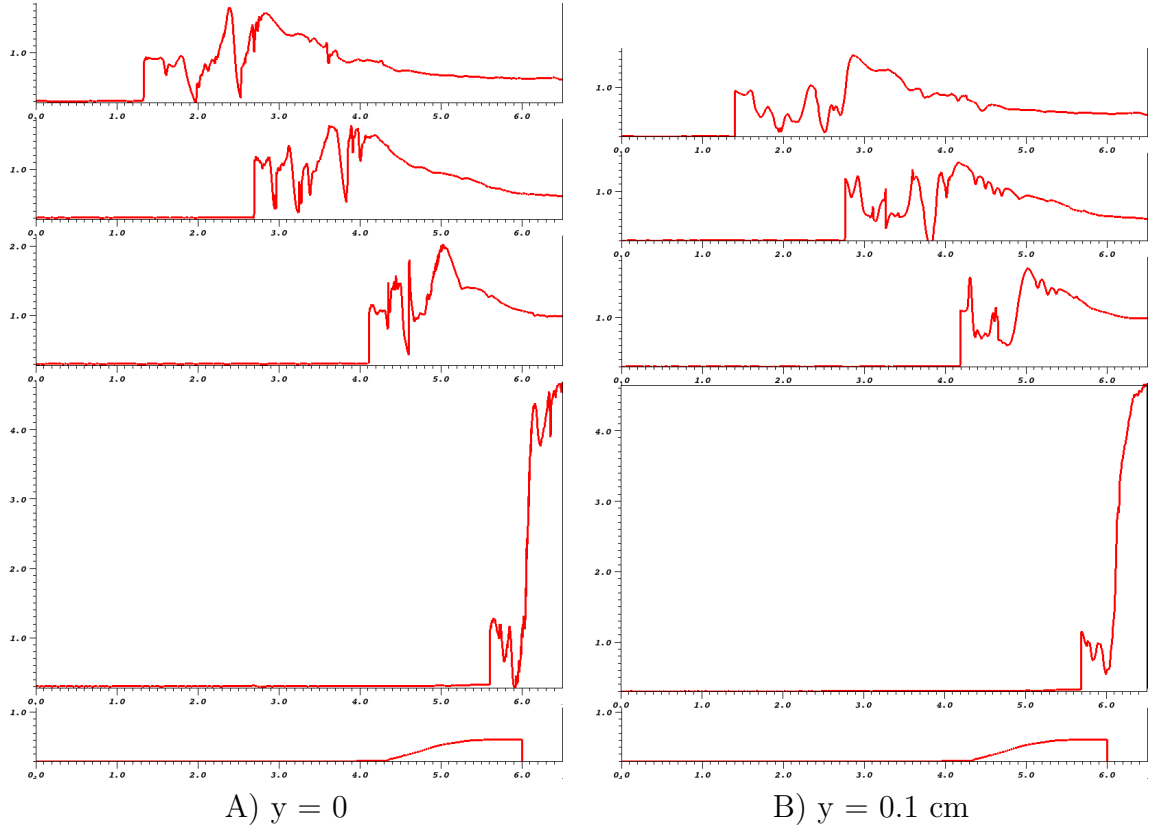


Figure 8.50: H<sub>2</sub>-N<sub>2</sub>O: Pressure (MPa) traces. The x-axis is cm and the tube end is at  $x = 6.5$  cm. Showing traces at times  $t = 0, 250, 500, 750, 1000$  (nondim) which is equivalent to  $t = 0, 8.846 \cdot 10^{-6}, 1.769 \cdot 10^{-5}, 2.654 \cdot 10^{-5}, 3.538 \cdot 10^{-5}$  sec.

### 8.7.5.4 Pressure Trace Discussion

The same trends as was found for the simplified detonation in § 8.6 are again seen. The pressure is typically lower at first in the foot closer to the wall, until strong shocklets of vortices or the reflected shock from the main triple point is traversed through. Farther from the wall, the solution appears more like the one-dimensional equivalent, with the exception being some oscillations in the tail of the shock due to the shocklets from the vortices traveling upwards into the flow. Another exception to the one dimensional solution is the effect of the pressure wave from the starting of the boundary layer which slowed down in the incident shock and creates a pressure peak in the main reflected wave.

Comparing the different results, as expected, the air case with its much smaller foot has the least effect on the shock pressure. The oscillations are less chaotic in



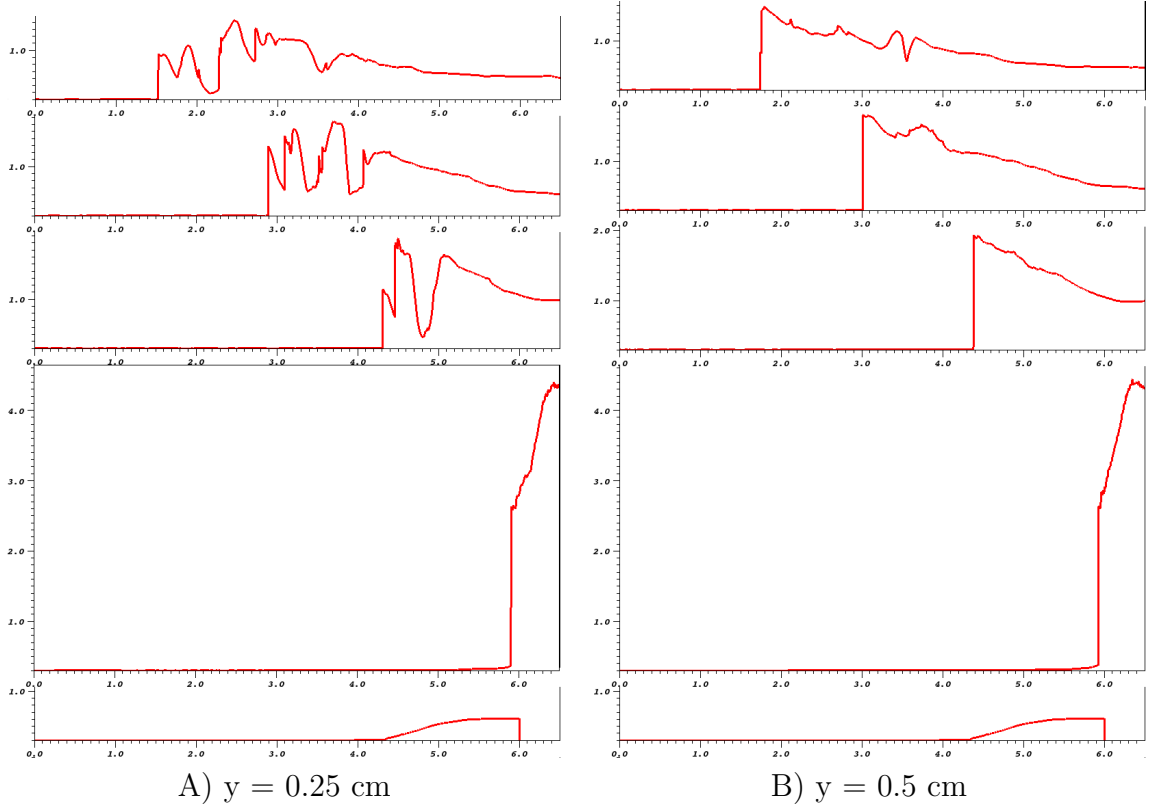


Figure 8.51:  $\text{H}_2\text{-N}_2\text{O}$ : Pressure (MPa) traces. The x-axis is cm and the tube end is at  $x = 6.5$  cm. Showing traces at times  $t = 0, 250, 500, 750, 1000$  (nondim) which is equivalent to  $t = 0, 8.846 \cdot 10^{-6}, 1.769 \cdot 10^{-5}, 2.654 \cdot 10^{-5}, 3.538 \cdot 10^{-5}$  sec.

general, have smaller amplitudes, and are more localized to the region close to the foot. For the  $\text{N}_2\text{O}$  and detonation cases, the vortices are much stronger in comparison and the influence of their shocklets is much stronger and span a larger upward space. Also, for the detonation case, the shear layer emanating from the foots main triple point is at an upward angle, leading to a larger relative (to the triple point height) coverage area than the  $\text{N}_2\text{O}$  case.

## 8.8 Discussion

Pressure measurements during detonation reflection are inconsistent with one-dimensional inviscid gas dynamic models. There is an inconsistency between the measured shock speed and the measured shock pressures if the flow is one-dimensional. We confirm that the pressure jump across the shock wave is larger in the center of the tube and there is a weaker shock wave leading the main front at the tube walls.

The preliminary simplified, two-dimensional, viscous, compressible simulation of

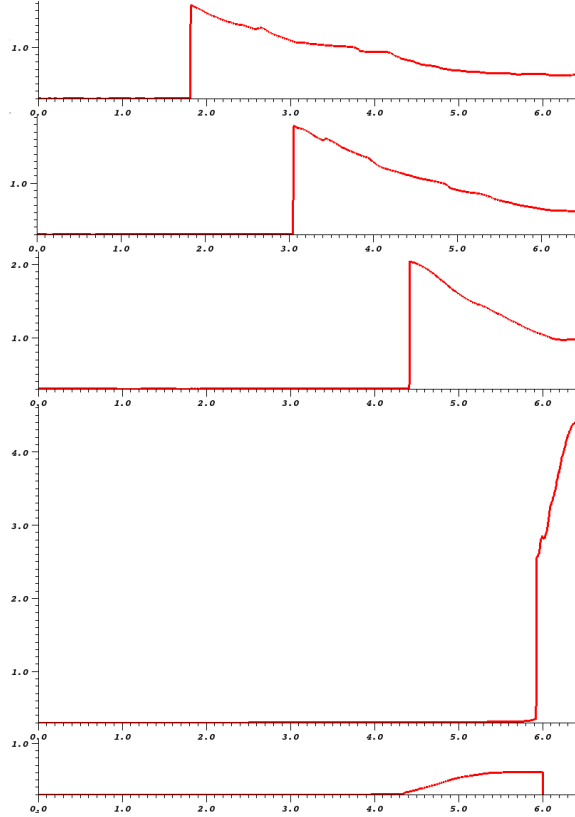


Figure 8.52:  $y = 1$  cm pressure (MPa) trace. The x-axis is cm and the tube end is at  $x = 6.5$  cm. Showing traces at times  $t = 0, 250, 500, 750, 1000$  (nondim) which is equivalent to  $t = 0, 8.846 \cdot 10^{-6}, 1.769 \cdot 10^{-5}, 2.654 \cdot 10^{-5}, 3.538 \cdot 10^{-5}$  sec.

the reflection process clearly demonstrates that the reflected shock wave-boundary layer interaction can result in separated flow and bifurcation of the reflected wave front. Many of the same features are observed in the computational pressure traces as in the experimentally measured pressure histories. These include the increase in the rise time of the pressure and the inconsistency between measured wave speed and pressures inferred from one-dimensional inviscid models.

More insight into the bifurcation process was gained with the simulations using detailed chemistry and transport in combination with comparisons with Mark's original theory (114). Two approaches were used: large-scale unresolved simulations were used for comparison to experimentally obtained schlieren images and small-scale resolved simulations were used to study foot formation during the early times of reflection. Also used for insight was a comparison between two nonreactive mixtures, air and  $N_2O$ , and a reactive  $H_2-N_2O$  mixture. This was instructive as the influence of resolution on the large-scale simulations was seen, with the largest effect on the simulation with the smallest foot.

The trends in our resolved small-scale and marginally resolved medium-scale simulations were compared to the historical experiments and theory outlined by the significant paper of Davies and Wilson (36) and the simulations of Weber *et al.* (159). In particular, the linear trend of foot height growth and the enlarging affect of an adiabatic wall were confirmed.

With these simulation results, certain trends were found for detonation bifurcations. As compared to nonreactive shocks with feet of similar heights, one should expect the detonation's foot's evolution to be more chaotic until the induction length of the incident detonation is reached. At that point, it is expected to act more like a very hot reflected shock. Also, due to the shocklets appearing from localized explosions in the foot during its early evolution, one should expect pressure traces above the wall to be chaotic even above the foot height.

## Chapter 9

# Spark-Ignited Deflagrations

### 9.1 Motivation

Determining the risk of accidental ignition of flammable mixtures is a topic of tremendous importance in industry and in aviation safety. Extensive work has been done (see (11)) to determine the flammability limits of various fuels in terms of mixture composition. When examining the amount of energy required to ignite a mixture within the flammability limits, the concept of a threshold minimum ignition energy (MIE) value has traditionally formed the basis in combustion science for studying ignition hazards of fuels. If an ignition source is not strong enough, or is below the minimum ignition energy (MIE) of the particular mixture, the mixture will not ignite. Standard test methods for determining the MIE have been developed which use a capacitive spark discharge for the ignition source. The MIE is determined from the energy stored in a capacitor at a known voltage that is then discharged through a specified gap. For more details and references see (12).

The view of ignition where the MIE is considered to be a single threshold value is vastly simplified. The first work of this century to tackle this problem was with simulations conducted by Thiele *et al.* (152). Their model for hydrogen-air included the compressible Navier-Stokes equations, detailed chemistry and molecular transport in the gas phase as well as heat conduction to the electrodes and solution with different geometries. Their spark is modeled for the phases subsequent to breakdown using the Maxwell equations for quasi-stationary conditions for the electric field. While using a shock-capturing finite-difference method, very accurate detailed chemistry and transport, and also modeling the initial plasma phase and realistic boundary conditions, it seems that they failed to resolve the viscous/diffusive scales in the simulations. They found that the length of the arc phase as well as the geometrical

shape of the electrodes did not influence the temporal development of the radial extension of the kernel significantly.

Oddly, all recent simulation works after the Thiele *et al.* paper contradict the independence of geometry findings. In research by Nakaya *et al.* (120) flame kernel initiation of methane/air mixtures in the spark ignition process were investigated with a shock-capturing scheme, diffusive molecular transport, and a simplified plasma model. In the early stage of their flame kernel development the hot gas expansion was dominated by a flow which was induced by the blast wave. They found that the induction time of the flame kernel initiation strongly depended on the ignition energy and effects of preferential diffusion of lighter molecules in the early phase of the flame kernel development.

In works by Han *et al.* (63, 64), the parameters which control spark ignition were studied in much more detail for methane-air and hydrogen air, albeit with a cruder (but more efficient) numerical method for the fluid dynamics. The SIMPLE method as proposed by Patankar was used to couple the velocity and pressure fields, a first-order upwind scheme was used for the convective terms, the implicit Euler method was used for the time advance, and the successive overrelaxation method was used to iterate each time step. They found that the MIE increased gradually below the quenching distance (critical spark gap) for the free-tipped electrode, but increased sharply starting at the quenching distance. Contrary to the work of Thiele *et al.*, the size of the electrodes significantly affected the value of the MIE within the quenching distance, but did not affect it beyond the quenching distance. They also found that for a short spark duration, the vortex gas motion and the temperature gradient around the flame kernel dramatically influenced the flame formation and the MIE.

The traditional MIE view criticized by the cited works and also by our simulation findings is deficient for reasons elaborated on in §9.6.3.3 and §9.6.3.4. The primary Goal of this numerical application on spark ignition is to, through numerical simulation, find the parameters and conditions which influence self-sustained flame propagation from accidental spark ignition of combustible mixtures.

A systemic approach was used to simulate the spark ignition problem. In collaboration with Bane (12), simulations of increasing levels of complexity were designed which matched as close as possible the initial conditions and geometries used in experiments.

## 9.2 Simulation Overview

Simulations and experimental comparisons are shown for increasing levels of complexity. Firstly, single- and two-component models are used for nonreactive and reactive sparks. Then, a four-component perfect gas model is used and lastly, a nine-component ideal gas model with detailed chemistry and transport is used. These are all compared to experimental schlieren images of Bane.

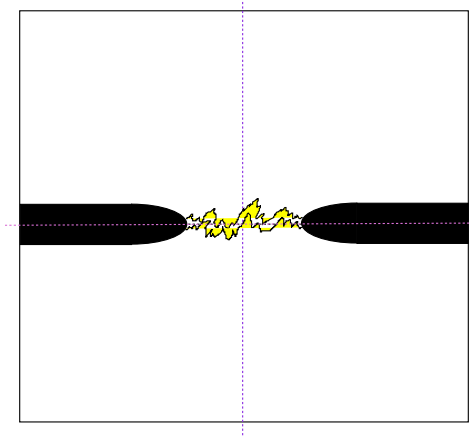


Figure 9.1: Cartoon of the spark ignition problem demonstrating the two planes in the axisymmetric symmetry

As shown in figure 9.1 the experimental apparatus for spark ignition testing displays two planes of symmetry. The electrode geometry itself is axisymmetric and thus great numerical simplification can be used by modeling the whole problem as a axisymmetric “quarter” of the whole geometry. There are two planes of symmetry. The vertical plane of symmetry is captured by requiring the  $y$  (radial) velocity to be symmetric. Numerically, this means that the boundary cells have a velocity that is the negative of its symmetric neighboring cells in the domain. Similarly on the bottom plane, the  $x$  (axial) velocity is symmetric.

### 9.2.1 Approximating a Spark

Simulation of the spark breakdown phase is beyond the scope of this work. Therefore, the following imposed initial conditions were used to model the plasma channel between the electrodes that results from the spark breakdown. The initial conditions are based on those used by Kravchik *et al.* (93) and Thiele *et al.* (153), which in turn

were motivated by the work of Maly and Vogel (113, 112). The initial conditions are those of the plasma channel at thermodynamic equilibrium approximately 60 ns after breakdown (113, 112). The plasma is modeled as a thin axisymmetric channel between the electrodes with a temperature of 35,000 K and a pressure of 1 MPa. The channel is 2 mm long, the length of the spark gap, and the radius of the channel is determined from the spark energy. Assuming the spark energy is deposited under constant volume conditions, the volume of the spark channel for a perfect gas with constant specific heat is

$$V_c = \frac{E_{spark}}{c_V \rho_0 (T_c - T_0)}, \quad (9.1)$$

where  $T_c$  is the temperature of the channel and  $\rho_0$  and  $T_0$  are the density and temperature of the ambient gas. Taking an axisymmetric channel of length  $L_{gap}$ , the channel radius is

$$r_c = \left( \frac{V_k}{\pi L_{gap}} \right)^{1/2}. \quad (9.2)$$

### 9.3 Single-Component Nonreactive Model Problem

Firstly, the nonreactive problem was simulated using a single-component fluid consisting of one perfect gas. This was done to separate the inviscid, nonreactive, convective parts of the physics from those in a simulation including detailed chemistry and transport. Both Euler and Navier-Stokes simulations were conducted for this model.

#### 9.3.1 Initial and Boundary Conditions

The initial conditions grossly approximate a spark as a diffused axisymmetric high temperature channel. A pressure increase and density decrease (temperature increase) models the “spark plasma”. figures 9.2 and 9.3 show the initial conditions and geometry used for the channel for this nonreactive case.



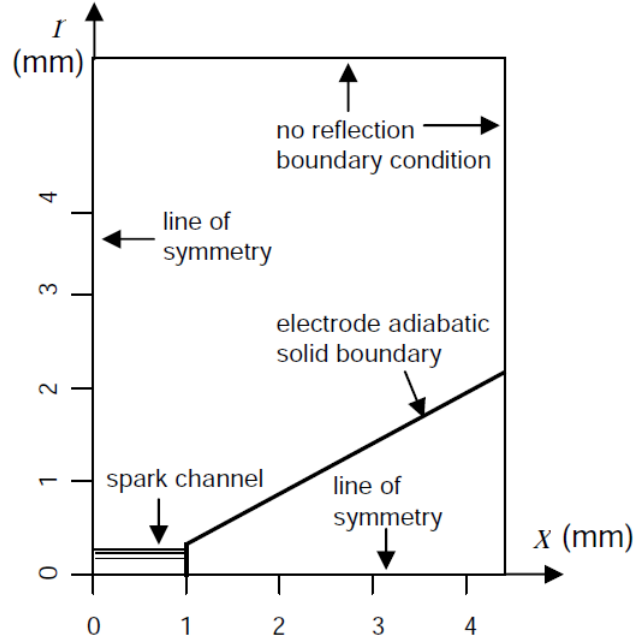


Figure 9.2: Computational domain for the spark ignition simulations.

$$\frac{p_{spark}}{p_{\infty}} = \frac{\rho_{\infty}}{\rho_{spark}} = 10^2 \quad (9.3)$$

$$\frac{T_{spark}}{T_{\infty}} = 10^4 \quad (9.4)$$

The Ghost Fluid Method (GFM) was used to model the solid electrode boundary. For the (inviscid) Euler equations the GFM was used to make the normal velocity zero, and for the Navier-Stokes equations, the no-slip boundary condition was used (zero fluid velocity on the electrode). Also, the boundaries were modeled as adiabatic.

In the spark discharge studies without ignition, the gas used in the simulations is a perfect gas modeling air and the following values were assumed within the spark channel:  $c_V = 721 \text{ J/kg}\cdot\text{K}$ ,  $\gamma = 1.4$ , viscosity  $= 2 \cdot 10^{-5} \text{ Pa}\cdot\text{s}$ , conductivity  $= 0.03 \text{ W/(m K)}$ ,  $\rho_0 = 1.15 \text{ kg/m}^3$ ,  $T_{spark} = 35,000 \text{ K}$ ; and outside the channel  $T_0 = 300 \text{ K}$  and  $p_0 = 0.1 \text{ MPa}$ . In these preliminary simulations, a larger spark gap of  $L_{gap} = 1 \text{ cm}$  was used.

Refinement criteria were used that capture the physics of each length scale in the problem. The gradient of the density is used to capture the convective length scale, the gradient of the radial and axial velocities is used for the viscous length scale, the

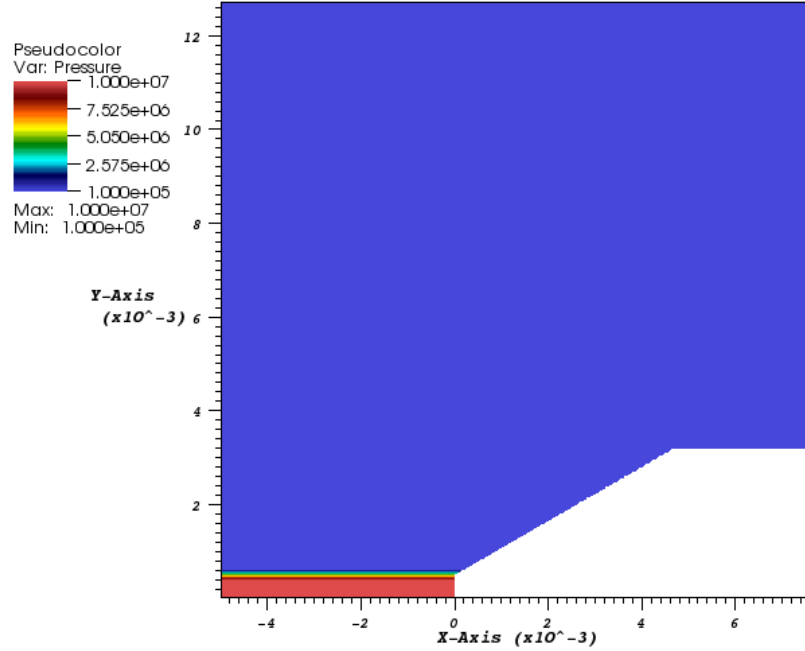


Figure 9.3: Initial Pressure

gradient of energy is used for the conduction length scale, and the gradients of the mass fractions are used to capture the flame thickness length scale.

### 9.3.2 Single-Component Nonreactive Results

Using 32 processors, the Navier-Stokes and Euler equations were simulated with three levels of refinement. The simulation time was the order of one day. Aside from the appearance of the boundary layer on the electrode surface, the viscous and inviscid simulations are very similar due to the small constant ambient value of the viscosity chosen. Therefore, only the viscous result is shown.

The evolution of the density field is shown in figures 9.6(a)-9.6(f). After the shock wave (shown in figure 9.4) has passed, a hot dense kernel remains that rolls up. This occurs as the result of the axisymmetric shock wave interacting with the conelike electrode surface. After the initial shock has passed the incline, the streamlines diverge causing a back flow and roll up. Note that this also occurs in the inviscid Euler simulation.

As show in figure 9.7, much later after the shock wave has passed, there remain hot vortical structures in which mixing, viscous shear, and heat conduction play a role. In a reactive simulation, it is presumed that these structures will influence the

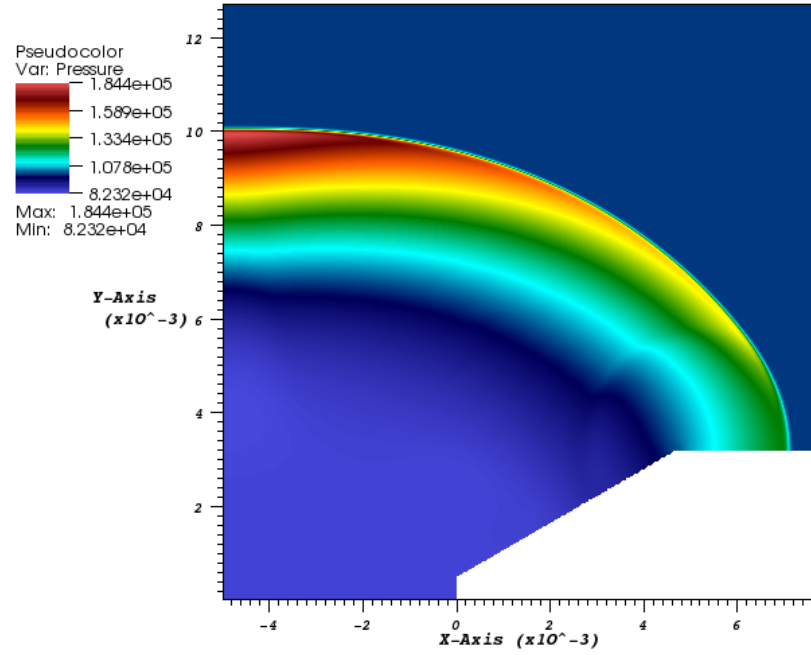


Figure 9.4: Pressure from axisymmetric shock wave in the early stages of the simulation at  $t = 1.5 \cdot 10^{-5}$  sec

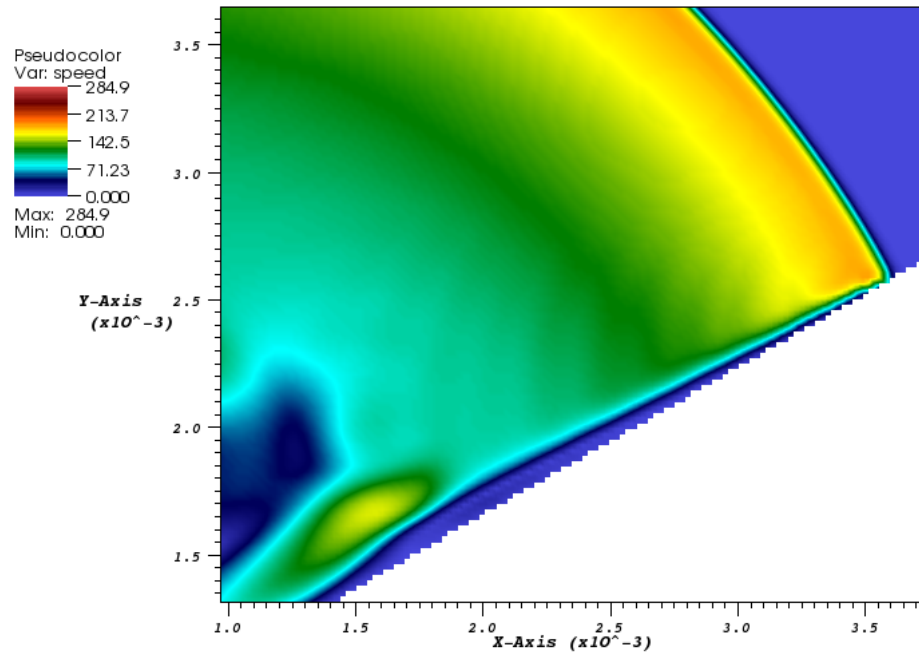
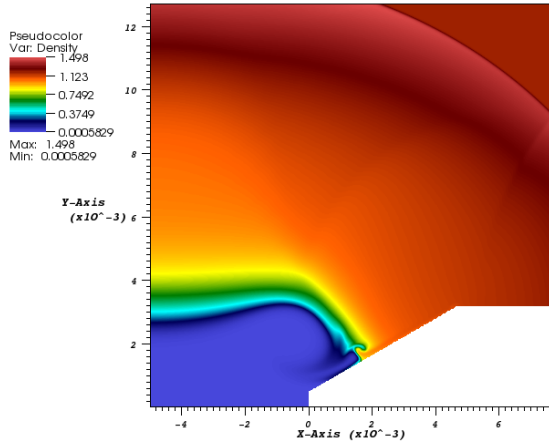
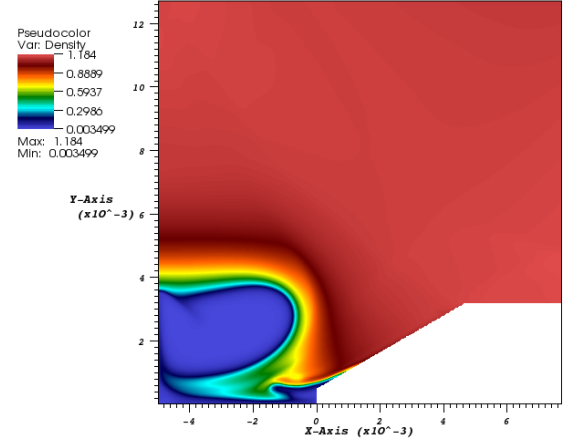
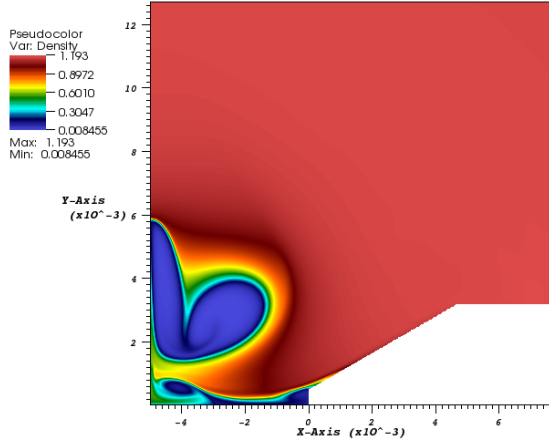
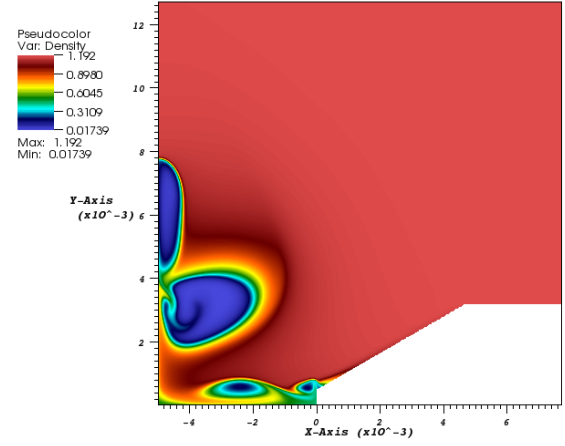
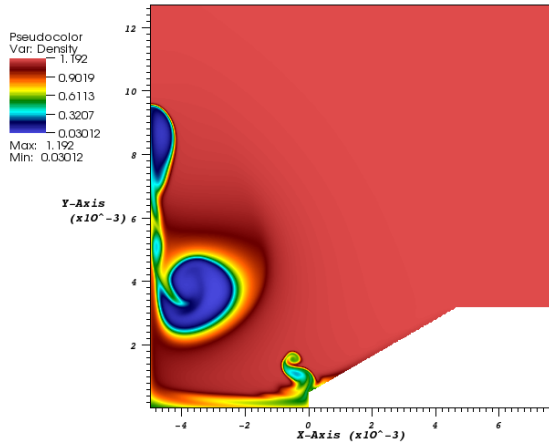
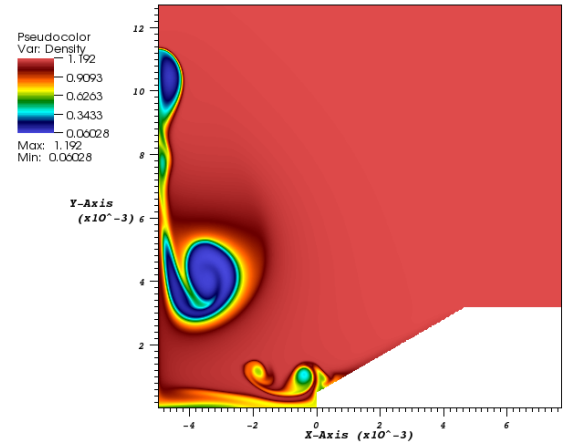


Figure 9.5: Zoomed in view of the velocity magnitude near the electrode surface at  $t = 6 \cdot 10^{-6}$  s. This illustrates the application of the no-slip boundary condition using the ghost fluid method

(a)  $t = 2.4 \cdot 10^{-5}$  s(b)  $t = 4.8 \cdot 10^{-5}$  s(c)  $t = 9.75 \cdot 10^{-5}$  s(d)  $t = 1.425 \cdot 10^{-4}$  s(e)  $t = 1.965 \cdot 10^{-4}$  s(f)  $t = 2.64 \cdot 10^{-4}$  sFigure 9.6: Evolution of density ( $\text{kg}/\text{m}^3$ ) for nonreactive viscous case.

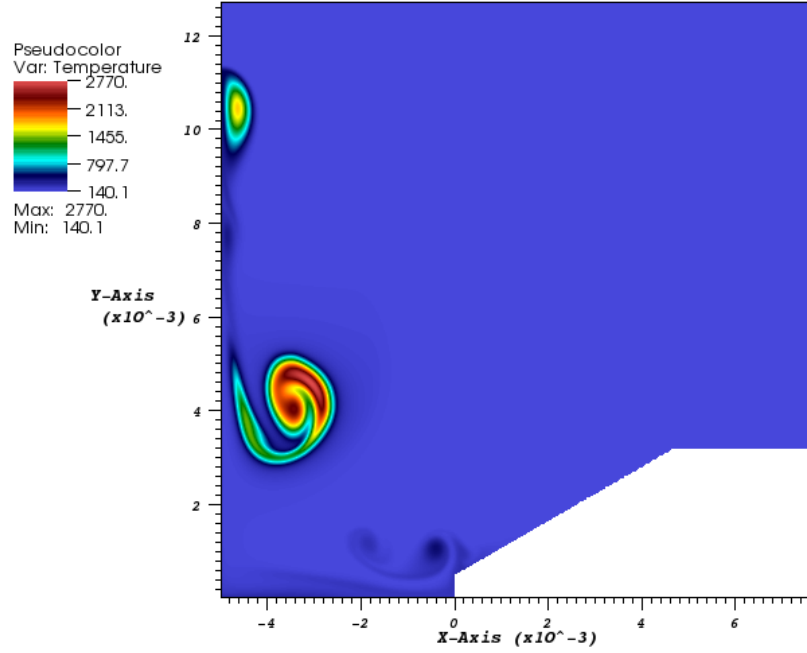


Figure 9.7: Temperature (K) at  $t = 2.64 \cdot 10^{-4}$  s for nonreactive viscous case.

growth of a self-sustained laminar flame.

For these particular initial and boundary conditions, there is little qualitative difference between the results for the Euler and Navier-Stokes equations. The shock waves and bulk vortical roll up of the hot dense region is essentially the same. The main difference between the results is the boundary layer on the electrode, caused by the no-slip boundary condition. For our simple nonreactive model with a small constant viscosity and conductivity, the effects of viscous shear and heat diffusion on the flow field are qualitatively small.

## 9.4 Two-Component Model

The influence of a flame on the the fluid dynamics was investigated by first using a simple model. A one-step reaction was assumed of the most simple form:  $R \rightarrow P$ , with constant perfect gas properties for the reactant, R, and the product, P. Both the reactant and product were assumed to have the molecular weight of  $N_2$  and a specific heat ratio of 1.4. The reaction rate parameters were for a rate of the form  $AT^n \exp(-(E_A/R_u)T)$  with  $A = 1.074926 \cdot 10^6 \text{ s}^{-1}$ ,  $n = 9.62 \cdot 10^7$ , and  $E_A = 71,128 \text{ J/mol}$ . Constant mass diffusivities of  $1.895 \cdot 10^{-5} \text{ m}^2/\text{s}$  were assumed.

Shown in figures 9.8(a)-9.8(f) and figures 9.9(a)-9.9(f) is a comparison of the density and temperature fields for the nonreactive and two-species reactive case started with the same initial conditions. It seems that for the small diffusivities selected for the reactive case, the flow is dominated by the hydrodynamics set up by the initial pressure and temperature gradient of the spark. Also shown in figure 9.10, is a visualization of the product mass fraction for the reactive case at  $t = 50 \cdot 10^{-6} \text{ s}$ . This roughly corresponds to the outline of the temperature which is visualized in figure 9.9(f). Overall, the reactive and nonreactive results are very similar. This is due to the fact that for this particular model, the diffusion terms are small, the spark energy dominates the chemical energy release, and the reactant and product, aside from the energy release, are assumed to have the same thermodynamic and transport properties.

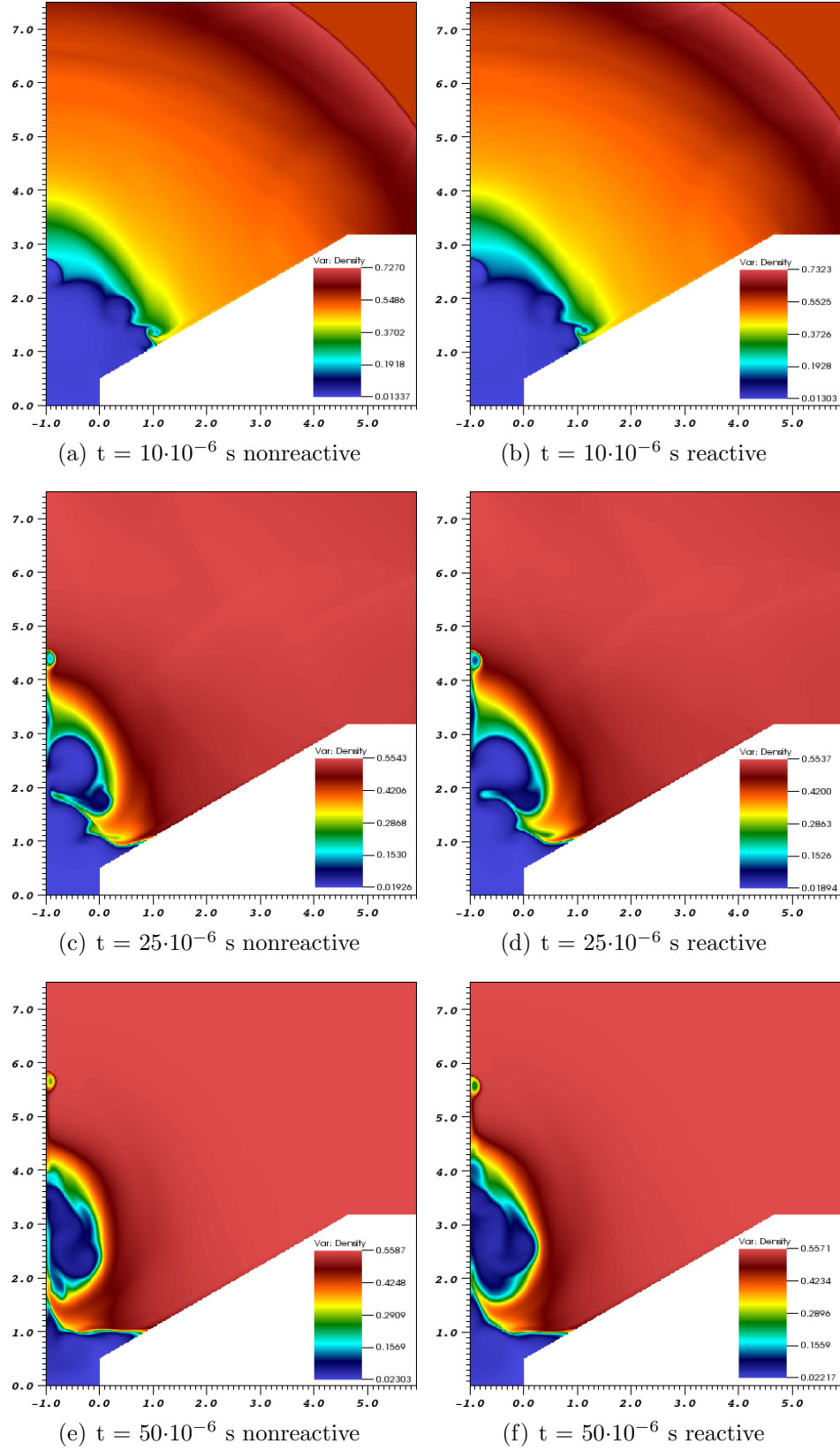


Figure 9.8: Two-component model: Evolution of density (kg/m³) for nonreactive and reactive case with 2 mm spark gap (2 mJ).



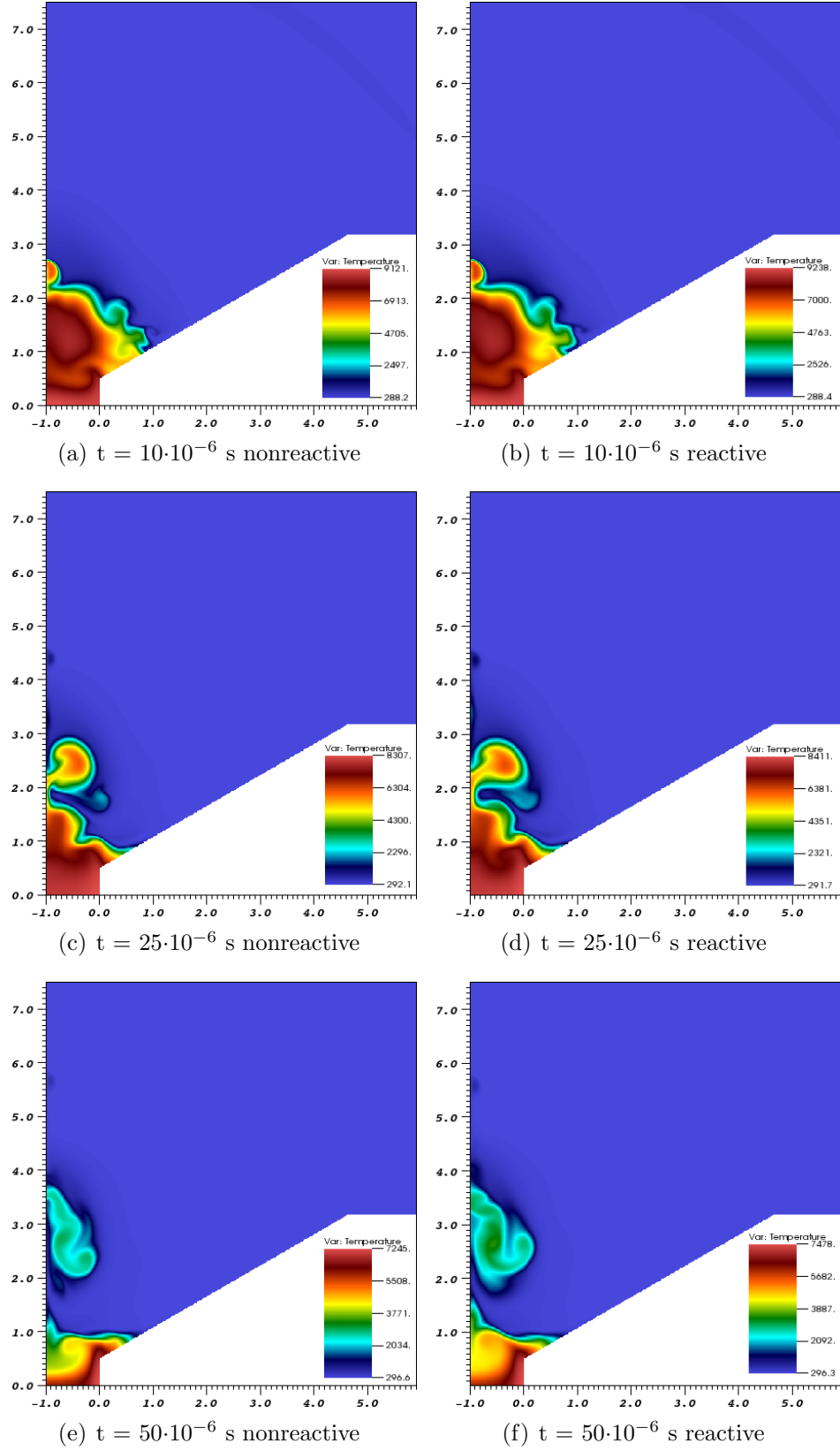


Figure 9.9: Two-component model: Evolution of temperature (K) for nonreactive and reactive case with 2 mm spark gap (2 mJ).

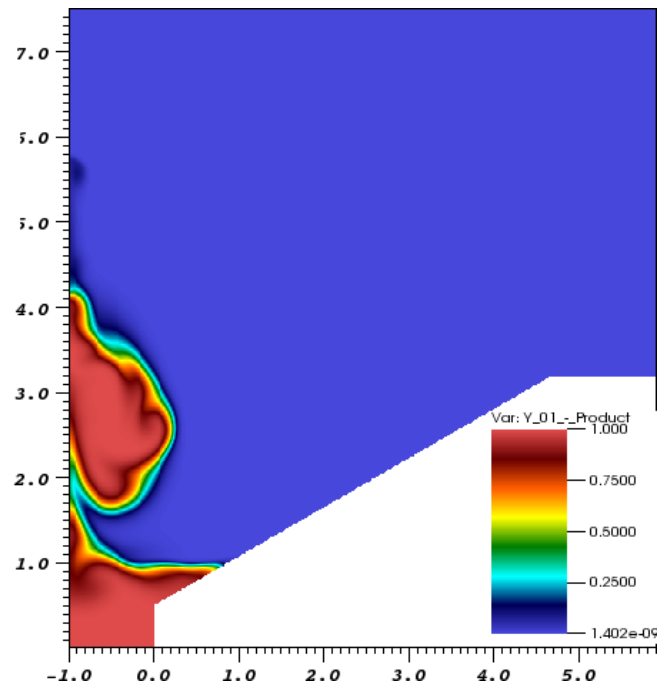


Figure 9.10: Two-component model: Product mass fraction at  $t = 50 \cdot 10^{-6}$  s for reactive case with 2mm spark gap (2 mJ).

## 9.5 Four-Species One-Step Model with Constant Transport Properties

To simulate spark ignition more accurately, and in particular, the straining behavior, the one-step model was modified to closer match the Lewis number obtained with a detailed chemistry CANTERA<sup>1</sup> simulation. This one-step model includes the four species  $\text{H}_2$ ,  $\text{O}_2$ ,  $\text{H}_2\text{O}$ , and  $\text{N}_2$ . The specific heats of  $\text{H}_2$ ,  $\text{O}_2$ , and  $\text{H}_2\text{O}$  were increased by a factor of approximately 3 to reduce the numerator of the Lewis number, but for  $\text{N}_2$  the actual thermodynamic coefficients for a nitrogen molecule were used. The full, detailed transport properties for all four-species were used. The one-step reaction was changed from  $\text{R} + \text{R} \rightarrow \text{P} + \text{P}$  to the model reaction  $\text{H}_2 + \frac{1}{2} \text{O}_2 \rightarrow \text{H}_2\text{O}$  with effective parameters  $E_A = 20.263 \text{ kcal/mol}$  and  $A = 2.85 \times 10^{14} \text{ s}^{-1}$ . Finally, since all the reactant species are included, the initial composition is the same as in the detailed chemistry case:  $0.42 \text{ H}_2 + 0.5 \text{ O}_2 + 1.88 \text{ N}_2$ . This corresponds to a 15 percent hydrogen-air mixture (10). After these changes were implemented, the Lewis number of the mixture obtained with the new one-step model was 0.42, which is now closer to the actual Lewis number of 0.38. This mechanism is documented in detail in appendix H of the GALCIT technical report (13).

In both the experiments and simulations, the spark energy used is  $E_{\text{spark}} = 2 \text{ mJ}$  and the spark gap is  $L_{\text{gap}} = 2 \text{ mm}$ . Using equations 9.1 and 9.2, the volume and radius of the spark channel used for the initial condition is approximately  $0.063 \text{ mm}^3$  and  $0.1 \text{ mm}$ , respectively. For more details on the experimental setup, see the thesis of Bane (10).

Simulations and experiments were performed for this 15 percent hydrogen-air mixture at the relatively high energy of 2 mJ. At this energy, ignition always occurs for the geometries we tested. By using a higher spark energy, the hydrodynamic forces in the flow are enhanced allowing easier analysis of the general fluid flow for each geometry. The 4-species one-step chemistry model with multi-component detailed transport (but with modified perfect gas thermodynamics) was used with the same initial temperature and pressure conditions as was used to model the spark for the simple two-species model. These simulations were performed with three different electrode geometries to investigate the effect of the geometry on the fluid mechanics of the evolving spark kernel and on flame formation. High-speed schlieren visualizations of spark and ignition kernels were compared to the computational results. It was found

---

<sup>1</sup><http://www.cantera.org>

that the electrode geometry had a significant effect on the fluid motion following spark discharge and thus could influence the ignition process (13).

### 9.5.1 Nonreactive Results

Images from the high-speed schlieren visualization of a 2 mJ spark discharge in air using the 0.38 diameter cylindrical electrodes and images from the two-dimensional simulation at approximately the same time steps are shown in figure 9.11. The video was taken at a rate of 79,069 frames per second with a total field of view of approximately 6.7 mm x 6.7 mm. Dimensions are given on the images in millimeters, and the computational region is indicated on the first schlieren image by a white box. The first image is taken less than  $12.6 \mu s$  after the spark breakdown. The spark breakdown creates a thin plasma channel at high temperature and pressure, as described in §9.3.1, and when the channel expands, a blast wave propagates outward while a rarefaction wave propagates inward toward the center of the channel. The rarefaction reflects at the center of the channel and propagates back outward and is seen trailing the blast wave in the pressure contours from the simulation. Initially, the shock wave is nearly a pure axisymmetric wave except for very close to the electrode surface, where the wave is spherical in nature. Because the pressure gradient following a axisymmetric shock wave is smaller than that following a spherical shock wave, the pressure is higher in the middle of the channel than next to the electrodes, causing gas to flow outward toward the electrode surface, as illustrated in figure 9.14. The flow separates and creates a clockwise-rotating vortex at the corner of the face and cylindrical body of the electrode, and additional vorticity is generated from the boundary layer due to the flow along the electrodes. The pressure gradient rapidly decreases and as the outward flow stops, the vortices propagate outward from the corner and pull fluid inward along the electrode as shown in both the schlieren visualization and simulation at approximately  $10 \mu s$ .

The vorticity contours from the computation reveal that by  $10 \mu s$  a counter-rotating vortex pair has formed near the tip of the electrode, shown in figure 9.15. The clockwise rotating vortex (top) is a result of the flow separation, and the counter clockwise rotating vortex (bottom) is a result of the shear layer that develops due to flow moving outward against the inflow. The temperature results from the simulation reveal that the vortex trapped a kernel of hot gas, preventing it from being cooled by the gas inflow, and this hot kernel continues to propagate vertically from the center of the channel. The kernel cools quickly and its temperature decreases below 1000 K by

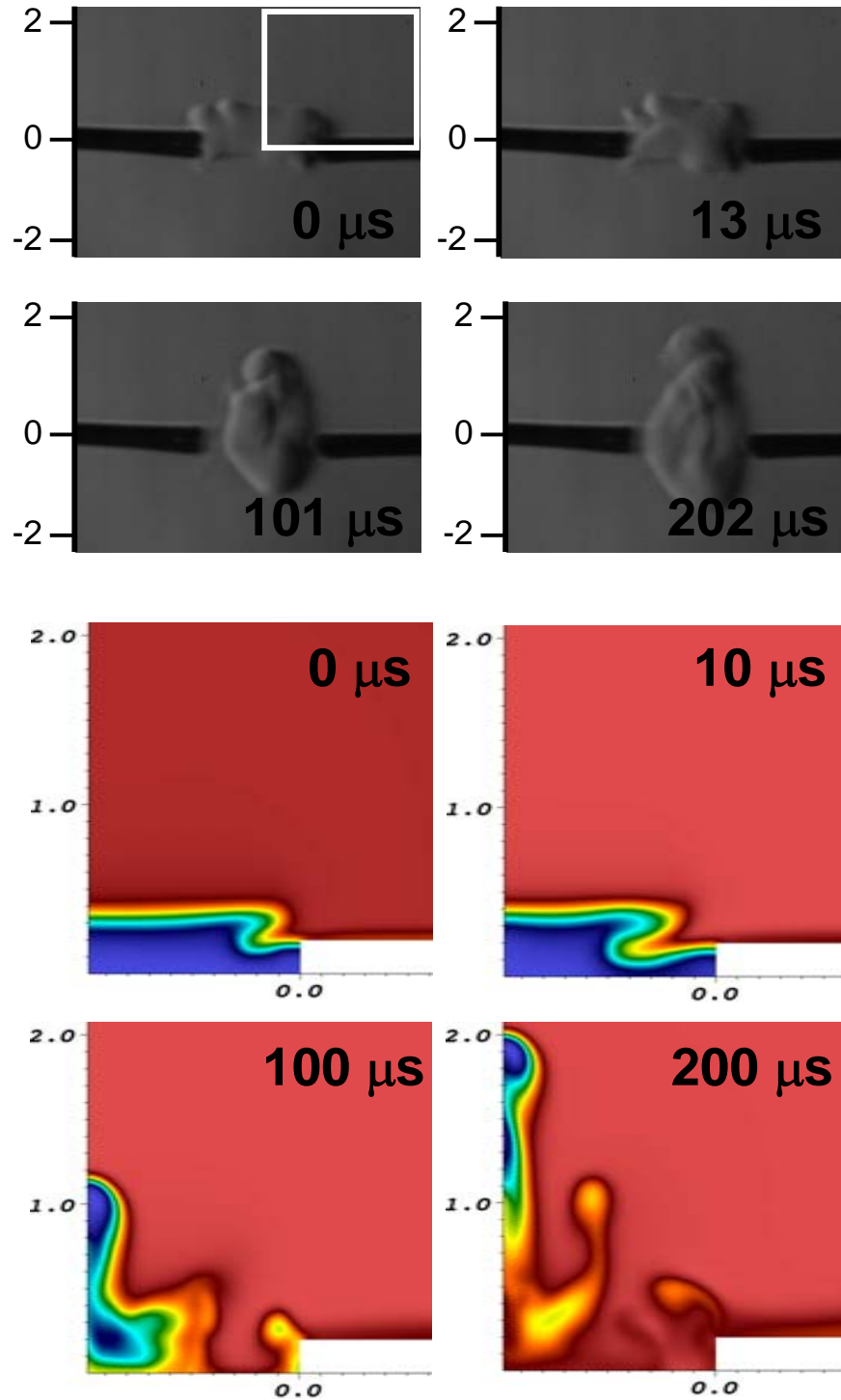


Figure 9.11: Four-component, nonreactive model: Images from high-speed schlieren visualization (upper set) and simulation density (lower set) of a 2 mJ spark discharge in air with 0.38 mm diameter cylindrical electrodes. Distances shown are in mm, simulation region corresponds to the quadrant outlined in white on the upper left schlieren image.

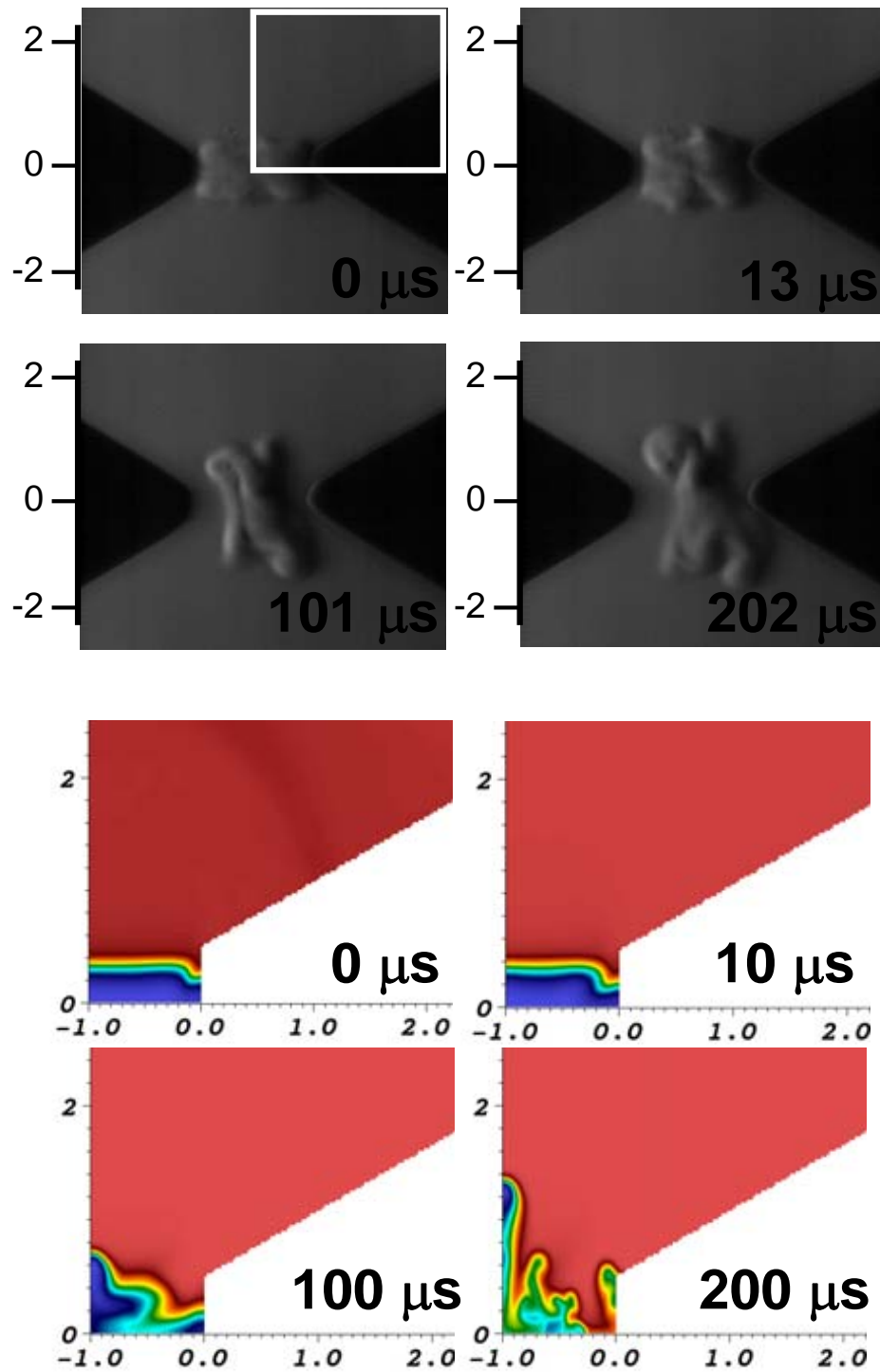


Figure 9.12: Four-component, nonreactive model: Images from high-speed schlieren visualization and simulation density of a 2 mJ spark discharge in air with conical electrodes.

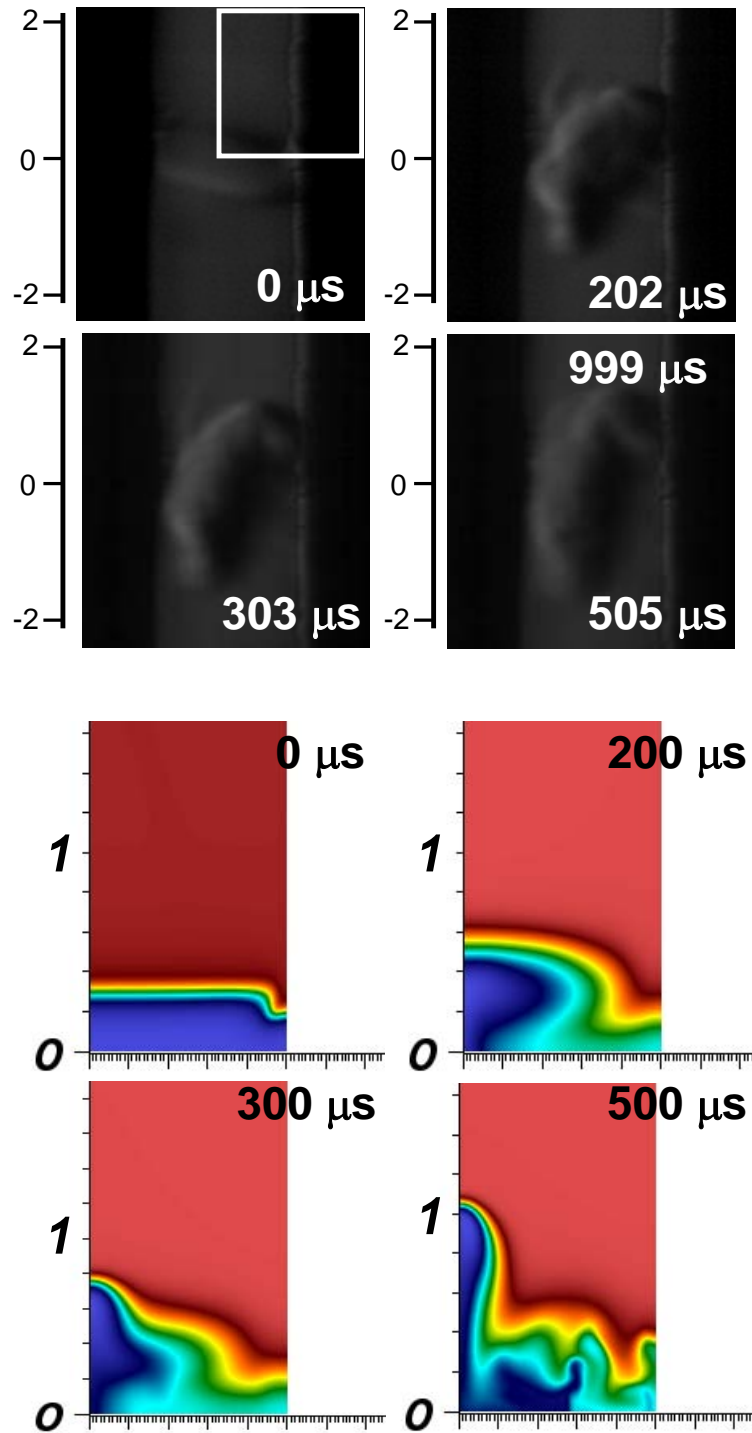


Figure 9.13: Four-component, nonreactive model: Images from high-speed schlieren visualization and simulation density of a 2 mJ spark discharge in air with 1.6 mm diameter cylindrical electrodes with 19 mm diameter Teflon flanges.



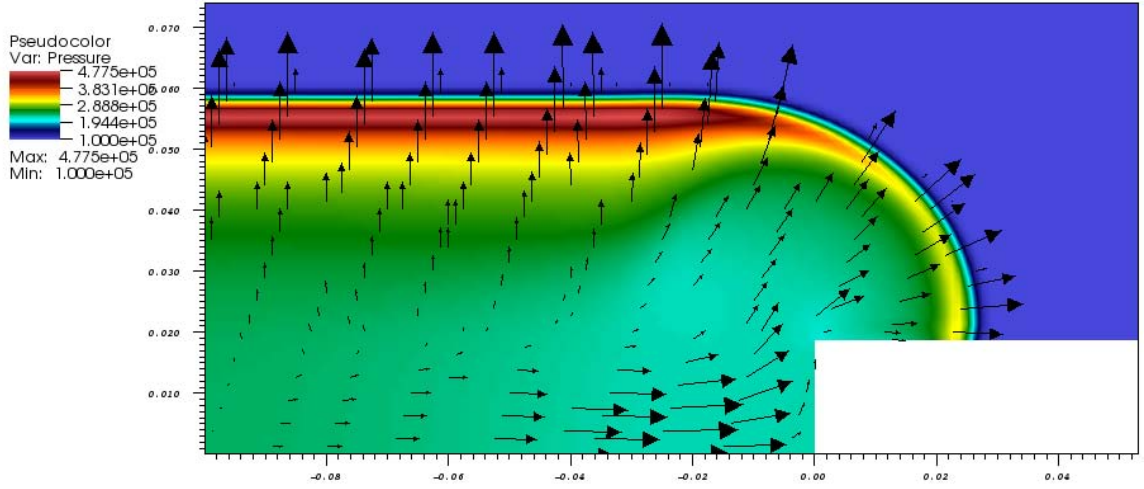


Figure 9.14: Four-component, nonreactive model: Simulated pressure field and velocity vectors showing the axisymmetric and spherical portions of the blast wave at time  $t = 0.5 \mu\text{s}$ .

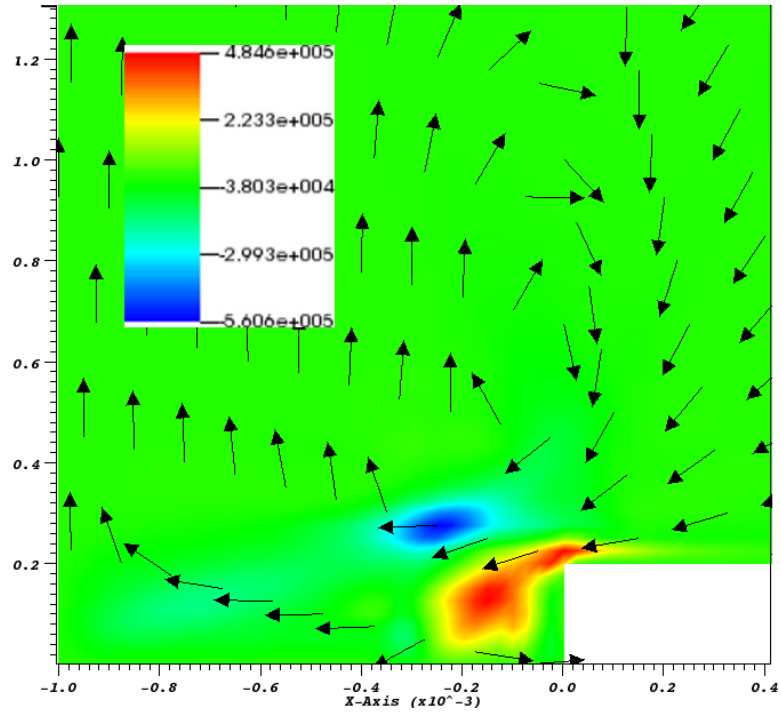


Figure 9.15: Four-component, nonreactive model: Simulation results (vorticity and velocity vectors) showing the vortex pair generated near the tip of the cylindrical electrode at time  $t = 10 \mu\text{s}$ .

80  $\mu s$ . There is also a mixing region near the channel and the inflow of cool gas causes this region to be significantly cooler than the rising kernel. The major features of the flow field in the simulation, including the inflow of cold gas immediately following expansion of the spark channel, the rising hot kernel, and the mixing region are also observed in the schlieren visualization.

For the second geometry, images from schlieren visualization of the spark discharge with the conical electrodes and the results from the two-dimensional simulation are shown in figure 9.12. The images were taken at the same time steps as those for the cylindrical electrode case for comparison. In this geometry, the competition between spherical and axisymmetric expansion is more predominant than in the cylindrical electrode case. Once again, clockwise-rotating vortices are generated near the tip of the electrode due to flow separation, and boundary layer vorticity induces inflow into the channel. The vortices are weaker in this geometry than in the cylindrical electrode geometry due to less flow separation, and as a result the inflow has a lower velocity. Due to the lower rates of convection and entrainment of cold gas, the kernel cools slower than in the cylindrical electrode case, maintaining a temperature above 1000 K until 140  $\mu s$ . The mixing region that forms near the gap is larger and at higher temperatures than in the cylindrical case. In comparison to the cylindrical electrodes, we have for the same energy a higher temperature gas kernel and larger mixing region, suggesting that for a given mixture, a lower spark energy could be needed for ignition.

The results of the schlieren visualization and computations for the third geometry, the 1.6 mm diameter electrodes with Teflon flanges, are shown in figure 9.13. In this geometry the expanding spark channel generates a purely axisymmetric blast wave, and therefore, there is no pressure gradient along the spark channel, due to (inviscid) hydrodynamics effects. However, in both the simulation and the schlieren visualization there is clearly inflow of gas toward the center of the channel caused by viscous effects. The vorticity field from the simulation shows that there is negative vorticity originating in the boundary layer at the right-hand flange and positive vorticity originating in the boundary layer at the left-hand flange. The kernel is hotter for a longer time than in the other cases, maintaining a temperature above 1000 K until 340  $\mu s$ . These results suggest that the lowest ignition energy would be required in this configuration and that the overall minimum ignition energy for a flammable gas is obtained using this geometry, as done by Lewis and von Elbe (102).

### 9.5.2 Reactive Results

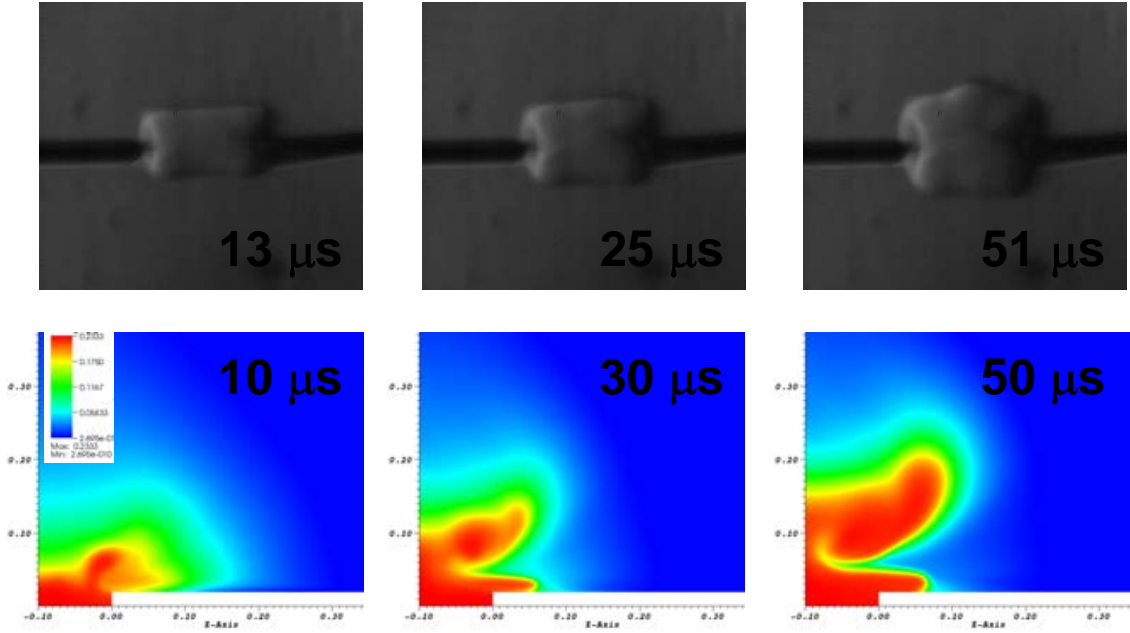


Figure 9.16: Four-component, one-step model: Images from high-speed schlieren visualization and simulation of ignition with the thin cylindrical electrodes.

The same set of experiments and simulations were repeated now with the combustible 15 percent hydrogen-air mixture. Images from the schlieren visualization and images of the product ( $\text{H}_2\text{O}$ ) from the simulation of ignition are shown in figure 9.16 for the cylindrical electrode case. Both the experiment and computation show the inflow of cold reactant gas along the electrode which then rolls up with the hot product gas expanding rapidly outward to form a large vortex with the flame front on its surface. This part of the flame continues to burn outward, while the small rising kernel in the center of the channel forms the rest of the flame front.

figure 9.17 shows images from the schlieren visualization and of the simulated product for the ignition with the conical electrodes. The flame formation is very similar to the cylindrical electrode case, as expected from the nonreactive results. Initially, there is inflow along the electrode which forms a vortex with the outward flowing product gas. The flame front propagates outwards on the surface of this vortical structure and the rising gas kernel in the center of the channel.

Lastly, the results for schlieren visualization and simulation of ignition with the flanged electrodes are shown in figure 9.18. In the simulation, the flame front is curved due to the viscous flow velocity profile in the channel. The kernel shape is

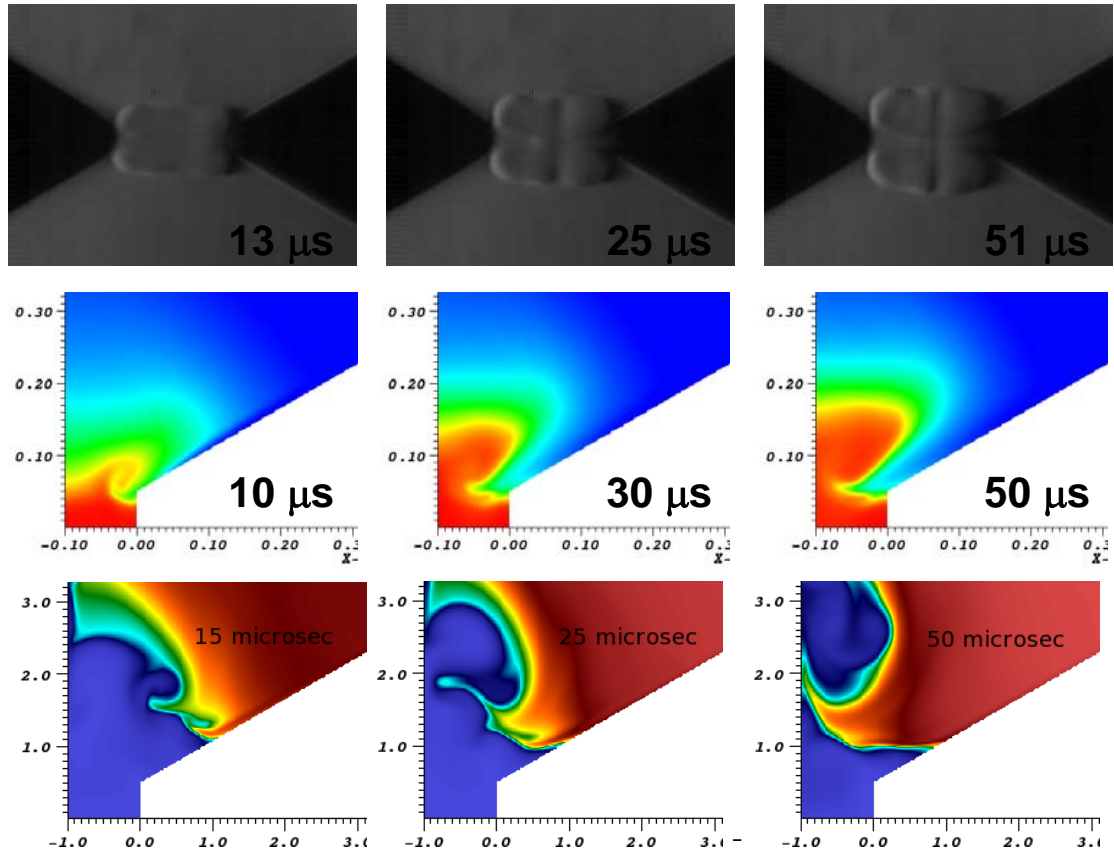


Figure 9.17: Four-component, one-step model: Images from high-speed schlieren visualization and simulations of ignition with the conical electrodes (four-species detailed transport and 2 species constant transport, both with one-step chemistry).

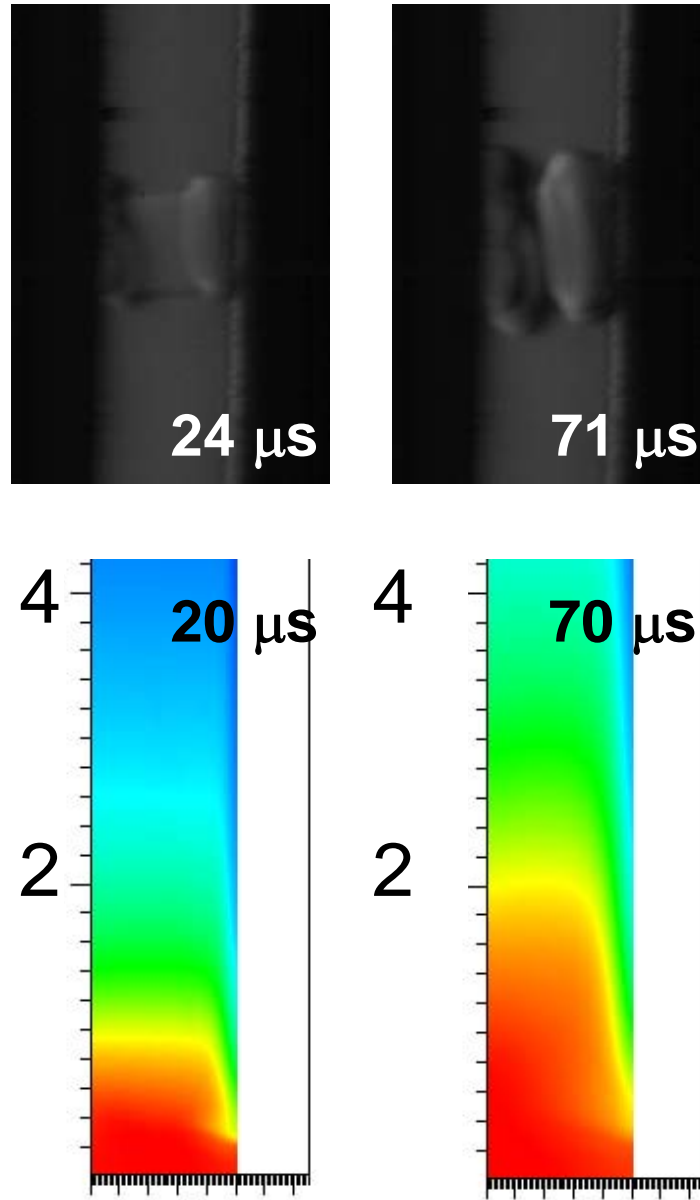


Figure 9.18: Four-component, one-step model: Images from high-speed schlieren visualization and simulation of ignition with the flanged electrodes.

more pronounced in the schlieren images, and there is also some asymmetry of the flame.

Theses results indicate that that the lowest minimum ignition energy would be obtained using the flanged electrodes due to a hotter gas kernel and confinement of the flow, and that the largest ignition energy would be required for the thin cylindrical electrode case. Schlieren visualization and two-dimensional simulations of ignition in a 15 percent hydrogen-air mixture demonstrated that the flame formation process was comparable in the cylindrical and conical electrode cases due to the similarities of the flow fields in the two geometries. Note, that this test was for the relatively high energy of 2 mJ, which is above the critical energy at which nonignition/ignition occurs.

## 9.6 Multi-Step Reduced Detailed Chemistry Model

Lastly, the spark ignition problem was repeated with multi-step, detailed chemistry, thermodynamics, and transport. In the previous case, only four perfect (rather than now ideal) gas species were used. Using this model for spark ignition is difficult as most CHEMKIN mechanisms are only defined to a temperature of 3,000 or 5,000 K maximum. In order to better model the initial high temperatures of the spark, a reduced  $\text{H}_2\text{-O}_2\text{-N}_2$  mechanism was extrapolated to 10,000 K. With these new polynomials for the thermodynamics, a higher initial temperature of approximately 9,000 K could be used. However, this is still lower than the experimentally measured temperatures of the plasma at approximately 35,000 K. Therefore, instead of modeling the hot plasma for which an entirely different mechanism would be needed, we opted to model the cooled mixture of radicals. To obtain the radical mole fractions, an arbitrary temperature and pressure were selected such that the cooled radicals had a temperature less than 10,000 K.

The Goal of using this model was to find cases in axisymmetric one- and two-dimensional simulations where specific spark thicknesses and energies lead to the ignition of a deflagration (a Go) or a dying flame (a no Go). By comparing these cases in this critical condition, the influence of the geometry, single and multi-dimensional mixing, and heat diffusion on the MIE and other possible global parameters that Govern ignition could be deduced.

### 9.6.1 Initial Conditions

Using the reduced CHEMKIN mechanism shown in appendix E.3, the hydrogen-air spark ignition for the conical electrode case was simulated. The demonstrative mixture with mole fractions of  $\text{H}_2$ :0.41,  $\text{O}_2$ :0.50,  $\text{N}_2$ :1.88 was again selected. The cooled radical mole fractions were found by using a zero-dimensional *constant volume explosion* calculation from the **Shock and Detonation Toolbox** which utilizes CANTERA. Above approximately 15,000 K, an equilibrium solution for a cooled radical mixture was not found. We were limited to a state with a cooled radical temperature less than 10,000 K as that was the maximum valid range of the extrapolated CHEMKIN mechanism. Constructing the initial condition in this manner made the thermodynamic and transport the most realistic as possible, however, at the price of having a less physical initial condition.

Firstly, the cooled radical mole fractions which match the 35,000 K temperature and 100 times pressure ratio prediction as close as possible were constructed with the following initial conditions,  $P = 1.1535 \cdot 10^7$  Pa and  $T = 14,000$  K, for the constant volume explosion. This led to the initial conditions for the 1D and 2D simulations with  $P = 1.0049 \cdot 10^7$  Pa,  $T = 9222.37$  K, and the mole fractions of

$\text{H}_2$ : 0.000683549,  $\text{O}_2$ : 0.000476917,  $\text{H}_2\text{O}$ : 3.21669e-6,  $\text{N}_2$ : 0.50952,  $\text{H}$ : 0.219253,  
 $\text{O}$ : 0.268453,  $\text{OH}$ : 0.00161064,  $\text{HO}_2$ : 3.47629e-7,  $\text{H}_2\text{O}_2$ : 3.31317e-10.

### 9.6.2 Experimental Comparison: 2 mJ Case

As was done in §9.5.2, a comparison with experiment was first conducted. Note that that in this case, all initial conditions are the same, except the initial temperature was limited to 14,000 K rather than the 35,000 K expected in experiment and used in the four-species constant  $C_p$  (perfect gas) one-step simulation. This leads to an energy slightly different from 2 mJ.

Using these initial conditions for a axisymmetric spark with a radius of 0.1 mm and width of 2mm yields an initial condition with an energy of 3.1 mJ and energy density of  $49 \text{ J/m}^3$ , as calculated using the change in enthalpy with the reduced mechanism in CANTERA. This is compared to the perfect gas four-species result (which has an energy of 2 mJ) in figures 9.19, 9.20, and 9.21 where the density field is shown for each of the three geometries. Note that even though the same spark thicknesses were used and the temperature is lower for the detailed chemistry case, the perfect gas case has a lower spark energy. This is due to the fact that the specific heats of the



detailed ideal gas species increase in a nonlinear fashion as the initial temperature is increased. Therefore, using an initial condition of radicals (rather than products or reactants) in this manner, has more stored energy and will lead to “a Go” for lower initial temperatures and thinner sparks.

In figure 9.19, the cylindrical case is compared. Even though the detailed case has a higher initial energy, the kernel is found to be smaller in size. Also, the flame fronts appear to be less diffused than in the four-species perfect gas case. Note that, the detailed case better matches the kernel size shown in the schlieren image, even though the energies are not the same.

In figure 9.20 for the conical electrode, the same trend of kernel size and diffusion is observed. The simple two-species model is also shown, for which the kernel is even larger; yet, the diffusion is still small in comparison. In figure 9.21 the flanged results are shown. At approximately 70 micros for the detailed case, the kernel is about half the size of the perfect gas case. Also, the observed diffusion is again smaller in extent. These differences highlight the importance of including detailed chemistry and transport in an ignition simulation. While using the perfect gas approximation allows one to easily use a higher initial temperature, this only occurs at the very early times of the simulation where the initial strong blast wave initially decays. After the initial decay, the temperature is much lower and the importance of having an accurate multi-species low temperature model becomes apparent.

### 9.6.2.1 Simulations Details

Shown in figures 9.22-9.25 are detailed visualizations highlighting the fluid flow in the detailed spark ignition problems. For the cylindrical geometry case in figure 9.22, the mass fraction of product,  $\text{H}_2\text{O}$ , is shown with superimposed flow velocity vectors. Initially, the deflagration/flame is localized on the outside surface of the hot kernel created by the blast wave. Also, vorticity is easily observed at the sharp electrode corner, causing a localized rollup of the flame. Soon after the blast wave has traveled past the electrode, a bulk backflow is created from the influence of the axisymmetric geometry as was discussed for the simpler model’s nonreactive cases. This back flow causes the vortex at the tip to be stretched into two pieces, both of which are pushed into the the  $x = 0$  symmetry plane. The top piece of the flame is pushed upward, and the bottom piece is pushed down and right into the electrode tip.

In figures 9.23 and 9.24 for the conical case, a very similar phenomenon is observed. A vortex, larger in this case is again formed at the electrode corner. Due to the larger

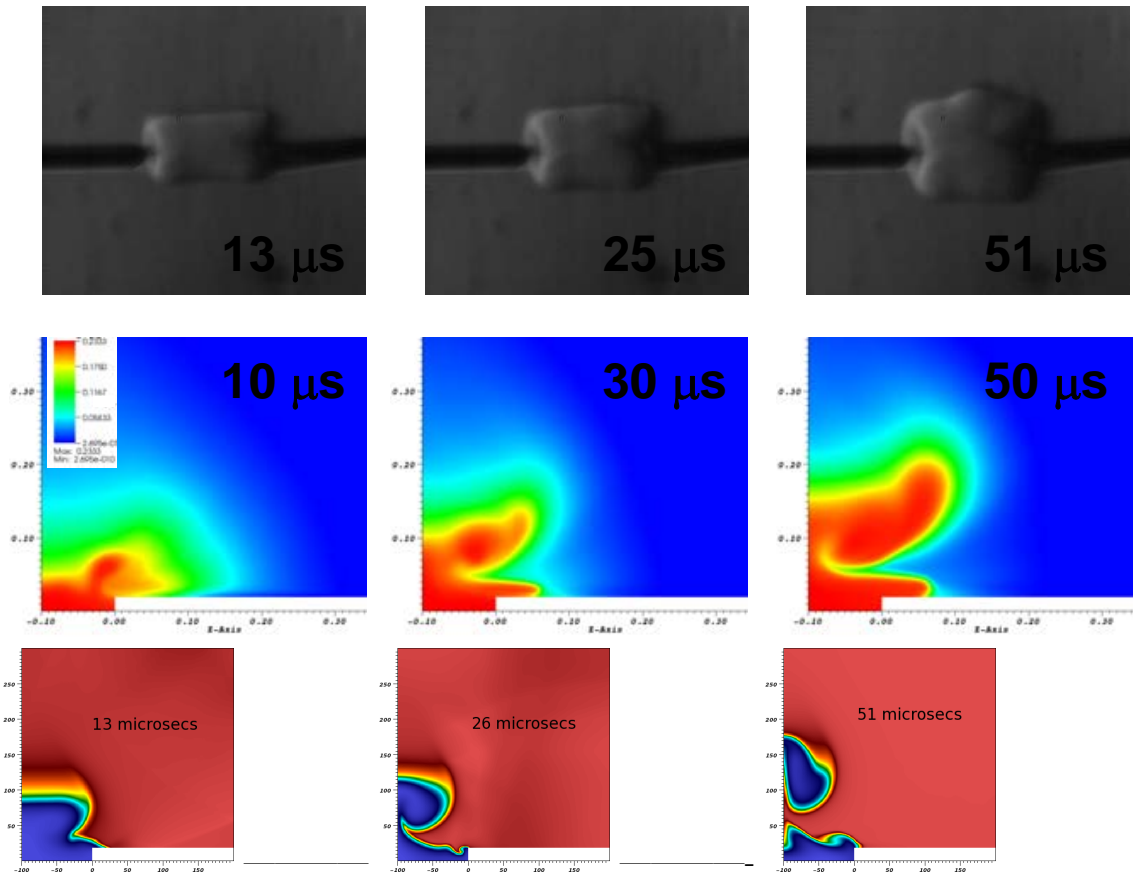


Figure 9.19: High-energy case: Images from high-speed schlieren visualization and pseudo-color density results from the simulation of ignition with the thin cylindrical electrodes. Comparing experiment, four-species one-step model with 35,000 K initial temperature, and detailed chemistry with 14,000 K initial temperature. Both simulations are at the same pressures.

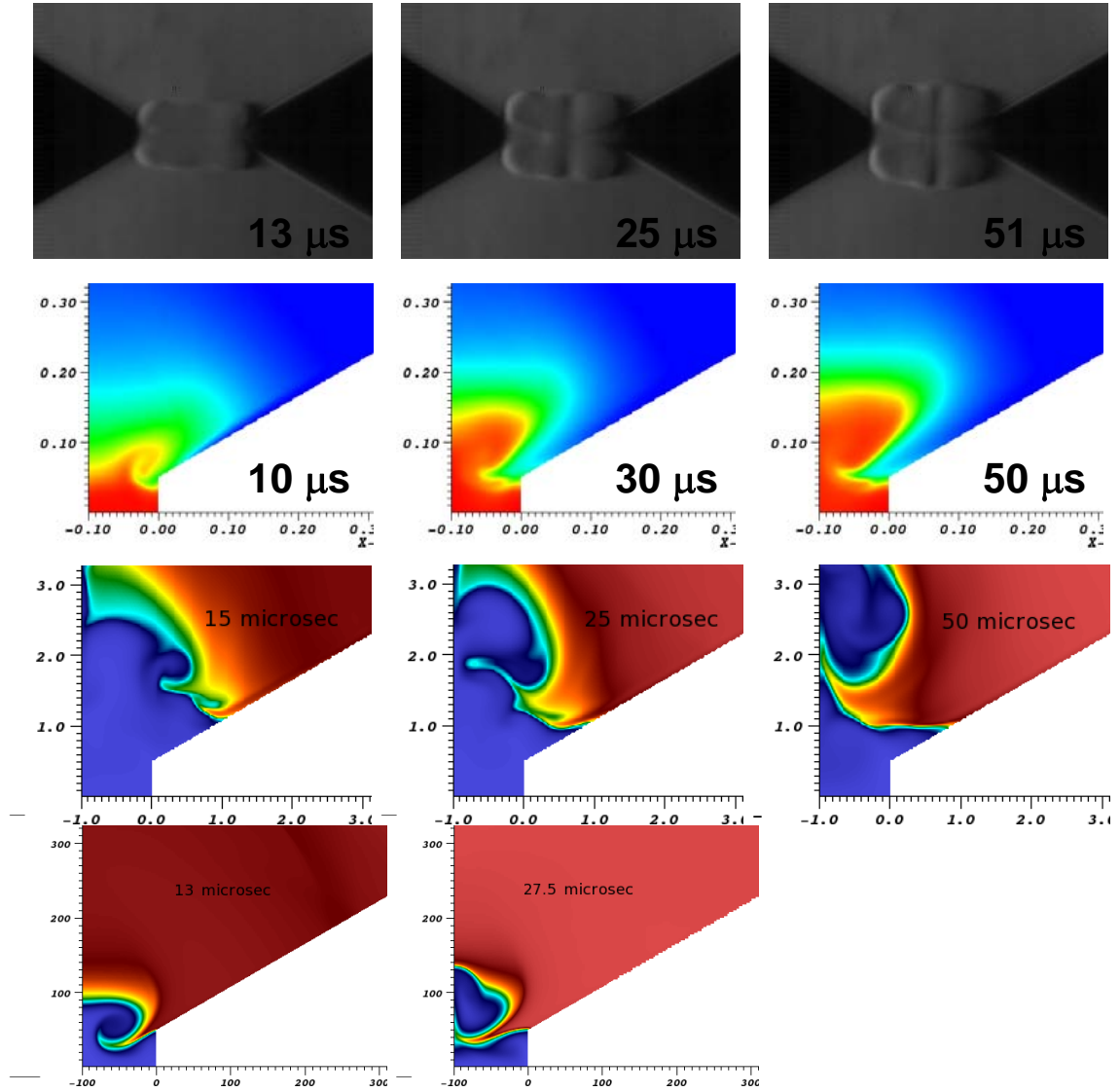


Figure 9.20: High-energy case: Images from high-speed schlieren visualization and pseudo-color density results from the simulation of ignition with the conical electrodes. Comparing experiment, 2 species one-step model, four-species one-step model with 35,000 K initial temperature, and detailed chemistry with 14,000 K initial temperature. Both simulations are at the same pressures.

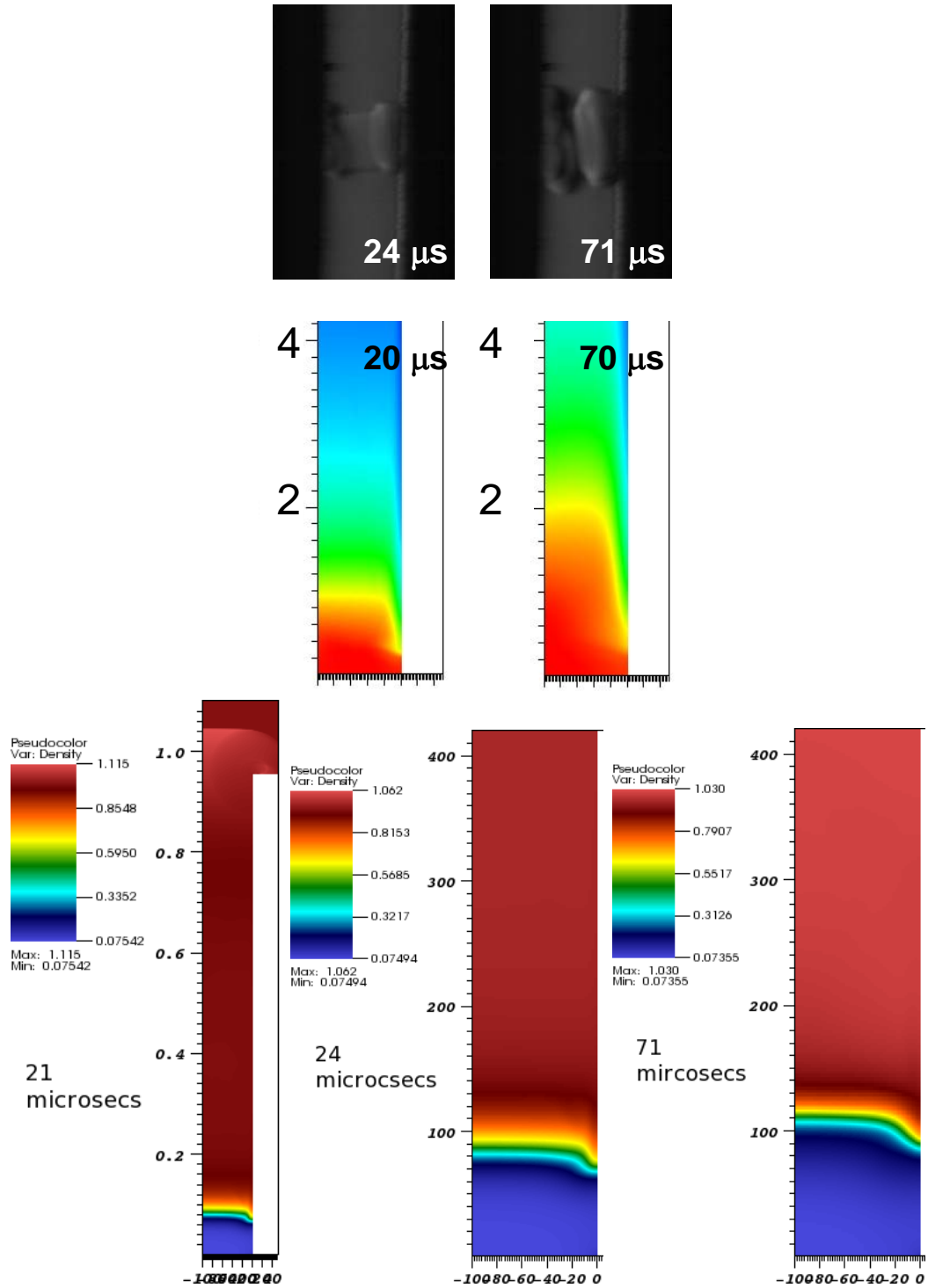


Figure 9.21: High-energy case: Images from high-speed schlieren visualization and pseudo-color density results from the simulation of ignition with the flanged electrodes. Comparing experiment, four-species one-step model with 35,000 K initial temperature, and detailed chemistry with 14,000 K initial temperature. Both simulations are at the same pressures.

and less sharp conical electrode geometry interacting with the blast wave, the vortex is allowed to rollup for a longer time and grow in size before it is stretched and broken in to an upper and lower piece by the back flow.

Lastly, from figure 9.25A) to B), the growth of the flame for the flanged geometry case is shown. Initially in A) near the wall, the flow directions are dominated by the influence of the boundary layer. Later in B), the flame and flow speed through the flame has grown in size and dominates the velocity flow direction even near the wall and very little back flow occurs.

A large difference found by including multi-component detailed chemistry with radicals is that for the early times involving the formation of the flame kernel, the chemical reactions are localized to a region centered at the kernel surface. In the one-step chemistry two- and four-species results the chemical reactions are seen to occur more uniformly throughout the hot kernel.

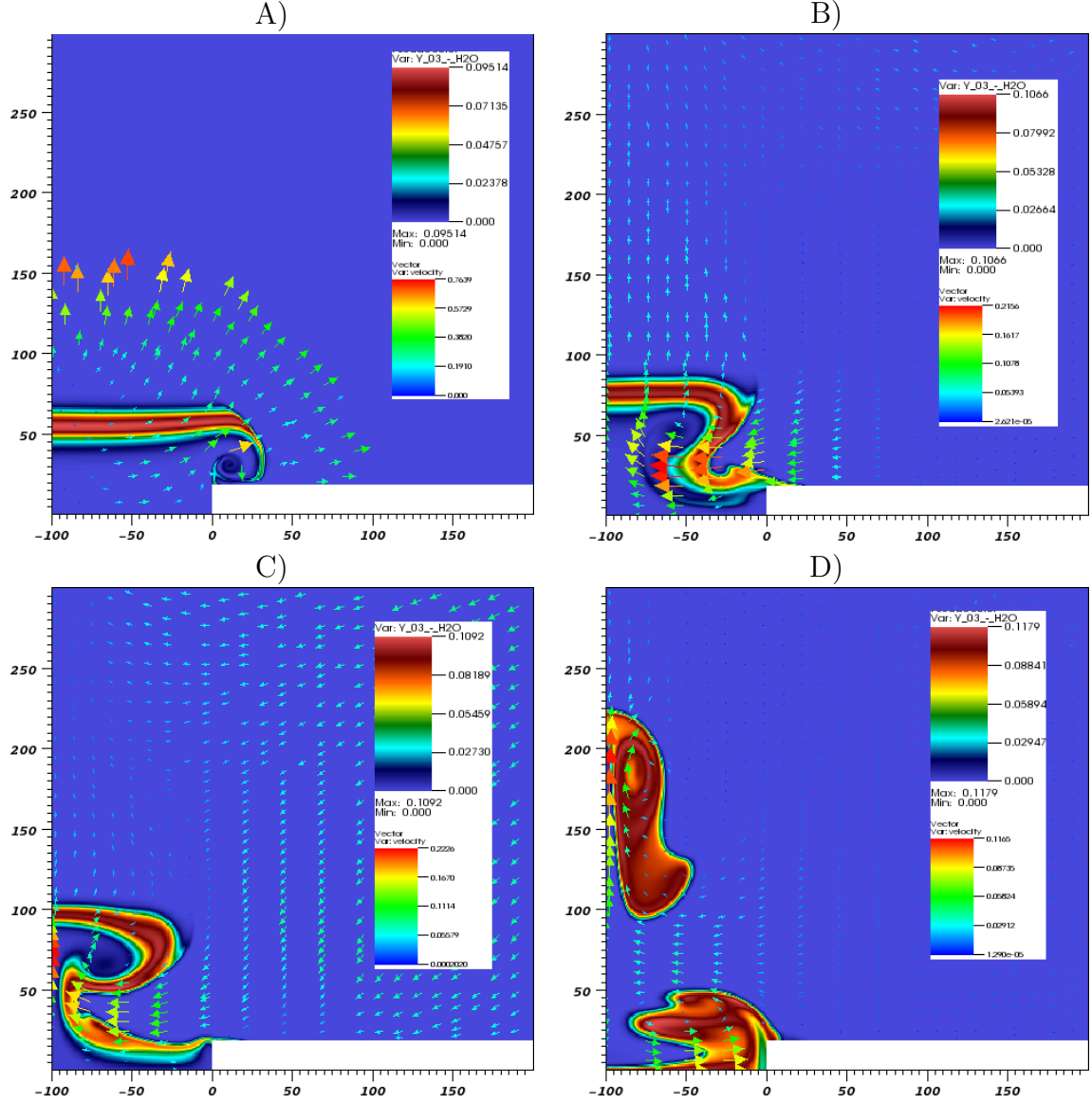
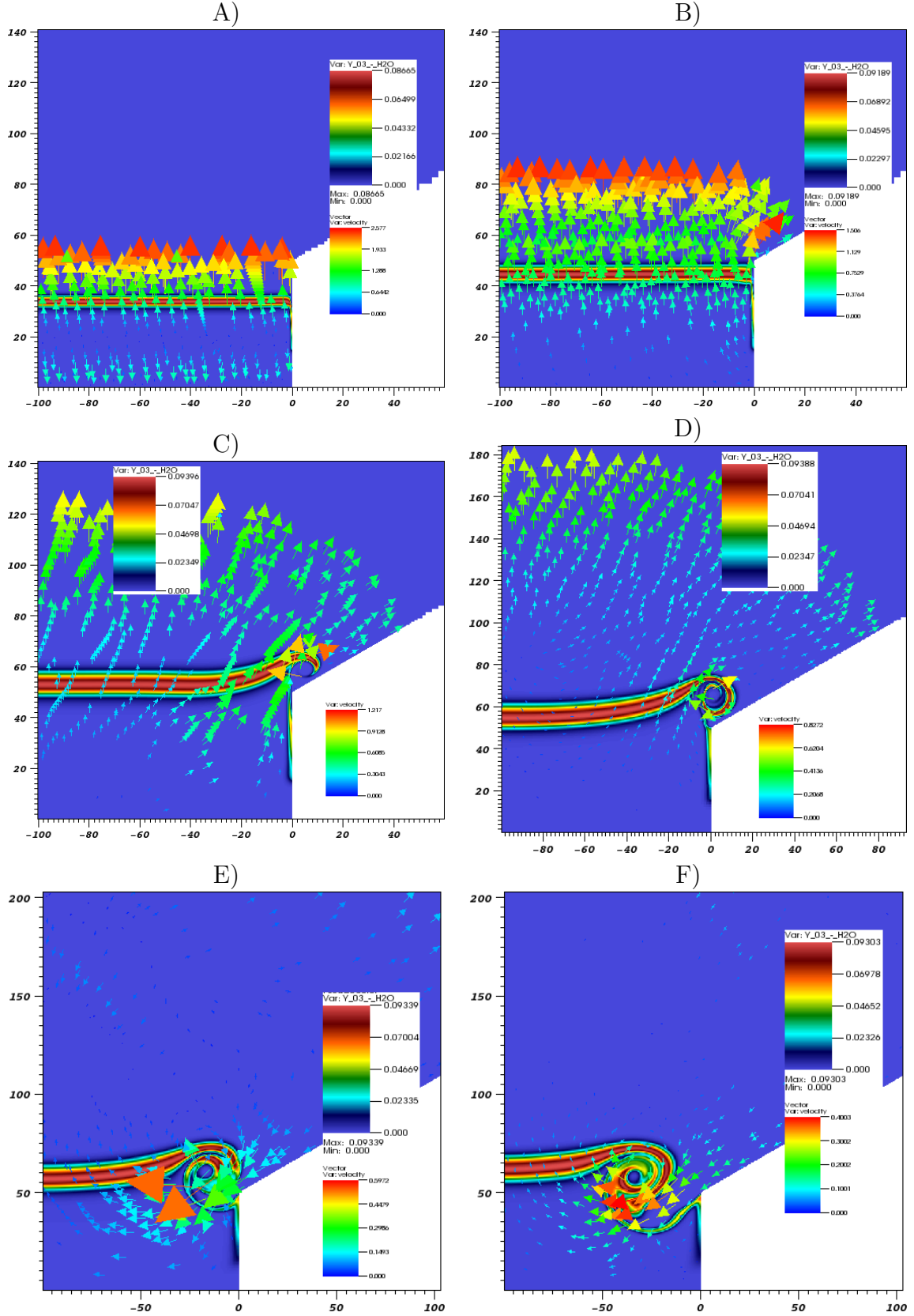


Figure 9.22: Velocity vectors superimposed on pseudo-color plots of  $\text{H}_2\text{O}$  mass fraction for the thin cylindrical electrode case with detailed chemistry and transport. Showing results for A) 60 nondim =  $1.602 \cdot 10^{-6}$  s, B) 480 nondim =  $1.2818 \cdot 10^{-5}$  s, C) 780 nondim =  $2.083 \cdot 10^{-5}$  s, and D) 3000 nondim =  $8.0114 \cdot 10^{-5}$  s. The units of the x- and y-axes are  $1 \cdot 10^{-3}$  cm.





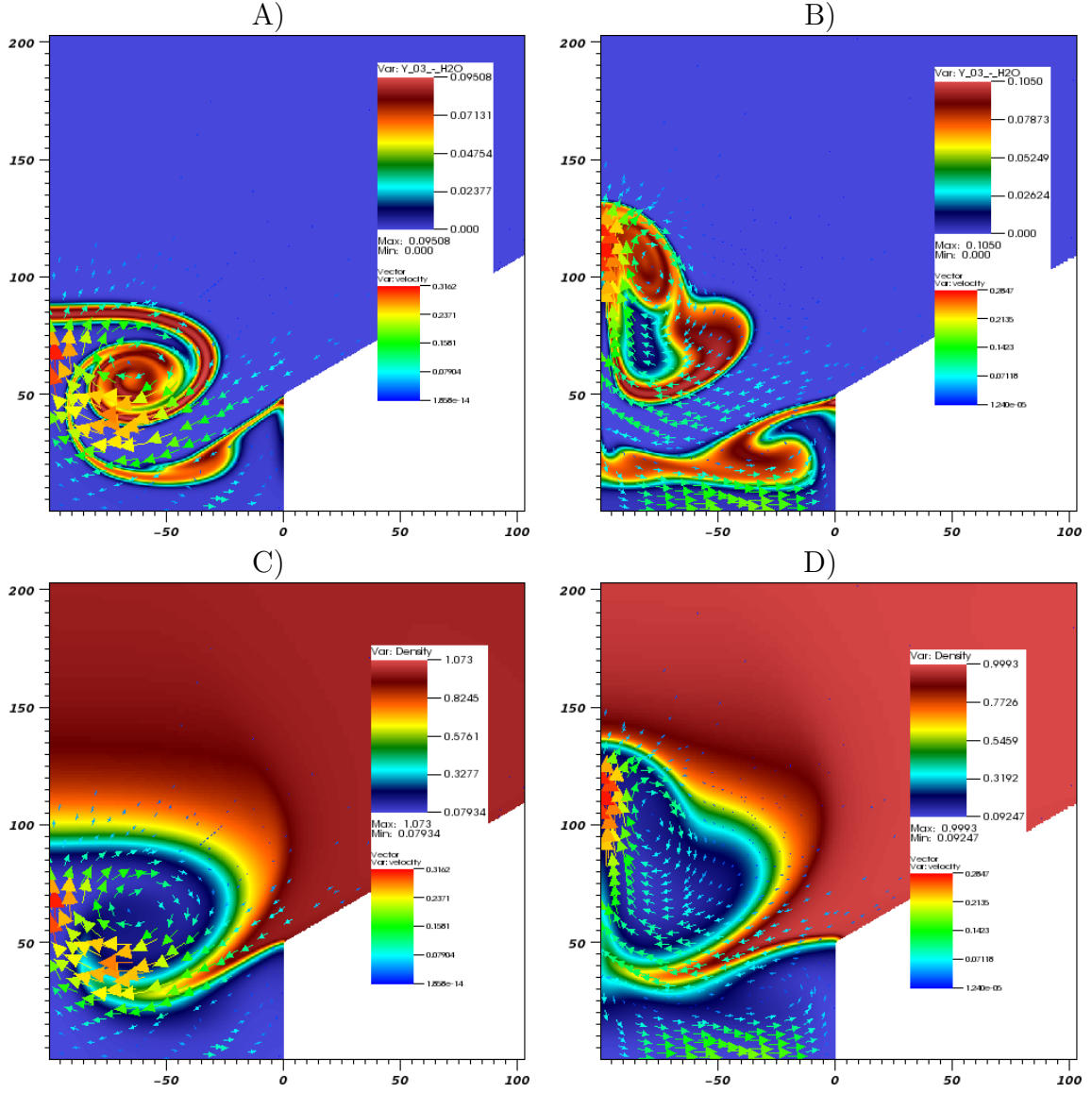


Figure 9.24: Velocity vectors superimposed on pseudo-color plots for the conical electrode case with detailed chemistry and transport. Showing results for H<sub>2</sub>O mass fraction in A)  $t = 560$  nondim =  $1.49 \cdot 10^{-5}$  s and B)  $t = 1030$  nondim =  $2.75 \cdot 10^{-5}$  s. Showing result for density in C)  $t = 560$  nondim =  $1.49 \cdot 10^{-5}$  s and D)  $t = 1030$  nondim =  $2.75 \cdot 10^{-5}$  s. The units of the x- and y-axes are  $1 \cdot 10^{-3}$  cm.

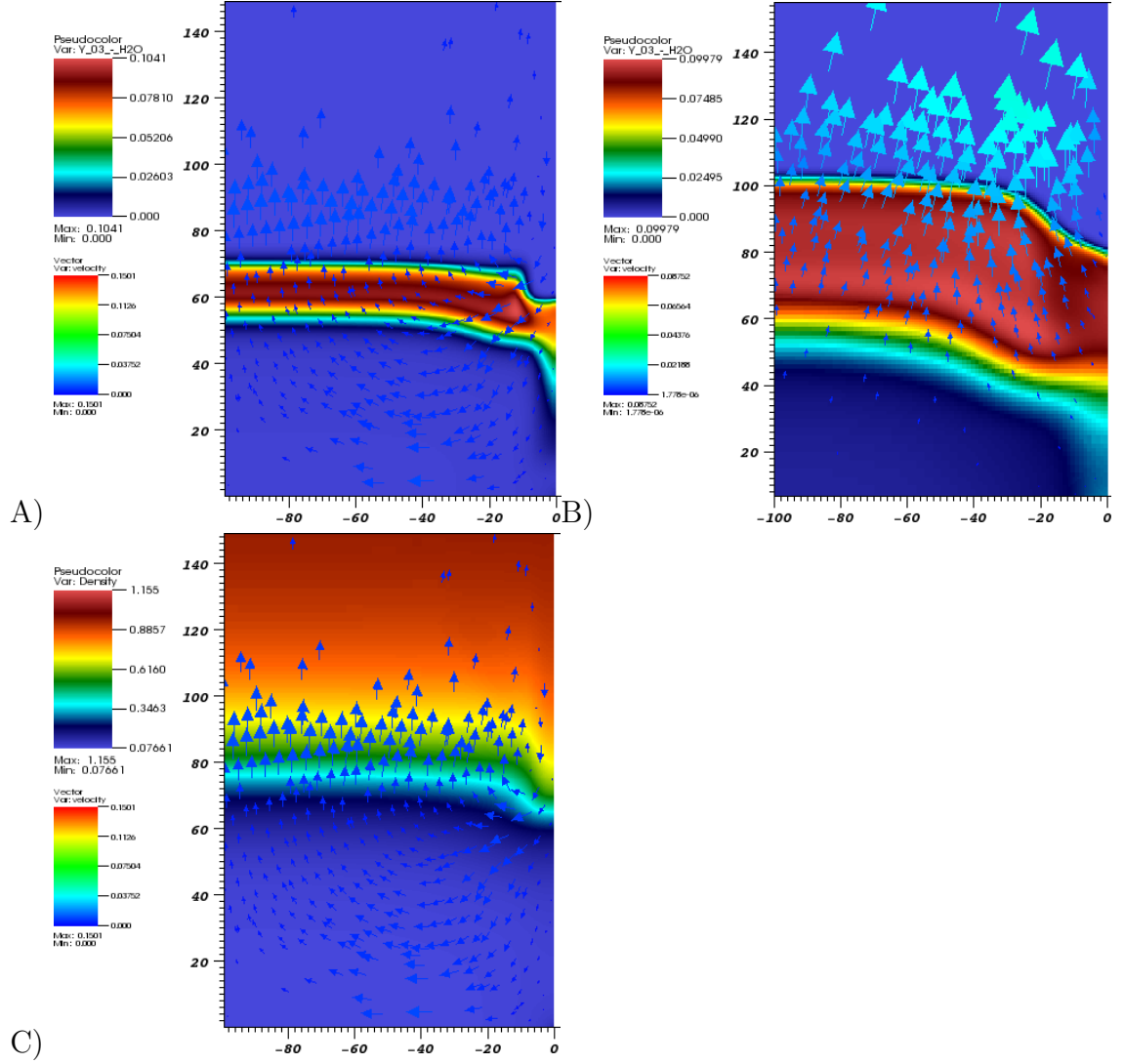


Figure 9.25: Velocity vectors superimposed on pseudo-color plots of various quantities for the flanged electrode case with detailed chemistry and transport. Showing results for A) and C)  $t = 600 \text{ nondim} = 1.6 \cdot 10^{-5} \text{ s}$  and B)  $t = 7.1 \cdot 10^{-5} \text{ s}$ . The units of the x- and y-axes are  $1 \cdot 10^{-3} \text{ cm}$ .

### 9.6.3 Critical Energy Results

All previously run experiments and simulations discussed in this chapter have been at energies that far exceed the minimum ignition energy (MIE). This has primarily been done such that an experimental/numerical comparison through the use of schlieren images was highly visible and repeatable. In particular, the use of a higher energy increased the relative influence of the geometry and boundary layers as compared to general mass and heat diffusion in the flame.

In the following sections, simulations in one and two dimensions were conducted at low ignition energies near the MIE value. Initial energy values just above and below the numerically discovered MIE values were used. The results from different initial spark thicknesses, pressure ratios, and ambient pressures and from different number of simulated dimensions were all compared to each other and also to a simplified theoretical model.

#### 9.6.3.1 One-Dimensional Axisymmetric Case

Firstly, one-dimensional axisymmetric simulations were carried out using the initial conditions specified in section 9.6.1, however, now with smaller spark thicknesses. The results for all time steps are shown in tables 9.2, 9.3, and 9.4. The boundary conditions at  $x = 0$  are symmetric and at the right boundary are outflow. These results are summarized in table 9.1. Here, it is found that the transition between a “Go” and a “No Go” is approximately at  $\frac{E}{V} \frac{P_{ratio}^2}{P_{initial}} = 4.91 \cdot 10^{-2} \text{ (J/(m}^3\text{))/Pa} = 1$  (nondimensional) ). Thus, a successful 1D axisymmetric flame propagation depends on the energy density, ambient pressure, and pressure ratio (or equivalently the spark pressure) of the spark.

As shown in table 9.2, with a initial pressure of 100,000 Pa and a ratio of approximately 100, three different spark radii were simulated: 0.02, 0.01, and 0.005 mm. The same initial conditions as specified for the experimental comparison in §9.6.2 were used.

In table 9.3, now with a initial pressure of 10,000 Pa and a ratio of approximately 100, three different spark radii were again simulated: 0.2, 0.1, and 0.05 mm. The cooled radical mole fractions for table 9.3 were found by using the initial conditions of  $P = 1.1535 \cdot 10^6 \text{ Pa}$  and  $T = 14,000 \text{ K}$ . This lead to the initial conditions for the 1D and 2D simulations with  $P = 1.00213 \cdot 10^6 \text{ Pa}$ ,  $T = 9,174.09 \text{ K}$ , and the mole fractions of

radius (cm)	energy E(J)	energy density $\frac{E}{V}$ (J/m <sup>3</sup> )	V (m <sup>3</sup> )	$P_{ratio}$	$P_{initial}$ (Pa)	$\frac{E}{V} \frac{P_{ratio}^2}{P_{initial}}$	$E \frac{P_{ratio}}{P_{initial}}$	Go?
$2 \cdot 10^{-4}$	$1.23 \cdot 10^{-4}$	$4.911 \cdot 10^7$	$2.513 \cdot 10^{-10}$	100	$1 \cdot 10^5$	$4.911 \cdot 10^{-2}$	$1.23 \cdot 10^{-7}$	Go
$1 \cdot 10^{-4}$	$3.08 \cdot 10^{-5}$	$4.911 \cdot 10^7$	$6.283 \cdot 10^{-11}$	100	$1 \cdot 10^5$	$4.911 \cdot 10^{-2}$	$3.08 \cdot 10^{-8}$	Go
$5 \cdot 10^{-5}$	$7.71 \cdot 10^{-6}$	$4.911 \cdot 10^7$	$1.571 \cdot 10^{-11}$	100	$1 \cdot 10^5$	$4.911 \cdot 10^{-2}$	$7.71 \cdot 10^{-9}$	No Go
$2 \cdot 10^{-3}$	$1.23 \cdot 10^{-5}$	$4.908 \cdot 10^6$	$2.513 \cdot 10^{-8}$	100	$1 \cdot 10^4$	$4.908 \cdot 10^{-2}$	$1.23 \cdot 10^{-7}$	Go
$1 \cdot 10^{-3}$	$3.08 \cdot 10^{-6}$	$4.908 \cdot 10^6$	$6.283 \cdot 10^{-9}$	100	$1 \cdot 10^4$	$4.908 \cdot 10^{-2}$	$3.08 \cdot 10^{-8}$	Go
$5 \cdot 10^{-4}$	$7.71 \cdot 10^{-7}$	$4.908 \cdot 10^6$	$1.571 \cdot 10^{-9}$	100	$1 \cdot 10^4$	$4.908 \cdot 10^{-2}$	$7.71 \cdot 10^{-9}$	No Go
$2 \cdot 10^{-2}$	$1.20 \cdot 10^{-3}$	$4.909 \cdot 10^5$	$2.513 \cdot 10^{-6}$	10	$1 \cdot 10^5$	$4.909 \cdot 10^{-2}$	$1.20 \cdot 10^{-7}$	Go
$1 \cdot 10^{-2}$	$3.084 \cdot 10^{-4}$	$4.909 \cdot 10^5$	$6.283 \cdot 10^{-7}$	10	$1 \cdot 10^5$	$4.909 \cdot 10^{-2}$	$3.084 \cdot 10^{-8}$	Go
$5 \cdot 10^{-3}$	$7.102 \cdot 10^{-5}$	$4.909 \cdot 10^5$	$1.571 \cdot 10^{-7}$	10	$1 \cdot 10^5$	$4.909 \cdot 10^{-2}$	$7.102 \cdot 10^{-9}$	No Go

Table 9.1: Summary of one- and two-dimensional spark ignition results for different initial spark and ambient conditions. Note that the transition between and Go and a No Go is between  $E \frac{P_{ratio}}{P_{initial}} = 3 \cdot 10^{-8}$  and  $7 \cdot 10^{-9}$  for all three test cases.

H<sub>2</sub>: 7.17764e-05, O<sub>2</sub>: 4.99156e-05, H<sub>2</sub>O: 3.51239e-08, N<sub>2</sub>: 0.508256, H: 0.221374,  
O: 0.27008, OH: 0.000168591, HO<sub>2</sub>: 3.71972e-09, H<sub>2</sub>O<sub>2</sub>: 3.66324e-13.

Lastly, in table 9.4 with a initial pressure of 10,000 Pa and a ratio of approximately 10, three different spark radii were simulated: 20, 10, and 5 mm. The cooled radical mole fractions for table 9.4 were found by using a constant volume explosion calculation from the Shock and Detonation Toolbox with the initial conditions of  $P = 1.1535 \cdot 10^5$  Pa and  $T = 14,000$  K. This lead to the initial conditions for the 1D and 2D simulations with  $P = 10,0184$  Pa,  $T = 9,169.01$  K, and the mole fractions of

H<sub>2</sub>: 7.21466e-06, O<sub>2</sub>: 5.01563e-06, H<sub>2</sub>O: 3.54512e-10, N<sub>2</sub>: 0.508123, H: 0.221597,  
O: 0.270251, OH: 1.69404e-05, HO<sub>2</sub>: 3.74636e-11, H<sub>2</sub>O<sub>2</sub>: 3.70224e-16.

The first thickness results in a clear Go. The last thickness results in a clear no Go. The middle spark thickness results in a simulation which at first shows a dying flame. Yet, after it has cooled to approximately 800 K, the temperature begins to slowly increase. The temperature then increases at an increasing rate until a Go is established. Note that in both Go cases, the self propagating flame temperature has a maximum of approximately 1,900 K.

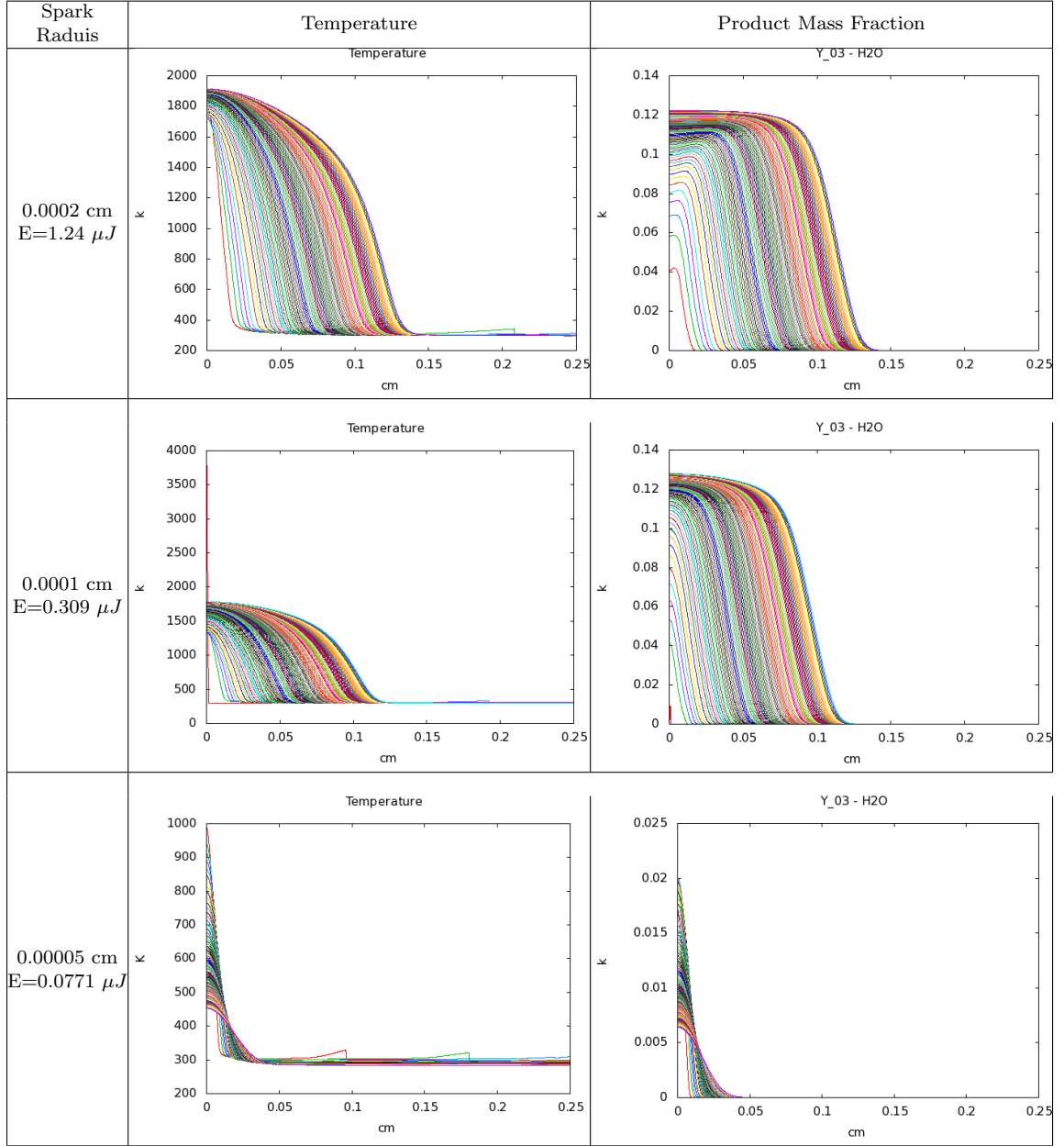


Table 9.2: Spark ignition results for the 1D axisymmetric problem with a pressure ratio of 100 at ambient (100,000 Pa = 1atm) conditions. Three different spark radii are shown: 0.0002, 0.0001, and 0.00005 cm. For each of these a time-elapsd Temperature (K) and product ( $H_2O_2$ ) mass fraction plot is shown. In these plots, a line is plotted every  $2 \cdot 10^{-6}$  s from 0 to  $2 \cdot 10^{-4}$  s. Observe that for the 0.0002 and 0.0001 cm radius case, a clear “Go” is found. For the 0.00005 radius case, a clear “no Go” is found.

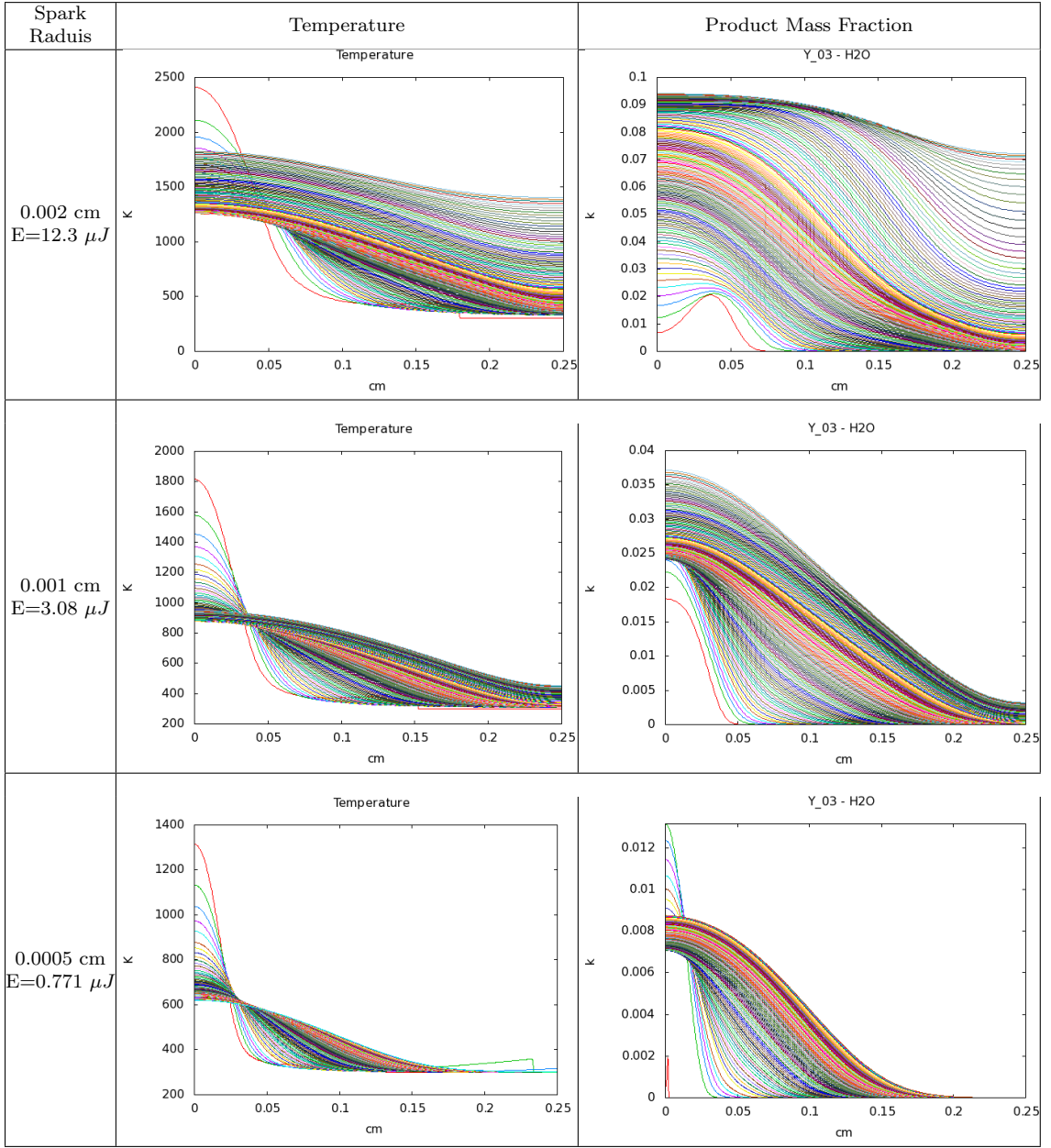


Table 9.3: Spark ignition results for the 1D axisymmetric problem with a pressure ratio of 100 at ambient ( $10,000 \text{ Pa} = 0.1 \text{ atm}$ ) conditions with three spark radii: 0.002, 0.001, and 0.0005 cm. For each of these a time-elapsd temperature (K) and product ( $\text{H}_2\text{O}_2$ ) mass fraction plot is shown. Here, lines are plotted every  $2 \cdot 10^{-6} \text{ s}$  from 0 to  $4 \cdot 10^{-4} \text{ s}$ . Observe that for the 0.002 cm radius case, a clear “Go” is found. For the 0.001 cm case an eventual “Go” is found. This is observed by noticing at approximately  $1 \cdot 10^{-4} \text{ s}$ , the temperature of the kernel stops decreasing and begins to increase. For the 0.0005 radius case, a clear “no Go” is found as the temperature continues to decrease.



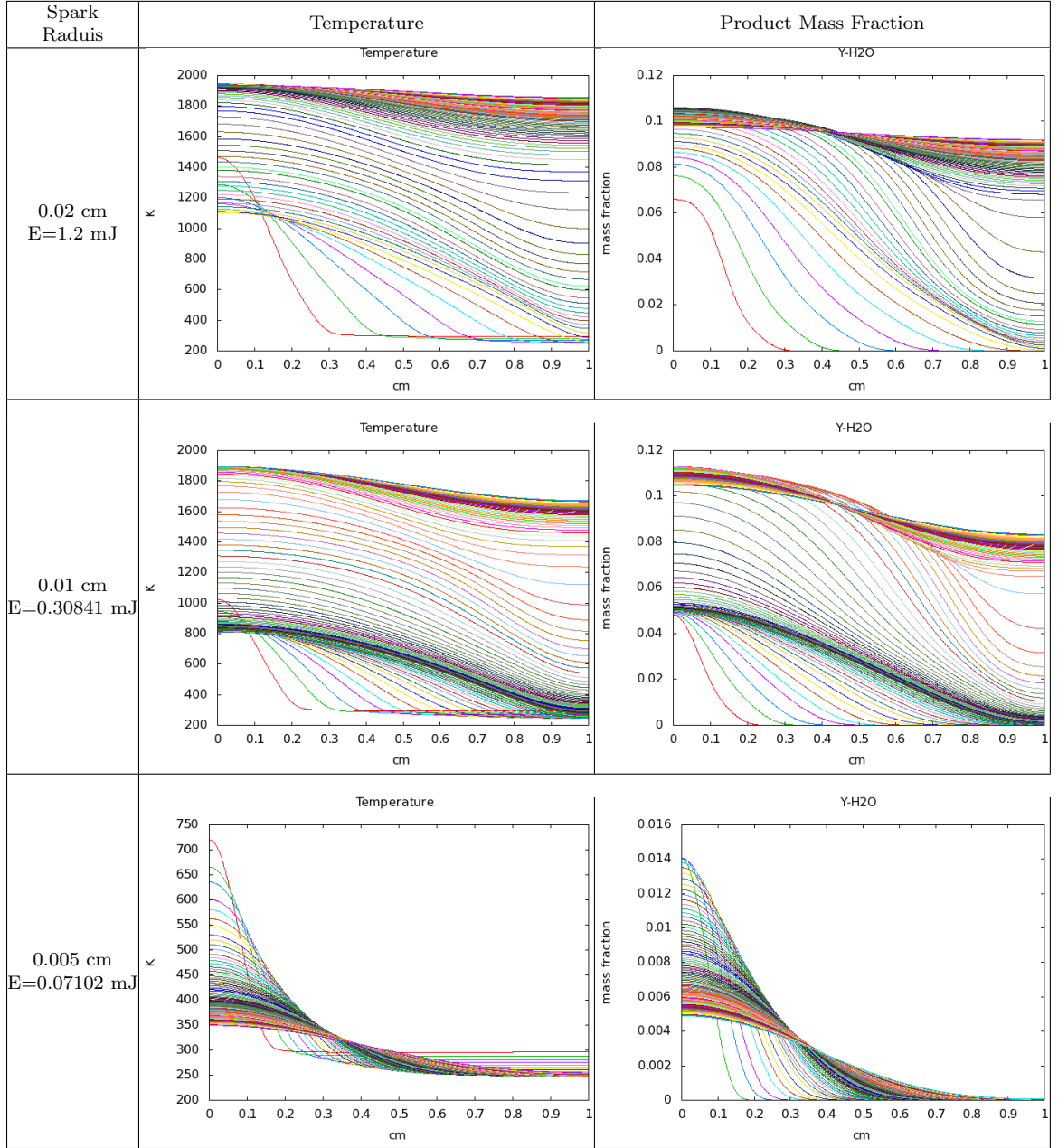


Table 9.4: Spark ignition results for the 1D axisymmetric problem with a pressure ratio of 10 with ambient conditions at 10,000 Pa. Three different spark radii are shown: 0.02, 0.01, and 0.005 cm. For each of these a time-elased Temperature (K) and product ( $\text{H}_2\text{O}_2$ ) mass fraction plot is shown. In these plots, a line is plotted every  $1 \cdot 10^{-4}$  s from 0 to  $1 \cdot 10^{-2}$  s. Observe that for the 0.02 cm radius case, a clear “Go” is found. For the 0.005 radius case, a clear “no g” is found. For the 0.01 cm radius case, after  $4 \cdot 10^{-3}$  s have passed, a “Go” is determined.



### 9.6.3.2 Two-Dimensional Axisymmetric Cone Case

Two-dimensional axisymmetric simulations of the spark ignition problem were carried out using the same initial and spark conditions in tables 9.3 (0.1 atm and a 100x pressure ratio) and 9.4 (1 atm and a 10x pressure ratio). The purpose of these simulations is to see how the multi-dimensional fluid dynamics can influence a flame in the limit of a Go/No Go case. Due to the large computational expense of these simulations, only the conical electrode case was simulated. Also, note that only two out of the three 1D cases were simulated in 2D. Difficulties were found with the 1 atm ambient, 100x pressure ratio case, as extremely small spark thicknesses were needed to show a No Go result. This made this case the most spatially multi-scale out of the three cases, requiring at least 8 refinement levels just to find nonignition. Because the spark is so thin, nonignition is established before the flame has time to be influenced by the geometry of the electrode, which is very large compared to the flame size, thus making a two-dimensional simulation comparable to its 1D simplification.

The results of the 0.1 atm ambient with 100x pressure ratio case are shown with the time-elapsed temperature in figures 9.26, 9.28, and 9.30 and  $\text{H}_2\text{O}$  mass fraction in figures 9.27, 9.29, and 9.31. In the first four figures, for the  $r = 0.002$  cm and  $r = 0.001$  cm sparks, a clear Go is found.

For the  $r = 0.002$  cm case, a Go is seen by observing that after the initial temperature decreases from the rarefaction behind the blast wave, there is an increasing maximum temperature, from 725 at  $0.87 \cdot 10^{-4}$  s to 744 K at  $2.3 \cdot 10^{-4}$ . Also, at these timesteps, the product mass fraction has largely increased from 0.0059 to 0.023, values which match the laminar flames found in the one-dimensional simulation. In fact, aside from the small effect of vorticity and the no-slip BC near the electrode surface, and a final spherical looking flame front, the 1D and 2D results are practically the same.

For the  $r = 0.001$  cm case, another Go is found. Because of the lower energy with this thinner spark, it takes a longer time for the flame to be established. At a time of approximately  $0.5 \cdot 10^{-4}$  s, the maximum temperature again begins to increase, going from 586 to 589 K at  $1.5 \cdot 10^{-4}$  s, yet, this time at a much smaller rate. The product mass fraction is also increasing, from 0.0029 to 0.0098 at these time steps. Comparing the 0.001 cm case to the 0.002 cm case, the flow fields are found to be similar, with diffusion (mass and heat) dominating flame evolution.

Now, for the  $r = 0.0005$  cm case, just as for the 1D axisymmetric result, a No Go is found. The temperature decreases from the the expansion of the blast wave,

and then continues to decrease from the effect of heat diffusion. A very small amount of combustion is occurring, however, at too small of a rate to heat up the fluid to support a laminar flame. These effects are observed by looking at the figures at times of  $0.64 \cdot 10^{-4}$  s and  $1.1 \cdot 10^{-4}$  s where the maximum temperature has decreased from 579 to 505 K, while the product mass fraction has decreased from 0.001107 to 0.001075 due to mass diffusion dominating the chemical reactions' product creation. At 500 K, the rate of chemical reaction is too small to increase the product concentration and fluid temperature.

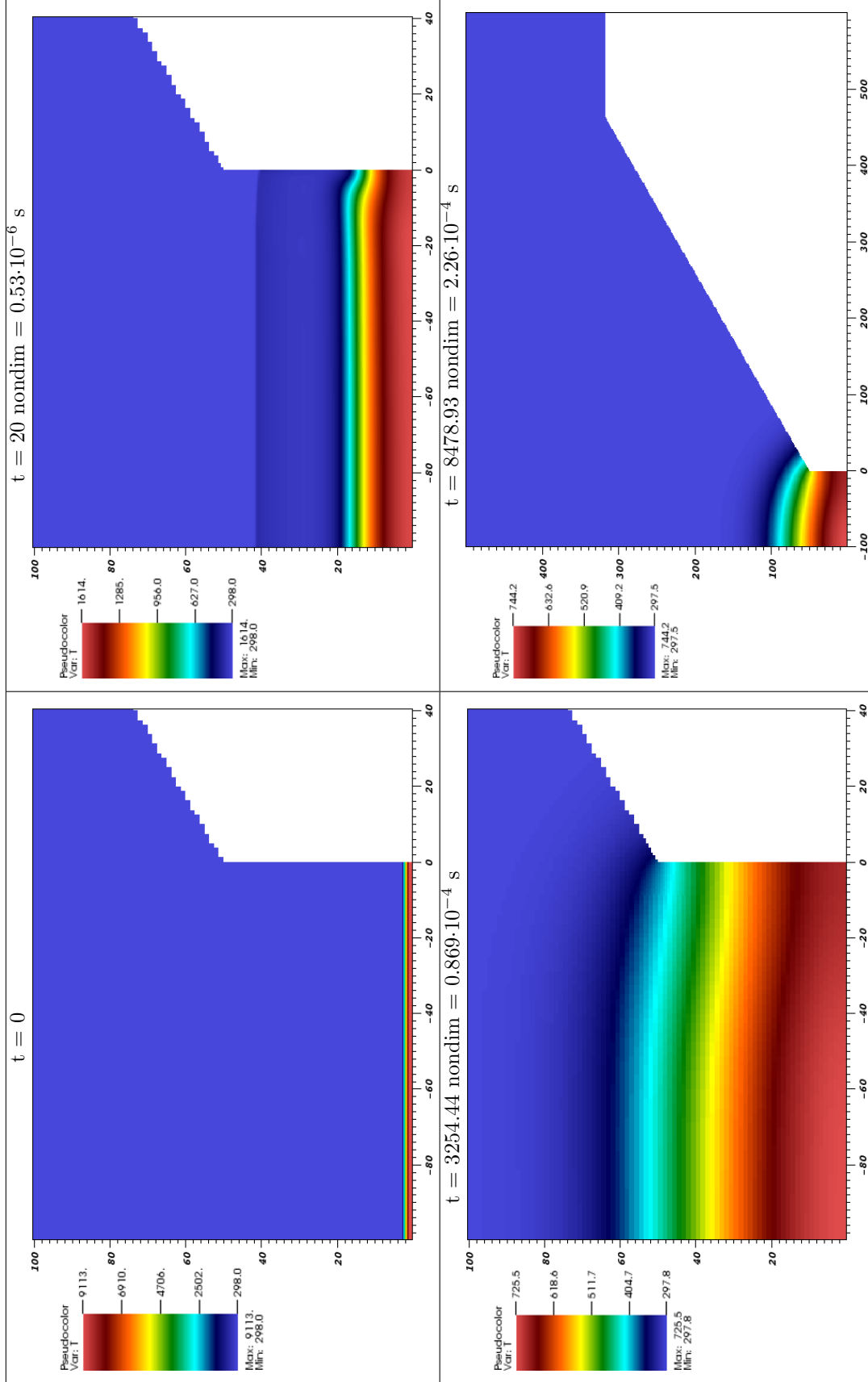


Figure 9.26:  $r = 0.002$  cm: Time-elapsing pseudo-color temperature plots for a spark radius  $= 0.002$  cm with a pressure ratio of 100 with ambient conditions at 10,000 Pa. Simulation was for  $x = (-0.1, 0.6)$  and  $y = (0, 0.5)$  cm with a  $560 \times 400$  base grid and 4 levels total (3 refinement levels  $2 \times$  finer each). The number of levels used in the simulation decreased as the gradients became smoother. Note that at  $t = 0.869 \cdot 10^{-4}$  s, the maximal temperature stops decreasing and begins to increase, marking the creation of a self-supported flame.

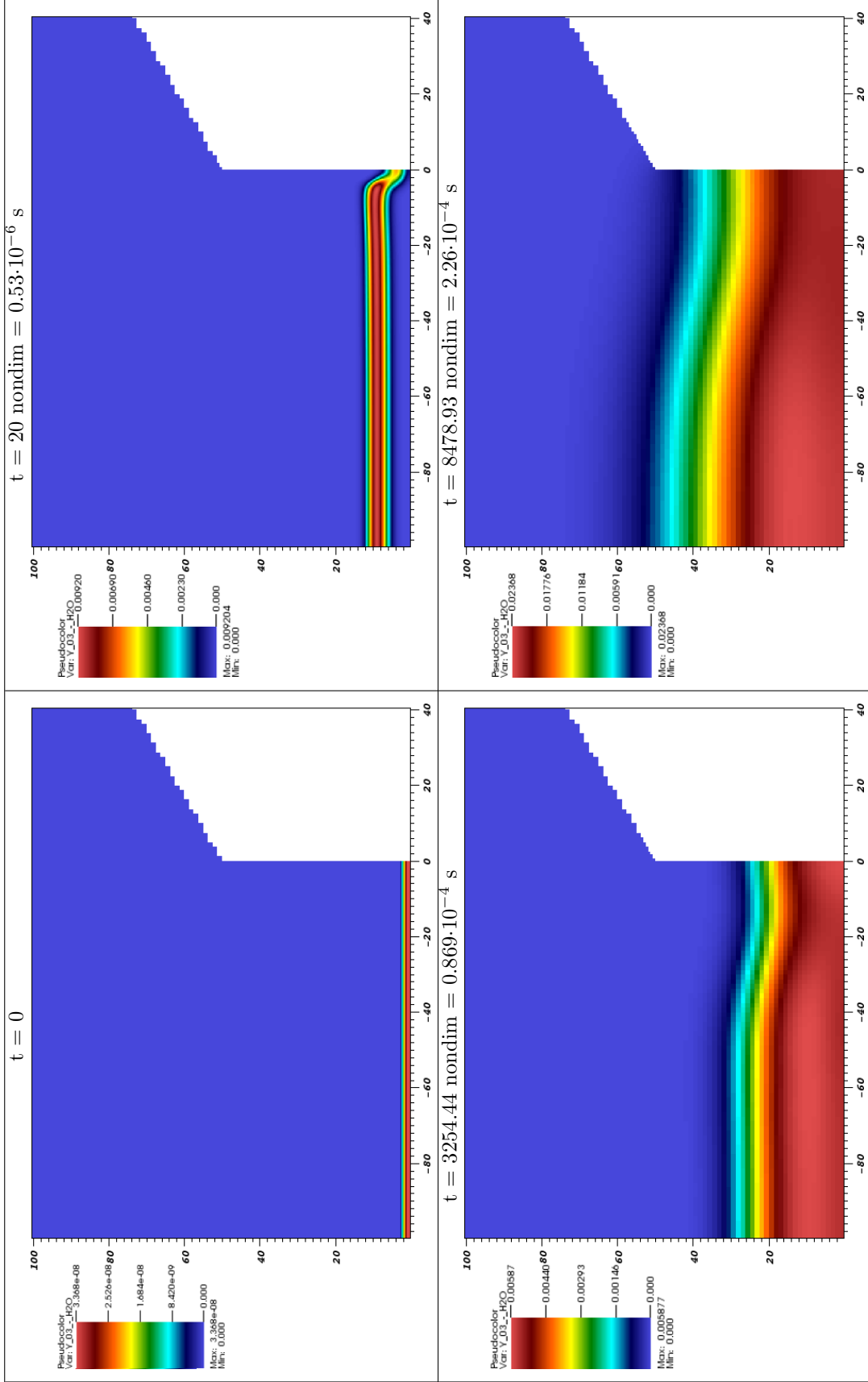


Figure 9.27:  $r = 0.002$  cm: Time-elapsed pseudo-color  $\text{H}_2\text{O}$  mass fraction plots for a spark radius  $= 0.002$  cm with a pressure ratio of 100 with ambient conditions at 10,000 Pa. Simulation was for  $x=(-0.1, 0.6)$  and  $y=(0, 0.5)$  cm with a  $560 \times 400$  base grid and 4 levels total (3 refinement levels 2x finer each). The number of levels used in the simulation decreased as the gradients became smoother.

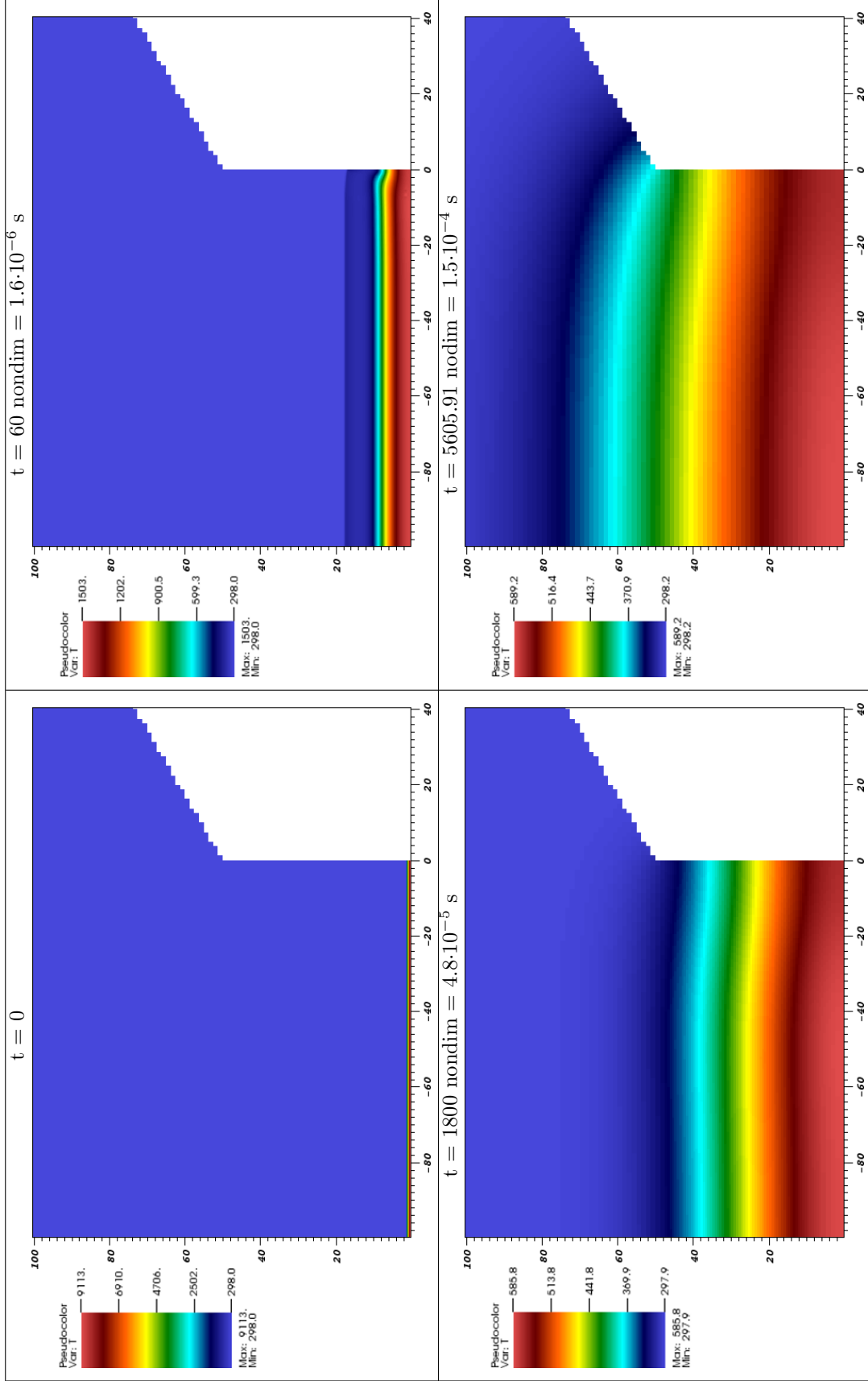


Figure 9.28:  $r = 0.001 \text{ cm}$ : Time-elapsing pseudo-color temperature plots for a spark radius = 0.001 cm with a pressure ratio of 100 with ambient conditions at 10,000 Pa. Simulation was for  $x=(-0.1,0.6)$  and  $y=(0,0.5)$  cm with a 560x400 base grid and 5 levels total (4 refinement levels 2x finer each). The number of levels used in the simulation decreased as the gradients became smoother.

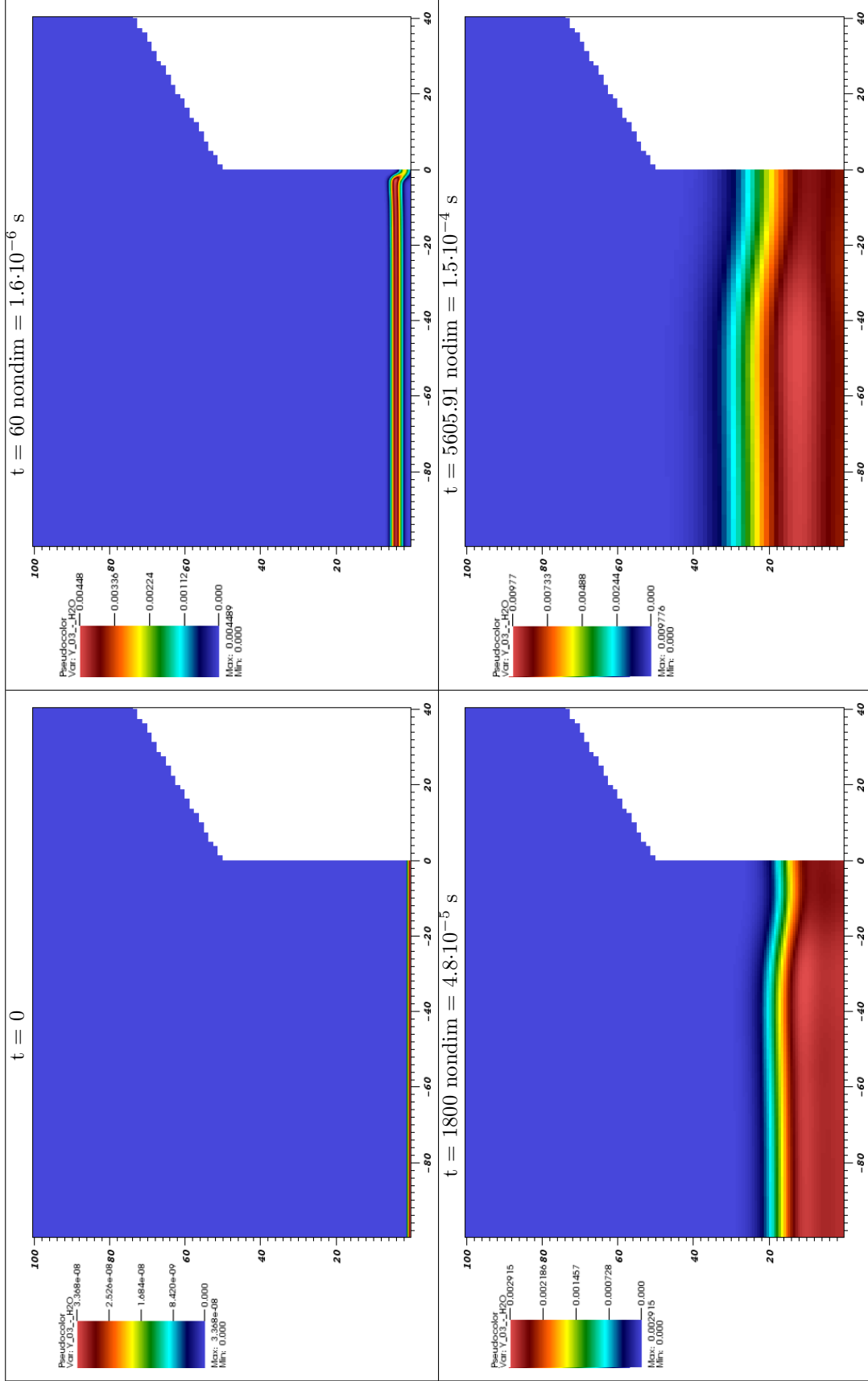


Figure 9.29:  $r = 0.001 \text{ cm}$ : Time-elapsed pseudo-color  $\text{H}_2\text{O}$  mass fraction plots for a spark radius = 0.001 cm with a pressure ratio of 100 with ambient conditions at 10,000 Pa. Simulation was for  $x=(0,1,0.6)$  and  $y=(0,0.5)$  cm with a 560x400 base grid and 5 levels total (4 refinement levels 2x finer each). The number of levels used in the simulation decreased as the gradients became smoother.

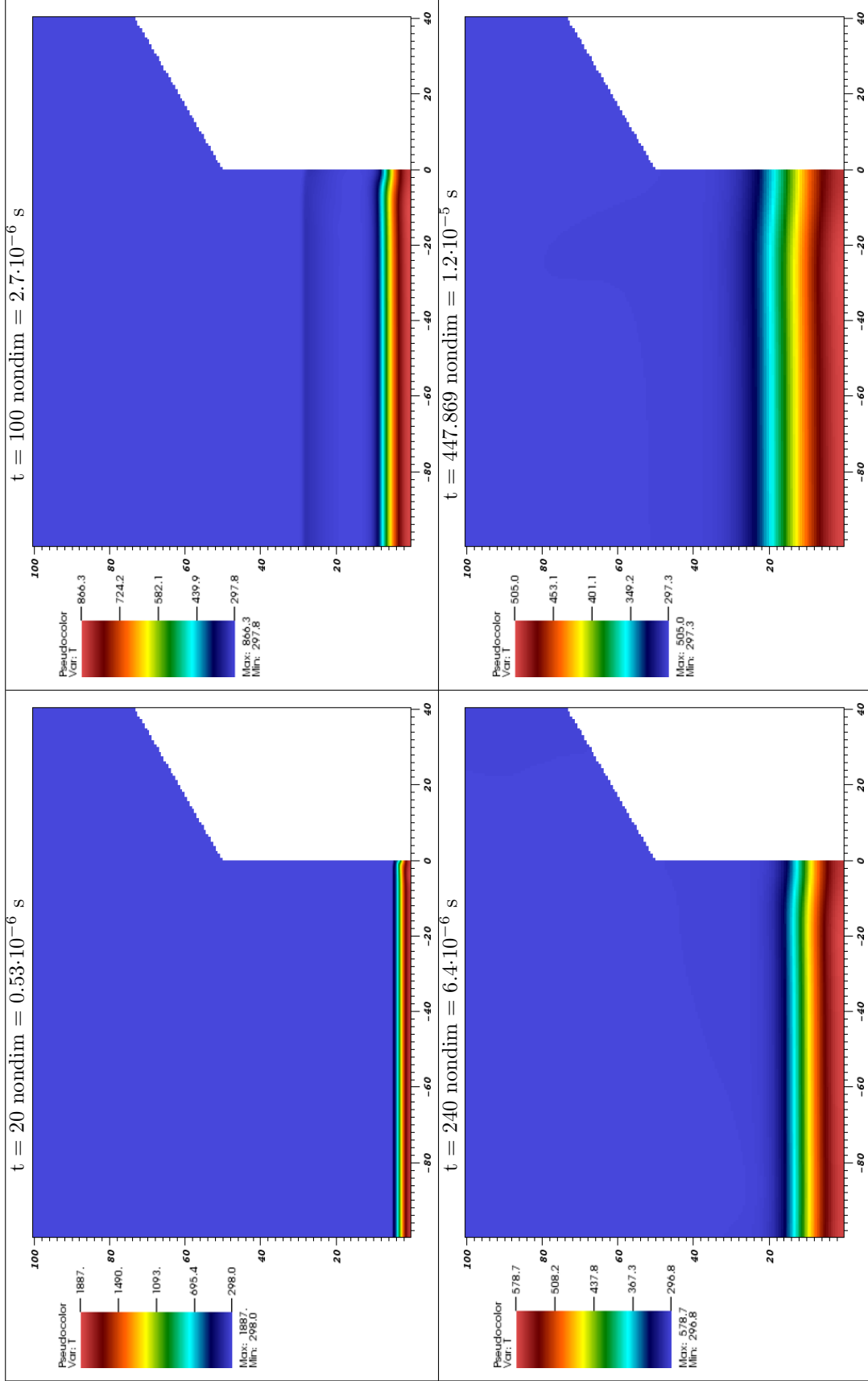


Figure 9.30: Time-elased pseudo-color temperature plots for a spark radius  $= 0.0005$  cm with a pressure ratio of 100 with ambient conditions at 10,000 Pa. Simulation was for  $x=(-0.1,0.6)$  and  $y=(0,0.5)$  cm with a 1120x800 base grid and 5 levels total (4 refinement levels 2x finer each). The number of levels used in the simulation decreased as the gradients became smoother.



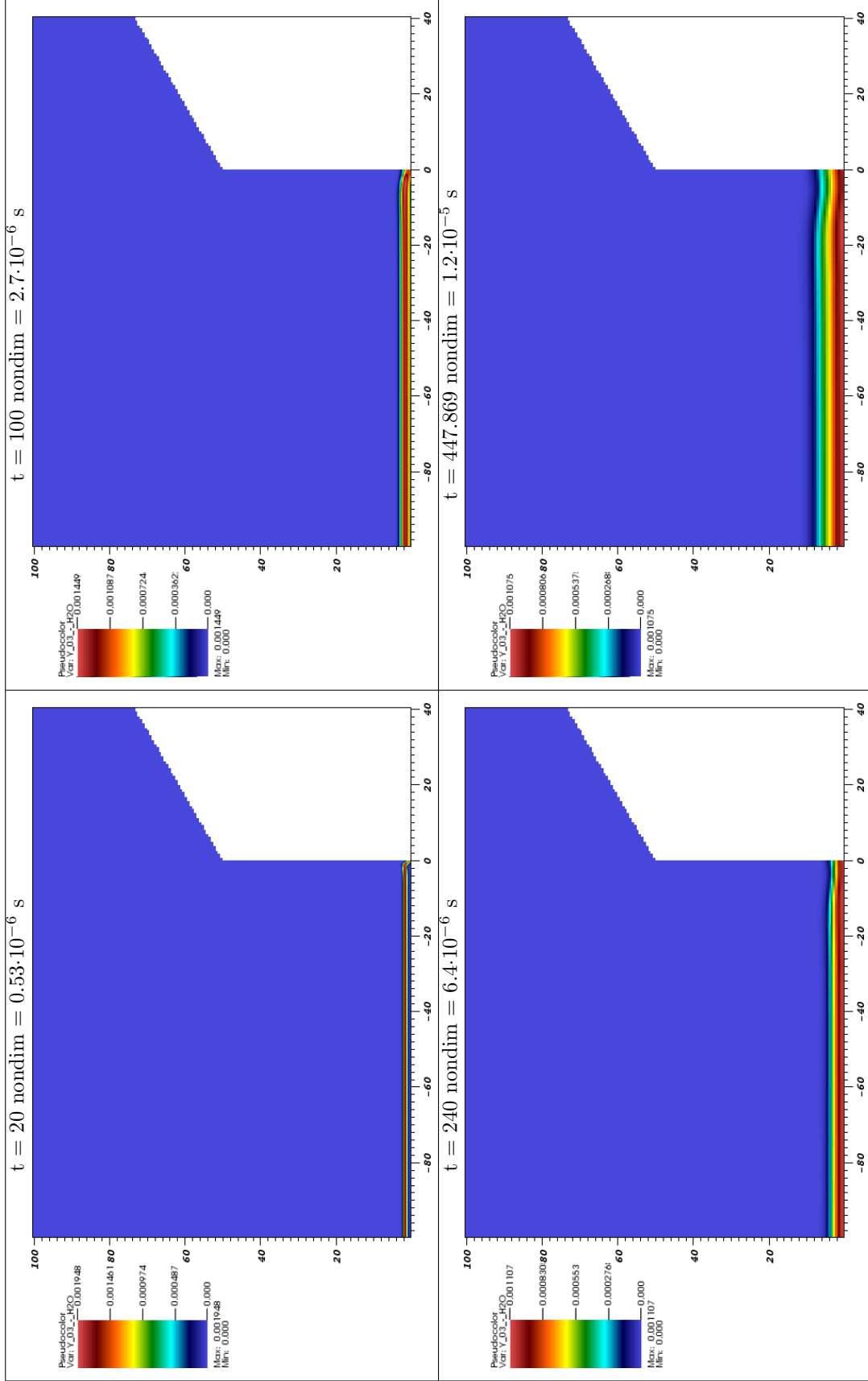


Figure 9.31:  $r = 0.0005$  cm: Time-elapsing pseudo-color  $\text{H}_2\text{O}$  mass fraction plots for a spark radius  $= 0.0005$  cm with a pressure ratio of 100 with ambient conditions at 10,000 Pa. Simulation was for  $x = (-0.1, 0.6)$  and  $y = (0, 0.5)$  cm with a  $1120 \times 800$  base grid and 5 levels total (4 refinement levels 2x finer each). The number of levels used in the simulation decreased as the gradients became smoother.

The results of the 1 atm ambient with 10x pressure ratio case are shown with the time-elapsed temperature in figures 9.32, 9.34, and 9.36 and H<sub>2</sub>O mass fraction in figures 9.33, 9.35, and 9.37. Like the previous set of cases, the first two result in a Go, and the last in a No Go.

The first case is for  $r = 0.02$  cm. In this case a flame is established at a much earlier time than in  $r = 0.002$  cm case with the lower initial pressure and higher pressure ratio. For this case, a flame kernel with a comparably high maximum product mass fraction is observed at a time of approximately  $1 \cdot 10^{-5}$  s. At  $6.4 \cdot 10^{-5}$  s this kernel is pushed into the center by the large scale cylindrical to spherical geometry change generated vorticity. Also at this time, the product mass fraction is still increasing, indicating the chemical reaction is dominating mass diffusion. In the range of timesteps shown, even up to  $1.1 \cdot 10^{-4}$  s, the maximum temperature is still high, being at 1062 K, although it is decreasing. This is due to the fact that the blast wave is weaker due to the pressure ratio being 10x rather than 100x larger initially in the spark. Because the shock is weaker, it travels slower and the temperature decrease due to the trailing expansion is lower and occurs at a slower rate allowing the flame to become established while the fluid is still hot.

For the  $r = 0.01$  cm case, another Go is found, and the fashion at which the flame forms (in regard to the temperature and product mass fraction changes) is similar. The main difference is that now due to the spark being half as thick, the blast wave is weaker than the previous case, in which the kernel was found to be pushed into the vertical center line. In this case, diffusion dominates convection as was also found for all the simulations in figures 9.28-9.31.

For the  $r = 0.005$  cm case, as was found for the 1D axisymmetric solution, a No Go is observed. This no Go is very marginal. At a time of  $8 \cdot 10^{-6}$  s (not shown) the expansion has decreased the maximum temperature from 9169 to 1154 K. Then at a time of  $1.0 \cdot 10^{-4}$  s, the temperature reaches a local minimum of 726 K. Here the temperature begins to increase until a time of  $2.0 \cdot 10^{-4}$  s, at which it has reached 733.8 K, and then at an increasing rate, begins to decrease again. At  $t = 7.5 \cdot 10^{-4}$  s, the temperature has reached 639 K and continues to decrease. The no Go is less marginal in the equivalent 1D simulation. In this 2D simulation, a flame started to form, and then died as it expanded from the confined region between the electrode tips into the larger ambient fluid. The differences in the 1D and 2D simulations could be due to the no-slip BC on the electrode surface which adds diffusion and vorticity to the fluid. Also, a possibility is the effect of numerical diffusion, which is larger in the 2D simulation due to the larger cell sizes which were used. For efficiency, refinement

levels were removed as the gradients of the solution became larger in time.

Overall, for both initial pressures and pressure ratios, the one-dimensional axisymmetric solution predicts the initial conditions at which a No Go or Go is found for a two-dimensional axisymmetric solution. Note that this only applies to the conditions tested for this 15 percent hydrogen mixture. With lower fuel concentrations, larger spark energies (which may critically induce multi-dimensional convection and enhanced mixing) are needed to produce a flame.

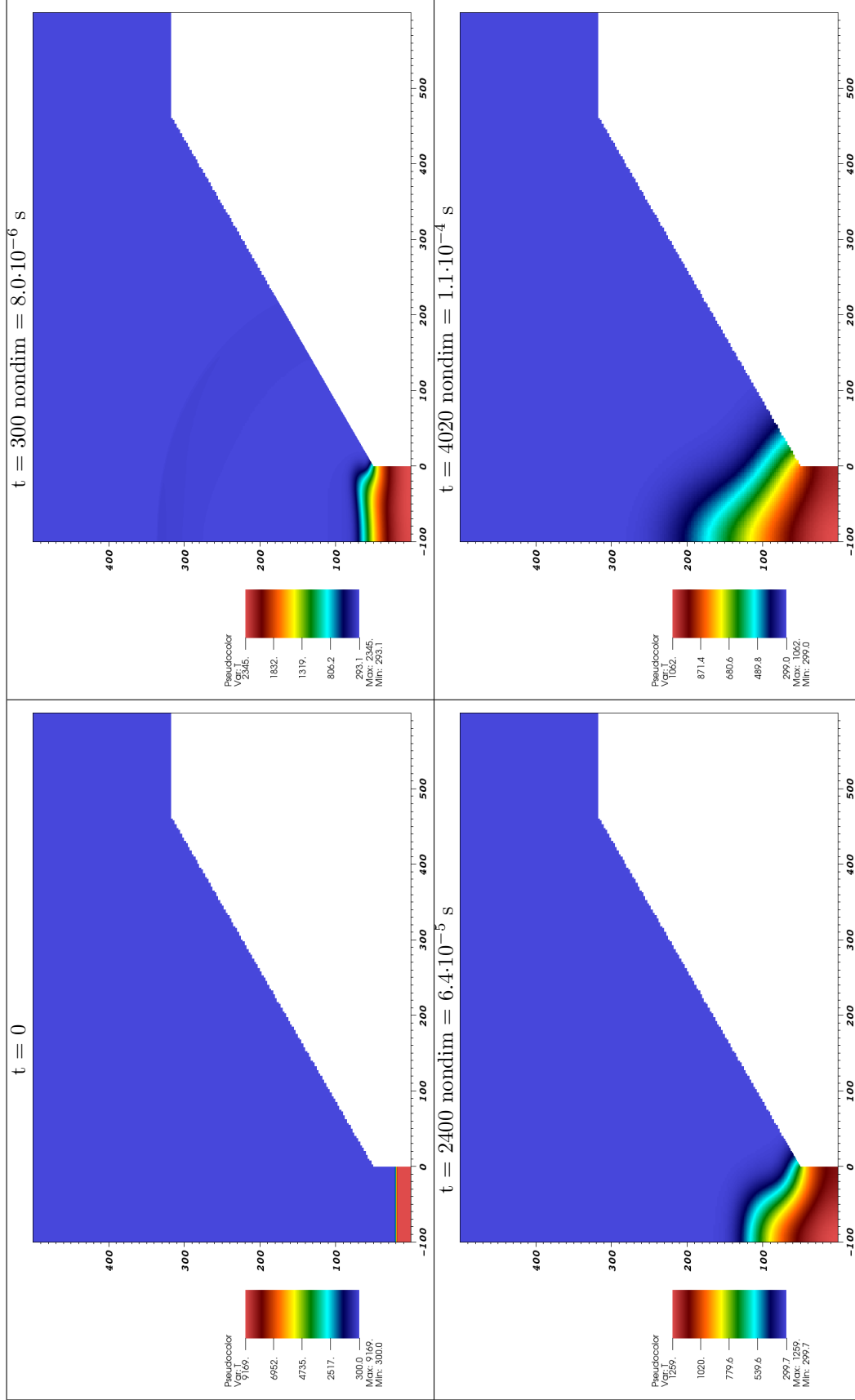


Figure 9.32:  $r = 0.02$  cm: Time-elapsed pseudo-color temperature plots for a spark radius = 0.02 cm with a pressure ratio of 10 with ambient conditions at 100,000 Pa. Simulation was for  $x=(0,1,0.6)$  and  $y=(0,0.5)$  cm with a 280x200 base grid and 4 levels total (3 refinement levels 2x finer each). The number of levels used in the simulation decreased as the gradients became smoother.

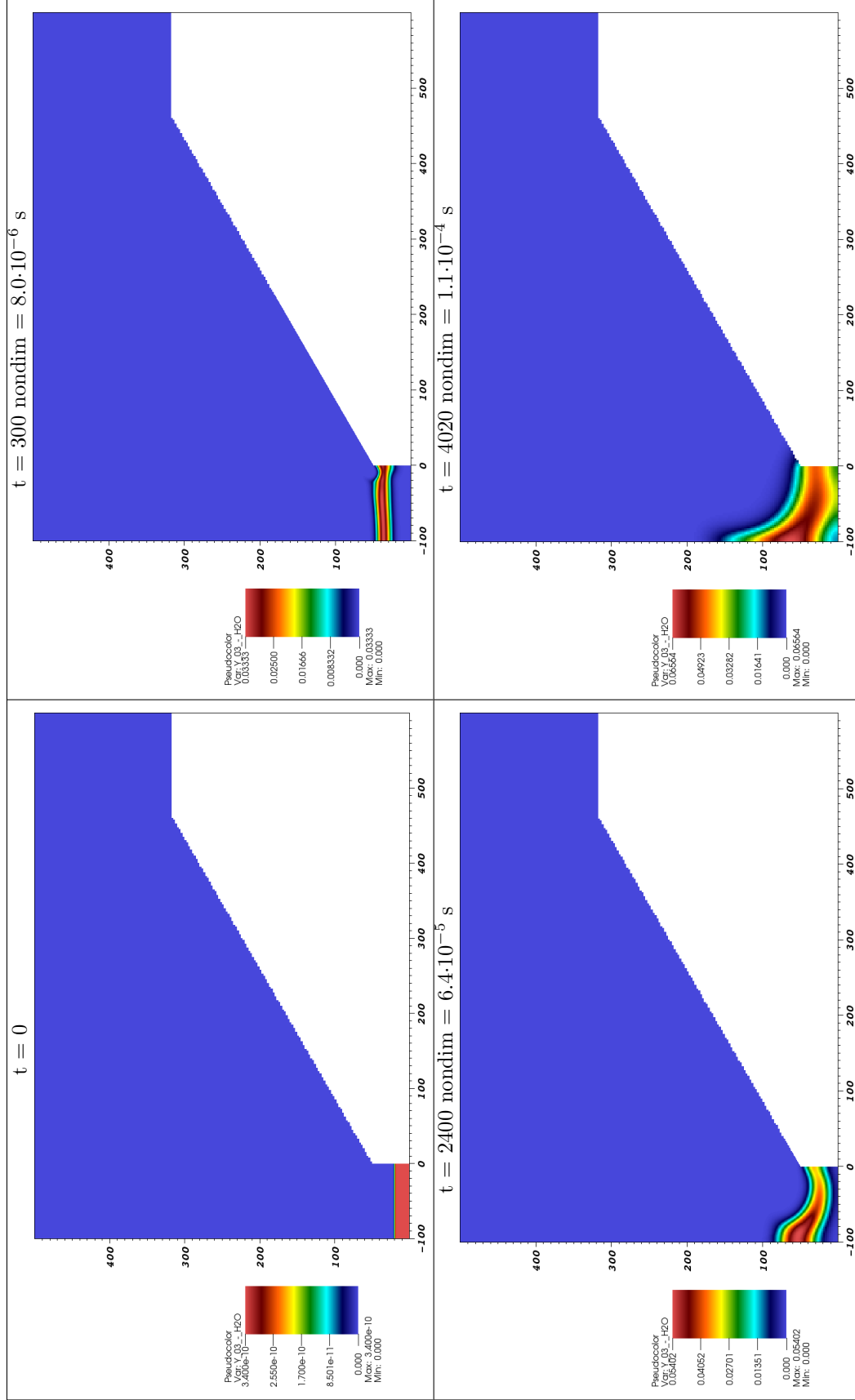


Figure 9.33:  $r = 0.02 \text{ cm}$ : Time-elapsed pseudo-color  $\text{H}_2\text{O}$  mass fraction plots for a spark radius  $= 0.02 \text{ cm}$  with a pressure ratio of 10 with ambient conditions at 100,000 Pa. Simulation was for  $x=(0,0.6)$  and  $y=(0,0.5) \text{ cm}$  with a  $280 \times 200$  base grid and 4 levels total (3 refinement levels 2x finer each). The number of levels used in the simulation decreased as the gradients became smoother.

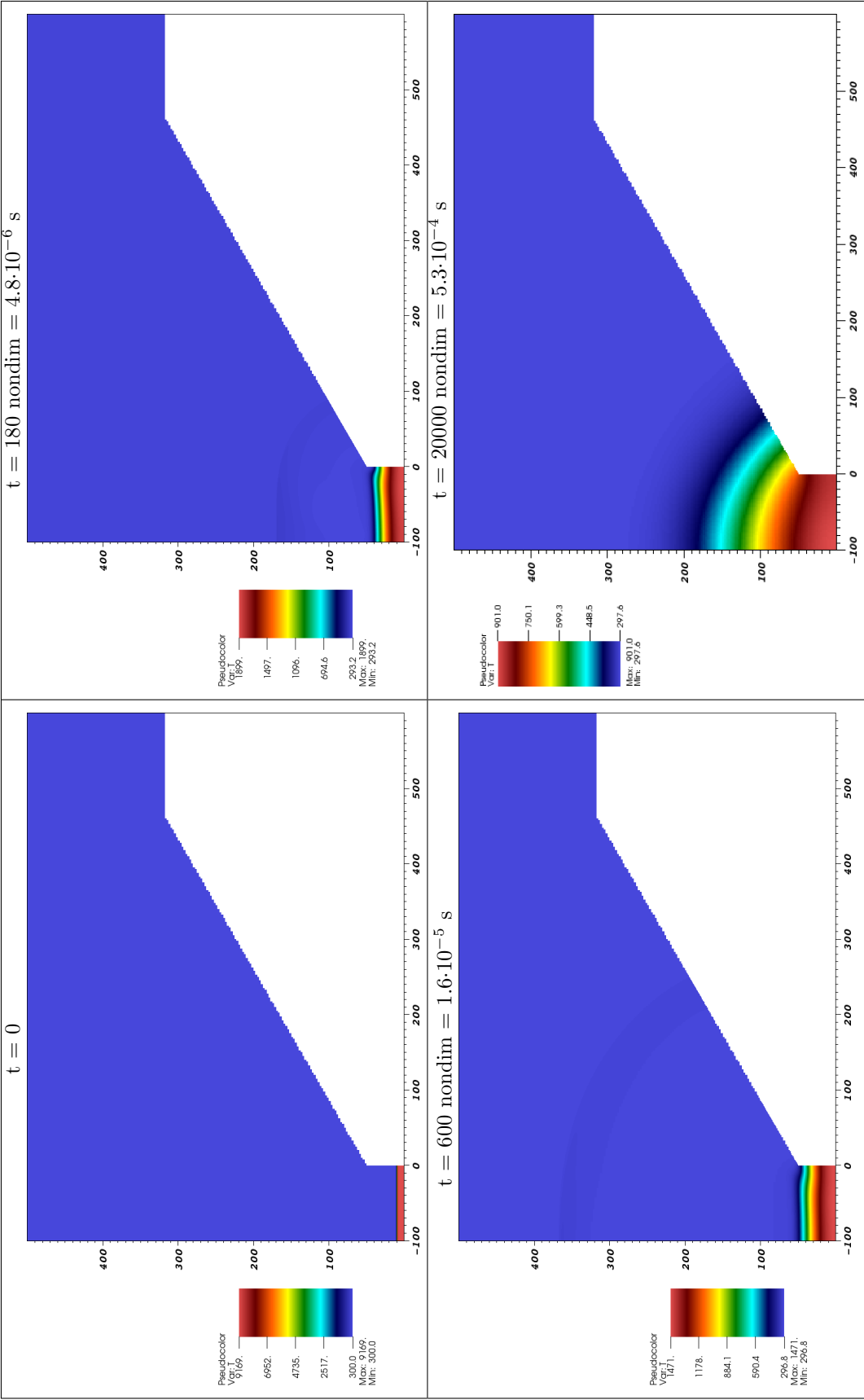


Figure 9.34:  $r = 0.01$  cm: Time-elapsed pseudo-color temperature plots for a spark radius = 0.01 cm with a pressure ratio of 10 with ambient conditions at 100,000 Pa. Simulation was for  $x = (-0.1, 0.6)$  and  $y = (0, 0.5)$  cm with a 280x200 base grid and 5 levels total (4 refinement levels 2x finer each). The number of levels used in the simulation decreased as the gradients became smoother.

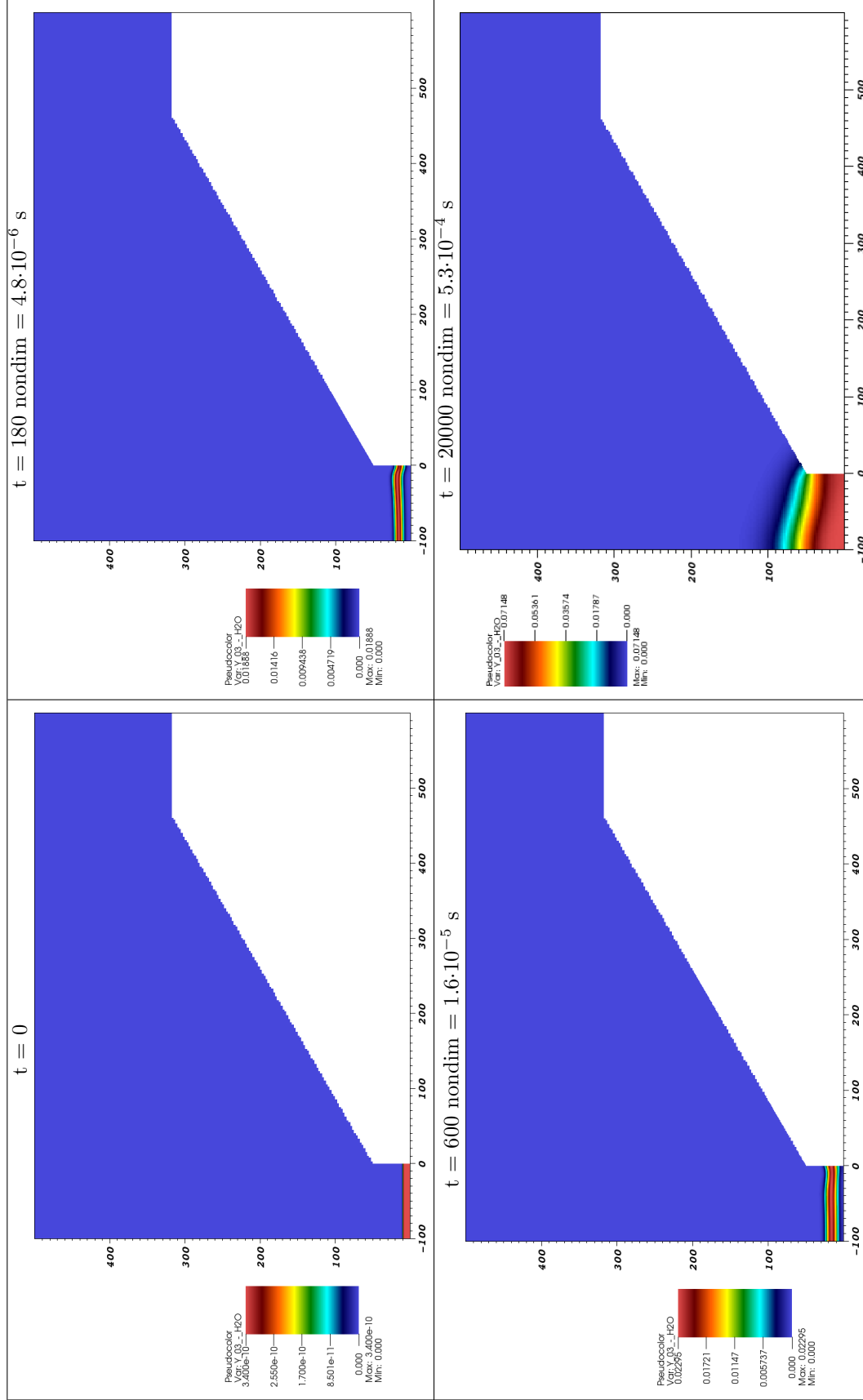


Figure 9.35:  $r = 0.01$  cm: Time-elapsed pseudo-color  $\text{H}_2\text{O}$  mass fraction plots for a spark radius  $= 0.01$  cm with a pressure ratio of 10 with ambient conditions at 100,000 Pa. Simulation was for  $x = (-0.1, 0.6)$  and  $y = (0, 0.5)$  cm with a  $280 \times 200$  base grid and 5 levels total (4 refinement levels  $2 \times$  finer each). The number of levels used in the simulation decreased as the gradients became smoother.

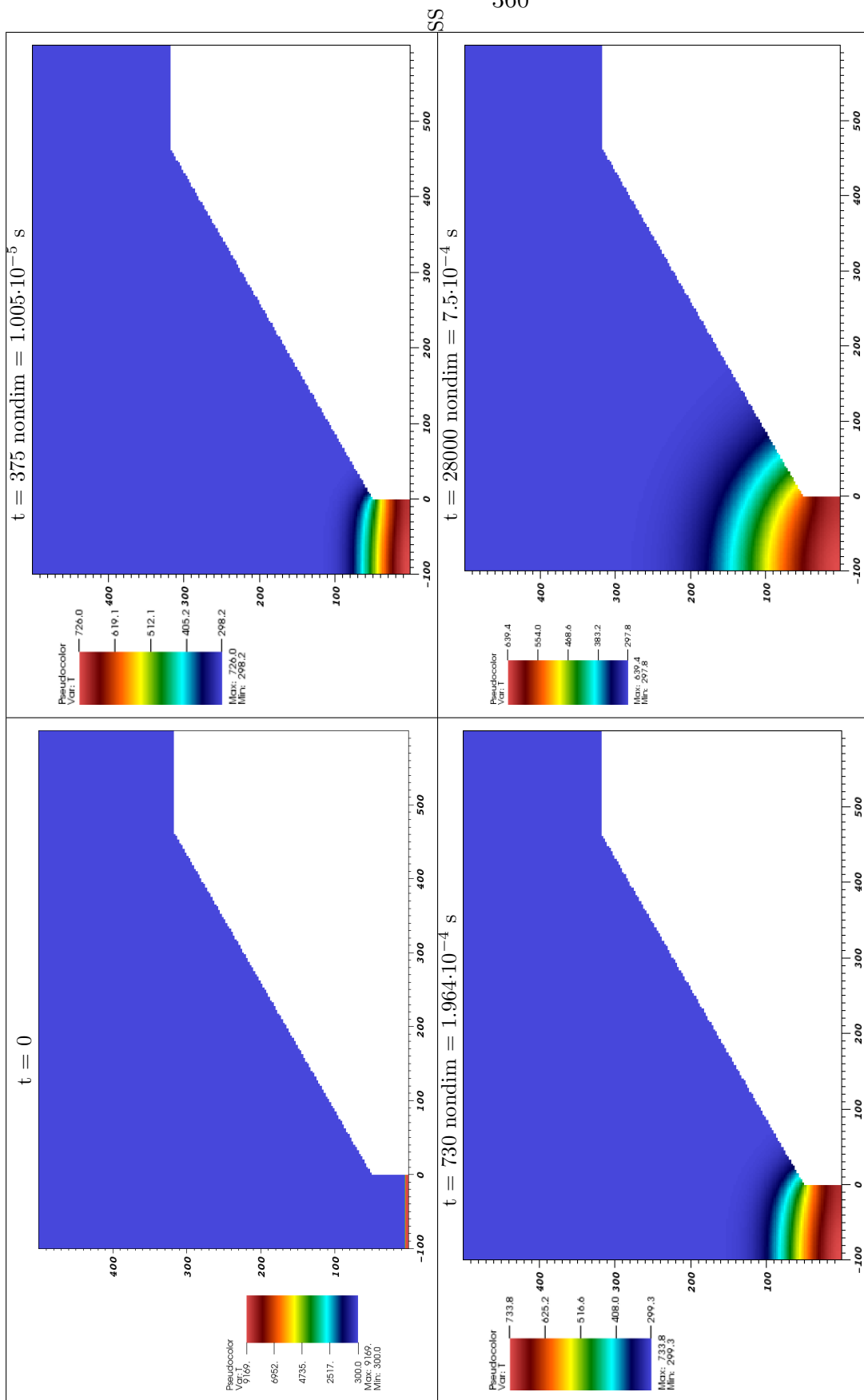


Figure 9.36: Time-elapsd pseudo-color temperature plots for a spark radius  $= 0.005$  cm with a pressure ratio of 10 with ambient conditions at 100,000 Pa. Simulation was for  $x=(-0.1,0.6)$  and  $y=(0,0.5)$  cm with a 280x200 base grid and 5 levels total (4 refinement levels 2x finer each). The number of levels used in the simulation decreased as the gradients became smoother.



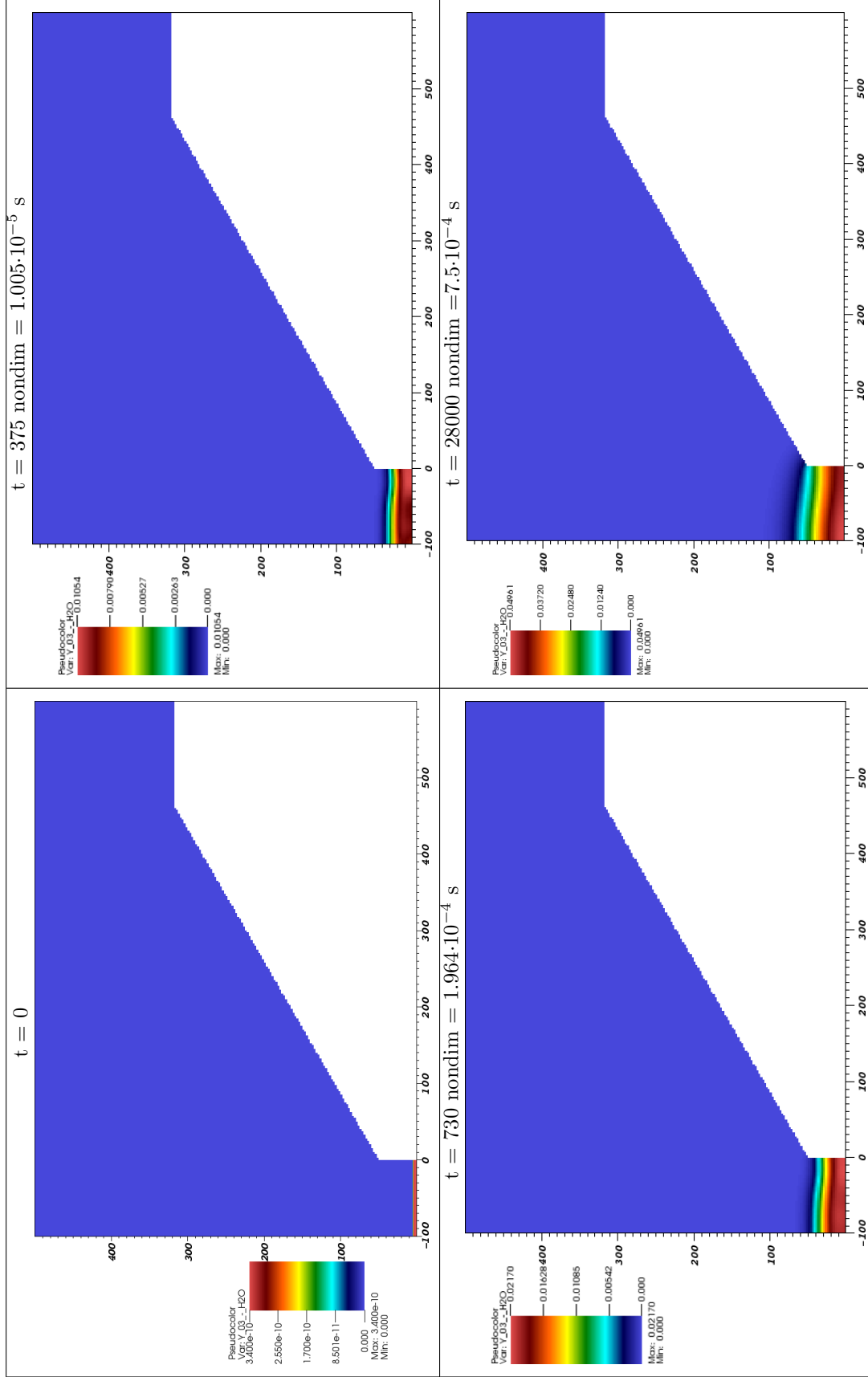


Figure 9.37:  $r = 0.005 \text{ cm}$ : Time-elapsed pseudo-color  $\text{H}_2\text{O}$  mass fraction plots for a spark radius = 0.005 cm with a pressure ratio of 10 with ambient conditions at 100,000 Pa. Simulation was for  $x = (-0.1, 0.6)$  and  $y = (0, 0.5)$  cm with a  $280 \times 200$  base grid and 5 levels total (4 refinement levels 2x finer each). The number of levels used in the simulation decreased as the gradients became smoother.

In the following sections, the “Go” and “no Go” results are compared to that gained from experiment and theory.

### 9.6.3.3 MIE Experimental Comparison

The view of ignition, where the minimum ignition energy (MIE) is considered to be a single threshold value, is the traditional viewpoint in combustion science. However, particularly in the aviation safety industry, a statistical approach to ignition characterization is being used and is more consistent with experimental observations of engineering test data. This statistical variation is most likely due to the chaotic nature of the initial spark. Simulating a probabilistic spark in a DNS framework is not practical and thus a single MIE and spark shape and distribution for each initial condition is considered. In figure 9.38, the historical MIE threshold data of the 1960s

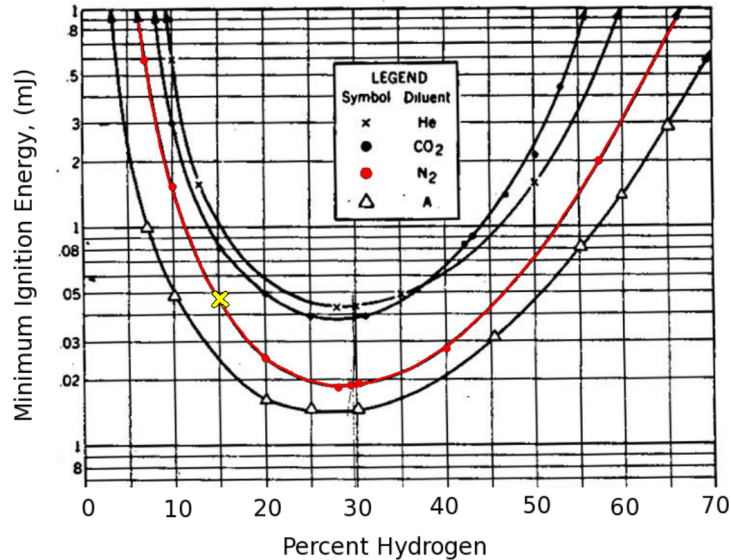


Figure 9.38: Minimum ignition energy results for hydrogen/inert gas mixtures at  $T = 298$  K and  $P = 1$  atm. Reprinted from Lewis and von Elbe (102).

(102) is shown. They tested for MIE values with different inert gas mixtures at atmospheric pressure. As a comparison, for the 15 percent hydrogen-air mixture, they found an energy of approximately 0.045 mJ. This can be compared to the numerically determined results shown in table 9.1 which shows a MIE between 0.00771 and 0.0308 mJ for the 100x pressure ratio case and 0.07202 and 0.3084 mJ for the 10x ratio case. The comparison is summarized in table 9.5. Due to the fact that the MIE depends on the exact initial condition formed by a spark and the geometry of the electrodes

and test vessel, these results do not match at all. Note that a 100x pressure ratio is the more physical representation of an actual spark after the plasma breakdown as is discussed in §9.2.1.

Analytical		Simulation		
$P_u$	$E_{ign}$	$P_u$	$P_{ratio}$	$E_{ign}$
$1.0 \cdot 10^5$ Pa	0.045 mJ	$1.0 \cdot 10^5$ Pa	100	0.00771-0.0308 mJ
		$1.0 \cdot 10^5$ Pa	10	0.07202-0.3084 mJ

Table 9.5: Comparing experimental ignition energy results for MIE to the 1D and 2D simulation values.

#### 9.6.3.4 MIE Analytical Comparison

An analytical model for the ignition energy of a cylindrical spark/kernel is discussed in the thesis of Bane (10). In this model, the flame is considered to be a cylindrical volume of gas ignited by a point spark, and a critical radius is defined under which the cylindrical wave cannot propagate. To determine the critical radius,  $r_{crit}$ , it is assumed that there is a balance between the heat generated by chemical reactions inside the gas volume and the heat lost to the surrounding cold gas through conduction. It is also assumed that the required ignition energy is the energy needed to heat the critical gas volume to the adiabatic flame temperature. These results which were originally for a spherical kernel are derived in Bane (10) for the more realistic case of a cylindrical spark and cylindrical flame. This analytical model greatly simplifies the spark ignition process ignoring mass diffusion, geometry of the electrodes and spark gap, and possible turbulence in the surrounding gas. This results in a critical radius of

$$r_{crit} = 2 \frac{\alpha_u}{s_L}, \quad (9.5)$$

where  $\alpha_u$  is the thermal diffusivity at the unburned condition and  $s_L$  is the laminar flame speed. This  $r_{crit}$  is approximately 20 percent smaller than the critical radius for a spherical kernel, when a 2 mm spark gap is used. Considering the heating of a cylindrical volume, the resulting ignition energy is

$$E_{ign} = \pi r_{crit}^2 L \rho_b c_{P_u} (T_b - T_u), \quad (9.6)$$

where  $b$  stands for burned and  $u$  unburned. In these cases, it was found that the exclusion of mass transport could be leading to overestimated ignition energies because hydrogen has such a high mass diffusivity. Neglecting the effect of preferential

diffusion has generally resulted in larger ignition energies than those observed in the experiments, as was found by Bane for 5 to 7 percent hydrogen mixtures (10).

Shown in table 9.6 are the analytical results for the critical radius and the ignition energy for the 15 percent hydrogen-air mixture. Also shown are the parameters used in this calculation. The laminar flame parameters were found by using the FreeFlame python routine of CANTERA. For consistency, the numerically determined flame speed, temperature, and densities were used rather than experimental values. These values do not differ significantly. For example, the 15 percent data of Lamoureux for hydrogen air at one atm shows an experimental value of 0.291 m/s as compared to our numerically determined value of 0.2235 m/s.

$P_u$	$T_b$	$c_P$	$s_L$	$\alpha$	$\rho_b$	$r_{crit}$	$E_{ign}$
$1 \cdot 10^5$ Pa	1413.9 K	1167.4	0.2235 m/s	$3.3649 \cdot 10^{-5} \text{ m}^2/\text{s}$	0.2323 kg/m <sup>3</sup>	$3.011 \cdot 10^{-4}$ m	$1.723 \cdot 10^{-4}$ J
$1 \cdot 10^4$ Pa	1418.8 K	1167.4	0.5069 m/s	$3.3649 \cdot 10^{-4} \text{ m}^2/\text{s}$	0.2310 kg/m <sup>3</sup>	$1.328 \cdot 10^{-3}$ m	$3.350 \cdot 10^{-4}$ J

Table 9.6: Analytical ignition energy results and flame parameters used in the calculation.

Analytical		Simulation		
$P_u$	$E_{ign}$	$P_u$	$P_{ratio}$	$E_{ign}$
$1.0 \cdot 10^5$ Pa	0.17232 mJ	$1.0 \cdot 10^5$ Pa	10	0.07102-0.3084 mJ
$1.0 \cdot 10^4$ Pa	0.33495 mJ	$1.0 \cdot 10^5$ Pa	100	0.00771-0.0308 mJ
		$1.0 \cdot 10^4$ Pa	100	0.000771-0.00308 mJ

Table 9.7: Comparing analytical ignition energy results for MIE to the 1D and 2D simulation values.

This comparison is summarized in table 9.7. The approximately 1 atm analytical  $E_{ign}$  result of 0.1732 mJ is right in the middle of the bounds (0.07102-0.3084 mJ) found for the 10x pressure ratio case that was simulated in 1D and 2D. Note that when the 100x pressure ratio is used, the MIE found is approximately 10 times smaller. This analytical model does not consider the initial condition of the spark at all. The approximately 0.1 atm analytical  $E_{ign}$  results of 0.3495 mJ are not close at all to the 100x pressure ratio MIE case which is between 0.000771 and 0.00308 mJ or the expected 10x pressure ratio results of 0.00771 and 0.0308 mJ. The analytical model fails to even get the trend of a decreasing MIE correct in the case where initial pressure is decreased. These results highlight the importance of initial spark and ambient conditions when formulating a MIE for an industrial application.

## 9.7 Discussion

For a prediction of spark ignition in combustible gas mixtures, the inclusion of multi-component detailed chemistry and transport was found to have a significant role in the process of ignition. Simplifications of this model where only a two-component model or a one-step reaction, four-component model were used yielded quite different sizes of the spark kernels for the three geometries tested. The choice of electrode geometry was found to influence the development and propagation of a flame, with the flanged electrode case (rather than the smaller radii conical or cylindrical cases) most likely leading to the smallest MIE. This is due to the flange's influence which tends to confine the flame kernel, keeping the temperature high.

In a set of simulations for one particular geometry, the conical electrode, using DNS for a 15 percent hydrogen-air mixture, critical ignition states were simulated and studied for three different initial pressure and pressure ratio conditions. In all simulations an ignition threshold was found. In the 2D and 1D axisymmetric geometries, for the particular 15 percent hydrogen-air mixture selected, the ignition was found to primarily depend on the approximately one-dimensional competition between temperature decrease from a blast wave and heat diffusion, and the temperature increase from chemical reaction. From the simulations, where the particular geometry tested did not have a large effect, parameters of the ambient state and spark state which affect ignition were determined. These are ambient pressure, pressure ratio, and spark energy density.

The MIE values from the DNS results were compared to an approximate analytical result and a historical experimental result. The deficiencies of the analytical model were determined, particularly the lack of mass diffusion and initial pressure ratio and ambient pressure effects. A comparison of experimentally determined MIE values to simulation results was also wildly different, highlighting the need for an exact knowledge of the spark and ambient initial conditions.

At the sacrifice of approximating the initial plasma phase of the spark, improvements on the contemporary results of (152, 120, 63, 64) were made in terms of using a more accurate shock-capturing method and resolution of the viscous and diffusive effects. Using a plasma model that also includes ions in addition to radicals makes the computation more expensive, making the production of resolved results more difficult. Despite this, our results agree with the findings of the most recent, yet less resolved, works of Nakaya *et al.* and Han *et al.* in terms of the finding of evidence that the geometry and initial spark conditions can affect the critical ignition cases.

## Chapter 10

### Conclusions

The study of high-speed reacting flows is important for assessing the threat of accidental ignition. In terms of detonations, most in depth numerical studies have concentrated on the less stable, computationally easier, hydrogen mixtures. However, a large number of industrial applications present a need for also simulating the largely unexplored hydrocarbon mixtures. For these mixtures, unlike others, diffusion can become a key driving force of the detonation. This has created a need for methods which both capture shocks and accurately model diffusive processes. In general, much is also unknown in the field of high-speed turbulent combustion, the realm between slow laminar flames and detonation waves. Numerical methods, such the one developed in this work, attempt to bridge that gap.

#### **10.1 Development and Verification of the 6th-Order Hybrid WENO-CD Method for the Multi-Component Reactive Navier-Stokes Equations**

The hybrid WENO-CD method was extended in the structured adaptive mesh refinement (SAMR) framework of AMROC and verified for 6th-order spatial accuracy for diffusive, reactive flows. Series of “simple” one- and two-dimensional test problems were used to verify the implementation, specifically the high-order accuracy of the diffusion terms. One-dimensional benchmarks included a viscous shock wave, laminar flame, and an unstable detonation. In two space dimensions, a viscous decaying Lamb-Oseen vortex with multiple fixed in space refinement levels was demonstrated. For all of these test, quantitative convergence, in particular 6th-order accuracy for both the viscous/diffusive and convection terms was demonstrated.

Further, “hard” convergence tests were carried out for three nonsteady two-dimensional double Mach reflection (DMR) problems for which many refinement levels in the SAMR framework were utilized. With a highly resolved case as the “exact” solution, low but conclusive converge rates were found when using adaptive levels for test problems with unresolved shock waves.

Using ORNL’s Jaguar and LBNL NERSC’s Carver supercomputers with up to 512 cores, the three tested DMR problems were subsequently simulated with increased complexity of the gas mixture. The first test was for a single component perfect case with constant transport properties. The second test was a two-component, one-step reaction, detonation case with temperature dependent transport. The third case was a multi-component hydrogen-argon mixture with detailed chemistry and transport. In all of these test cases the viscous/diffusive scales were resolved

The present convergence results for the nonreactive and reactive DMR simulations support the case that, with our implementation and detailed simulations, diffusive processes within chemically reacting zones can be resolved. The advances that have allowed this are as follows: First, careful use of a hybrid method, where WENO is activated *only* at strong shock waves (using an approximate Riemann-problem based shock detection), allowed the sixth-order accurate centered difference stencils to be uniformly active on shear layers and surrounding regions. Additionally, away from the shocks, fifth-order accurate prolongation/restriction operators were utilized on the fine/coarse mesh boundaries and overlaps while first-order operators were used near the strong shocks in order to provide stability.

Second, the detailed inclusion of a reliable diffusive stability condition for the explicit RK4 and RK3 integration allowed to take maximum time steps. Third, appropriate nondimensionalization using physically relevant parameters was found to be necessary for the elimination of underflow errors. Finally, a study of mesh refinement indicated that a minimum coverage, at the finest refinement level, was required in the region surrounding the shear layers in order to obtain convergence. This usage of minimum coverage was found to be essential because these simulations benefit substantially not only from high resolution provided by SAMR but also from the efficiency. The results produced using the present implementation, together with advancements in resolving capability and accuracy, demonstrate possible future directions for converged SAMR simulations.

## 10.2 Reduced, Detailed Mechanism Development for the Simulation of a Highly Irregular, Hydrocarbon Detonation

Through the use of the efficient and accurate, hybrid numerical method, novel two-dimensional simulations of irregular hydrocarbon detonations were conducted. The development of a highly accurate, reduced propane-air mechanism also enabled these results. The detailed hydrocarbon mechanism of Blanquart was minimally reduced from 161 species and 1,055 reactions to 22 species and 53 reversible reactions. This reduction is for only one mixture and initial state, in particular the  $\text{C}_3\text{H}_8\text{-5O}_2\text{-9N}_2$  mixture at an initial pressure of 20 kPa and temperature of 298 K.

The reduction was carried by using the steady ZND solution as a reference over the range of 0.8 to 1.4 overdrives, matching the temperature and pressure profiles very closely. Also matched were the induction times and the rate of energy release or the thermicity profiles. In this mechanism, the slow nitrogen chemistry and the formation of hydrocarbons with more than 3 carbon atoms were neglected and found to be negligible.

## 10.3 Resolved Multi-Component Irregular Detonation Double Mach Reflection

With this mechanism, a double Mach reflection direct numerical simulation for a diffusive, multi-component, highly irregular detonation was carried out. With our two highest resolved simulations, all scales, including reactive, viscous, diffusive, and weak shock scales were resolved, except for the strong shocks of the reflected, incident, and mach stem waves which were only marginally resolved. This simulation, with 384-768 cores on LBNL NERSC's Hopper supercomputer was conducted over four differently sized domains, with each twice as large as the previous. For each subsequently simulated domain, on refinement level was removed making the simulation two times coarser. For each domain, a viscous/diffusive and an inviscid model were utilized. By comparing inviscid and viscous results at different resolutions, a qualitative measure of the relative magnitude and influence of the numerical viscosity was determined. Comparisons to the lower-order accurate MUSCL method at the same resolution were also made, with the expected result of its numerical viscosity



dissipating out the many of the small scale shear/mixing layers of the solution.

The fluid dynamics of the detonation DMR were analyzed in detail. Initially the DMR resembled its nonreactive variant, but shortly after reflection, new triple points appeared. Firstly, a triple point in the Mach stem developed from an interaction with the jet from the primary shear layer. This phenomenon did not arise in the previously simulated nonreactive and reactive hydrogen-air detonation DMRs. Then, triple points appeared on the main reflected shock and the reflected shock of the secondary triple point of the DMR. These triple points grew in strength and in instability. Shortly thereafter triple points appeared on the Mach stem of the primary triple point. As the DMR grew in size, it eventually became larger than the induction length of the incident detonation, and in those regions no longer bounded by this length, it gained stability as the chemical reactions approached equilibrium and the triple points disappeared.

Also, at a lower resolution, the transition of the initially steady, slightly overdriven, incident detonation to a transversely unstable, selfpropagating detonation and its interaction with the DMR below it was simulated. This extremely unstable, multiple triple-point interaction of a weaker unstable detonation with a stronger (hotter and higher pressure) detonation is similar to what happens in real irregular detonation mixtures when triple points, which bound under- and overdriven waves, also collide. With these simulation results, a qualitative comparison was made with schlieren images of detonation structures of similar size. The triple-point spacing length-scales were also measured, but found to be significantly smaller than those that are visible through experimental methods.

## 10.4 Validation Through Comparisons to Thin Channel Detonation Experiments

Also, through the use of a large-scale computation utilizing 3072 cores on the Hopper supercomputer, 8 and 16 cm wide, periodic detonation channels were simulated for a propane-air mixture, enabling the first experimental comparison with the largest and most unstable hydrocarbon mixture studied experimentally to date. The results, while being unresolved for the viscous and diffusive terms, agreed with the 45 mm dominant cell width found on soot foils of an experiment with a 15 cm wide, thin channel. The results were also shown to be statistically stationary, while being centered at the equilibrium pressure (speed) of the initial,  $f = 1.008$ , overdriven steady

ZND detonation.

Qualitative agreement was also found for comparisons with schlieren and chemiluminescence images, in particular the formation of keystone structures, pockets of unreacted fuel which lead to localized explosions, and a chaotic range of scales between triple points depending on the overdriven or underdriven state of the local main shock/detonation front.

This large-scale simulation was found to be the coarsest resolution which would support a self-propagating detonation. With even coarser cells, no triple points would appear and the detonation would fail. Also investigated was the influence of smaller channel widths on the resulting unstable detonation solution. The 16 cm wide channel was the smallest channel which had cells comparable to experiment. The 8 cm wide channel could be compared in some periods of its oscillation. However, the enhanced shock reflections with its smaller domain caused it to create a strong explosion which engulfed the whole channel going well over the expected maximum dominant cell size. With simulations in a 1-4 cm wide channel the number of possible triple points was controlled. With a 0.5 cm wide channel, a marginally resolved simulation was conducted, but due small transverse confinement, the results showed no triple points.

## 10.5 Contribution to Detonation and Shock Bifurcations

While nonreactive perfect gas shock bifurcations have been simulated in detail in past works, no attempt has been made for multi-component and reactive flows with detailed chemistry and transport. Bifurcation simulations of a  $\text{H}_2\text{-N}_2\text{O}$  detonation reflecting off a shock tube end wall and its interaction with the wall boundary layer were conducted and analyzed in detail for the first time with detailed chemistry and transport. The complete understanding of, and our ability to simulate shock and detonation bifurcations are important for interpreting measurement and visualizations of shock tube experiments.

These simulations were conducted on GALCIT's Millikan parallel computer, using up to 128 cores. With the enhanced accuracy, efficiency, and confidence of a viscous and diffusive simulation result with the WENO-CD method, the detonating bifurcation was compared in detail to nonreactive shock bifurcations in air and  $\text{N}_2\text{O}$  mixtures. Also compared for the nonreactive mixtures was the influence of isothermal as compared to adiabatic boundary conditions. These simulations were conducted at

multiple resolutions, with the coarsest case running the reflected wave up to a distance of 5 cm from the end wall. With these simulations, conclusive comparisons with experimentally obtained schlieren images were made, with the isothermal wall case showing the best agreement. The adiabatic wall boundary condition had the effect of enlarging the foot height by approximately 50 percent.

Also studied was the effect of resolution on the bifurcation solution. For all non-reactive cases, except the isothermal air case which had a very small foot, the foot length and height all showed a similar trend when plotted as a function of the distance from the end wall. However, the triple point angle  $\beta$  and less so the angle  $\alpha$ , however, were more sensitive and were offset as the resolution was changed. The detonation case also showed a high sensitivity to resolution, but more so due to the fact that the initially steady detonation went transversely unstable upon reflection from the end wall. This was due to the affect of the interaction of the shock waves with the now much hotter, unreacted fuel which has a much shorter induction time than the incident detonation. These instabilities are very similar to those that occurred in the double Mach reflection simulation with the propane mixture. In the bifurcation, however, the instabilities die out as soon as the induction length of the incident detonation is reached.

The shock and detonation bifurcations were also compared to calculations from Mark's original theory and nonreactive trends found in experiment and in the computations of Weber et al. Considering the simplicity of the theory, agreement with the nonreactive simulations was good, and with equilibrium shocks assumed for the detonations case, agreement was also good. The previously numerically and experimentally found trend, a linearly growing foot height, was also found by making polynomial fits with the resolved and marginally resolved simulations which were run no farther than 1 cm from the end wall. The unresolved large-scale simulations showed a slight steeping above linear.

With the reactive calculations and comparisons, general trends for detonation end-wall reflection-produced bifurcations were found. The pressure traces will be extremely chaotic up to the induction length of the incident wave. At farther distances as compared to nonreactive slower speed variants, the influence of shocklets in terms of strength and extend will be larger. Also, the geometry will differ in that foot angle will be much larger and the main shear layer will be tilted upward rather than downward.

## 10.6 Contribution to Spark Ignition

Two-dimensional, axisymmetric spark ignition simulations of hydrogen-air with the resolution of solid boundary layers were also conducted. At the sacrifice of approximating the initial plasma phase of the spark, improvements on the contemporary results were made in the accuracy and resolution of the reactive and fluid dynamical processes.

Through the use of high-energy computations with three different geometries, the finding that the electrode geometry can influence the development of the flame kernel was confirmed. Three geometries were tested, small cylindrical electrodes, large conical electrodes, and even larger flanged electrodes. The spark energy and spark gap were the same in all three cases. It was found for the nonreactive and reactive simulations that the smaller the confinement region, the longer the flame kernel will remain hot enough to accelerate chemical reactions. Therefore, the flanged electrodes were determined to most likely produce the smallest minimum ignition energies (MIE).

Also compared for these high energy test cases was the effect of the complexity in the numerical model. Three models of increasing complexity were tested: a two-component one-step perfect gas model, a four-component perfect gas one-step model with simplified chemistry and detailed transport, and a multi-component ideal gas multi-step model with detailed chemistry and transport. While the general shapes of the kernels were all the same, the sizes and temperatures of the kernels differed greatly, showing the need for multi-component detailed chemistry and transport models.

Using the multicomponent model, an investigation of the “Go” and “No Go” ignition process at low critical ignition energies was conducted. Using the same spark gap in all tests, the parameters of initial pressure, spark pressure ratio, and spark radius were varied. This led to the finding that the critical ignition or nonignition state depends on the energy density, initial pressure, and the pressure ratio of the spark. These results supported the importance of using a detailed mechanism, modeling the geometry, and capturing the exact initial spark conditions for simulations of MIE tests.

A comparison of experimentally and theoretically determined MIE values to our simulation results was also made. This highlighted the deficiency of the current theory in terms of neglecting the initial pressure and the pressure in the spark state. The need for an exact knowledge of the spark and ambient initial conditions was also confirmed with the experimental comparison, which also did not agree. This disagreement was

most likely due to our approximation of the initial spark state, yet, it brings to our attention that sparks of the same energy but with different properties overall could result in different ignition/nonignition results.

## 10.7 Future Work and Outlook

The WENO-CD numerical method/SAMR framework combination with improvements in both parallel efficiency and numerical accuracy has enabled first of its kind, resolved, detailed, diffusive irregular detonation DMR simulations. Even more efficient strategies would enable fully resolved two-dimensional irregular detonation channel flow simulations and a marginally resolved three-dimensional equivalent. This would require the use of tens to hundreds of thousands of cores on a supercomputer, a feat which has yet to be implemented for a sixth-order accurate hybrid method and SAMR together. Another possibility is a “brute” force uniform grid computation with hundreds of thousands of cores, however, SAMR and AMR in general is still needed as not all researchers have access to that many cores, and even with that access one would like to run more than one configuration. This will be possible with future development of AMR for high-order methods. The same could also be said for resolving shock and detonation bifurcations at the large scales encountered shock-tube experiments and for using larger chemistry models which model both the plasma stage and fluid dynamics in spark ignition simulations. More efficiency would also enable one to simulate the largely unexplored detonation to deflagation process for the expensive hydrocarbon mixtures.

SAMR with higher-order, stable boundary conditions, possibly using upwinded stencils, is needed to model the isothermal wall using the WENO-CD method. First-order boundary conditions are very efficient and robust with the usual second-order accurate SAMR methods, however, with larger stencils, more stability and accuracy is needed.

Another improvement in accuracy and efficiency would be a hybrid WENO-like prolongation and restriction routine. By measuring the smoothness/gradient of the solution and finding shocks in a similar way that the WENO method does, the option of using efficient low-order stencils or more expensive highly stable upwinded, or maximally accurate (but prone to instability) centered stencils would enhance the efficiency, accuracy, and stability of a high-order method in a SAMR framework.

The ultimate future goal is through the use of DNS, the development of subgrid scale models for high-speed turbulent combustion, a clear need for simulating det-

onation and high-speed deflagration problems at scales encountered in engineering applications. The key challenge, as in low speed flows, is in the statistical characterization of a turbulent flow field. This would enable quantitative engineering predictions of macroscopic detonation behavior.

## Appendix A

# Similarity Solution of the One-Dimensional Euler equations

$$(v - \xi) \frac{d\rho}{d\xi} + \rho \frac{d(v)}{d\xi} = 0, \quad (\text{A.1})$$

$$(v - \xi) \frac{dv}{d\xi} = -\frac{1}{\rho} \frac{dp}{d\xi}. \quad (\text{A.2})$$

These two equations can be reduced to one integral equation by considering the entropy,  $s$ , and the speed of sound,  $c$ . For this derivation, it must be assumed that the entropy is conserved or constant. Therefore, there cannot be any discontinuities such as shock waves. This assumption,

$$(v - \xi) \frac{ds}{d\xi} = 0, \quad (\text{A.3})$$

forces  $\frac{ds}{d\xi}$  to be zero, and thus  $s$  is constant. Therefore, the general definition for the speed of sound,

$$c^2 = \left( \frac{\partial p}{\partial \rho} \right)_s, \quad (\text{A.4})$$

reduces to

$$c^2 = \frac{dp}{d\rho} = \frac{\frac{dp}{d\xi}}{\frac{d\rho}{d\xi}}. \quad (\text{A.5})$$

Now, by eliminating the pressure derivative with the simplified definition for  $c^2$ , the

continuity and momentum equations reduce to

$$(v - \xi)\rho' + \rho v' = 0, \quad (\text{A.6})$$

$$(v - \xi)v' = -\frac{c^2 \rho'}{\rho}, \quad (\text{A.7})$$

where the ' denotes differentiation with respect to  $\xi$ . From this hyperbolic system of equations,  $p'$  and  $v'$  can be eliminated, thus obtaining,

$$(v - \xi)^2 = c^2, \quad (\text{A.8})$$

$$x/t = v \pm c. \quad (\text{A.9})$$

Using this result in the continuity equation, the integral relation for  $v$  as a function of the thermodynamic state of the system is obtained

$$c\rho' = \rho v', \quad (\text{A.10})$$

$$v(\rho) = \pm \int \frac{cd\rho}{\rho} = \pm \int \frac{dp}{\rho c}. \quad (\text{A.11})$$

The significance of this result is that the any variable representing a quality of the flow  $(v, p, \rho, c)$ , can be expressed as a function of one of the others. For example, valid options are  $\{p(v), \rho(v), c(v)\}$  or  $\{v(\rho), p(\rho), c(\rho)\}$ .

Now, by selecting  $\rho$  as the independent parameter,  $\frac{\partial x}{\partial t}$  at constant  $v$ , is obtained by solving the momentum equation.

$$\frac{\frac{\partial v}{\partial x}}{\frac{\partial v}{\partial t}} = \left( \frac{\partial x}{\partial t} \right)_v = v + \frac{1}{\rho} \frac{dp}{dv}, \quad (\text{A.12})$$

or equivalently,

$$\left( \frac{\partial x}{\partial t} \right)_v = v + \pm c(v). \quad (\text{A.13})$$

This result is then integrated to yield a solution of the form

$$x = t[v \pm c(v)] + f(v), \quad (\text{A.14})$$

where  $f(v)$  is an arbitrary function. A more useful form is derived by inverting the



function  $f(v)$  to obtain

$$v = F[x - t(v \pm c(v))], \quad (A.15)$$

where  $F(v)$  is another function which is related to the arbitrary, smooth waveform of the initial conditions. With a thermodynamic relation between  $c$  and  $\rho$  defined, a nonlinear equation solver is easily used to obtain a solution. See (94) §101.

Assuming a polytropic gas, the thermodynamic relation required is

$$\rho = \rho_0 (c/c_0)^{2/(\gamma-1)}, \quad (A.16)$$

where  $\gamma$  is the specific heat ratio and the subscript, 0, denotes a reference state. Using this in the integral relation A.11,

$$v = \pm \int \frac{cd\rho}{\rho} = \frac{2}{\gamma-1} \int dc = \frac{2}{\gamma-1} (c - c_0), \quad (A.17)$$

$c$  is expressed as a function of  $v$ ,

$$c = c_0 \pm \frac{1}{2}(\gamma-1)v. \quad (A.18)$$

This is then used in A.15, where now

$$v = F \left\{ x - t[\pm c_0 + (\frac{1}{2}\gamma + 1)v] \right\}. \quad (A.19)$$

Therefore, given any continuous function,  $F$ , and a set of reference conditions,  $(c_0, p_0, \rho_0)$ , this nonlinear equation is solved for  $v$ , at each  $x$  and  $t$ . With the velocity now known, the pressure and density are found with the following  $p = p(v)$  and  $\rho = \rho(v)$  relations,

$$\rho = \rho_0 \left( 1 \pm \frac{1}{2}(\gamma-1)v/c_0 \right)^{2/(\gamma-1)}, \quad (A.20)$$

$$p = p_0 \left( 1 \pm \frac{1}{2}(\gamma-1)v/c_0 \right)^{2\gamma/(\gamma-1)}. \quad (A.21)$$

This similarity solution is not valid for all time, as compression waves tend to steepen the profile to the point where discontinuities appear. The discontinuity known as a shock wave forms when the derivatives of the velocity, pressure, and density become infinite.

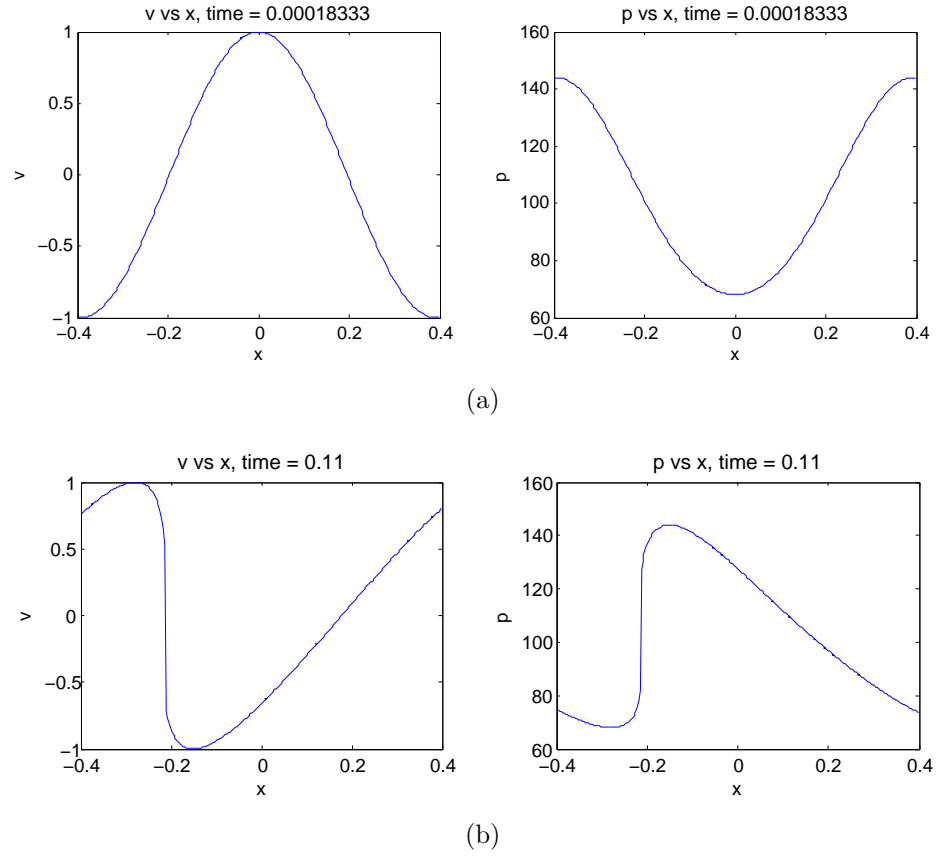


Figure A.1: a) Velocity and pressure for the similarity solution at a time,  $t = 0.0021$  seconds. b) Velocity and pressure for the similarity solution at a time,  $t = 0.11$  seconds.

This is realized when an inflection point is encountered, which occurs when

$$\left(\frac{\partial x}{\partial v}\right)_t = 0, \quad (\text{A.22})$$

$$\left(\frac{\partial^2 x}{\partial v^2}\right)_t = 0. \quad (\text{A.23})$$

For polytropic gases, these equations are satisfied when

$$t = -2f'(0)/(\gamma + 1), \quad (\text{A.24})$$

where  $f'(0)$  is found from the function  $f(v)$  appearing in equation A.14. As an example, consider the following function  $F = F(v)$ ,

$$F(w) = \cos(8w), \quad (\text{A.25})$$

$$w = x - t[\pm c_0 + (\frac{1}{2}\gamma + 1)v], \quad (\text{A.26})$$

$$v = F(w), \quad (\text{A.27})$$

where the  $+$  in the  $\pm$  of equation A.15 has been taken for a left-going wave. This solution at a time of 0.00018333 seconds is shown in figure A.1(a). In this example,  $p_0 = 100$ ,  $\rho_0 = 10$ ,  $\gamma = 1.4$ , and  $a1 = \sqrt{(\frac{\gamma p_0}{\rho_0})}$ . Thus, with  $f(v) = F^{-1}$ ,

$$f(v) = \frac{1}{8} \arccos(v), t_{\text{breaking}} = -2f'(0)/(\gamma + 1), f'(0) = \frac{-1}{8}, t = 0.1041666667 \quad (\text{A.28})$$

At a time of 0.11 s  $< t_{\text{breaking}}$ , the discontinuity is present as shown in figure A.1(b).

# Appendix B

## Shock Reflection Theory

In this appendix previous research literature on shock and detonation reflections are described. Using theories developed from these Mach reflection and reactive Mach reflection (detonation triple point) theories are developed. In the following appendix algorithms that implement these theories are tested and described.

### B.1 Shock Reflection Background Research

Ben-Dor and Glass (18) gives computational and experimental results for the perfect, and real nitrogen Mach reflections. The real gas model is described as being in dissociative equilibrium. The results shown in appendix C using equilibrium shocks in CANTERA (dissociative and internal degrees of freedom (translational, rotational, and vibrational)) match Ben-Dor's computational results. The frozen result are noticeably different.

Ben-Dor's book (16) shows additional and repeated nitrogen plots as in (18) for the real and perfect gas. Note that he has mislabeled almost half of his graphs (particularly pages 70-90), labeling the perfect as imperfect (real) and the imperfect as perfect. The first group of graphs is incorrect and the later group is correct. Their 1979 paper is correct (18). The discussion in this book about the qualitative differences of the perfect and real cases in some sections is based on this mislabeling and is not correct. Ben-Dor also gives a discussion and estimates for relaxation length scales for real gas effects. This book was written before any Navier-Stokes real gas simulations we conducted.

Ben-Dor (15) also gives nice presentation of the three-shock theory and results for N<sub>2</sub> at 15 torr. He compares these results to Takayama's experimental results for yet another unnamed gas. Also in these document he shows how to find corrections

by adding in the effects of the boundary layer. He also mentions vibrational and relaxation time scales.

In the paper of Hornung *et al.* (72) three shock theory with dissociative relaxation is modeled. Also, in Hornung and Talyor (74) it is demonstrated experimentally that the influence of viscosity on the transition condition in pseudosteady flow as predicted is very significant. A mechanism is proposed for the usual persistence of regular reflection beyond the sonic condition.

Burtschell *et al.* (26) investigated regular and Mach reflections in steady nonequilibrium hypersonic air flows at Mach 7,  $T=773$  K, and  $P = 6.5$  kPa. The computations were performed using a multi-block MUSCL-TVD finite-volume scheme. The comparison with and without thermochemical effects revealed a strong dependence of the transition angles, of the height and location of the Mach stem on the physical modeling of the gas flow.

Hornung (71) used the reactive Euler equations to discuss the gradients across curved reactive shock waves. Using the normal and parallel derivatives across the shock the gradients and substantial derivatives are found to be proportional to the rate of removal of enthalpy by reactions and the local shock curvature.

Meltzer *et al.* (118) shows work analogous to the nonreacting simulations of Mach reflections, experimental and analytical transitions and triple point angles for RR and MR were determined for the stable  $H_2-O_2$  detonation. The two and three shock theories were used and found to have similar properties of the nondetonating real gas cases of previous researchers. Still though, computations and experiments quantitatively differ.

Sanderson *et al.* (139) presents a dimensionless framework for real gas effects on normal, oblique and interacting shock waves. They consider dissociation reactions and vibrational equilibrium. They develop a set of nondimensional parameters, particularly a reaction rate parameter that relates the chemical and fluid time scales. Oblique shock jump conditions are presented for all of the dimensionless parameters.

### B.1.1 Relaxation Effects Relevant to Detonations

Relaxation effects are processes that can have a large effect on the dynamics of shock waves. (79), (27), (28), (37) and (81) are contemporary examples of how vibrational relaxation is computationally modeled in hypersonics. Clark (31) and Williamrich and Treanor (163) are past reviews of real gas effects and vibrational relaxation.

(30, 14, 150) are some older references which looked the effect that vibrational relaxation may have on detonations. Belles and Lauver(14) concluded that existing data exhibit little or no effect of slow vibrational relaxation. Calculations were presented to show that the greatest possible effect of slow  $O_2$  relaxation would, in fact, be a small one. The calculations were carried out by making the assumption that all the activation energy of the slow chain-branching step must be supplied by vibrational energy of  $O_2$ . Their data covered different compositions and temperatures and included observations in  $H_2$ -air,  $H_2$ - $O_2$ -argon, and  $H_2$ - $O_2$  mixtures. They did not look at  $N_2$ . Chesick and Kistiakowsky (30) has similar conclusions for  $H_2$ - $O_2$  detonations, that are based on comparing the ZND theory to experimental results. Soloukhin (150) has similar views on  $O_2$  and shows graphically how vibrational relaxation changes the temperature behind the compression wave. Belles (14) states that at 1500 K, for  $H_2$ - $O_2$ -air, the induction times at 6 and 10 times longer than the vibrational relaxation times in 5 and 20 percent mixtures mainly due to the presence of  $H_2$  and  $O_2$ .

In a contemporary set of examples by Lu and Fan, (110), (108), and (109) modeled for a pulse detonation engine the chemical reaction for a stoichiometric  $H_2/O_2/N_2$  flow by a simple two-step reaction involving five species:  $H_2$ ,  $O_2$ ,  $N_2$ ,  $H_2O$  and  $OH$ . The model consisted of a 2D unsteady and steady detonation hitting a wedge. The code that was used included a two-temperature model for vibrational nonequilibrium, but they found this effect to be negligibly small.

## B.2 Steady Reflection

When a *steady compressible flow* impinges on a wedge, multiple flow configurations are possible, depending on the initial Mach number  $M_0$ , and the wedge deflection angle  $\theta_w$ . For subsonic flow,  $M_0 < 1$ , no shocks can exist and the flow deflection will take place with a continuous turning, as in figure B.1(a). For supersonic flow,  $M_0 > 1$ , two cases are possible, an attached straight shock or a curved detached shock as in figure B.1(b) and B.1(c). An attached shock is approximately straight far from the tip of the wedge and the detached shock is curved. The fluid dynamics of the steady straight shock are governed by the oblique shock relations. When the wedge angle is less than the detachment angle (which is a function of  $M_0$  and the initial thermodynamic state), two attached shock configurations are possible. The strong shock at a large angle and the weak shock at a small angle. The strong and weak post shock states are respectively subsonic and supersonic. In an actual flow only one of

these can occur, the one which satisfies the boundary conditions, or if both are valid the weak wave will occur.

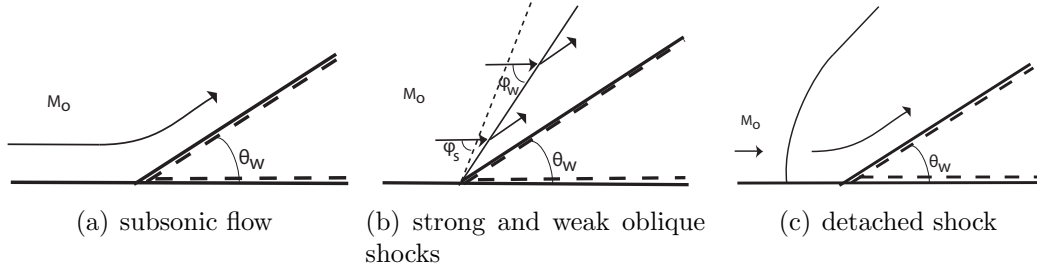


Figure B.1: Possible steady wedge flows

### B.3 Unsteady Reflection

Consider the flow depicted in figure B.2(a). Here a planar incident shock impinges on a sharp wedge. As a result of the new boundary condition experienced by the flow, a reflected wave appears and follows the incident wave up the wedge, as shown for one possible solution in figure B.2(b). Now to analyze this flow, the reference frame which is steady relative to the reflection point is used. In this frame, where the incident and reflected shocks meet and travel up the wedge, the flow is deemed pseudo-steady and the oblique shock relations can be used. This described flow configuration, regular reflection (RR) in figure B.2(b), is possible when the Mach number (relative to the reflection point frame of reference) behind the reflected shock wave is greater than one. If the post reflected shock Mach number is less than one, an irregular reflection (IR) is realized. Physically, the subsonic flow interacts with the reflection point, causing the MR or vNR type configuration to emerge.

Similar to the steady case, in an unsteady flow there are two basic types of shock reflection, regular and irregular reflection (RR and IR). And again there are two basic ways for flow deflection, through an attached bow shock or a detached bow shock. However, unlike the steady case, for unsteady flows, the complexities and the different variants of MRs are more numerous. One such variant, a single Mach reflection (SMR), with an attached bow shock is shown in figure B.3(a).

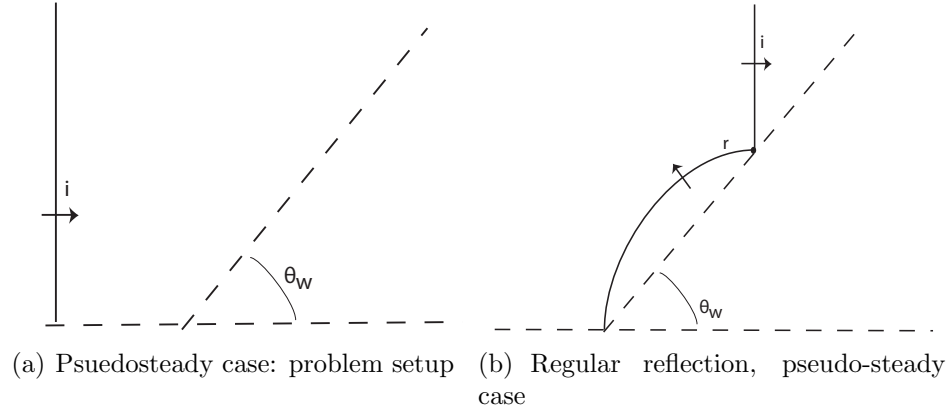


Figure B.2: Unsteady reflection

### B.3.1 Regular Reflection

The analysis of regular reflection is carried out in the stationary frame relative to the reflection point, where the incident shock  $i$ , and the reflected shock  $r$  meet, as labeled in figure B.2(b). The boundary condition is that the net deflection of  $i$  and  $r$  (in the reflection point frame moving up the wedge) be zero, such the flow behind the wedge is parallel the wedge surface.

The above problem thus has 9 equations (B.16-B.24) and 13 unknowns. The solution is found by specifying the initial pressure,  $P_0$ , and temperature,  $T_0$ , and by the geometrical relations below for the incident shock wave and frame of reference

$$\phi_1 = 90^\circ - \theta_w, \quad (\text{B.1})$$

$$u_0 = u_s \sec(\theta_w). \quad (\text{B.2})$$

### B.3.2 Irregular Reflection

In general for unsteady flow, the shock-wave reflection configurations are regular reflection (RR), or irregular reflection (IR). The irregular reflection could be either a von Neumann reflection (vNR), or a Mach reflection (MR). Unlike the steady case, the MR can be further broken down into more configurations. The Mach reflection could be one of the following three types, each depending on the direction the triple point,  $T$ , travels: a direct Mach reflection (DiMR) where  $T$  moves away from the wedge, a stationary Mach reflection (StMR) where  $T$  moves parallel to the wedge and an inverse-Mach reflection (InMR) where  $T$  moves towards the reflecting wedge surface. Upon the collision of the triple point with the wedge, the InMR terminates and a



transitioned regular reflection (TRR) appears. In pseudo-steady flows (for which the theories and algorithms discussed in this document are valid), the Mach reflection is always a DiMR, with the triple point moving away from the wedge surface.

The DiMR can be further divided into three different types: a single Mach reflection (SMR), a transitional Mach reflection (TMR), and a double-Mach reflection (DMR) depending on whether the triple point trajectory angle of the first triple point is larger or smaller than that of the second triple point, the DMR can be further divided into two types. This summary only touches the different types of unsteady reflections, and will be discussed no further, as this document is concerned mostly with the SMR in pseudo-steady flow.

### B.3.3 Single Mach Reflection

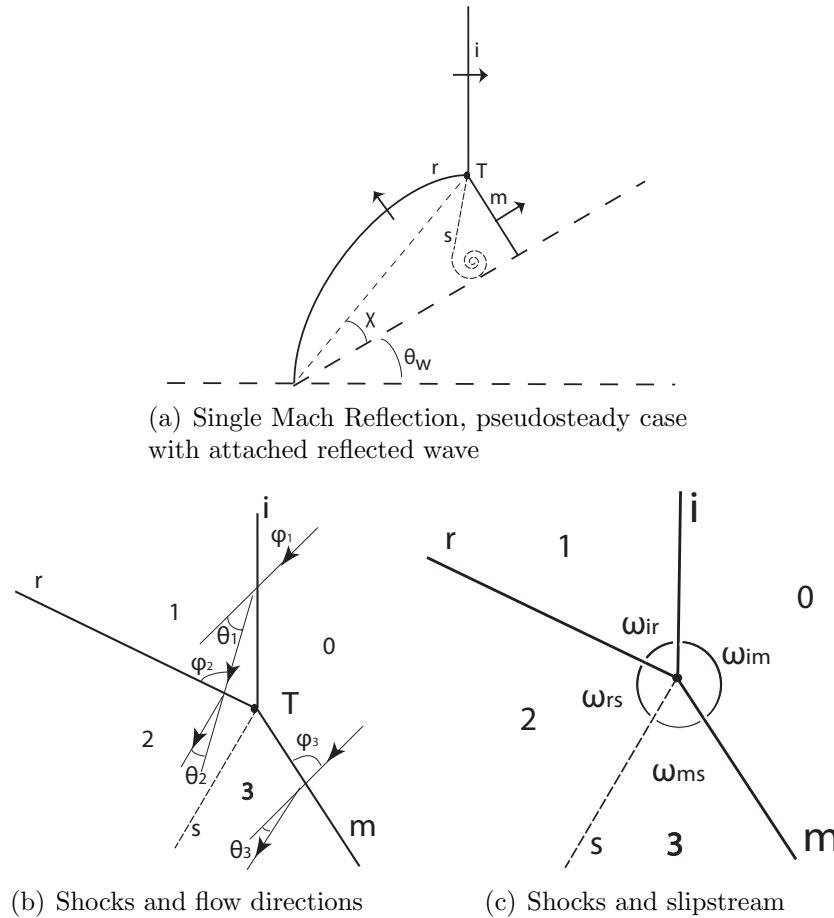


Figure B.3: Single Mach Reflection, pseudosteady case

The unsteady reflection process can be approximated as a self similar, pseudo-

steady problem (103), (15), (18). For this simplification, the Mach stem is assumed to be straight and perpendicular to the wedge, and the fluid is modeled as inviscid. By attaching a reference frame to the triple point, the three shock pseudo-steady solution is found. In this frame, the reflected wave of a SMR relative to the triple point path, is straight in the pseudo-steady reference frame.

For each shock, there are 4 sets of oblique shock relations. The first 14 equations (B.27-B.40) of the steady model are again used. However, the additional equations resulting from the geometry and straight Mach stem assumption must be modified to include the triple point angle,  $\chi$ ,

$$\phi_1 = \frac{\pi}{2} - \theta_w - \chi, \quad (\text{B.3})$$

$$u_o = \frac{u_s}{\cos(\theta_w + \chi)}. \quad (\text{B.4})$$

The 16 equations (B.27-B.40, B.3, B.4) and 16 unknowns above can be solved given the appropriate thermodynamic relations and initial conditions.

### B.3.4 Unsteady Transition Criterion

For pseudo-steady flows, the transition from RR to MR occurs at what is known as the sonic condition, as described by (72). The sonic condition occurs when the post-reflected shock state becomes sonic,  $M = 1$ . On a shock polar diagram this occurs when the sonic point of the reflected shock polar coincides with the pressure axis. This point is lower than the detachment point of the shock polar, and thus transition to MR will occur at a smaller incident shock angle than when using the detachment condition. Experimentally, the sonic and detachment conditions are almost indistinguishable, and different books and papers state the unsteady transition criteria as either the detachment condition or sonic condition.

A single condition encompassing both the von Neumann condition for steady flows and the sonic condition for pseudosteady flows is the information condition, as described by (70). The condition states that in order for a Mach stem to exist, it is necessary that information about a length scale can reach the region near the reflection point in order to scale the Mach stem length.

In pseudo-steady flows, RR transitions to MR when the flow behind the reflection point becomes sonic in a frame of reference attached to the RR point. When  $M_2 > 1$ , the corner generated signals catch up with the reflection point, and a Mach stem is formed, causing an irregular reflection, IR. The IR can be either an MR or a

vNR depending on the angle of incidence,  $\phi_2$ , between the flow in state (1) behind the incident shock wave, i, and the reflected shock wave, r, in a frame of reference attached to the triple point, T. The transition to a vNR takes place when

$$\phi_2 \geq 90^\circ. \quad (\text{B.5})$$

$\phi_2 = 90^\circ$  occurs when the flow in state (1) is perpendicular to the reflected shock wave, r, and afterward remains perpendicular to the reflected shock wave. This also occurs when

$$\omega_{rs} = 90^\circ. \quad (\text{B.6})$$

where  $\omega_{rs}$  is the angle between the reflected shock wave r, and the slipstream s, as shown in figure B.3(c).

The transition boundaries for MR can be seen by looking at the solution of the triple point path as a function of Mach number and wedge angle as shown in figure C.9. The left side of the plot for  $\chi(M)$  at various  $\theta_w$  shows that for a particular wedge angle, there is a Mach number below which the MR does not physically exist. This represents the transition to vNR. Not that using the shock polars, a MR solution for  $\phi_2 \geq 90^\circ$  can be found, but can only physically exist in the steady case. In the pseudo-steady case the vNR is found experimentally. Also, at the bottom of the figure the transition to RR is found. Again for particular Mach number, there is a wedge angle above which MR cannot exist and RR will be observed.

Once the condition for the existence of a Mach reflection is met, the value of the Mach number,  $M_2$ , in state (2) behind the reflected shock wave, r, of the Mach reflection with respect to the triple point T, becomes the main parameter for determining what type of Mach reflection will be observed.

For  $M_2 < 1$ , the reflection is an SMR with a reflected shock wave curved along its entire length. When the flow in state (2) becomes supersonic with respect to T, the reflected shock wave develops a straight portion that terminates at a point known as the kink, K, which indicates the part of r that has been reached by the corner-generated signals. The SMR changes to a transitional Mach reflection (TMR) when  $M_2 = 1$ .

Once a kink is formed in the reflected shock wave, the value of the Mach number in state (2) behind the reflected shock wave, r, of the MR with respect to the kink, K, becomes the significant parameter in determining whether the reflection remains

a TMR or changes to a double Mach reflection (DMR). When a DMR forms, the band of the compression waves from the TMR converge to form a shock wave, and a second triple point,  $T'$ , appears. In the past, the kink of the TMR and the second triple point, of the DMR were assumed to be practically the same point. However, recent research has developed more accurate, but complex theories (17).

In figure B.4(a) and B.4(b) the transition criterion for vNR, TMR, and RR are shown as a function of  $\theta_w$ ,  $\phi_1$ , and  $M_s$ , for the entire solution domain up to  $M_s = 10$  for the perfect gas case with  $\gamma = \frac{7}{5}$ . In figure B.4(c) they are shown for the domain with the triple point angle rather than explicitly calculating the transition boundaries with a computationally expensive solution of the MR and RR equations for each criterion, the points of transition within the solution algorithm have been recognized as they first occur. For example, as soon as  $\phi_2 = 90^\circ$  or  $\theta_2$  switches sign, the vNR transition boundary has been crossed. When  $M_2$  passed through one, the TMR boundary has been crossed. The RR transition boundary can be calculated explicitly, using and nonlinear equation solve for the sonic criterion, for which the results are shown in figure B.4(c). This is fairly expensive, however, this boundary can be estimated using the historical *mechanical equilibrium transition criterion* for RR as shown in figure B.3.4. For these results it is assumed that transition occurs when the RR reflected shock polar first crosses incident shock polar at  $\theta_1 - \theta_2 = \theta_3 = 0$ . For this criterion the transition wedge angle is overestimated, however, it is straight forward to implement algorithmically. For the algorithms discussed later in this document, this criterion is used as an estimate of the solution domain for SMR, however, attention must still be paid when interpreting the results to rule out the physically invalid solutions. Note that this computationally sensitive implementation of the transition criterion is most important when dealing the real case models to limit the computational expense.

### B.3.5 Oblique Shock Relations

The Euler equations for compressible flow are used to derive a general solution for a gas which travels through a planar oblique shock wave. These equations are written for the normal velocity component of the gas as the tangential component is unchanged. An additional required equation is the equation of state, which can be (for perfect and imperfect gases) the ideal gas law or a more complex one, such as the Van der Waals equation of state. For this, the temperature and pressure are chosen as the independent thermodynamic parameters. With the pre-shock state, 0, and the

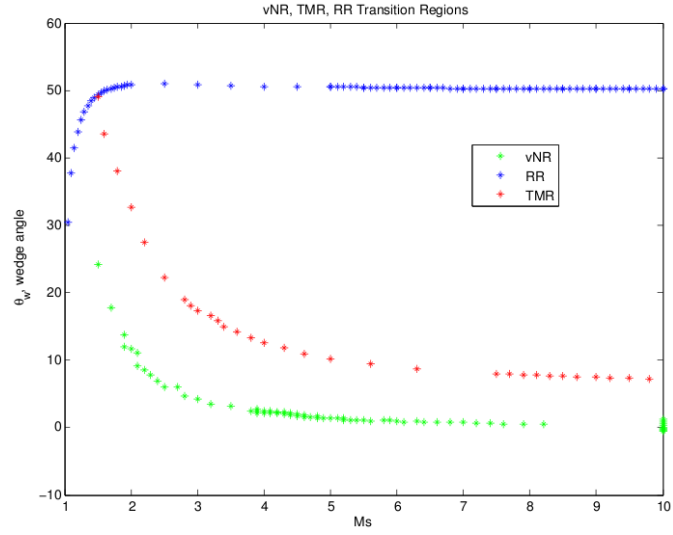
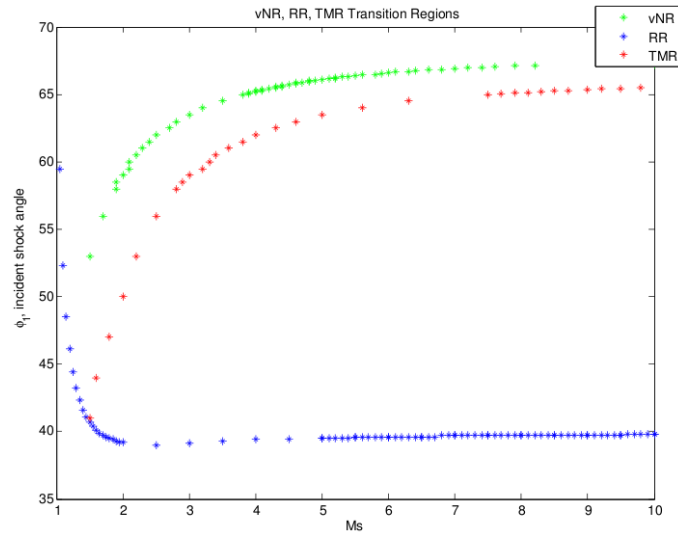
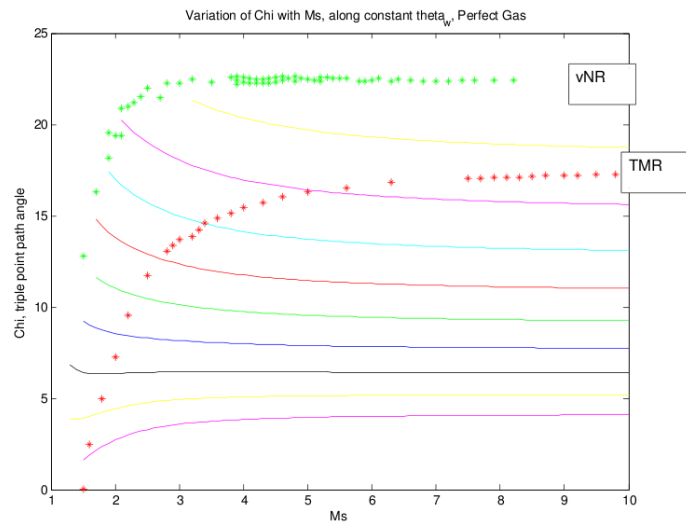
(a)  $\theta_w$  vs  $M_s$ (b)  $\phi_1$  vs  $M_s$ (c)  $\chi$  vs  $M_s$ 

Figure B.4: Psuedo-steady transition regions, perfect gas

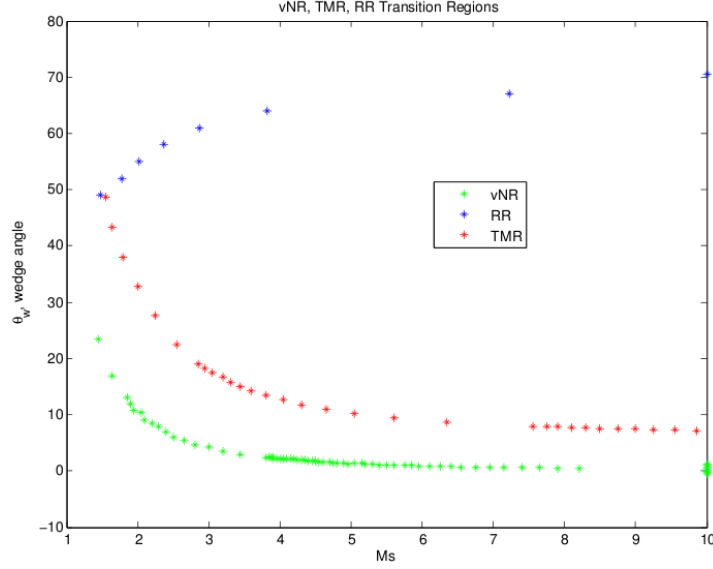


Figure B.5: Psuedo-steady mechanical equilibrium RR transition criterion,  $\theta_3 = 0$ .

post-shock state, 1, the systems of equations are

$$\rho_0 u_0 \sin \phi_1 = \rho_1 u_1 \sin(\phi_1 - \theta_1), \quad (\text{B.7})$$

$$\rho_0 \tan \phi_1 = \rho_1 \tan(\phi_1 - \theta_1), \quad (\text{B.8})$$

$$p_0 + \rho_0 u_0^2 \sin^2 \phi_1 = p_1 + \rho_1 u_1^2 \sin^2(\phi_1 - \theta_1), \quad (\text{B.9})$$

$$h_0 + \frac{1}{2} u_0^2 \sin^2 \phi_1 = h_1 + \frac{1}{2} u_1^2 \sin^2(\phi_1 - \theta_1). \quad (\text{B.10})$$

The solution is found when given the wedge angle,  $\theta_1 = \theta_w$ , and the thermodynamic and chemical state at the initial state 0, for example, Mach number  $M_0$ , temperature  $T_0$ , pressure  $P_0$ , and species mole fractions  $q_0$ . In this case, the solution is the shock angle,  $\phi_1$ , which as shown in figure B.1(b) can be equal to  $\phi_w$  or  $\phi_s$ . The inverse problem of finding the deflection angle in terms of the shock angle is also of interest. These oblique shock relations as presented are valid for two-dimensional, steady, inviscid, compressible flows.

For a perfect gas solution, the only required input information is the wedge angle and the initial flow Mach number  $M_0$ . The above equations are reduced, for example,

from state 0 to state 1 across an oblique shock to

$$M_{n0} = M_0 \sin(\phi_1), \quad (\text{B.11})$$

$$M_{n1} = \sqrt{\frac{1 + ((\gamma - 1)/2)M_{n0}^2}{\gamma M_{n0}^2 - (\gamma - 1)/2}}, \quad (\text{B.12})$$

$$\frac{p_1}{p_0} = 1 + 2\gamma(M_{n0}^2 - 1)/(\gamma + 1), \quad (\text{B.13})$$

$$\theta_1 = \arctan \left( \frac{2 \cot(\phi_1)((M_0 \sin(\phi_1))^2 - 1)}{M_0^2(\gamma + \cos(2\phi_1)) + 2} \right), \quad (\text{B.14})$$

$$M_1 = \frac{M_{n1}}{\sin(\phi_1 - \theta_1)}. \quad (\text{B.15})$$

### B.3.5.1 Shock Polars

The shock polar is a graphical tool for visualizing and assisting the solution of multiple shock interactions. A shock polar for one shock in figure B.6, represents the pressure ratios,  $p_1/p_0$ , that are available through an oblique shock with a flow deflection,  $\theta$ . The polars have different sizes and shapes, depending on the initial thermodynamic state, the flow Mach number, and the thermodynamic and chemical model, for example, real or perfect gas and reacting or nonreacting. For perfect gases, the shock polar shape depends solely on the Mach number and the specific heat ratio. figure B.7 shows the shock polar, for perfect ( $\gamma = 1.4$ ) and imperfect reacting nitrogen. For a given wedge angle, there are two solutions, the weak and strong. The asterisks mark the sonic condition, below which the downstream flow is supersonic (the weak solution) and above which it is subsonic (the strong solution). For  $\theta = 0$  there is either no disturbance or a normal shock wave. There is also the maximum angle (left and rightmost points), the detachment angle, beyond which there is no solution at all for an upstream Mach number.

### B.3.6 Regular Reflection

The regular reflection case generally occurs for larger angles of incidence, in which the incident shock is closer to the wall boundary. A schematic is shown in figure B.8(a). Here, a steady wave that could have been caused by a wedge in the free stream is in contact with a wall at an oblique angle, causing a reflected wave to appear. If the angle of incidence between the incident wave and the wall is less than the detachment angle, then a straight attached reflected wave is a possible solution. More precisely, the RR is the only solution when the incident shock angle is below the von Neumann

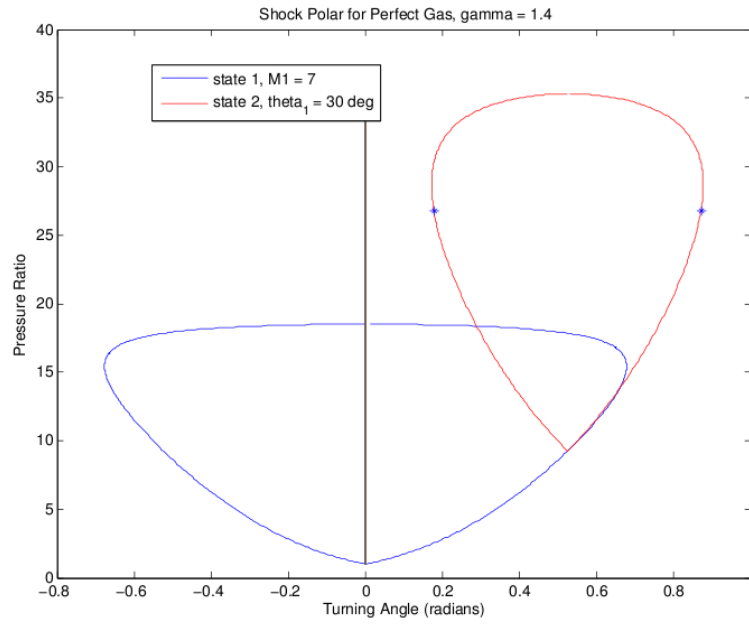


Figure B.6: Incident (state 1) and Reflected shocks (state 2), Perfect gas shock polars for air,  $M_1 = 1.6$  and  $\theta_1 = 8^\circ$

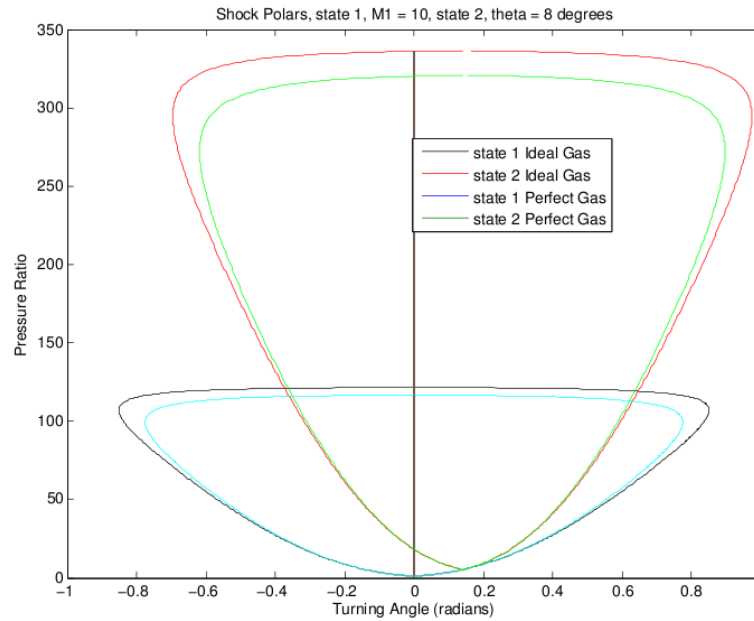
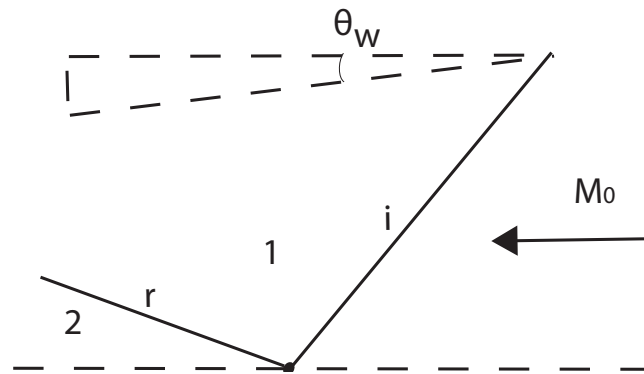
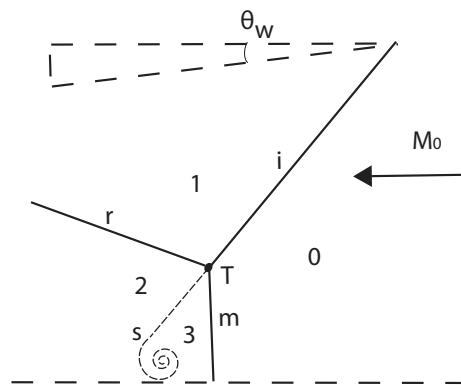


Figure B.7: Incident (state 1) and Reflected shocks (state 2), shock polars: Comparing Perfect gas and real gas mixture cases for air at 300 K and 100 kPa,  $M_1 = 10$  and  $\theta_1 = 8^\circ$



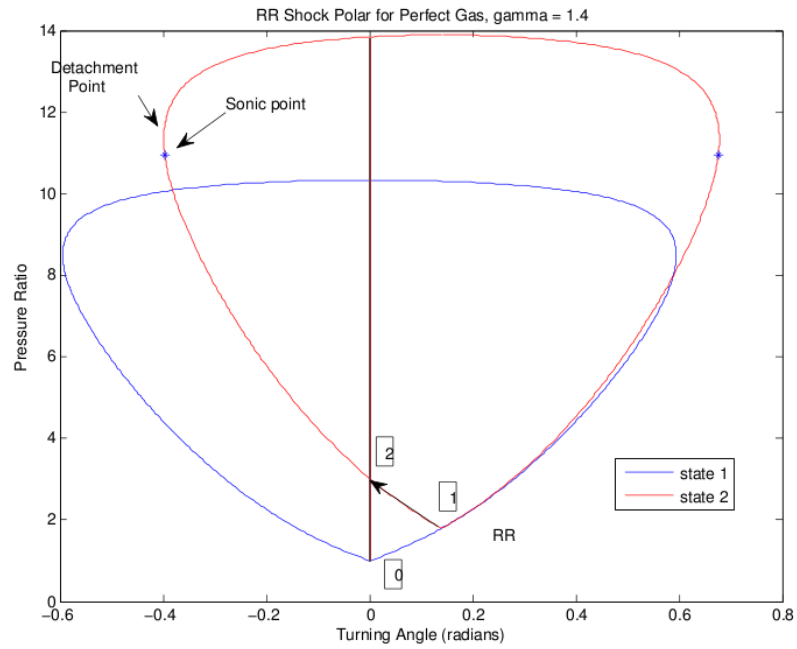


(a) Regular reflection (RR)

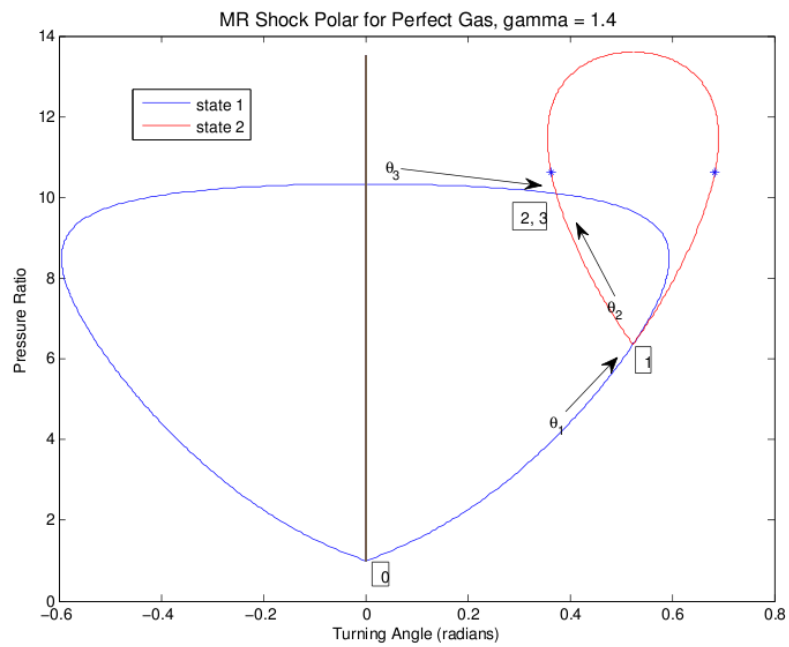


(b) Mach reflection (MR)

Figure B.8: Steady flow reflections



(a) Regular reflection (RR)



(b) Mach reflection (MR)

Figure B.9: Steady flow reflection shock polars

angle (not to be confused with the von Neumann Reflection), and RR or MR is possible between the von Neumann angle and the detachment angle, as discussed in the steady transition criterion section. The von Neumann angle is the angle at which the reflected shock polar intersects the incident shock polar at the top. On the  $(P, \theta)$  shock polar diagram, this is where  $\theta = 0$ . Here the two shocks together have the same effect on the pressure ratio that one normal shock would. A valid RR is demonstrated with its incident and reflected shock polars, as shown in figure B.9(a).

For inviscid flow, this two-shock configuration can be accurately modeled using the oblique shock relations twice. Starting at state 0, where the angle of incidence,  $\phi_1$ , of the incident wave is known, the flow deflection and thermodynamic state can be found across the incident shock. Then, this post-shock thermodynamic state and the known flow deflection angle (parallel to the wall) are used to find the angle of the reflected shock wave.

The solution from *two shock theory* is formulated by applying the oblique shock relations twice and enforcing the BC,

State (0) to State (1)

$$\rho_0 u_0 \sin \phi_1 = \rho_1 u_1 \sin(\phi_1 - \theta_1), \quad (\text{B.16})$$

$$\rho_0 \tan \phi_1 = \rho_1 \tan(\phi_1 - \theta_1), \quad (\text{B.17})$$

$$p_0 + \rho_0 u_0^2 \sin^2 \phi_1 = p_1 + \rho_1 u_1^2 \sin^2(\phi_1 - \theta_1), \quad (\text{B.18})$$

$$h_0 + \frac{1}{2} u_0^2 \sin^2 \phi_1 = h_1 + \frac{1}{2} u_1^2 \sin^2(\phi_1 - \theta_1). \quad (\text{B.19})$$

State (1) to State (2)

$$\rho_1 u_1 \sin \phi_2 = \rho_2 u_2 \sin(\phi_2 - \theta_2), \quad (\text{B.20})$$

$$\rho_1 \tan \phi_2 = \rho_2 \tan(\phi_2 - \theta_2), \quad (\text{B.21})$$

$$p_1 + \rho_1 u_1^2 \sin^2 \phi_2 = p_2 + \rho_2 u_2^2 \sin^2(\phi_2 - \theta_2), \quad (\text{B.22})$$

$$h_1 + \frac{1}{2} u_1^2 \sin^2 \phi_2 = h_2 + \frac{1}{2} u_2^2 \sin^2(\phi_2 - \theta_2). \quad (\text{B.23})$$

and enforcing the BC,

$$\theta_1 - \theta_2 = 0. \quad (\text{B.24})$$

Note that equations B.17 and B.21 are the result of dividing the conservation of

the normal mass equation,

$$\rho_i u_i \sin \phi_i = \rho_j u_j \sin(\phi_i - \theta_j), \quad (\text{B.25})$$

by the continuity of tangential velocity equation,

$$u_i \cos \phi_i = u_j \cos(\phi_i - \theta_j). \quad (\text{B.26})$$

### B.3.7 Mach Reflection

Again consider the following straight incident shock wave, that originated from the free stream and became steady, as in figure B.8(b). Now, consider the case when the angle of incidence between shock i and the wall is greater than the von Neumann angle. In the unsteady starting problem for this steady solution, an initially curved shock wave resulted at the reflection point. This “detached” wave propagated away from the wall and approached a new steady solution. The resulting solution configuration is known as a Mach reflection (MR).

MR is the appearance of three main shock waves jointing at a common point, the triple point, T. The Mach stem m, starting straight and perpendicular to the wall “displaces” the reflection point up to the triple point at which m is curved. For this configuration, the flow is supersonic behind the incident shock, subsonic or supersonic behind the reflected shock, and subsonic behind the Mach stem. The flow field coming from the reflected shock above is different from that coming from the Mach stem below. However, physically the pressures and flow deflection (normal velocity), must be equal for the slipstream to be at a constant angle. The surface (or line in two dimensions), called the slipstream, at which these flows meet can thus support differing densities, temperatures, and species concentrations.

At the triple point T in a MR, there are four discontinuities (in regard to inviscid flow), the incident shock, labeled i, reflected shock r, Mach stem m, and the slipstream s. These all coincide at the triple point T. The Mach stem is curved at the triple point, concave for weak waves (supersonic post-reflected shock state) and convex for strong waves (subsonic post-reflected shock state). A valid MR is demonstrated with its incident and reflected shock polars, as shown in figure B.9(b).

The solution is found by applying the *three shock theory*, equivalently applying the oblique shock relations once for each shock.

Incident Shock, State (0) to State (1):

$$\rho_0 u_0 \sin \phi_1 = \rho_1 u_1 \sin(\phi_1 - \theta_1), \quad (\text{B.27})$$

$$\rho_0 \tan \phi_1 = \rho_1 \tan(\phi_1 - \theta_1), \quad (\text{B.28})$$

$$p_0 + \rho_0 u_0^2 \sin^2 \phi_1 = p_1 + \rho_1 u_1^2 \sin^2(\phi_1 - \theta_1), \quad (\text{B.29})$$

$$h_0 + \frac{1}{2} u_0^2 \sin^2 \phi_1 = h_1 + \frac{1}{2} u_1^2 \sin^2(\phi_1 - \theta_1). \quad (\text{B.30})$$

Reflected Shock, State (1) to State (2):

$$\rho_1 u_1 \sin \phi_2 = \rho_2 u_2 \sin(\phi_2 - \theta_2), \quad (\text{B.31})$$

$$\rho_1 \tan \phi_2 = \rho_2 \tan(\phi_2 - \theta_2), \quad (\text{B.32})$$

$$p_1 + \rho_1 u_1^2 \sin^2 \phi_2 = p_2 + \rho_2 u_2^2 \sin^2(\phi_2 - \theta_2), \quad (\text{B.33})$$

$$h_1 + \frac{1}{2} u_1^2 \sin^2 \phi_2 = h_2 + \frac{1}{2} u_2^2 \sin^2(\phi_2 - \theta_2). \quad (\text{B.34})$$

Mach Stem, State (0) to State (3):

$$\rho_0 u_0 \sin \phi_3 = \rho_1 u_1 \sin(\phi_3 - \theta_3), \quad (\text{B.35})$$

$$\rho_0 \tan \phi_3 = \rho_1 \tan(\phi_3 - \theta_3), \quad (\text{B.36})$$

$$p_0 + \rho_0 u_0^2 \sin^2 \phi_3 = p_1 + \rho_1 u_1^2 \sin^2(\phi_3 - \theta_3), \quad (\text{B.37})$$

$$h_0 + \frac{1}{2} u_0^2 \sin^2 \phi_3 = h_1 + \frac{1}{2} u_1^2 \sin^2(\phi_3 - \theta_3). \quad (\text{B.38})$$

and enforcing the BC's across the slipstream,

$$p_2 = p_3, \quad (\text{B.39})$$

$$\theta_1 - \theta_2 = \theta_3. \quad (\text{B.40})$$

Note that  $\theta_3$  is not zero and the flow travels to the wall, where it can curl in a counter clockwise or clockwise direction. In the present framework, two alternatives exist in finding a solution. If the angle of curvature of the Mach stem is known experimentally or estimated, this can be used to close the equations. Otherwise, the curvature is neglected and the approximation  $\phi_3 = 90^\circ$  is used. In either case, the 14 equations (B.27-B.40) and 14 unknowns above can then be solved given the incident shock and wall angles and the appropriate thermodynamic relations at the initial state 0, for example, Mach number  $M_0$ , temperature  $T_0$ , pressure  $p_0$ , and species mole fractions  $q_0$ .

### B.3.8 Von Neumann Reflection

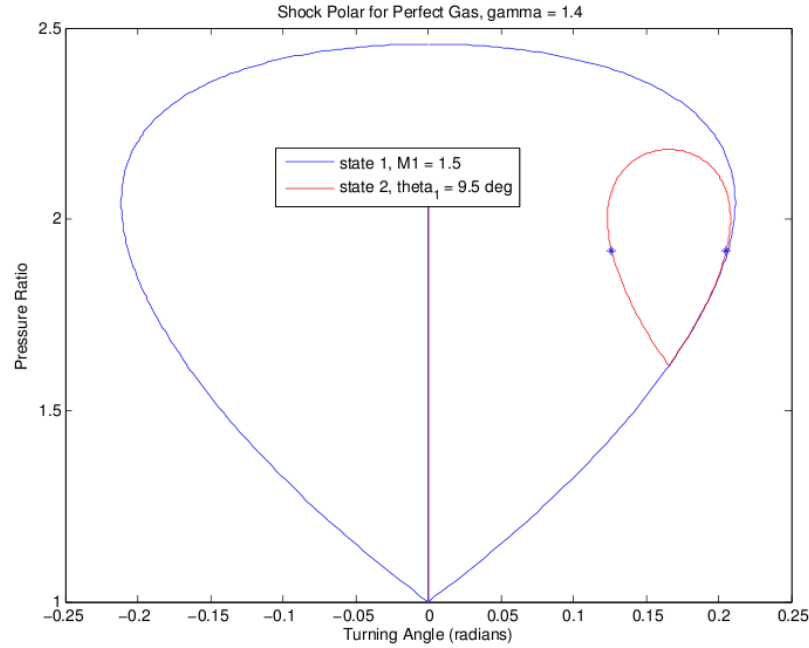


Figure B.10: Shock polar for vNR

Von Neumann reflection, visually similar but different than MR, occurs when the reflected shock polar never intersects the incident shock polar, as shown in figure B.10.

In a von Neumann reflection (vNR), is unlike the clear and sharp change in the orientation of the Mach stem and the incident shock wave at the triple point of a Mach reflection. The Mach stem smoothly merges into the incident shock wave. In addition, while the reflected wave is a clear shock wave in a Mach reflection, it is instead a band of compression waves in a von Neumann reflection. Experimentally, to the unaided eye the vNR looks like an SMR. Skews and Ashworth, showed the experimental verification of steady vNR, (148).

### B.3.9 Steady Transition Criterion

The transition criterion of reflections in compressible flows are governed by disturbances and the existence or lack of information pathways. These pathways are similar to the regions of influence and dependence in countered in hyperbolic equations. In steady flow, any disturbance in the flow that is strong enough to set up a small Mach reflection would open an information path to the reflection point. Once the Mach stem is set up a permanent information path is established from the subsonic flow

to the triple point. Without any disturbances, regular reflection is possible at shock angles greater than that at the von Neumann angle (also known as the von Neumann condition). Therefore, in steady flow, between the von Neumann condition and the detachment condition there exists the dual-solution domain where both RR and MR are possible (73), (104), (119). Note that once the vNR is established, the two and three shock theories can no longer be used, as solution is now governed by weak compressive waves.

In general, reflection phenomenon are labeled as either regular reflection (RR) or irregular reflection (IR). For steady flow, IR encompasses MR and vNR. The vNR results whenever a reflected shock wave is insufficient to match the state behind the incident shock with that behind the Mach stem. This occurs when the theoretically possible reflected shock polar is totally inside of the incident shock polar.

## Appendix C

# Mach Reflection Solution Algorithms

Algorithms have been developed to model the case of a pseudo-steady MR. These results are valid in the neighborhood of the triple point of any MR, for example DMR or TMR, but are most useful for the case of a single Mach reflection (SMR).

Two types of algorithms have been implemented, a general one which iterates on the triple point angle while keeping the wedge angle constant, and the (97) algorithm which iterates on the triple point angle while keeping the angle of incidence,  $\phi_1$ , between the flow and the incident shock constant. Both have been implemented for perfect gases and real gases (ideal gas mixtures with nonconstant  $c_P$  and frozen or equilibrium chemistry to be precise).

The solution algorithms iterate on the triple point angle until the system of equations is satisfied. The additional information needed from the above formulation is that across the slipstream, in the frame of reference of the triple point, the pressures and flow deflections of states 2 and 3 must be equal. The equality of pressure and flow deflection is used as criterion for evaluating the residual at each iteration.

### C.1 Perfect Gas Algorithm

For a desired Mach number and wedge angle, this algorithm iterates to find the triple point angle,  $\chi$ , until a residual is zero, corresponding to the difference in deflections on both sides of the slipstream.

For the perfect gas case, one starts with an initial guess for the triple point angle. If the solution is desired for all possible  $M$  and  $\theta_w$ , it is easiest to start at the largest Mach number, for example  $M = 10$ , and slowly decrease it to obtain the  $\chi = \chi(\theta)$



relation at each  $\theta_w$ , which is varied in an outer loop. Below is a sketch of a Matlab function which is called at every iteration by a nonlinear equation solver such as Newton's method, equivalently Matlab's *fsolve* function. figure C.1(a) and C.1(b) show how in the algorithm, the i and r shock polars can be matched while keeping  $\theta_w$  constant and varying the Mach number. figure C.1(a) shows an example inner loop of the algorithm where  $M$  is varied, and figure C.1(b) shows this loop and the subsequent loop at the next wedge angle. As the shock polars are varied, the solution (in terms of  $\chi(M, \theta_w)$  for the perfect case), is tracked and extrapolated to ensure better convergence properties of the nonlinear equation solver at the next iteration in both the inner and outer loops.

In figures C.2(b) and C.2(a), the results are summarized by showing the triple point angle and pressure ratio across the Mach stem as functions of the initial incident wave Mach number for different wedge angles.

For a particular  $M$  and  $\theta_w$ , the algorithm starts with an extrapolated guess for  $\chi$ . Initial parameters are first found by transforming to the triple point frame of reference and using geometrical relations,

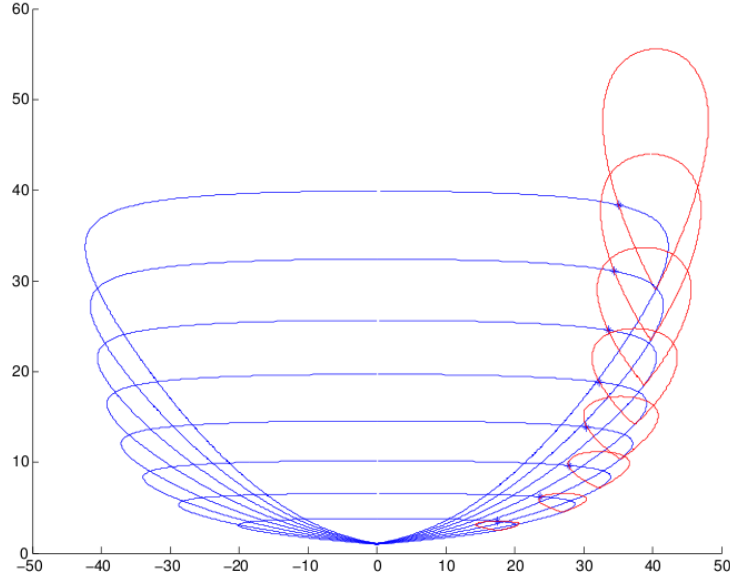
$$M_0 = \frac{M_s}{\cos(\theta_w + \chi)}, \quad (\text{C.1})$$

using  $\chi = \frac{\pi}{2} - \phi_3$ ,

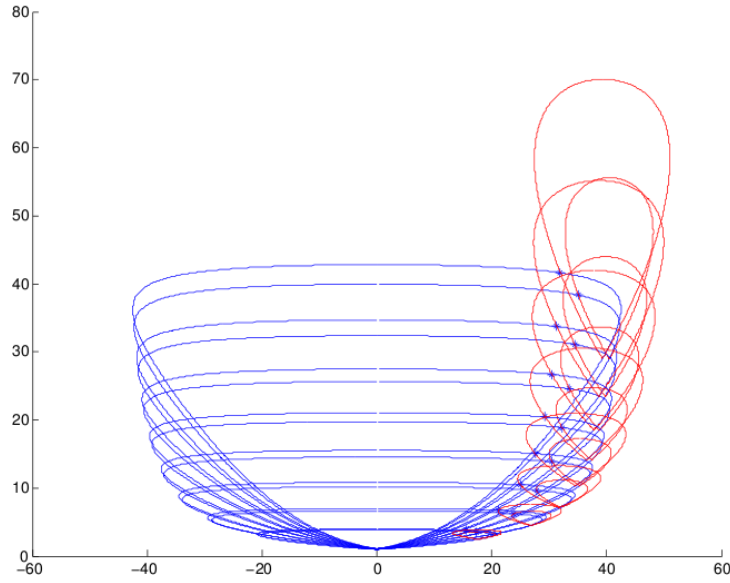
$$\phi_3 = \frac{\pi}{2} - \chi, \quad (\text{C.2})$$

$$\phi_1 = \frac{\pi}{2} - \theta_w - \chi, \quad (\text{C.3})$$

$$M_s = M_0 \sin(\phi_1). \quad (\text{C.4})$$



(a) Example solution path for  $\theta_w = 20^\circ$  starting at a Mach number of 5 and decreasing to 1.5 in .5 increments.



(b) Example solution path for  $\theta_w = 20^\circ$  starting at a Mach number of 5 and decreasing to 1.5 in .5 increments, and then repeating for  $\theta_w = 25^\circ$

Figure C.1: Evolution of the solution in the general algorithm, perfect gas

State (0) to State (1): Incident Shock

$$M_{n0} = M_0 \sin(\phi_1), \quad (\text{C.5})$$

$$M_{n1} = \sqrt{\frac{1 + ((\gamma - 1)/2)M_{n0}^2}{\gamma M_{n0}^2 - (\gamma - 1)/2}}, \quad (\text{C.6})$$

$$\frac{p_1}{p_0} = 1 + 2\gamma(M_{n0}^2 - 1)/(\gamma + 1), \quad (\text{C.7})$$

$$\theta_1 = \arctan \left( \frac{2 \cot(\phi_1)((M_0 \sin(\phi_1))^2 - 1)}{M_0^2(\gamma + \cos(2\phi_1)) + 2} \right), \quad (\text{C.8})$$

State (0) to State (3): Mach Stem

$$M_{n0} = M_0 \sin(\phi_3), \quad (\text{C.10})$$

$$M_{n3} = \sqrt{\frac{1 + ((\gamma - 1)/2)M_{n0}^2}{\gamma M_{n0}^2 - (\gamma - 1)/2}}, \quad (\text{C.11})$$

$$\frac{p_3}{p_0} = 1 + 2\gamma(M_{n0}^2 - 1)/(\gamma + 1), \quad (\text{C.12})$$

$$\theta_3 = \arctan\left(\frac{2 \cot(\phi_3)((M_0 \sin(\phi_3))^2 - 1)}{M_0^2(\gamma + \cos(2\phi_3)) + 2}\right), \quad (\text{C.13})$$

$$M_3 = \frac{M_{n3}}{\sin(\phi_3 - \theta_3)}. \quad (\text{C.14})$$

Matching Reflected Shock and Mach Stem Pressure and Deflections of States (2) and (3)

$$\frac{p_2}{p_1} = \frac{p_0}{p_1} * \frac{p_3}{p_0}, \quad (\text{C.15})$$

$$M_{n1} = \sqrt{\left(\left(\frac{p_2}{p_1} - 1\right)\frac{\gamma + 1}{2\gamma} + 1\right)}, \quad (\text{C.16})$$

$$\phi_2 = \arcsin \frac{M_{n1}}{M_1}, \quad (\text{C.17})$$

$$\theta_2 = \arctan\left(\frac{2 \cot(\phi_1)((M_1 \sin(\phi_2))^2 - 1)}{M_1^2(\gamma + \cos(2\phi_2)) + 2}\right), \quad (\text{C.18})$$

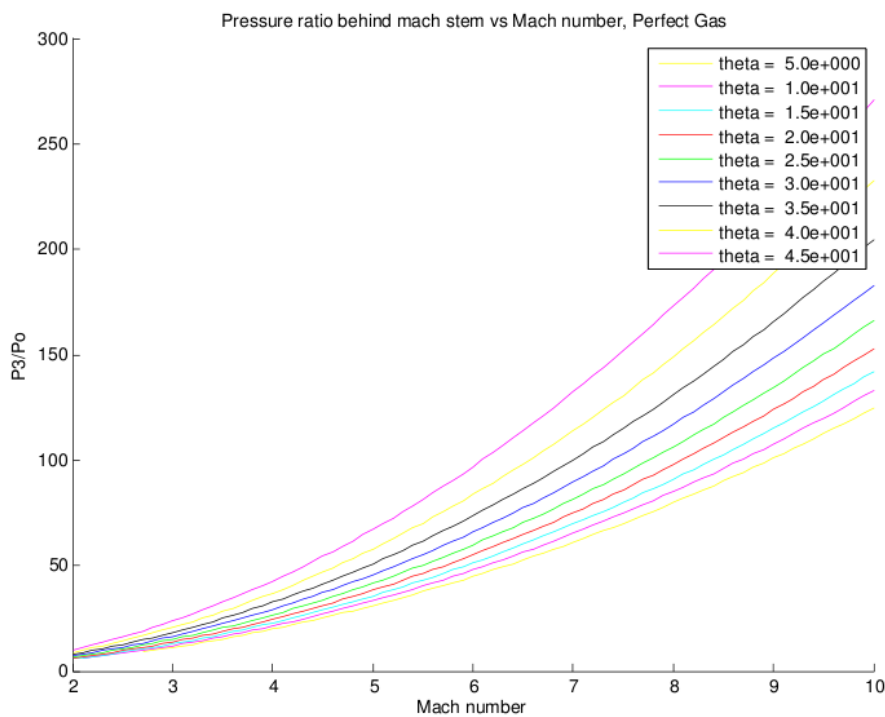
$$residual = (\theta_1 - \theta_3) - \theta_2. \quad (\text{C.19})$$

At this point the residual from the current iteration is used by the nonlinear equation solver to find the next  $\chi$  value and so on until residual converges to zero. Then the solution can be used for extrapolating to the triple point angle at the next Mach number.

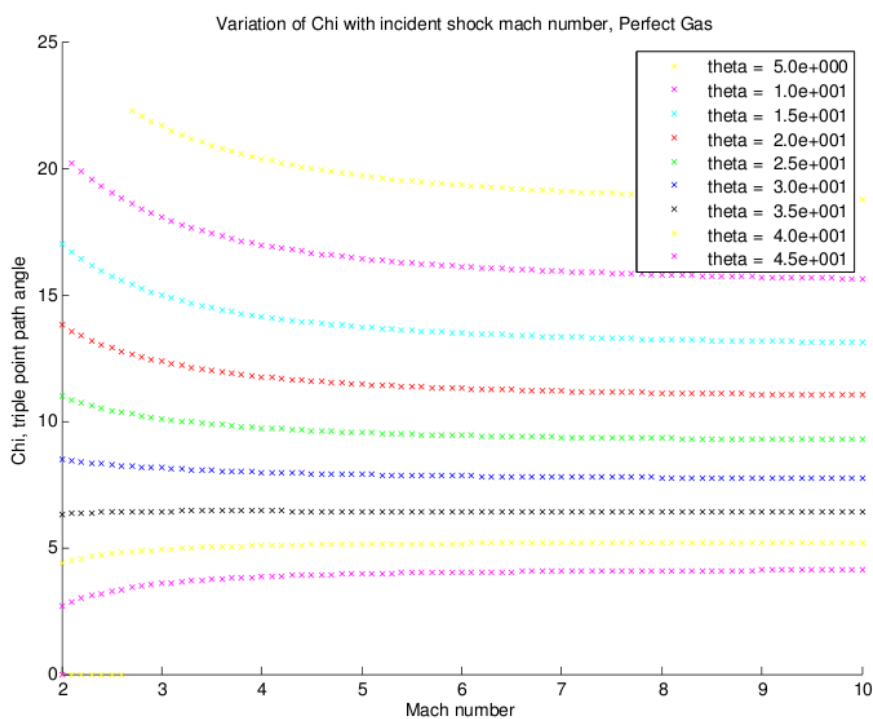
## C.2 Real Gas Algorithm

The real gas algorithm works in a similar fashion to the perfect gas algorithm. The main changes are the use of CANTERA and the **Shock and Detonation Toolbox** to find the post-shock state. Another difference is the use of a two- rather than one-dimensional nonlinear equation solver.

The below example algorithm is for the equilibrium (rather than frozen) shock gas case. This involves a two dimensional Newton Solve, requiring two guesses to start,



(a) Mach Stem Pressure Ratio vs Mach number



(b) Triple point angle vs Mach number

Figure C.2: Perfect gas results for general algorithm

the initial guess for the triple point angle,  $\chi$ , and the angle of incidence of the flow with the reflected shock,  $\phi_2$ . Within the algorithm, one iterates on the triple point angle,  $\chi$ , while simultaneously solving the nonlinear oblique shock equation for  $\phi_2$ , until both of components of the residual are zero, corresponding to the pressure and deflection matching errors. In figures C.2 and C.2 the results are summarized by showing the triple point angle and pressure ratio across the Mach stem as functions of the initial incident wave Mach number for different wedge angles.

Transform to the triple point frame of reference

$$M_0 = \frac{M_s}{\cos(\theta_w + \chi)}, \quad (\text{C.20})$$

$$\phi_3 = \frac{\pi}{2} - \chi, \quad (\text{C.21})$$

$$\phi_1 = \frac{\pi}{2} - \theta_w - \chi, \quad (\text{C.22})$$

$$M_s = M_0 \sin(\phi_1). \quad (\text{C.23})$$

State (0) to State (1): Incident Shock

$$M_{n0} = M_0 \sin(\phi_1) \quad (\text{C.24})$$

$$(\rho_1, p_1, T_1, q_1, M_{n1}) = \text{Post\_Equilibrium\_Shock}(M_{n0}, p_0, T_0, q_0), \quad (\text{C.25})$$

$$\theta_1 = \frac{\arctan(\tan(\phi_1)(\frac{\rho_1}{\rho_0} - 1))}{(\tan(\phi_1)^2 + \frac{\rho_1}{\rho_0})}, \quad (\text{C.26})$$

$$M_1 = \frac{M_{n1}}{\sin(\phi_1 - \theta_1)}. \quad (\text{C.27})$$

State (0) to State (3): Mach Stem

$$M_{n0} = M_0 \sin(\phi_3) \quad (\text{C.28})$$

$$(\rho_3, p_3, T_3, q_3, M_{n3}) = \text{Post\_Equilibrium\_Shock}(M_{n0}, p_0, T_0, q_0), \quad (\text{C.29})$$

$$\theta_3 = \frac{\arctan(\tan(\phi_3)(\frac{\rho_3}{\rho_0} - 1))}{\tan(\phi_3)^2 + \frac{\rho_3}{\rho_0}}, \quad (\text{C.30})$$

$$M_3 = \frac{M_{n3}}{\sin(\phi_3 - \theta_3)}. \quad (\text{C.31})$$

Matching Reflected Shock and Mach Stem Pressure and Deflections of States (2) and

(3)

$$Error(\phi_2) \leftarrow \phi_2(M_1, \theta_2, gas, T_1, p_1, q_1), \quad (C.32)$$

$$M_2 = \frac{M_{n2}}{\sin(\phi_2 - \theta_2)}, \quad (C.33)$$

$$M_{n1} = M_1 \sin(\phi_2), \quad (C.34)$$

$$(\rho_2, p_2, T_2, q_2, M_{n2}) = Post\_Equilibrium\_Shock(M_{n1}, p_1, T_1, q_1), \quad (C.35)$$

$$residual(1) \leftarrow \frac{p_0 p_1}{p_1 p_2} - \frac{p_0}{p_3}, \quad (C.36)$$

$$residual(2) \leftarrow Error(\phi_2). \quad (C.37)$$

Similar to the perfect gas algorithm, the residual from the current iteration is used by the nonlinear equation solver to find the next  $\chi$  and  $\phi_2$  values and so on until residual converges to zero. Then the solution can be used for extrapolating to  $\chi$  and  $\phi_2$  at the next Mach number. Below are a sketch of the post-equilibrium shock calculation of the algorithm and the general, oblique shock relation used.

*Post\_Equilibrium\_Shock* calculation using the SDToolbox

Example for pre- and post-shock states (0) and (1):

$$set(gas(T_0, p_0, q_0). \quad (C.38)$$

$$\rho_0 = density(gas1). \quad (C.39)$$

$$a_0 = soundspeed\_frozen(gas1). \quad (C.40)$$

$$u_{0n} = a_0 M_{n0}. \quad (C.41)$$

$$(\rho_1, p_1, T_1, q_1, a_1) = equilibrated\_shock(u_{0n}, p_0, T_0, q_0). \quad (C.42)$$

$$u_{1n} = \frac{\rho_0 u_{0n}}{\rho_1}. \quad (C.43)$$

$$M_{n1} = \frac{u_{1n}}{a_1}. \quad (C.44)$$

$$(C.45)$$

Oblique shock relation used for finding the deflections or evaluating the error of  $\phi_{i2}$  for a given  $\theta_2$ ,  $M_{n2}$ , and density ratio.

$$\rho_1 \tan \phi_2 = \rho_2 \tan(\phi_2 - \theta_2) \quad (C.46)$$

$$\tan(\phi_2) = \frac{\rho_2 / \rho_1 (\tan(\phi_2) - \tan(\theta_2))}{(1 + \tan(\phi_2) \tan(\theta_2))}. \quad (C.47)$$

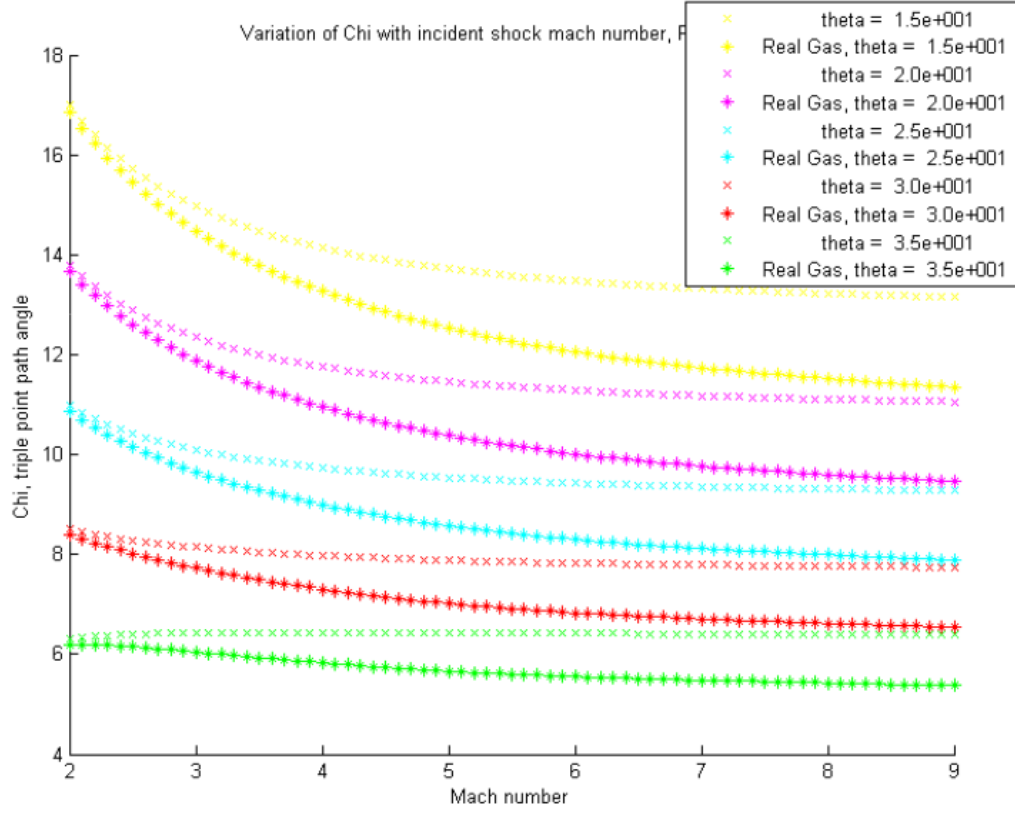


Figure C.3: Triple point angle vs Mach number, "\*" real gas (frozen), "x" perfect gas

### C.3 Law and Glass Algorithm

The Law and Glass graphical method involves iterating on the triple point angle while keeping constant the angle of incidence,  $\phi_1$ , between the flow and the incident shock (97). As in the previous section, the perfect gas case one iterates on  $\chi$ , and the real gas case iterates on  $\chi$  and  $\phi_2$ . The basis for this method is that for a MR, the incident and reflected shock polars will always intersect some where in the right plane, where  $\theta_2 = \theta_1 - \theta_3$  and  $p_2 = p_3$ . This algorithm is more intuitive and insightful than the previous, however, it has the extra hassle that  $\chi(M)$  for constant  $\theta_w$  is not explicitly given. Interpolation is used in the final results to find this relation. Figures C.3 and C.3 show how in the algorithm, the i and r shock polars can be matched while keeping  $\phi_1$  constant and varying the Mach number. Figure C.3 shows an example inner loop of the algorithm, and figure C.3 shows this loop and the subsequent loop. As the shock polars are varied, the solution (in terms of  $\phi_3$  and  $\phi_2$  for the real gas case, and just  $\phi_3$  for the perfect case), is tracked and extrapolated to ensure better convergence properties of the nonlinear equation solver at the next iteration. This

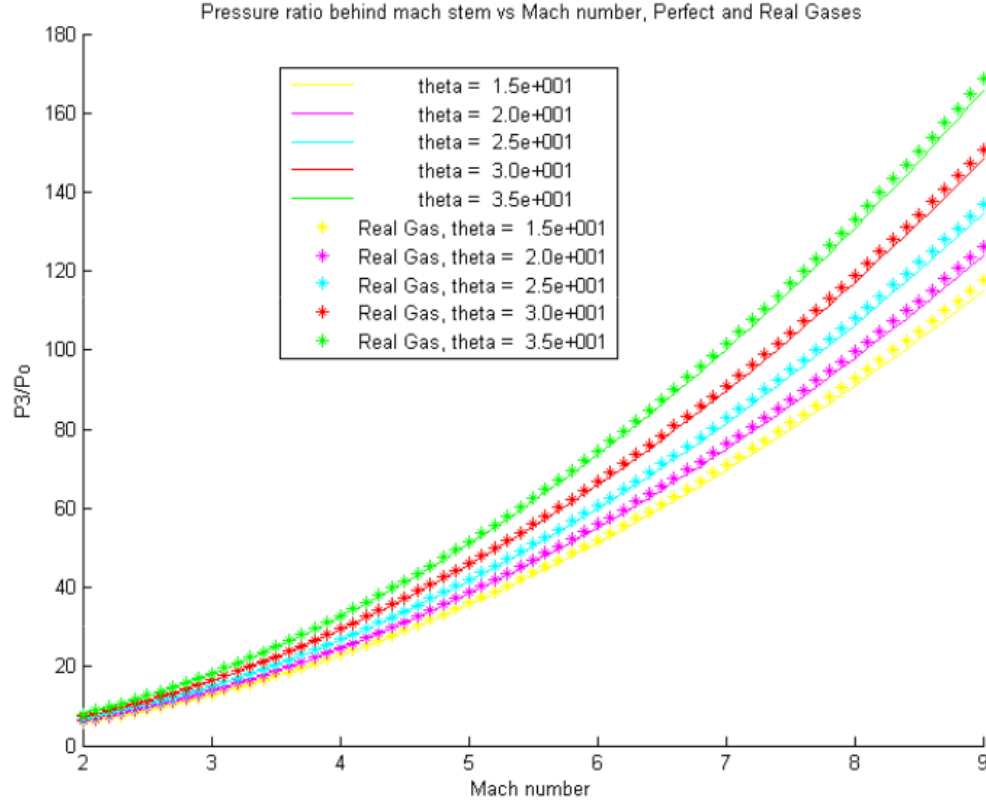


Figure C.4: Mach stem pressure ratio vs Mach number, “\*” real gas (frozen), “x” perfect gas

is done for both  $\phi_1$  and  $M$  in the outer and inner loops, using up to third-order extrapolation. Near the vNR transition limit, the r polar can become very small relative to the i polar or it can be very close to it on the right side. This seems to make the solution very sensitive and is the reason for the high-order extrapolation.

### C.3.1 Perfect Gas Case

for  $\phi_1 = 30^\circ, 30.5^\circ, \dots (0 < \phi_1 < 90^\circ)$

for  $M_s = 10, 9.9, 9.8 \dots (M_s > 1)$

$$M_0 = M_s / \sin(\phi_1)$$

State (0) to State (1): Incident Shock

$$M_{n0} = M_0 \sin(\phi_1)$$

$$M_{n1} = \sqrt{\frac{1 + ((\gamma - 1)/2) M_{n0}^2}{\gamma M_{n0}^2 - (\gamma - 1)/2}}$$

$$\frac{p_1}{p_0} = 1 + 2\gamma(M_{n0}^2 - 1)/(\gamma + 1)$$

$$\theta_1 = \arctan\left(\frac{2 \cot(\phi_1)((M_0 \sin(\phi_1))^2 - 1)}{M_0^2(\gamma + \cos(2\phi_1)) + 2}\right)$$



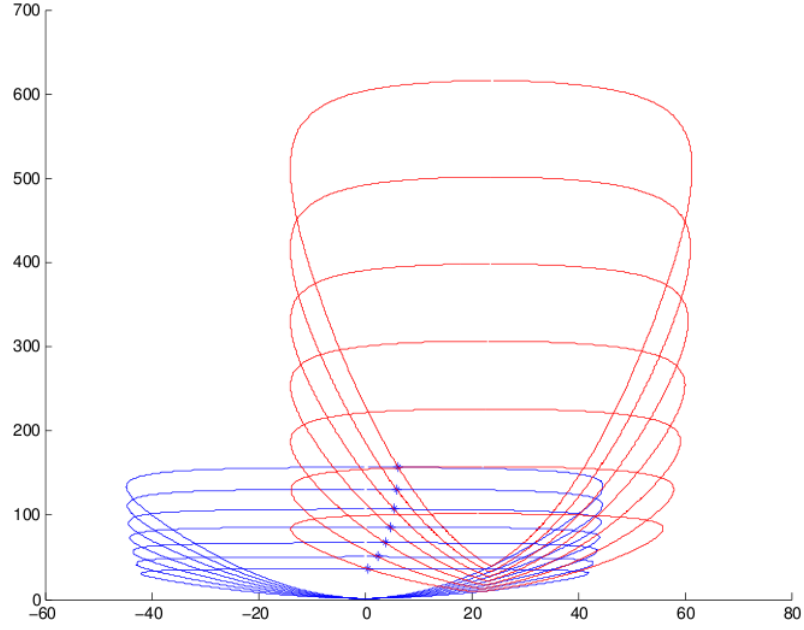


Figure C.5: Evolution of the Law and Glass graphical method, showing the matching of the incident and reflected shock polars, for the perfect gas case decreasing  $M$  from 6 by 0.5 increments at a constant  $\phi_1$  value of  $30^\circ$ .

$$M_1 = \frac{M_{n1}}{\sin(\phi_1 - \theta_1)}$$

if  $M_1 > 1$

Extrapolate for  $\phi_{3guess}$

$\phi_3 \leftarrow$  Match I and R Shock Polars

State (0) to State (3): Mach stem

$$M_{n0} = M_0 \sin(\phi_3)$$

$$M_{n3} = \sqrt{\frac{1 + ((\gamma - 1)/2)M_{n0}^2}{\gamma M_{n0}^2 - (\gamma - 1)/2}}$$

$$\frac{p_3}{p_0} = 1 + 2\gamma(M_{n0}^2 - 1)/(\gamma + 1)$$

$$\theta_3 = \arctan\left(\frac{2 \cot(\phi_3)((M_0 \sin(\phi_3))^2 - 1)}{M_0^2(\gamma + \cos(2\phi_3)) + 2}\right)$$

$$M_3 = \frac{M_{n3}}{\sin(\phi_3 - \theta_3)}$$

$$\theta_2 = \theta_1 - \theta_3$$

Check the RR and vNR transition limits

if  $\theta_3 > 0$  and  $\theta_2 > 0$

$$\chi(M_s, \phi_1) = \pi/2 - \phi_3$$

$$\theta_w(M_s, \phi_1) = \pi/2 - \phi_1 - \chi$$

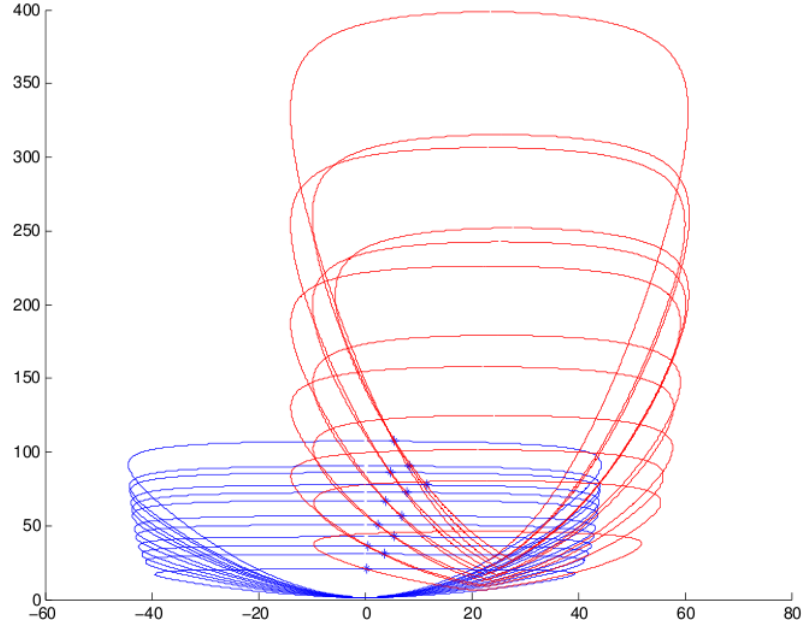


Figure C.6: Evolution of the Law and Glass graphical method, showing the matching of the incident and reflected shock polars, for the perfect gas case decreasing  $M$  from 5 by 0.5 increments at a constant  $\phi_1$  value of  $30^\circ$ , and then starting the next loop at  $\phi_1 = 33^\circ$

end

end

Variation of  $\chi$  with  $M_s$ , along constant  $\theta_w$

Choose  $\theta_w = 5, 10, \dots, 45$ , for example

for each  $M_s$

$$\chi(\theta_w, M_s) = \text{interpolate}(\theta_w(M_s, \chi), \theta_w)$$

For the above calculations we obtain the following functions  $\chi(M_s)$  along constant  $\chi + \theta_w = \pi/2 - \phi_1$  and  $\chi(\theta_w)$  along constant  $M_s$ . Another relation desired but not exactly calculated by this algorithm is  $\chi(M_s)$  along constant  $\theta_w$ . In order to obtain this, the above calculated data points must be interpolated. Given enough points this is accurate.

The below function is iterated upon with the nonlinear equation solver, matching the incident and reflected shock polars when the residual approaches zero.

$$\text{MatchIRPolars}(\phi_3, M_0, p_1/p_0, \gamma, M_1, \theta_1)$$

$$M_{n0} = M_0 \sin(\phi_3) \quad (\text{C.48})$$

$$M_{n3} = \sqrt{\frac{1 + ((\gamma - 1)/2)M_{n0}^2}{\gamma M_{n0}^2 - (\gamma - 1)/2}} \quad (\text{C.49})$$

$$\frac{p_3}{p_0} = 1 + 2\gamma(M_{n0}^2 - 1)/(\gamma + 1) \quad (\text{C.50})$$

$$\theta_3 = \arctan\left(\frac{2 \cot(\phi_3)((M_0 \sin(\phi_3))^2 - 1)}{M_0^2(\gamma + \cos(2\phi_3)) + 2}\right) \quad (\text{C.51})$$

$$M_3 = \frac{M_{n3}}{\sin(\phi_3 - \theta_3)} \frac{p_2}{p_1} = \frac{p_0}{p_1} * \frac{p_3}{p_0} \quad (\text{C.52})$$

$$M_{n1} = \sqrt{\left(\left(\frac{p_2}{p_1} - 1\right)\frac{\gamma + 1}{2\gamma} + 1\right)} \quad (\text{C.53})$$

$$\phi_2 = \arcsin \frac{M_{n1}}{M_1} \quad (\text{C.54})$$

$$\theta_2 = \arctan\left(\frac{2 \cot(\phi_1)((M_1 \sin(\phi_2))^2 - 1)}{M_1^2(\gamma + \cos(2\phi_2)) + 2}\right) \quad (\text{C.55})$$

$$residual = (\theta_1 - \theta_3) - \theta_2 \quad (\text{C.56})$$

### C.3.2 Real Gas Case

Similar to the perfect gas case,  $\phi_1$  and  $M$  are varied in the outer and inner loops. CANTERA and the SDToolbox are used for the real gas normal shock calculations. Also, just as in the general algorithm, a two-dimensional nonlinear equation solver is used to match the i and r shock polars. The below algorithm is for the frozen shock case, at an initial  $q_0, p_0, T_0, M_s$  for a particular real gas model, using a CANTERA mechanism file for the temperature variable thermodynamic properties.

for  $\phi_1 = 30^\circ, 30.5^\circ, \dots, (0 < \phi_1 < 90^\circ)$

for  $M_s = 10, 9.9, 9.8, \dots, (1 < M_s < (M_s)_{max})$

$$M_0 = M_s / \sin(\phi_1)$$

State (0) to State (1): Incident Shock

$$M_{n1} = M_1 \sin(\phi_1)$$

$$(\rho_1, p_1, T_1, q_1, M_{n1}) = Post\_Frozen\_Shock(M_{n0}, p_0, T_0, q_0)$$

$$\theta_1 = \frac{\arctan(\tan(\phi_1)(\frac{p_1}{p_0} - 1))}{(\tan(\phi_1)^2 + \frac{p_1}{p_0})}$$

$$M_1 = \frac{M_{n1}}{\sin(\phi_1 - \theta_1)}$$

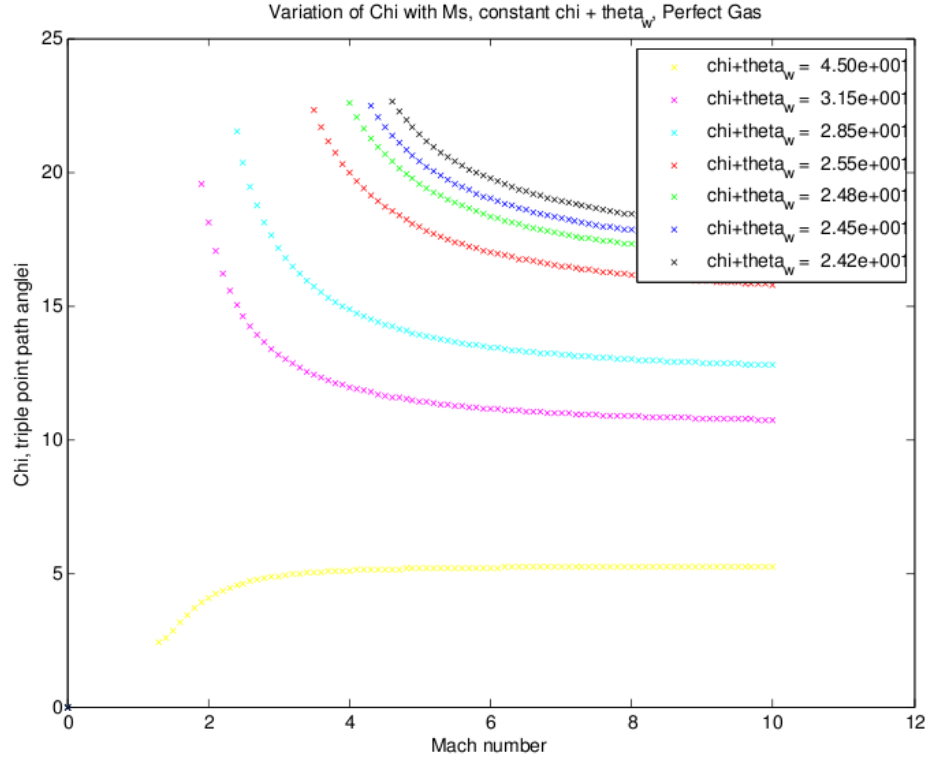


Figure C.7: For  $N_2$  perfect gas:  $\chi(M_s)$  along constant  $\chi + \theta_w = \pi/2 - \phi_1$

if  $M_1 > 1$

Extrapolate for  $\phi_{3guess}$  and  $\phi_{2guess}$

$\phi_3 \leftarrow$  Match I and R Shock Polars

State (0) to State (3): Mach stem

$$M_{n0} = M_0 \sin(\phi_3)$$

$$(\rho_3, p_3, T_3, q_3, M_{n3}) = \text{Post\_Frozen\_Shock}(M_{n0}, p_0, T_0, q_0)$$

$$\theta_3 = \frac{\arctan(\tan(\phi_3)(\frac{\rho_3}{\rho_0} - 1))}{\tan(\phi_3)^2 + \frac{\rho_3}{\rho_0}}$$

$$\theta_2 = \theta_1 - \theta_3$$

Check the RR and vNR transition limits

if  $\theta_3 > 0$  and  $\theta_2 > 0$

$$\chi(M_s, \phi_1) = \pi/2 - \phi_3$$

$$\theta_w(M_s, \phi_1) = \pi/2 - \phi_1 - \chi$$

end

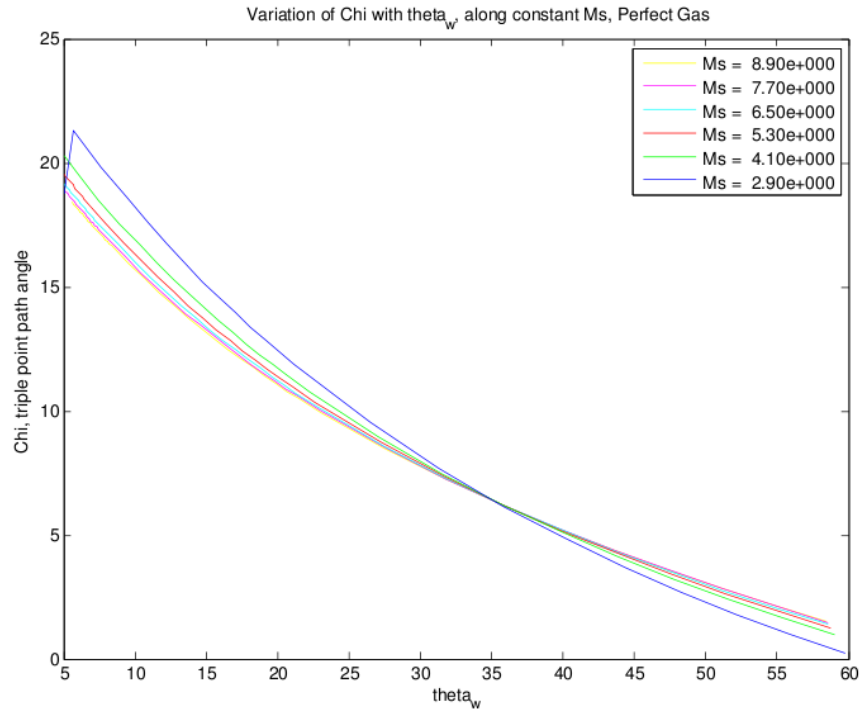


Figure C.8: For  $N_2$  perfect gas:  $\chi(\theta_w)$  along constant  $M_s$

end

Find the variation of  $\chi$  with  $M_s$ , along constant  $\theta_w$

Choose  $\theta_w = 5, 10, \dots, 45$

for each  $M_s$

$$\chi(\theta_w, M_s) = \text{interpolate}(\theta_w(M_s, \chi), \theta_w)$$

*Post\_Frozen\_Shock* calculation using the SDToolbox, example for pre- and post-shock

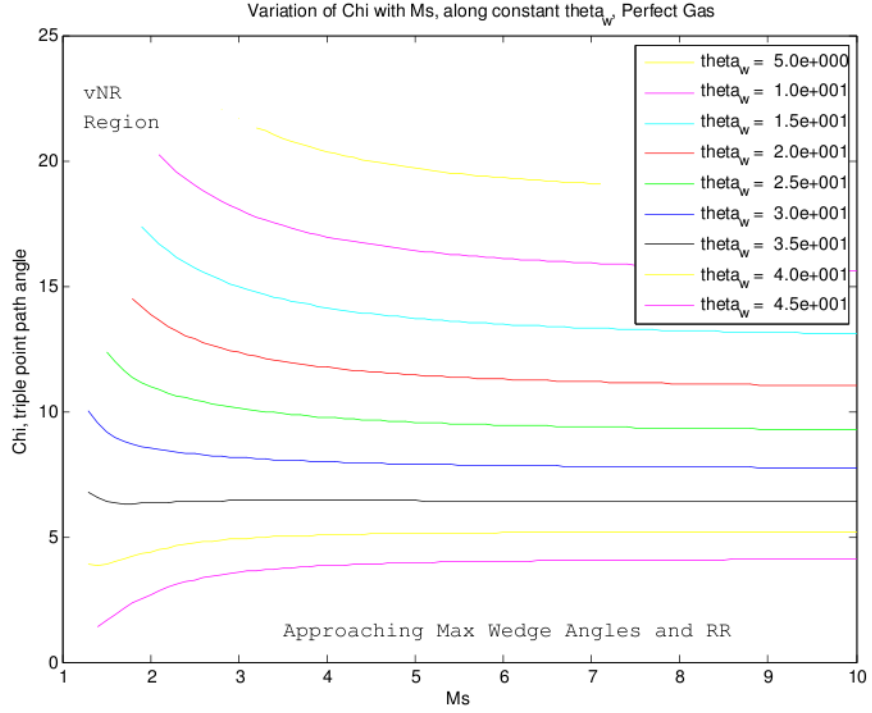


Figure C.9: For  $N_2$  perfect gas:  $\chi(M_s)$  along constant  $\theta_w$

states (0) and (1):

$$set(gas(T_0, p_0, q_0)) \quad (C.57)$$

$$\rho_0 = density(gas1) \quad (C.58)$$

$$a_0 = soundspeed\_frozen(gas1) \quad (C.59)$$

$$u_{0n} = a_0 M_{n0} \quad (C.60)$$

$$(\rho_1, p_1, T_1, q_1, a_1) = frozen\_shock(u_{0n}, p_0, T_0, q_0) \quad (C.61)$$

$$u_{1n} = \frac{\rho_0 u_{0n}}{\rho_1} \quad (C.62)$$

$$M_{n1} = \frac{u_{1n}}{a_1} \quad (C.63)$$

$$(C.64)$$

The below function is iterated upon with the nonlinear equation solver, matching the incident and reflected shock polars when the residual approaches zero.

$$\text{matchIRpolar}(\phi_3, \phi_2, M_0, p_1/p_0, M_1, \theta_1, T_1, p_1, \rho_1, P_0, T_0, \rho_0, q_0)$$

$$M_{n0} = M_0 \sin(\phi_3) \quad (\text{C.65})$$

$$(\rho_3, p_3, T_3, q_3, M_{n3}) = \text{Post\_Equilibrium\_Shock}(M_{n0}, p_0, T_0, q_0) \quad (\text{C.66})$$

$$\theta_3 = \frac{\arctan(\tan(\phi_3)(\frac{\rho_3}{\rho_0} - 1))}{\tan(\phi_3)^2 + \frac{\rho_3}{\rho_0}} \quad (\text{C.67})$$

$$M_3 = \frac{M_{n3}}{\sin(\phi_3 - \theta_3)} \text{Error}(\phi_2) \leftarrow \phi_2(M_1, \theta_2, \text{gas}, T_1, p_1, q_1) \quad (\text{C.68})$$

$$M_2 = \frac{M_{n2}}{\sin(\phi_2 - \theta_2)} \quad (\text{C.69})$$

$$M_{n1} = M_1 \sin(\phi_2) \quad (\text{C.70})$$

$$(\rho_2, p_2, T_2, q_2, M_{n2}) = \text{Post\_Equilibrium\_Shock}(M_{n1}, p_1, T_1, q_1) \quad (\text{C.71})$$

$$\text{residual}(1) \leftarrow \frac{p_0}{p_1} \frac{p_1}{p_2} - \frac{p_0}{p_3} \quad (\text{C.72})$$

$$\text{residual}(2) \leftarrow \text{Error}(\phi_2) \quad (\text{C.73})$$

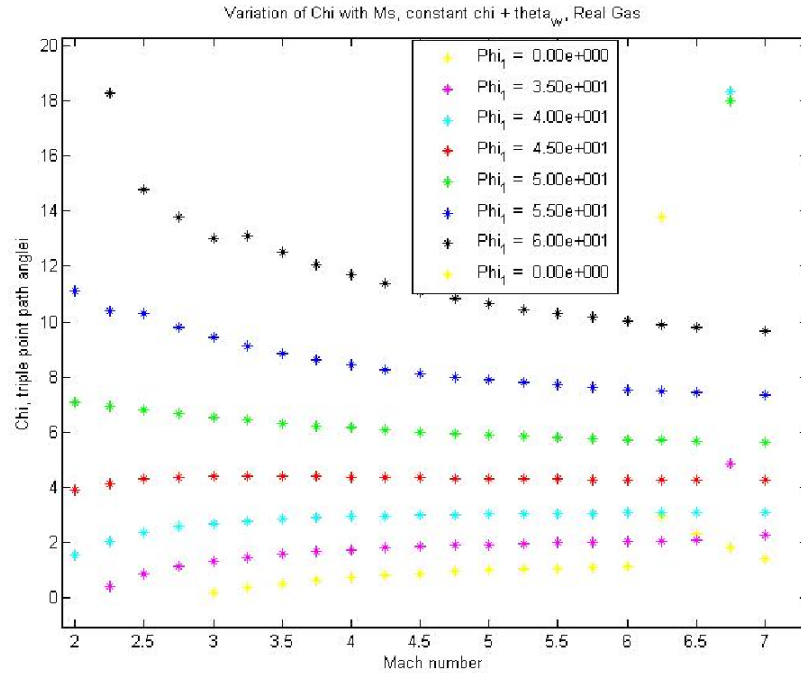


Figure C.10: Law and Glass algorithm  $\chi(M)$  along constant  $\phi_1$ , real gas results for  $\text{N}_2$  imperfect gas (frozen):  $\chi(M_s)$  along constant  $\chi + \theta_w = \pi/2 - \phi_1$

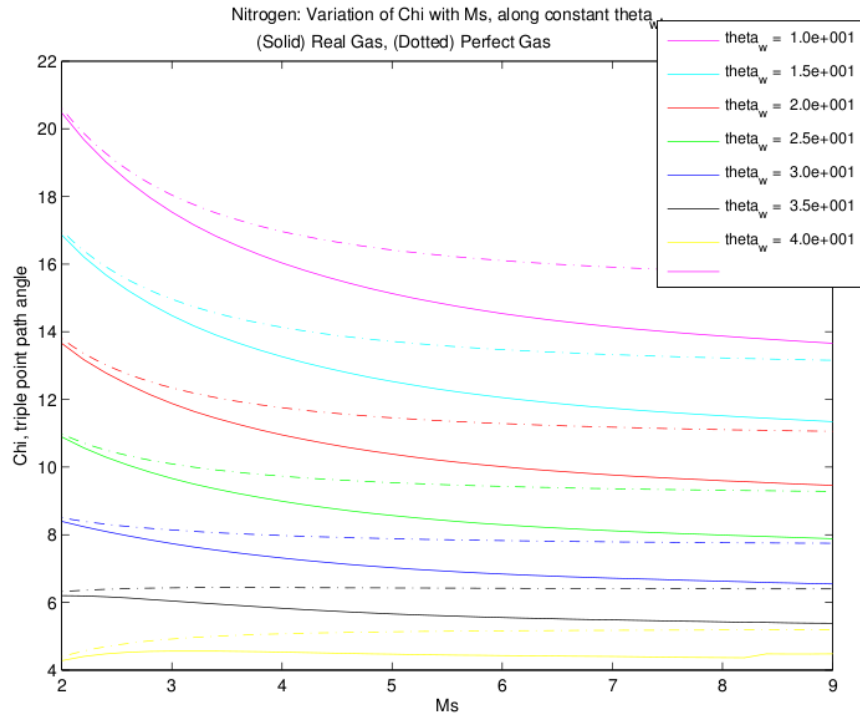


Figure C.11: Law and Glass algorithm  $\chi(M)$  along constant  $\theta_w$ , real gas results for  $N_2$  imperfect gas (frozen):  $\chi(M_s)$  along constant  $\theta_w$



### C.3.3 Comparison of Results with Ben-Dor and Glass

The real gas results from the implementation of the Law and Glass algorithm have been compared to the results from (18). In figure C.12, the calculated results are compared for  $N_2$  with equilibrium chemistry across the shock waves. In both models the specific heat is a function of temperature, and the diatomic nitrogen is modeled to dissociate more and more into monatomic nitrogen at higher temperatures. The results are equivalently the same, while allowing for the errors gathered while visually picking the data points from Ben-Dor's plot.

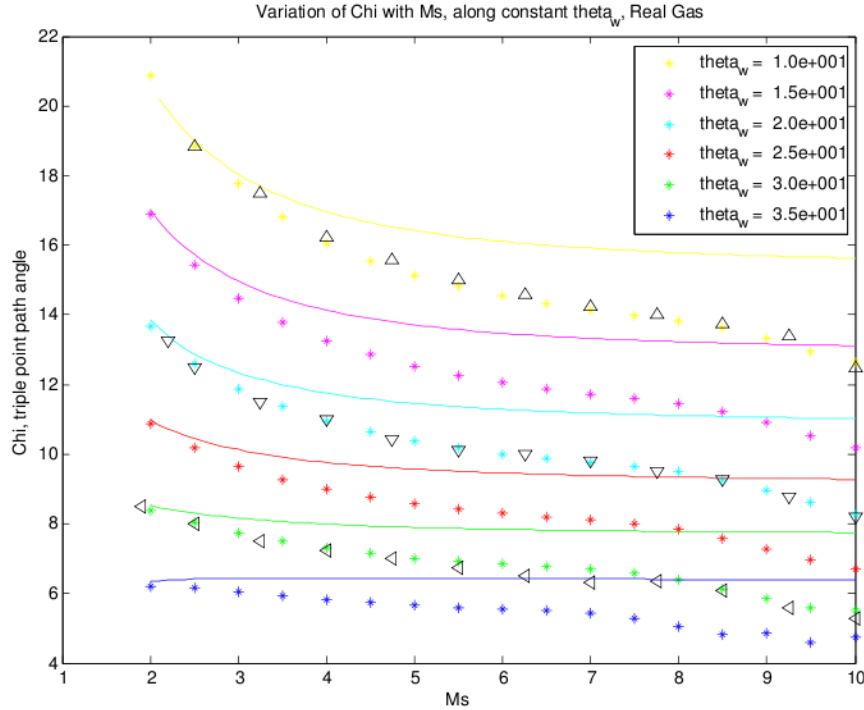


Figure C.12: Comparing Law and Glass algorithm  $N_2$  results with Ben-Dor and Glass's results for  $N_2$  imperfect gas (equilibrium chemistry,  $T = 300K$ ,  $p = 2000Pa$ ):  $\chi(M_s)$  along constant  $\theta_w$ . The triangle's correspond to the computational results from (18)

The real gas results from the implementation of the Law and Glass algorithm have also been compared to the experimental data from (18). In figure C.13, the calculated results are compared for imperfect air ( $q_0 = (N_2:3.76, O_2:1)$ ) with equilibrium chemistry across the shock waves, and perfect air with a specific heat ration of  $\frac{7}{5}$ . The results are very different and appear so even for Ben-Dor. This shows the limitations of the assumptions used in the three shock theory for the MR problem.

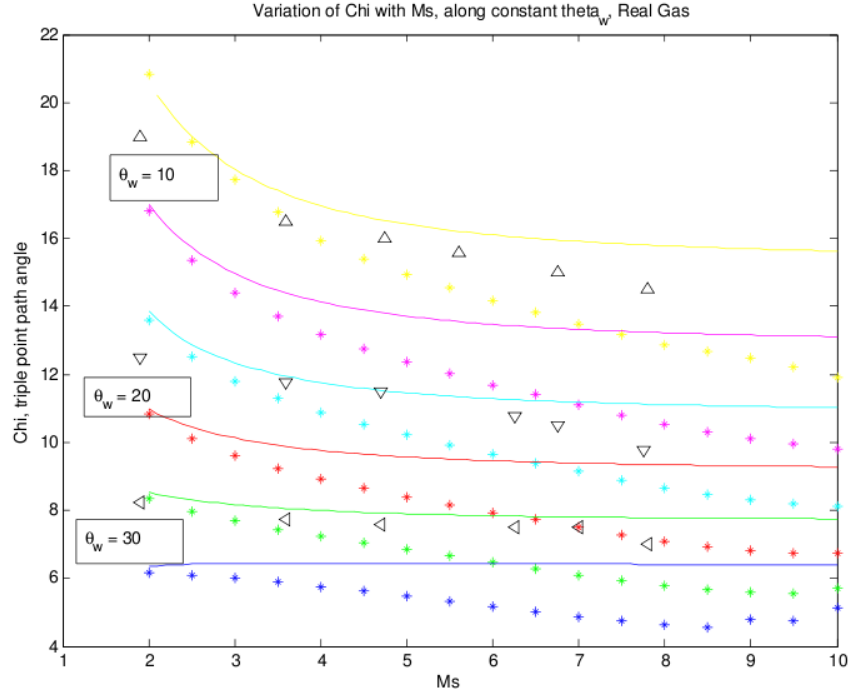


Figure C.13: Comparing Law and Glass algorithm air results with Ben-Dor and Glass's experimental results for air with perfect and imperfect gas models (equilibrium chemistry,  $T = 300$  K,  $p = 2000$  Pa):  $\chi(M_s)$  along constant  $\theta_w$ . The triangle's correspond to the experimental results from (18), at  $10^\circ$ ,  $20^\circ$ , and  $30^\circ$  wedge angles.

As shown in figure C.11, the real and perfect gas models for  $N_2$  were compared. At low Mach numbers (equivalently lower temperatures), the real gas effects are small and the solutions are seen to approach each other. At larger Mach numbers the solutions diverge as the nonconstant enthalpy of the imperfect nitrogen is the most different from the constant specific heat value a higher temperatures.

## Appendix D

# Viscous Flow Physics

In this section theory on free shear layers is discussed in detail. Using approximate analytical methods to calculate boundary layer thicknesses and inviscid shear layer instabilities was useful for increasing the confidence and understanding the the Mach reflection simulations where shear and mixing layers are created at the triple points.

### D.1 Blasius Solution

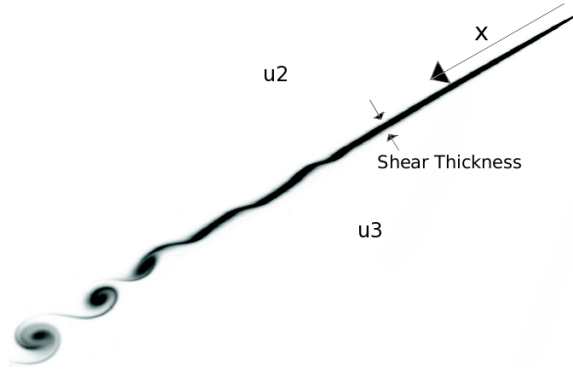


Figure D.1: Vorticity in the Mixing layer

Directly behind the triple point, as shown in figure [D.1](#), the flow is laminar and the Reynolds number is high. Therefore, for constant viscosity, the boundary layer equations apply. The similarity solution obeys the same ODE as the well-known Blasius flat plat case, with the difference being the boundary conditions for the free Blasius mixing layer.

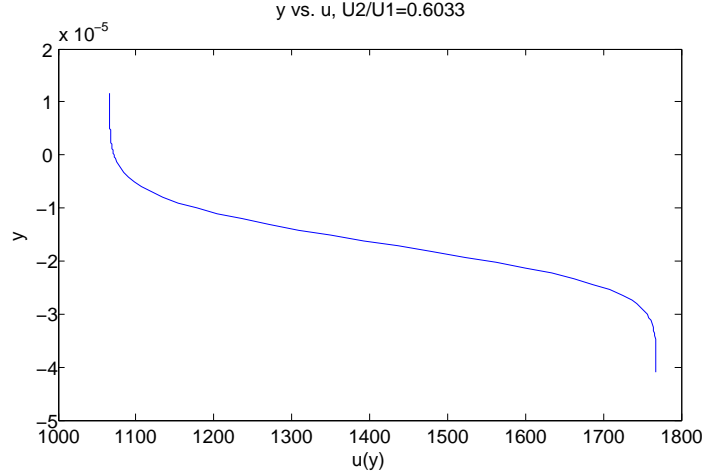


Figure D.2: Blasius laminar mixing layer solution

$$\eta = y \sqrt{\frac{U}{2\nu x}}, \quad (\text{D.1})$$

$$\psi = \sqrt{2\nu x U} f(\eta), \quad (\text{D.2})$$

$$\nu = \frac{\mu}{\rho}, \quad (\text{D.3})$$

$$u = \frac{\partial \psi}{\partial y} = U f'(\eta), \quad (\text{D.4})$$

$$v = -\frac{\partial \psi}{\partial x} = \sqrt{\frac{U}{2\nu x}} (\eta f'(\eta) - f), \quad (\text{D.5})$$

$$(\text{D.6})$$

when the stream function  $\psi$  is substituted into the boundary layer equations, the Blasius ODE is obtained in terms of the dimensionless stream function  $f$ . Integration of this ODE with the proper BCs leads to solution  $f$  in terms of the similarity variable  $\eta$ , for which the velocities,  $u$  and  $v$  can be found. Now, let  $U$  be the velocity of the high speed region behind the Mach stem (note this is not in the triple point frame of reference, yet the results are equivalent with a reference frame change) and let  $\lambda U$  be the slower velocity behind the reflected shock on top of the mixing layer. Then the boundary conditions follow as

$$\eta \rightarrow +\infty : f' = \lambda, \quad (\text{D.7})$$

$$\eta \rightarrow -\infty : f' = 1, \quad (\text{D.8})$$

$$\lim(\eta \rightarrow -\infty) : (\eta - f) = \lim(\eta \rightarrow +\infty) : -\lambda(\eta\lambda - f). \quad (\text{D.9})$$

The last boundary condition comes from a global momentum balance across the  $y$  direction of the boundary layer where  $v_{-\infty} = -\lambda v_{\infty}$ . (140)

This boundary value problem was solved in MATLAB using an iterative newton solver around an ODE integrator. The ODE is third order, and is put in vector form as follows,

$$y_1 = f, \quad (\text{D.10})$$

$$y_2 = \frac{df}{d\eta}, \quad (\text{D.11})$$

$$y_3 = \frac{d^2 f}{d\eta^2} = \frac{d}{d\eta} \left( \frac{df}{d\eta} \right), \quad (\text{D.12})$$

$$Y = [y_1, y_2, y_3], \quad (\text{D.13})$$

$$\frac{dY}{d\eta} = [y_2, y_3, -y_1 y_3]. \quad (\text{D.14})$$

The algorithm is as follows. One guesses the solution of  $y_1$ ,  $y_2$ , and  $y_3$  at  $\eta = 0$  and solves two Blasius boundary layers toward positive and negative infinity. For a  $\lambda$  value of  $0.6033 \pm 6$  is sufficient for an approximate infinity. At plus and minus “infinity” the third boundary condition is evaluated, yielding an error estimate for the Newton iteration. The solution of  $u(y)$  for  $\lambda = 0.6033$  and  $\nu = \frac{\mu}{\rho} = 3.035e - 5$  evaluated at  $x = 0.001m$  is shown in figure D.1.

## D.2 Von Karman Momentum-Integral Technique

The mixing thickness can be obtained using the von Karman momentum-integral technique (15). It is assumed in the that the flows on both sides of the shear layer are incompressible and that there is no pressure gradient along the layer. The upper and lower velocities,  $u_2$  and  $u_3$ , are assumed to have a laminar profile and are approximated with third order polynomials. The coefficients for the upper slower fluid are determined with the boundary conditions,

$$u(y = \delta_2) = V_2, u(y = \delta_2) = V_c, \quad (\text{D.15})$$

$$\frac{\partial^2 u}{\partial y^2}(y = \delta_2) = 0, \frac{\partial^2 u}{\partial y^2}(y = 0) = 0, \quad (\text{D.16})$$

where  $\delta_2$  is the displacement thickness and  $V_c$  is the velocity at the interface. This leads to,

$$u_2 = \frac{1}{2}V_2(\eta_2 - 1)\left(\frac{y}{\delta_2}\right)^3 - \frac{3}{2}V_2(\eta_2 - 1)\left(\frac{y}{\delta_2}\right) + V_c, \quad (\text{D.17})$$

and similarly for the lower fluid,

$$u_3 = \frac{1}{2}V_3(\eta_3 - 1)\left(\frac{y}{\delta_3}\right)^3 - \frac{3}{2}V_3(\eta_3 - 1)\left(\frac{y}{\delta_3}\right) + V_c, \quad (\text{D.18})$$

where  $\eta_2 = V_c/V_2$  and  $\eta_3 = V_c/V_3$  are yet to be determined, yet it is known that

$$\frac{\eta_2}{\eta_3} = \frac{V_3}{V_2}. \quad (\text{D.19})$$

These velocity profiles are substituted into the von Karman momentum integral to get the following result,

$$\mu_i \frac{\partial u_i}{\partial y_i} \Big|_{y_i=0} = \partial \partial x \int_0^{\delta_i} (u_i^2 - u_i V_i) dy \quad (\text{D.20})$$

$$\frac{\delta_i}{x} = \left( \frac{280}{22\eta_i + 13} \right)^{\frac{1}{2}} (Re_{ix})^{-\frac{1}{2}}. \quad (\text{D.21})$$

Now, to determine  $\eta_2$  and  $\eta_3$  the magnitudes of the displacement thicknesses for the upper and lower fluids are matched. This yields a nonlinear algebraic equation relating the unknowns to the far field ratios of density, viscosity, and velocity.

$$\frac{1 - \eta_2}{\eta_3 - 1} \left( \frac{22\eta_3 + 13}{22\eta_2 + 13} \right)^{\frac{1}{2}} = \left( \frac{\mu_3 \rho_2 V_2}{\mu_2 \rho_3 V_3} \right)^{\frac{1}{2}} \quad (\text{D.22})$$

One then solves this equation along with  $\frac{\eta_2}{\eta_3} = \frac{V_3}{V_2}$  to obtain the displacement thickness above and below the mixing layer. The total length scale of the mixing layer is simply the sum of the two. The utility of von Karman integral method is that it approximates the effects of the density difference across the layer, unlike the Blasius method for which an average density was used. Of equal importance is that it also allows for the viscosity to be different. The lower fluid is much hotter than the upper fluid yielding a physically unnegligible change in viscosity. Yet, for the sake of simplicity, the total displacement thick was calculated and shown in figure [D.3](#).

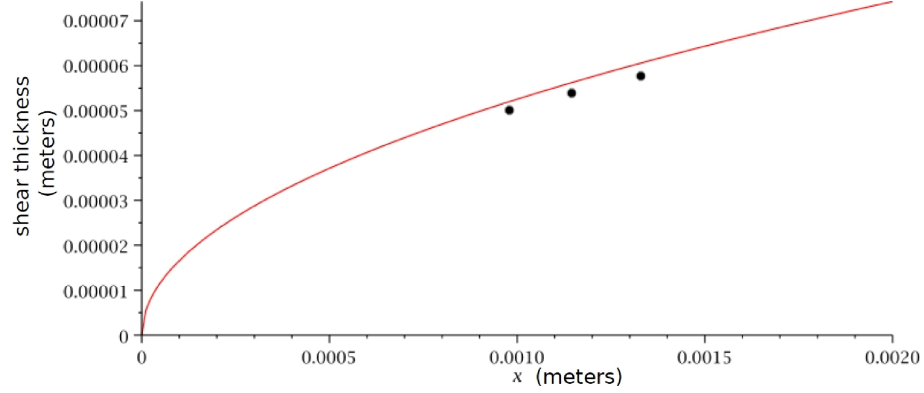


Figure D.3: Laminar mixing layer thickness as a function of distance from the triple point, von Karman momentum-integral technique

### D.3 Inviscid Mixing Layer Linear Stability

The initial growth of a laminar free shear/mixing layer depends on effects of the linearized inviscid instability mode. This linearized growth rate is a function of the density ratio, velocity ratio, and a convective Mach number (149). The convective mach number is found by considering a pair of vortices that are convecting at a common speed. In this case there is a stagnation point of common pressure where

$$\left(1 + \frac{\gamma_1 - 1}{2} M_{c1}^2\right)^{\frac{\gamma_1}{\gamma_1 - 1}} = \left(1 + \frac{\gamma_2 - 1}{2} M_{c2}^2\right)^{\frac{\gamma_2}{\gamma_2 - 1}}, \quad (\text{D.23})$$

with  $M_{c1} = (U_1 - U_c)/a_1$  and  $M_{c2} = (U_2 - U_c)/a_2$  as the convective Mach numbers in the top and bottom fluids. For low convective Mach numbers,

$$M_{c1} = \left(\frac{\gamma_1}{\gamma_2}\right)^{\frac{1}{2}} M_{c2}. \quad (\text{D.24})$$

In the case  $\gamma_1 = \gamma_2$ ,

$$\frac{U_c}{U_1} = \frac{1 + q\sqrt{s}}{1 + \sqrt{s}}, \quad (\text{D.25})$$

where  $s = \rho_2/\rho_1$  and  $q = U_2/U_1$ . Also if the flow is isentropic,  $M_{c1} = M_{c2} = M_c$ ,

$$M_c = \frac{\Delta U}{a_1 + a_2}, \quad (\text{D.26})$$

$$U_c = \frac{a_2 U_1 + a_1 U_2}{a_1 + a_2}. \quad (\text{D.27})$$

Note that in this analysis,  $U_c$  is the speed of the stagnation point, not the speed of the eddies themselves. Now, to get a growth rate for the size of the eddies, we assume for a subsonic variable density mixing layer that the turbulent diffusion rate is constant in a frame of reference convected by the eddies and that the spreading rate is inversely proportional to the convection velocity,

$$\frac{\delta}{x} = \delta'_0 \propto \frac{\Delta U}{U_c}, \quad (\text{D.28})$$

$$\delta'_0 = \delta'_{ref} \frac{(1-q)(1+\sqrt{s})}{2(1+q\sqrt{s})}, \quad (\text{D.29})$$

where  $\delta'_{ref}$  is the spreading rate for  $s = 1$  and  $U_2 = 0$ . This result is only valid for low Mach numbers. For higher Mach numbers it is found that this growth rate scales with an empirical function that depends solely on the convective Mach number. Dimotakis's semi-empirical relation for this function is commonly used. With a  $\delta'_{ref}$  of 0.16,  $s = 1.431$  and  $q = 0.6029$  the resulting growth rate dependence on  $M_c$  is shown in figure D.3.

$$\delta'_0 = \delta'_{ref} \frac{(1-q)(1+\sqrt{s})}{2(1+q\sqrt{s})} \Phi(M_c), \quad (\text{D.30})$$

$$\Phi(M_c) = 0.8e^{-M_c^2} + 0.2. \quad (\text{D.31})$$



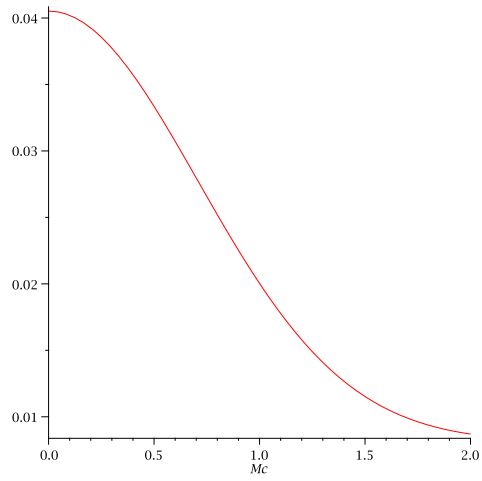


Figure D.4: Inviscid growth rate dependence on the convective Mach number for  $\delta'_{ref} = 0.16$ ,  $s = 1.431$ , and  $q = 0.6029$

# Appendix E

## Reduced CHEMKIN Mechanisms

### E.1 Reduced Propane-Air Mechanism

#### E.1.1 Chemistry

ELEMENTS

N H O C

END

SPECIES

C3H8 O2 N2 H O OH H2 H2O CO2 H2O2

CO HCO TCH2 CH3 CH2O HCCO

C2H2 CH4 C2H3 C2H4

C2H5 NC3H7

END

REACTIONS

H+O2 = O+OH 2.640e+16 -0.670 17041.11

O+H2 = H+OH 4.590e+04 2.700 6259.56

OH+H2 = H+H2O 1.730e+08 1.510 3429.73

2OH = O+H2O 3.970e+04 2.400 -2110.42

H+OH+M = H2O+M 4.400e+22 -2.000 0.000

CH4/2.00/ CO/1.75/ CO2/3.60/ H2/2.00/ H2O/6.30/

H+O2(+M) = H2O(+M) 5.120e+12 0.440 0.00

O2/0.85/ H2/0.75/ H2O/11.89/ CO2/2.18/ CO/1.09/

LOW / 6.330e+19 -1.400 0.00 /

TR0E/ 0.5 0.00 10000000000.00 /

H2+O2 = H2O+H 5.920e+05 2.430 53501.43

H2O+H = 2OH 7.490e+13 0.000 635.76

H2O+OH = H2O+O2 1.000e+16 0.000 17330.31

CO+OH = CO2+H 8.000e+11 0.140 7351.82

DUPLICATE

CO+OH = CO2+H 8.780e+10 0.030 -16.73

DUPLICATE

HCO+H = CO+H2 1.200e+14 0.000 0.00

HCO+OH = CO+H2O 3.020e+13 0.000 0.00

HCO+M = CO+H+M 1.870e+17 -1.000 17000.48

H2/2.00/ H2O/0.00/ CO2/3.60/ CO/1.75/ CH4/2.00/

HCO+H2O = CO+H+H2O 2.240e+18 -1.000 17000.48

HCO+O2 = CO+H2O2 1.200e+10 0.810 -726.58

TCH2+O = HCO+H 8.000e+13 0.000 0.00

TCH2+OH = CH20+H	2.000e+13	0.000	0.00
TCH2+O2 => CO2+2H	5.800e+12	0.000	1500.96
TCH2+O2 = CH20+O	2.400e+12	0.000	1500.96
TCH2+O2 => OH+H+CO	5.000e+12	0.000	1500.96
2TCH2 = C2H2+H2	1.600e+15	0.000	11943.12
CH20+H = HCO+H2	5.740e+07	1.900	2741.40
CH20+OH = HCO+H2O	3.430e+09	1.180	-446.94
CH3+H(+M) = CH4(+M)	6.920e+13	0.180	0.00
H2/2.00/ H2O/6.00/ CO2/2.00/ CO/1.50/ CH4/3.00/			
LOW / 3.470e+38 -6.300 5074.09 /			
TROE/ 0.783 74.00 2941.00 6964.00 /			
CH3+O = CH20+H	5.060e+13	0.000	0.00
CH3+O => H+H2+CO	3.370e+13	0.000	0.00
CH3+OH = TCH2+H2O	5.600e+07	1.600	5420.65
CH3+TCH2 = C2H4+H	1.000e+14	0.000	0.00
2CH3 = C2H5+H	6.840e+12	0.100	10599.90
CH4+H = CH3+H2	6.600e+08	1.620	10841.30
CH4+OH = CH3+H2O	1.000e+08	1.600	3119.02
HCCO+O = H+2CO	1.000e+14	0.000	0.00
HCCO+TCH2 = C2H3+CO	3.000e+13	0.000	0.00
C2H2+H(+M) = C2H3(+M)	1.710e+10	1.270	2707.93
H2/2.00/ H2O/12.00/ CO2/3.60/ CO/1.75/ CH4/2.00/			
LOW / 6.340e+31 -4.660 3781.07 /			
TROE/ 0.2122 1.00 -10212.00 /			
C2H2+O = HCCO+H	8.100e+06	2.000	1900.10
C2H2+O = TCH2+CO	1.250e+07	2.000	1900.10
C2H3+H = C2H2+H2	3.000e+13	0.000	0.00
C2H3+O2 = C2H2+HO2	1.340e+06	1.610	-384.80
C2H3+O2 = HCO+CH2O	4.580e+16	-1.390	1015.77
C2H4+H(+M) = C2H5(+M)	1.370e+10	1.460	1355.16
H2/2.00/ H2O/12.00/ CO2/3.60/ CO/1.75/ CH4/2.00/			
LOW / 4.060e+39 -6.640 5769.60 /			
TROE/ -0.569 299.00 -9147.00 152.40 /			
C2H4+H = C2H3+H2	1.270e+05	2.750	11649.14
C2H4+O = TCH2+CH2O	7.150e+04	2.470	929.73
C2H4+O = CH3+HCO	3.890e+08	1.360	886.71
C2H4+OH = C2H3+H2O	1.310e-01	4.200	-860.42
C2H4+CH3(+M) = NC3H7(+M)	2.550e+06	1.600	5700.29
H2/2.00/ H2O/12.00/ CO2/3.60/ CO/1.75/ CH4/2.00/			
LOW / 3.000e+63 -14.600 18169.22 /			
TROE/ 0.1894 277.00 8748.00 7891.00 /			
C2H5+O2 = C2H4+HO2	1.920e+07	1.020	-2033.94
C3H8(+M) = C2H5+CH3(+M)	1.290e+37	-5.840	97387.67
H2/2.00/ H2O/12.00/ CO2/3.60/ CO/1.75/ CH4/2.00/			
LOW / 1.1000e+74 -15.740 98718.93 /			
TROE/ 0.31 50.00 3000.00 9000.00 /			
NC3H7+O = C2H5+CH2O	3.170e+13	0.030	-394.36
C3H8+H = NC3H7+H2	5.800e-02	4.710	6211.76
C3H8+OH = NC3H7+H2O	5.360e+06	2.010	365.68
HCCO+CH3 = C2H4+CO	5.000e+13	0.000	0.00
HCCO+OH = 2 HCO	1.000e+13	0.000	0.00

END

## E.1.2 Thermodynamics

### THERMO

	298.000	1000.000	5000.000								
N2	121286N	2		G	0300.00	5000.00	1000.00				1
	0.02926640E+02	0.14879768E-02	-0.05684760E-05	0.10097038E-09	-0.06753351E-13						2
	-0.09227977E+04	0.05980528E+02	0.03298677E+02	0.14082404E-02	-0.03963222E-04						3
	0.05641515E-07	-0.02444854E-10	-0.10208999E+04	0.03950372E+02							4
O	L 1/900	1	00	00	00G	200.000	3500.000	1000.000			1
	2.56942078E+00	-8.59741137E-05	4.19484589E-08	-1.00177799E-11	1.22833691E-15						2
	2.92175791E+04	4.78433864E+00	3.16826710E+00	-3.27931884E-03	6.64306396E-06						3
	-6.12806624E-09	2.11265971E-12	2.91222592E+04	2.05193346E+00	6.72540300E+03						4
O2	TPIS890	2	00	00	00G	200.000	3500.000	1000.000			1
	3.28253784E+00	1.48308754E-03	-7.57966669E-07	2.09470555E-10	-2.16717794E-14						2
	-1.08845772E+03	5.45323129E+00	3.78245636E+00	-2.99673416E-03	9.84730201E-06						3
	-9.68129509E-09	3.24372837E-12	-1.06394356E+03	3.65767573E+00	8.68010400E+03						4
H	L 7/88H	1	00	00	00G	200.000	3500.000	1000.00			1
	2.50000001E+00	-2.30842973E-11	1.61561948E-14	-4.73515235E-18	4.98197357E-22						2
	2.54736599E+04	-4.46682914E-01	2.50000000E+00	7.05332819E-13	-1.99591964E-15						3
	2.30081632E-18	-9.27732332E-22	2.54736599E+04	-4.46682853E-01	6.19742800E+03						4
H2	TPIS78H	2	00	00	00G	200.000	3500.000	1000.00			1
	3.33727920E+00	-4.94024731E-05	4.99456778E-07	-1.79566394E-10	2.00255376E-14						2
	-9.50158922E+02	-3.20502331E+00	2.34433112E+00	7.98052075E-03	-1.94781510E-05						3
	2.01572094E-08	-7.37611761E-12	-9.17935173E+02	6.83010238E-01	8.46810200E+03						4
OH	S 9/010	1H	1	0	OG	200.000	6000.000	1000.00			1
	2.86472886E+00	1.05650448E-03	-2.59082758E-07	3.05218674E-11	-1.33195876E-15						2
	3.71885774E+03	5.70164073E+00	4.12530561E+00	-3.22544939E-03	6.52764691E-06						3
	-5.79853643E-09	2.06237379E-12	3.38153812E+03	-6.90432960E-01	4.51532273E+03						4
H2O	L 8/89H	20	1	00	00G	200.000	3500.000	1000.000			1
	3.03399249E+00	2.17691804E-03	-1.64072518E-07	-9.70419870E-11	1.68200992E-14						2
	-3.00042971E+04	4.96677010E+00	4.19864056E+00	-2.03643410E-03	6.52040211E-06						3
	-5.48797062E-09	1.77197817E-12	-3.02937267E+04	-8.49032208E-01	9.90409200E+03						4
HO2	L 5/89H	10	2	00	00G	200.000	3500.000	1000.000			1
	4.01721090E+00	2.23982013E-03	-6.33658150E-07	1.14246370E-10	-1.07908535E-14						2
	1.11856713E+02	3.78510215E+00	4.30179801E+00	-4.74912051E-03	2.11582891E-05						3
	-2.42763894E-08	9.29225124E-12	2.94808040E+02	3.71666245E+00	1.00021620E+04						4
TCH2	L S/93C	1H	2	00	00G	200.000	3500.000	1000.000			1
	2.87410113E+00	3.65639292E-03	-1.40894597E-06	2.60179549E-10	-1.87727567E-14						2
	4.62636040E+04	6.17119324E+00	3.76267867E+00	9.68872143E-04	2.79489841E-06						3
	-3.85091153E-09	1.68741719E-12	4.60040401E+04	1.56253185E+00	1.00274170E+04						4
CH3	L11/89C	1H	3	00	00G	200.000	3500.000	1000.000			1
	2.28571772E+00	7.23990037E-03	-2.98714348E-06	5.95684644E-10	-4.67154394E-14						2
	1.67755843E+04	8.48007179E+00	3.67359040E+00	2.01095175E-03	5.73021856E-06						3
	-6.87117425E-09	2.54385734E-12	1.64449988E+04	1.60456433E+00	1.03663400E+04						4
CH4	L 8/88C	1H	4	00	00G	200.000	3500.000	1000.000			1
	7.48514950E-02	1.33909467E-02	-5.73285809E-06	1.22292535E-09	-1.01815230E-13						2
	-9.46834459E+03	1.84373180E+01	5.14987613E+00	-1.36709788E-02	4.91800599E-05						3
	-4.84743026E-08	1.66693956E-11	-1.02466476E+04	-4.64130376E+00	1.00161980E+04						4
CO	TPIS79C	10	1	00	00G	200.000	3500.000	1000.000			1
	2.71518561E+00	2.06252743E-03	-9.98825771E-07	2.30053008E-10	-2.03647716E-14						2
	-1.41518724E+04	7.81868772E+00	3.57953347E+00	-6.10353680E-04	1.01681433E-06						3
	9.07005884E-10	-9.04424499E-13	-1.43440860E+04	3.50840928E+00	8.67100000E+03						4
CO2	L 7/88C	10	2	00	00G	200.000	3500.000	1000.000			1
	3.85746029E+00	4.41437026E-03	-2.21481404E-06	5.23490188E-10	-4.72084164E-14						2
	-4.87591660E+04	2.27163806E+00	2.35677352E+00	8.98459677E-03	-7.12356269E-06						3

```

2.45919022E-09-1.43699548E-13-4.83719697E+04 9.90105222E+00 9.36546900E+03 4
HCO          L12/89H  1C  10  1  00G  200.000  3500.000  1000.000  1
2.77217438E+00 4.95695526E-03-2.48445613E-06 5.89161778E-10-5.33508711E-14 2
4.01191815E+03 9.79834492E+00 4.22118584E+00-3.24392532E-03 1.37799446E-05 3
-1.33144093E-08 4.33768865E-12 3.83956496E+03 3.39437243E+00 9.98945000E+03 4
CH2O         L 8/88H  2C  10  1  00G  200.000  3500.000  1000.000  1
1.76069008E+00 9.20000082E-03-4.42258813E-06 1.00641212E-09-8.83855640E-14 2
-1.39958323E+04 1.36563230E+01 4.79372315E+00-9.90833369E-03 3.73220008E-05 3
-3.79285261E-08 1.31772652E-11-1.43089567E+04 6.02812900E-01 1.00197170E+04 4
C2H2         L 1/91C  2H  2  00  00G  200.000  3500.000  1000.000  1
4.14756964E+00 5.96166664E-03-2.37294852E-06 4.67412171E-10-3.61235213E-14 2
2.59359992E+04-1.23028121E+00 8.08681094E-01 2.33615629E-02-3.55171815E-05 3
2.80152437E-08-8.50072974E-12 2.64289807E+04 1.39397051E+01 1.00058390E+04 4
C2H3         L 2/92C  2H  3  00  00G  200.000  3500.000  1000.000  1
3.01672400E+00 1.03302292E-02-4.68082349E-06 1.01763288E-09-8.62607041E-14 2
3.46128739E+04 7.78732378E+00 3.21246645E+00 1.51479162E-03 2.59209412E-05 3
-3.57657847E-08 1.47150873E-11 3.48598468E+04 8.51054025E+00 1.05750490E+04 4
C2H4         L 1/91C  2H  4  00  00G  200.000  3500.000  1000.000  1
2.03611116E+00 1.46454151E-02-6.71077915E-06 1.47222923E-09-1.25706061E-13 2
4.93988614E+03 1.03053693E+01 3.95920148E+00-7.57052247E-03 5.70990292E-05 3
-6.91588753E-08 2.69884373E-11 5.08977593E+03 4.09733096E+00 1.05186890E+04 4
C2H5         L12/92C  2H  5  00  00G  200.000  3500.000  1000.000  1
1.95465642E+00 1.73972722E-02-7.98206668E-06 1.75217689E-09-1.49641576E-13 2
1.28575200E+04 1.34624343E+01 4.30646568E+00-4.18658892E-03 4.97142807E-05 3
-5.99126606E-08 2.30509004E-11 1.28416265E+04 4.70720924E+00 1.21852440E+04 4
HCCO         SRIC91H  1C  20  1  G  0300.00  4000.00  1000.00  1
0.56282058E+01 0.40853401E-02-0.15934547E-05 0.28626052E-09-0.19407832E-13 2
0.19327215E+05-0.39302595E+01 0.22517214E+01 0.17655021E-01-0.23729101E-04 3
0.17275759E-07-0.50664811E-11 0.20059449E+05 0.12490417E+02 4
C3H8         P11/94C  3H  8  0  OG  300.000  3000.000  1
0.75244152E+01 0.18898282E-01-0.62921041E-05 0.92161457E-09-0.48684478E-13 2
-0.16564394E+05-0.17838375E+02 0.92851093E+00 0.26460566E-01 0.60332446E-05 3
-0.21914953E-07 0.94961544E-11-0.14057907E+05 0.19225538E+02 4
NC3H7        P11/94C  3H  7  0  OG  300.000  3000.000  1
0.77097479E+01 0.16031485E-01-0.52720238E-05 0.75888352E-09-0.38862719E-13 2
0.79762236E+04-0.15515297E+02 0.10491173E+01 0.26008973E-01 0.23542516E-05 3
-0.19595132E-07 0.93720207E-11 0.10312346E+05 0.21136034E+02 4
ENDOFDATA

```

## E.1.3 Transport

! \*\* Transport properties taken from \*\*

!

! " An optimized kinetic model of H2/CO combustion"

! Davis, Joshi, Wang, and Egolfopoulos

! Proc. Comb. Inst. 30 (2005) 1283-1292

!

N2	1	97.530	3.621	0.000	1.760	4.000
H	0	145.000	2.050	0.000	0.000	0.000
H2	1	38.000	2.920	0.000	0.790	280.000
H2O	2	572.400	2.605	1.844	0.000	4.000
HO2	2	107.400	3.458	0.000	0.000	1.000
O	0	80.000	2.750	0.000	0.000	0.000
O2	1	107.400	3.458	0.000	1.600	3.800

OH	1	80.000	2.750	0.000	0.000	0.000
CO	1	98.100	3.650	0.000	1.950	1.800
CO2	1	244.000	3.763	0.000	2.650	2.100
HCO	2	498.000	3.590	0.000	0.000	0.000
TCH2	1	144.000	3.800	0.000	0.000	0.000
CH3	1	144.000	3.800	0.000	0.000	0.000
CH4	2	141.400	3.746	0.000	2.600	13.000
CH2O	2	498.000	3.590	0.000	0.000	2.000
C2H2	1	209.000	4.100	0.000	0.000	2.500
C2H3	2	209.000	4.100	0.000	0.000	1.000
C2H4	2	280.800	3.971	0.000	0.000	1.500
C2H5	2	252.300	4.302	0.000	0.000	1.500
HCCO	2	150.000	2.500	0.000	0.000	1.000
NC3H7	2	266.800	4.982	0.000	0.000	1.000
C3H8	2	266.800	4.982	0.000	0.000	1.000
ENDDIFF						

## E.2 Reduced Hydrogen-N<sub>2</sub>O Mechanism

### E.2.1 Chemistry

!H3-N2O-Air mechanism - BOWMAN-MILLER APPENDIX B (+ A FEW JES 3/93)

!Reduced model

ELEMENTS

H O N

END

SPECIES

H2 N2O O O2 OH H2O HO2 N H

NO HNO N2 NH N2H

END

REACTIONS

OH+H2=H2O+H	1.1700E+09	1.300	3626.000	! 100 %
O+OH=O2+H	3.6100E+14	-0.500	0.000	! 56 %
O+H2=OH+H	5.0600E+04	2.670	6290.000	! 100 %
H+O2+M=HO2+M	3.6100E+17	-0.720	0.000	! 67 %
H2O/18.6/, H2/2.9/, N2/1.3/				
OH+HO2=H2O+O2	7.5000E+12	0.000	0.000	! 33 %
H+HO2=OH+OH	1.4000E+14	0.000	1073.000	! 78 %
2OH=O+H2O	6.0000E+08	1.300	0.000	! 33 %
NH+NO=N2O+H	4.3300E+14	-0.500	0.000	! 89 %
N2O+H=N2+OH	7.6000E+13	0.000	15200.000	! 100 %
N2O(+M)=N2+O(+M)	1.3000E+11	0.000	59610.000	! 100 %
LOW/6.94E23 -2.5 64995./				
N2O+O=N2+O2	1.0000E+14	0.000	28020.000	! 89 %
N2O+O=NO+NO	6.9200E+13	0.000	26630.000	! 67 %
N2O+OH=N2+HO2	2.0000E+12	0.000	10000.000	! 56 %
NH+N2O=HNO+N2	2.0000E+12	0.000	6000.000	! 67 %
N2H+M=N2+H+M	2.0000E+14	0.000	2000.000	! 67 %
N2H+O=N2O+H	1.0000E+14	0.000	0.000	! 67 %
HNO+M=H+NO+M	1.5000E+16	0.000	48680.000	! 56 %
H2O/10.0/, O2/2.0/, H2/2.0/				
N+NO=N2+O	3.2700E+12	0.500	0.000	! 78 %
N+O2=NO+O	6.4000E+09	1.000	6280.000	! 56 %
END				

## E.2.2 Thermodynamics

H2	REF ELEMENT	RUS 78H	2	0	0	OG	200.000	6000.000	1000.	1		
							0.29328305E+01	0.82659802E-03	-0.14640057E-06	0.15409851E-10	-0.68879615E-15	2
							-0.81305582E+03	-0.10243164E+01	0.23443029E+01	0.79804248E-02	-0.19477917E-04	3
							0.20156967E-07	-0.73760289E-11	-0.91792413E+03	0.68300218E+00	0.00000000E+00	4
N2O		L 7/88N	20	1	0	OG	200.000	6000.000	1000.	1		
							0.48230729E+01	0.26270251E-02	-0.95850872E-06	0.16000712E-09	-0.97752302E-14	2
							0.80734047E+04	-0.22017208E+01	0.22571502E+01	0.11304728E-01	-0.13671319E-04	3
							0.96819803E-08	-0.29307182E-11	0.87417746E+04	0.10757992E+02	0.98141682E+04	4
O		L 1/90O	1	0	0	OG	200.000	6000.000	1000.	1		
							2.54363697E+00	-2.73162486E-05	-4.19029520E-09	4.95481845E-12	-4.79553694E-16	2
							2.92260120E+04	4.92229457E+00	3.16826710E+00	-3.27931884E-03	6.64306396E-06	3
							-6.12806624E-09	2.11265971E-12	2.91222592E+04	2.05193346E+00	2.99687009E+04	4
O2	REF ELEMENT	RUS 89O	2	0	0	OG	200.000	6000.000	1000.	1		
							3.66096083E+00	6.56365523E-04	-1.41149485E-07	2.05797658E-11	-1.29913248E-15	2
							-1.21597725E+03	3.41536184E+00	3.78245636E+00	-2.99673415E-03	9.84730200E-06	3
							-9.68129508E-09	3.24372836E-12	-1.06394356E+03	3.65767573E+00	0.00000000E+00	4
OH	HYDROXYL RADI	IU3/03O	1.H	1.	0.	O.G	200.000	6000.000	1000.	1		
							2.83853033E+00	1.10741289E-03	-2.94000209E-07	4.20698729E-11	-2.42289890E-15	2
							3.69780808E+03	5.84494652E+00	3.99198424E+00	-2.40106655E-03	4.61664033E-06	3
							-3.87916306E-09	1.36319502E-12	3.36889836E+03	-1.03998477E-01	4.48613328E+03	4
H2O		L 5/89H	20	1	0	OG	200.000	6000.000	1000.	1		
							0.26770389E+01	0.29731816E-02	-0.77376889E-06	0.94433514E-10	-0.42689991E-14	2
							-0.29885894E+05	0.68825500E+01	0.41986352E+01	-0.20364017E-02	0.65203416E-05	3
							-0.54879269E-08	0.17719680E-11	-0.30293726E+05	-0.84900901E+00	-0.29084817E+05	4
HO2		L 5/89H	10	2	0	OG	200.000	6000.000	1000.	1		
							0.41722659E+01	0.18812098E-02	-0.34629297E-06	0.19468516E-10	0.17609153E-15	2
							0.61818851E+02	0.29577974E+01	0.43017880E+01	-0.47490201E-02	0.21157953E-04	3
							-0.24275961E-07	0.92920670E-11	0.29480876E+03	0.37167010E+01	0.15096500E+04	4
N		L 6/88N	1	0	0	OG	200.000	6000.000	1000.	1		
							0.24159429E+01	0.17489065E-03	-0.11902369E-06	0.30226244E-10	-0.20360983E-14	2
							0.56133775E+05	0.46496095E+01	0.25000000E+01	0.00000000E+00	0.00000000E+00	3
							0.00000000E+00	0.00000000E+00	0.56104638E+05	0.41939088E+01	0.56850013E+05	4
N2	REF ELEMENT	G 8/02N	2.	0.	0.	O.G	200.000	6000.000	1000.	1		
							2.95257637E+00	1.39690040E-03	-4.92631603E-07	7.86010195E-11	-4.60755204E-15	2
							-9.23948688E+02	5.87188762E+00	3.53100528E+00	-1.23660988E-04	-5.02999433E-07	3
							2.43530612E-09	-1.40881235E-12	-1.04697628E+03	2.96747038E+00	0.00000000E+00	4
H		L 6/94H	1	0	0	OG	200.000	6000.000	1000.	1		
							0.25000000E+01	0.00000000E+00	0.00000000E+00	0.00000000E+00	0.00000000E+00	2
							0.25473660E+05	-0.44668285E+00	0.25000000E+01	0.00000000E+00	0.00000000E+00	3
							0.00000000E+00	0.00000000E+00	0.25473660E+05	-0.44668285E+00	0.26219035E+05	4
NO		RUS 89N	10	1	0	OG	200.000	6000.000	1000.	1		
							3.26071234E+00	1.19101135E-03	-4.29122646E-07	6.94481463E-11	-4.03295681E-15	2
							9.92143132E+03	6.36900518E+00	4.21859896E+00	-4.63988124E-03	1.10443049E-05	3
							-9.34055507E-09	2.80554874E-12	9.84509964E+03	2.28061001E+00	1.09770882E+04	4
HNO		L12/89H	1N	10	1	OG	200.000	3500.000	1000.	1		
							0.31655229E+01	0.30000862E-02	-0.39436619E-06	-0.38575815E-10	0.70807189E-14	2
							0.11194426E+05	0.76477833E+01	0.45352475E+01	-0.56853972E-02	0.18519850E-04	3
							-0.17188273E-07	0.55583207E-11	0.11039881E+05	0.17431919E+01	0.12271645E+05	4
N2H		T07/93N	2H	1	0	OG	200.000	6000.000	1000.	1		
							0.37667545E+01	0.28915081E-02	-0.10416620E-05	0.16842594E-09	-0.10091896E-13	2
							0.28650697E+05	0.44705068E+01	0.43446927E+01	-0.48497072E-02	0.20059459E-04	3
							-0.21726464E-07	0.79469538E-11	0.28791973E+05	0.29779411E+01	0.30009829E+05	4

## E.2.3 Transport

```
! edited 20/06/00
H          0   145.000   2.050   0.000   0.000   0.000
H2         1    38.000   2.920   0.000   0.790  280.000
H2O        2   572.400   2.605   1.844   0.000   4.000
HNO        2   116.700   3.492   0.000   0.000   1.000  !(*)
HO2        2   107.400   3.458   0.000   0.000   1.000  !(*)
N          0    71.400   3.298   0.000   0.000   0.000  !(*)
N2         1    97.530   3.621   0.000   1.760   4.000
N2O        1   232.400   3.828   0.000   0.000   1.000  !(*)
NH         1    80.000   2.650   0.000   0.000   4.000
N2H        2    71.400   3.798   0.000   0.000   1.000  !(*)
NO         1    97.530   3.621   0.000   1.760   4.000
O          0    80.000   2.750   0.000   0.000   0.000
O2         1   107.400   3.458   0.000   1.600   3.800
OH         1    80.000   2.750   0.000   0.000   0.000
```

## E.3 Reduced Hydrogen-Air Mechanism

### E.3.1 Chemistry

```
ELEMENTS
H O N
END
SPECIES
H2 O2 H2O N2 H O OH HO2 H2O2
END
REACTIONS
!H2-O2 Chain Reactions
! Hessler, J. Phys. Chem. A, 102:4517 (1998)
H+O2=O+OH          3.547e+15 -0.406  1.6599E+4
! Sutherland et al., 21st Symposium, p. 929 (1986)
O+H2=H+OH          0.508E+05  2.67  0.629E+04
! Michael and Sutherland, J. Phys. Chem. 92:3853 (1988)
H2+OH=H2O+H        0.216E+09  1.51  0.343E+04
! Sutherland et al., 23rd Symposium, p. 51 (1990)
O+H2O=OH+OH        2.97e+06  2.02  1.34e+4
!H2-O2 Dissociation Reactions
! Tsang and Hampson, J. Phys. Chem. Ref. Data, 15:1087 (1986)
H2+M=H+H+M         4.577E+19 -1.40  1.0438E+05
      H2/2.5/ H2O/12/
! Tsang and Hampson, J. Phys. Chem. Ref. Data, 15:1087 (1986)
O+O+M=O2+M         6.165E+15 -0.50  0.000E+00
      H2/2.5/ H2O/12/
! Tsang and Hampson, J. Phys. Chem. Ref. Data, 15:1087 (1986)
O+H+M=OH+M         4.714E+18 -1.00  0.000E+00
      H2/2.5/ H2O/12/
! Tsang and Hampson, J. Phys. Chem. Ref. Data, 15:1087 (1986)
!H+OH+M=H2O+M      2.212E+22 -2.00  0.000E+00
H+OH+M=H2O+M      3.800E+22 -2.00  0.000E+00
      H2/2.5/ H2O/12/
!Formation and Consumption of HO2
! Cobos et al., J. Phys. Chem. 89:342 (1985) for kinf
```



```

! Michael, et al., J. Phys. Chem. A, 106:5297 (2002) for k0
!*****
! MAIN BATH GAS IS N2 (comment this reaction otherwise)
!
H+O2(+M)=HO2(+M)      1.475E+12  0.60  0.00E+00
      LOW/6.366E+20  -1.72  5.248E+02/
      TROE/0.8  1E-30  1E+30/
      H2/2.0/  H2O/11./  O2/0.78/
!*****
!
!H+O2(+M)=HO2(+M)      1.475E+12  0.60  0.00E+00
!      LOW/9.042E+19  -1.50  4.922E+02/
!      TROE/0.5  1E-30  1E+30/
!      H2/3.0/  H2O/16/  O2/1.1/
! Tsang and Hampson, J. Phys. Chem. Ref. Data, 15:1087 (1986) [modified]
HO2+H=H2+O2      1.66E+13  0.00  0.823E+03
! Tsang and Hampson, J. Phys. Chem. Ref. Data, 15:1087 (1986) [modified]
HO2+H=OH+OH      7.079E+13  0.00  2.95E+02
! Baulch et al., J. Phys. Chem. Ref Data, 21:411 (1992)
HO2+O=O2+OH      0.325E+14  0.00  0.00E+00
! Keyser, J. Phys. Chem. 92:1193 (1988)
HO2+OH=H2O+O2      2.890E+13  0.00  -4.970E+02
!Formation and Consumption of H2O2
! Hippler et al., J. Chem. Phys. 93:1755 (1990)
HO2+HO2=H2O2+O2      4.200e+14  0.00  1.1982e+04
      DUPLICATE
HO2+HO2=H2O2+O2      1.300e+11  0.00  -1.6293e+3
      DUPLICATE
! Brouwer et al., J. Chem. Phys. 86:6171 (1987) for kinf
! Warnatz, J. in Combustion chemistry (1984) for k0
H2O2(+M)=OH+OH(+M)      2.951e+14  0.00  4.843E+04
      LOW/1.202E+17  0.00  4.55E+04/
      TROE/0.5  1E-30  1E+30/
      H2/2.5/  H2O/12/
! Tsang and Hampson, J. Phys. Chem. Ref. Data, 15:1087 (1986)
H2O2+H=H2O+OH      0.241E+14  0.00  0.397E+04
! Tsang and Hampson, J. Phys. Chem. Ref. Data, 15:1087 (1986)
H2O2+H=HO2+H2      0.482E+14  0.00  0.795E+04
! Tsang and Hampson, J. Phys. Chem. Ref. Data, 15:1087 (1986)
H2O2+O=OH+HO2      9.550E+06  2.00  3.970E+03
! Hippler and Troe, J. Chem. Phys. Lett. 192:333 (1992)
H2O2+OH=HO2+H2O      1.000E+12  0.00  0.000
      DUPLICATE
H2O2+OH=HO2+H2O      5.800E+14  0.00  9.557E+03
      DUPLICATE
END

```

## E.3.2 Thermodynamics

THERMO ALL

300.0 1000.0 5000.0

H	120186H	1	G	0300.00	5000.00	1000.00	1
	2.50000000E+00	0.00000000E+00	0.00000000E+00	0.00000000E+00	0.00000000E+00	0.00000000E+00	2
	2.54716270E+04	-4.60117638E-01	2.50000000E+00	0.00000000E+00	0.00000000E+00	0.00000000E+00	3

```

0.00000000E+00 0.00000000E+00 2.54716270E+04-4.60117608E-01      4
O      120186D      1      G      0300.00      5000.00      1000.00      1
2.54205966E+00-2.75506191E-05-3.10280335E-09 4.55106742E-12-4.36805150E-16      2
2.92308027E+04 4.92030811E+00 2.94642878E+00-1.63816649E-03 2.42103170E-06      3
-1.60284319E-09 3.89069636E-13 2.91476445E+04 2.96399498E+00      4
OH      S 9/010      1H      1      0      OG      200.000      6000.000      1000.      1
2.86472886E+00 1.05650448E-03-2.59082758E-07 3.05218674E-11-1.33195876E-15      2
3.68362875E+03 5.70164073E+00 4.12530561E+00-3.22544939E-03 6.52764691E-06      3
-5.79853643E-09 2.06237379E-12 3.34630913E+03-6.90432960E-01 4.51532273E+03      4
H2      121286H      2      G      0300.00      5000.00      1000.00      1
2.99142337E+00 7.00064411E-04-5.63382869E-08-9.23157818E-12 1.58275179E-15      2
-8.35033997E+02-1.35511017E+00 3.29812431E+00 8.24944174E-04-8.14301529E-07      3
-9.47543433E-11 4.13487224E-13-1.01252087E+03-3.29409409E+00      4
O2      121386D      2      G      0300.00      5000.00      1000.00      1
3.69757819E+00 6.13519689E-04-1.25884199E-07 1.77528148E-11-1.13643531E-15      2
-1.23393018E+03 3.18916559E+00 3.21293640E+00 1.12748635E-03-5.75615047E-07      3
1.31387723E-09-8.76855392E-13-1.00524902E+03 6.03473759E+00      4
H2O      20387H      20      1      G      0300.00      5000.00      1000.00      1
2.67214561E+00 3.05629289E-03-8.73026011E-07 1.20099639E-10-6.39161787E-15      2
-2.98992090E+04 6.86281681E+00 3.38684249E+00 3.47498246E-03-6.35469633E-06      3
6.96858127E-09-2.50658847E-12-3.02081133E+04 2.59023285E+00      4
HO2      L 5/89H      10      2      00      OOG      200.000      3500.000      1000.000      1
4.01721090E+00 2.23982013E-03-6.33658150E-07 1.14246370E-10-1.07908535E-14      2
1.11856713E+02 3.78510215E+00 4.30179801E+00-4.74912051E-03 2.11582891E-05      3
-2.42763894E-08 9.29225124E-12 2.94808040E+02 3.71666245E+00 1.00021620E+04      4
H2O2      120186H      20      2      G      0300.00      5000.00      1000.00      1
4.57316685E+00 4.33613639E-03-1.47468882E-06 2.34890357E-10-1.43165356E-14      2
-1.80069609E+04 5.01136959E-01 3.38875365E+00 6.56922581E-03-1.48501258E-07      3
-4.62580552E-09 2.47151475E-12-1.76631465E+04 6.78536320E+00      4
AR      120186AR      1      G      0300.00      5000.00      1000.00      1
0.02500000E+02 0.00000000E+00 0.00000000E+00 0.00000000E+00 0.00000000E+00      2
-0.07453750E+04 0.04366001E+02 0.02500000E+02 0.00000000E+00 0.00000000E+00      3
0.00000000E+00 0.00000000E+00-0.07453750E+04 0.04366001E+02      4
N2      121286N      2      G      0300.00      5000.00      1000.00      1
0.02926640E+02 0.01487977E-01-0.05684761E-05 0.01009704E-08-0.06753351E-13      2
-0.09227977E+04 0.05980528E+02 0.03298677E+02 0.01408240E-01-0.03963222E-04      3
0.05641515E-07-0.02444855E-10-0.01020900E+05 0.03950372E+02      4
HE      120186HE      1      G      0300.00      5000.00      1000.00      1
0.02500000E+02 0.00000000E+00 0.00000000E+00 0.00000000E+00 0.00000000E+00      2
-0.07453750E+04 0.09153489E+01 0.02500000E+02 0.00000000E+00 0.00000000E+00      3
0.00000000E+00 0.00000000E+00-0.07453750E+04 0.09153488E+01      4
CO      121286C      10      1      G      0300.00      5000.00      1000.00      1
0.03025078E+02 0.01442689E-01-0.05630828E-05 0.01018581E-08-0.06910952E-13      2
-0.01426835E+06 0.06108218E+02 0.03262452E+02 0.01511941E-01-0.03881755E-04      3
0.05581944E-07-0.02474951E-10-0.01431054E+06 0.04848897E+02      4
CO2      121286C      10      2      G      0300.00      5000.00      1000.00      1
0.04453623E+02 0.03140169E-01-0.01278411E-04 0.02393997E-08-0.01669033E-12      2
-0.04896696E+06-0.09553959E+01 0.02275725E+02 0.09922072E-01-0.01040911E-03      3
0.06866687E-07-0.02117280E-10-0.04837314E+06 0.01018849E+03      4
END

```

### E.3.3 Transport

```

CO      1      98.100      3.650      0.000      1.950      1.800

```

H2O	2	572.400	2.605	1.844	0.000	4.000
H2	1	38.000	2.920	0.000	0.790	280.000
CO2	1	244.000	3.763	0.000	2.650	2.100
O2	1	107.400	3.458	0.000	1.600	3.800
H2O2	2	107.400	3.458	0.000	0.000	3.800
OH	1	80.000	2.750	0.000	0.000	0.000
HO2	2	107.400	3.458	0.000	0.000	1.000 ! *
H	0	145.000	2.050	0.000	0.000	0.000
O	0	80.000	2.750	0.000	0.000	0.000
AR	0	136.500	3.330	0.000	0.000	0.000
N2	1	97.530	3.621	0.000	1.760	4.000
HE	0	10.200	2.576	0.000	0.000	0.000 ! *

! Transport data for H2/O2 reaction mechanism

! Li, J., Zhao, Z., Kazakov, A., and Dryer, F.L. "An Updated Comprehensive Kinetic Model  
! for H2 Combustion", Fall Technical Meeting of the Eastern States Section of the  
! Combustion Institute, Penn State University, University Park, PA, October 26-29, 2003.

# Bibliography

- [1] E. S. Oran and J. S. Weber Jr., E. I. Stefaniw, M. H. Lefebvre, and J. D. Anderson Jr. A numerical study of a two-dimensional  $H_2$ - $O_2$ -Ar detonation using a detailed chemical reaction model. *Combustion Flame*, 113:147–163, 2006. [93](#)
- [2] N. A. Adams and K. Sharif. A high-resolution hybrid compact-ENO scheme for shock-turbulence interaction problems. *J. Comput. Physics*, 127:27–51, 1996. [29](#)
- [3] M. Akram. Two-dimensional model for spark discharge simulation in air. *AIAA Journal*, 34(9):1835–1842, 1996. [12](#)
- [4] M. Arienti and J. E. Shepherd. The role of diffusion in irregular detonations. In *The 4th Joint Meeting of the US Sections of the Combustion Institute, Philadelphia, PA, March 20-23.*, 2005. [91](#)
- [5] M. Arienti and J. E. Shepherd. The role of diffusion in irregular detonations. In *22nd International Symposium on Shock Waves, Imperial College, London, UK, July 18-23*, 2005. [95](#)
- [6] J. M. Austin. *The role of instability in gaseous detonation*. PhD in aeronautics, California Institute of Technology, 2003. [xviii](#), [93](#), [194](#), [195](#), [198](#), [230](#), [231](#), [234](#)
- [7] J. M. Austin, F. Pintgen, and J. E. Shepherd. Reaction zones in highly unstable detonations. In *Proceedings of the Combustion Institute 30*, page 1849, 2005. [xvii](#), [91](#), [93](#), [199](#)
- [8] V. Babrauskas. *Ignition Handbook: Principles and Applications to Fire Safety Engineering, Fire Investigation, Risk Management and Forensic Science*. Fire Science Publishers, Issaquah, WA, 2003. [1](#)
- [9] D. S. Balsara and C. W. Shu. Monotonicity preserving weighted essentially non-oscillatory schemes with increasingly high order of accuracy. *J. Comput. Physics*, 160:405–452, 2000. [31](#)
- [10] S. P. M. Bane. *Spark ignition: Experimental and numerical investigation with application to aviation safety*. PhD in aeronautics, California Institute of Technology, 2010. [xiii](#), [11](#), [320](#), [363](#), [364](#)
- [11] S. P. M. Bane, J. E. Shepherd, E. Kwon, and A. C. Day. Statistical analysis of electrostatic spark ignition of lean  $H_2$ - $O_2$ -Ar mixtures. In *In Proceedings of the 3rd International Conference on Hydrogen Safety. Ajaccio, Corsica, Sept 16-18, 2009*, 2009. [12](#), [307](#)

- [12] S. P. M. Bane, J. E. Shepherd, E. Kwon, and A. C. Day. Statistical analysis of electrostatic spark ignition of lean  $\text{H}_2/\text{O}_2/\text{Ar}$  mixtures. *Inter. J. of Hydrogen Energy*, 46:2344–2350, 2011. [12](#), [307](#), [308](#)
- [13] S. P. M. Bane, J. L. Ziegler, and J. E. Shepherd. Development of one-step chemistry models for flame and ignition simulation. Galcit report galcitfm:2010.002, California Institute of Technology, 2010. [320](#), [321](#)
- [14] F. E. Belles and M. R. Lauver. Effects of concentration and vibrational relaxation on induction period of hydrogen-oxygen reaction. Technical note d-2540, NASA, 1964. [382](#)
- [15] G. Ben-Dor. A reconsideration of the three-shock theory for a pseudo-steady Mach reflection. *J. Fluid Mechanics*, 121:467–484, 1987. [18](#), [72](#), [74](#), [380](#), [386](#), [421](#)
- [16] G. Ben-Dor. *Shock Wave Reflection Phenomena*. Springer-Verlag, New York, 1992. [18](#), [380](#)
- [17] G. Ben-Dor. A state-of-the-knowledge review on pseudo-steady shock-wave reflections and their transition criteria. *Shock Waves*, 15, 2006. [388](#)
- [18] G. Ben-Dor and I. I. Glass. Domains and boundaries of non-stationary oblique shock-wave reflexions: 1. Diatomic gas. *J. Fluid Mechanics*, 92:459–496, 1979. [xxiii](#), [18](#), [380](#), [386](#), [417](#), [418](#)
- [19] M. Berger and P. Colella. Local adaptive mesh refinement for shock hydrodynamics. *J. Comput. Phys.*, 82:64–84, 1988. [41](#), [46](#)
- [20] M. Berger and J. Oliger. Adaptive mesh refinement for hyperbolic partial differential equations. *J. Comput. Phys.*, 53:484–512, 1984. [41](#)
- [21] G. Blanquart, P. Pepiot-Desjardins, and H. Pitsch. Chemical mechanism for high temperature combustion of engine relevant fuels with emphasis on soot precursors. *Comb. Flame*, 156:588–607, 2008. [xiv](#), [8](#), [96](#), [99](#), [100](#), [110](#)
- [22] G. Blanquart and H. Pitsch. Analyzing the effects of temperature on soot formation with a joint volume-surface-hydrogen model. *Comb. Flame*, 156:1614–1626, 2009. [xiv](#), [8](#), [96](#), [99](#), [100](#), [110](#)
- [23] R. Borges, M. Carmona, B Costa, and W. S. Don. An improved weighted essentially non-oscillatory scheme for hyperbolic conservation laws. *J. Comput. Physics*, 227:3191–3211, 2008. [31](#)
- [24] S. Browne, Z. Liang, R. Deiterding, and J. E. Shepherd. Detonation front structure and the competition for radicals. *Proc. of the Combustion Institute*, 31(2):2445–2453, 2007. [8](#), [42](#)
- [25] S. T. Browne and J. E. Shepherd. Linear stability of detonations with reversible chemical reactions. In *007 Fall Meeting of the Western States Section of the Combustion Institute, Livermore, CA October 16-17*, pages Paper 07F–70, 2007. [6](#)
- [26] Y. Burtschell1, D. E. Zeitoun, and G. Ben-Dor. Steady shock wave reflections in thermochemical nonequilibrium flows. *Shock Waves*, 11:15–21, 2001. [381](#)

- [27] G. V. Candler, J. D. Kelley, S. O. Macheret, M. N. Shneider, and I. V. Adamovich. Vibrational excitation, thermal nonuniformities, and unsteady effects on supersonic blunt bodies. *AIAA*, 40, 2002. [381](#)
- [28] G. V. Candler, I. Nompelis, and M. S. Holden. Effect of vibrational nonequilibrium on hypersonic double-cone experiments. *AIAA*, 41, 2003. [381](#)
- [29] J. Chao, A. Haselbacher, and S. Balachandar. A massively parallel multi-block hybrid compactWENO scheme for compressible flows. *J. Comput. Physics*, 228:7473–7491, 2009. [29](#)
- [30] J. P. Chesick and G. B. Kistiakowsky. Gaseous detonations. X. Study of reaction zones. *J. of Chemical Physics*, 28, 1958. [382](#)
- [31] J. F. Clarke. Gas dynamics with relaxation effects. *Rep. Prog. Phys.*, 41, 1978. [381](#)
- [32] P. Colella, M. Dorr, J. Hittinger, D. F. Martin, and P. McCorquodale. High-order finite-volume adaptive methods on locally rectangular grids. In *J. Phys.: Conf. Ser.*, volume 180 012010, 2009. [29](#)
- [33] B. Costa and W. S. Don. High order hybrid central-WENO finite difference scheme for conservation laws. *J. Comput. and App. Math.*, 204:209–218, 2007. [29](#)
- [34] H. F. Coward and G. W. Jones. The limits of flammability of gases and vapors. Technical report, 1952. Bulletin 503, Bureau Mines. [1](#)
- [35] J. Damazo, J. Ziegler, J. Karnesky, and J. E. Shepherd. Investigating shock wave-boundary layer interaction caused by reflecting detonations. In *8th ISHPMIE September 5-10, 2010, Yokohama, Japan*, 2010. [xiii](#), [xviii](#), [4](#), [237](#), [238](#), [239](#), [240](#)
- [36] L. Davies and J. L. Wilson. Influence of reflected shock and boundary-layer interaction on shock-tube flows. *Phys. Fluids Supplement I*, pages I–37–I–43, 1969. [4](#), [235](#), [288](#), [306](#)
- [37] M. J. Davis. Dynamics of a nonlinear master equation: Low-dimensional manifolds and the nature of vibrational relaxation. *J. of Chemical Physics*, 116, 2002. [381](#)
- [38] M. S. Day, J. B. Bell, R. K. Cheng, S. Tachibana, V. E. Beckner, and M. J. Lijewski. Cellular burning in lean premixed turbulent hydrogen-air flames: Coupling experimental and computational analysis at the laboratory scale. In *SciDAC 2009, J. of Physics: Conference Series, San Diego, California*, July 2009. [29](#)
- [39] M. De-Kang. Towards front-tracking based on conservation in two space dimensions II, tracking discontinuities in capturing fashion. *J. Comput. Physics*, 226:1550–1588, 2007. [33](#)
- [40] R. Deiterding. *Parallel adaptive simulation of multi-dimensional detonation structures*. PhD thesis, Brandenburgische Technische Universität Cottbus, 2003. [26](#), [28](#), [30](#), [42](#), [49](#), [63](#), [65](#), [66](#), [86](#), [93](#)
- [41] R. Deiterding. Construction and application of an AMR algorithm for distributed memory computers. In T. Plewa, T. Linde, and V. G. Weirs, editors, *Adaptive Mesh Refinement - Theory and Applications*, volume 41 of *Lecture Notes in Computational Science and Engineering*,

pages 361–372. Springer, 2005. 42

- [42] R. Deiterding. Detonation structure simulation with AMROC. In L. T. Yang, editor, *High Performance Computing and Communications 2005*, volume 3726 of *Lecture Notes in Computer Science*, pages 916–927. Springer, 2005. 42
- [43] R. Deiterding. A parallel adaptive method for simulating shock-induced combustion with detailed chemical kinetics in complex domains. *Computers & Structures*, 87:769–783, 2009. 42, 71
- [44] R. Deiterding. Parallel adaptive simulation of weak and strong detonation transverse-wave detonation structures in  $H_2$ - $O_2$  detonations. In R. Biswas, editor, *Parallel CFD 2009: 21st Int. Conf. on Parallel Computational Fluid Dynamics*, pages 519–534. DEStech Publications, 2010. 42
- [45] R. Deiterding and G. Bader. High-resolution simulation of detonations with detailed chemistry. In G. Warnecke, editor, *Analysis and Numerics for Conservation Laws*, pages 69–91. Springer, 2005. 49
- [46] R. Deiterding, F. Cirak, S. P. Mauch, and D. I. Meiron. A virtual test facility for simulating detonation- and shock-induced deformation and fracture of thin flexible shells. *Int. J. Multiscale Computational Engineering*, 5(1):47–63, 2007. 41
- [47] R. Deiterding, R. Radovitzki, S. P. Mauch, F. Cirak, D. J. Hill, C. Pantano, J. C. Cummings, and D. I. Meiron. Virtual Test Facility: A virtual shock physics facility for simulating the dynamic response of materials. Available at <http://www.cacr.caltech.edu/asc>. 41
- [48] R. Deiterding, R. Radovitzky, S. P. Mauch, L. Noels, J. C. Cummings, and D. I. Meiron. A virtual test facility for the efficient simulation of solid materials under high energy shock-wave loading. *Engineering with Computers*, 22(3-4):325–347, 2006. 41
- [49] C. A. Eckett. *Numerical and analytical studies of the dynamics of gaseous detonations*. PhD in aeronautics, California Institute of Technology, 2000. 93
- [50] C. A. Eckett, J. J. Quirk, and J. E. Shepherd. The role of unsteadiness in direct initiation of gaseous detonation. *J. Fluid Mech.*, 441:142–183, 2000. 63
- [51] O. Ekici, O. A. Ezekoye, M. J. Hall, and R. D. Matthews. Thermal and flow fields modeling of fast spark discharges in air. *Journal of Fluids Engineering*, 129:55–65, 2007. 12
- [52] R. P. Fedkiw, B. Merriman, and S. Osher. High accuracy numerical methods for thermally perfect gas flows with chemistry. *J. Comput. Phys.*, 132:175–190, 1997. 19, 29, 77
- [53] D. Fernandez-Galisteo, A. L. Sanchez, A. Linan, and F. A. Williams. One-step reduced kinetics for lean hydrogen-air deflagration. *Comb. Flame*, 156:985–996, 2009. 8
- [54] W. Fickett and Davis W. C. *Detonation: Theory and Experiment*. Dover Publications, 1979. 7
- [55] V. N Gamezo, D. Desbordes, and E. S. Oran. Formation and evolution of two-dimensional

- cellular detonations. *Combust. Flame*, 116:154–165, 1999. [94](#)
- [56] V. N. Gamezo, D. Desbordes, and E. S. Oran. Two-dimensional reactive flow dynamics in cellular detonation waves. *Shock Waves*, 9:11–17, 1999. [94](#)
- [57] V. N. Gamezo, A. M. Khokhlov, and E. S. Oran. The influence of shock bifurcations on shock-flame interactions and ddt. *Comb. and Flame*, 126:18101826, 2001. [236](#)
- [58] S. Gottlieb, D. I. Ketcheson, and C. W. Shu. High order strong stability preserving time discretizations. *J. of Scientific Computing*, 38(3):251, 2009. [39](#), [40](#), [41](#)
- [59] S. Gottlieb and C.W. Shu. Total variation diminishing Runge-Kutta schemes. *Combustion and Flame*, 67:73–85, 1998. [41](#)
- [60] J. A. Greenough and W. J. Rider. A quantitative comparison of numerical methods for the compressible Euler equations: fifth-order WENO and piecewise-linear Godunov. *J. Comput. Phys.*, 196:259281, 2004. [32](#)
- [61] B. Gustafsson, H.-O. Kreiss, and J. Oliger. *Time Dependent Problems and Difference Methods*. John Wiley and Sons, 1995. [29](#)
- [62] F. Haloua, M. Brouillette, V. Lienhart, and G. Dupr. Characteristics of unstable detonations near extinction limits. *Combustion and Flame*, 22, 2000. [93](#)
- [63] J. Han, H. Yamashita, and N. Hayashi. Numerical study on the spark ignition characteristics of a methane-air mixture using detailed chemical kinetics. *Combustion and Flame*, 157:1414–1421, 2010. [12](#), [308](#), [365](#)
- [64] J. Han, H. Yamashita, and N. Hayashi. Numerical study on the spark ignition characteristics of a hydrogen-air mixture using detailed chemical kinetics. *Inter. J. Hydrogen Energy*, 36:9286–9297, 2011. [12](#), [308](#), [365](#)
- [65] A. K. Henrick, T. D. Aslam, and J. M. Powers. Mapped weighted essentially non-oscillatory schemes: Achieving optimal order near critical points. *J. Comput. Physics*, 207:542–567, 2005. [31](#)
- [66] A. K. Henrick, T. D. Aslam, and J. M. Powers. Simulations of pulsating one-dimensional detonations with true fifth order accuracy. *J. Comput. Physics*, 213:311–329, 2006. [31](#), [32](#)
- [67] D. J. Hill and D. I. Pullin. Hybrid tuned center-difference-WENO method for large eddy simulations in the presence of strong shocks. *J. Comput. Phys.*, 194(2):435–450, 2004. [28](#), [37](#), [44](#)
- [68] A. C. Hindmarsh and P. M. Gresho. The stability of explicit Euler time-integration for certain finite difference approximations of the multi-dimensional advection-diffusion equation. *Inter. J. for Num. Meth. in Fluids*, 4:853–897, 1984. [50](#)
- [69] A. E. Honein and P. Moin. Higher entropy conservation and numerical stability of compressible turbulence simulations. *J. Comput. Phys.*, 201(2):531, 2004. [38](#)



- [70] H. Hornung. Regular and Mach reflection of shock waves. *Annual Review of Fluid Mechanics*, 18:33–58, 1986. [386](#)
- [71] H. G. Hornung. Gradients at a curved shock in reacting flow. *Shock Waves*, 8:11–21, 1998. [381](#)
- [72] H. G. Hornung, H. Oertel, and R. J. Sandeman. Transition to Mach reflection of shock waves in steady and psuedo-steady flow with and without relaxation. *J. Fluid Mechanics*, 90:541–547, 1979. [381](#), [386](#)
- [73] H. G. Hornung and M. L. Robinson. Transition from regular to Mach reflection of shock-waves Part 2: The steady-flow criterion. *J. Fluid Mechanics*, 123:155–164, 1982. [399](#)
- [74] H. G. Hornung and J. R. Talyor. Transition from regular to Mach reflection of shock waves Part 1. The effect of viscosity in the pseudosteady case. *J. of Fluid Mchanics*, 123:143–153, 1982. [381](#)
- [75] P. Hwang, R. P. Fedkiw, B. Merriman, T. D. Aslam, A. R. Karagozian, and S. J. Osher. Numerical resolution of pulsating detonation waves. *Appl. Numer. Math.*, 3:217–240, 2000. [63](#), [65](#)
- [76] E. I. Vas Ilev, G. Ben-Dor, T. Elperin, and L. F. Henderson. The wall-jetting effect in Mach reflection: Navier-Stokes simulations. *Shock Waves*, 511:363–379, 2004. [30](#), [71](#), [72](#)
- [77] K. Inaba, A. Matsuo, K. Tanaka, A. K. W. Lam, F. Pintgen, E. Wintenberger, and J. E. Shepherd. Soot track generation by mach reflection over a wedge. *Japanese Symp. Shock Waves, Ibarki, Japan, March 14-16*, 2002. [93](#)
- [78] K. Ishii, T. Tsukamoto, Y. Ujiie, and M. Kono. Analysis of ignition mechanism of combustible mixtures by composite sparks. *Combustion and Flame*, 91:153–164, 1992. [12](#)
- [79] R. Jaffe, D. W. Schwenke, and G. Chaban. Appendix 2. Vibrational and rotational excitation and relaxation of nitrogen from accurate theoretical calculations. *Meeting paper AIAA-2008-1208-273*, 2008. [381](#)
- [80] G. S. Jiang and C. W. Shu. Efficient implementation of weighted ENO schemes. *J. Comput. Physics*, 126:202–228, 1996. [31](#)
- [81] E. Josyula and W. F. Bailey. Vibration-dissociation coupling using master equations in nonequilibrium hypersonic blunt-body flow. *J. of Thermophysics and Heat Transfer*, 15, 2001. [381](#)
- [82] P. Kaps and P. Rentrop. Generalized Runge-Kutta methods of order four with step size control for stiff ordinary differential equations. *Num. Math.*, 33:55–68, 1979. [40](#)
- [83] J. Karnesky. *Detonation induced strain in tubes*. PhD in aeronautics, California Institute of Technology, 2010. [236](#)
- [84] J. Karnesky, J. Damazo, J. E. Shepherd, and A. Rusinek. Plastic response of thin-walled tubes to detonation. In *Proceedings of the ASME 2010 Pressure Vessels and Piping Conference: 2010*

*Jul 18-22; Bellevue, USA*, 2009. [235](#), [237](#)

- [85] R. J. Kee, F. M. Rupley, and J. A. Miller. Chemkin-II: A Fortran chemical kinetics package for the analysis of gas-phase chemical kinetics. Sand89-8009, Sandia National Laboratories, Livermore, California, 1989. [48](#)
- [86] C. A. Kennedy and M. H. Carpenter. Several new numerical methods for compressible shear layer simulations. *Appl. Numer. Math.*, 14:397–433, 1994. [30](#)
- [87] D. A. Kessler, V. N. Gamezo, and E. S. Oran. Three-dimensional reactive shock bifurcations. *Proceedings of the Combustion Institute*, 30:1841–1847, 2005. [4](#), [236](#)
- [88] D. A. Kessler, V. N. Gamezo, and E. S. Oran. Simulations of flame acceleration and deflagration-to-detonation transitions in methane-air systems. *Combustion and Flame*, 157:2063–2077, 2010. [90](#), [96](#)
- [89] A. M. Khokhlov, J. M. Austin, F. Pintgen, and J. E. Shepherd. Numerical study of the detonations in ethylene-oxygen mixtures. *AIAA*, 153, 2004. [93](#), [94](#)
- [90] P. Knupp and S. Kambiz. *Verification of Computer Codes in Computational Science and Engineering*. Chapman and Hall/CRC, 2002. [66](#)
- [91] M. Kono, K. Niu, T. Tsukamoto, and Y. Ujiie. Mechanism of flame kernel formation produced by short duration sparks. *Proceedings of the Combustion Institute*, 22:1643–1649, 1988. [12](#)
- [92] R. M. J. Kramer, C. Pantano, and D. I. Pullin. A class of energy stable, high-order finite-difference interface schemes suitable for adaptive mesh refinement of hyperbolic problems. *J. Comput. Phys.*, 226:1458–1484, 2007. [53](#)
- [93] T. Kravchik, E. Sher, and J. B. Heywood. From spark ignition to flame initiation. *Combustion Science and Technology*, 108:1–30, 1995. [12](#), [309](#)
- [94] Landau and Lifshitz. *Fluid Mechanics 2nd Edition: Landau and Lifshitz Course of Theoretical Physics Volume 6*. Pergamon Books Ltd., NY, 1987. [16](#), [377](#)
- [95] J. Larson and S. K. Lele. Direct numerical simulation of canonical shock/turbulence interaction. *Phys. Fluids*, 21, 2009. [29](#)
- [96] J. Larsson and B. Gustafsson. Stability criteria for hybrid difference methods. *J. Comput. Physics*, 227:2886–2898, 2008. [29](#)
- [97] C. K. Law and I. I. Glass. Diffraction of strong shock waves by a sharp compressive corner. *CASI Trans.*, 4:2–12, 1971. [400](#), [407](#)
- [98] J. H. S. Lee. *The Detonation Phenomenon*. Cambridge University Press, 2008. [2](#), [3](#), [7](#)
- [99] J. H. S. Lee and M. I. Radulescu. On the hydrodynamic thickness of cellular detonations. *Combustion, Explosion, and Shock Waves*, 41:745–765, 2005. [93](#)
- [100] S. K. Lele. Compact finite difference schemes with spectral like resolution. *J. Comput. Phys.*, 103:16–42, 1992. [36](#)

- [101] R. J. Leveque. *Finite Volume Methods for Hyperbolic Problems*. Cambridge University Press, NY, 2002. [38](#), [39](#), [40](#), [49](#)
- [102] B. Lewis and G. von Elbe. *Combustion, Flames and Explosions of Gases*. Academic Press, New York, 1961. [xxii](#), [326](#), [362](#)
- [103] H. Li and G. Ben-Dor. Reconsideration of pseudo-steady shock wave reflections and the transition criterion between them. *Shock Waves*, 5:59–73, 1995. [18](#), [386](#)
- [104] H. Li and G. Ben-Dor. A parametric study of Mach reflection in steady flows. *J. Fluid Mechanics*, 341:101–125, 1997. [399](#)
- [105] Z. Liang, S. Browne, R. Deiterding, and Shepherd J. E. Detonation front structure and the competition for radicals. In *Proc. Combust. Inst.* 31, pages 2445–2453, 2007. [90](#)
- [106] M. Lombardini. *Richtmyer-Meshkov instability in converging geometries*. PhD thesis, California Institute of Technology, 2008. [28](#), [44](#), [45](#)
- [107] M. Lombardini and D. I. Pullin. Small-amplitude perturbations in the three-dimensional cylindrical Richtmyer-Meshkov instability. *Physics of Fluids*, 21, 2009. [29](#)
- [108] F. K. Lu and H. Fan. Numerical modelling of oblique shock and detonation waves induced in a wedged channel. In *Proceedings of the Institute of Mechanical Engineers*, 2006. [382](#)
- [109] F. K. Lu, H. Y. Fan, and D. R. Wilson. Comparison of detonation processes in a variable cross section chamber and a simple tube. *J. of Propulsion and Power*, 21, 2006. [382](#)
- [110] F. K. Lu, H. Y. Fan, and D. R. Wilson. Detonation waves induced by a confined wedge. *Aerospace Science and Technology*, 10, 2006. [382](#)
- [111] T. Lu, Y. Ju, and C. K. Law. Complex CSP for chemistry reduction and analysis. *Comb. Flame*. [8](#)
- [112] R. Maly. *Spark Ignition: Its Physics and Effect on the Internal Combustion Engine*, chapter 3. Springer, 1984. [310](#)
- [113] R. Maly and M. Vogel. Initiation and propagation of flame fronts in lean CH<sub>4</sub>-air mixtures by the three modes of the ignition spark. *Proceedings of the Combustion Institute*, 17:821–831, 1979. [310](#)
- [114] H. Mark. The interaction of a reflected shock wave with the boundary layer in a shock tube. *Ithica, NY, USA: Cornell University; 1958 Mar. NACA TM1418*, 1958. [3](#), [235](#), [239](#), [284](#), [288](#), [305](#)
- [115] M. P. Martin, E. M. Taylor, M. Wu, and V. G. Weirs. A bandwidth-optimized WENO scheme for the effective direct numerical simulation of compressible turbulence. *J. Comput. Physics*, 220:270–289, 2006. [29](#)
- [116] L. Massa, J. M. Austin, and T. L. Jackson. Triple-point shear layers in gaseous detonation waves. *J. Fluid Mech.*, 586:205–248, 2007. [10](#), [29](#), [91](#), [94](#), [96](#), [199](#)

- [117] G. Matheou, A. M. Bonanos, C. Pantano, and P. E. Dimotakis. Large-eddy simulation of mixing in a recirculating shear flow. *J. Fluid Mech.*, 646:375–414, 2010. [29](#)
- [118] J. Meltzer, J. E. Shepherd, E. Akbar, and A. Sabet. Mach reflection of detonation waves. In *Progress in Astronautics and Aeronautics*, AIAA, 153, 1993. [381](#)
- [119] C. A. Mouton. *Transition between regular reflection and Mach reflection in the dual-solution domain*. PhD in aeronautics, California Institute of Technology, 2006. [399](#)
- [120] S. Nakaya, K. Hatori, M. Tsue, M. Kono, D. Segawa, and T. Kadota. Numerical analysis on flame kernel in spark ignition methane/air mixtures. *J. Propul. and Power*, 27, 2011. [12](#), [308](#), [365](#)
- [121] S. Osher and S. Chakravarthy. High resolution schemes and the entropy condition. *SIAM J. Numer. Anal.*, 21:955–984, 1984. [39](#)
- [122] T. Pang. *An Introduction to Computational Physics*. Cambridge University Press, 1997. [46](#)
- [123] C. Pantano, R. Deiterding, D. J. Hill, and D. I. Pullin. A low numerical dissipation patch-based adaptive mesh refinement method for large-eddy simulation of compressible flows. *J. Comput. Phys.*, 221(1):63–87, 2006. [28](#), [29](#), [37](#), [38](#), [43](#)
- [124] E. L. Petersen and R. K. Hanson. Measurement of reflected-shock bifurcation over a wide range of gas composition and pressure. *Shock Waves*, 15:333–340, 2006. [3](#), [235](#), [236](#), [239](#)
- [125] M. V. Petrova and F. A. Williams. A small detailed chemical-kinetic mechanism for hydrocarbon combustion. *Comb. Flame*, 144:526–544, 2005. [8](#)
- [126] M. V. Petrova and F. A. Williams. A phenomenological model for hydrocarbon high-temperature autoignition. *Combust. Theory and Modeling*, 10:349–360, 2006. [8](#)
- [127] M. V. Petrova and F. A. Williams. Reduced chemistry for autoignition of C<sub>3</sub> hydrocarbons in air. *Combust. Sci. and Tech.*, 179:961–986, 2007. [8](#)
- [128] F. Pintgen, C. A. Eckett, J. M. Austin, J. E. Shepherd, and H. Hornung. Direct observations of reaction zone structure in propagating detonations. *Combustion and Flame*, 133(3):211–229, 2003. [90](#), [93](#)
- [129] S. Pirozzoli. Conservative hybrid compact-WENO schemes for shock-turbulence interaction. *J. Comput. Physics*, 178:81–117, 2002. [29](#)
- [130] A. Y. Poludnenko and E.S. Oran. The interaction of high-speed turbulence with flames: Global properties and internal flame structure. *Combustion and Flame*, 157:995–1011, 2010. [30](#)
- [131] J. M. Powers. Review of multiscale modeling of detonation. *J. of Propuls. and Power*, 22:6:1217–1229, 2006. [7](#), [95](#)
- [132] J. M. Powers and S. Paolucci. Accurate spatial resolution estimates for reactive supersonic flow with detailed chemistry. *AIAA*, 43, 2005. [7](#)
- [133] J. C. Prince, C. Trevino, and F. A. Williams. Reduced kinetic mechanism for high-

temperature propane ignition. *Int. J. Chem. Kinetics*. 8

- [134] M. I. Radulescu, G. J. Sharpe, C. K. Law, and J. H. S. Lee. The hydrodynamic structure of unstable cellular detonations. *J. Fluid Mech.*, 580:31–81, 2007. [90](#), [94](#)
- [135] M. I. Radulescu, G. J. Sharpe, C. K. Law, J. H. S. Lee, C. B. Kiyanda, A. J. Higgins, and R. K. Hanson. The ignition mechanism in irregular structure gaseous detonations. In *Proc. Combust. Inst.* 30, pages 1859–1867, 2005. [91](#), [94](#)
- [136] R. Reinmann and M. Akram. Temporal investigation of a fast spark discharge in chemically inert gases. *Journal of Physics D - Applied Physics*, 30:1125–1134, 1997. [12](#)
- [137] P. G. Saffman, M. J. Ablowitz, E. J. Hinch, J. R. Ockendon, and P. J. Olver. *Vortex Dynamics*. Cambridge University Press, 2006. [66](#)
- [138] S. Sanderson, J. Austin, Z. Liang, F. Pintgen, J. E. Shepherd, and H. Hornung. Reactant jetting in unstable detonation. *Progress in Aerospace Sciences*, 46(2-3):116–131, 2010. [90](#)
- [139] S. R. Sanderson, H. G. Hornung, and B. Sturtevant. Aspects of planar, oblique and interacting shock waves in an ideal dissociating gas. *Physics of Fluids*, 15, 2003. [381](#)
- [140] H. Schlichting and K. Gersten. *Boundary Layer Theory: 8th Edition*. Springer, 2003. [421](#)
- [141] E. Schultz and J. E. Shepherd. Detonation analysis using detailed reaction mechanisms. In *22nd International Symposium on Shock Waves, Imperial College, London, UK, July 18-23, 1999*. 8
- [142] J. E. Shepherd. Detonation in gases. In *Proc. Combust. Inst.* 32, pages 83–98, 2009. [1](#), [3](#), [7](#), [90](#)
- [143] J. E. Shepherd, G. A. Melhem, and P. Athens. Unconfined vapor cloud explosions: A new perspective. In *International Conference and Workshop on Modelling and Mitigating the Consequences of Accidental Releases of Hazardous Materials. CCPS of AIChE, New Orleans, 1991*. [235](#)
- [144] C. W. Shu. Essentially non-oscillatory and weighted essentially non-oscillatory schemes for hyperbolic conservation laws. Technical Report No. 97-65, Institute for Computer Applications in Science and Engineering NASA Langley Research Center, 1997. [31](#), [32](#), [34](#), [36](#)
- [145] S. Singh, D. Lieberman, and J. E. Shepherd. Combustion behind shock waves. In *Fall 2003 Western States Section/Combustion Institute*, 2003. [96](#)
- [146] S. Singh, J. M. Powers, and S. Paolucci. Detonation solutions from reactive NavierStokes equations. *AIAA Paper 99-0966*, 1999. [95](#)
- [147] S. Singh, Y. Rastigejev, S. Palolucci, and J. M. Powers. Viscous detonation in H<sub>2</sub>-O<sub>2</sub>-Ar using intrinsic low-dimensional manifolds and wavelet adaptive multilevel representation. *Combust. Theory Modelling*, 5, 2001. [95](#)
- [148] B. W. Skews and J. T. Ashworth. The physical nature of weak shock wave reflection. *J. Fluid*

*Mechanics*, 2005. [398](#)

- [149] A. Smits and J. Dussauge. *Turbulent Shear Layers in Supersonic Flow: 2nd Edition*. Springer, 2006. [423](#)
- [150] R. I. Soloukhin. Detonation waves in gases. *Soviet Physics Uspekhi*, 80:525–551, 1964. [382](#)
- [151] M. Thiele, S. Selle, U. Riedel J. Warnatz, and U. Maas. Numerical simulation of spark ignition including ionization. *Combustion Theory and Modelling*, 4:413–434, 2000. [12](#)
- [152] M. Thiele, J. Warnatz, A. Dreizler, S. Lindenmaier, R. Schießl, U. Maas, A. Grant, and P. Ewart. Spark ignited hydrogen/air mixtures: Two dimensional detailed modeling and laser based diagnostics. *Combustion and Flame*, 128:74–87, 2002. [12](#), [307](#), [365](#)
- [153] M. Thiele, J. Warnatz, and U. Maas. Geometrical study of spark ignition in two dimensions. *Combustion Theory and Modelling*, 4:413–434, 2000. [12](#), [309](#)
- [154] P. A. Thompson. *Compressible Fluid Dynamics*. New York: McGraw-Hill, 1972. [237](#)
- [155] B. Varatharajan, M. V. Petrova, F. A. Williams, and V. Tangirala. Two-step chemical-kinetic descriptions for hydrocarbon-oxygen-diluent ignition and detonation applications. In *Proceedings of the Combustion Institute*, volume 30, pages 1869–1877, 2005. [8](#)
- [156] J. von Neumann. Oblique reflection of shocks. Technical report, Bureau of Ordnance, 1943. [17](#)
- [157] R. Wang and R. J. Spiteri. Linear instability of the fifth-order weno method. *SIAM J. Numer. Anal.*, 45:1871–1901, 2007. [39](#)
- [158] G. Ward and D. I. Pullin. A hybrid, center-difference, limiter method for simulations of compressible multicomponent flows with Mie-Gruneisen equation of state. *J. Comput. Physics*, 229:2999–3018, 2010. [29](#)
- [159] J. S. Weber, E. S. Oran, J. P. Boris, and J. D. Anderson Jr. The numerical simulation of shock bifurcation near the end wall of a shock tube. *Phys. Fluids*, 7(10):2475–2488, 2006. [4](#), [235](#), [288](#), [306](#)
- [160] V. G. Weirs and G. V. Candler. Optimization of weighted ENO schemes for DNS of compressible turbulence. *AIAA*, 97-1940:1–11, 1997. [35](#), [36](#)
- [161] C. K. Westbrook. Chemical kinetics of hydrocarbon oxidation in gaseous detonations. *Combustion & Flame*, 46:191–210, 1982. [86](#)
- [162] F. M. White. *Viscous fluid flow*. New York: McGraw-Hill, 1974. [241](#)
- [163] J. Williamrich and C. Treanor. Vibrational relaxation in gas-dynamic flows. *Annual Reviews Journal*, 1970. [381](#)
- [164] F. A. Williams. *Combustion Theory*. Addison-Wesley, Reading, MA, 1985. [19](#), [20](#), [57](#)
- [165] T. Yuasa, S. Kadota, M. Tsue, M. Kono, H. Nomura, and Y. Ujiej. Effects of energy deposition

schedule on minimum ignition energy in spark ignition of methane/air mixtures. *Proceedings of the Combustion Institute*, 29:743–750, 2002. [12](#)

- [166] J. L. Ziegler, R. Deiterding, J. E. Shepherd, and D. I. Pullin. An adaptive high-order hybrid scheme for compressive, viscous flows with detailed chemistry. *J. Comput. Physics*, 230:7598–7630, 2011. [53](#)